



STUDY OF BIOCOMPATIBILITY OF NANOSTRUCTURED MATERIALS ON IN VITRO AND IN VIVO MODELS

Anna Barbara Orłowska

ADVERTIMENT. L'accés als continguts d'aquesta tesi doctoral i la seva utilització ha de respectar els drets de la persona autora. Pot ser utilitzada per a consulta o estudi personal, així com en activitats o materials d'investigació i docència en els termes establerts a l'art. 32 del Text Refós de la Llei de Propietat Intel·lectual (RDL 1/1996). Per altres utilitzacions es requereix l'autorització prèvia i expressa de la persona autora. En qualsevol cas, en la utilització dels seus continguts caldrà indicar de forma clara el nom i cognoms de la persona autora i el títol de la tesi doctoral. No s'autoritza la seva reproducció o altres formes d'explotació efectuades amb finalitats de lucre ni la seva comunicació pública des d'un lloc aliè al servei TDX. Tampoc s'autoritza la presentació del seu contingut en una finestra o marc aliè a TDX (framing). Aquesta reserva de drets afecta tant als continguts de la tesi com als seus resums i índexs.

ADVERTENCIA. El acceso a los contenidos de esta tesis doctoral y su utilización debe respetar los derechos de la persona autora. Puede ser utilizada para consulta o estudio personal, así como en actividades o materiales de investigación y docencia en los términos establecidos en el art. 32 del Texto Refundido de la Ley de Propiedad Intelectual (RDL 1/1996). Para otros usos se requiere la autorización previa y expresa de la persona autora. En cualquier caso, en la utilización de sus contenidos se deberá indicar de forma clara el nombre y apellidos de la persona autora y el título de la tesis doctoral. No se autoriza su reproducción u otras formas de explotación efectuadas con fines lucrativos ni su comunicación pública desde un sitio ajeno al servicio TDR. Tampoco se autoriza la presentación de su contenido en una ventana o marco ajeno a TDR (framing). Esta reserva de derechos afecta tanto al contenido de la tesis como a sus resúmenes e índices.

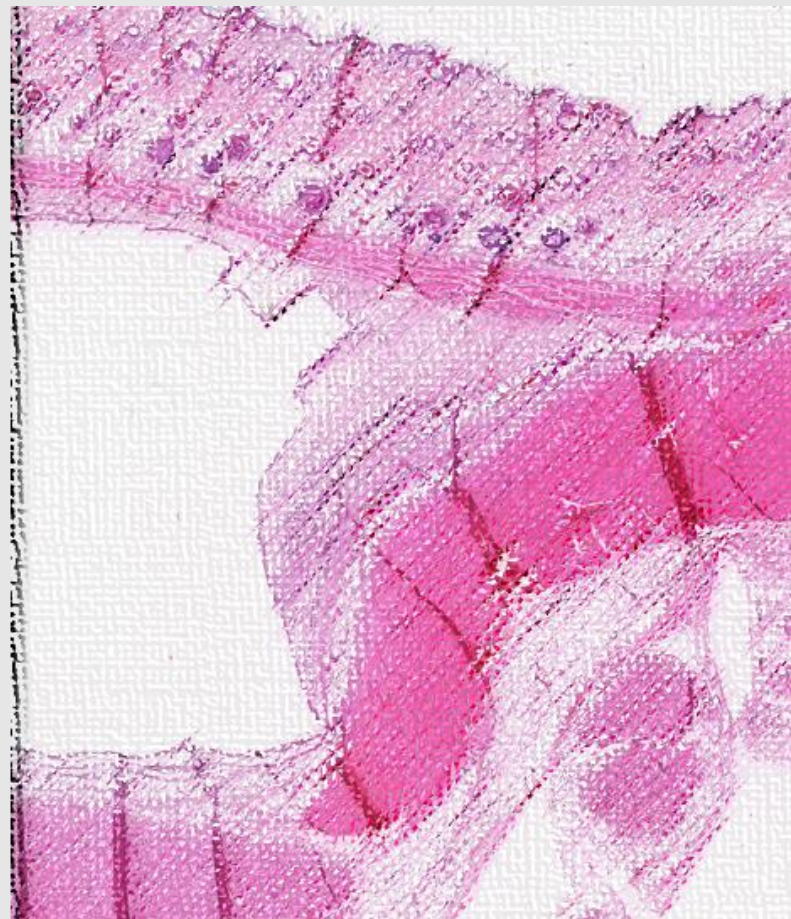
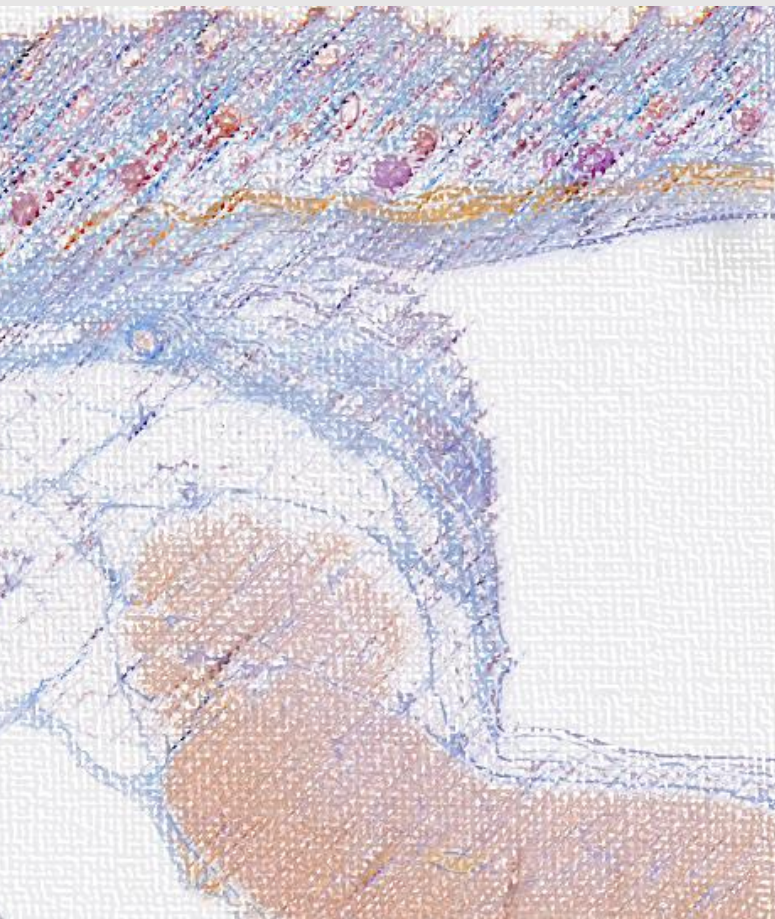
WARNING. Access to the contents of this doctoral thesis and its use must respect the rights of the author. It can be used for reference or private study, as well as research and learning activities or materials in the terms established by the 32nd article of the Spanish Consolidated Copyright Act (RDL 1/1996). Express and previous authorization of the author is required for any other uses. In any case, when using its content, full name of the author and title of the thesis must be clearly indicated. Reproduction or other forms of for profit use or public communication from outside TDX service is not allowed. Presentation of its content in a window or frame external to TDX (framing) is not authorized either. These rights affect both the content of the thesis and its abstracts and indexes.



UNIVERSITAT
ROVIRA i VIRGILI

Study of biocompatibility of nanostructured materials on *in vitro* and *in vivo* models

Anna Barbara Orłowska



DOCTORAL THESIS
2022

UNIVERSITAT ROVIRA I VIRGILI

STUDY OF BIOCOMPATIBILITY OF NANOSTRUCTURED MATERIALS ON IN VITRO AND IN VIVO MODELS

Anna Barbara Orłowska





Anna Barbara Orłowska

Study of biocompatibility of nanostructured materials on *in vitro* and *in vivo* models

Doctoral Thesis

Supervised by Dr. Vladimir A. Baulin

Departament de Química Física i Inorgànica



UNIVERSITAT
ROVIRA i VIRGILI

Tarragona, 2022



Departament de Química Física i Inorgànica

C/ Marcel·lí Domingo s/n, Edifici N4

43007 Tarragona

Tel.: +34 977 55 8675

Fax.: +34 977 55 9621

I STATE that the present study, entitled “Study of biocompatibility of nanostructured materials on *in vitro* and *in vivo* models”, presented by Anna Barbara Orłowska for the award of the degree of Doctor, has been carried out under my supervision at the Department d’Enginyeria Química and Departament de Química Física i Inorgànica of Universitat Rovira I Virgili.

Tarragona, May 17, 2022

Doctoral Thesis Supervisor/s



Dr. Vladimir A. Baulin

Acknowledgments

I would first and foremost like to express my sincerest gratitude to my advisor, Dr. Vladimir A. Baulin. His unending support during my Ph.D. studies and research, as well as his patience, motivation, and enthusiasm were integral in my development. His guidance helped me throughout the research and writing process of this thesis. I could not have asked for a better advisor and mentor during my Ph.D. studies.

I would also like to thank FP7-funded ITN-SNAL, which I have been a part of as an Early Stage Researcher and which has funded my Ph.D. The process has been a fantastic learning experience for me, which would not have been possible otherwise.

Moreover, I would also like to express my gratitude to Prof. Elena Ivanova, currently from RMIT, who has hosted me at Swinburne University and mentored me through my entire visit in Australia. As well as Dr. Shahram Ghanaati, from Frankfurt University Hospital, who I collaborated with during this Ph.D. in a very prosperous manner. I hope in future to find a possible way of working together.

Additionally, I would like to thank my co-worker, Dr. Andre Dias for many stimulating discussions, for the sleepless nights we were working together before deadlines, for all the fun we have had in the last years, and mostly for his friendship.

Finally, I would like to thank my family for all the support, especially my loving husband, Lukasz who helps me to go through the ups and downs in this tough journey of my PhD studies. Especially in this difficult coronavirus pandemic, his love and support give me a lot of strength and courage. Without you none of those things would be possible.

Summary

Biomaterials play a substantial role in the health care industry. Each year, the number of medical devices used in humans is estimated to be around 1.5 million individual devices, according to the World Health Organization, with about 10 000 types of generic device groups available worldwide. As new devices emerge, the topic of the biocompatibility of these materials becomes more relevant.

This thesis studies biocompatibility of biomaterials and their interaction with tissues and cells combining *in vitro* and *in vivo* models. The studied biomaterials are classified in synthetic (polymers, silicon, titanium, and alloys) and nature-derived biomaterials, which in turn, classify in xenogenic, derived from natural materials but foreign for the organism and autologous biomaterials, derived from the tissues of the same organism.

In the case of synthetic materials, it was shown how different functionalization strategies of surfaces (in particular, the effect of protein coating and surface topography) affect mammalian cell response. Autologous biomaterials were represented by platelet rich fibrin (PRF), derived from the blood of the patient. Their potential as implantable system was studied *in vitro* and *in vivo*. PRF matrixes were characterized by growth factors storage capacity and release as well as their cellular retention. In regard to xenogenic biomaterials, cell permeation and liquid absorption into different collagen membranes were studied *in vitro*, while evaluation of the host's tissue response was studied with *in vivo* implantation model. Results show that all tested collagen membranes were biocompatible, showcasing the formation of new blood vessels regardless of the presence of multinucleated giant cells.

Contents

1. Introduction	3
1.1. Types of biomaterials	3
1.2. Historical background of biomaterials	5
1.3. Nanoscaling of biomaterials	8
1.4. Functionalization of biomaterials.....	12
1.5. Application of biomaterials in medicine.....	13
1.6. Biocompatibility of Biomaterials	15
1.7. Evaluation methods of biocompatibility	23
1.7.1. <i>In vitro</i> models	26
1.7.2. <i>In vivo</i> models	29
1.8. Goals and research overview	36
1.9. References.....	37
2. Study of biocompatibility of synthetic biomaterials.....	46
2.1. Adsorption of Human Plasma Albumin and Fibronectin onto Nanostructured Black Silicon Surfaces.....	48
2.2. The Effect of Coatings and Nerve Growth Factor on Attachment and Differentiation of Pheochromocytoma Cells	70
2.3. Race for the Surface: Eukaryotic Cells Can Win	85
2.4. Pheochromocytoma (PC12) Cell Response on Mechanobactericidal Titanium Surfaces.....	110
2.5. Synthetic biomaterials conclusions	129
3. Study of biocompatibility of nature-derived biomaterials	132
3.1. The case of autologous materials.....	132
3.1.1. Reduction of relative centrifugal forces increases growth factor release within solid platelet-rich-fibrin (PRF)-based matrices: a proof of concept of LSCC (low speed centrifugation concept).....	134
3.1.2. Reduction of the relative centrifugal force influences cell number and growth factor release within injectable PRF-based matrices	157

3.1.3. A low-speed centrifugation concept leads to cell accumulation and vascularization of solid plateletrich fibrin: an experimental study <i>in vivo</i>	177
3.1.4. Autogenous biomaterials conclusions.....	204
3.2. The case of xenogenic materials	207
3.2.1. Biologization of Collagen-Based Biomaterials Using Liquid-Platelet-Rich Fibrin: New Insights into Clinically Applicable Tissue Engineering.....	210
3.2.2. Sugar-based collagen membrane cross-linking increases barrier capacity of membranes	233
3.2.3. <i>In vivo</i> Implantation of a Bovine-Derived Collagen Membrane Leads to Changes in the Physiological Cellular Pattern of Wound Healing by the Induction of Multinucleated Giant Cells: An Adverse Reaction?.....	257
3.2.4. Multinucleated giant cells within the <i>in vivo</i> implantation bed of a collagen-based biomaterial determine its degradation pattern.....	282
3.2.5. Xenogenic biomaterial conclusions	309
4. Study of biocompatibility of PP-13	312
4.1. The pyrrolopyrimidine colchicine-binding site agent PP-13 reduces the metastatic dissemination of invasive cancer cells <i>in vitro</i> and <i>in vivo</i>	312

1. Introduction

Biomaterials are a substantial part of the health care industry. Each year, the number of medical devices used in humans is estimated to be around 1.5 million individual devices, according to the World Health Organization, with about 10 000 types of generic device groups available worldwide. Furthermore, the use of biomaterials is steadily growing, by integrating the knowledge and ideas from multiple disciplines, such as medicine, biology, chemistry, physics, material and engineering sciences.¹ A biomaterial is any material that is intended to interact with biological systems for a medical purpose – either to support or replace damaged tissue, or to function as a medical device.^{2,3}

1.1. Types of biomaterials

There are many different types of biomaterials, each with their own unique properties and applications. The three main categories of biomaterials are: (1) nature-derived (*e.g.*, plant-derived, tissue-derived), (2) synthetic (*e.g.*, metals, polymers, ceramics, and composites) and (3) semi-synthetic or hybrid (Figure 1).^{1,4}

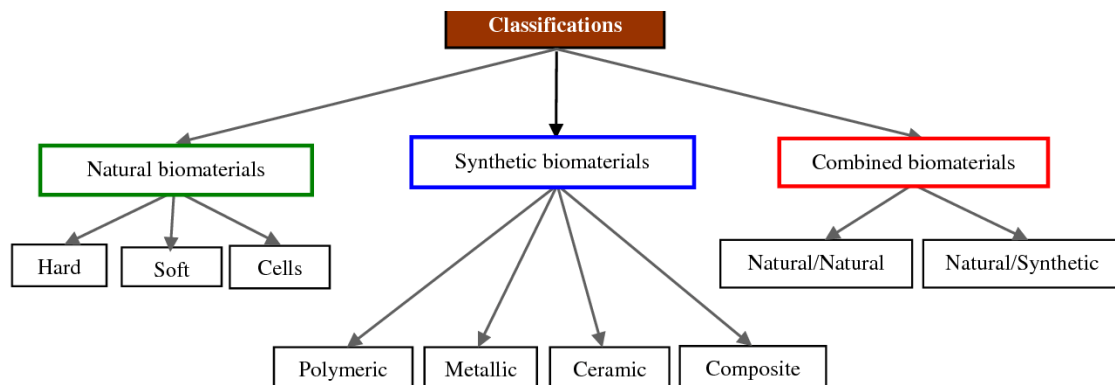


Figure 1. Classification tree of biomaterials. Reprinted from Ali *et al*, 2013.⁴

Natural biomaterials originate from living organisms, such as plants, animals (xenogenic) and humans (allogenic/autogenous) - or their derivatives. Examples include proteins (silk, collagen, elastin, fibrin), polysaccharides (chitin, glycosaminoglycans), and polynucleotides (DNA, RNA).¹ They might be present in the non-viable form of decellularized extracellular matrix (ECM) and other products, or in the form of allogenic or autologous viable living cells. These materials are often used in reconstructive, reparative and regenerative medicine due to their

ability to integrate with the body, as it can recognize the material and process it through its metabolic pathways due to material similarity to native tissue. The significant challenge with natural polymers is that they may denature or decompose at relatively low temperatures, thus making their processing and sterilization challenging.⁵

Synthetic biomaterials can be divided into the following types: metals, polymers, ceramics and composites.^{1,6} Regarding metals, titanium and stainless steel the most employed in orthopedic (wires, plates, screws) and dental implants, due to their strength, load-bearing capability and body compatibility.^{7,8} Ceramics, such as hydroxyapatite, are often used in bone replacement and regeneration thanks to their similar chemical and physical properties to natural bone. Also, in powder form, they can be applied in conjunction with polymers to fill cavities, as cements in dental applications.⁹ Polymers, including polyurethanes and polyethylenes, are commonly seen in artificial joints, vascular grafts, and drug delivery devices due to their flexibility and biocompatibility.^{5,6} Composites, which are made from a combination of two or more different materials (*e.g.* natural and synthetic), are frequently present in prosthetic devices and tissue engineering scaffolds, as they can mimic the mechanical properties of the natural tissues. Examples include carbon fiber and metal matrix composites.^{1,5}

Each type of biomaterial has its own advantages and disadvantages. For example, metals are strong and durable, but they can be difficult to shape and they can cause inflammation at the implant site. Ceramics are also strong and durable, but they are brittle and can fracture if they are not designed properly. Polymers are relatively easy to shape and are biocompatible, but they can degrade over time. Composites have the advantage of being customizable to the specific needs of the application, but they can be more difficult to work with. As such, the choice of biomaterial for a particular application depends on a variety of factors, including the intended function of the device, the mechanical properties required, the chemical compatibility with the body, and the manufacturing process. In general, the ideal biomaterial for a given application should include all of the following features: be biocompatible, strong, durable, and easy to work with.^{3,10}

1.2. Historical background of biomaterials

In 1982, at the "National Institutes of Health Consensus Development Conference Statement on the Clinical Applications of Biomaterials" held in Bethesda, Maryland, a widely accepted definition of biomaterials was formulated for the first time.

*"A substance (other than a drug) or combination of substances, synthetic or natural in origin, which can be used for any period of time, as a whole or as a part of a system which treats, augments, or replaces any tissue, organ, or function of the body"*¹¹

However, the history of biomaterials can be traced back to the early days of medicine, when simple materials such as wood, metal and stone were used to treat injuries and diseases.¹¹ Over time, more sophisticated materials such as glass, ceramic and plastic were developed, and these have been used in a variety of medical applications (Figure 2).³ Together with industrial revolution, major development in biomaterials could be observed as scientists and doctors started to realize that biocompatibility of materials was a key factor in the success of using materials within a biological system.

Among the most profound advancements in the biomaterial field, was the technique for bone fracture fixation with metal wire, presented in 1775. In the mid-1800, comparative study into the biocompatibility of metal implants (gold, silver, lead, and platinum) and bone fixation plates in dogs was performed. Additionally, huge impact had an introduction of sterilization techniques by Joseph Lister; the discovery of first antibiotic, penicillin G, by Alexander Fleming; and the isolation of 99.9% pure titanium by Matthew Hunter - all leading towards the development of material science field (Table 1).^{1,10}

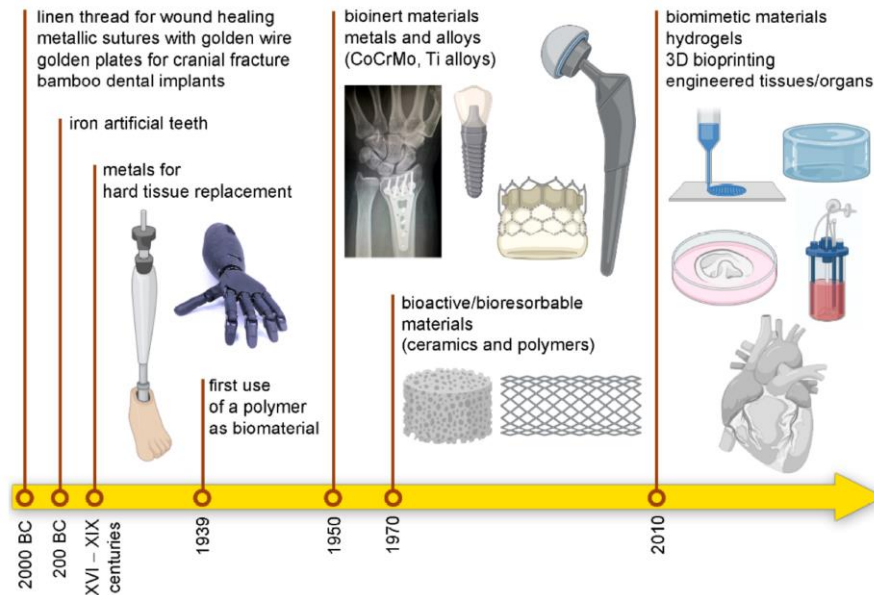


Figure 2. The history of the biomaterials from regeneration to replacement. Reprinted from Todros *et al*, 2021.³

Today, biomaterials are an essential part of modern medicine. They are used in a wide range of medical applications, from artificial hips^{13,14} and knees¹⁵ to pacemakers¹⁶ and stents¹⁷.

The future of biomaterials is likely to be even more exciting as new materials and technologies are developed. For example, 3D printing is being used to create customized biomaterials for use in medical implants, and nanotechnology is being used to create materials with unique properties that could be applied in a variety of medical applications.^{18,19} Biomaterials have been an essential part of medicine for many years and will continue to play an important role in the future of healthcare.

Table 1. Important event in the history of biomaterials. Adapted from Kulintes, 2015.¹

Year	Event
1775	Doctors Lapuyade and Sicre from Toulouse presented the earliest technique for bone fracture fixation with metal wire.
1829	Comparative study of biocompatibility of metal (gold, silver, lead and platinum) implants and bone fixation plates in dogs by H. S. Levert.
1860	Aseptic surgical technique is introduced by Joseph Lister, a British Surgeon.
1870	Lister's antiseptic Lister's methods of infection control and aseptic surgical techniques were used by Germany during the Franco-Prussian war.
1888	Adolf Flick developed first glass contact lens.
1886	H. Hansmann in Hamburg, Germany, was the first surgeon to use plates for internal bone fixation in human. The metal plate was L-shaped with six screw holes.
1910	Isolation of 99.9% pure titanium by Matthew Hunter.
1930	Introduction of new biomaterials suitable for orthopaedic applications, such as stainless steel, titanium, and cobalt chromium alloys.
1931	Smith Peterson, a Boston surgeon, introduced a metal cup for partial hip replacement.
1938	P. Wiles develops the concept of total hip prosthesis.
1939-45	Development of many new materials and surgical techniques for implants, including materials made mostly of metals and a few from plastic.
1940	Polymers became available as biomaterials. Polymethyl methacrylate (PMMA) was introduced for bone defect repair; cellulose was introduced as a filtration material for dialysis; nylon strings were used as sutures.
1947	Ingraham published a first paper related to polyethylene as an implant material.
1949	Ingraham commented on plastics leaching ('sweating out') additives, resulting in a strong (negative) biological reaction to some plastics, such as cellophane, lucite, and nylon, and mild reaction to 'new plastics' such as teflon.
1952	The mechanical heart valve was first conceived, made from metals and polymers.
1953	Vascular graft prostheses were made from Dacron (polymer fiber).
1958	A combination of polymers and metals was utilized in the first cemented (PMMA) joint replacement.
1960	Introduction of first heart valves in a clinical setting.
1962	Passage of Food and Drug Act and Consumer Bill of Rights.
1970	Development of protein resistant thin films to be used as coatings for implants, such as polyethylene oxide (PEO).
1976	Amendment to Food and Drug Act and subsequent FDA regulations outlining requirements to testing and production of medical devices.
1982	A widely accepted definition of biomaterials was formulated at the "National Institutes of Health Consensus Development Conference Statement on the Clinical Applications of Biomaterials" held in Maryland,

1.3. Nanoscaling of biomaterials

As the world progresses, so does the technology used to create various materials. In the past, biomaterials were limited to those that could be produced through traditional means. However, with the advent of nanotechnology (the ability to manipulate structures having dimensions from 1–1000 nanometres), biomaterials can now be created on a much smaller scale.²⁰ This has led to the development of new and improved biomaterials that has far greater properties based on nanoscale systems. They can be stronger, more durable, resilient than ever before, because of their ultra-small size, large surface area and large surface to volume ratio (Figure 3).²¹

The use of nanotechnology in medicine, also known as nanomedicine, has created a multitude of possibilities in healthcare, including: disease diagnosis,²² drug, gene and vaccine delivery;²³⁻²⁵ *in vivo* imaging,^{26,27} tissue engineering and regenerative medicine.^{28,29} Nanomaterials have been utilized in many therapies, such as cancer, diabetes, infection and inflammation treatment.^{30,31} Recently, widespread public awareness was achieved by use of nanomaterials in medicine as a bearer framework in m-RNA based Covid-19 vaccines.^{32,33}

As previously mentioned, one of the most significant advantages of nanoscaling biomaterials is that it allows for the creation of materials with unique properties. For example, nanowires can be used to create materials that are both electrically conductive and biocompatible. This is a major breakthrough, as it opens up the possibility for the development of new medical devices that can be used safely in the body.³⁴ Carbon nanotubes have also been investigated as potential drug delivery vehicles because they can target specific cells and release their payloads directly into them.³⁵ Silicone or titanium surfaces with high aspect-ratio nanofeatures generate a mechanical bactericidal effect, independent of its chemical composition. Both of these surfaces pose highly bactericidal features against all tested Gram-negative and Gram-positive bacteria, and endospores, and exhibit estimated average killing rates of up to $\sim 450,000$ cells $\text{min}^{-1} \text{cm}^{-2}$, which allows the fabrication of materials with antibacterial surfaces.³⁶

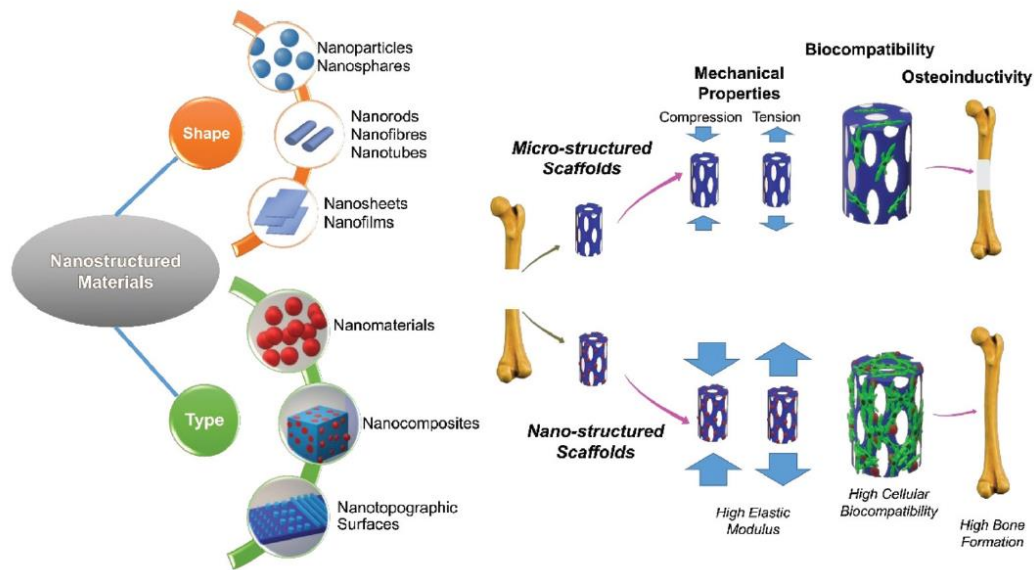


Figure 3. Different shape and type of nanostructured materials and application of nanotechnology in the improvement of 3 main properties of tissue engineering scaffolds including mechanical properties, biocompatibility, and osteoinductivity. Reprinted from Hajiali *et al*, 2021.²¹

Finally, introducing nanoscale level features to biomaterials can also help to improve their biocompatibility. This is because smaller particles are less likely to cause an immune reaction in the body.^{30,37} This is extremely important for medical applications, where biomaterials are often required to be in close contact with the body. The impact of topographical features at length scales ranging from nano- to micrometres on cell adhesion and morphology has been shown to be significant. It has been discussed in the literature that there could be an optimum size range in which cell adhesion would be most significantly enhanced but this is dependent on cell type.³⁷⁻⁴⁰

Furthermore, it has been recently reported, by several groups, that the outcome of cell adhesion influences cell migration, proliferation and differentiation processes, which are main steps of tissue re-organization in wound healing (Figure 4).⁴¹⁻⁴³ The results of studies conducted to investigate the biocompatibility of nanomaterials and nanocomposites are summarized in (Table 2).

Overall, the nanoscaling of biomaterials is a major breakthrough that has led to the development of new and improved materials. This has had a major impact in the medical field, where stronger and more biocompatible materials are now available.

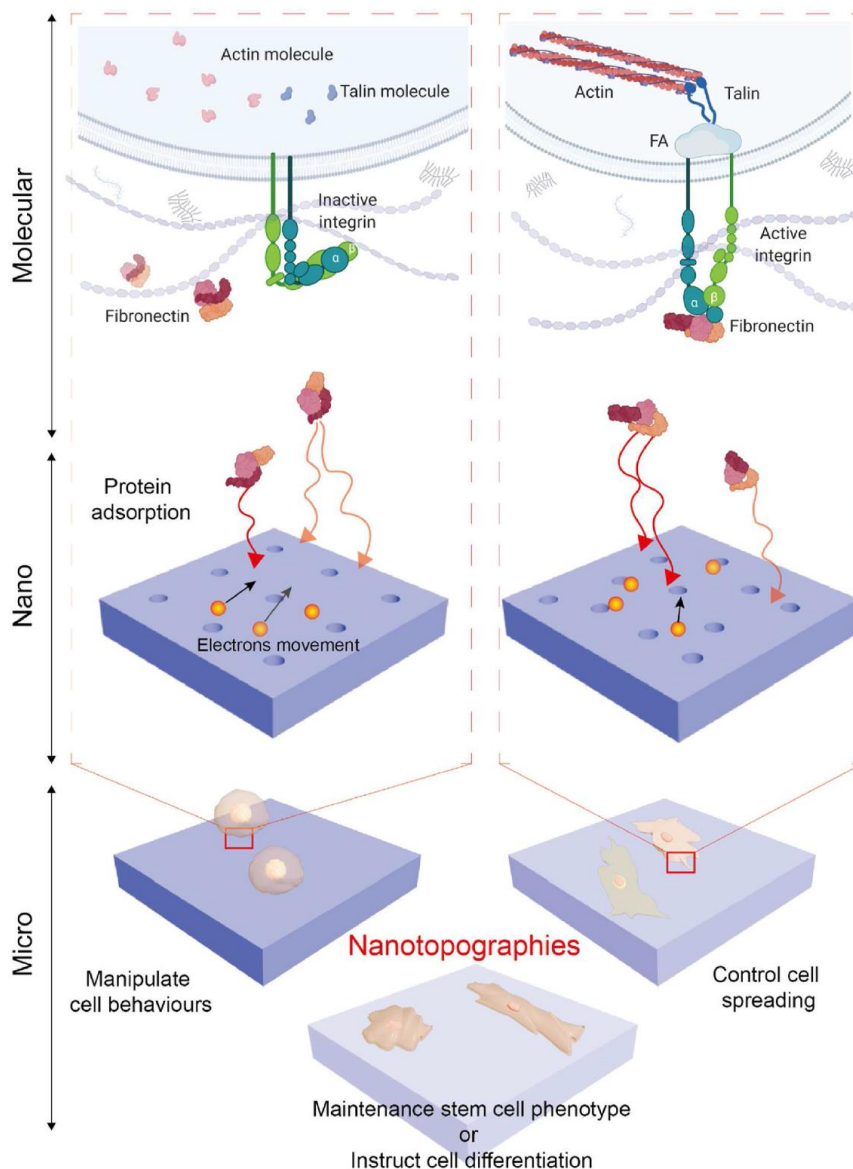


Figure 4. Schematic demonstrating influence of nanotopography on cell behaviour through interaction with extracellular matrix. Cellular behaviours under microscale such as adhesion, spreading and differentiation are influenced by fibronectin interacts with on nanotopography surface electrons and adsorption under nanoscale. Transmembrane receptors like integrins can further interact to fibronectin adsorbed on nanotopography, then behave active or inactive. Upon ligand bonding, the focal adhesions (FAs) are assembled and cytoskeletal filaments are aggregated by actin and talin molecules. Reprinted from Luo *et al*, 2022.⁴⁰

Table 2. Summary of recent studies that assess the biocompatibility of nanostructures for bone regeneration. Adapted from Hajjali *et al*, 2021.

Nanomaterials	Cell type	Tests	Results
Nanoapatite	MC3T3-E1 osteoblast-like cells	Cell viability with calcein-AM, ethidium-homodimer-1	No significant difference in cell attachment and proliferation between nanoapatite scaffolds and controls. Cells infiltrate into the macro pores and anchor to the nano-apatite crystals
Nanobioglass (nBG)	MG63 osteoblast-like cells	LDH and mitochondrial activity, alkaline phosphatase (ALP) activity	High cytocompatibility of the nBG particles compared with micro-BG
Nano fluorhydroxyapatite	Extracted osteoblast-like cells from adult rabbit, L929 mouse fibroblast cell line	Haemocytometer	Biocompatibility of fluorhydroxyapatite was higher than hydroxyapatite and fluorapatite
Gold nanoparticles-miRNA	Rat BMSCs	Alamar blue as say, ALP activity	High cellular biocompatibility of nanoparticles
Whitlockite inorganic nanoparticles nWH: Ca18Mg2(HPO4)2(PO4)12)	Human tonsil-derived mesenchymal stem cells (hTMSCs)	LIVE/DEAD cell viability kit, click-iT EdU, flow cytometry assay, ALP activity	No significant difference in cell viability and proliferation between hydroxyapatite and WH nanoparticles. Significantly enhanced ALP activity in nWH compared to nHAP
Nanohydroxyapatite silk fibroin	Rat marrow mesenchymal cells	DNA contents, alkaline phosphatase (ALP) activity, the osteocalcin contents	Support cell proliferation, and osteogenic differentiation of the cells
Poly(3-hydroxybutyrate)/nBG scaffolds	MG63 osteoblast-like cells	MTT assay, ALP activity	Improve cell proliferation, and induce a high level of ALP activity
Poly(3-hydroxybutyrate)/nHA nanofibers	Rat bone marrow stroma cells	Methylthiazol tetrazolium (MTT) assay, ALP activity	Positive effect on attachment, proliferation, and differentiation of cells
Gelatin methacrylate/nanosilicates (LAPONITE®) hydrogels	MC3T3 E1-4	Alamar blue assay, ALP activity	Nanocomposites are cytocompatible, enhanced ALP activity
Whitlockite/chitosan scaffolds	Human bone derived mesenchymal stem cells (hBMSCs)	Cell counting Kit-8 [CCK-8], ALP activity	Greatest proliferation and significantly higher ALP activity when cells cultured on WH/chitosan membranes compared to HAP/chitosan membranes and control

1.4. Functionalization of biomaterials

The functionalization of biomaterials is a process by which the materials are modified to perform a specific function, for instance: cell adhesion, neovascularization, cell proliferation and differentiation.

The functionalization of biomaterials can be achieved by a variety of modifications:

- **Physical** – topographies with different features (nanorough glass,⁴⁴ nanopillar titanium,^{45,46} nanoholes silicon,⁴⁷ nanogrooves PDMS⁴⁸) and arrangements (e.g. nanopits-ordered/disordered PCL,⁴⁹ ordered/disordered gold nanoparticles combined with PEG substrate⁵⁰)
- **Chemical** – incorporation or modification (oxidation,⁵¹ reduction⁵²) of existing functional groups (acetylation,⁵³ fluorination,⁵⁴ silanization,⁵⁵ incorporation of sulfonate groups⁵⁶) or the addition of nanoparticles,⁵⁷ grafting macromolecules (e.g. polyethylene glycol)⁵⁸, plasma treatment with reactive gases (O₂)⁵⁹, UV radiation treatment⁶⁰ and polymeric cross-linking⁶¹
- **Biological** – covalent and non-covalent biomolecules immobilization,^{63,63} heparin coating,⁶⁴ natural ECM protein coating,⁶⁵ addition of peptide sequences,⁶⁶ growth factor augmentation⁶⁷

The functionalization of biomaterials is a critical step in the development of new materials, as well as improving existing ones. The process can enhance their biocompatibility, increase durability, and enable additional characteristics, as for instance control of bacterial biofilm formation and surgical site infection (SSI) prevention.

Since SSI is a serious complication and can delay healing, increase the risk of re-operation, and lead to prolonged hospitalization, numerous approaches aiming to reduce SSI and secondary infections are in the centre of functionalization focus in material science. Frequent approach is to incorporate antimicrobial agents (*e.g.*, methicillin, vancomycin, amoxicillin), which can kill or inhibit the growth of the bacteria.⁶⁸ However, nowadays antimicrobial resistance (AMR) is an increasing problem, which prompted development of another strategies, such as: antifouling coatings,⁶⁹⁻⁷² antiadhesive surface modifications,⁷³ addition of metal oxide nanoparticles and ammonium compounds to the surfaces of medical devices,^{74,75} coating devices with polymer products,⁷⁶ surface engineering with chemical fragments,⁷⁷⁻⁷⁹ coating, lamination, adsorption, or immobilization of biomolecules⁸⁰ and engineering of different microtopographic and nanotopographic structures (black silicone, nanostructured titanium).

1.5. Application of biomaterials in medicine

As mentioned above, biomaterials are designed to interact with biological systems. They can be used in a variety of medical applications, from replacing damaged tissue to delivering drugs, and several fields of medicine can benefit from them.

Orthopedics

Biomaterials have found significant use in orthopedic implant devices. Autoimmune and inflammatory diseases such as osteoarthritis and rheumatoid arthritis can both damage the structure of synovial joints, inhibiting their function. These articulations include hip, knee, shoulder, ankle, and elbow. In the case of joints, pain can be quite intense, especially in weight-bearing joints such as hip and knee, which can have devastating effects on the ability to walk. Only recently, with the inception of anaesthesia, antisepsis, and antibiotics during surgical procedures, has it become possible to replace joints with prostheses while still providing relief of pain and improving mobility for countless number of patients. In terms of fractures, fixation devices are vital for proper healing. This category of devices includes bone plates, screws, nails, rods, wires, and other similar items. Traditionally, metals have been used for fracture fixation due to their strength and durability. However, some non-metallic materials (e.g. carbon-carbon composite bone plates) are being investigated as possible substitutes.^{7,81-85}

Cardiovascular applications

Implant devices are also used to treat cardiovascular issues. The circulatory system comprises the heart and blood vessels which transport blood around the body. Problems with heart valves or arteries can occur, and both can be remedied by implants. The heart valves can become structurally changed, preventing the valve from either opening or closing all the way. This can be replaced with a number of substitutes. Atherosclerosis, or the build-up of fatty deposits, is also a common problem affecting arteries. In some cases, it is possible to replace blocked segments of arteries with artificial arteries. This is often performed in cases involving the coronary arteries or the vessels of the lower limbs.⁸⁶⁻⁹¹

Ophthalmics

Several diseases can affect vision and ultimately lead to blindness due to eye tissue damage. One of such diseases is cataracts, which causes the lens to develop cloudy patches. In such cases, the lens may be replaced with a synthetic (polymer) intraocular lens. Such surgeries

have a high successful rate in improving eyesight. Contact lenses are also considered biomaterials, as they have direct contact with sensitive eye tissue. Like intraocular lenses, they can be used for vision correction and restoration.⁹¹⁻⁹⁵

Dental Applications

Bacterial diseases can destroy both teeth and gum tissues in the mouth. For instance, dental caries (cavities) demineralizes and dissolve teeth due to metabolic activity in a plaque (a film of bacteria-trapping mucus on teeth surfaces). Extensive tooth loss can occur as a result. There are various materials that can be used to replace or restore teeth, either in their entirety or in segments.⁹⁶⁻¹⁰²

Wound healing

The number of chronic wounds is rising as our population ages and more people develop diabetes. With a greater understanding of the biological processes involved in these diseases, new medical technologies are being introduced into the wound care market. Treatment of chronic wounds typically varies depending on the underlying cause of the wound. Therefore, semi-occlusive or occlusive specialized dressing materials are required. They can be produced in various forms: films, foams, hydrogels, or hydrocolloids and are usually fabricated from synthetic materials, like poly(vinyl) alcohol (PVA), poly(lactic-co-glycolic acid) (PLGA), polyurethanes, polyethylene glycol (PEG), polycaprolactone (PCL), nylon, or silicone. In terms of wound closure, modern synthetic suture materials can be made from polymers or metals, with the former being the most common.¹⁰³⁻¹⁰⁷

Drug delivery systems

Implantable devices for controlled and targeted drug delivery are becoming increasingly popular. Many of these technologies make use of new polymeric materials to act as drug reservoirs, allowing for sustained and controlled release. For example, non-biodegradable polymeric implantable systems are commonly used as a contraception method or menopausal symptom prevention by long lasting slow and controlled hormone release.¹⁰⁸⁻¹¹¹

1.6. Biocompatibility of Biomaterials

The human body is constantly exposed to foreign materials, whether through the air we breathe, the food we eat, or the water we drink. In most cases, the body is able to recognize foreign materials and mount an appropriate response to eliminate them. When foreign materials are introduced into the body as medical devices (e.g. implants), the body may react to them in numerous ways. The type of response depends on the material itself, as well as the location of the implant and the individual response of the host^{113,115}

Biocompatibility is a major concern in the development of new biomaterials and the use of existing ones. The degree to which a biomaterial is compatible with its host is determined by how much the host's homeostasis is disrupted during implantation surgery, and which pathological consequences may arise from the ensuing inflammatory response, wound healing process, and reaction to the foreign body itself.¹¹⁶ Once the foreign object (*i.e.* biomaterial) is introduced into the body, it triggers a physiological sequence of events, starting from the surgical injury to the host tissue: blood proteins adsorption and provisional matrix formation, acute and subsequently chronic inflammation, granulation tissue formation, foreign body reaction and possible fibrous encapsulation (Figure 5). All these reactions may differ in severity and occurrence, depending on the biomaterial.¹¹⁷

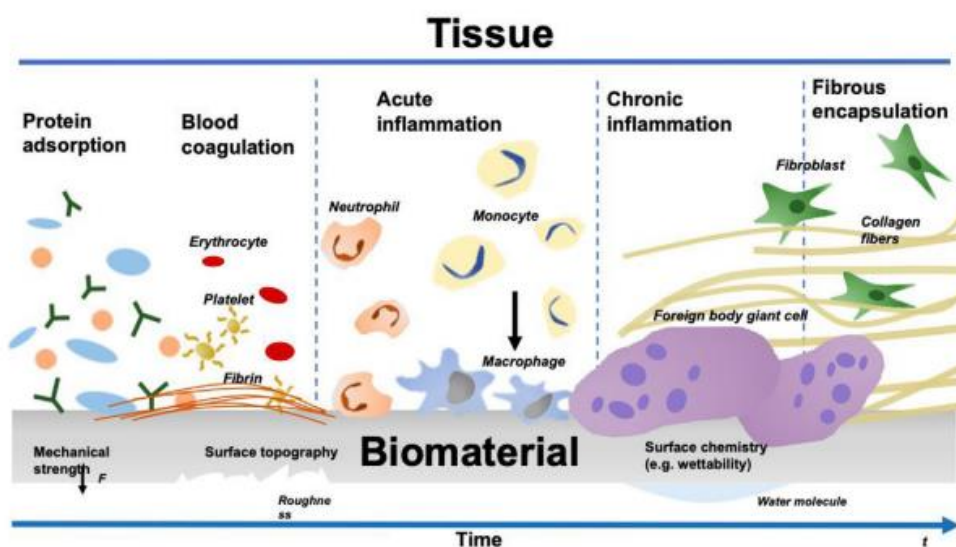


Figure 5. Schematic representation of foreign body response of host tissue to implanted biomaterials. In addition to biological and biochemical responses, biomaterials experience physical (e.g., mechanical, dynamic, topography), and temporal effects (e.g., change of interaction over time, degradation), indicating the interplay of factors that could influence biocompatibility of a biomaterial. Reprinted from Raut *et al*, 2020¹¹⁷

Protein adsorption

Protein adsorption to materials surfaces is a complex phenomenon. The term refers to accumulation and adhesion of plasma proteins to a surface but without surface penetration. It has been described that there are more than 300 different protein types in blood plasma,¹¹⁸ and the type and amount of adsorbed proteins on a surface play an important role in determining the material's ultimate biocompatibility and biofunctionality when exposed to a biological environment.¹¹⁹ This process is one of the first interactions and begins mere seconds after blood plasma components comes into contact with a foreign surface. The initial contact sets off all subsequent interactions between the host tissue and the biomaterial surface. Cell-biomaterial interactions are mediated by the type and conformation of the adsorbed proteins that can interact with specific integrins which are expressed by the cells on their membranes (integrins $\beta 1$ and 2 on macrophages). These host components include leukocytes involved in inflammation and immunity (Table 3).¹¹³

Table 3. Selected protein – cell interactions. Reprinted from Tengvall, 2011.¹¹⁴

<i>Protein</i>	<i>Major function</i>	<i>Cell receptor</i>	<i>Cell type</i>
Serum albumin	Body transport and clearance protein, binds to certain cell surfaces ('passivates'), maintains the osmotic balance	gp30 and gp18	Endothelial, hepatocytes?
Fibrinogen (Fib)	Forms fibrin during blood coagulation	CD11b,c, CD41a, CD51, CD61	Platelet, endothelial, myeloid, NK, osteoclast, tumor
Fibronectin (FNT)	Extracellular matrix protein that binds cells via RGD-sequence	CD49c, d, e, CD41a, CD61	Platelet, B lymphocyte, monocyte, fibroblast, epithelial, keratinocyte, tumor
Immunoglobulin G (IgG)	Opsonizes a nonself cell surface, activates complement	Fc	PMN, macrophage
High molecular weight kininogen (HMWK)	Component of the intrinsic pathway of coagulation, binds to negatively charged surfaces	$\beta 1$ and $\beta 2$ receptors	Endothelium, platelets and neutrophils, monocytes, macrophages
Complement factor 1q (C1q)	Binds to IgG and IgM and initiates classical complement activation, related to collagen activation of platelets	cC1q-RI, C1q-Rq, gC1q-R	B lymphocyte, T lymphocyte, monocyte/macrophage, PMN, eosinophil, platelet, fibroblast, endothelial, epithelial, smooth muscle, mesengial
Complement factor 3b (C3b) and C4b	Key adsorbed complement proteins, formed by cleavage of C3 to C3a and C3b, C4 to C4a and C4b	CR1(CD35)	Erythrocyte, phagocyte, B lymphocyte, T lymphocyte, eosinophil
Complement factor 3dg/3d (C3dg,C3d)	Surface-bound complement peptide after proteolytic cleavage of C3b, opsonin	CR2(CD21)	B lymphocyte, T lymphocyte
Complement factor 3bi (C3bi)	Inactivated C3b	CR3 (CD11b and CD18) and CR4 (CD11c)	Monocytes, macrophages, PMNL dendritic cells, myeloid cells, NK, B cells, T cell subset

There are two main factors that affect protein adsorption such as surface affinity of the protein and its concentration. In general, the surface affinity of the protein stands for how energetically favourable it is for the protein to be adsorbed to a surface. Protein surface affinity can be affected by the size of the protein (the larger the protein the more contact area it has), the charge (protein can be attracted or repelled), hydrophobicity (more hydrophobic proteins tend to adsorb to the surface in greater amount) and also structural stability (the lower the stability, the more contact points possible when unfolding). In terms of concentration, the higher

the protein concentration, the more likely contact with the surface is, and the higher the probability of interaction.¹²⁰

In case of biomaterials and protein surface attachment, it is important to mention the Vroman effect, also described as protein displacement phenomena. It is a competitive deposition of protein onto a surface of high molecular weight proteins, in which albumin, immunoglobulins, fibrinogen, factor XII (Hageman factor) and high molecular weight kininogen (HMWK) are subsequently adsorbed onto the membrane surface, one replacing the other (Figure 6). In the early phase of the plasma adsorption, HSA adsorbs first due to the high concentration in blood plasma, relatively flexible structure and low molecular weight. The adsorbed proteins cause modification of electrodynamic conditions on the material surface and are eventually replaced by other proteins with higher surface affinity but lower bulk concentration. The adsorption process can take a very long time, and in many cases might be irreversible.¹¹⁴ This distinction is important to mention specifically for practical applications, especially in cardiovascular implant where protein adsorption to such extent is not desired.¹²²

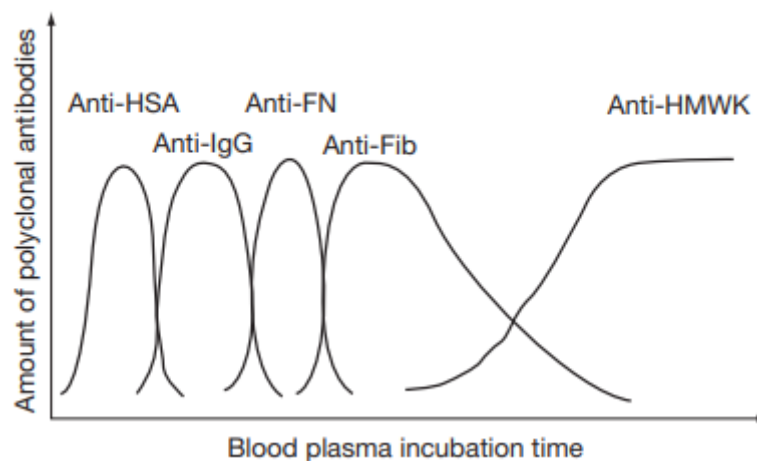


Figure 6. The Vroman plasma protein displacement phenomenon. The x-axis shows time elapse of incubation of a negatively charged surface, such as glass, Ta-oxide, or Ti-oxide in blood plasma, and the y-axis the amount of surface-bound polyclonal antibodies after different plasma incubation times. Reprinted from Tengvall, 2011.¹¹⁴

Acute and chronic inflammation

Acute inflammation is a process brief in duration and can last anywhere from minutes to days. It can be described by exudation of fluid and plasma proteins (edema), and migration of leukocytes, predominantly polymorphonuclear (PMNs) leukocytes. Inflamed area can be described by increased number of white blood cells due to their specific interactions between complementary adhesion molecules presented on them and endothelial cells interaction.^{10, 113,115,120} PMNs and other white blood cells move from the blood vessels towards the tissues surrounding the injury site in response to chemotactic stimuli. These include:

(1) margination, (2) adhesion, (3) emigration, (4) phagocytosis, and (5) extracellular release of leukocyte products. One of the main function of PMNs is phagocytosis, which can be described as a clearing out process of damaged tissue, foreign materials or microorganisms. Phagocytosis is seen as a three-step process in which the injurious agent undergoes recognition and neutrophil attachment, engulfment, and killing or degradation. With regards to biomaterials, engulfment and degradation may or may not occur, depending on the properties of the biomaterial (Figure 7).¹²³

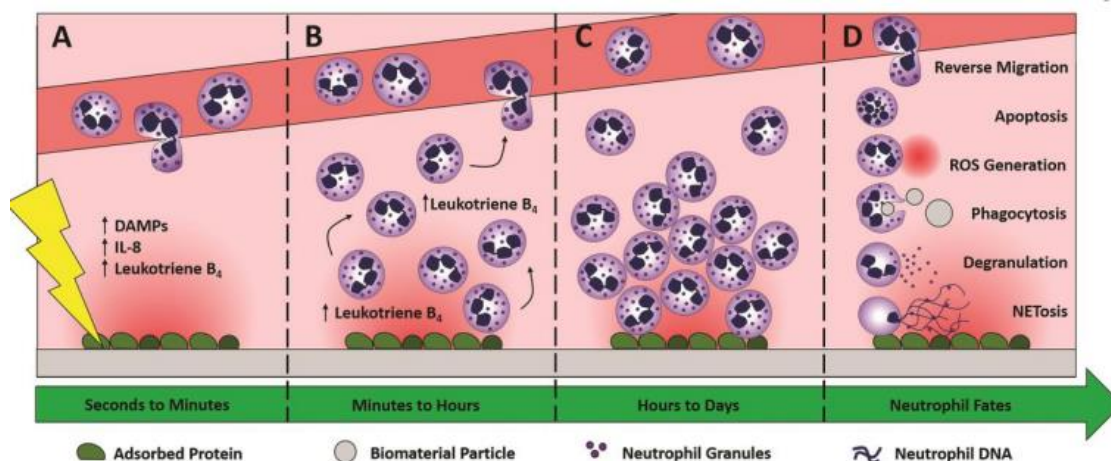


Figure 7. Implantation of a biomaterial triggers an innate immune response and neutrophil recruitment. (A) Injury up-regulates DAMPs, IL-8, and leukotriene B₄ to recruit neutrophils from circulation. (B) Neutrophils are recruited to a biomaterial-induced injury through leukotriene B₄ secretion in a feed-forward manner. (C) Swarming neutrophils interact with the biomaterial directly or indirectly through surface adsorbed proteins. (D) Neutrophils respond to the biomaterial and modulate the microenvironment through the production of ROS, phagocytosis, degranulation, and the release of NETs. Additionally, neutrophils can undergo apoptosis or reverse migrate back into circulation. Reprinted from Fetz *et al*, 2020.¹²³

Although biomaterials are not generally phagocytosed by neutrophils or macrophages due to the size disparity (i.e., the surface of the biomaterial is greater than the size of the cell, more than 50 μm). In addition, during this brief phase, they are modulating immune response by secreting cytokines which can influence the character and degree of subsequent inflammatory cell recruitment and activation.

Chronic inflammation due to the presence of biocompatible materials is marked by the infiltration of mononuclear leukocytes – macrophages derived from monocytes, lymphocytes and plasma cells.¹²⁰ These cells are accompanied by the development of new blood vessels (neovascularization) and connective tissue development (Table 4). With materials that are biocompatible, this phase usually lasts for around 2 to maximum 4 weeks (Figure 8). Macrophages are longer lasting cell in comparison to neutrophils and also have greater phagocytic and synthetic abilities.^{113,115,116,121} It is believed that macrophages play a key role in controlling the inflammatory response and subsequent wound healing/fibrosis processes.¹²⁰ The

activation of macrophages for cytokine production and phenotypic expression appears to be dependent on the surface chemistry of the biomaterial. For example, several key biomaterial-dependent chemokine and cytokine mediators, such as interleukin (IL)-1 β , IL-6, IL-8, and tumour necrosis factor (TNF)- α , have been shown to have autocrine and paracrine effects during the wound healing phases.^{124,125} The role of lymphocytes in these scenarios is not well understood, but it is believed that their significance is far greater than described in literature. Plasma cells presence can also be observed during the chronic inflammation phase, however as they are part of humoral response, they are not at the core focus of biomaterial research.^{113,115,126}

Table 4. General list of cell types involved in tissue-biomaterial interactions.

Cell types	Antigens used in immunohistochemistry	Host tissue response / Stages of wound healing
Erythrocytes / Red Blood Cells/RBC	TER-119	Surgical Injury
Leukocytes / White Blood Cells / WBC		Acute and chronic inflammation
Platelets / Thrombocytes	CD61	Surgical injury, protein adsorption
Neutrophils / Polymorphonuclear cells	CD15	Acute inflammation
Monocytes	CD68	Dilatated blood vessels
Macrophages	CD68, CD163	Acute and chronic inflammation
Multinucleated Giant Cells	CD68, CD206	Foreign Body Response
Lymphocytes	CD20	Chronic inflammation
Plasma cells	CD138	Chronic inflammation
Fibroblasts	Vimentin	Granulation tissue
Endothelial cells	CD31	Granulation tissue

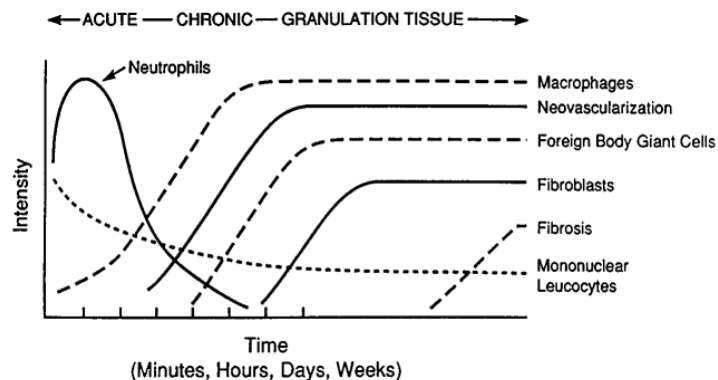


Figure 8. The temporal variation in the acute inflammatory response, chronic inflammatory response, granulation tissue development, and foreign body reaction to implanted biomaterials. The intensity and time variables are dependent upon the extent of injury created in the implantation and the size, shape, topography, and chemical and physical properties of the biomaterial. Reprinted from Anderson, 2001.¹¹⁵

Foreign body response (FBR)

When macrophages are unable to eliminate foreign particles / objects through the process of phagocytosis, they instead fuse to form multinucleated giant cells (MNGCs). This process is known as a foreign body reaction also often called “macrophages frustration fusion”. These MNGCs can be found in foreign body granulomas. Their nuclei are round, generally heterogeneously distributed throughout the cytoplasm, in contrast to tuberculosis MNGCs, and can amount to 100 (Figure 9).¹²¹ It has been shown that the formation of foreign body MNGCs is activated via macrophage fusion, depending on interleukin-4 and 13 pathways, induced by lymphocyte Th2.¹¹⁵ Contrary to osteoclasts (physiologically existing cells present during bone resorption and remodelling), MNGC formation is related to a different type of integrins, such as $\beta 1$ and $\beta 2$. Similar to their precursors, foreign body MNGCs express CD-68 antigen on their outer membrane, a glycoprotein expressed in monocytes and macrophages (Table 4). Furthermore, the mannose receptor (CD-206) was found in foreign body MNGCs during and after fusion in vitro.^{113,115,116,121, 126}

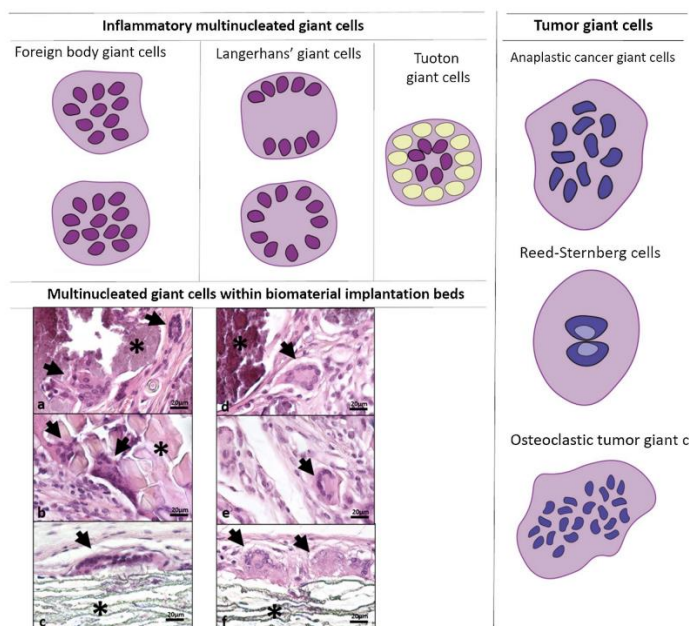


Figure 9. Illustrative artwork of the histopathological characteristics of different MNGCs subtypes. Exemplary histological micrographs of the morphologically different subtypes of MNGCs observed within the subcutaneous implantation beds of biomaterials. (a) Foreign body MNGCs with heterogeneously distributed nuclei (black arrows) within the implantation bed of a nanostructured bone substitute material (*) on day 15. (b) Foreign body MNGCs with heterogeneously distributed nuclei (black arrows) within the implantation bed of silk fibroin (*) on day 60. (c) Foreign body MNGCs with heterogeneously distributed nuclei (black arrows) within the implantation bed of expanded polytetrafluoroethylene (*) on day 60. (d) Langerhans'-like MNGCs with peripherally oriented nuclei in a circle (black arrow) within the implantation bed of a nanostructured bone substitute material (*) on day 10. (e) Langerhans'-like MNGCs with peripherally oriented nuclei in a horseshoe arrangement (black arrow) within the implantation bed of silk fibroin (*) on day 15. (f) Langerhans'-like MNGCs with peripherally oriented nuclei in a circle (black arrow) within the implantation bed of expanded polytetrafluoroethylene (*) on day 30. All histological stains are Haematoxylin & Eosin. Adapted from Al-Maawi *et al*, 2017.¹²¹

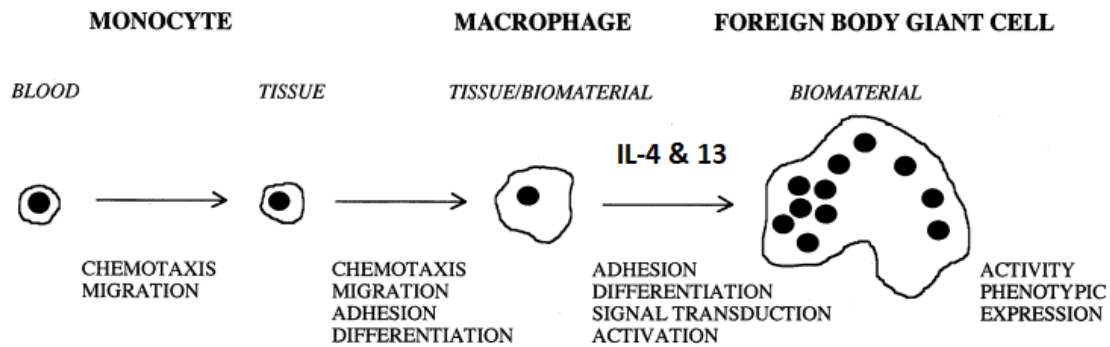


Figure 10. Transition from blood-borne monocyte to biomaterial adherent monocyte/macrophage to foreign body giant cell at the tissue/biomaterial interface. Adapted from Anderson 2001.¹¹⁵

Granulation Tissue

One of the body's responses to a biomaterial implant is the formation of granulation tissue. This tissue is characterized by the proliferation of small new blood vessels and fibroblasts. The formation of granulation tissue begins within the first day of biomaterial implantation, with the action of monocytes and macrophages, followed by proliferation of fibroblasts and neoangiogenesis. The granulation tissue formation often refers to the healing response, and its names come from the fact of its pink, soft, granular appearance of wounds healing. Its key histological features include the proliferation of capillaries and fibroblasts. Depending on the extent of injury, fully developed granulation tissue may be seen as early as three to five days post-implantation of a biomaterial.^{113,115,116} The new, small blood vessels are formed by budding or sprouting of pre-existing vessels in a process known as neoangiogenesis. It involves proliferation, maturation, and reorganization of endothelial cells into capillary tubes (Figure 11).¹²⁷ Moreover, fibroblasts also proliferate in developing granulation tissue and are responsible for synthesizing proteoglycans (more prevalent at the beginning) and collagen (especially collagen type I, which is a main component of the fibrous capsule). Some fibroblasts, during the development of granulation tissue, are associated with wound contraction properties by mimicking characteristic of smooth muscle cells and are, therefore, called myofibroblasts. The wound healing outcome depends largely on extent and degree of the primary injury. The complete reconstitution of the original architecture is often impossible in case more granulation tissue is formed, resulting in larger areas of fibrosis and subsequently scar.^{115,116,127}

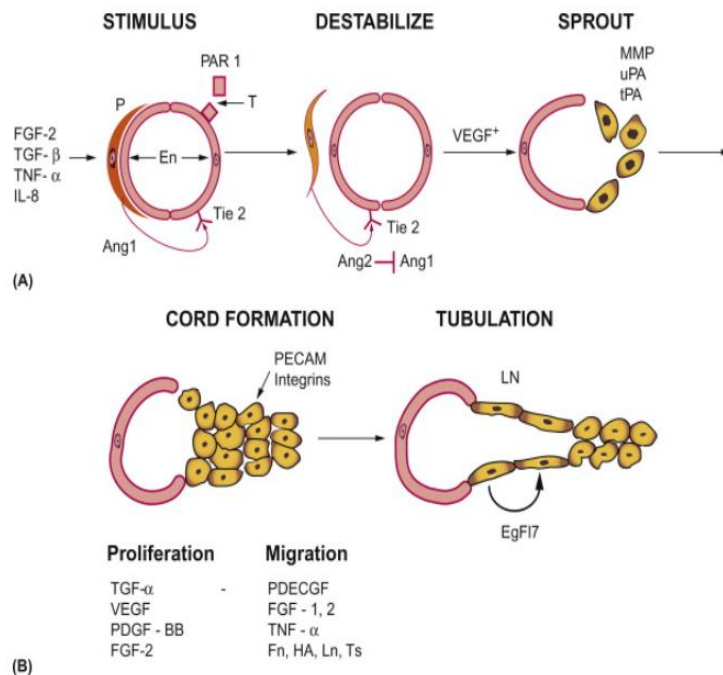


Figure 11. Molecular factors regulating angiogenesis. (A) Initiating of sprouting. Endothelial cells (En) are stabilized by their interactions with pericytes (P), mediated by Ang1/Tie 2. Thrombin (T) cleaves protease-activated receptor (PAR-1), allowing it to activate endothelial cells. The endothelial cells respond to a combination of growth factors and cytokines released from platelets and ECM, and synthesized by macrophages, fibroblasts, endothelial cells and pericytes. Pericytes now synthesize Ang 2, which competes with Ang 1 for binding to Tie 2, allowing dissociation of pericytes from the endothelium and its destabilization. In the presence of VEGF, the endothelial cells secrete proteases (MMP, uPA, tPA) that degrade the basement membrane of the blood vessel, allowing division of endothelial cells to form a sprout from the injured vessel. (B) Endothelial cells of the sprout proliferate to form cords of migrating cells that express PECAM and integrins on their surfaces. Cell division and migration are promoted by different sets of growth factors. Migration also requires several substrate molecules such as fibronectin (Fn), thrombospondin (Ts), hyaluronic acid (HA), and laminin (Ln). As the cords grow, the cells closest to the old vessel flatten and arrange themselves into tubules, which requires the secreted protein, EgF17. Reprinted from Stocum, 2012.

127

Fibrosis / Fibrous encapsulation

The final stage of healing response to biomaterials is considered as fibrosis or fibrous encapsulation. Nevertheless, there may be exceptions to this outcome if porous material has been inoculated with cells or porous material have been implanted into the bone and created a scaffold which can be integrated and replaced by newly formed structure.¹¹³

The repair of implant sites occurs through either regeneration or replacement. Regeneration is the reconstitution of damaged tissue by identical cells. Whereas replacement is the substitution of damaged tissue with connective tissue that forms a fibrous capsule. Both processes are usually determined by the either proliferative capacity of the cells in the receiving tissue, the degree of injury in relation to destruction, and/or by the persistence of the tissue framework of the implant site. Moreover, the cells which take place in regeneration can be

divided into three groups depending on their replicative capacity. Labile cells include the epithelia of ducts, hematopoietic stem cell, and epidermis. Injury to labile cells is rapidly repaired due to the fast tissue repair response. Stable (expanding) cells have a long-life span and divide at a very slow rate (parenchymal cells of the liver, kidney, and pancreas). Whereas, permanent (static) cells do not replicate and cannot recreate themselves, e.g. neurons, skeletal myocytes and cardiomyocytes.^{113,115} Therefore, in theory, only tissues involving labile and stable cells can be perfectly repaired with reconstitution of normal structure. To overpass that, pluripotent cells are being introduced nowadays to the biomaterial field. By adequate stimulation, these cells can potentially differentiate to the desired tissue. Alternatively, a different mechanism executed by the body is individual cellular adaptation to injury. In other words, cells may adapt their growth proliferation and differentiation and be described as follows: atrophy (decrease in cell size or function), hypertrophy (increase in cell size), hyperplasia (increase in cell number, only relevant to labile and stable cells), and metaplasia (change in cell type).^{116,121}

1.7. Evaluation methods of biocompatibility

As previously stated, in order for biomaterials to be clinically applicable, they must be biocompatible while retaining high levels of functionality. Biocompatibility in this context refers to a biomaterial's ability to function without causing toxic or injurious effects on biological systems. Nowadays, the biocompatibility concept also encompasses biofunctionality and biostability in addition to bio-inertia. A biomaterial's chemical, mechanical, and structural properties, as well as its interaction with the biological environment, can all affect its biocompatibility.¹¹² Biological evaluation of biomaterials includes a broad spectrum of *in vitro* and *in vivo* tests related to cytocompatibility, genotoxicity, sensitization, irritation, acute and chronic toxicity, hemocompatibility, reproductive and developmental toxicity, carcinogenicity, implantation and material degradation, as specified in different international standards (Table 5).¹¹²⁻¹²⁹

Table 5. The ISO Standard 10993-1 Guidance for Selection of Biocompatibility; Devices, type of contact, and potential biological effects/endpoints. Reprinted from Myers *et al*, 2017.¹²⁸

Device categories			Initial evaluation								Supplemental evaluation	
	Body contact	Contact duration	Cytotoxicity	Sensitization	Irritation or intracutaneous reactivity	Systemic toxicity (acute)/pyrogenicity	Subchronic toxicity	Genotoxicity	Implantation	Hemocompatibility	Chronic toxicity	Carcinogenicity
Surface devices	Skin	A	●	●	●							
		B	●	●	●							
		C	●	●	●							
	Mucosal Membranes	A	●	●	●							
		B	●	●	●	○	○		○			
		C	●	●	●	○	●	●	○		○	
	Breached/ compromised surface	A	●	●	●	○						
		B	●	●	●	○	○		○			
		C	●	●	●	○	●	●	○		○	
External communication devices	Blood path indirect	A	●	●	●	●				●		
		B	●	●	○	●	○			●		
		C	●	●	●	●	●	●	○	●	●	●
	Tissue/bone/dentin communicating	A	●	●	●	○						
		B	●	●	○	○	○		●			
		C	●	●	○	○	○		●		○	●
	Circulating blood	A	●	●	●	●					●	
		B	●	●	●	○	○	●	○	●		
		C	●	●	●	●	●	●	○	●	●	●
Implant devices	Bone/tissue	A	●	●	●	○		○				
		B	●	●	○	○	○	●	●			
		C	●	●	○	○	○	●	●		●	●
	Blood	A	●	●	●	●				●	●	
		B	●	●	●	●	○	●	●	●		
		C	●	●	●	●	●	●	●	●	●	●

A, limited exposure (5-24 hours); B, prolonged exposure (24 hours-30 days); C, permanent contact (> 30 days)

● FDA and ISO evaluation tests; ○ Additional tests for FDA

Materials meant for internal use must be able to function in a living organism without causing any negative local or systemic reactions, such as immune, allergic, or inflammatory. The evaluation process for a biomaterial is not only about it being bio-inert, but also biostable and biofunctional. This is a key concept that depends heavily on the material's properties (texture, crystallinity, wettability, surface chemistry, breakdown products, charges, stiffness), its interaction with the biological environment of the targeted tissues (adsorption of proteins, inflammatory processes), the length of time the device is meant to be used, and the type of application.¹³⁰

In order to fully assess a biomaterial's potential usefulness, a wide variety of *in vitro* and *in vivo* tests must be conducted. According to North American Material Science Association

(NAMSA), medical devices safety is divided into a four-phase approach (Figure 12)¹¹² The first phase of material characterization involves assessing the chemical, physical and biological properties of the components. The second phase is biocompatibility testing to determine which, if any, tests need to be performed. The biocompatibility of biomaterials is typically evaluated using guidelines from the International Organization for Standardization (ISO10993). The third phase pertains to product and process validation while the last phase covers release and audit testing procedures. The last phase refers to animal testing which is a final point before clinical trials. It is important to mention that the final product as well as its solo components should be tested as their (cyto)toxicity might be related to their individual status.^{112,129}

Phase	
I	Characterization of material <ul style="list-style-type: none"> • Chemical characterization • Physical characterization • Biological characterization
II	Biocompatibility of material
III	Product and process validation <ul style="list-style-type: none"> • Environment control • Manufacturing process control • Sterility Finished product quality
IV	Release and animal testing <ul style="list-style-type: none"> • Release testing • Periodic audit testing Product release




Figure 12. A four-phase approach for safety evaluation of medical devices (NAMSA). Reprinted from Inayat-Hussain *et al*, 2009.¹¹²

The use of *in vitro* and *in vivo* models is crucial for the evaluation of biomaterials. *In vitro* models allow for the study of biomaterials under controlled conditions, in the absence of a living organism while, *in vivo* models involve the study of biomaterials in a living organism. Each of these models has its own advantages and disadvantages, and the choice of which model to use depends on the specific question being asked.¹³¹

1.7.1. *In vitro* models

In vitro models are generally quicker and less expensive to set up and run than *in vivo* models. They also allow for a greater degree of control over variables, as it is easier to manipulate conditions in a closed fully monitored environment. However, *in vitro* models may not always represent the full scope of the *in vivo* situation, as they do not consider the complex interactions between the biomaterial and the living organism. *In vitro* tests, especially cytotoxicity assays are mandatory almost for all medical devices and their components and their task is to detect potential future hazards.¹³² *In vitro* models involve a wide selection of cell systems such as immortalized cells, genetically modified cells, primary cells, and more recently stem cells, however the last are still not fully accepted due to their uncontrolled modalities. Often, the first cell type choice used by researchers to evaluate biocompatibility are fibroblast or fibroblast-like cells with usually incubation time no longer than 7 days. Unfortunately, frequently the time and cell type utilized in assay is not adequate to the future application of the material. In the case of testing materials which would be applied for bone regeneration or foreign body response evaluation, designing the study utilizing fibroblast / fibroblast-like cells as a cell model may provide misleading information because for this particular application fibroblast overexpression is not desired. Additionally, often it is not taken into consideration the tumour origins of cell lines used as a model which application may not fully represent required specific cell/ tissue profile (Table 6).¹³¹ On the other hand, cell lines maintain their genetic and morphological characteristics throughout an entire lifespan, are more stable and easier to handle. It is important that suitable experimental design must weigh the advantages and disadvantages and be aware of it possible pitfalls to properly address scientific question.¹¹²

Table 6. Macrophages and macrophages-like cell lines used in biomaterial studies. Reprinted from Anderson, 2016.¹³¹

Cell line	Source
HL-60	Human: promyelocytic leukemia
IC-21	Mouse: transformed peritoneal macrophages
J774	Mouse: histocytic lymphoma
J774A.1	Mouse: histocytic lymphoma
P388D1	Mouse: transformed lymphoma
RAW	Mouse: transformed lymphoma
RAW 264.7	Mouse: transformed lymphoma
THP-1	Human: acute monocytic lymphoma
U937	Human: histiocytic lymphoma
'Macrophages'	Mouse: peritoneal surface

The cytotoxicity endpoints aim to demonstrate the level of harm that a biomaterial may cause, for instance: decreased membrane stability, increased release of cytosolic enzymes, metabolic impairment (ATP production), and decreased DNA synthesis or cell replication. As shown in Table 7, various assays have been devised to analyse the cytotoxic effect of biomaterials.¹¹² In this section, most of methods applied in the thesis will be described, namely MTS, Crystal Violet, Live/Dead and LDH.

Table 7. Common examples of cytotoxicity test, Adapted from Inayat-Hussain *et al*, 2009.¹¹²

Test	Principle
MTT assay	Reduction of tetrazolium salts by succinate dehydrogenase
Lactate dehydrogenase (LDH) leakage assay	Detection of LDH release into culture medium after cell membrane damage
Neutral red uptake (NRU) assay	Uptake of neutral red by lysosomes in viable cells
Alamar blue assay	Reduction of resazurin (alamar blue) to resorufin (pink fluorescent)
Colony forming assay (CFA)	Measurement of cell viability by colony-forming efficiency (survival) and colony size (proliferation)
Dye exclusion assay	Determine cell viability by dyes (e.g. trypan blue); cell with intact membranes exclude the dye and remain unstained
Sulforhodamine B (SRB) protein staining	Measures cell proliferation and chemosensitivity testing; the dye binds to basic amino acids of cellular proteins and colorimetric evaluation provides an estimate of total protein mass which is related to cell number

Cell Proliferation Assay, MTS Assay

The MTS (3-(4,5-dimethylthiazol-2-yl)-5-(3-carboxymethoxyphenyl)-2-(4-sulfophenyl)-2H-tetrazolium) assay is a colorimetric method for determining the number of viable cells or cells which undergo proliferation, it is associated with cell metabolic activity. In the presence of phenazine methosulfate (PMS), the MTS is reduced by viable and metabolically active cells into a formazan product by NADPH-dependent dehydrogenase enzymes (Figure 13). The produced formazan dye can be quantified by measuring the absorbance at 490–500 nm. The test is often defined as an upgrade and simplification of MTT assay, so called “one step”, MTT which offers the convenience of adding the reagent straight to the cell culture without the further steps

required in the MTT assay that uses 3-(4,5-dimethylthiazol-2-yl)-2,5-diphenyltetrazolium bromide. Additionally, the other benefit of MTS over MTT is that it is more soluble and nontoxic, allowing the cells to be returned to culture for further evaluation if necessary.¹³³

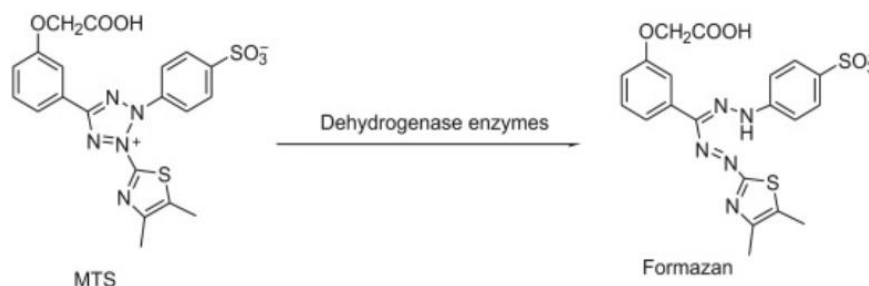


Figure 13. Structure of MTS tetrazolium and its formazan product. Reprinted from Technical Bulletin CellTiter 96® Aqueous One Solution Cell Proliferation Assay, Promega133

Crystal violet viability assay and direct contact test

The Crystal Violet (CV) assay uses triarylmethane dye, which attaches to ribose type molecules such as DNA in cell nuclei. The method is based on staining cells which remain attached to cell culture plates (viable / adherent cells). While performing the assay, detached cells are washed away during the sample preparation step. The remaining attached, live cells are stained with CV. Afterwards, the crystal violet dye is solubilized and measured by absorbance at 570 nm. There are several pitfalls to that method, for example tested samples require homogenous, single-cell suspension as cell need to be adherent. There can be also high variability between the same samples therefore it is recommended to have more replicates. Crystal violet can be used also as a staining dye for viable cells. The morphological changes such as vacuolization, rounding and swelling can be observed through an inverted microscope. This test can be used only for the adjacent cells because it is based on the concept that dead cells lose their capability to remain attached. Viable cells, however, remain and can be stained with CV. The toxic effect of a substance is evaluated by the absence of stained cells in the vicinity of the test material.¹³⁴

Live/Dead Assay

The LIVE/DEAD test is a two-colour assay to determine viability of cells by means of plasma membrane integrity and esterase activity. The outcome can be read using variable tools like flow cytometry, fluorescence microscopy, and fluorescence microplate readers. Ubiquitous intracellular esterase activity and an intact plasma membrane are differentiating features. The cellular differentiation of live from dead cells is performed by simultaneously staining with

green, fluorescent calcein-AM to indicate intracellular esterase activity and red-fluorescent ethidium homodimer-1 to indicate loss of plasma membrane integrity.¹³⁵

Non-Radioactive Cytotoxicity Assay, LDH

The Non-Radioactive Cytotoxicity Assay is an alternative to ⁵¹Cr release cytotoxicity analyses. In general, the assay quantitatively measures lactate dehydrogenase (LDH), which is a stable cytoplasmic enzyme that is released upon cell lysis. The half-life of LDH enzyme that has been released from cells into the cell culture medium is approximately 9 hours. Released of LDH in culture supernatants is measured with coupled enzymatic assay, which results in the conversion of a idonitrotetrazolium violet (INT) into a red formazan product (Figure 14). The absorbance data are collected using a plate reader.¹³⁶

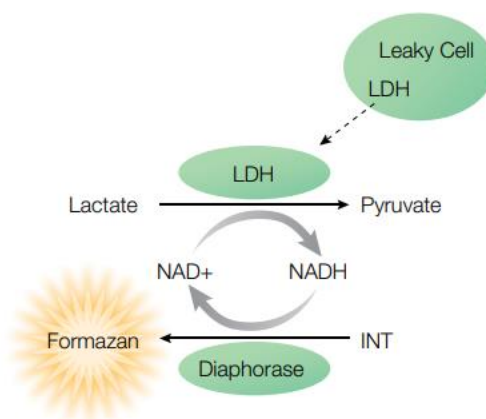


Figure 14. Release of LDH from damaged cells is measured by supplying lactate, NAD⁺ and INT as substrates in the presence of diaphorase. Reprinted from Technical Bulletin CytoTox 96[®] Non-Radioactive Cytotoxicity Assay, Promega.¹³⁶

1.7.2. *In vivo* models

In vivo models in biomaterials compatibility study remain the gold standard for the development and assessment of new biomaterials. Their use allows for the assessment of a material's biocompatibility in a living system, which is the best way to determine how a material will interact with the human body. *In vivo* models also allow for the study of long-term effects of biomaterials, which is important for the development of materials for implantable devices. Additionally, *in vivo* models can be used to study the interactions between biomaterials and cells, which is essential for the development of new biomaterials. Nonetheless, their use is associated with a number of ethical and practical issues.^{137,138}

In vivo models are more representative of the real situation, as they allow for the study of biomaterials in their natural environment. However, they are more expensive and time-consuming to set up and run than *in vitro* models. In addition, it is more difficult to control variables in an animal model, as the interactions between the biomaterial and the living organism are more complex. The ISO 10993-6:2016 guidelines refer to the assessment of the local effects post implantation of biomaterials proposed for use in medical devices such as: solid and non-absorbable, non-solid, such as porous materials, liquids, gels, pastes, and particulates, and degradable and/or absorbable, which may be solid or non-solid.^{137,138} For the evaluation of the biological safety of the material, the test sample is implanted into a site and animal species appropriate for the evaluation and intended application. The purpose of these test methods is to study the history and evolution of the tissue reaction to medical device/biomaterial implants, including the extent fibrosis and inflammation, tissue degeneration, immune cell response in terms of numbers and distribution, necrosis and apoptosis, tissue alterations (vascularization, bone formation, fat infiltration and granuloma development), quality and quantity of tissue ingrowth and final absorption or degradation of the material. These tests are particularly important for degradable/absorbable materials, in order to determine the degradation characteristics of the material and the resulting tissue response.¹³⁹

The ISO 10993-6:2016 guidelines does not specifically address systemic toxicity, carcinogenicity, teratogenicity, or mutagenicity. However, long-term implantation studies evaluating local biological effects might provide some insight into these properties. Both control and test samples should be implanted under identical conditions in research animals that are the same species, age, sex, and line. The number and size of the implants per animal depend on the size of the animal and the anatomical placement of the specimen. For the most accurate results, it is recommended that control and test specimens be implanted in the same animal. While choosing a species of laboratory animal for testing in conformity with ISO 10993-2, various factors should be considered, such as the size of the test specimens to be implanted, the number of test specimens per animal, the expected duration of the test, the lifespan of the animal, and potential species differences in biological response. Often, short-term studies are performed on small rodents or rabbits mostly due to economic reasons and long-term studies can be carried out on small rodents, rabbits, dogs, sheep, goats, pigs and other suitable animals with a relatively long lifespan.¹³⁹⁻¹⁴⁶ There are many animals' models to study biocompatibility of soft and hard tissue however the most common are:

Subcutaneous (subcutis) implantation model in small rodent

Rodents (mice and rats) are frequently used to evaluate the ability of tissues repair to its damage. Their skin regeneration capacity is much faster and more efficient than in other animal species. The subcutaneous pocket interchangeably called subcutis screening test might be used to evaluate the compatibility of both soft and hard tissue materials, specifically inflammatory response, cellularization of the extracellular matrix, and angiogenesis validation. Screening tests evaluating biocompatibility (by measuring the host's reaction to foreign material) in the subcutis can give insights into potential risks of harm associated with any substance entering the body. Thus, subcutis is often the first tissue where biocompatibility of any material for clinical application is assessed. Additionally, different hard biomaterials intended for bone treatment are also firstly tested for biocompatibility and harmlessness in soft tissue (*e.g.*, the subcutis). The concept behind this is that if a material is not biocompatible with subcutaneous tissue, it is unlikely to be compatible with bone tissue. Testing in this order is more humane to experimental animals as well as is more efficient in terms of time, costs, and low complexity level of the procedure (Figure 15).¹³⁸

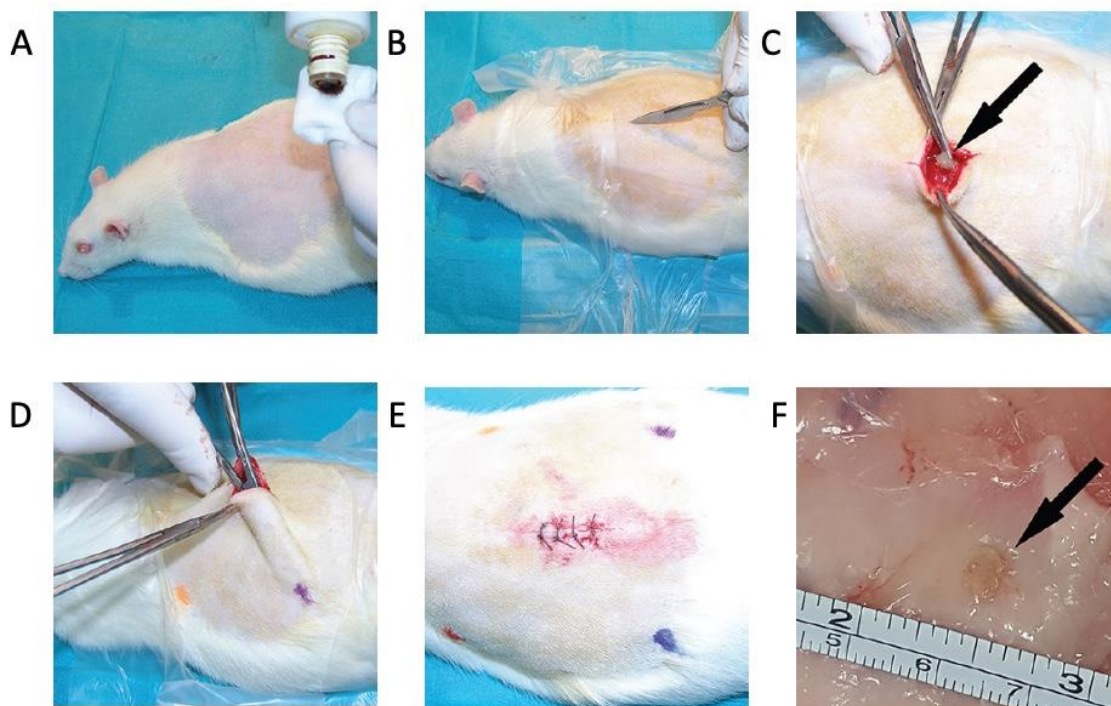


Figure 15. Subcutaneous implantation model in rat, (A) 3–4 month Wistar rat with average weight of 250-350 g, animal preparation for the procedure, (B) Perpendicular, midline scalpel incision performed under sterile conditions in subscapular region in dorsal part of the animal (C, D) Four hydrogel disc implantation into 4 different subcutaneous pockets (E) Wound closure with sutures (F) Explant, black arrows indicate the material area. Adapted from Prokic et al, 2022.¹³⁸

Cranial critical size defect (CSD) model in rabbit

Rabbits are a popular choice for animal experiments as they are easy to handle and have a high bone turnover rate. They also reach full maturity within 6 months. Rabbit cranial and femur CSD are the first choice for basic verification of bone graft materials and evaluations of bone tissue regeneration, repair, and remodelling. A CSD is a size defect in bone which is beyond body's ability to repair it naturally. These defects are studied in different bones used in implantology. Though there are only slight variations in bone composition between rabbits and humans, it is crucial to take these into account when selecting an animal model, as they can influence the results of the experiment. Most bone defect models are located in the femur, tibia, radius, mandible, and the cranium. The cranial model is best suited for implantation among the options available, given its biological inertness due to factors such as poor blood supply and limited bone marrow. Scar tissue formation is not a common occurrence in bone when compared to other tissues such as cartilage. Despite its regenerative potential, bone is not able to completely heal in more extensive fractures or when faced with bigger defects. Bone grafting is the process of implanting bone tissue, either alone or in combination with other materials, in order to promote bone regeneration. This is done through processes such as osteogenesis, osteoinduction and osteoconduction (Figure 16).¹⁴⁷ There are several factors to consider when choosing the ideal bone graft, such as tissue viability, damage size, graft size, shape, graft volume, biocompatibility, biomechanical capabilities, and cost (Figure 17).¹³⁸

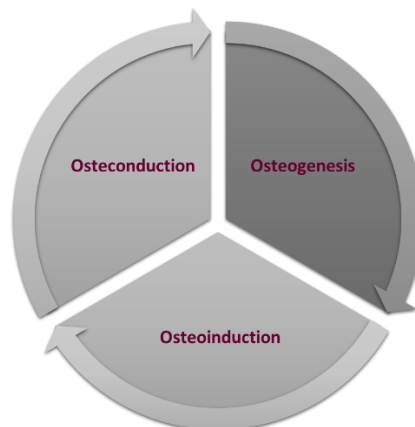


Figure 16. The three vital processes for bone regeneration. The scaffold network allows the migration of the cells (osteoconduction). Subsequently, the growth factors provided by the vascular supply induce the cellular proliferation (osteoinduction). Finally, the osteoblasts form new bone tissue (osteogenesis). Adapted from Bernardi *et al*, 2020.¹⁴⁷

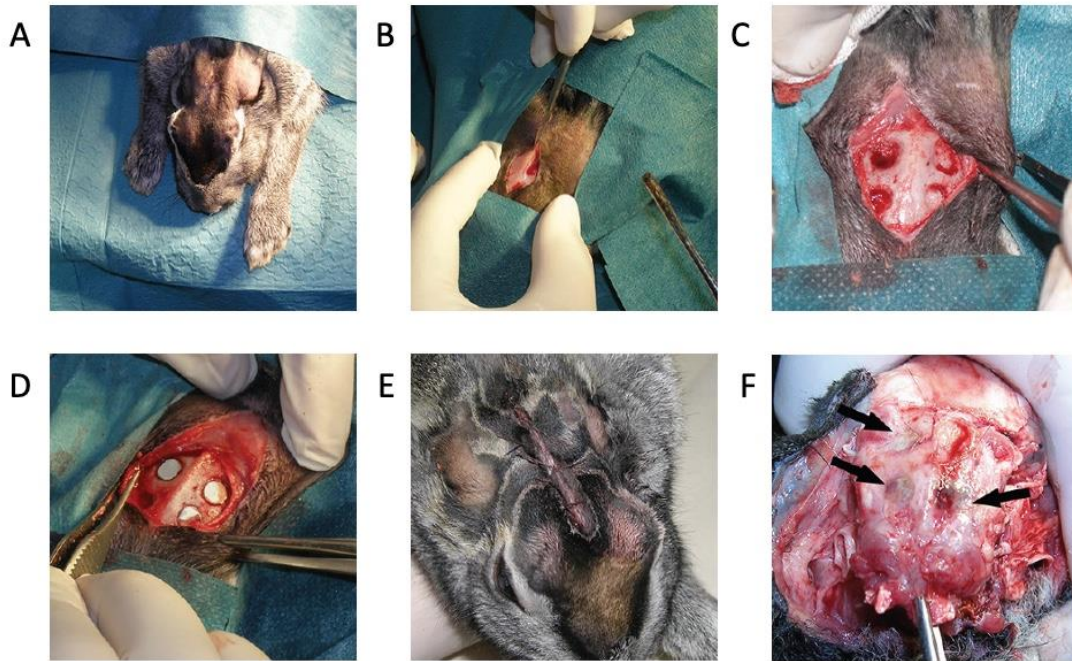


Figure 17. Cranium critical size defect model in rabbit (A) Animal preparation for the procedure (B) Perpendicular, midline scalpel incision performed under sterile conditions in dorsal part of the cranium, (C-D) Four defects of 5 mm diameter were made in each calvaria and implantation of material was performed (E) Wound closure with sutures (F) Explant, black arrows indicate the material area. Adapted from Prokic et al, 2022.¹³⁸

Any animal research necessary for the development of new drugs or biomaterials that will be used in both veterinary and human medicine must follow current ethical standards and justification must be provided for any experimental work performed. Research assessing the biocompatibility of new biomaterials generally utilize rats and rabbits instead of dogs, pigs or monkeys. To minimize the number of additional and repeated experiments, it is crucial that the research results are clear and precise. This not only reduces the pain, suffering and stress experienced by experimental animals, but also provides valid data for further evaluation and use of the biomaterial for clinical purposes. Finally, it is crucial to validate *in vitro* results with *in vivo* studies before any claims are made or hypotheses proposed. In the literature, it is common to find overstated claims based only on *in vitro* results that are not verified by *in vivo* studies. If a biomaterial is being considered for use in a medical device or prosthesis, *in vivo* validation of any *in vitro* results is essential.¹³⁷

Histological analysis

The biological/host response to the material is evaluated by the results of macroscopic and histopathological analysis gained at specified time intervals after implantation, for example 3, 10, 15, 30, and 60 days. After humane euthanasia, the specimens are removed together with up to 5mm of surrounding macroscopically unchanged tissue. For most materials and dyes, chemical fixation in 10% formalin for at least 24 hours without light exposure is advised. Other fixative methods such as methanol based, or cryopreservation are also possible. After fixation in case of hard materials as for example titanium, plastic *etc.*, the implants need to be removed prior further processing. In these situations, capsule and it surrounding tissue reflects the implantation area. When samples contain bone tissue decalcification step is required by usually using EDTA solution until it softens. In case of most common paraffin embedding of specimens, the samples need to overgo progressing concentrations of alcohol (70-100%) followed by xylene clearance and paraffin wax infiltration. Afterwards, paraffin blocks with a specimen present in the middle can be cut using microtome into 3-5 μm section, affixed on the polarized glass slide and deparaffinized for further staining procedure. Different staining techniques are used to identify particular structures, cells, tissues, or collagen depositions.¹⁴⁶⁻¹⁵¹

The most common staining is Hematoxylin-Eosin (HE) which as combination of two histological stain: hematoxylin that stains nuclei in dark purple or blue and eosin that stains the cytoplasm and extracellular matrix (ECM) of cells in pink. Hematoxylin, when used with a mordant, is often said to produce a basic, positively charged, or cationic stain. Eosin is a negatively charged stain that is acidic in nature.^{148,152} However, structures do not have to be acidic or basic to be called “basophilic” or “eosinophilic”; these terms originated from the affinity of cellular elements for the dyes. HE stains does not always give enough contrast to differentiate all tissues parts, cellular structures, therefore more specific stains, and methods are being employed in biomaterial research, such as: Heidenhain's AZAN trichrome stain (AZAN), Masson-Goldner's trichrome stain and Tartrate-resistant acid phosphatase (TRAP) stain, immunohistochemistry (IHC) and immunofluorescence (IF).

Heidenhain's Azan Stain

Heidenhain's Azan stain is a trichrome staining technique described by Martin Heidenhain, and later named after two of the dyes used: azokarmin and anilinblau. It contains different composites: azocarmine B or G, aniline-alcohol, phosphotungstic acid and a mixture of aniline blue and orange G. The differentiation of the azocarmine (aniline-alcohol followed by PTA) is a critical step that leaves red color only in nuclei, erythrocytes, some secretory granules, and glial scar tissue. Most of the cytosol is orange. Collagen fibers (including reticulin) and basement

membranes are blue. AZAN staining is often applied to visualize fibrotic alterations in the tissue (e.g., liver sclerosis).¹⁵³

Masson-Goldner Stain

Masson-Goldner trichrome staining is a method used to stain muscle fibers and collagen in tissues. The Fast Green dye in the staining method binds to collagen, which turns the collagen green. Masson-Goldner's trichrome is used to visualize an increase in collagen in functional tissues. This is particularly useful for identifying scar tissue but can also be used to differentiate smooth muscle fibers and collagens. The components of the Masson-Goldner trichrome are three dyes: Weigert's hematoxylin for nuclei, a mixture of acid dyes (Fuschine Biebrich acid scarlet) for cytoplasm and brilliant green for collagen.¹⁴⁹

TRAP Stain

The TRAP Staining is used for the staining of tartrate-resistant acid phosphatase presence in osteoclasts, activated macrophages, osteoblast and MNGCs. Bone mass is controlled by the balance between the activity of osteoblasts and osteoclasts. The role of TRAP in osteoclast migration and differentiation has been widely studied in the context of biomaterial research. It has been suggested that presence of TRAP positive cells may result in higher vascularization rate. Additionally, TRAP-null mice have been found to have irregular bone microarchitecture, in addition to the condition of osteopetrosis. This has led to the hypothesis that TRAP is necessary for the proper initiation and proliferation of osteoclasts.¹⁵⁴

Immunohistochemistry (IHC) and immunofluorescence (IF)

Immunohistochemistry (IHC) and immunofluorescence (IF) are staining techniques based on the reaction of antibodies with specific antigens. These methods can be used to examine the distribution of targeted proteins within a cell or tissue inspected sample. The specific antigens to which the antibodies may bind to can be found in a number of areas of the cells, including the cytoplasm, nucleus, lipids, proteins and cell membrane. The main difference between these two techniques is visualization method. While IHC utilizes chromogen, and the obtained result can be observed using brightfield microscope. IF technique uses fluorochrome, which once excited emits a light at a specific wavelength and the outcome can be observed with a fluorescence microscope.^{155,156}

1.8. Goals and research overview

Biomaterials have had an enormous importance on the development of medicine over the course of history. In particular, the advancement of fabrication and functionalization methods has contributed towards the creation of safer and more specialized materials. However, despite all the improvements so far, there is much we do not understand regarding our bodies' response to a given substance.

In this thesis, I aim to study the biological response against different types of biomaterials:

- Synthetic materials
- Nature-derived materials
 - Autologous materials
 - Xenogenic materials

In the case of synthetic materials, the aim was to study understand the role of different functionalization strategies (biological and physical) of polystyrene, silicone, and titanium in the initial host response. In particular, cell attachment to the materials was evaluated. Additionally, I have investigated cell differentiation and adherence to these materials *in vitro* and assessed the tissue response to silicone during *in vivo* implantation.

The study of nature-derived materials has been divided in two different categories depending on their origin: autologous and xenogenic.

The investigation of autologous materials focuses on platelet rich fibrin, a naturally derived hydrogel obtained from the host peripheral blood. Here the objective was to determine how different preparation methods by varying relative centrifugal force and centrifugation time were tested for growth factors storage capacity and release as well as cellular retention within the matrix. Moreover, an *in vivo* implantation model was employed to evaluate tissue reaction.

Different collagen membranes were studied as representative of xenogenic materials. The goal of this study was to measure cellular permeation into the membrane and its liquid absorption by applying liquid PRF system. Furthermore, an *in vivo* implantation model was utilized to establish host tissue response, in particular, multinucleated giant cell formation and their impact on neovascularization.

Finally, in addition to previously described work, I participated in the study of potential therapeutic effect of a novel anti-cancer agent, pyrrolopyrimidine (PP-13).

1.9. References

1. Kulinets, I. (2015). Biomaterials and their applications in medicine. In *Regulatory Affairs for Biomaterials and Medical Devices* (pp. 1–10). Elsevier Inc. <https://doi.org/10.1533/9780857099204.1>
2. Marin, E., Boschetto, F., & Pezzotti, G. (2020). Biomaterials and biocompatibility: An historical overview. In *Journal of Biomedical Materials Research - Part A* (Vol. 108, Issue 8, pp. 1617–1633). John Wiley and Sons Inc. <https://doi.org/10.1002/jbm.a.36930>
3. Todros, S., Todesco, M., & Bagno, A. (2021). Biomaterials and their biomedical applications: From replacement to regeneration. In *Processes* (Vol. 9, Issue 11). MDPI. <https://doi.org/10.3390/pr9111949>
4. Ali, S. H., Almaatoq, M. M., & Mohamed, A. S. (2013). Classifications, surface characterization and standardization of nanobiomaterials. In *International Journal of Engineering and Technology* (Vol. 2, Issue 3). www.sciencepubco.com/index.php/IJET
5. Ratner, B. D., & Zhang, G. (n.d.). *A History of Biomaterials*.
6. Samavedi, S., Poindexter, L. K., van Dyke, M., & Goldstein, A. S. (2014). Synthetic biomaterials for regenerative medicine applications. In *Regenerative Medicine Applications in Organ Transplantation* (pp. 81–99). Elsevier Inc. <https://doi.org/10.1016/B978-0-12-398523-1.00007-0>
7. Kaur, M., & Singh, K. (2019). Review on titanium and titanium based alloys as biomaterials for orthopaedic applications. In *Materials Science and Engineering C* (Vol. 102, pp. 844–862). Elsevier Ltd. <https://doi.org/10.1016/j.msec.2019.04.064>
8. Hanawa, T. (2019). Titanium-tissue interface reaction and its control with surface treatment. In *Frontiers in Bioengineering and Biotechnology* (Vol. 7, Issue JUL). Frontiers Media S.A. <https://doi.org/10.3389/fbioe.2019.00170>
9. Huzum, B., Puha, B., Necoara, R., Gheorghevi, S., Puha, G., Filip, A., Sirbu, P., & Alexa, O. (2021). Biocompatibility assessment of biomaterials used in orthopedic devices: An overview (Review). *Experimental and Therapeutic Medicine*, 22(5). <https://doi.org/10.3892/etm.2021.10750>
10. Overview of Biomaterials and Their Use in Medical Devices. (2003). www.asminternational.org
11. Huebsch, N., & Mooney, D. J. (2009). Inspiration and application in the evolution of biomaterials. In *Nature* (Vol. 462, Issue 7272, pp. 426–432). <https://doi.org/10.1038/nature08601>
12. Wwww, W. :, Patel, N. R., & Gohil, P. P. (2012). International Journal of Emerging Technology and Advanced Engineering A Review on Biomaterials: Scope, Applications & Human Anatomy Significance (Vol. 2, Issue 4). www.ijetae.com
13. Pezzotti, G., & Yamamoto, K. (2014). Artificial hip joints: The biomaterials challenge. *Journal of the Mechanical Behavior of Biomedical Materials*, 31, 3–20. <https://doi.org/10.1016/j.jmbbm.2013.06.001>
14. Zhang, W., Titze, M., Cappi, B., Wirtz, D. C., Telle, R., & Fischer, H. (2010). Improved mechanical long-term reliability of hip resurfacing prostheses by using silicon nitride. *Journal of Materials Science: Materials in Medicine*, 21(11), 3049–3057. <https://doi.org/10.1007/s10856-010-4144-z>
15. Pritchett, J. W. (2020). Total Articular Knee Replacement Using Polyurethane. *Journal of Knee Surgery*, 33(3), 242–246. <https://doi.org/10.1055/s-0039-1677816>
16. Kypta, A., Blessberger, H., Lichtenauer, M., Lambert, T., Kammler, J., & Steinwender, C. (2015). Gold-coated pacemaker implantation for a patient with type IV allergy to titanium. *Indian Pacing and Electrophysiology Journal*, 15(6), 291–292. <https://doi.org/10.1016/j.ipej.2016.02.009>
17. Bowen, P. K., Shearier, E. R., Zhao, S., Guillory, R. J., Zhao, F., Goldman, J., & Drelich, J. W. (2016). Biodegradable Metals for Cardiovascular Stents: From Clinical Concerns to Recent Zn-Alloys. In *Advanced Healthcare Materials* (Vol. 5, Issue 10, pp. 1121–1140). Wiley-VCH Verlag. <https://doi.org/10.1002/adhm.201501019>
18. Wasti, S., & Adhikari, S. (2020). Use of Biomaterials for 3D Printing by Fused Deposition Modeling Technique: A Review. In *Frontiers in Chemistry* (Vol. 8). Frontiers Media S.A. <https://doi.org/10.3389/fchem.2020.00315>
19. Tappa, K., & Jammalamadaka, U. (2018). Novel biomaterials used in medical 3D printing techniques. In *Journal of Functional Biomaterials* (Vol. 9, Issue 1). MDPI AG. <https://doi.org/10.3390/jfb9010017>
20. Mansoori, G. A., & Soelaiman, T. A. F. (2005). Nanotechnology-An Introduction for the Standards Community. In *Journal of ASTM International* (Vol. 2, Issue 6). www.astm.org

21. Hajiali, H., Ouyang, L., Llopis-Hernandez, V., Dobre, O., & Rose, F. R. A. J. (2021). Review of emerging nanotechnology in bone regeneration: Progress, challenges, and perspectives. In *Nanoscale* (Vol. 13, Issue 23, pp. 10266–10280). Royal Society of Chemistry. <https://doi.org/10.1039/d1nr01371h>
22. Misra, R., Acharya, S., & Sahoo, S. K. (2010). Cancer nanotechnology: Application of nanotechnology in cancer therapy. In *Drug Discovery Today* (Vol. 15, Issues 19–20, pp. 842–850). <https://doi.org/10.1016/j.drudis.2010.08.006>
23. Panyam, J., Sahoo, S. K., Prabha, S., Bargar, T., & Labhasetwar, V. (2003). Fluorescence and electron microscopy probes for cellular and tissue uptake of poly(D,L-lactide-co-glycolide) nanoparticles. *International Journal of Pharmaceutics*, 262(1–2), 1–11. [https://doi.org/10.1016/S0378-5173\(03\)00295-3](https://doi.org/10.1016/S0378-5173(03)00295-3)
24. Gregory, A. E., Titball, R., & Williamson, D. (2013). Vaccine delivery using nanoparticles. In *Frontiers in Cellular and Infection Microbiology* (Vol. 4, Issue MAR). <https://doi.org/10.3389/fcimb.2013.00013>
25. Li, C., Wang, J., Wang, Y., Gao, H., Wei, G., Huang, Y., Yu, H., Gan, Y., Wang, Y., Mei, L., Chen, H., Hu, H., Zhang, Z., & Jin, Y. (2019). Recent progress in drug delivery. In *Acta Pharmaceutica Sinica B* (Vol. 9, Issue 6, pp. 1145–1162). Chinese Academy of Medical Sciences. <https://doi.org/10.1016/j.apsb.2019.08.003>
26. Cardoso Dos Santos, M., Colin, I., Ribeiro Dos Santos, G., Susumu, K., Demarque, M., Medintz, I. L., & Hildebrandt, N. (2020). Time-Gated FRET Nanoprobes for Autofluorescence-Free Long-Term *In vivo* Imaging of Developing Zebrafish. *Advanced Materials*, 32(39). <https://doi.org/10.1002/adma.202003912>
27. Wallyn, J., Anton, N., & Vandamme, T. F. (2019). Synthesis, principles, and properties of magnetite nanoparticles for *in vivo* imaging applications—A review. In *Pharmaceutics* (Vol. 11, Issue 11). MDPI AG. <https://doi.org/10.3390/pharmaceutics11110601>
28. Hasan, A., Morshed, M., Memic, A., Hassan, S., Webster, T. J., & Marei, H. E. S. (2018). Nanoparticles in tissue engineering: Applications, challenges and prospects. In *International Journal of Nanomedicine* (Vol. 13, pp. 5637–5655). Dove Medical Press Ltd. <https://doi.org/10.2147/IJN.S153758>
29. Fathi-Achachelouei, M., Knopf-Marques, H., Ribeiro da Silva, C. E., Barthès, J., Bat, E., Tezcaner, A., & Vrana, N. E. (2019). Use of Nanoparticles in Tissue Engineering and Regenerative Medicine. *Frontiers in Bioengineering and Biotechnology*, 7. <https://doi.org/10.3389/fbioe.2019.00113>
30. Roma-rodrigues, C., Rivas-garcía, L., Baptista, P. v., & Fernandes, A. R. (2020). Gene therapy in cancer treatment: Why go nano? In *Pharmaceutics* (Vol. 12, Issue 3). MDPI AG. <https://doi.org/10.3390/pharmaceutics12030233>
31. Yuan, K., Jiang, Z., Jurado-Sánchez, B., & Escarpa, A. (2020). Nano/Micromotors for Diagnosis and Therapy of Cancer and Infectious Diseases. In *Chemistry - A European Journal* (Vol. 26, Issue 11, pp. 2309–2326). Wiley-VCH Verlag. <https://doi.org/10.1002/chem.201903475>
32. Pardi, N., Hogan, M. J., Porter, F. W., & Weissman, D. (2018). mRNA vaccines—a new era in vaccinology. In *Nature Reviews Drug Discovery* (Vol. 17, Issue 4, pp. 261–279). Nature Publishing Group. <https://doi.org/10.1038/nrd.2017.243>
33. Patil-Sen, Y. (2021). Advances in nano-biomaterials and their applications in biomedicine. In *Emerging Topics in Life Sciences* (Vol. 5, Issue 1, pp. 169–176). Portland Press Ltd. <https://doi.org/10.1042/ETLS20200333>
34. Choi, S., Han, S. I., Jung, D., Hwang, H. J., Lim, C., Bae, S., Park, O. K., Tschabrunn, C. M., Lee, M., Bae, S. Y., Yu, J. W., Ryu, J. H., Lee, S. W., Park, K., Kang, P. M., Lee, W. B., Nezafat, R., Hyeon, T., & Kim, D. H. (2018). Highly conductive, stretchable and biocompatible Ag–Au core–sheath nanowire composite for wearable and implantable bioelectronics. *Nature Nanotechnology*, 13(11), 1048–1056. <https://doi.org/10.1038/s41565-018-0226-8>
35. Zare, H., Ahmadi, S., Ghasemi, A., Ghanbari, M., Rabiee, N., Bagherzadeh, M., Karimi, M., Webster, T. J., Hamblin, M. R., & Mostafavi, E. (2021). Carbon nanotubes: Smart drug/gene delivery carriers. In *International Journal of Nanomedicine* (Vol. 16, pp. 1681–1706). Dove Medical Press Ltd. <https://doi.org/10.2147/IJN.S299448>
36. Linklater, D. P., Juodkazis, S., & Ivanova, E. P. (2017). Nanofabrication of mechano-bactericidal surfaces. In *Nanoscale* (Vol. 9, Issue 43, pp. 16564–16585). Royal Society of Chemistry. <https://doi.org/10.1039/c7nr05881k>
37. Wandiyanto, J. v., Truong, V. K., Kobaisi, M. al, Juodkazis, S., Thissen, H., Bazaka, O., Bazaka, K., Crawford, R. J., & Ivanova, E. P. (2019). The fate of osteoblast-like mg-63 cells on pre-infected

- bactericidal nanostructured titanium surfaces. *Materials*, 12(10). <https://doi.org/10.3390/ma12101575>
38. Variola, F., Vetrone, F., Richert, L., Jedrzejowski, P., Yi, J. H., Zalzal, S., Clair, S., Sarkissian, A., Perepichka, D. F., Wuest, J. D., Rosei, F., & Nanci, A. (2009). Improving biocompatibility of implantable metals by nanoscale modification of surfaces: An overview of strategies, fabrication methods, and challenges. In *Small* (Vol. 5, Issue 9, pp. 996–1006). <https://doi.org/10.1002/sml.200801186>
39. Loesberg, W. A., te Riet, J., van Delft, F. C. M. J. M., Schön, P., Figdor, C. G., Speller, S., van Loon, J. J. W. A., Walboomers, X. F., & Jansen, J. A. (2007). The threshold at which substrate nanogroove dimensions may influence fibroblast alignment and adhesion. *Biomaterials*, 28(27), 3944–3951. <https://doi.org/10.1016/j.biomaterials.2007.05.030>
40. Luo, J., Walker, M., Xiao, Y., Donnelly, H., Dalby, M. J., & Salmeron-Sanchez, M. (2022). The influence of nanotopography on cell behaviour through interactions with the extracellular matrix – A review. In *Bioactive Materials* (Vol. 15, pp. 145–159). KeAi Communications Co. <https://doi.org/10.1016/j.bioactmat.2021.11.024>
41. Dalby, M. J., Gadegaard, N., & Oreffo, R. O. C. (2014). Harnessing nanotopography and integrin-matrix interactions to influence stem cell fate. *Nature Materials*, 13(6), 558–569. <https://doi.org/10.1038/nmat3980>
42. Donnelly, H., Dalby, M. J., Salmeron-Sanchez, M., & Sweeten, P. E. (2018). Current approaches for modulation of the nanoscale interface in the regulation of cell behavior. In *Nanomedicine: Nanotechnology, Biology, and Medicine* (Vol. 14, Issue 7, pp. 2455–2464). Elsevier Inc. <https://doi.org/10.1016/j.nano.2017.03.020>
43. Wickström, S. A., & Niessen, C. M. (2018). Cell adhesion and mechanics as drivers of tissue organization and differentiation: local cues for large scale organization. In *Current Opinion in Cell Biology* (Vol. 54, pp. 89–97). Elsevier Ltd. <https://doi.org/10.1016/j.ceb.2018.05.003>
44. Qian, W., Gong, L., Cui, X., Zhang, Z., Bajpai, A., Liu, C., Castillo, A., Teo, J. C. M., & Chen, W. (2017). *Nanotopographic Regulation of Human Mesenchymal Stem Cell Osteogenesis*. <http://pubs.acs.org>
45. Wandiyanto, J. v., Truong, V. K., Kobaisi, M. al, Juodkasis, S., Thissen, H., Bazaka, O., Bazaka, K., Crawford, R. J., & Ivanova, E. P. (2019). The fate of osteoblast-like mg-63 cells on pre-infected bactericidal nanostructured titanium surfaces. *Materials*, 12(10). <https://doi.org/10.3390/ma12101575>
46. Sjöström, T., Dalby, M. J., Hart, A., Tare, R., Oreffo, R. O. C., & Su, B. (2009). Fabrication of pillar-like titania nanostructures on titanium and their interactions with human skeletal stem cells. *Acta Biomaterialia*, 5(5), 1433–1441. <https://doi.org/10.1016/j.actbio.2009.01.007>
47. Xiao, Q. R., Zhang, N., Wang, X., Man, X. Y., Yang, K., Lü, L. X., & Huang, N. P. (2017). Oriented Surface Nanotopography Promotes the Osteogenesis of Mesenchymal Stem Cells. *Advanced Materials Interfaces*, 4(3). <https://doi.org/10.1002/admi.201600652>
48. Yim, E. K. F., Darling, E. M., Kulangara, K., Guilak, F., & Leong, K. W. (2010). Nanotopography-induced changes in focal adhesions, cytoskeletal organization, and mechanical properties of human mesenchymal stem cells. *Biomaterials*, 31(6), 1299–1306. <https://doi.org/10.1016/j.biomaterials.2009.10.037>
49. McMurray, R. J., Gadegaard, N., Tsimbouri, P. M., Burgess, K. v., McNamara, L. E., Tare, R., Murawski, K., Kingham, E., Oreffo, R. O. C., & Dalby, M. J. (2011). Nanoscale surfaces for the long-term maintenance of mesenchymal stem cell phenotype and multipotency. *Nature Materials*, 10(8), 637–644. <https://doi.org/10.1038/nmat3058>
50. Wang, X., Yan, C., Ye, K., He, Y., Li, Z., & Ding, J. (2013). Effect of RGD nanospacing on differentiation of stem cells. *Biomaterials*, 34(12), 2865–2874. <https://doi.org/10.1016/j.biomaterials.2013.01.021>
51. Silvestri, A., Boffito, M., Sartori, S., & Ciardelli, G. (2013). Biomimetic materials and scaffolds for myocardial tissue regeneration. *Macromolecular Bioscience*, 13(8), 984–1019. <https://doi.org/10.1002/mabi.201200483>
52. Hiraba, H., Koizumi, H., Kodaira, A., Takehana, K., Yoneyama, T., & Matsumura, H. (2021). Effects of copper surface oxidation and reduction on shear-bond strength using functional monomers. *Materials*, 14(7). <https://doi.org/10.3390/ma14071753>
53. Thevarajah, J. J., van Leeuwen, M. P., Cottet, H., Castignolles, P., & Gaborieau, M. (2017). Determination of the distributions of degrees of acetylation of chitosan. *International Journal of Biological Macromolecules*, 95, 40–48. <https://doi.org/10.1016/j.ijbiomac.2016.10.056>

54. Mali, A., Kaijzel, E. L., Lamb, H. J., & Cruz, L. J. (2021). 19F-nanoparticles: Platform for *in vivo* delivery of fluorinated biomaterials for 19F-MRI. *Journal of Controlled Release*, 338, 870–889. <https://doi.org/10.1016/j.jconrel.2021.09.001>
55. Lee, T. J., Chau, L. K., & Huang, C. J. (2020). Controlled Silanization: High Molecular Regularity of Functional Thiol Groups on Siloxane Coatings. *Langmuir*, 36(21), 5935–5943. <https://doi.org/10.1021/acs.langmuir.0c00745>
56. Xue, R., Zhang, X., Wei, Y., Zhao, Z., Liu, H., Yang, F., Yin, L., Song, Z., Luan, S., & Tang, H. (2021). A sulfonate-based polypeptide toward infection-resistant coatings. *Biomaterials Science*, 9(19), 6425–6433. <https://doi.org/10.1039/d1bm00951f>
57. Song, W., & Ge, S. (2019). Application of antimicrobial nanoparticles in dentistry. In *Molecules* (Vol. 24, Issue 6). MDPI AG. <https://doi.org/10.3390/molecules24061033>
58. Thalla, P. K., Contreras-García, A., Fadlallah, H., Barrette, J., de Crescenzo, G., Merhi, Y., & Lerouge, S. (2013). A versatile star PEG grafting method for the generation of nonfouling and nonthrombogenic surfaces. *BioMed Research International*, 2013. <https://doi.org/10.1155/2013/962376>
59. Esposito, A. R., Kamikawa, C. M., Lucchesi, C., Ferreira, B. M. P., & de Rezende Duek, E. A. (2013). Benefits of oxygen and nitrogen plasma treatment in Vero cell affinity to poly(Lactide-Co-Glycolide Acid). *Materials Research*, 16(4), 695–702. <https://doi.org/10.1590/S1516-14392013005000056>
60. Gozdecka, A., & Wiącek, A. E. (2018). Effect of UV radiation and chitosan coating on the adsorption-photocatalytic activity of TiO₂ particles. *Materials Science and Engineering C*, 93, 582–594. <https://doi.org/10.1016/j.msec.2018.08.022>
61. Zhao, H., Liao, J., Wu, F., & Shi, J. (2021). Mechanical strength improvement of chitosan/hydroxyapatite scaffolds by coating and cross-linking. *Journal of the Mechanical Behavior of Biomedical Materials*, 114. <https://doi.org/10.1016/j.jmbbm.2020.104169>
62. Casanova, M. R., Reis, R. L., Martins, A., & Neves, N. M. (2020). Surface biofunctionalization to improve the efficacy of biomaterial substrates to be used in regenerative medicine. *Materials Horizons*, 7(9), 2258–2275. <https://doi.org/10.1039/d0mh00542h>
63. Batalov, I., Stevens, K. R., Deforest, C. A., & Blau, H. M. (n.d.). *Photopatterned biomolecule immobilization to guide three-dimensional cell fate in natural protein-based hydrogels*. <https://doi.org/10.1073/pnas.2014194118/-/DCSupplemental>
64. Facchetti, D., Hempel, U., Martocq, L., Smith, A. M., Koptuyg, A., Surmenev, R. A., Surmeneva, M. A., & Douglas, T. E. L. (2022). Heparin enriched-wpi coating on ti6al4v increases hydrophilicity and improves proliferation and differentiation of human bone marrow stromal cells. *International Journal of Molecular Sciences*, 23(1). <https://doi.org/10.3390/ijms23010139>
65. Santiago, L. Y., Nowak, R. W., Rubin, J. P., & Marra, K. G. (2006). Peptide-surface modification of poly(caprolactone) with laminin-derived sequences for adipose-derived stem cell applications. *Biomaterials*, 27(15), 2962–2969. <https://doi.org/10.1016/j.biomaterials.2006.01.011>
66. Boateng, S. Y., Lateef, S. S., Mosley, W., Hartman, T. J., Hanley, L., Russell, B., & Russell RGD, B. (2005). RGD and YIGSR synthetic peptides facilitate cellular adhesion identical to that of laminin and fibronectin but alter the physiology of neonatal cardiac myocytes. *Am J Physiol Cell Physiol*, 288, 30–38. <https://doi.org/10.1152/ajpcell.00199.2004.-ln>
67. Bauer, S. M., Bauer, R. J., Liu, Z. J., Chen, H., Goldstein, L., & Velazquez, O. C. (2005). Vascular endothelial growth factor-C promotes vasculogenesis, angiogenesis, and collagen constriction in three-dimensional collagen gels. *Journal of Vascular Surgery*, 41(4), 699–707. <https://doi.org/10.1016/j.jvs.2005.01.015>
68. Polívková, M., Hubáček, T., Staszek, M., Švorčík, V., & Siegel, J. (2017). Antimicrobial treatment of polymeric medical devices by silver nanomaterials and related technology. In *International Journal of Molecular Sciences* (Vol. 18, Issue 2). MDPI AG. <https://doi.org/10.3390/ijms18020419>
69. Banerjee, I., Pangule, R. C., & Kane, R. S. (2011). Antifouling coatings: Recent developments in the design of surfaces that prevent fouling by proteins, bacteria, and marine organisms. In *Advanced Materials* (Vol. 23, Issue 6, pp. 690–718). <https://doi.org/10.1002/adma.201001215>
70. Hasan, J., Crawford, R. J., & Ivanova, E. P. (2013). Antibacterial surfaces: The quest for a new generation of biomaterials. In *Trends in Biotechnology* (Vol. 31, Issue 5, pp. 295–304). <https://doi.org/10.1016/j.tibtech.2013.01.017>
71. Tedjo, C., Neoh, K. G., Kang, E. T., Fang, N., & Chan, V. (2007). Bacteria-surface interaction in the presence of proteins and surface attached poly(ethylene glycol) methacrylate chains. *Journal of Biomedical Materials Research - Part A*, 82(2), 479–491. <https://doi.org/10.1002/jbm.a.31172>

72. Saldarriaga Fernández, I. C., van der Mei, H. C., Lochhead, M. J., Grainger, D. W., & Busscher, H. J. (2007). The inhibition of the adhesion of clinically isolated bacterial strains on multi-component cross-linked poly(ethylene glycol)-based polymer coatings. *Biomaterials*, 28(28), 4105–4112. <https://doi.org/10.1016/j.biomaterials.2007.05.023>
73. Neoh, K. G., & Kang, E. T. (2011). Combating bacterial colonization on metals via polymer coatings: Relevance to marine and medical applications. *ACS Applied Materials and Interfaces*, 3(8), 2808–2819. <https://doi.org/10.1021/am200646t>
74. Shintani, H. (2004). Modification of Medical Device Surface to Attain Anti-Infection. In *Trends Biomater. Artif. Organs* (Vol. 18, Issue 1). <http://www.sbaoi.org>
75. Kwok, C. S., Horbett, T. A., & Ratner, B. D. (1999). Design of infection-resistant antibiotic-releasing polymers II. Controlled release of antibiotics through a plasma-deposited thin film barrier. In *Journal of Controlled Release* (Vol. 62). www.elsevier.com/locate/jconrel
76. Li, L., Molin, S., Yang, L., & Ndoni, S. (2013). Sodium dodecyl sulfate (SDS)-loaded nanoporous polymer as anti-biofilm surface coating material. *International Journal of Molecular Sciences*, 14(2), 3050–3064. <https://doi.org/10.3390/ijms14023050>
77. Antoci, V., Adams, C. S., Parvizi, J., Davidson, H. M., Composto, R. J., Freeman, T. A., Wickstrom, E., Ducheyne, P., Jungkind, D., Shapiro, I. M., & Hickok, N. J. (2008). The inhibition of Staphylococcus epidermidis biofilm formation by vancomycin-modified titanium alloy and implications for the treatment of periprosthetic infection. *Biomaterials*, 29(35), 4684–4690. <https://doi.org/10.1016/j.biomaterials.2008.08.016>
78. Hume, E. B. H., Baveja, J., Muir, B., Schubert, T. L., Kumar, N., Kjelleberg, S., Griesser, H. J., Thissen, H., Read, R., Poole-Warren, L. A., Schindhelm, K., & Willcox, M. D. P. (2004). The control of Staphylococcus epidermidis biofilm formation and in vivo infection rates by covalently bound furanones. *Biomaterials*, 25(20), 5023–5030. <https://doi.org/10.1016/j.biomaterials.2004.01.048>
79. Pavluchina, S. v., Kaplan, J. B., Xu, L., Chang, W., Yu, X., Madhyastha, S., Yakandawala, N., Mentbayeva, A., Khan, B., & Sukhishvili, S. A. (2012). Noneluting enzymatic antibiofilm coatings. *ACS Applied Materials and Interfaces*, 4(9), 4708–4716. <https://doi.org/10.1021/am3010847>
80. Khoo, X., Hamilton, P., O'Toole, G. A., Snyder, B. D., Kenan, D. J., & Grinstaff, M. W. (2009). Directed assembly of PEGylated-peptide coatings for infection-resistant titanium metal. *Journal of the American Chemical Society*, 131(31), 10992–10997. <https://doi.org/10.1021/ja9020827>
81. El-Zayat, B. F., Ruchholtz, S., Efe, T., Paletta, J., Kreslo, D., & Zettl, R. (2013). Results of titanium locking plate and stainless steel cerclage wire combination in femoral fractures. *Indian Journal of Orthopaedics*, 47(5), 454–458. <https://doi.org/10.4103/0019-5413.118200>
82. Prakasam, M., Locs, J., Salma-Ancane, K., Loca, D., Largeteau, A., & Berzina-Cimdina, L. (2017). Biodegradable materials and metallic implants-A review. In *Journal of Functional Biomaterials* (Vol. 8, Issue 4). MDPI AG. <https://doi.org/10.3390/jfb8040044>
83. Girón, J., Kerstner, E., Medeiros, T., Oliveira, L., Machado, G. M., Malfatti, C. F., & Pranke, P. (2021). Biomaterials for bone regeneration: An orthopedic and dentistry overview. *Brazilian Journal of Medical and Biological Research*, 54(9). <https://doi.org/10.1590/1414-431X2021E11055>
84. Sharma, B., & Varghese, S. (2016). Progress in orthopedic biomaterials and drug delivery. In *Drug Delivery and Translational Research* (Vol. 6, Issue 2, pp. 75–76). Springer Verlag. <https://doi.org/10.1007/s13346-016-0288-9>
85. Vojtěch, D., Kubásek, J., Šerák, J., & Novák, P. (2011). Mechanical and corrosion properties of newly developed biodegradable Zn-based alloys for bone fixation. *Acta Biomaterialia*, 7(9), 3515–3522. <https://doi.org/10.1016/j.actbio.2011.05.008>
86. Okada, N., Tajima, K., Takami, Y., Kato, W., Fujii, K., Hibino, M., Munakata, H., Sakai, Y., Hirakawa, A., & Usui, A. (2015). Valve selection for the aortic position in dialysis patients. *Annals of Thoracic Surgery*, 99(5), 1524–1531. <https://doi.org/10.1016/j.athoracsur.2014.11.055>
87. Sipahi, I., Akay, M. H., Dagdelen, S., Blitz, A., & Alhan, C. (2014). Coronary artery bypass grafting vs percutaneous coronary intervention and long-term mortality and morbidity in multivessel disease : Meta-analysis of randomized clinical trials of the arterial grafting and stenting ERA. *JAMA Internal Medicine*, 174(2), 223–230. <https://doi.org/10.1001/jamainternmed.2013.12844>
88. Giustino, G., Baber, U., Sartori, S., Mehran, R., Mastoris, I., Kini, A. S., Sharma, S. K., Pocock, S. J., & Dangas, G. D. (2015). *Duration of Dual Antiplatelet Therapy After Drug-Eluting Stent Implantation A Systematic Review and Meta-Analysis of Randomized Controlled Trials*.
89. Byrne, R. A., Kastrati, A., Massberg, S., Wiecek, A., Laugwitz, K. L., Hadamitzky, M., Schulz, S., Pache, J., Fusaro, M., Hausleiter, J., Schömig, A., & Mehilli, J. (2011). Biodegradable polymer versus

- permanent polymer drug-eluting stents and everolimus- versus sirolimus-eluting stents in patients with coronary artery disease: 3-year outcomes from a randomized clinical trial. *Journal of the American College of Cardiology*, 58(13), 1325–1331. <https://doi.org/10.1016/j.jacc.2011.06.027>
90. Stettler, C., Wandel, S., Allemann, S., Kastrati, A., Morice, M. C., Schömig, A., Pfi, M. E., Stone, G. W., Leon, M. B., Suarez De Lezo, J., Goy, J.-J., Park, S.-J., Sabaté, M., Suttorp, M. J., Kelbaek, H., Spaulding, C., Menichelli, M., Vermeersch, P., Dirksen, M. T., ... Jüni, P. (2007). Outcomes associated with drug-eluting and bare-metal stents: a collaborative network meta-analysis. In *www.thelancet.com* (Vol. 370). www.tctmd.com,
 91. Bharadwaj, A. (2021). An Overview on Biomaterials and Its Applications in Medical Science. *IOP Conference Series: Materials Science and Engineering*, 1116(1), 012178. <https://doi.org/10.1088/1757-899x/1116/1/012178>
 92. Anaya-Alaminos, R., Ibáñez-Flores, N., Aznar-Peña, I., & González-Andrades, M. (2015). Antimicrobial biomaterials and their potential application in ophthalmology. *Journal of Applied Biomaterials and Functional Materials*, 13(4), e346–e350. <https://doi.org/10.5301/jabfm.5000253>
 93. Fenton, O. S., Paolini, M., Andresen, J. L., Müller, F. J., & Langer, R. (2020). Outlooks on Three-Dimensional Printing for Ocular Biomaterials Research. In *Journal of Ocular Pharmacology and Therapeutics* (Vol. 36, Issue 1, pp. 7–17). Mary Ann Liebert Inc. <https://doi.org/10.1089/jop.2018.0142>
 94. Wang, T.-J., Wang, † ‡ § I-Jong, Hu, F.-R., & Young, T.-H. (2016). *Applications of Biomaterials in Corneal Endothelial Tissue Engineering*. www.corneajrnl.com
 95. Musgrave, C. S. A., & Fang, F. (2019). Contact lens materials: A materials science perspective. In *Materials* (Vol. 12, Issue 2). MDPI AG. <https://doi.org/10.3390/ma12020261>
 96. Zhang, X. M., Li, Y., Gu, Y. X., Zhang, C. N., Lai, H. C., & Shi, J. Y. (2019). Ta-coated titanium surface with superior bacteriostasis and osseointegration. *International Journal of Nanomedicine*, 14, 8693–8706. <https://doi.org/10.2147/IJN.S218640>
 97. Smeets, R., Stadlinger, B., Schwarz, F., Beck-Broichsitter, B., Jung, O., Precht, C., Kloss, F., Gröbe, A., Heiland, M., & Ebker, T. (2016). Impact of Dental Implant Surface Modifications on Osseointegration. In *BioMed Research International* (Vol. 2016). Hindawi Limited. <https://doi.org/10.1155/2016/6285620>
 98. Bencharit, S., Byrd, W. C., Altarawneh, S., Hosseini, B., Leong, A., Reside, G., Morelli, T., & Offenbacher, S. (2014). Development and applications of porous tantalum trabecular metal-enhanced titanium dental implants. *Clinical Implant Dentistry and Related Research*, 817–826. <https://doi.org/10.1111/cid.12059>
 99. Yang, Y., Ren, S., Zhang, X., Yu, Y., Liu, C., Yang, J., & Miao, L. (2018). Safety and efficacy of PLGA(Ag-Fe₃O₄)-Coated dental implants in inhibiting bacteria adherence and osteogenic inducement under a magnetic field. *International Journal of Nanomedicine*, 13, 3751–3762. <https://doi.org/10.2147/IJN.S159860>
 100. Heyman, O., Koren, N., Mizraji, G., Capucha, T., Wald, S., Nassar, M., Tabib, Y., Shapira, L., Hovav, A. H., & Wilensky, A. (2018). Impaired differentiation of Langerhans cells in the murine oral epithelium adjacent to titanium dental implants. *Frontiers in Immunology*, 9(AUG). <https://doi.org/10.3389/fimmu.2018.01712>
 101. Shemtov-Yona, K., & Rittel, D. (2015). An Overview of the Mechanical Integrity of Dental Implants. In *BioMed Research International* (Vol. 2015). Hindawi Publishing Corporation. <https://doi.org/10.1155/2015/547384>
 102. al Zahrani, S., & al Mutairi, A. A. (2019). Crestal Bone Loss Around Submerged and Non-Submerged Dental Implants in Individuals with Type-2 Diabetes Mellitus: A 7-Year Prospective Clinical Study. *Medical Principles and Practice*, 28(1), 75–81. <https://doi.org/10.1159/000495111>
 103. Blanco-Fernandez, B., Castaño, O., Mateos-Timoneda, M. Á., Engel, E., & Pérez-Amodio, S. (2021). Nanotechnology Approaches in Chronic Wound Healing. In *Advances in Wound Care* (Vol. 10, Issue 5, pp. 234–256). Mary Ann Liebert Inc. <https://doi.org/10.1089/wound.2019.1094>
 104. Chaudhari, A. A., Vig, K., Baganizi, D. R., Sahu, R., Dixit, S., Dennis, V., Singh, S. R., & Pillai, S. R. (2016). Future prospects for scaffolding methods and biomaterials in skin tissue engineering: A review. In *International Journal of Molecular Sciences* (Vol. 17, Issue 12). MDPI AG. <https://doi.org/10.3390/ijms17121974>
 105. Alven, S., & Aderibigbe, B. A. (2021). Fabrication of hybrid nanofibers from biopolymers and poly (Vinyl alcohol)/poly (ε-caprolactone) for wound dressing applications. In *Polymers* (Vol. 13, Issue 13). MDPI AG. <https://doi.org/10.3390/polym13132104>

106. Alven, S., Peter, S., Mbese, Z., & Aderibigbe, B. A. (2022). Polymer-Based Wound Dressing Materials Loaded with Bioactive Agents: Potential Materials for the Treatment of Diabetic Wounds. In *Polymers* (Vol. 14, Issue 4). MDPI. <https://doi.org/10.3390/polym14040724>
107. You, D., Li, K., Guo, W., Zhao, G., & Fu, C. (2019). Poly (lactic-co-glycolic acid)/graphene oxide composites combined with electrical stimulation in wound healing: Preparation and characterization. *International Journal of Nanomedicine*, 14, 7039–7052. <https://doi.org/10.2147/IJN.S216365>
108. Saghazadeh, S., Rinoldi, C., Schot, M., Kashaf, S. S., Sharifi, F., Jalilian, E., Nuutila, K., Giatsidis, G., Mostafalu, P., Derakhshandeh, H., Yue, K., Swieszkowski, W., Memic, A., Tamayol, A., & Khademhosseini, A. (2018). Drug delivery systems and materials for wound healing applications. In *Advanced Drug Delivery Reviews* (Vol. 127, pp. 138–166). Elsevier B.V. <https://doi.org/10.1016/j.addr.2018.04.008>
109. Zhuo, S., Zhang, F., Yu, J., Zhang, X., Yang, G., & Liu, X. (2020). pH-sensitive biomaterials for drug delivery. In *Molecules* (Vol. 25, Issue 23). MDPI AG. <https://doi.org/10.3390/molecules25235649>
110. Hakim, L. K., Yazdani, M., Alam, M., Abbasi, K., Tebyaniyan, H., Tahmasebi, E., Khayatan, D., Seifalian, A., Ranjbar, R., & Yazdani, A. (2021). Biocompatible and Biomaterials Application in Drug Delivery System in Oral Cavity. In *Evidence-based Complementary and Alternative Medicine* (Vol. 2021). Hindawi Limited. <https://doi.org/10.1155/2021/9011226>
111. Stewart, S. A., Domínguez-Robles, J., Donnelly, R. F., & Larrañeta, E. (2018). Implantable polymeric drug delivery devices: Classification, manufacture, materials, and clinical applications. In *Polymers* (Vol. 10, Issue 12). MDPI AG. <https://doi.org/10.3390/polym10121379>
112. Inayat-Hussain, S., Rajab, N. F., & Siew, E. L. (2008). In vitro testing of biomaterials toxicity and biocompatibility. In *Cellular Response to Biomaterials* (pp. 508–537). Elsevier Ltd. <https://doi.org/10.1533/9781845695477.3.508>
113. Anderson, J. M., & McNally, A. K. (2011). Biocompatibility of implants: Lymphocyte/macrophage interactions. In *Seminars in Immunopathology* (Vol. 33, Issue 3, pp. 221–233). <https://doi.org/10.1007/s00281-011-0244-1>
114. Tengvall, P. (2011). Protein interactions with biomaterials. In *Comprehensive Biomaterials* (Vol. 4, pp. 63–73). Elsevier. <https://doi.org/10.1016/b978-0-08-055294-1.00006-4>
115. Anderson, J. M. (2001). BIOLOGICAL RESPONSES TO MATERIALS.
116. Anderson, J. M., Rodriguez, A., & Chang, D. T. (n.d.). *FOREIGN BODY REACTION TO BIOMATERIALS*.
117. Raut, H. K., Das, R., Liu, Z., Liu, X., & Ramakrishna, S. (2020). Biocompatibility of Biomaterials for Tissue Regeneration or Replacement. In *Biotechnology Journal* (Vol. 15, Issue 12). Wiley-VCH Verlag. <https://doi.org/10.1002/biot.202000160>
118. Liu, Y., Buil, A., Collins, B. C., Gillet, L. C., Blum, L. C., Cheng, L., Vitek, O., Mouritsen, J., Lachance, G., Spector, T. D., Dermitzakis, E. T., & Aebbersold, R. (2015). Quantitative variability of 342 plasma proteins in a human twin population. *Molecular Systems Biology*, 11(2), 786. <https://doi.org/10.15252/msb.20145728>
119. Yu, Q., & Chen, H. (2015). Interaction of switchable biomaterials surfaces with proteins. In *Switchable and Responsive Surfaces and Materials for Biomedical Applications* (pp. 167–188). Elsevier Inc. <https://doi.org/10.1016/B978-0-85709-713-2.00007-9>
120. Stanciu, L., & Diaz-Amaya, S. (2022). Tissue-biomaterials interactions. In *Introductory Biomaterials* (pp. 171–200). Elsevier. <https://doi.org/10.1016/b978-0-12-809263-7.00008-1>
121. Al-Maawi, S., Orłowska, A., Sader, R., James Kirkpatrick, C., & Ghanaati, S. (2017). In vivo cellular reactions to different biomaterials—Physiological and pathological aspects and their consequences. In *Seminars in Immunology* (Vol. 29, pp. 49–61). Academic Press. <https://doi.org/10.1016/j.smim.2017.06.001>
122. Erbulut, D. U., & Lazoglu, I. (2010). Biomaterials for improving the blood and tissue compatibility of total artificial hearts (TAH) and ventricular assist devices (VAD). In *Biomaterials for Artificial Organs* (pp. 207–235). Elsevier Inc. <https://doi.org/10.1533/9780857090843.2.207>
123. Fetz, A. E., Radic, M. Z., & Bowlin, G. L. (2021). Neutrophils in Biomaterial-Guided Tissue Regeneration: Matrix Reprogramming for Angiogenesis. In *Tissue Engineering - Part B: Reviews* (Vol. 27, Issue 2, pp. 95–106). Mary Ann Liebert Inc. <https://doi.org/10.1089/ten.teb.2020.0028>
124. Jones, J. A., Advisor, D., & Anderson, J. M. (2007). BIOMATERIALS AND THE FOREIGN BODY REACTION: SURFACE CHEMISTRY DEPENDENT MACROPHAGE ADHESION, FUSION, APOPTOSIS, AND CYTOKINE PRODUCTION by.

125. Jones, J. A., Chang, D. T., Meyerson, H., Colton, E., II, K. K., Matsuda, T., & Anderson, J. M. (2007). Proteomic analysis and quantification of cytokines and chemokines from biomaterial surface-adherent macrophages and foreign body giant cells. *Journal of Biomedical Materials Research - Part A*, 83(3), 585–596. <https://doi.org/10.1002/jbm.a.31221>
126. Brodbeck, W. G., & Anderson, J. M. (2009). Giant cell formation and function. In *Current Opinion in Hematology* (Vol. 16, Issue 1, pp. 53–57). <https://doi.org/10.1097/MOH.0b013e32831ac52e>
127. Stocum, D. (2012). *Regenerative Biology and Medicine*, 2nd edition. Academic Press, Paperback ISBN: 9780123848604
128. Myers, D. K., Goldberg, A. M., Poth, A., Wolf, M. F., Carraway, J., McKim, J., Coleman, K. P., Hutchinson, R., Brown, R., Krug, H. F., Bahinski, A., & Hartung, T. (2017). From in vivo to in vitro: The medical device testing paradigm shift. *Altex*, 34(4), 479–500. <https://doi.org/10.14573/altex.1608081>
129. Biological evaluation of medical devices-ISO-10992-1-2009. (2009).
130. Derelanko, M. J., & Hollinger, M. A. (2002). *Handbook of toxicology*. CRC Press.
131. Anderson, J. M. (2016). Future challenges in the in vitro and in vivo evaluation of biomaterial biocompatibility. In *Regenerative Biomaterials* (Vol. 3, Issue 2, pp. 73–77). Oxford University Press. <https://doi.org/10.1093/RB/RBW001>
132. Biological evaluation of medical devices- ISO10993-5:2009 (2009).
133. Corporation, P. (n.d.). CellTiter 96[®] AQueous One Solution Cell Proliferation Assay Instructions for Use of Products G3580, G3581 and G3582. www.promega.com
134. Feoktistova, M., Geserick, P., & Leverkus, M. (2016). Crystal violet assay for determining viability of cultured cells. *Cold Spring Harbor Protocols*, 2016(4), 343–346. <https://doi.org/10.1101/pdb.prot087379>
135. MP 03224 LIVE/DEAD[®] Viability/Cytotoxicity Kit Product Information. (n.d.). www.omegafilters.com
136. Corporation, P. (n.d.). CytoTox 96[®] Non-Radioactive Cytotoxicity Assay Instructions for Use of Product G1780. www.promega.com
137. Biological evaluation of medical devices- ISO10993-6:2009 (2009).
138. Prokic, B., Luzajic-Bozinovski, T., Gajdov, V., Milosevic, I., Todorovic, V., Djosic, M., Miskovic-Stankovic, V., & Markovic, D. (2021). Animal models in biocompatibility assessments of implants in soft and hard tissues. *Veterinarski Glasnik*, 00, 5–5. <https://doi.org/10.2298/vetgl210322005p>
139. Fini, M., Giardino, R., (2003) In vitro and in vivo tests for the biological evaluation of candidate orthopedic materials: Benefits and limits. *J Appl Biomater Biomech*. Sep-Dec;1(3):155-63. PMID: 20803452.
140. Nuss, K. M. R., Auer, J. A., Boos, A., & von Rechenberg, B. (2006). An animal model in sheep for biocompatibility testing of biomaterials in cancellous bones. *BMC Musculoskeletal Disorders*, 7. <https://doi.org/10.1186/1471-2474-7-67>
141. Pearce, A. I., Richards, R. G., Milz, S., Schneider, E., & Pearce, S. G. (2007). Animal models for implant biomaterial research in bone: A review. In *European Cells and Materials* (Vol. 13, pp. 1–10). AO Research Institute Davos. <https://doi.org/10.22203/eCM.v013a01>
142. Wancket, L. M. (2015). Animal Models for Evaluation of Bone Implants and Devices: Comparative Bone Structure and Common Model Uses. *Veterinary Pathology*, 52(5), 842–850. <https://doi.org/10.1177/0300985815593124>
143. Williams, D. F. (1987). Review Tissue-biomaterial interactions. In *JOURNAL OF MATERIALS SCIENCE* (Vol. 22).
144. Reis, H. R., & Gilsonkhagg, A. (n.d.). Advances in Experimental Medicine and Biology 1250 Biomimicked Biomaterials Advances in Tissue Engineering and Regenerative Medicine. <http://www.springer.com/series/5584>
145. Costa-Pinto, A., Santos, T. C., Neves, N. M., & Reis, R. L. (2016). 30 TESTING NATURAL BIOMATERIALS IN ANIMAL MODELS.
146. Faleris, J. A., Hernandez, R. M. C., Wetzels, D., Dodds, R., & Greenspan, D. C. (2011). In-vivo and in-vitro histological evaluation of two commercially available acellular dermal matrices. *Hernia*, 15(2), 147–156. <https://doi.org/10.1007/s10029-010-0749-x>
147. Bernardi, S., Macchiarelli, G., & Bianchi, S. (2020). Autologous materials in regenerative dentistry: Harvested bone, platelet concentrates and dentin derivatives. In *Molecules* (Vol. 25, Issue 22). MDPI AG. <https://doi.org/10.3390/molecules25225330>
148. Paramitha, D., Ulum, M. F., Purnama, A., Wicaksono, D. H. B., Noviana, D., & Hermawan, H. (2017). Monitoring degradation products and metal ions in vivo. In *Monitoring and Evaluation of*

- Biomaterials and their Performance In Vivo* (pp. 19–44). Elsevier Inc. <https://doi.org/10.1016/B978-0-08-100603-0.00002-X>
149. Hartmann-Fritsch, F., & Biedermann, T. (2019). Murine models for in vivo evaluation of new biomaterials for skin scaffolds. In *Biomaterials for Skin Repair and Regeneration* (pp. 253–295). Elsevier. <https://doi.org/10.1016/B978-0-08-102546-8.00009-1>
150. Jung, O., Hesse, B., Stojanovic, S., Seim, C., Weitkamp, T., Batinic, M., Goerke, O., Kačarević, Ž. P., Rider, P., Najman, S., & Barbeck, M. (2021). Biocompatibility analyses of hf-passivated magnesium screws for guided bone regeneration (Gbr). *International Journal of Molecular Sciences*, 22(22). <https://doi.org/10.3390/ijms222212567>
151. Audouard, E., Rousselot, L., Folcher, M., Cartier, N., & Piguet, F. (2021). Optimized Protocol for Subcutaneous Implantation of Encapsulated Cells Device and Evaluation of Biocompatibility. *Frontiers in Bioengineering and Biotechnology*, 9. <https://doi.org/10.3389/fbioe.2021.620967>
152. Fischer, A. H., Jacobson, K. A., Rose, J., & Zeller, R. (2008). Hematoxylin and eosin staining of tissue and cell sections. *Cold Spring Harbor Protocols*, 3(5). <https://doi.org/10.1101/pdb.prot4986>
153. Barbeck, M., Serra, T., Booms, P., Stojanovic, S., Najman, S., Engel, E., Sader, R., Kirkpatrick, C. J., Navarro, M., & Ghanaati, S. (2017). Analysis of the in vitro degradation and the in vivo tissue response to bi-layered 3D-printed scaffolds combining PLA and biphasic PLA/bioglass components – Guidance of the inflammatory response as basis for osteochondral regeneration. *Bioactive Materials*, 2(4), 208–223. <https://doi.org/10.1016/j.bioactmat.2017.06.001>
154. Hayman, A. (2008). Tartrate-resistant acid phosphatase (TRAP) and the osteoclast/immune cell dichotomy. *Autoimmunity*, 41(3), 218–223. <https://doi.org/10.1080/08916930701694667>
155. Khorramirouz, R., Go, J. L., Noble, C., Jana, S., Maxson, E., Lerman, A., & Young, M. D. (2018). A novel surgical technique for a rat subcutaneous implantation of a tissue engineered scaffold. *Acta Histochemica*, 120(3), 282–291. <https://doi.org/10.1016/j.acthis.2018.02.010>
156. Gao, H., Liu, C., Wu, B., Cui, H., Zhao, Y., Duan, Y., Gao, F., Gu, Q., Wang, H., & Li, W. (2020). Effects of Different Biomaterials and Cellular Status on Testicular Cell Self-Organization. *Advanced Biosystems*, 4(7). <https://doi.org/10.1002/adbi.201900292>

2. Study of biocompatibility of synthetic biomaterials

By nature, synthetic materials are not biocompatible and special treatment or surface functionalization needs to be applied to make them both functional and biocompatible. During the past 50 years, many medical devices made of metal have been replaced by those alloys made of ceramic and polymers. This is due to advances in ceramic and polymer technology, as well as their improved biocompatibility and biofunctionality. Even so, more than 70% of surgical implants and over 95% of orthopedic implants still consist of metal.¹ This is because metal materials have large fracture toughness and durability. Titanium (Ti) and its alloys are widely used in the medical and dental fields because of their corrosion resistance, large specific strength, and high performance. However, there are several disadvantages to using metals as biomaterials with the major one being the lack of biofunctionality. To make metals more biocompatible and biofunctional, surface modifications are necessary.²⁻⁵ This is because merely manufacturing metals through processes such as melting, casting, forging, and heat treatment will not promote biologically adequate qualities. Surface functionalization is a process that alters the surface morphology, structure, and composition, without affecting the bulk mechanical properties. Additionally, arising problem of antimicrobial resistance as well surgical secondary infections due to implantations raise a call for development of surfaces with bactericidal properties. A variety of surface treatment techniques have been investigated however most can lead to a raise in bacterial resistance, which may ultimately lead to the birth of superbacteria (i.e. bacteria resistant to known antibiotics). Recently the idea of mimicking cicada or dragonfly wings was brought to light. These surfaces contain nanoscale structures which have mechanical bactericidal properties, opposed to traditional chemical-based approaches. In principle this new approach may counter the formation of biofilms as well as bypass bacteria drug resistance.

In order to investigate and understand how different functionalization strategies of surfaces (polystyrene, silicon, and titanium) affect mammalian cell response *in vitro* and *in vivo* studies were performed. In particular, protein adsorption to black silicon (BSi), a silicon-based nanostructured surface, was investigated to determine the effect of the nanoscale topography on protein adsorption. The effects of protein coating to promote cell attachment and differentiation were also studied using PC12 cells. *In vitro* and *in vivo* studies were performed on BSi to assess its biocompatibility while still displaying bactericidal properties. Additionally, a similar surface topography has been applied to titanium in order to improve the cellular response.

References

1. Hanawa, T. (2019). Titanium-tissue interface reaction and its control with surface treatment. *In Frontiers in Bioengineering and Biotechnology* (Vol. 7, Issue JUL). Frontiers Media S.A. <https://doi.org/10.3389/fbioe.2019.00170>
2. Variola, F., Vetrone, F., Richert, L., Jedrzejowski, P., Yi, J. H., Zalzal, S., Clair, S., Sarkissian, A., Perepichka, D. F., Wuest, J. D., Rosei, F., & Nanci, A. (2009). Improving biocompatibility of implantable metals by nanoscale modification of surfaces: An overview of strategies, fabrication methods, and challenges. *In Small* (Vol. 5, Issue 9, pp. 996–1006). <https://doi.org/10.1002/sml.200801186>
3. Luo, J., Walker, M., Xiao, Y., Donnelly, H., Dalby, M. J., & Salmeron-Sanchez, M. (2022). The influence of nanotopography on cell behaviour through interactions with the extracellular matrix – A review. *In Bioactive Materials* (Vol. 15, pp. 145–159). KeAi Communications Co. <https://doi.org/10.1016/j.bioactmat.2021.11.024>
4. Dalby, M. J., Gadegaard, N., & Oreffo, R. O. C. (2014). Harnessing nanotopography and integrin-matrix interactions to influence stem cell fate. *Nature Materials*, 13(6), 558–569. <https://doi.org/10.1038/nmat3980>
5. Donnelly, H., Dalby, M. J., Salmeron-Sanchez, M., & Sweeten, P. E. (2018). Current approaches for modulation of the nanoscale interface in the regulation of cell behavior. *In Nanomedicine: Nanotechnology, Biology, and Medicine* (Vol. 14, Issue 7, pp. 2455–2464). Elsevier Inc. <https://doi.org/10.1016/j.nano.2017.03.020>
6. Linklater, D. P., Juodkasis, S., & Ivanova, E. P. (2017). Nanofabrication of mechano-bactericidal surfaces. *In Nanoscale* (Vol. 9, Issue 43, pp. 16564–16585). Royal Society of Chemistry. <https://doi.org/10.1039/c7nr05881k>
7. Linklater, D. P., Baulin, V. A., Juodkasis, S., Crawford, R. J., Stoodley, P., & Ivanova, E. P. (2021). Mechano-bactericidal actions of nanostructured surfaces. *In Nature Reviews Microbiology* (Vol. 19, Issue 1, pp. 8–22). Nature Research. <https://doi.org/10.1038/s41579-020-0414-z>

2.1. Adsorption of Human Plasma Albumin and Fibronectin onto Nanostructured Black Silicon Surfaces

Langmuir, **2016**, 32(41), 10744–10751.

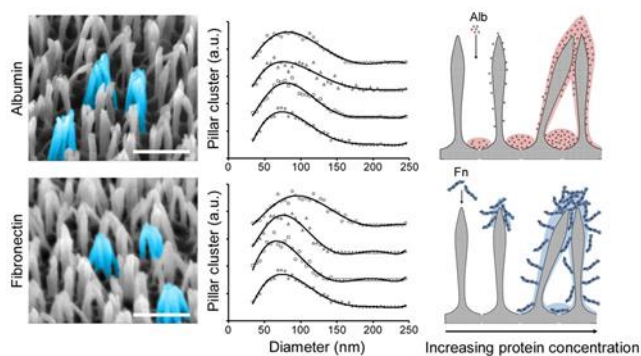
Nguyen, D. H. K.^a, Pham, V. T. H.^a, Al Kobaisi, M.^a, Bhadra, C.^a, **Orłowska, A.**^b, Ghanaati, S.^b, Manzi, B. M.^c, Baulin, V. A.^c, Joudkazis, S.^a, Kingshott, P., Crawford, R. J.^d, & Ivanova, E. P.^a

^a Department of Chemistry and Biotechnology, Faculty of Science, Engineering and Technology, Swinburne University of Technology, Hawthorn VIC 3122, Australia

^b Frankfurt Orofacial Regenerative Medicine, University Hospital Frankfurt, Theodor-Stern-Kai 7, D-60590 Frankfurt am Main, Germany

^c Department d'Enginyeria Química, Universitat Rovira i Virgili, 26 Av. dels Paisos Catalans, 43007 Tarragona, Spain

^d School of Science, College of Science, Engineering and Health, RMIT University, Melbourne VIC 3001, Australia



3.2.1 Abstract

The protein adsorption of two human plasma proteins, albumin (Alb) and fibronectin (Fn) onto synthetic nanostructured bactericidal material, black silicon (bSi) surfaces (that contain an array of nanopillars) and silicon wafer (non-structured) surfaces, were investigated. The adsorption behavior of Alb and Fn onto two types of substrata were studied using a combination of complementary analytical techniques. A two-step Alb adsorption mechanism onto the bSi surface has been proposed. At low bulk concentrations (below 40 $\mu\text{g/mL}$), the Alb preferentially adsorbed at the base of the nanopillars. At higher bulk concentrations, the Alb adsorbed on the top of the nanopillars. In the case of Fn, the protein preferentially adsorbed on the top of the nanopillars, irrespective of its bulk concentration.

3.2.1 Introduction

The interactions of proteins with nanostructured biomaterials have been in focus of intensive research for several years.¹⁻⁵ High aspect ratio nanostructured surfaces have been utilized in various applications such as drug delivery systems,⁶⁻⁷ biosensors,⁸⁻⁹ cell guidance¹⁰⁻¹¹ and in the construction of antibacterial biomaterials.¹²⁻¹⁴ When an implantable material is introduced into the host, a conditioning film of adsorbed plasma proteins is instantaneously formed on its surface.¹⁵⁻¹⁷ This protein layer may either stimulate the repair of the wound, cell adhesion and tissue integration, or trigger the clotting of blood, or initiate a severe inflammatory response and the subsequent isolation of the implanted material.¹⁶⁻¹⁹ In some instances, an enhanced degree of protein adsorption has been observed on these nanostructured surfaces, however there have been some inconsistencies in the reported results. For example, Hammarin *et al.* showed that laminin, a component of the extracellular matrix, could trigger the formation of cellular focal adhesions.²⁰ This resulted in a four-fold increase in the adsorption of laminin onto gallium phosphide nanostructured surfaces containing nanowires compared to that obtained on flat gallium phosphide control surfaces. Kim *et al.* reported that the adsorption of bovine serum albumin, IgG and fibronectin increased 1.2 – 3 times depending on the proteins, on nanopillar structured polyethylene glycol (PEG) surfaces compared to that observed on the non-structured PEG control surfaces.²¹ Whereas, a series of titanium films containing different grain sizes at nanoscale roughness (root mean square roughness, Sq) ranging from 2 nm to 21 nm has been shown to have no statistically significant difference on either bovine serum albumin or human plasma fibrinogen adsorption.²²

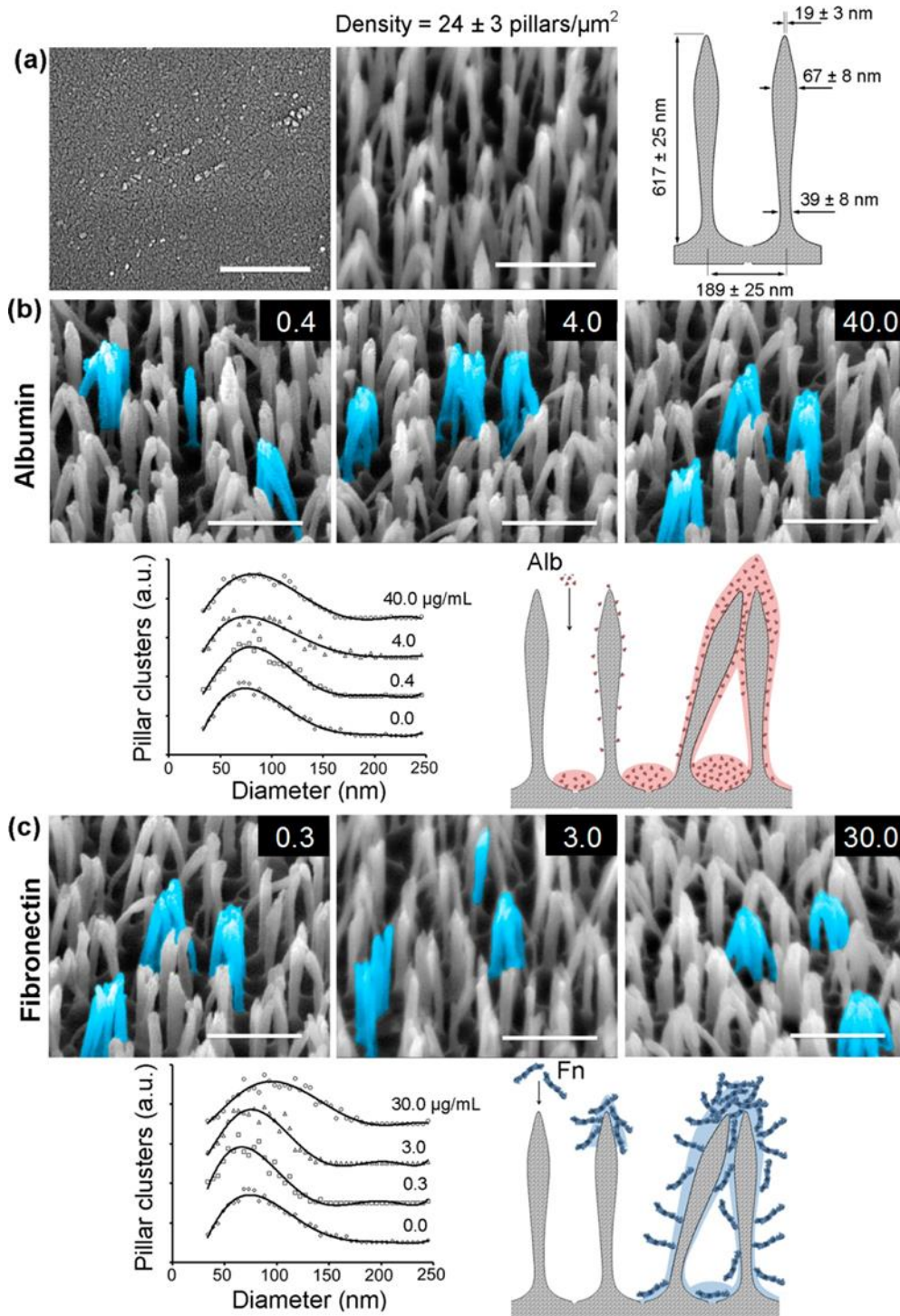


Figure 1. Visualization of black silicon (bSi) with adsorbed proteins after 1 h of interaction. (a) Surface of flat control silicon wafer and nanopillar bSi after 1 h incubation with PBS solution ($0 \mu\text{g/mL}$ protein concentration), and the typical dimension and spacing of the nanopillar structure of bSi surface. Typical 45° tilted SEM images of bSi interacted with (b) albumin (Alb) at concentrations of 0.4 , 4.0 , and $40.0 \mu\text{g/mL}$, and with (c) fibronectin (Fn) at concentrations of 0.3 , 3.0 , and $30.0 \mu\text{g/mL}$. The pillar clusters were highlighted by false color for comparison. The corresponding distributions of nanopillar clusters were presented to indicate the changes in the cluster size (diameter) as the concentrations of proteins increase. A stepwise adsorption behavior was also proposed for each of the protein when interacting on bSi surface at different concentrations. Scale bar = 500 nm .

Despite several excellent papers being published on this topic,²³⁻²⁵ the interaction of plasma proteins with nanostructured surfaces is not fully understood due to the complex interplay of chemical and physical interactions taking place when these proteins come into contact with the liquid-solid interface.^{22-23,26-28} This study aimed to investigate the adsorption behavior of two plasma proteins, fibronectin and albumin, on the surface of nanostructured black silicon (bSi). Fibronectin is the extracellular matrix protein responsible for cell adhesion and wound healing,²⁹⁻³⁰ and albumin is one of the most abundant proteins found in blood plasma.^{18,31} Black silicon is a high aspect ratio nanostructured surface, which has recently been reported to possess broad spectrum antibacterial behavior that arises from the surface having the ability to mechanically rupture any bacterial cells coming into contact with its surface, leading to their death.¹⁴ This type of mechano-bactericidal surface is an attractive alternative for existing biomaterial surfaces, as it allows the surface to eliminate bacterial contamination. Therefore, studying the human plasma protein adsorption on such potential topography is necessary to understand the role that this adsorption plays in medical implant application. Here, we comparatively analyzed the protein specific adsorption of human serum albumin and fibronectin onto nanostructured black silicon surfaces. In order to clarify the adsorption patterns of the Alb and Fn proteins, a combination of complementary analytical techniques was employed; AFM was used to perform an extended surface roughness analysis, Raman spectroscopy was used for surface characterization, XPS was used for protein quantification, and AFM with SEM were applied for visualization and topographical analysis of the protein adsorption.

3.2.2 Experimental

Surface fabrication

A 100 mm diameter silicon wafer (Atecom Ltd, Taiwan), possessing a thickness of $525 \mu\text{m} \pm 25 \mu\text{m}$ and a particular resistivity of $10\text{-}20 \Omega \text{ cm}^{-1}$, was subjected to reactive ion etching (RIE) using SF_6 and O_2 over five minutes to produce the black silicon (bSi) using an Oxford PlasmaLab 100 ICP380 instrument (Oxford Instruments, Concord, MA, USA) as described elsewhere.^{14, 32} Each bSi and 'as-received' silicon control surface wafer was cut into 1.0 cm^2 squares and sterilized using a 70% ethanol solution prior to each experiment.

Protein adsorption

Human plasma fibronectin (Fn) and albumin (Alb) were obtained from Invitrogen and Sigma-Aldrich, respectively. The protein solutions were prepared in sterile 10 mM phosphate buffered saline (PBS, pH 7.4) at the concentrations of 0.3, 3.0, 30.0 $\mu\text{g}/\text{mL}$ for Fn and 0.4, 4.0, 40.0 $\mu\text{g}/\text{mL}$ for Alb. The bSi samples were placed into contact with these protein solutions by immersing them into 300 μL volumes of the protein solution at each concentration and allowed to incubate for one hour at 37 °C. The samples were then washed with copious quantities of MilliQ water to remove any unbound protein molecules prior to further analysis. The final results were derived from the average of at least three independent experiments, with two technical replicates being performed for each experiment.

Raman spectroscopy

Detection of air, which may be trapped within the nanopillar-structured surface of the bSi, was performed using a Raman micro-spectrometer (WiTEC, Ulm, Germany) with a laser wavelength of 532 nm ($h\nu = 2.33$ eV). A water-immersion 60 \times magnification objective lens (numerical aperture = 0.9) was employed to map the homogeneity of the water distribution over the middle-top plane of the bSi nanopillars, located 200 nm from the base of the pillars. A grid of 100 spectra \times 100 spectra was acquired for a 2 $\mu\text{m} \times 10 \mu\text{m}$ scanning area, with an integration time of 0.2255 s per spectrum. Scanning was conducted after the bSi samples had been allowed a period of one hour of contact with the water at room temperature.

Scanning electron microscopy (SEM) and image analysis

High resolution SEM images were obtained at 3 kV under 50,000 \times , 100,000 \times and 200,000 \times magnification at three different angles, including top view, 45° tilted view and a 90° tilted view using a ZEISS SUPRA 40VP field-emission scanning electron microscope (Carl Zeiss NTS GmbH, Oberkochen, BW, Germany). A quantitative morphological analysis was carried out with top-viewed images at 50,000 \times and 100,000 \times magnification using ImageJ software ver. 1.61 (<http://imagej.nih.gov/ij>). The threshold in the SEM images was altered to portray the boundary of the nanopillars and their clusters at the uppermost plane, the location at which the protein came into contact with the surface of the BSi. A particle analyser plugin was utilized to estimate the size and distribution of clusters within a specific population.

X-ray photoelectron spectroscopy (XPS)

XPS analysis was performed using a Thermo Scientific™ K-alpha X-ray Photoelectron Spectrometer (ThermoFischer™), equipped with a monochromatic X-ray source (Al K α , $h\nu = 1486.6$ eV) operating at 150 W. The spectrometer energy scale was calibrated using the Au 4f_{7/2} photoelectron peak at a binding energy (E_B) of 83.98 eV. During analysis, the samples were flooded with low-energy electrons to counteract any surface charging that may take place. The hydrocarbon component of the C 1s peak (binding energy 285.0 eV) was used as a reference for charge correction. Photoelectrons emitted at 90° to the surface from an area of 700 $\mu\text{m} \times 300 \mu\text{m}$ were analyzed with 160 eV for survey spectra and then with 20 eV for region spectra. Survey spectra were recorded at 1.0 eV/step, while the region spectra were taken at 0.1 eV/step. The Shirley algorithm was used to measure the background core level spectra and chemically distinct species in the high-resolution regions of the spectra were resolved using synthetic Gaussian–Lorentzian components after the background was removed (using the Thermo Scientific™ Avantage Data System). The relative atomic concentration of elements determined using XPS was quantified on the basis of the peak area in the selected high resolution region, with the appropriate sensitivity factors for the instrument being used. High resolution scans were performed across each of the nitrogen 1s and silicon 2p_{3/2} and _{1/2} peaks.

Atomic force microscopy (AFM)

The surface topography of the bSi (both with and without adsorbed protein) was examined by using an Innova® atomic force microscope (AFM) (Bruker, USA). The tapping mode of analysis was employed for all samples, and all experiments were conducted under ambient temperature conditions using a phosphorus doped silicon probe (MPP- 31120-10, Bruker, USA). AFM scans obtained from 10 $\mu\text{m} \times 10 \mu\text{m}$ surface areas were processed using Gwyddion software (available at www.gwyddion.net).³³ A set of roughness parameters, including arithmetic average height, also known as average roughness (S_a), root mean square deviation from the mean plane (S_q), maximum roughness (S_{max}), skewness (S_{skw}), kurtosis (S_{kur}), mean of maximum peak to valley height (S_{tm}) and average wavelength (λ_a) was determined, as described elsewhere.³⁴

Statistical analysis

The data were statistically analyzed using one-way ANOVA using the SPSS 16.0.1 software (SPSS Inc., Chicago, IL, USA). Statistically significant differences were considered if p-values were less than 0.05 (* $p < 0.05$).

3.2.4 Results and discussion

Surface topology of bSi

The adsorption of two human plasma proteins onto nanopatterned black silicon surfaces was studied. bSi surfaces are composed of a disordered array of hierarchical nanopillars (Figure 1a). The nanopillars existed as random single pillars or in small clusters, such as dimers or trimers. The upper part of the nanopillars have a conical shape, with the tip being approximately 19 nm wide, and the diameter of the middle and base being typically 67 nm and 39 nm, respectively. The average length of the nanopillars is approximately 617 nm and the pillar density was approximately 24 pillars/ μm^2 . The average distance between adjacent pillars was 185 nm, with no preferential orientation. The detailed physicochemical properties of the black silicon surfaces, comprising surface chemical composition, surface hydrophobicity and surface crystallinity, have been reported elsewhere.^{14, 35} The surface geometry of the bSi, including the pillar cluster distribution and the average frequency of adjacent nanopillars, were as previously described.³²

Detection of micro/nano air bubbles trapped within the nanopillars

In order to determine the adsorption behavior of the proteins as a function of the surface area of the bSi, it was important to determine the surface area of the bSi that was exposed to the aqueous solution. Any trapped air in the form of micro-/nano-bubbles within the nanopillars on the bSi surface would reduce the surface area³⁶⁻³⁷ that was available for protein adsorption. A depth Raman spectroscopic analysis of a bSi sample immersed in water showed that homogenous spreading of the water took place over the surface, filling the interspace between pillars, clearly indicating the absence of entrapped air (Figure S1). If micro- or nano-air bubbles had been retained on the bSi surface after it was immersed in water, they would have been visible when mapping the distribution of the O-H bonds on the surface (being part of the water phase) using Raman spectroscopy, with a significant reduction in the O-H peak intensity being observed when bubbles were present on the surface.³⁷⁻³⁹ No such reduction was observed, and hence the total bSi surface area was available for protein adsorption.

SEM visualization and image analysis of the proteins adsorbed onto the bSi substrata

Typical SEM images, together with analysis of the nanopillar distribution with adsorbed Alb and Fn, are presented in Figure 1b and 1c. It can be seen that pillar clustering took place upon Alb adsorption, with the clusters being an average size of approximately 83 ± 3.5 nm for

each of the different protein concentrations. In contrast, a shift in the nanopillar clustering was observed during Fn adsorption with an increasing cluster size being observed as the bulk protein concentration levels were increased. At a concentration of 0.3 $\mu\text{g}/\text{mL}$, the greatest number of clusters appeared, with a diameter of approximately 70 nm. This value slightly increased to 108 nm when a concentration of 3 $\mu\text{g}/\text{mL}$ of fibronectin was applied, rising to approximately 129 nm when the highest applied fibronectin concentration of 30 $\mu\text{g}/\text{mL}$ was applied.

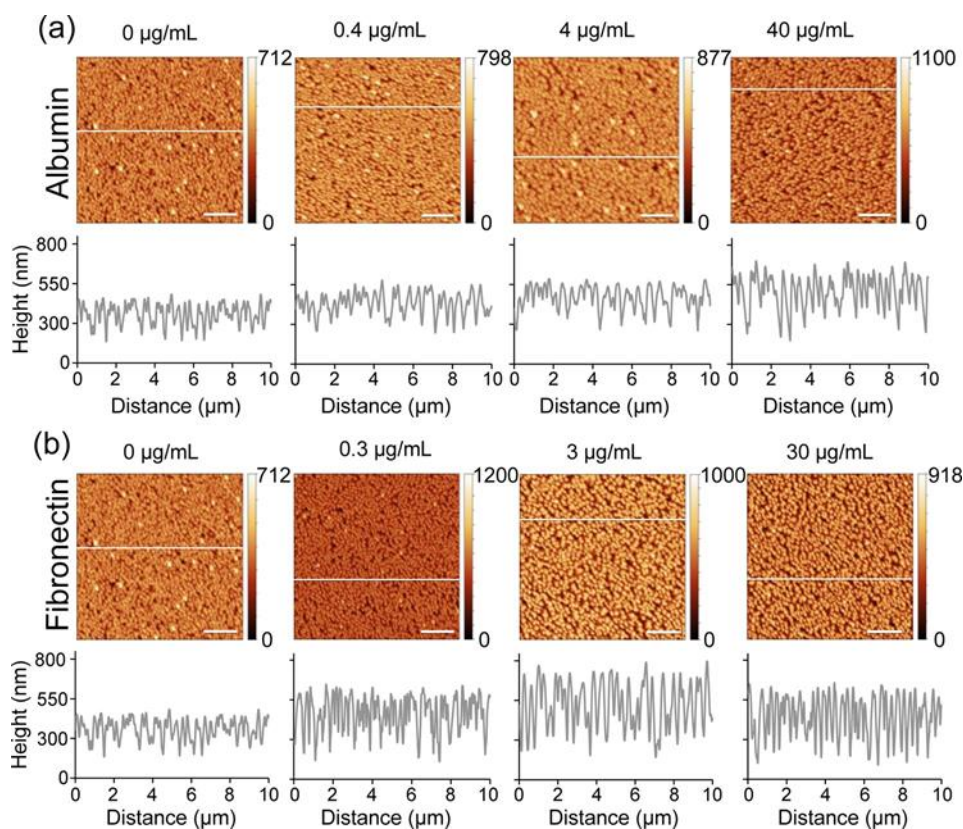


Figure 2. Atomic force microscopy (AFM) images of bSi surfaces with adsorbed proteins after 1 h of interaction. Each image represented a $10\ \mu\text{m} \times 10\ \mu\text{m}$ scanning area with a typical surface line profile of bSi interacted with (a) albumin (Alb) at concentrations of 0, 0.4, 4.0, and 40.0 $\mu\text{g}/\text{mL}$ and (b) fibronectin (Fn) at concentrations of 0, 0.3, 3.0, and 30.0 $\mu\text{g}/\text{mL}$. Scale bar = 2.0 μm . False color scale bar is shown in units of nm.

AFM analysis of the changes in bSi surface topography as the adsorption of proteins

An AFM surface roughness analysis showed that the average roughness of the bSi surface was 58.8 nm. With increased levels of protein adsorption, the surface roughness gradually increased. For example, the average roughness (S_a), of the surface increased from 64 nm to 115 nm for Alb and from 84 nm to 113 nm for the increasing bulk protein concentrations of Fn (as shown in Figure 1b and c, Figure 2 and Table 1). An analysis of the other typical surface roughness parameters revealed a similar trend, the results of which are presented in Table S1. Despite being recognized as the most commonly used surface roughness parameter, the average roughness alone is not sufficient to describe the amplitudinal variations of a surface; it is

common for two surfaces to have very different surface structures but exhibit identical S_a values.⁴⁰⁻⁴² Two complementary surface parameters are the ‘mean of maximum peak to valley height’ (S_{tm}) and the ‘average wavelength’ (λ_a). These parameters were employed to allow a more detailed surface characterization to be undertaken. S_{tm} is the mean of the maximum peak to valley heights measured within the length of a profile; in this case, any change in the S_{tm} would provide information regarding the location of adsorbed protein, whether it is on the tips of the pillars (increasing the S_{tm}) or in the valley between the nanopillars (decreasing the S_{tm}). Another parameter, λ_a is the average spacing between the local peaks and valleys, which is taking into account the relative amplitudes and individual spatial frequencies. Any change in this parameter would imply the presence of a possible build-up of adsorbed proteins along the nanopillars. An AFM analysis of S_{tm} and λ_a parameters confirmed that the adsorption behavior of the albumin on the bSi surface was dissimilar to that observed for the fibronectin.

Table 1. Statistical Analysis of the Black Silicon (bSi) Surface Topography, as a Function of the Initial Applied Protein Concentrations, Including the Control bSi Sample with PBS, Starting at 0.0 $\mu\text{g/mL}$

	protein concentration ($\mu\text{g/mL}$)	arithmetic average height, S_a (nm)	mean of maximum peak-to-valley height, S_{tm} (nm)	average wavelength, λ_a (nm)
PBS	0.0	58.8 \pm 7.7	149.9 \pm 33.8	160.7 \pm 26.3
albumin	0.4	64.4 \pm 14.3	106.3 \pm 33.5	189.3 \pm 7.0
	4.0	72.4 \pm 18.5	101.7 \pm 19.4	164.2 \pm 18.1
	40.0	115.4 \pm 16.7	215.9 \pm 38.6	154.7 \pm 13.6
fibronectin	0.3	83.7 \pm 6.9	235.8 \pm 23.6	160.0 \pm 7.6
	3.0	118.8 \pm 6.1	236.3 \pm 42.3	177.3 \pm 13.3
	30.0	113.0 \pm 4.6	247.8 \pm 30.7	172.7 \pm 7.0

XPS analysis of adsorbed proteins

Adsorption of Alb and Fn from the bulk protein solutions of concentration 0.4, 4.0, 40.0 $\mu\text{g/mL}$ and 0.3, 3.0, 30.0 $\mu\text{g/mL}$, respectively, was analyzed according to the XPS data (Figure 3 and Table 2) based on the amount of nitrogen retained on the bSi.⁴³ Both proteins were found to be equally weakly absorbed from low bulk concentrations on both the bSi and control silicon surfaces. Similar results were reported for glass (flat) surfaces, bare silica and the hydrophobic surface of self-assembled mono-layers (SAMs).⁴⁴⁻⁴⁶

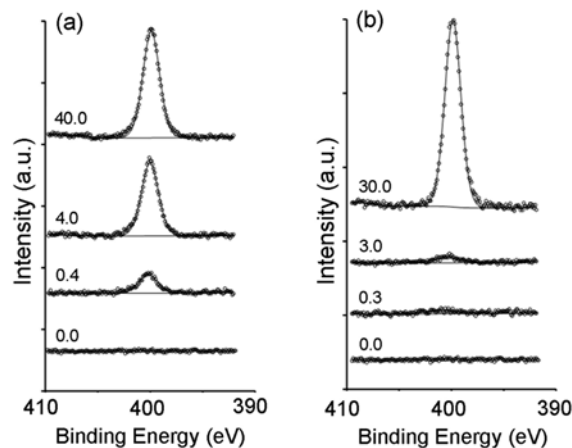


Figure 3. XPS spectra showing the elemental nitrogen (N 1s) present on bSi after the adsorption of (a) albumin (at 0.0, 0.4, 4.0, and 40.0 $\mu\text{g}/\text{mL}$) and (b) fibronectin (0.0, 0.3, 3.0, and 30.0 $\mu\text{g}/\text{mL}$).

With increasing bulk protein concentration, the level of Alb adsorption onto the bSi surfaces increased in comparison to that observed on the control silicon surfaces; with the converse being observed for the Fn adsorption experiments. After one hour of incubation, the amount of protein that had adsorbed onto the bSi substrate was found to be less than that observed on the flat silicon wafer substrate, despite the substantially greater bSi substrate surface area. This phenomenon can be attributed to a change in the conformation of the protein, which caused the protein molecules to occupy a greater surface area per molecule within a specific time frame. This increased conformational surface area would effectively mask the influence of the increased surface area, leading to a lower than expected protein surface coverage being observed. This effect has been previously reported for Fn adsorption onto rough tantalum surfaces.⁴⁶

The attachment behaviour of the two proteins investigated in this study was found to be protein-specific, as shown in Table 2. With increasing bulk concentrations, the amount of Alb that was adsorbed onto the surface incrementally increased. The Fn displayed rather poor adsorption under low bulk concentration conditions on the bSi substrate in particular, while at the higher bulk concentration of 30.0 $\mu\text{g}/\text{mL}$, the surface coverage was found to increase substantially. This result is in agreement with a previous report, which indicated that Fn adsorption on hydroxyapatite significantly increased with increased bulk concentration.⁴⁷ It was suggested by these authors that under high Fn concentrations, the process of fibril self-assembly to form a dense network was induced, resulting in higher levels of protein adsorption.⁴⁷

Table 2. XPS Elemental Data, Given in Terms of Atomic Percentagea of C, O, Si, and N, on bSi and Si Wafer Surfaces after One Hour of Protein Incubation

	protein concentration ($\mu\text{g}/\text{mL}$)	at. % C	at. % O	at. % Si	at. % N
Black Silicon (bSi)					
PBS	0.0	9.5 ± 1.9	40.9 ± 0.8	49.4 ± 1.5	<dl ^b
albumin	0.4	9.4 ± 0.4	39.0 ± 1.6	51.2 ± 1.2	0.5 ± 0.1
	4.0	12.7 ± 0.7	37.3 ± 0.2	48.3 ± 0.7	1.7 ± 0.2
	40.0	25.0 ± 0.1	31.1 ± 3.2	39.3 ± 0.1	4.6 ± 0.1
fibronectin	0.3	8.4 ± 0.7	40.7 ± 1.6	50.5 ± 1.0	0.4 ± 0.1
	3.0	11.4 ± 1.2	38.5 ± 0.1	49.3 ± 1.3	0.8 ± 0.2
	30.0	31.8 ± 0.7	27.5 ± 3.0	33.5 ± 1.4	7.3 ± 0.4
Silicon Wafer					
PBS	0.0	5.2 ± 0.8	29.5 ± 0.3	65.4 ± 1.1	<dl ^b
albumin	0.4	6.8 ± 0.4	31.4 ± 0.7	61.2 ± 0.2	0.8 ± 0.1
	4.0	9.9 ± 1.8	30.5 ± 0.1	57.9 ± 2.3	1.8 ± 0.4
	40.0	11.8 ± 2.8	30.9 ± 0.2	55.1 ± 3.3	2.3 ± 0.6
fibronectin	0.3	5.7 ± 1.1	31.8 ± 0.3	62.6 ± 1.5	<dl ^b
	3.0	8.7 ± 0.4	32.1 ± 0.4	57.9 ± 0.1	1.4 ± 0.2
	30.0	21.9 ± 3.3	27.2 ± 0.3	45.6 ± 3.8	5.4 ± 0.8

Step-wise Alb attachment onto the BSi surface

Statistical analysis of the surface roughness topographical parameters obtained from AFM scans showed that the S_{tm} value of the BSi in the absence of protein adsorption was 150 nm (Table 1). When exposed to the lowest bulk concentration of Alb (0.4 $\mu\text{g}/\text{mL}$), the S_{tm} reduced to 106 nm, implying a decreased distance between the tip of the pillar and the valley, thus suggesting that the Alb was most likely being deposited in the valley areas between the nanopillars. This scenario was supported by the changes observed in the λ_a parameter, which increased from 160 nm (BSi without protein) to 189 nm when exposed to a bulk Alb concentration of 0.4 $\mu\text{g}/\text{mL}$, indicating that the slope of the peaks had decreased as a result of the Alb preferentially adsorbing onto the valley sections between nanopillars. Alb has the ability to adopt various conformations when interacting with a surface.^{42, 48} The observed Alb adsorption behavior on the bSi is similar to previously reported theoretical prediction of adsorption behavior for lysozyme.⁴⁹⁻⁵² In this theory, it was stipulated that the preferential adsorption of small globular proteins, such as lysozyme, on curved surfaces occurs as a consequence of increased levels of contact area being present on concave surfaces, which in turn increases the interaction forces existing between the protein and the surface, resulting in a greater level of perturbation of the protein secondary structure.⁴⁹⁻⁵² Recently, it was reported that lysozyme preferentially adsorbs onto concave gold nanoparticle surfaces by undergoing a

greater internal structural change than occurs in the presence of both flat and convex gold surfaces.⁵³

Since the values of S_{tm} and λ_a were similar for Alb adsorption from both 0.4 and 4.0 $\mu\text{g/mL}$ bulk concentration (Table 1), it could be suggested that adsorption patterns at these two concentrations would be similar. When the concentration was increased to 40.0 $\mu\text{g/mL}$, however, the S_{tm} significantly increased to 216 nm, indicating that the Alb preferentially adsorbed onto the top of the nanopillars rather in the sessions between the nanopillars. Here, the λ_a decreased, most likely due to the consequential increase in the peak slope. This switch in the adsorption pattern of Alb compared to that of Fn could be considered in light of the two-step adsorption model for lysozyme adsorption proposed by Elter *et al.*⁵⁴ In this work it was shown that in the first stage of adsorption, the small globular protein would preferentially adsorb at the convex edges of the nano-structured surface since these edges afford the protein greater accessibility and increased electrostatic forces (Schematic illustration presented in Figure 1b). In the second step, proteins migrated via surface diffusion into the concave corners of the surface, or the inner space, where they were stabilized by higher dispersion interactions.⁵⁴

Fn attachment on bSi surfaces

In contrast to Alb, Fn was most likely preferentially adsorbed onto the top of the nanopillars present on the bSi (Figures 1c) even at the lowest protein bulk concentration of 0.3 $\mu\text{g/mL}$, as inferred from the increased S_{tm} value of 236 nm (indicating an increased distance between the peaks and valleys). Both the S_{tm} and λ_a parameters reached a plateau when the bulk concentration was increased to 30.0 $\mu\text{g/mL}$ (Table 1). This result suggested that the Fn was adsorbing and forming layers after the initial deposition took place at the top of the nanopillars (Schematic illustration presented in Figure 1c), resulting in an unchanging peak-to-valley distance and average spacing between pillar clusters, as confirmed by the AFM data. A similar attachment pattern for bovine Fn was reported on the polymeric nanostructured surfaces, with the attachment pattern being attributed to the variation in surface energy being present along the nanostructure, as reported by Kim *et al.*²¹ Thus, it is likely that at low protein bulk concentrations, the fibre-like large (440 kDa, 120 nm in length and 2 nm in diameter^{45, 55-56}) molecules of Fn were readily adsorbed on the upper part of the nanopillars, whereas smaller globular albumin (66.5 kDa, a native ellipsoidal shape of 14.1 nm \times 4.1 nm was reported⁵⁷⁻⁵⁹) would have preferentially attached to the concave sections between the nanopillars.^{18, 31, 60} At increased protein concentrations, both proteins were found to adsorb onto the top of the bSi nanopillars.

3.2.5 Conclusions

The data reported in this study clearly demonstrated that the adsorption pattern of two human plasma proteins (Alb and Fn) on the surface of bSi was different and a function of the bulk protein concentration. Overall, both proteins adsorbed to a greater extent on the non-structured silicon wafers than the nanostructured bSi surfaces at low concentrations. This mechanism involved the efficiency of protein molecule occupation on rough surface like bSi than Si wafer. A step-wise mechanism for Alb adsorption onto the bSi surface was proposed; at low bulk concentrations up to 40.0 µg/mL, the Alb preferentially adsorbed onto the surface in the valleys between nanopillars. At bulk protein concentrations above 40.0 µg/mL, the Alb preferentially adsorbed onto the top of the nanopillars. The Fn was found to preferentially adsorb onto the top of the nanopillars, independent of the bulk protein concentration. With increasing levels of protein adsorption taking place at the top of the nanopillars, an increased amount of nanopillar clustering was observed as a result of the increased protein concentration at that location. In this case, the inter-pillar space was not filled with proteins, despite the inter-pillar space being filled with water. Further work is underway to investigate this phenomenon and to identify the bulk protein concentrations required to achieve saturation of the bSi surface.

3.2.6 Acknowledgments

VB, BM and EI acknowledge funding from Marie Curie Actions under EU FP7 Initial Training Network SNAL 608184. Authors gratefully acknowledge the RMIT Microscopy and Microanalysis Facility (RMMF) for providing access to the characterization instruments. DHKN is the recipient of Swinburne University Postgraduate Research Award (SUPRA).

3.2.7 References

1. Rabe, M.; Verdes, D.; Seeger, S. Understanding Protein Adsorption Phenomena at Solid Surfaces. *Adv. Colloid Interface Sci.* **2011**, 162 (1–2), 87-106.
2. Stevens, M. M.; George, J. H. Exploring and Engineering the Cell Surface Interface. *Science* **2005**, 310 (5751), 1135-1138.
3. Khang, D.; Kim, S. Y.; Liu-Snyder, P.; Palmore, G. T. R.; Durbin, S. M.; Webster, T. J. Enhanced Fibronectin Adsorption on Carbon Nanotube/Poly(Carbonate) Urethane: Independent Role of Surface Nano-Roughness and Associated Surface Energy. *Biomaterials* **2007**, 28 (32), 4756-4768.

4. Gray, J. J. The Interaction of Proteins with Solid Surfaces. *Curr. Opin. Struct. Biol.* **2004**, 14 (1), 110-115.
5. Roach, P.; Farrar, D.; Perry, C. C. Interpretation of Protein Adsorption: Surface-Induced Conformational Changes. *J. Am. Chem. Soc.* **2005**, 127 (22), 8168-8173.
6. McAllister, D. V.; Wang, P. M.; Davis, S. P.; Park, J. H.; Canatella, P. J.; Allen, M. G.; Prausnitz, M. R. Microfabricated Needles for Transdermal Delivery of Macromolecules and Nanoparticles: Fabrication Methods and Transport Studies. *Proc. Natl. Acad. Sci. U. S. A.* **2003**, 100 (24), 13755-13760.
7. Park, J. H.; Allen, M. G.; Prausnitz, M. R. Biodegradable Polymer Microneedles: Fabrication, Mechanics and Transdermal Drug Delivery. *J. Control. Release* **2005**, 104 (1), 51-66.
8. Engel, Y.; Elnathan, R.; Pevzner, A.; Davidi, G.; Flaxer, E.; Patolsky, F. Supersensitive Detection of Explosives by Silicon Nanowire Arrays. *Angew. Chem. Int. Edit.* **2010**, 49 (38), 6830-6835.
9. Krivitsky, V.; Hsiung, L.-C.; Lichtenstein, A.; Brudnik, B.; Kantaev, R.; Elnathan, R.; Pevzner, A.; Khatchourints, A.; Patolsky, F. Si Nanowires Forest-Based On-Chip Biomolecular Filtering, Separation and Preconcentration Devices: Nanowires Do it All. *Nano Lett.* **2012**, 12 (9), 4748-4756.
10. Baranes, K.; Chejanovsky, N.; Alon, N.; Sharoni, A.; Shefi, O. Topographic Cues of Nano-Scale Height Direct Neuronal Growth Pattern. *Biotechnol. Bioeng.* **2012**, 109 (7), 1791-1797.
11. Piret, G.; Perez, M. T.; Prinz, C. N. Neurite Outgrowth and Synaptophysin Expression of Postnatal CNS Neurons on GaP Nanowire Arrays in Long-Term Retinal Cell Culture. *Biomaterials* **2013**, 34 (4), 875-887.
12. Hasan, J.; Raj, S.; Yadav, L.; Chatterjee, K. Engineering a Nanostructured "Super Surface" with Superhydrophobic and Superkilling Properties. *RSC Adv.* **2015**, 5 (56), 44953-44959.
13. Serrano, C.; García-Fernández, L.; Fernández-Blázquez, J. P.; Barbeck, M.; Ghanaati, S.; Unger, R.; Kirkpatrick, J.; Arzt, E.; Funk, L.; Turón, P.; del Campo, A. Nanostructured Medical Sutures with Antibacterial Properties. *Biomaterials* **2015**, 52 (1), 291-300.
14. Ivanova, E. P.; Hasan, J.; Webb, H. K.; Gervinskis, G.; Juodkasis, S.; Truong, V. K.; Wu, A. H. F.; Lamb, R. N.; Baulin, V. A.; Watson, G. S.; Watson, J. A.; Mainwaring, D. E.; Crawford, R. J. Bactericidal Activity of Black Silicon. *Nat. Commun.* **2013**, 4, 2838.
15. Anderson, J. M. Biological Responses To Materials. *Annu. Rev. Mater. Res.* **2001**, 31 (1), 81-110.

16. Puleo, D. A.; Nanci, A. Understanding and Controlling the Bone–Implant Interface. *Biomaterials* **1999**, *20* (23–24), 2311-2321.
17. Wilson, C. J.; Clegg, R. E.; Leavesley, D. I.; Pearcy, M. J. Mediation of Biomaterial-Cell Interactions by Adsorbed Proteins: A Review. *Tissue Eng.* **2005**, *11* (1-2), 1-18.
18. Hindié, M.; Camand, E.; Agniel, R.; Carreiras, F.; Pauthe, E.; Van Tassel, P. Effects of Human Fibronectin and Human Serum Albumin Sequential Adsorption on Preosteoblastic Cell Adhesion. *Biointerphases* **2014**, *9* (2), 029008.
19. Allen, L. T.; Tosetto, M.; Miller, I. S.; O'Connor, D. P.; Penney, S. C.; Lynch, I.; Keenan, A. K.; Pennington, S. R.; Dawson, K. A.; Gallagher, W. M. Surface-Induced Changes in Protein Adsorption and Implications for Cellular Phenotypic Responses to Surface Interaction. *Biomaterials* **2006**, *27* (16), 3096-3108.
20. Hammarin, G.; Persson, H.; Dabkowska, A. P.; Prinz, C. N. Enhanced Laminin Adsorption on Nanowires Compared to Flat Surfaces. *Colloids Surf. B Biointerfaces* **2014**, *122*, 85-89.
21. Kim, P.; Kim, D. H.; Kim, B.; Choi, S. K.; Lee, S. H.; Khademhosseini, A.; Langer, R.; Suh, K. Y. Fabrication of Nanostructures of Polyethylene Glycol for Applications to Protein Adsorption and Cell Adhesion. *Nanotechnology* **2005**, *16* (10), 2420-2426.
22. Cai, K.; Bossert, J.; Jandt, K. D. Does the Nanometre Scale Topography of Titanium Influence Protein Adsorption and Cell Proliferation? *Colloids Surf. B* **2006**, *49* (2), 136-144.
23. Lord, M. S.; Foss, M.; Besenbacher, F. Influence of Nanoscale Surface Topography on Protein Adsorption and Cellular Response. *Nano Today* **2010**, *5* (1), 66-78.
24. Lynch, I.; Dawson, K. A. Protein-Nanoparticle Interactions. *Nano Today* **2008**, *3* (1–2), 40-47.
25. Scopelliti, P. E.; Borgonovo, A.; Indrieri, M.; Giorgetti, L.; Bongiorno, G.; Carbone, R. Podesta, A.; Milani, P. The Effect of Surface Nanometre-Scale Morphology on Protein Adsorption. *PloS One* **2010**, *5* (7), e11862.
26. Han, M.; Sethuraman, A.; Kane, R. S.; Belfort, G. Nanometer-Scale Roughness Having Little Effect on the Amount or Structure of Adsorbed Protein. *Langmuir* **2003**, *19* (23), 9868- 9872.
27. Rechendorff, K.; Hovgaard, M. B.; Foss, M.; Zhdanov, V. P.; Besenbacher, F. Enhancement of Protein Adsorption Induced by Surface Roughness. *Langmuir* **2006**, *22* (26), 10885-10888.
28. Riedel, M.; Müller, B.; Wintermantel, E. Protein Adsorption and Monocyte Activation on Germanium Nanopyramids. *Biomaterials* **2001**, *22* (16), 2307-2316.

29. García, A. J.; Vega, M. a. D.; Boettiger, D. Modulation of Cell Proliferation and Differentiation through Substrate-Dependent Changes in Fibronectin Conformation. *Mol. Biol. Cell.* **1999**, 10 (3), 785-798.
30. Pierschbacher, M. D.; Ruoslahti, E. Variants of the Cell Recognition Site of Fibronectin that Retain Attachment-Promoting Activity. *Proc. Natl. Acad. Sci. U. S. A.* **1984**, 81 (19), 5985- 5988.
31. Rondeau, P.; Bourdon, E. The Glycation of Albumin: Structural and Functional Impacts. *Biochimie* 2011, 93 (4), 645-658.
32. Pham, V. T. H.; Truong, V. K.; Mainwaring, D. E.; Guo, Y.; Baulin, V. A.; Al Kobaisi, M.; Gervinskas, G.; Juodkasis, S.; Zeng, W. R.; Doran, P. P.; Crawford, R. J.; Ivanova, E. P. Nanotopography as a Trigger for the Microscale, Autogenous and Passive Lysis of Erythrocytes. *J. Mater. Chem. B* **2014**, 2 (19), 2819-2826.
33. Nečas, D.; Klapetek, P. Gwyddion: An Open-Source Software for SPM Data Analysis. *Cent. Eur. J. Phys.* **2012**, 10 (1), 181-188.
34. Gadelmawla, E. S.; Koura, M. M.; Maksoud, T. M. A.; Elewa, I. M.; Soliman, H. H. Roughness Parameters. *J. Mater. Process. Technol.* **2002**, 123 (1), 133-145.
35. Pham, V. T.; Truong, V. K.; Orłowska, A.; Ghanaati, S.; Barbeck, M.; Booms, P.; Fulcher, A. J.; Bhadra, C. M.; Buividas, R.; Baulin, V.; Kirkpatrick, C. J.; Doran, P.; Mainwaring, D. E.; Juodkasis, S.; Crawford, R. J.; Ivanova, E. P. "Race for the Surface": Eukaryotic Cells Can Win. *ACS applied materials & interfaces* **2016**, 8 (34), 22025-31.
36. Wu, Z.; Zhang, X.; Zhang, X.; Sun, J.; Dong, Y.; Hu, J. In Situ AFM Observation of BSA Adsorption on HOPG with Nanobubble. *Chinese Sci. Bull.* **2007**, 52 (14), 1913-1919.
37. Truong, V. K.; Webb, H. K.; Fadeeva, E.; Chichkov, B. N.; Wu, A. H. F.; Lamb, R.; Wang, J. Y.; Crawford, R. J.; Ivanova, E. P. Air-Directed Attachment of Coccolid Bacteria to the Surface of Superhydrophobic Lotus-Like Titanium. *Biofouling* **2012**, 28 (6), 539-550.
38. Nguyen, S. H.; Webb, H. K.; Mainwaring, D. E.; Mahon, P. J.; Crawford, R. J.; Ivanova, E. P. Bacterial patterning at the three-phase line of contact with microtextured alkanes. *Biofouling* **2015**, 31 (3), 297-307.
39. Bhushan, B.; Jung, Y. C.; Koch, K. Micro-, Nano- and Hierarchical Structures for Superhydrophobicity, Self-Cleaning and Low Adhesion. *Philos. Trans. A, Math. Phys. Eng. Sci.* **2009**, 367 (1894), 1631-1672.
40. Crawford, R. J.; Webb, H. K.; Truong, V. K.; Hasan, J.; Ivanova, E. P. Surface Topographical Factors Influencing Bacterial Attachment. *Adv. Colloid Interface Sci.* **2012**, 179-182, 142-149.

41. Truong, V. K.; Pham, V. T. H.; Medvedev, A.; Lapovok, R.; Estrin, Y.; Lowe, T. C.; Baulin, V.; Boshkovikj, V.; Fluke, C. J.; Crawford, R. J.; Ivanova, E. P. Self-Organised Nanoarchitecture of Titanium Surfaces Influences the Attachment of *Staphylococcus aureus* and *Pseudomonas aeruginosa* Bacteria. *Appl. Microbiol. Biotechnol.* **2015**, 99 (16), 6831-6840.
42. Wu, Y.; Zitelli, J. P.; TenHuisen, K. S.; Yu, X.; Libera, M. R. Differential Response of Staphylococci and Osteoblasts to Varying Titanium Surface Roughness. *Biomaterials* **2011**, 32 (4), 951-960.
43. Singh, G.; Pillai, S.; Arpanaei, A.; Kingshott, P. Highly Ordered Mixed Protein Patterns Over Large Areas from Self-Assembly of Binary Colloids. *Adv. Mater.* **2011**, 23 (13), 1519-1523.
44. Roach, P.; Farrar, D.; Perry, C. C. Surface Tailoring for Controlled Protein Adsorption: Effect of Topography at the Nanometer Scale and Chemistry. *J. Am. Chem. Soc.* **2006**, 128 (12), 3939-3945.
45. Baujard-Lamotte, L.; Noinville, S.; Goubard, F.; Marque, P.; Pauthe, E. Kinetics of Conformational Changes of Fibronectin Adsorbed onto Model Surfaces. *Colloids Surf. B Biointerfaces* **2008**, 63 (1), 129-137.
46. Hovgaard, M. B.; Rechendorff, K.; Chevallier, J.; Foss, M.; Besenbacher, F. Fibronectin Adsorption on Tantalum: the Influence of Nanoroughness. *J. Phys. Chem. B* **2008**, 112 (28), 8241-8249. (47)
47. Pellenc, D.; Berry, H.; Gallet, O. Adsorption-Induced Fibronectin Aggregation and Fibrillogenesis. *J. Colloid Interface Sci.* **2006**, 298 (1), 132-144.
48. Nakanishi, K.; Sakiyama, T.; Imamura, K. On the Adsorption of Proteins on Solid Surfaces, a Common but Very Complicated Phenomenon. *J. Biosci. Bioeng.* **2001**, 91 (3), 233-244.
49. Billsten, P.; Wahlgren, M.; Arnebrant, T.; McGuire, J.; Elwing, H. Structural Changes of T4 Lysozyme upon Adsorption to Silica Nanoparticles Measured by Circular Dichroism. *J. Colloid Interface Sci.* **1995**, 175 (1), 77-82.
50. Lundqvist, M.; Sethson, I.; Jonsson, B. H. Protein Adsorption onto Silica Nanoparticles: Conformational Changes Depend on the Particles' Curvature and the Protein Stability. *Langmuir* **2004**, 20 (24), 10639-10647.
51. Tian, M.; Lee, W. K.; Bothwell, M. K.; McGuire, J. Structural Stability Effects on Adsorption of Bacteriophage T4 Lysozyme to Colloidal Silica. *J. Colloid Interface Sci.* **1998**, 200 (1), 146-154.

52. Vertegel, A. A.; Siegel, R. W.; Dordick, J. S. Silica Nanoparticle Size Influences the Structure and Enzymatic Activity of Adsorbed Lysozyme. *Langmuir* **2004**, 20 (16), 6800-6807.
53. Qian, X.; Rameshbabu, U.; Dordick, J. S.; Siegel, R. W. Selective Characterization of Proteins on Nanoscale Concave Surfaces. *Biomaterials* **2016**, 75, 305-312.
54. Elter, P.; Lange, R.; Beck, U. Electrostatic and Dispersion Interactions During Protein Adsorption on Topographic Nanostructures. *Langmuir* **2011**, 27 (14), 8767-8775.
55. Bergkvist, M.; Carlsson, J.; Oscarsson, S. Surface-Dependent Conformations of Human Plasma Fibronectin Adsorbed to Silica, Mica, and Hydrophobic Surfaces, Studied with Use of Atomic Force Microscopy. *J. Biomed. Mater. Res. A* **2003**, 64A (2), 349-356.
56. Erickson, H. P.; Carrell, N.; McDonagh, J. Fibronectin Molecule Visualized in Electron Microscopy: a Long, Thin, Flexible Strand. *J. Cell. Biol.* **1981**, 91 (3), 673-78.
57. Burns, N. L.; Holmberg, K.; Brink, C. Influence of Surface Charge on Protein Adsorption at an Amphoteric Surface: Effects of Varying Acid to Base Ratio. **1996**, 178 (1), 116-122.
58. Peters, T. Serum albumin. *Advances in protein chemistry* **1985**, 37, 161-245.
59. Rixman, M. A.; Dean, D.; Ortiz, C. Nanoscale Intermolecular Interactions between Human Serum Albumin and Low Grafting Density Surfaces of Poly(ethylene oxide). **2003**, 19 (22), 9357-9372.
60. Ruoslahti, E. Fibronectin in Cell Adhesion and Invasion. *Cancer Metast. Rev.* **1984**, 3 (1), 43-51.

3.2.8 Supplementary Data

S1. Quantification of adsorbed protein

The thickness and surface coverage of human serum albumin and plasma fibronectin on the bSi surfaces were calculated from the XPS data. The thickness of adsorbed proteins (z) was calculated using the overlayer equation shown below,¹⁻⁸ where the bSi surface is assumed to have random roughness and variable emission angles:

$$z = -\lambda_{IMFP} \times \cos \theta \times \ln \left(1 - \frac{I}{I_{\infty}} \right)$$

where I and I_{∞} are the %N recorded on the protein coated bSi surfaces, and %N present in each protein, respectively. λ_{IMFP} is the mean free path of N 1s photoelectrons generated from the protein overlayers (it is assumed to be 2.5 nm), and $\cos \theta$ is the angle between the sample and analyser.⁸ In this case we use $\theta=57.3^{\circ}$: the average angle of emission for a randomly rough

particle-like surface for bSi surfaces and $\theta=0^\circ$ for control silicon wafers.⁸ The reference value for I_∞ is determined by calculating % N from the atomic composition for each protein which is obtained by submitting the sequence or the SwissProt/TrEMBL accession number for the protein into the PortParam calculator (<http://web.expasy.org/protparam/>). For human fibronectin this is determined to be 17.7 %N and for human serum albumin this is 16.7 %N.

Once the thickness of each protein is determined; the surface coverage (Θ) is calculated in ng/cm² assuming the density of dry protein to be 1.4 g/cm³.⁶ The calculation assumes the surface is uniformly covered with protein and occupies a volume of 1 cm × 1 cm × z.⁸

$$\theta = z \times 1.4 \times 10^2$$

Table S1. Protein Uptake on bSi and Si Wafer Surfaces Using the Overlayer Equation Obtained from XPS Elemental Analysis

	protein concentration ($\mu\text{g/mL}$)	adsorbed protein mass (ng/cm^2)		protein molecule uptake ($\times 10^9$) (molecule/cm^2)	
		bSi	Si wafer	bSi	Si wafer
albumin	0.4	5.7 ± 0.2	17.2 ± 3.1	51.6 ± 1.8	155.8 ± 28.1
	4.0	20.3 ± 2.3	38.8 ± 8.3	183.8 ± 20.8	351.4 ± 75.2
	40.0	60.8 ± 0.6	52.0 ± 13.8	550.6 ± 5.4	470.9 ± 125.0
fibronectin	0.3	4.5 ± 0.3	*	6.2 ± 0.4	*
	3.0	8.4 ± 1.9	27.8 ± 4.5	11.5 ± 2.6	38.0 ± 6.2
	30.0	100.0 ± 6.5	126.3 ± 22.1	136.9 ± 8.9	172.9 ± 30.2

* Below detection limit

Table S2. Topographical Analysis of the bSi Surface with Protein Adsorption Taking Place at Different Bulk Protein Concentrations over a Scanning Area of $10 \mu\text{m} \times 10 \mu\text{m}$

roughness parameter	PBS	albumin ($\mu\text{g/mL}$)			
		0.4	4.0	40.0	
S (nm) _q	76.5 ± 9.4	82.3 ± 16.9	96.3 ± 21.4	141.3 ± 18.7	
S (nm) _{max}	803.4 ± 96.8	804.6 ± 67.9	1097.3 ± 249.0	1103.4 ± 46.4	
S _{skw}	-0.4 ± 0.1	-0.5 ± 0.1	0.2 ± 0.5	-0.5 ± 0.1	
S _{kur}	1.4 ± 0.2	1.0 ± 0.5	2.4 ± 0.4	-0.1 ± 0.3	
		fibronectin ($\mu\text{g/mL}$)			
		PBS	0.3	3.0	30.0
S (nm) _q	76.5 ± 9.4	104.1 ± 7.5	144.0 ± 6.3	135.4 ± 4.6	
S (nm) _{max}	803.4 ± 96.8	1010.4 ± 126.3	1033.9 ± 60.1	1019.7 ± 142.1	
S _{skw}	-0.4 ± 0.1	-0.7 ± 0.1	-0.6 ± 0.2	-0.4 ± 0.1	
S _{kur}	1.4 ± 0.2	0.3 ± 0.2	-0.3 ± 0.2	-0.5 ± 0.1	

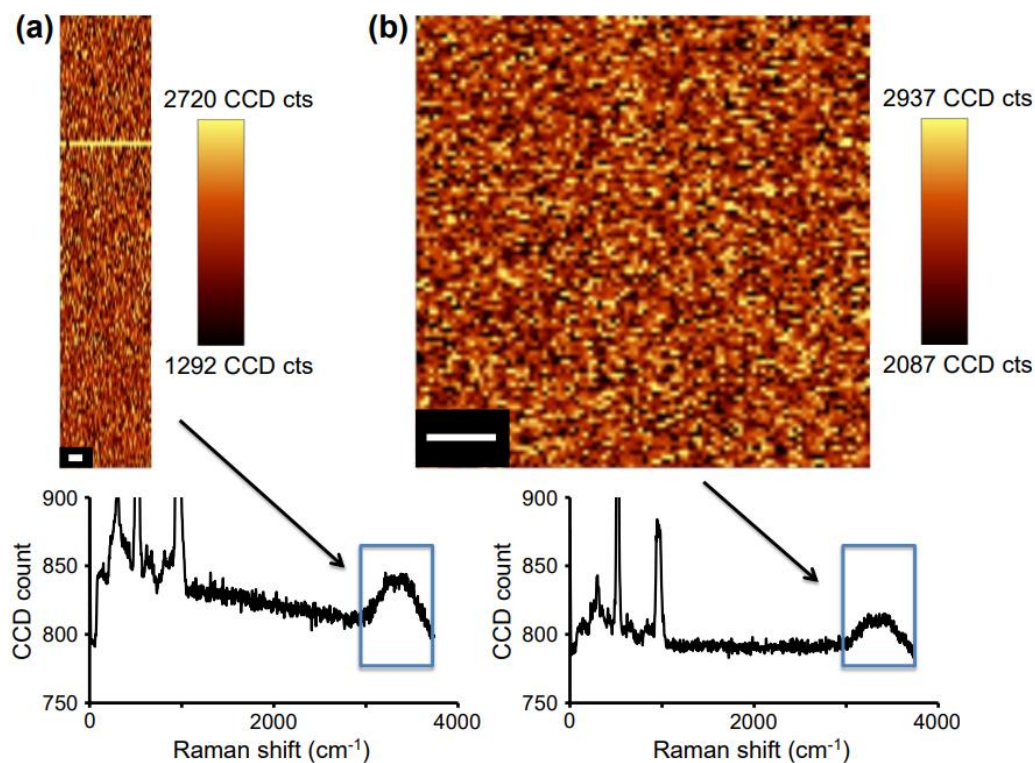


Figure S1. Raman activity of the water distribution on bSi surfaces. (a) Depth profile of 10 μm (height) × 2 μm (width) areas showing the penetrating depth of water from the tip to the foot of the pillars, demonstrating the absence of air retained between the nanopillars. (b) The space between the pillar tips and water layer, showing a homogenous spreading of water on the surface of bSi. Scale bar is 0.3 μm.

Reference

1. Bramblett, A. L.; S. Boeckl, M.; Hauch, K. D.; Ratner, B. D.; Sasaki, T.; Rogers, J. W. Determination of Surface Coverage for Tetraphenylporphyrin Monolayers Using Ultraviolet Visible Absorption and X-Ray Photoelectron Spectroscopies. *Surf. Interface Anal.* **2002**, *33*, 506-515.
2. Caruso, F.; Niikura, K.; Furlong, D. N.; Okahata, Y. 1. Ultrathin Multilayer Polyelectrolyte Films on Gold: Construction and Thickness Determination. *Langmuir* **1997**, *13*, 3422-3426.
3. Chatelier, R. C.; Gengenbach, T. R.; Griesser, H. J.; Brighamburke, M.; Oshannessy, D. J. A General Method to Recondition and Reuse Biacore Sensor Chips Fouled with Covalently Immobilized Protein/Peptide. *Anal. Biochem.* **1995**, *229*, 112-118.
4. Frydman, A.; Castner, D. G.; Schmal, M.; Campbell, C. T. A Method for Accurate Quantitative XPS Analysis of Multimetallic or Multiphase Catalysts on Support Particles. *J. Catal.* **1995**, *157*, 133-144.

5. Meyer, R. L.; Arpanaei, A.; Pillai, S.; Bernbom, N.; Enghild, J. J.; Ng, Y. Y.; Gram, L.; Besenbacher, F.; Kingshott, P. Physicochemical Characterization of Fish Protein Adlayers with Bacteria Repelling Properties. *Colloids Surf. B* **2013**, 102, 504-510.
6. Paynter, R. W.; Ratner, B. D.; Horbett, T. A.; Thomas, H. R. XPS Studies on The Organization of Adsorbed Protein Films on Fluoropolymers. *J. Colloid Interface Sci.* **1984**, 101, 233-245.
7. Ray, S.; Shard, A. G. Quantitative Analysis of Adsorbed Proteins by X-Ray Photoelectron Spectroscopy. *Anal. Chem.* **2011**, 83, 8659-8666.
8. Singh, G.; Pillai, S.; Arpanaei, A.; Kingshott, P. Highly Ordered Mixed Protein Patterns Over Large Areas from Self-Assembly of Binary Colloids. *Adv. Mater.* **2011**, 23, 1519-1523.

2.2. The Effect of Coatings and Nerve Growth Factor on Attachment and Differentiation of Pheochromocytoma Cells

Materials, **2017**, *11*(1).

Orłowska, A.^{a,b}, Perera, P. T.^c, Al Kobaisi, M.^c, Dias, A.^{a,b}, Nguyen, H. K. D.^c, Ghanaati, S.^a, Baulin, V.^b, Crawford, R. J.^c, & Ivanova, E. P.^c

^a Frankfurt Orofacial Regenerative Medicine, University Hospital Frankfurt, Theodor-Stern-Kai 7, D-60590 Frankfurt am Main, Germany

^b Departament d'Enginyeria Química, Universitat Rovira i Virgili, 26 Avenue dels Països Catalans, 43007 Tarragona, Spain

^c Department of Chemistry and Biotechnology, School of Science, Swinburne University of Technology, P.O. Box 218, Hawthorn VIC 3122, Australia

^d School of Science, RMIT University, P.O. Box 2476, Melbourne VIC 3001, Australia

3.3.1 Abstract

Cellular attachment plays a vital role in the differentiation of pheochromocytoma (PC12) cells. PC12 cells are noradrenergic clonal cells isolated from the adrenal medulla of *Rattus norvegicus* and studied extensively as they have the ability to differentiate into sympathetic neuron-like cells. The effect of several experimental parameters including (i) the concentration of nerve growth factor (NGF); (ii) substratum coatings, such as poly-L-lysine (PLL), fibronectin (Fn), and laminin (Lam); and (iii) double coatings composed of PLL/Lam and PLL/Fn on the differentiation process of PC12 cells were studied. Cell morphology was visualised using brightfield phase contrast microscopy, cellular metabolism and proliferation were quantified using a 3-(4,5-dimethylthiazol-2-yl)-5-(3-carboxymethoxyphenyl)-2-(4-sulfophenyl)-2H-tetrazolium (MTS) assay, and the neurite outgrowth and axonal generation of the PC12 cells were evaluated using wide field fluorescence microscopy. It was found that double coatings of PLL/Lam and PLL/Fn supported robust adhesion and a two-fold enhanced neurite outgrowth of PC12 cells when treated with 100 ng/mL of NGF while exhibiting stable metabolic activity, leading to the accelerated generation of axons.

3.3.2 Introduction

The pheochromocytoma (PC12) cell line is commonly used in *in vitro* studies to examine neuronal differentiation and neurotoxicity implicated in neurodegenerative disease.^{1,2} PC12 cells are noradrenergic clonal cells originating from *Rattus norvegicus* transplantable pheochromocytoma.¹ They exhibit a reversible response to nerve growth factor (NGF). After NGF exposure, PC12 cells acquire characteristic phenotypic properties associated with sympathetic neuron-like cells, which includes the inhibition of proliferation, outgrowth of neurites, and the possibility of being electrically excitable.¹⁻³ Upon differentiation, the neuron-like PC12 cells start to express various integral proteins that are responsible for neurite growth¹ and can transmit signals along the axons.^{4,5}

In laboratory conditions, PC12 cells attach poorly to polystyrene (PS) tissue culture surfaces^{4,6} where they grow mostly as floating cell aggregates.⁶ This poor adhesion ultimately results in insufficient levels of neurite outgrowth.⁴ Functionalization of the surface can improve the attachment of the PC12 cells. Previously, it was shown that the pre-treatment of the substratum surface with proteins, especially the extracellular matrix components, enhanced not only cell adhesion, but also their growth, morphology, migration, and differentiation, increasing their life-span.⁷

Various substratum coatings used in the formation of PC12 neuronal processes have been reported, e.g., glycoproteins, collagen (type IV from human placenta, type I),⁸⁻¹¹ laminin (Lam),¹² and fibronectin (Fn).³ In addition, it was shown that polyornithine,^{3,13-16} poly-D-lysine, and poly-L-lysine (PLL) can be used to enhance the attachment of PC12 cells.⁸⁻¹¹ Although Tomaselli *et al.*¹⁷ have shown that Lam and collagen type IV coated surfaces promoted PC12 adhesion to a greater degree than Fn, no systematic assessment of the suitability of various coatings that would enhance the attachment and differentiation of PC12 cells has been performed. Therefore, the aim of our study was to investigate the effect of five coating types, including Lam, Fn, and PLL (and various combinations of these coatings) on the attachment, proliferation, and differentiation of PC12 cells. The extent of differentiation of the PC12 cells using different coatings was monitored by measuring a set of parameters related to cellular functions as a function of NGF concentration. The proliferation and metabolic activity of the PC12 cells were analyzed using an MTS (3-(4,5-dimethylthiazol-2-yl)-5-(3-carboxymethoxyphenyl)-2-(4-sulfophenyl)-2H-tetrazolium) assay. The morphology and neuron-like characteristics of the cells were analyzed by using brightfield phase contrast microscopy and wide field fluorescence microscopy.

3.3.3 Experimental

PC12 Cell Line

Commercially-available PC12 CRL-1721™ cells were obtained from the American Type Culture Collection (American Type Culture Collection (ATCC), Manassas, VA, USA). The cells were cultured in 75 mm² tissue culture flasks with complete Gibco™ 1640 RPMI medium supplemented with 10% horse serum (HS, Thermo Fisher Scientific Australia Pty Ltd., Melbourne, Australia), 5% fetal bovine serum (FBS, Thermo Fisher Scientific Australia Pty Ltd., Melbourne, Australia) and 1% Penicillin/Streptomycin (Pen/Strep, Thermo Fisher Scientific Australia Pty Ltd., Melbourne, Australia). The cells were maintained according to standard protocols^{4,18} at 37°C in a 95% humidified incubator with 5% CO₂. The medium was changed every 2 days, and passaged accordingly when the confluence reached 90%.

Coatings

Poly-L-lysine

Sterile-filtered poly-L-lysine (PLL) (molecular weight 150,000–300,000 Da) was purchased from Sigma-Aldrich (Sydney, Australia) and used at the recommended concentration of 0.01% w/v in water. The sterile filtered solution was stored at 4 °C until required.

Fibronectin

Fibronectin (Fn) was purchased from Sigma-Aldrich (Sydney, Australia) in lyophilized powder form. An aqueous working solution of 40 µg/mL concentration was prepared and stored at -20 °C until required.

Laminin

Laminin (Lam) derived from a mouse Engelbreth-Holm-Swarm (EHS) sarcoma was purchased from Sigma-Aldrich (Sydney, Australia). An aqueous working solution of 10 µg/mL concentration was prepared and stored at -20 °C until required.

Atomic Force Microscopy

The surface topography of the various substrata was visualized using an Innova® atomic force microscope (Bruker, Billerica, MA, USA). A phosphorous-doped silicon probe (MPP-31120-10, Bruker, Billerica, MA, USA) was employed in tapping mode for all measurements performed in air, at a temperature of approximately 22 °C. The atomic force microscopy (AFM, Veeco, Bruker, Billerica, MA, USA) scans, obtained over a 10 µm x 10 µm surface area with 512 x 512 data points, were processed using Gwyddion software (Version 2.49, Czech Metrology Institute, Brno, Czech).¹⁹ Analysis was conducted using three AFM micrographs for each sample, and for two samples of each substratum surface. The surface roughness parameters derived from the AFM data included the arithmetic average height (S_a), root mean square deviation from the mean plane (S_q), maximum height of the profile (S_{max}), skewness (S_{skw}), and kurtosis (S_{kur}), as described in detail elsewhere.²⁰

Differentiation of PC12 Cells

PC12 cells were seeded onto 24-well polystyrene (PS) tissue culture plates at a density of 3×10^4 cells/mL in Gibco™ 1640 Roswell Park Memorial Institute (RPMI) medium (1% HS, 1% FBS and 1% Pen/Strep) supplemented with 0, 25, 50, and 100 ng/mL Nerve Growth Factor (NGF) (mouse recombinant NGF 7S, Sigma-Aldrich, Sydney, Australia). Prior to seeding, the tissue culture dish (Sarstedt AG & Co., Nümbrecht, Germany) was prepared with different coatings, with each being prepared in triplicate. Non-coated plates were employed as control surfaces.

PLL was added to cover the entire surface area and incubated at 25 °C for 2 h. The wells were washed with phosphate-buffered saline (PBS) and a second coating of Fn or Lam was added and incubated at 25 °C for 2 h. The non-coated wells of the tissue culture dishes were used as control surfaces. At least two technical replicates were completed. The culture medium on the samples was changed every second day.

Metabolic Activity

The metabolic activity of the PC12 cells was determined using the CellTiter 96® AQueous One Solution Cell Proliferation Assay (Promega, Sydney, Australia). The assay was performed by adding the tetrazolium compound to the PC12 cell culture at a 10% ratio of the final volume. This allowed the reduction of (3-(4,5-dimethylthiazol-2-yl)-5-(3-carboxymethoxyphenyl)-2-(4-sulfophenyl)-2H-tetrazolium) (MTS) to formazan, resulting in the formation of a coloured precipitate. The absorbance of the resultant solution was recorded at a wavelength of 490 nm after incubation for 90 min at 37 °C using a FLUOstar Omega microplate reader (BMG LABTECH, Cary, NC, USA).

Assessment of Neurite Outgrowth

A neurite outgrowth analysis was performed using representative digitized photomicrographs of each well, obtained using a phase contrast brightfield inverted Olympus microscope (CKX41, Olympus, Tokyo, Japan) equipped with a Panasonic camera (DMC-GH3). The quantity of differentiated cells was established by the visual detection of neurites. Evaluation of neurite growth was carried out by manually tracking the length of the neurites on each cell using NeuronJ software (ImageJ plugin; NIH, Bethesda, MD, USA). This procedure was conducted for all cells in a field where the entire neurite could be visualized.

Widefield Fluorescence Microscopy

After a 5-day incubation period, the cells were washed with PBS and fixed with 4% paraformaldehyde for 15 min. After fixation, the cells were washed with PBS and cell membranes were stained using Wheat Germ Agglutinin, Alexa Flour™ 488 (WGA, Thermo Fisher Scientific Australia Pty Ltd., Melbourne, Australia). The nucleus was stained using DAPI (4',6-diamidino-2-phenylindole). Samples were then imaged using a Nikon Eclipse Ti-E epifluorescence inverted microscope (Nikon Instruments Inc., Tokyo, Japan). Sequential images were acquired using DAPI and GFP-B standard series filter cubes and analysed using FIJI (ImageJ) software (k.1.45, National Institute of Mental Health, Bethesda, MD, USA).²¹

Statistical Analysis

Statistically significant differences ($p < 0.05$, $p < 0.01$, $p < 0.001$, $p < 0.0001$) were calculated among the various groups using a two-way ANOVA analysis followed by Tukey's multiple comparison test. All statistical analyses were carried out using the GraphPad Prism 7 statistical software package (GraphPad Software, Inc., San Diego, CA, USA).

3.3.4 Results and Discussions

Single- and two-component coatings were investigated in this study. The glycoproteins, such as Lam and Fn, were selected because they are typical components of the extracellular matrix.^{5,17,22,23} It has been reported that Lam and Fn positively influenced the outgrowth of neurons, axonal guidance, differentiation and cell proliferation.^{5,22} Since PLL was reported to facilitate cell attachment and improve the differentiation of PC12 cells,²⁴ PLL was also selected for analysis. In addition to single component coatings, PLL/Lam and PLL/Fn combination coatings were also studied.

Protein Distribution on the Substratum

An AFM analysis confirmed that an even distribution of the coatings was present on the plastic surfaces of the cell culture wells (Figure 1A). The S_a of the control (2.2 ± 0.2 nm) was found to be similar to that present on the substrata with a single coating, namely, Fn (1.8 ± 0.1 nm) and PLL (2.1 ± 0.7 nm). The Lam coating exhibited a higher S_a of 2.9 ± 0.4 nm. The PLL/Fn and PLL/Lam dual component coatings were found to have S_a of 3.4 ± 0.4 nm and 5.8 ± 1.2 nm, respectively.

PC12 Cell Attachment and Initial Differentiation in the Presence of NGF

The extent of growth of the PC12 cells on substrata containing the five different coating types, together with various concentrations of NGF, was investigated in order to identify the most suitable growth conditions for the stimulated attachment and differentiation of PC12 cells into neuron-like cells. Cell attachment, growth, and differentiation patterns were monitored over a five-day period (Figures 1B and 2). The initial differentiation and attachment propensity of the PC12 cells after 48 h (day 2) was studied using phase-contrast brightfield microscopy (Figure 1B).

The densities of attached cells on the substrata possessing a single Lam coating and dual-component coatings were found to be comparable, whereas isolated, spherically-shaped cells

were observed without protrusions on substrata containing the PLL and Fn coatings. Enhanced levels of cell attachment were detected on substrata containing the PLL/Fn and Lam coatings in the presence of 50 ng/mL NGF (Figure 1B). In the absence of 50 ng/mL NGF, only a few cells were observed to have attached to these surfaces. These results confirmed that the presence of a coating is essential for robust cell attachment to be supported, whereas it was apparent that NGF could act as a co-factor for achieving enhanced levels of cell attachment.

In order to compare and confirm the cell differentiation processes on the various substrata being investigated, PC12 cells were stained with a membrane specific protein and imaged using wide field fluorescence microscopy (Figure 2). Analysis of the fluorescence micrographs indicated that the dual component PLL/Fn and PLL/Lam coatings supported enhanced levels of PC12 cell differentiation, as evidenced by the presence of neurite outgrowth. In contrast, on PLL- and Lam-coated surfaces, the PC12 cells exhibited a lower degree of differentiation, with no or just a few non-differentiated cells being observed on the Fn- and non-coated surfaces.

PC12 cells incubated on Fn- or non-coated surfaces exhibited little to no attachment propensity in both the presence and absence of NGF. These results are consistent with previously reported data that suggested that NGF acted as a co-factor in enhancing the attachment and differentiation of cells, however, the surface coating itself was found to be the main factor determining the extent to which cells would attach to surfaces.

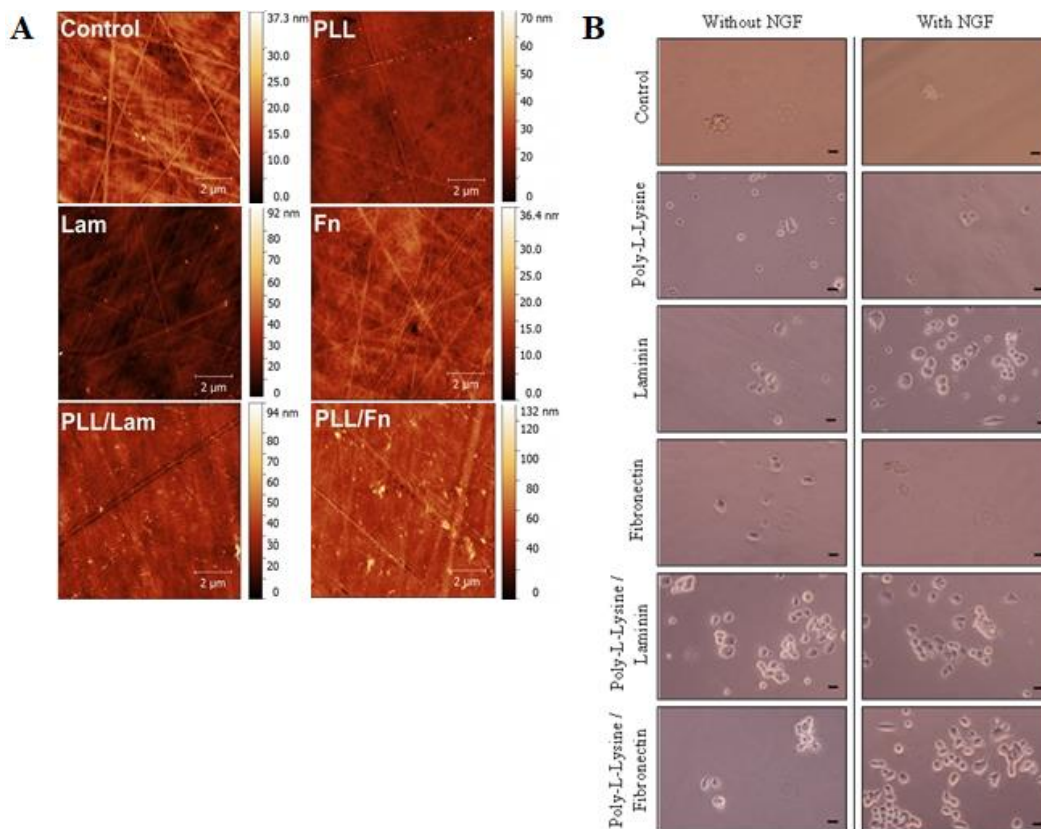


Figure 1. (A) AFM analysis of surfaces with different coatings. The AFM micrographs show an even distribution of single and two-component coatings on the surfaces of the polystyrene substratum. (B) Attachment and initial differentiation of PC12 cells after two days of incubation in the presence and absence of NGF solution. Cells were seeded at a density of 3×10^4 cells/mL on poly-L-lysine, laminin, fibronectin, poly-L-lysine/laminin, and poly-L-lysine/fibronectin-coated wells. The cells were grown in a medium that was supplemented with human recombinant NGF (50 ng/mL). The control wells did not contain any coating. In these experiments the PC12 cells appeared to attach to the surface in clusters. Scale bar is 5 μm.

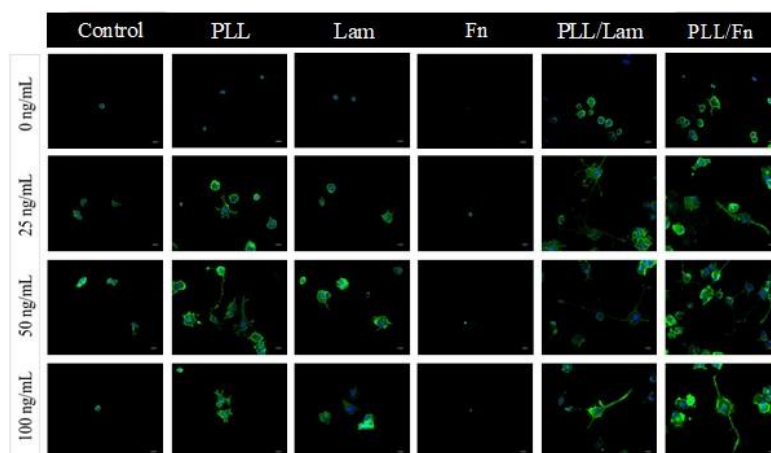


Figure 2. Comparative differentiation of PC12 cells on substrata with single- and two-component coatings in the presence of NGF solution. The NGF concentrations used were 0, 25, 50, and 100 ng/mL. Cells were grown over a period of five days; fixed in 4% PFA for 15 min and stained with WGA-488(membrane, green), DAPI (nuclei, blue). Significant neurite outgrowth was observed for cells grown on substrata with double coatings containing poly-L-lysine/laminin and poly-L-lysine/fibronectin. Substrata containing single coatings of poly-L-lysine and laminin exhibited poor cell differentiation.

PC12 Cells Metabolic Activity and Proliferation

The differentiation of PC12 cells into neuron-like cells has been found to be accompanied by an arrest in the post-mitotic G0 stage in the cell cycle, which in turn decreased their potential to proliferate.^{1-3,25} A commonly used method for the evaluation of proliferation activity is through monitoring cell metabolic activity via an MTS assay.²⁶ In this work, an MTS assay was employed to study the metabolic activity of the PC12 cells while attached to the different substratum surfaces. PC12 cells grown on PLL-coated substrata exhibited an increased growth after five days when both 25 and 50 ng/mL NGF was present, compared to growth in the absence of NGF (Figure 3). At a concentration of 100 ng/mL NGF, however, a decrease in cell growth was observed. This decrease is likely to be associated with a progression of the cells into an arrested G0 stage, which is characteristic of PC12 cells that have undergone a differentiation to form neuron-like cells. Analysis of the metabolic activity of the PC12 cells 24 h after seeding (day 1) indicated that the metabolic activity of the cells increased in the presence of NGF, however, when cells were incubated on a PLL-coated substratum, an increase in metabolic activity was not observed. After the third day of growth, a similar metabolic activity was observed for all cells attached to all surfaces.

After the 5th day, cell proliferation was found to increase with increasing NGF concentration for all substrata. Cells incubated in the presence of substrata coated with PLL, Fn and PLL/Fn, and 100 ng/mL NGF exhibited a statistically significant decrease in proliferation compared to that observed in the presence of 50 ng/mL NGF.

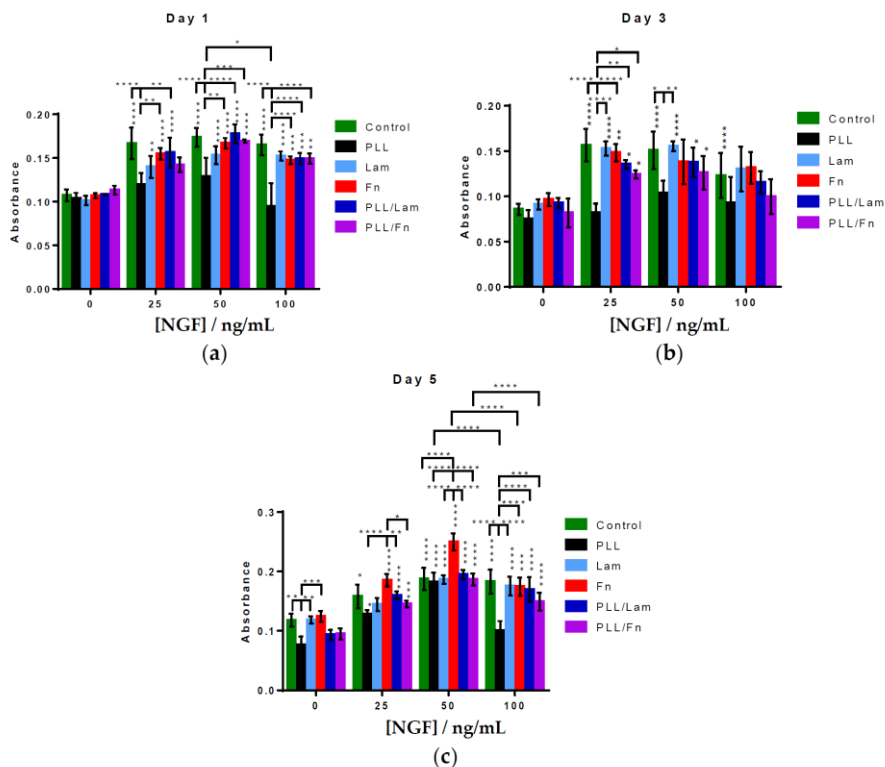


Figure 3. Comparative analysis of the proliferation of PC12 cells on substrata with different coatings in the presence of NGF solution. PC12 cells were grown over a period of 5 days in the presence of 0, 25, 50, or 100 ng/mL NGF. Incubation of PC12 cells on substratum surfaces in the presence of 50 ng/mL NGF resulted in an increased amount of attachment on day (a) 1, (b) 3 and (c) 5 compared to the other NGF solutions. Results are presented as the mean \pm standard deviation. Unless otherwise specified, statistically significant differences in cell proliferation grown on the different substrata are shown versus the absence of NGF solution. “*” indicates the degree of statistically significant differences.

Neurite Outgrowth

The neurite outgrowth was evaluated for individual cells, grown under different experimental conditions. The results are presented in Figure 4. A comparative analysis of these data indicated that increases in NGF concentration stimulated the outgrowth of neurites, despite the metabolic activity of the cells being greater at 50 ng/mL (Figure 3). It was also found that substrata with two-component coatings stimulated the outgrowth of neurites in the presence of a 100 ng/mL NGF solution (Figure 4). PC12 cells incubated in the presence of substrata with or without a single coating showed reduced levels or no outgrowth of neurites, most likely because of low cell attachment occurring on these surfaces. The substrata possessing dual component coatings stimulated the differentiation of neurites (Figure 4) after cell proliferation had been arrested (in the presence of 100 ng/mL NGF) after the 5th day of incubation (Figure 3).

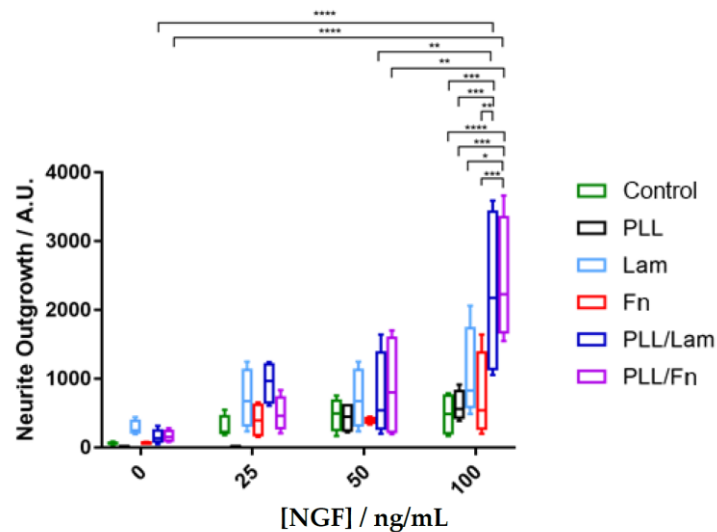


Figure 4. Quantification of neurite extension. The PC12 cells were grown on various coatings over a period of five days and in the presence of 0, 25, 50, and 100 ng/mL NGF. Over fifty fields of view were analyzed for each condition. The results indicated a two-fold greater neurite outgrowth occurring on substrata containing the dual-component coatings of poly-L-lysine/laminin and poly-L-lysine/fibronectin with increasing NGF concentrations. Results are presented as minimum, 1st quartile, median, 3rd quartile, and maximum. “*” indicates the degree of statistically significant differences.

Discussion

The results of this study have demonstrated that PC12 cells incubated in the presence of substrata with dual-component coatings composed of PLL/Lam or PLL/Fn exhibited enhanced attachment, proliferation, and outgrowth of neurites. It is likely that this enhancement has occurred because PLL offers an increased number of cationic sites that can bind to the ionic sites present on the polystyrene surfaces of the tissue culture wells via hydrogen bonding or electrostatic interactions (Figure 5A). The glycoproteins, while effectively binding to PLL via electrostatic interactions (Fn and Lam isoelectric point of 5.5–6.0²⁷ and 6.4²⁸, respectively (Figure 5B,C)), also provided specific binding sites for the PC12 cells, allowing greater levels of cell attachment to take place,²⁹ because cell surface receptors that promote cellular adhesion to extracellular matrices are known to facilitate adherence the PC12 cells.³⁰ It was also demonstrated that the cell attachment domain of Fn consists of potential chains of β -turns, which form the most hydrophilic region for cell attachment.²⁹ The integrin binding domain present on Lam²⁷ can bind with the integrin receptors present on the surface of PC12 cells (Figure 5C), resulting in adhesion and the initiation of cell differentiation. The PC12 cells strongly attached to the substrata containing a PLL coating due to the negatively-charged cell membrane and nonspecific electrostatic interactions with the highly positively-charged PLL surface (Figure 5A).²⁴ The single-component coatings composed of only glycoproteins were most likely not able

to support a robust attachment onto the surfaces of the tissue culture wells because of the weak binding affinity of this protein to the well surface. As a result, the PC12 cells would not have been able to withstand the washing procedures taking place during the incubation period.

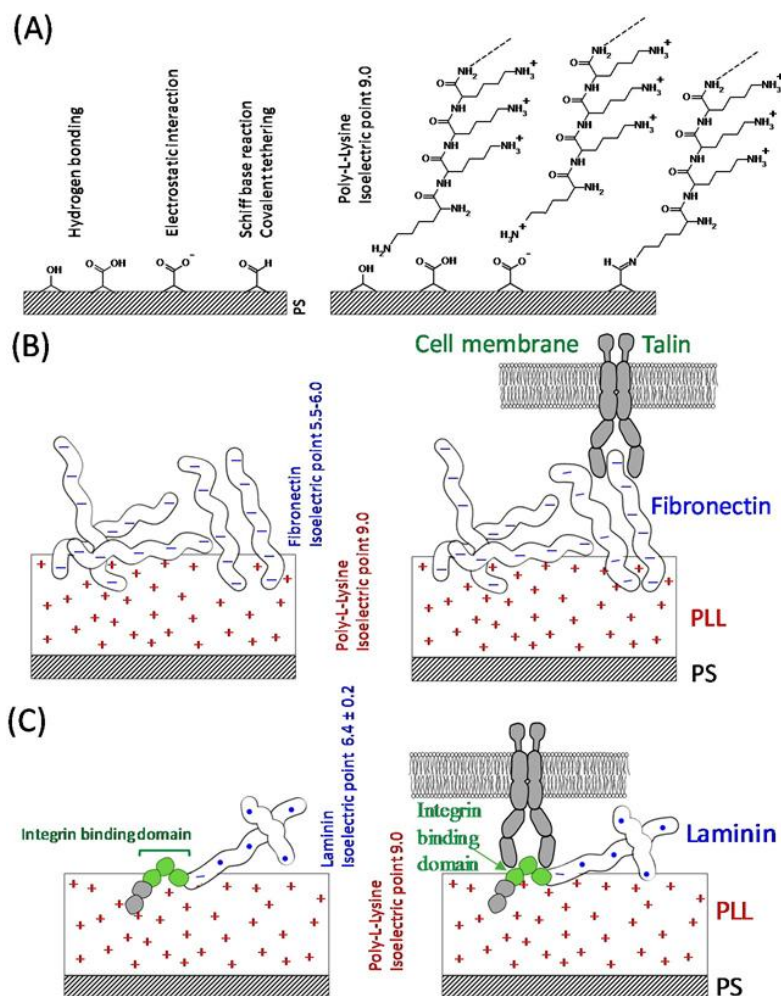


Figure 5. Schematic interpretation of the bio-interfaces of the PC12 cells undergoing attachment onto the substratum samples. (A) Possible chemical interactions between the polystyrene substratum and the coating materials. The aldehyde and ketone groups present on the surface of polystyrene undergo a Schiff base reaction and bind covalently with the amine groups. (B) negatively-charged fibronectin (pI 5.5–6.0) binding to the positively charged poly-L-lysine coating via electrostatic interactions. (C) laminin (pI 6.4) with a net negative charge also binds electrostatically to the poly-L-lysine layer. Laminin interacts with the PC12 cell surface receptors via the integrin binding domain.

3.3.5 Conclusions

In summary, substrata containing the two-component coatings of PLL/Lam and PLL/Fn in the presence of 100 ng/mL NGF solution were found to result in the greatest levels of attachment of PC12 cells followed by early stimulation of cell differentiation and neurite outgrowth.

3.3.6 Acknowledgements

Anna Orłowska, Andre Dias, Vladimir A. Baulin, Shahram Ghanaati, and Elena P. Ivanova acknowledge partial support from the Marie Curie Actions under the EU FP7 Initial Training Network SNAL 608184.

3.3.7 References

1. Jesky, R.; Chen, H. The neuritogenic and neuroprotective potential of senegenin against A β -induced neurotoxicity in PC12 cells. *BMC Complement. Altern. Med.* **2016**, *16*, 26.
2. Westerink, H.R.; Ewing, A.G. The PC12 cell as model for neurosecretion. *Acta Physiol.* **2008**, *192*, 273–285.
3. Gordon, J.; Amini, S.; White, M.K. General overview of neuronal cell culture. *Methods Mol. Biol.* **2013**, 1078,
4. Fuji, D.K.; Massoglia, S.L.; Savion, N.; Gospodarowicz, D. Neurite outgrowth and protein synthesis by PC12 cells as a function of substratum and nerve growth factor. *J. Neurosci.* **1982**, *2*, 1157–1175.
5. Akeson, R.; Warren, S.L. PC12 adhesion and neurite formation on selected substratums are inhibited by some glycosaminoglycans and a fibronectin-derived tetrapeptide. *Exp. Cell Res.* **1986**, *162*, 347–362.
6. Attiah, G.D.; Kopher, R.A.; Desai, T.A. Characterization of PC12 cell proliferation and differentiation-stimulated by ECM adhesion proteins and neurotrophic factors. *J. Mater. Sci. Mater. Med.* **2003**, *14*, 1005–1009.
7. Kleinman, H.K.; Luckenbill-Edds, L.; Cannon, F.W.; Sephel, G.C. Use of extracellular matrix components for cell culture. *Anal. Biochem.* **1987**, *166*, 1–13.
8. Ergin, V.; Erdogan, M.; Menevse, A. Regulation of shootin1 gene expression involves ngf-induced alternative splicing during neuronal differentiation of PC12 cells. *Sci. Rep.* **2015**, *5*, 17931.
9. Ogra, Y.; Tejima, A.; Hatakeyama, N.; Shiraiwa, M.; Wu, S.; Ishikawa, T.; Yawata, A.; Anan, Y.; Suzuki, N. Changes in intracellular copper concentration and copper-regulating gene expression after PC12 differentiation into neurons. *Sci. Rep.* **2016**, *6*, 33007.
10. Boczek, T.; Kozaczuk, A.; Ferenc, B.; Kosiorek, M.; Pikula, S.; Zylinska, L. Gene expression pattern in PC12 cells with reduced PMCA2 or PMCA3 isoform: Selective up-regulation of calmodulin and neuromodulin. *Mol. Cell. Biochem.* **2012**, *360*, 89–102.

11. Marino, A.; Ciofani, G.; Filippeschi, C.; Pellegrino, M.; Pellegrini, M.; Orsini, P.; Pasqualetti, M.; Mattoli, V.; Mazzolai, B. Two-photon polymerization of sub-micrometric patterned surfaces: Investigation of cell-substratum interactions and improved differentiation of neuron-like cells. *ACS Appl. Mater. Interfaces* **2013**, *5*, 13012–13021.
12. Cowley, S.; Paterson, H.; Kemp, P.; Marshall, C.J. Activation of MAP kinase is necessary and sufficient for PC12 differentiation and for transformation of NIH 3T3 cells. *Cell* **1994**, *77*, 841–852.
13. Shafer, J.T.; Atchison, W.D. Transmitter, ion channel and receptor properties of pheochromocytoma (PC12) cells: A model for neurotoxicological studies. *Neurotoxicology* **1991**, *12*, 473–492.
14. Chen, T.-I.; Chiu, H.-W.; Pan, Y.-C.; Hsu, S.-T.; Lin, J.-H.; Yang, K.-T. Intermittent hypoxia-induced protein phosphatase 2A activation reduces PC12 cell proliferation and differentiation. *J. Biomed. Sci.* **2014**, *21*, 1–11.
15. Pandey, A.; Singh, P.; Jauhari, A.; Singh, T.; Khan, F.; Pant, A.B.; Parmar, D.; Yadav, S. Critical role of the miR-200 family in regulating differentiation and proliferation of neurons. *J. Neurochem.* **2015**, *133*, 640–652.
16. Connolly, L.J.; Green, S.A.; Greene, L.A. Comparison of rapid changes in surface morphology and coated pit formation of PC12 cells in response to nerve growth factor epidermal growth factor and dibutylryl cyclid AMP. *J. Cell Biol.* **1984**, *98*, 457–465.
17. Tomaselli, J.K.; Damsky, C.H.; Reichardt, L.F. Purification and characterization of mammalian integrins expressed by a rat neuronal cell line (PC12) evidence that they function as α/β heterodimeric receptors for laminin and type IV collagen. *J. Cell Biol.* **1988**, *107*, 1241–1252.
18. Garcia-Parra, P.; Cavaliere, F.; Maroto, M.; Bilbao, L.; Obieta, I.; de Munain, A.L.; Álava, J.I.; Izeta, A. Modeling neural differentiation on micropatterned substratums coated with neural matrix components. *Front. Cell. Neurosci.* **2012**, *6*, 1–12.
19. Nečcas, D.; Klapetek, P. Gwyddion: An open-source software for SPM data analysis. *Open Phys.* **2012**, *10*, 181–188.
20. Gadelmawla, E.S.; Koura, M.M.; Maksoud, T.M.A.; Elewa, I.M.; Soliman, H.H. Roughness parameters. *J. Mater. Process. Technol.* **2002**, *123*, 133–145.
21. Schindelin, J.; Arganda-Carreras, I.; Frise, E.; Kaynig, V.; Longair, M.; Pietzsch, T.; Preibisch, S.; Rueden, C.; Saalfeld, S.; Schmid, B.; et al. Fiji: An open-source platform for biological-image analysis. *Nat. Methods* **2012**, *9*, 676–682.

22. Freire, E.; Gomes, F.C.; Linden, R.; Neto, V.M.; Coelho-Sampaio, T. Structure of laminin substratum modulates cellular signalling for neuritogenesis. *J. Cell Sci.* **2002**, 115, 4867–4876.
23. Rogers, S.L.; Letourneau, P.C.; Palm, S.L.; McCarthy, J.; Furcht, L.T. Neurite extension by peripheral and central nervous system neurons in response to substratum-bound fibronectin and laminin. *Dev. Biol.* **1983**, 98, 212–220.
24. Mazia, D.; Schatten, G.; Sale, W. Adhesion of cells to surfaces coated with polylysine. *J. Cell Biol.* **1975**, 66, 198–200.
25. Ajioka, I. Coordination of proliferation and neuronal differentiation by the retinoblastoma protein family. *Dev. Growth Differ.* **2014**, 56, 324–334.
26. Berridge, M.V.; Tan, A.S. Characterization of the cellular reduction of 3-(4,5-dimethylthiazol-2-yl)-2,5-diphenyltetrazolium bromide (MTT): subcellular localization, substratum dependence, and involvement of mitochondrial electron transport in MTT reduction. *Arch. Biochem. Biophys.* **1993**, 303, 474–482.
27. Vartio, T. Characterization of the binding domains in the fragments cleaved by cathepsin G from human plasma fibronectin. *FEBS J.* **1982**, 123, 223–233.
28. Paulsson, M.; Deutzmann, R.; Timpl, R.; Dalzoppo, D.; Odermatt, E.; Engel, J. Evidence for coiled-coil α -helical regions in the long arm of laminin. *EMBO J.* **1985**, 4, 309–316.
29. Pierschbacher, D.M.; Ruoslahti, E. Cell attachment activity of fibronectin can be duplicated by small synthetic fragments of the molecule. *Nature* **1984**, 309, 30–33.
30. Hynes, R.O. Integrins: Versatility, modulation and signalling in cell adhesion. *Cell* **1992**, 69, 11–25.

2.3. Race for the Surface: Eukaryotic Cells Can Win

ACS Applied Materials and Interfaces, **2016**, 8(34), 22025–22031.

Pham, V. T. H.^a, Truong, V. K.^a, **Orłowska, A.**^b, Ghanaati, S.^b, Barbeck, M.^b, Booms, P.^b, Fulcher, A. J.^c, Bhadra, C. M.^a, Buividas, R.^a, Baulin, V.^d, Kirkpatrick, C. J.^b, Doran, P.^a, Mainwaring, D. E.^a, Juodkazis, S.^a, Crawford, R. J.^{a,e}, & Ivanova, E. P.^a

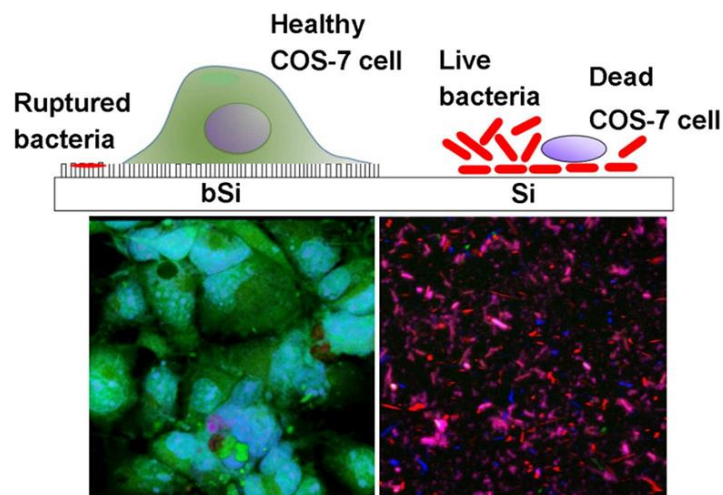
^e School of Science, Swinburne University of Technology, P.O. Box 218, Hawthorn, Victoria, 3122, Australia

^f Frankfurt Orofacial Regenerative Medicine, University Hospital Frankfurt, Theodor-Stern-Kai 7, D-60590 Frankfurt am Main, Germany

^g Monash Micro Imaging, Monash University, Clayton, Victoria, 3800, Australia

^h Departament d'Enginyeria Química, Universitat Rovira i Virgili, 26 Avenue dels Paisos Catalans, Tarragona 43007, Spain

ⁱ School of Science, RMIT University, P.O. Box 2476, Melbourne, Victoria 3001, Australia



3.1.1 Abstract

With an aging population and the consequent increasing use of medical implants, managing the possible infections arising from implant surgery remains a global challenge. Here, we demonstrate for the first time, that a precise nanotopology provides an effective intervention in bacterial co-colonization enabling the proliferation of eukaryotic cells on a substratum surface, pre-infected by both live Gram-negative, *Pseudomonas aeruginosa*, and Gram-positive, *Staphylococcus aureus*, pathogenic bacteria. The topology of the model black silicon (bSi) substratum not only favors the proliferation of eukaryotic cells, but is biocompatible not triggering an inflammatory response in the host. The attachment behavior and development of filopodia when COS-7 fibroblast cells are placed in contact with the bSi surface is demonstrated in the dynamic study, which is based on the use of real-time sequential confocal imaging. Bactericidal nanotopology may enhance the prospect for further development of inherently responsive antibacterial nanomaterials for bionic applications such as prosthetics and implants.

3.1.2 Introduction

Biomaterial-associated infections arising from implant surgery have been a global challenge despite the development of modern sterilization methods. The mechanism by which host cells compete with live bacteria that may be present on an implant material for their effective surface colonization remains poorly understood.¹⁻⁸ This process was initially termed “the race for the surface” by Gristina.⁹ If won by the tissue cells of the host, the implant becomes protected from invading pathogens, ensuring that appropriate tissue integration takes place. If pathogenic bacteria become the primary surface colonizers, the formation of a bacterial biofilm will occur, which leads to severe inflammatory responses in the host, and a subsequent cascade of infective issues, including the risk of mortality.⁹⁻¹¹ Hence, investigations that allow an insight of infective issues, into how eukaryotic cells and bacteria compete for the colonization of biomaterial surfaces forming an essential aspect of the effective design of antibacterial biomaterials.¹⁰ A majority of studies assessing biomaterial surface interactions with bacteria and mammalian cells have used laboratory models, which evaluated possible interactions of either cell type.^{10, 12-14} Several detailed experimental *in vitro* and *in vivo* approaches have been proposed aimed at demonstrating the “race for the surface”.^{3-4, 6, 8, 12-13} Busscher *et al.*, for example, investigated the *in vitro* co-culturing of bacterial and mammalian cells on substratum surfaces, where it was shown that growth of *S. epidermidis* cells on substrata can be partially

inhibited whilst simultaneously allowing a limited growth of U2OS osteosarcoma cells to occur within a flow cell.⁴ It was further shown that neither the alteration of the wettability characteristics of the surface, nor the addition of polymer coatings could effectively prevent further overgrowth of the pathogenic bacteria on the surface.^{3, 12} A post-contamination model was also introduced showing the successful attachment of U2OS osteosarcoma cells on a substratum in the presence of *S. epidermidis* cells when the mammalian cells were seeded at an high initial cell densities and allowed to adhere to the surface for twenty four hours prior to the surface being exposed to the bacteria.¹³ These authors also reported an *in vivo* model for studying the fate of contaminated biomaterials by using a genetically modified bioluminescent bacterial strain, which monitored the *in vivo* infected sites over a long period.¹⁴ Trentin *et al.* have shown that a selective reduction in the formation of an *S. epidermidis* biofilm could be achieved while simultaneously supporting the growth of Vero cells when both cell types were co-cultured on a surface coated with an antifouling agent.⁵ Although this antimicrobial coating was found to be less effective against other bacteria such as *P. aeruginosa*, *S. aureus* and *K. pneumoniae*⁵ and in fact may have served to promote the extent of bacterial resistance to the coating over time. Chow *et al.* were able to co-culture heat-inactivated *E. coli* and lung cancer cells (H59) in order to investigate the role of the receptors that mediate postoperative pneumonia associated with cancer treatments. Here it is reported that the presence of *E. coli* cells enhanced the *in vitro* adhesion and migration of the eukaryotic cells and significantly increased the *in vivo* formation of hepatic metastases.¹⁵ There is however, lack of a demonstration of an effective material surface that has the ability to simultaneously enhance mammalian cell growth while preventing bacterial invasion, without the surface chemical agent.

It was recently shown that the high aspect ratio nanostructured surfaces of *Psaltoda claripennis* cicada wings,¹⁶⁻¹⁷ *Diplacodes bipunctata* dragonfly wings and their synthetic analogue, black silicon (bSi), were highly bactericidal to different types of bacteria and spores.¹⁸ Bacterial cells coming into contact with the surface were extensively deformed through nanomechanical stresses imposed by the nanopillar arrays present on the substratum surfaces. The resulting high levels of cell lysis, and therefore the bactericidal efficiency of the surface, was found to be independent of the surface chemical composition.¹⁹ When placed in contact with red blood cells, these surfaces also proved to actively promote autogenous lysis.²⁰ It remains unclear, however, whether or not eukaryotic cells would be affected by the action of the surface topology of the bSi. Therefore, the aim of the current work was to investigate the ability of the bSi topology to provide an effective intervention in the competitive colonization between fibroblast-like cells derived from monkey kidney tissue (COS-7) on this surface pre-infected with viable *Staphylococcus aureus* and *Pseudomonas aeruginosa* cells. The immune response of the

host to the topology of the bSi using a subcutaneous implantation model in mouse was also evaluated.

3.1.3 Experimental

Preparation of black silicon

The black silicon (bSi) samples were prepared using a p-type boron doped, 100 mm diameter Si wafer, with a specific resistivity of $10 - 20 \Omega \text{ cm}^{-1}$, a $\langle 100 \rangle$ oriented surface and a substratum thickness of $525 \pm 25 \mu\text{m}$ (Atecom Ltd, Taiwan). The samples were subjected to mixed mode reactive ion etching (RIE) using SF_6 and O_2 over a 5 minute period to produce the bSi using an Oxford PlasmaLab 100 ICP380 instrument (Oxford Instruments, Concord, MA, USA) as described previously.²⁰⁻²¹ The characterization of bSi surface is detailed in Supporting Information S1.1, S2.1 and Figure S1.

Infecting the bSi surfaces with pathogenic bacteria

Pseudomonas aeruginosa ATCC 9027 and *Staphylococcus aureus* CIP 65.8T were obtained from the American Type Culture Collection (ATCC, USA) and Culture Collection of the Institute Pasteur (CIP, France), respectively. Bacterial stocks were prepared in 20% glycerol with 80% nutrient broth (Oxoid) and stored at -80°C . A fresh bacterial suspension was prepared for each of the strains at the infective dose of 10^3 cells per mL for *S. aureus* and 10^5 cells per mL for *P. aeruginosa*, according to Federal Drug Administration (FDA) guidelines.²¹⁻²² Black silicon (nanostructured) and non-structured silicon wafer surfaces were incubated with the bacterial suspensions for 6 hours at 37°C under dark conditions.

Growth of COS-7 cells on bacteria pre-infected surfaces

COS-7 cells were cultured in Dulbecco's Modified Eagle's medium (DMEM) (Invitrogen) supplemented with 10% fetal bovine serum (FBS) and 1% penicillin-streptomycin. The use of the cell line was approved by the Biosafety Project 2014/SBC01. Cells were grown to reach 80% confluency; then were trypsinized using 0.25% Trypsin/EDTA (Invitrogen). Cells were seeded on pre-infected bSi and silicon substrata at the density of 10,000 cells per cm^2 for every independent experiment. All of the following assessments were performed after 1, 3 and 7 days of seeding, when 100% confluency was reached, and three independent experiments were performed for each type of surfaces.

Scanning electron microscopy (SEM)

After incubation all specimen were fixed in 2.5% glutaraldehyde (Sigma) for 30 min and progressively dehydrated in graded of ethanol solutions (30%, 50%, 70%, 90% and 100% v/v), in 10 min for each solution, and visualized using SEM. The ZEISS SUPRA 40VP field-emission SEM (Carl Zeiss NTS GmbH, Oberkochen, BW, Germany) was used to image the morphology of bacteria and COS-7 cells on two types of surfaces, operated at 3 kV.

Confocal laser scanning microscopy

Live cell imaging was conducted using the Leica SP5 Multiphoton confocal microscope with a dipping 20× objective lens. Simultaneous fluorescent imaging of bacteria and COS-7 was achieved by labeling mammalian cells with a LIVE/DEAD® Viability/Cytotoxicity Kit (Invitrogen) which is composed of calcein AM and ethidium homodimer-1 for live cell and dead cell staining, respectively, while bacteria were labeled with SYTO® 17 Red Fluorescent Nucleic Acid Stain (Invitrogen). Viable COS-7 cells were quantified based on the confocal imaging data, expressing in the number of attached cells per cm² based on nine images of about 100 cells.

To analyze the interactions of COS-7 cells on the bSi surface in real time, COS-7 cells pre-labeled with CellTracker™ OrangeCMRA (Invitrogen) were seeded and allowed to adhere onto the bSi surface 24 hours prior to a second batch of COS-7 cells, pre-labeled with CellTracker™ Green GMFDA Dye (Invitrogen), being seeded onto the same bSi specimen. Imaging commenced from the time the COS-7 cell labeled with CellTracker™ GreenGMFDA was seeded, where the z-range was determined using the COS-7 cells labeled with CellTracker™ Orange CMRA that had been previously adhered to the surface. Images were collected every 10 min using the Leica SP5 Multiphoton microscope with the 20× dipping objective lens (part number 507701). The image data was analyzed using the 3D possessing software Imaris (Bitplane), where snapshots were measured at representative time points, a time lapse movie recorded and surface rendering of the data was performed to highlight local contact points of COS-7 cell with bSi nanotopology.

Implantation and excision of samples in CD-1 mice

The *in vivo* pilot study was performed on 8 female, 6-8 weeks old, CD-1 mice that were obtained from Military Medical Academy (Belgrade, Serbia) with the approval of the Local Ethical Committee (Faculty of Medicine, University of Niš, Serbia). See also Supporting Information S1.2, S1.3 and S1.4.

3.1.4 Results and discussion

Eukaryotic cell growth over the pathogenic bacteria

Whilst the bactericidal efficiency of the bSi nanotopology has been well documented,¹⁸ it is unclear as to whether eukaryotic cells would be able to attach and proliferate on the bSi surface when pre-infected by live pathogenic bacteria. To address this question, bSi surfaces were inoculated with live *S. aureus* CIP 65.8^T or *P. aeruginosa* ATCC 9027 cells for six hours at their respective infective doses (Figure 1).²²⁻²³ The first 6 hours of bacterial contact with an implant surface is considered to be critical for the initiation of infection²⁴ which is generally designed as the “decisive period”, particularly for medical implant-associated infections.²⁵⁻²⁶ During this stage, the host immune system can potentially neutralize the invading pathogenic bacteria with the aid of prophylactic antibiotics.²⁵⁻²⁷ The pathogenic bacteria were therefore equilibrated with the bSi surface for 6 hours to evaluate the effectiveness of the bSi surface to passively eliminate the bacterial cells (Figure 1).

The subsequent colonization of COS-7 cells of the pre-infected surfaces was then monitored for seven days until 100% confluency was reached. It was confirmed that after 6 hours, all of the bacteria appeared to be dead, with only cell debris being detected on the bSi surface after a 24-hour incubation period (Figure 1 and Figure S2(A)). This was confirmed by examination of the surfaces using SEM (Figure 2) and confocal microscopy (Figure 3), the results of which were consistent with our previously reported bactericidal studies.¹⁸ The bacteria remained viable on the equivalent non-structured silicon wafer surfaces, which used as control (Figure 3). Notably, the growth of the two pathogenic bacteria on this control surfaces was not inhibited by the presence of antibiotics (penicillin-streptomycin (1%)), present as supplements in the DMEM used for the cultivation of the COS-7 cells.

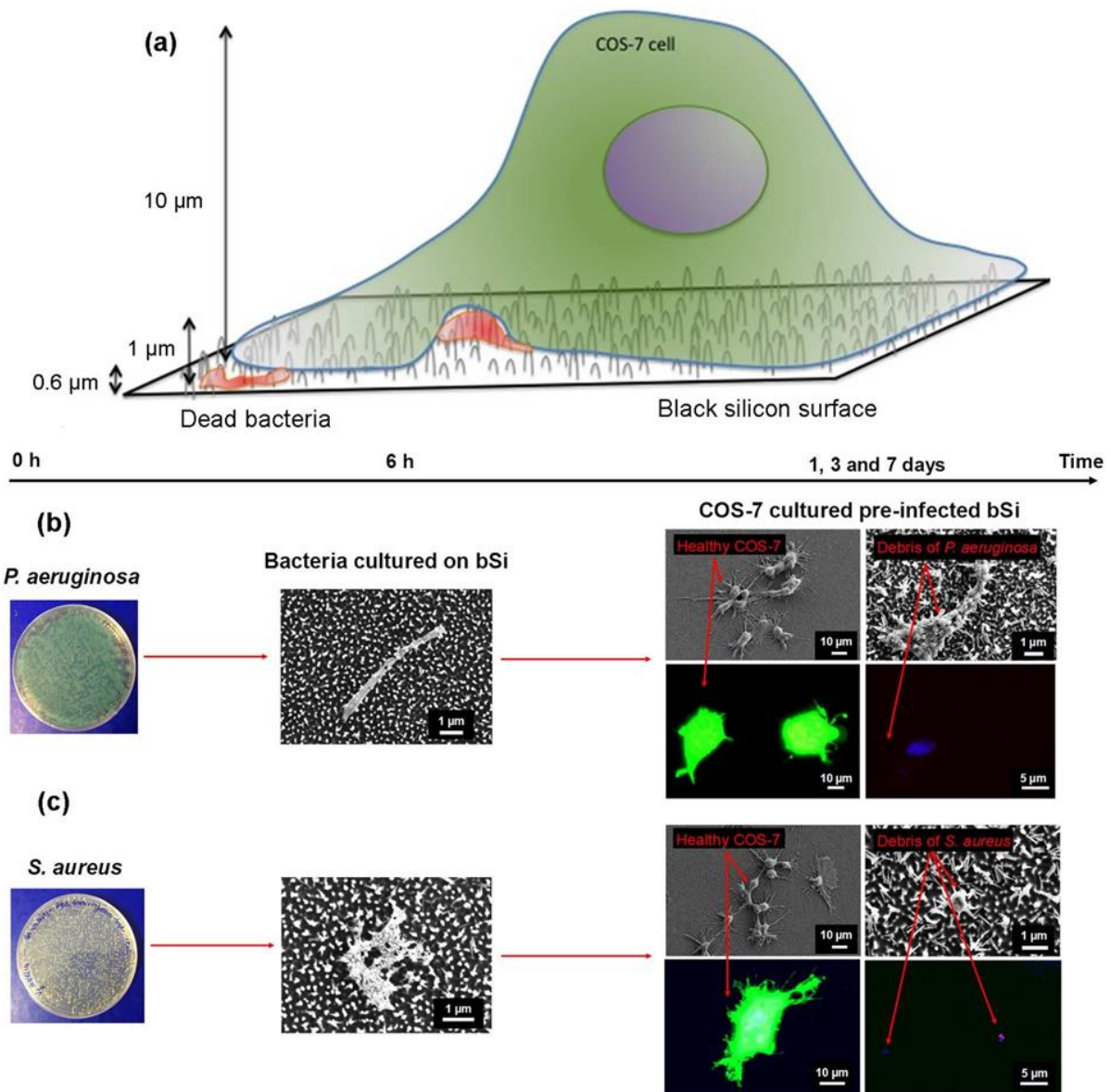


Figure 1. (a) Schematic demonstration of the relative dimensions of COS-7 cells (10 μm), bacterium (1 μm) and nanopillars (0.6 μm). Two stages in evaluating the colonization of pathogenic *P. aeruginosa* ATCC 9027 (b) and *S. aureus* CIP 65.8T (c) with fibroblast-like COS-7 cells on the bSi surfaces. In the first stage, bSi surfaces were infected by the pathogenic bacteria and allowed to equilibrate for 6 h. Altered bacterial morphology indicating dead bacteria after 6 hours in contact with bSi surfaces inferred from SEM images. The next stage, the preinfected surfaces were seeded with COS-7 cells, and simultaneously growth of bacteria and eukaryotic cells were maintained and analyzed up to 7 days. It was demonstrated that COS-7 cells were able to attach and grow on pre-infected bSi surfaces while only debris of bacterial cells were found after one day of co-culturing on the bSi surfaces.

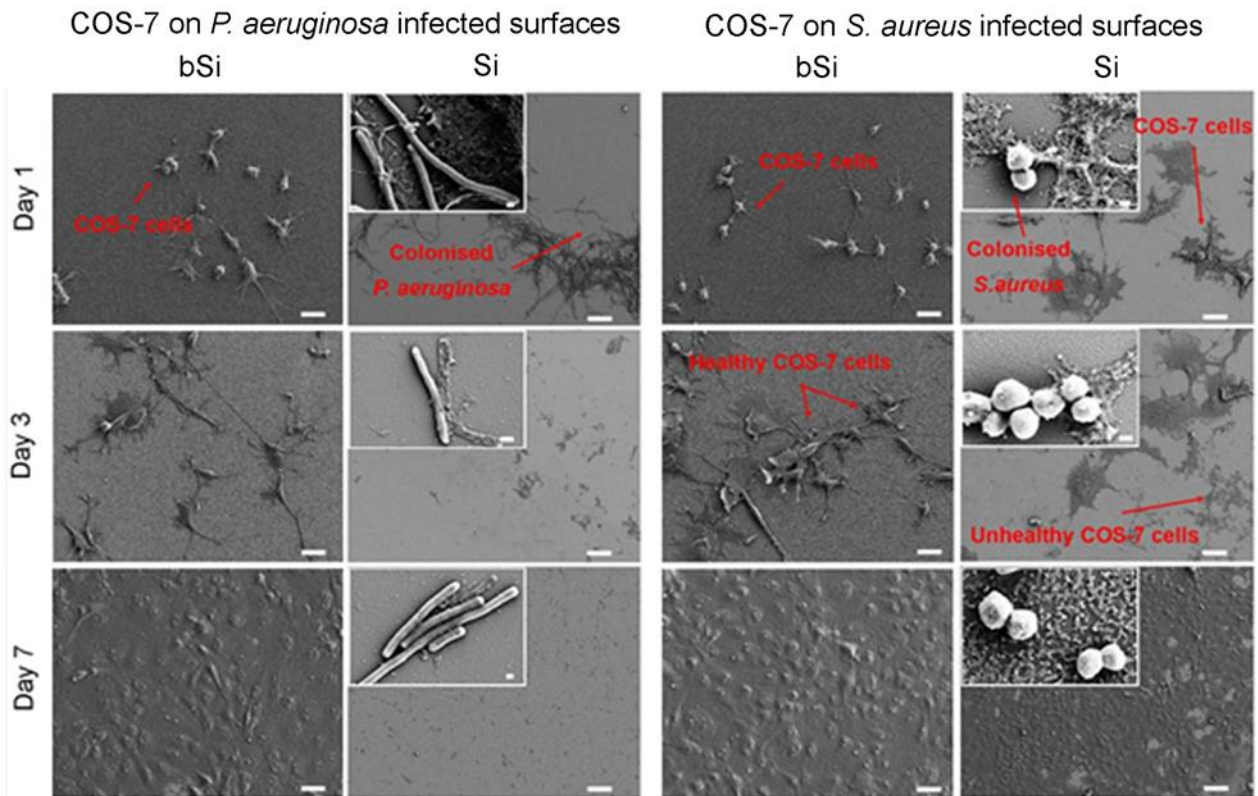


Figure 2. SEM images showing the colonization of COS-7 cells onto nanostructured bSi and non-structured Si control surfaces infected with *P. aeruginosa* and *S. aureus* bacterial cells. Overgrowth of COS-7 observed on the infected bSi surface with the absence of bacteria colonization over 7 days, while the growth of COS-7 cells appeared inhibited by the presence of pathogenic bacteria on the non-structured Si surfaces. Scale bar is 10 μm , inset is 1 μm .

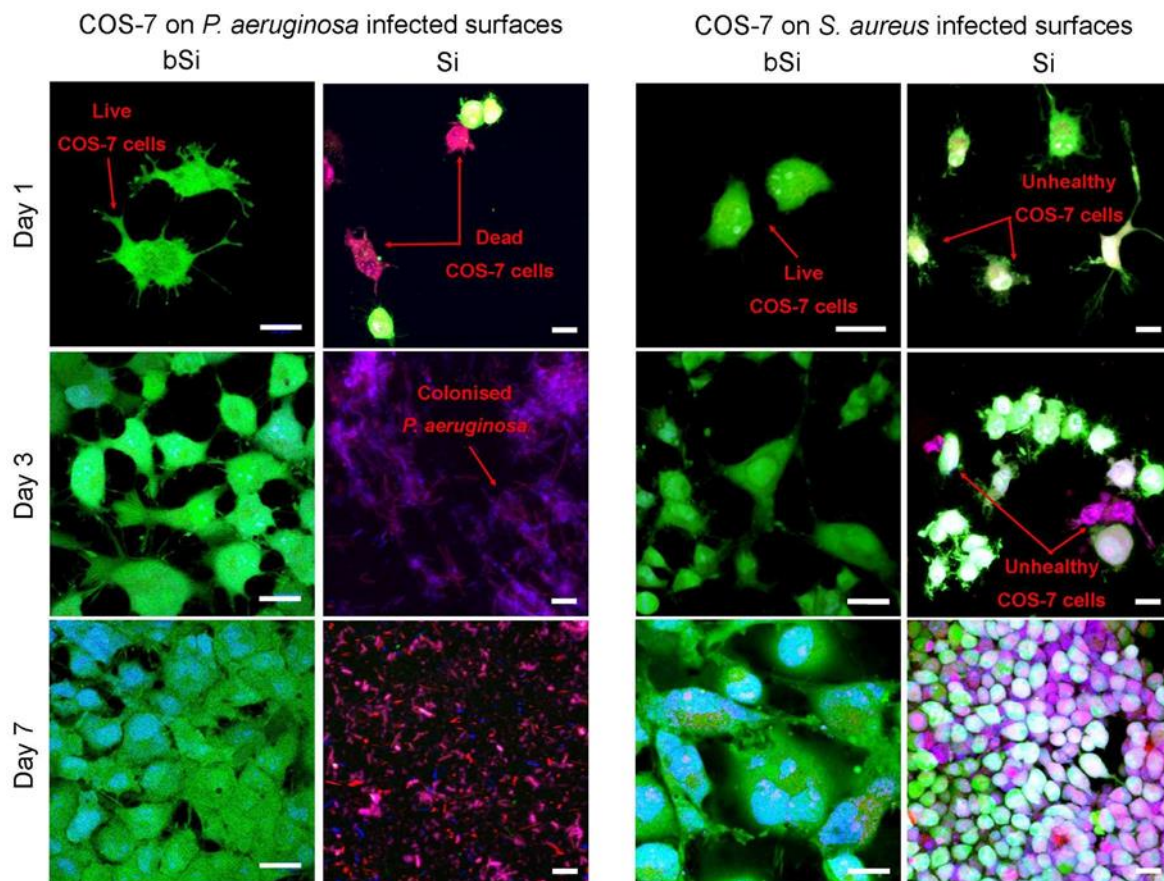


Figure 3. CLSM images demonstrating the robust adhesion and proliferation behaviors of COS-7 cells during seven days on the infected bSi surface, contrasting with the inhibited COS-7 cell growth induced by the colonization of pathogenic bacteria on the non-structured Si surfaces. Live cells stained with Calcein AM (green), dead cells stained with ethidium homodimer-1 (red), viable bacteria were stained with SYTO® 17 (blue). Scale bars are 20 μm (separate channels of fluorescent images are presented in Supporting Information, Fig. S5).

The morphological changes of bacteria grown on bSi and non-structured Si wafer surfaces are shown in Fig. S4. After 6 hours of contact, *P. aeruginosa* and *S. aureus* cells appeared to be completely ruptured on the nanopillars of bSi surfaces, while both strains maintained their integrity on non-structured Si surfaces under identical conditions (Figure S4). The morphology, attachment and viability of the COS-7 fibroblasts on the infected surfaces were correlated after 1, 3 and 7 days using both SEM and CLSM (Figure 2 & 3). The seeded COS-7 cells appeared to be viable on the infected surfaces after 1 day, with a significant increase in cell growth being apparent after 3 days, and 100% confluency achieved after 7 days. By contrast, both the *P. aeruginosa* and *S. aureus* cells formed biofilms on the non-structured control surfaces and subsequently inhibited the growth of the fibroblasts after 7 days of incubation. The *P. aeruginosa* cells completely overgrew the COS-7 fibroblast cells, whereas a limited number of fibroblast cells remained viable in the presence of the *S. aureus* cells on the non-structured control surfaces (Figure 3). Initiating at the same cell seeding density of 5×10^4 cells per cm^2 for all surfaces, both of the groups seeded on the infected bSi surface exhibited a similar growth

rate, eventually reaching approximately 9×10^5 cells per cm^2 after 7 days, which covered 100% surface areas of the substratum (Figure S2(B)). The silicon control surfaces, however, showed a selective growth of COS-7 cells on the *S. aureus* infected surface, reaching coverage of approximately 3.9×10^5 cells per cm^2 after one week. The *P. aeruginosa* infected control silicon surface showed an initial attachment observed at day 1, however the COS-7 cells failed to maintain long-term viability, with no growth being detected after day 3. These final two control examples (Si) approximate the current *in vitro* scenarios for implant materials containing a pathogenic bacterial biofilm. Notably, even with application of antibiotics, these biofilms would persist. As illustrated in Fig. S4, one day after the pre-infected surfaces were introduced to COS-7 cultured in DMEM (containing antibiotic supplements), *S. aureus* retained on Si surfaces and co-existed with COS-7 cells while *P. aeruginosa* cells outgrew the surface of non-structured Si wafer. Biomaterials containing a surface nanotopography similar to that of bSi appear required to ensure that successful cell attachment and subsequent tissue integration takes place, whilst at the same time eliminating any bacterial contamination.

It is noteworthy that the traces of bacterial debris that were present one day after the initial seeding of the surface were not observed after 3 and 7 days of incubation, indicating that the debris had diffused from the surface, thereby not interfering with the growth of the COS-7 cells (Figure 2 & 3). To our knowledge, this is the first model demonstrating that the eukaryotic cells were able to grow over and successfully colonize surfaces that had been infected with live pathogenic bacteria. Previous work had reported that human-bone-marrow-mesenchymal-stem (hBMMS) cells could not survive in the presence of *S. epidermidis* contamination when present on activated bactericidal titanium surfaces.⁶ Recently, human U2OS osteoblast-like cells were also seen to be capable of growing over both *P. aeruginosa* and *S. aureus* bacteria present on PMMA surfaces even in presence of macrophages, and with a domination rate that was however, dependent on the virulence of the particular bacteria being studied.²⁸

Ability of eukaryotic cells to proliferate on bSi substrata

The attachment and development of filopodia of COS-7 fibroblasts on the bSi surfaces was determined in a dynamic study based on real-time sequential confocal imaging (Figure 4), which provided an insight into the initial attachment of the COS-7 cells onto the bSi surface. The cells began to form filaments within 20 minutes of the initial surface contact. After 3 hours, the cells were immobilized, forming local contact points with the surface, demonstrating welldefined membrane protrusions (filopodia) as seen in Figure 4a and in the Supporting Movie 1. The formation of these protrusions is recognized as a “cue” parameter in the initial attachment of

cells to nano-structured substrata,²⁹⁻³² with the nanopillars providing anchoring points for the attachment of cells. To visualize the cell-surface interface, the focal plane was adjusted to the base of a single cell in contact with the surface (Figure 4b). The membrane was then observed to deform under the imposed stress from the nanopillars (red arrows). SEM imaging of freeze fractured samples of the bSi substrata with attached COS-7 cells is shown in Figure 4c. It appears that the deformation of the cell membrane allowed for the cells to engulf the pillars. A number of studies have reported the similar phenomenon that nanopillar structured materials exhibited the ability to modulate the proliferation and differentiation of eukaryotic cells, whereas non-structured surfaces did not show a similar behavior.^{29, 32-38} The recent study of the embryonic rat neurons interacting with substrata containing a nanopillar structure represents an example of this.³⁹ Using transmission electron microscopy, it was demonstrated that at the local nanopillar contact point, the membrane was stretched and distorted, following the shape of the nanopillar and engulfing the entire pillar without disrupting the internal cytosolic materials of the cells.³⁹

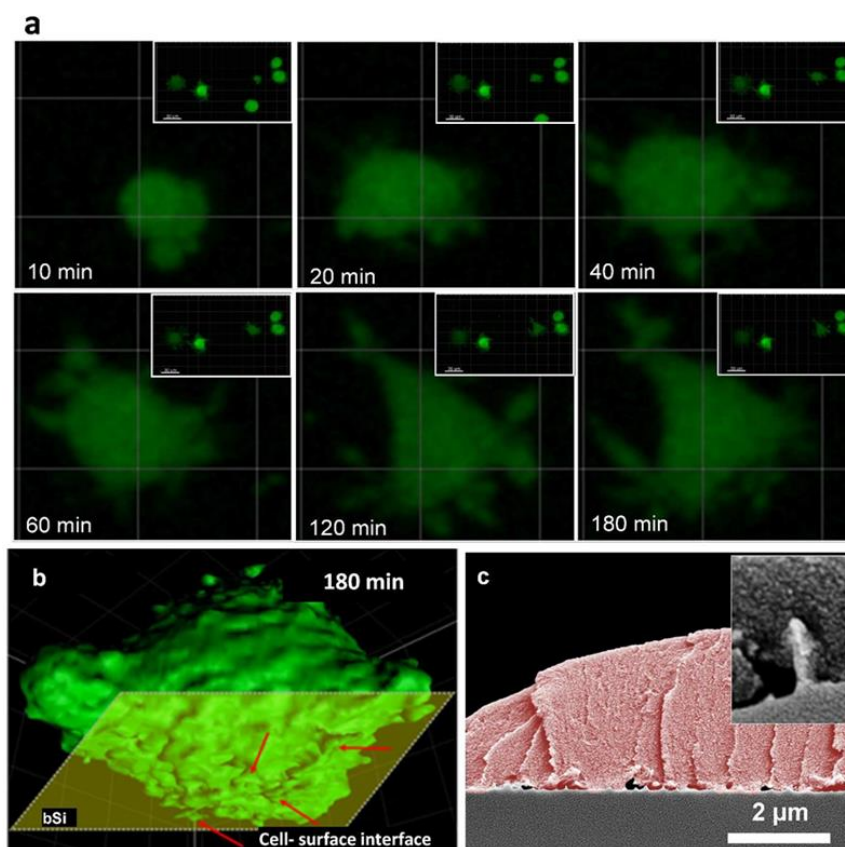


Figure 4. Dynamic interactions between COS-7 cells and the nanostructured bSi surfaces. (a) Real-time interactions of COS-7 cells on the nanostructured bSi surfaces visualized by CLSM over three hours. Arrows indicate the characteristic cell morphology producing filopodia during the initial attachment to the bSi surface. (b) Visualization of the interface between a single cell and the bSi surface. Arrows indicate local contact points with the nanopillars. Snapshots are taken from real-time interactions of COS-7 cells with the bSi surfaces (Supporting Movie 1). Cells were stained with the CellTracker CMFDA (green). (c) SEM images of freeze fractured COS-7 cells attached onto the bSi surfaces, showing the cell membrane covering the nanopillars.

Inflammatory responses to substratum surfaces

The nanostructured and non-structured silicon substrata were implanted into the subcutaneous connective tissue of CD-1 mice to assess the respective *in vivo* tissue reactions to these substrata. During 15 day-study, nor mild neither severe clinical symptoms of inflammation were observed. Macroscopically, on third day post-surgery, wound healing of implanted area was detected without implication of bacterial infection. Furthermore, post mortem examination revealed no morphological changes in any of axillary lymph nodes. The histological investigation of the interscapular region (implantation area) showed minor tissue reaction, manifested by presence of mononuclear cells surrounding implanted surface in both groups of animals. The immunohistochemical staining against macrophages allowed identifying the majority of invading mononuclear cells. Furthermore, histomorphometrical analysis was performed in order to count and compare the number of macrophages in both groups (Figure 5c, d). The results indicated that a larger foreign body response was prompted by the planar, nonstructured surface, with higher number of material-associated macrophages and thicker fibrous capsule in comparison to nanostructured surface (Figure S3). The images presented in Figure 5 highlight that the implanted bSi surfaces induced a lower level of inflammatory tissue reaction, which is consistent with previously reported studies for a range of other nanostructured materials, where the surface structure appeared to reduce the extent of this response⁴⁰.

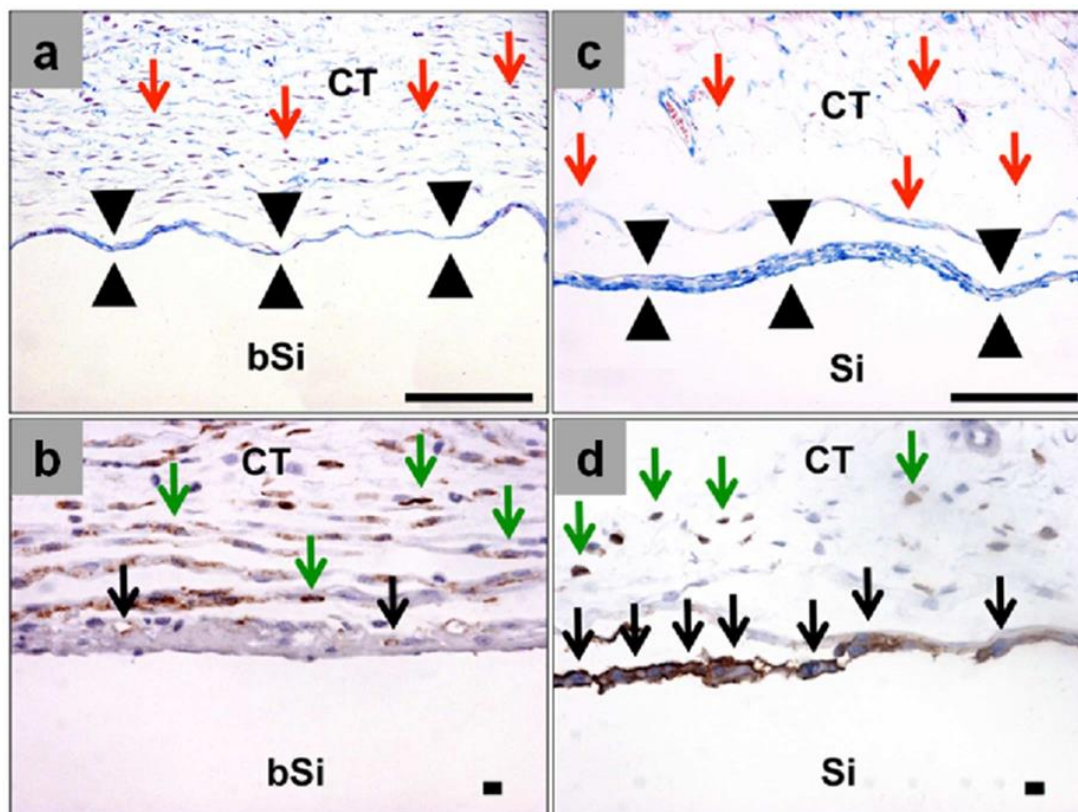


Figure 5. Representative microphotographs of the tissue reactions to the implanted bSi and control Si surfaces within the subcutaneous connective tissue (CT) of the CD-1 mouse at day 15 after implantation. (a) On the surface of bSi, a thin layer of mononuclear cells and extracellular matrix clearly indicated. Within the surrounding CT, an increased number of mononuclear cells (red arrows) detected. (b) The immunohistochemical detection showed that only a small number of the cells that had adhered to the bSi surface were macrophages (black arrows). Most of the cells within the surrounding CT were also identified as macrophages (green arrows). (c) At the surface of the implanted control Si substrata, a thicker layer (arrows) composed of mononuclear cells was detected. In the peri-implant CT, a greater number of mononuclear cells (red arrows) were detected. (d) Most of the cells that had attached to the control Si surfaces were identified as macrophages (black arrows), whereas numerous macrophages (green arrows) were detected within the peri-implant CT. All scale bars are 10 μm .

3.1.5 Conclusions

This work now provides the first demonstration of the dual behavior of a specific surface nanotopology, which not only exhibits bactericidal properties, but also affords the surface the ability to selectively eliminate only bacterial cells whilst promoting the growth and proliferation of eukaryotic cells. Furthermore, the nanotopology of the bSi surface is biocompatible and resulted in a reduced inflammatory response compared to its non-nanostructured equivalent when implanted into mice, despite its inherent bactericidal functionality.

With the demand for prosthetics and implants rising as a direct result of an ageing population, some of which is immuno-compromised,¹¹ the prevention of infection resulting from medical biomaterials remains a global challenge. Given that the bSi nanotopology has now been

shown to exhibit substantial biocompatibility and a lack of an inflammatory response upon implantation, together with its ability to eliminate bacterial contamination without the need for antimicrobial agents, this particular nanotopology represents a significant prospect for use in the design of antibacterial nanomaterials, especially in an era of increasing concern for antibiotic resistance.

3.1.6 Acknowledgements

The authors would like to thank Predrag Kovacevic and Stevo Najman, Faculty of Medicine, Department for Cell and Tissue Engineering; Institute of Biology and Human Genetics, and University of Niš, and Clinic of Plastic and Reconstructive Surgery, Clinical Center Niš, Serbia, for their excellent technical assistance. The authors acknowledge partial support of the SNAL Marie Curie ITN Network of the Seventh Framework Program of the European Commission 2012.

3.1.7 References

1. Foss, B. L.; Ghimire, N.; Tang, R.; Sun, Y.; Deng, Y. Bacteria and Osteoblast Adhesion to Chitosan Immobilized Titanium Surface: A Race for The Surface. *Colloids Surf. B Biointerfaces* **2015**, 134, 370-376.
2. Subbiahdoss, G.; Aleyt, T.; Kuijjer, R.; Busscher, H. J.; van der Mei, H. C. Influence of Prophylactic Antibiotics on Tissue Integration Versus Bacterial Colonization on Poly(methyl methacrylate). *Int. J. Artif. Organs* **2012**, 35 (10), 840-846.
3. Subbiahdoss, G.; Pidhatika, B.; Coullerez, G.; Charnley, M.; Kuijjer, R.; van der Mei, H. C.; Textor, M.; Busscher, H. J. Bacterial Biofilm Formation Versus Mammalian Cell Growth on Titanium-Based Mono-and Bi-Functional Coatings. *Eur. Cells and Mater.* **2010**, 19, 205-213.
4. Subbiahdoss, G.; Kuijjer, R.; Grijpma, D. W.; van der Mei, H. C.; Busscher, H. J. Microbial Biofilm Growth vs. Tissue Integration: "The Race for The Surface" Experimentally Studied. *Acta Biomater.* **2009**, 5 (5), 1399-1404.
5. Trentin, D. S.; Silva, D. B.; Frasson, A. P.; Rzhepishevskaya, O.; da Silva, M. V.; de L. Pulcini, E.; James, G.; Soares, G. V.; Tasca, T.; Ramstedt, M.; Giordani, R. B.; Lopes, N. P.; Macedo, A. J. Natural Green Coating Inhibits Adhesion of Clinically Important Bacteria. *Sci. Rep.* **2015**, 5, 8287.

6. Yue, C.; Kuijper, R.; Kaper, H. J.; van der Mei, H. C.; Busscher, H. J. Simultaneous Interaction of Bacteria and Tissue Cells with Photocatalytically Activated, Anodized Titanium Surfaces. *Biomaterials* **2014**, 35 (9), 2580-2587.
7. Lee, J. H.; Gu, Y.; Wang, H.; Lee, W. Y. Microfluidic 3D Bone Tissue Model for High-Throughput Evaluation of Wound-Healing and Infection-Preventing Biomaterials. *Biomaterials* **2012**, 33 (4), 999-1006.
8. Saldarriaga Fernández, I. C.; Busscher, H. J.; Metzger, S. W.; Grainger, D. W.; van der Mei, H. C. Competitive Time- and Density-Dependent Adhesion of Staphylococci and Osteoblasts on Crosslinked Poly(Ethylene Glycol)-Based Polymer Coatings in Co-Culture Flow Chambers. *Biomaterials* **2011**, 32 (4), 979-984.
9. Gristina, A. Biomaterial-Centered Infection: Microbial Adhesion Versus Tissue Integration. *Science* **1987**, 237 (4822), 1588-1595.
10. Busscher, H. J.; van der Mei, H. C.; Subbiahdoss, G.; Jutte, P. C.; van den Dungen, J. J.; Zaat, S. A.; Schultz, M. J.; Grainger, D. W. Biomaterial-Associated Infection: Locating The Finish Line in The Race for The Surface. *Sci. Transl. Med.* **2012**, 4 (153), 153rv10.
11. Dryden, M. Prosthetic Joint Infection: Managing Infection in A Bionic Era. *J. Antimicrob. Chemother.* **2014**, 69 (SUPPL1), i3-i4.
12. Chua, P. H.; Neoh, K. G.; Kang, E. T.; Wang, W. Surface Functionalization of Titanium With Hyaluronic Acid/Chitosan Polyelectrolyte Multilayers and RGD for Promoting Osteoblast Functions and Inhibiting Bacterial Adhesion. *Biomaterials* **2008**, 29 (10), 1412-1421.
13. Bhadra, C. M.; Truong, V. K.; Pham, V. T.; Al Kobaisi, M.; Seniutinas, G.; Wang, J. Y.; Juodkazis, S.; Crawford, R. J.; Ivanova, E. P. Antibacterial Titanium Nano-Patterned Arrays Inspired by Dragonfly Wings. *Sci. Rep.* **2015**, 5, 16817.
14. Hsu, S. H.; Tseng, H. J.; Lin, Y. C. The Biocompatibility and Antibacterial Properties of Waterborne Polyurethane-Silver Nanocomposites. *Biomaterials* **2010**, 31 (26), 6796-6808.
15. Engelsman, A. F.; van der Mei, H. C.; Francis, K. P.; Busscher, H. J.; Ploeg, R. J.; van Dam, G. M. Real Time Noninvasive Monitoring of Contaminating Bacteria in A Soft Tissue Implant Infection Model. *J. Biomed. Mater. Res. Part B Appl. Biomater.* **2009**, 88B (1), 123-129.
16. Ivanova, E. P.; Hasan, J.; Webb, H. K.; Truong, V. K.; Watson, G. S.; Watson, J. A.; Baulin, V. A.; Pogodin, S.; Wang, J. Y.; Tobin, M. J.; Løbbe, C.; Crawford, R. J. Natural Bactericidal Surfaces: Mechanical Rupture of *Pseudomonas aeruginosa* Cells by Cicada Wings. *Small* **2012**, 8 (16), 2489-2494.

17. Ivanova, E. P.; Hasan, J.; Truong, V. K.; Wang, J. Y.; Raveggi, M.; Fluke, C.; Crawford, R. J. The Influence of Nanoscopically Thin Silver Films on Bacterial Viability and Attachment. *Appl. Microbiol. Biotechnol.* **2011**, 91 (4), 1149-1157.
18. Ivanova, E. P.; Hasan, J.; Webb, H. K.; Gervinskas, G.; Juodkazis, S.; Truong, V. K.; Wu, A. H. F.; Lamb, R. N.; Baulin, V. A.; Watson, G. S.; Watson, J. A.; Mainwaring, D. E.; Crawford, R. J. Bactericidal Activity of Black Silicon. *Nat. Commun.* **2013**, 4, 2838.
19. Pogodin, S.; Hasan, J.; Baulin, V. A.; Webb, H. K.; Truong, V. K.; Nguyen, T. H. P.; Boshkovikj, V.; Fluke, C. J.; Watson, G. S.; Watson, J. A.; Crawford, R. J.; Ivanova, E. P. Biophysical Model of Bacterial Cell Interactions With Nanopatterned Cicada Wing Surfaces. *Biophys. J.* **2013**, 104 (4), 835-840.
20. Pham, V. T. H.; Truong, V. K.; Mainwaring, D. E.; Guo, Y.; Baulin, V. A.; Al Kobaisi, M.; Gervinskas, G.; Juodkazis, S.; Zeng, W. R.; Doran, P. P.; Crawford, R. J.; Ivanova, E. P. Nanotopography As a Trigger for The Microscale, Autogenous and Passive Lysis of Erythrocytes. *J. Mater. Chem. B* **2014**, 2 (19), 2819-2826.
21. Ivanova, E. P.; Hasan, J.; Webb, H. K.; Gervinskas, G.; Juodkazis, S.; Truong, V. K.; Wu, A. H. F.; Lamb, R. N.; Baulin, V. A.; Watson, G. S.; Watson, J. A.; Mainwaring, D. E.; Crawford, R. J. Bactericidal activity of black silicon. *Nat. Commun.* **2013**, 4.
22. FDA. *Bad Bug Book: Foodborne Pathogenic Microorganisms and Natural Toxins Handbook*. Food and Drug Administration (FDA): U.S. Department of Health and Human Services, **2012**.
23. Schmid-Hempel, P.; Frank, S. A. Pathogenesis, Virulence, and Infective Sose. *PLoS Pathog.* **2007**, 3 (10), 1372-1373.
24. Emmerson, M. A Microbiologist's View of Factors Contributing to Infection. *New Horiz.* **1998**, 6 (2 Suppl), S3-10.
25. Poelstra, K. A.; Barekzi, N. A.; Rediske, A. M.; Felts, A. G.; Slunt, J. B.; Grainger, D. W. Prophylactic Treatment of Gram-Positive and Gram-Negative Abdominal Implant Infections Using Locally Delivered Polyclonal Antibodies. *J. Biomed. Mater. Res.* **2002**, 60 (1), 206-215.
26. Hetrick, E. M.; Schoenfisch, M. H. Reducing Implant-Related Infections: Active Release Strategies. *Chem. Soc. Rev.* **2006**, 35 (9), 780-9.
27. Davies, D. Understanding Biofilm Resistance to Antibacterial Agents. *Nat. Rev. Drug. Discov.* **2003**, 2 (2), 114-122.
28. Subbiahdoss, G.; Fernández, I. C. S.; da Silva Domingues, J. F.; Kuijjer, R.; van der Mei, H. C.; Busscher, H. J. *In vitro* Interactions Between Bacteria, Osteoblast-Like Cells and

- Macrophages in The Pathogenesis of Biomaterial-Associated Infections. *PLoS ONE* **2011**, 6 (9).
29. Jahed, Z.; Molladavoodi, S.; Seo, B. B.; Gorbet, M.; Tsui, T. Y.; Mofrad, M. R. K. Cell Responses to Metallic Nanostructure Arrays with Complex Geometries. *Biomaterials* **2014**, 35 (34), 9363-9371.
30. Albuschies, J.; Vogel, V. The Role of Filopodia in The Recognition of Nanotopographies. *Sci. Rep.* **2013**, 3, 01658.
31. Beckwith, K. S.; Cooil, S. P.; Wells, J. W.; Sikorski, P. Tunable High Aspect Ratio Polymer Nanostructures for Cell Interfaces. *Nanoscale* **2015**, 7 (18), 8438-8450.
32. Kuo, S. W.; Lin, H. I.; Hui-Chun Ho, J.; Shih, V.; Chen, H. F.; Yen, T. J.; Lee, O. K. Regulation of The Fate of Human Mesenchymal Stem Cells by Mechanical and Stereo-Topographical Cues Provided by Silicon Nanowires. *Biomaterials* **2012**, 33 (20), 5013-5022.
33. Bucaro, M. A.; Vasquez, Y.; Hatton, B. D.; Aizenberg, J. Fine-Tuning The Degree of Stem Cell Polarization and Alignment on Ordered Arrays of High-Aspect-Ratio Nanopillars. *ACS Nano* **2012**, 6 (7), 6222-6230.
34. Brammer, K. S.; Choi, C.; Frandsen, C. J.; Oh, S.; Jin, S. Hydrophobic Nanopillars Initiate Mesenchymal Stem Cell Aggregation and Osteo-Differentiation. *Acta Biomater.* **2011**, 7 (2), 683-690.
35. Loya, M. C.; Brammer, K. S.; Choi, C.; Chen, L. H.; Jin, S. Plasma-Induced Nanopillars on Bare Metal Coronary Stent Surface for Enhanced Endothelialization. *Acta Biomater.* **2010**, 6 (12), 4589-4595.
36. Kuo, C. W.; Shiu, J. Y.; Chien, F. C.; Tsai, S. M.; Chueh, D. Y.; Chen, P. Polymeric Nanopillar Arrays for Cell Traction Force Measurements. **2010**, 31 (18), 3152-3158.
37. Cacchioli, A.; Ravanetti, F.; Alinovi, R.; Pinelli, S.; Rossi, F.; Negri, M.; Bedogni, E.; Campanini, M.; Galetti, M.; Goldoni, M.; Lagonegro, P.; Alfieri, R.; Bigi, F.; Salviati, G. Cytocompatibility and Cellular Internalization Mechanisms of SiC/SiO₂ Nanowires. *Nano Lett.* **2014**, 14 (8), 4368-4375.
38. Robinson, J. T.; Jorgolli, M.; Shalek, A. K.; Yoon, M. H.; Gertner, R. S.; Park, H. Vertical Nanowire Electrode Arrays As a Scalable Platform for Intracellular Interfacing to Neuronal Circuits. *Nat. Nanotechnol.* **2012**, 7 (3), 180-184.
39. Hanson, L.; Lin, Z. C.; Xie, C.; Cui, Y.; Cui, B. Characterization of The Cell-Nanopillar Interface by Transmission Electron Microscopy. *Nano Lett.* **2012**, 12 (11), 5815-5820.
40. Anderson, J. M.; Rodriguez, A.; Chang, D. T. Foreign Body Reaction to Biomaterials. *Semin. Immunol.* **2008**, 20 (2), 86-100.

3.1.8 Supplementary Data

S1. Experimental Section

S1.1. Characterization of bSi surface

The surface morphology of bSi and the geometry of the single nanopillar were visualized using SEM (ZEISS SUPRA, Germany), operated at 3 kV. Tilted scanning electron micrographs, operated at an angle of 45°, were obtained to determine the pillar heights, tip widths and pillar density. The physico-chemical properties of the bSi surfaces were characterized by X-ray diffractometry (XRD) and Raman spectroscopy. Un-modified silicon wafers were used as the control surface in all experiments. The crystallinity of the surfaces was measured using a Bruker D8 Advance XRD, operated at ambient conditions using Cu-K α radiation ($\lambda = 0.15406$ nm). The samples were scanned over a 2θ range of 30 - 80° at a scanning rate of 1 degree per minute. The surface chemical properties were characterized using a Raman microspectrometer (WITEC, Ulm, Germany) with a laser wavelength of 532 nm ($h\nu = 2.33$ eV) under a 100 × magnification objective lens (numerical aperture = 1.0). Scanning was performed independently on 5 different areas of 5 different substrata. The surface wettability of bSi was determined via contact angle measurements using an FTA 1000C device equipped with a nanodispenser (First Ten Angstroms Inc.). All imaging and measurements were performed in triplicate with 5 different samples.

S1.2. Implantation and explantation of specimens in CD-1 mice

The *in vivo* pilot study was performed on 8 female, 6-8 weeks old, CD-1 mice that were obtained from Military Medical Academy (Belgrade, Serbia) with the approval of the Local Ethical Committee (Faculty of Medicine, University of Niš, Serbia). Animal housing was provided under standard conditions, *i.e.*, regular mouse pellets and access to water *ad libitum* as well as an artificial light–dark cycle of 12 h each.

Prior to implantation, the animals were randomly categorized into two study groups with 4 animals per group for subcutaneous implantation of the nanostructured bSi and nonstructured silicon samples for 15 days. Animals of group 1 obtained implantation of the bSi samples, while animals of the group 2 received the non-structured silicon samples (*i.e.*, control group).

The implantation of the samples was performed according to a previously established protocol.¹⁻⁵ Briefly, an intra-peritoneal anesthesia (10 ml of 50 mg mL⁻¹ ketamine with 1.6 mL of 2% xylazine), shaving and disinfection of the rostral region were initially conducted. After this was completed, the silicon samples were implanted in a preformed subcutaneous pocket in the

subscapular region under sterile conditions and the implantation sides were finally closed using 5.0 Prolene (Ethicon, New Jersey, USA). After the implantation procedure the animals were housed individually until the explantation of the materials took place.

After 15 days of implantation, the peri-implant tissue, together with the implanted silicon samples, was obtained after sacrifice of the animals via an overdose of the abovementioned anesthetics and the implanted samples were carefully expurgated using a surgical forceps due to their non-cutability after paraffin embedding.

S1.3. Histological analyses

The peri-implant tissue was histologically prepared for qualitative and quantitative analyses as described elsewhere.¹⁻⁵ These explants were initially preserved in 4% formaldehyde solution for 24 h. Afterwards, the formalin fixed tissue was cut into several segments for further embedding, processed in automatic tissue processor (Leica TP1020, Germany) and embedded in paraffin blocks. This procedure allowed for producing multiple 2 - 4 μm thick sections using a rotary microtome (Leica, Germany). These tissue sections were immediately affixed on charged glass slides (VWR International, SuperFrost® Plus) and incubated at 37 °C for 12 hours.

Shortly before staining, a dewaxing- and rehydration process took place by sequential immersion of the slides in xylene and graded concentration of ethanol. Initially, samples were stained by hematoxylin and eosin (HE) to evaluate the section quality. After selection of the tissue blocks with the best quality, Azan- and Giemsa staining techniques were applied. Furthermore, murine macrophages were immunohistochemically detected by using an anti-F4/80 primary antibody (rat anti-mouse antibody, clone: BM8, Dianova, Germany) and an autostainer (Autostainer 360, ThermoScientific, Germany). Endogenous peroxidase was then quenched with 3% H_2O_2 and epitope unmasking was by proteinase K application, while blocking was conducted via Avidin-Biotin Complex (ABC Vector Elite, Vector Laboratories, US). A mixture of Tris-Buffered Saline and Tween-20 was used as a washing buffer. For visualization by light microscopy, slides were additionally stained with 3,3'-diaminobenzidine (DAB); and for increased sensitivity of the DAB chromogen, the VECTASTAIN Elite ABC peroxidase reagent (Vector Laboratories, US) was used to remove undesirable "background" due to non-specific immune-labeling. Negative controls for each slide were prepared by the same process, but by omitting the primary antibodies.

S1.4. Qualitative and quantitative histomorphometrical analyses

Qualitative histological analyses were conducted using an established protocol.⁴⁻⁵ Bright field light microscopy (Nikon Eclipse 80i, Japan) was used to determine interactions between the tissue and the biomaterials. The focus was on the description of the biomaterial induced inflammatory responses and the cells involved in this process. A DS-F1 digital camera and a digital sight control unit (both: Nikon, Tokyo, Japan) that were connected to the above-mentioned microscope were used for making microphotographs.

A quantitative histomorphometrical analysis was performed after digitalization of the sections that were immunohistochemically stained by F4/80 for macrophage detection by a specialized scanning microscope system composed of an Eclipse 80i microscopy (Nikon, Japan), a DS-F1 digital camera and an automatic scanning table (EK 75 × 50 Pilot, Marzhauser, Germany) connected to computer running the NIS-elements AR software (version 4.10.03, Nikon, Japan) as previously described.¹⁻⁵ Briefly, the length of every biomaterial-induced capsule was measured (in mm). Furthermore, the amount of positive immune-labeled cells, *i.e.*, murine macrophages, adherent to the material surfaces was manually counted for each section. In order to compare the material-adherent macrophages the numbers of macrophages in relation to the biomaterial surfaces (macrophages mm⁻²) was calculated. The data were statistically analyzed by a Student's *t*-test using the SPSS 16.0.1 software (SPSS Inc., Chicago, IL, USA). Statistically, significant differences were considered if *p*-values were less than 0.05 (* *p* < 0.05), and highly significant if *p*-values less than 0.01 (** *p* < 0.01) or less than 0.001 (***) *p* < 0.001). Finally the histomorphometrical data were displayed as means ± standard deviations (SD) using the GraphPad Prism 6.0c software (GraphPad Software Inc., La Jolla, USA).

S2. Results and Discussion Section

S2.1 Characterization of bSi surfaces

The physico-chemical properties of the bSi were evaluated using SEM, Raman spectroscopy and XRD. The nanopillars were shown to be typically 652 nm ± 10.3 nm in length, with a typical tip diameter of 100 nm ± 1.8 nm, randomly distributed in an array of approximately 12.2 pillars per μm² (Fig. S1a-c). The Raman spectrum of the bSi surface showed the typical peaks of silicon at 520 nm with a slight enhancement in peak intensity compared to the as-received silicon wafer, considered to be due to the presence of the “hot spots” created by the clusters of nanopillars (Fig. S1d).⁶⁻⁷ Similarly, in the X-ray diffractogram, the nanopillar surface of the bSi exhibited an intensive peak at 69° of crystallite Si <400> which were barely detected on the flat

Si wafer (Fig. S1e).⁸⁻⁹ The water contact angle was found to be $40.1^\circ \pm 0.3^\circ$ which indicates that the surface is hydrophilic.

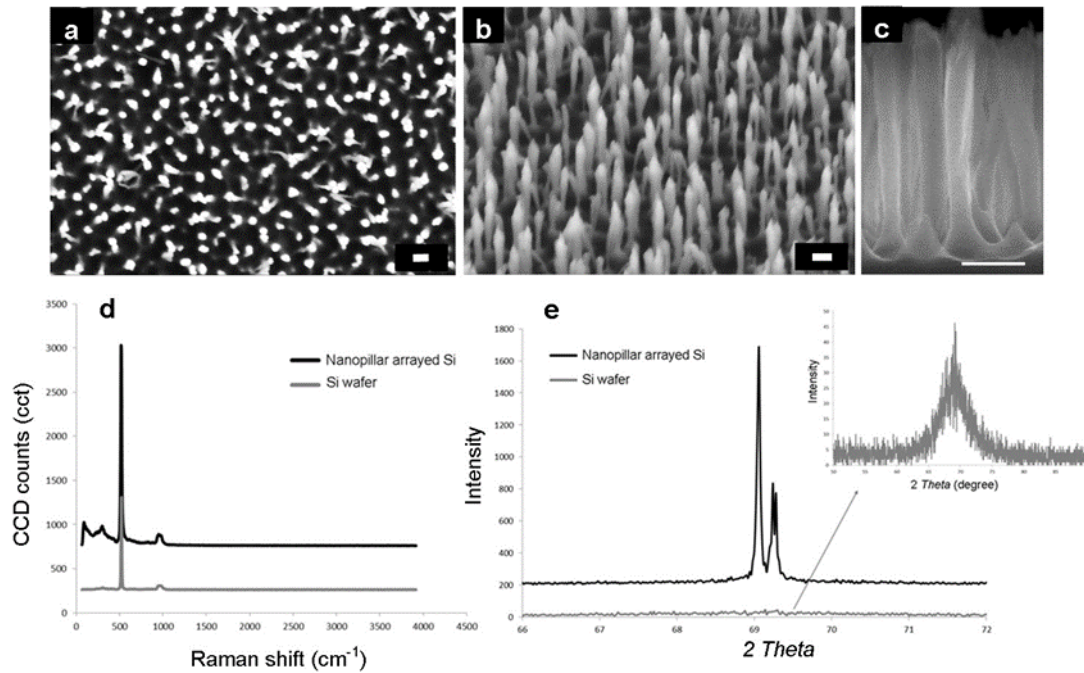


Figure S1. Characterization of the bSi using SEM (a – c, scale bar 200 nm), Raman spectroscopy (d), and X-ray diffractometry (e), the enhanced characteristic peaks (inset) of the silicon nanopillars.

S2.2 Quantification of COS-7 cultured on pre-infected bSi

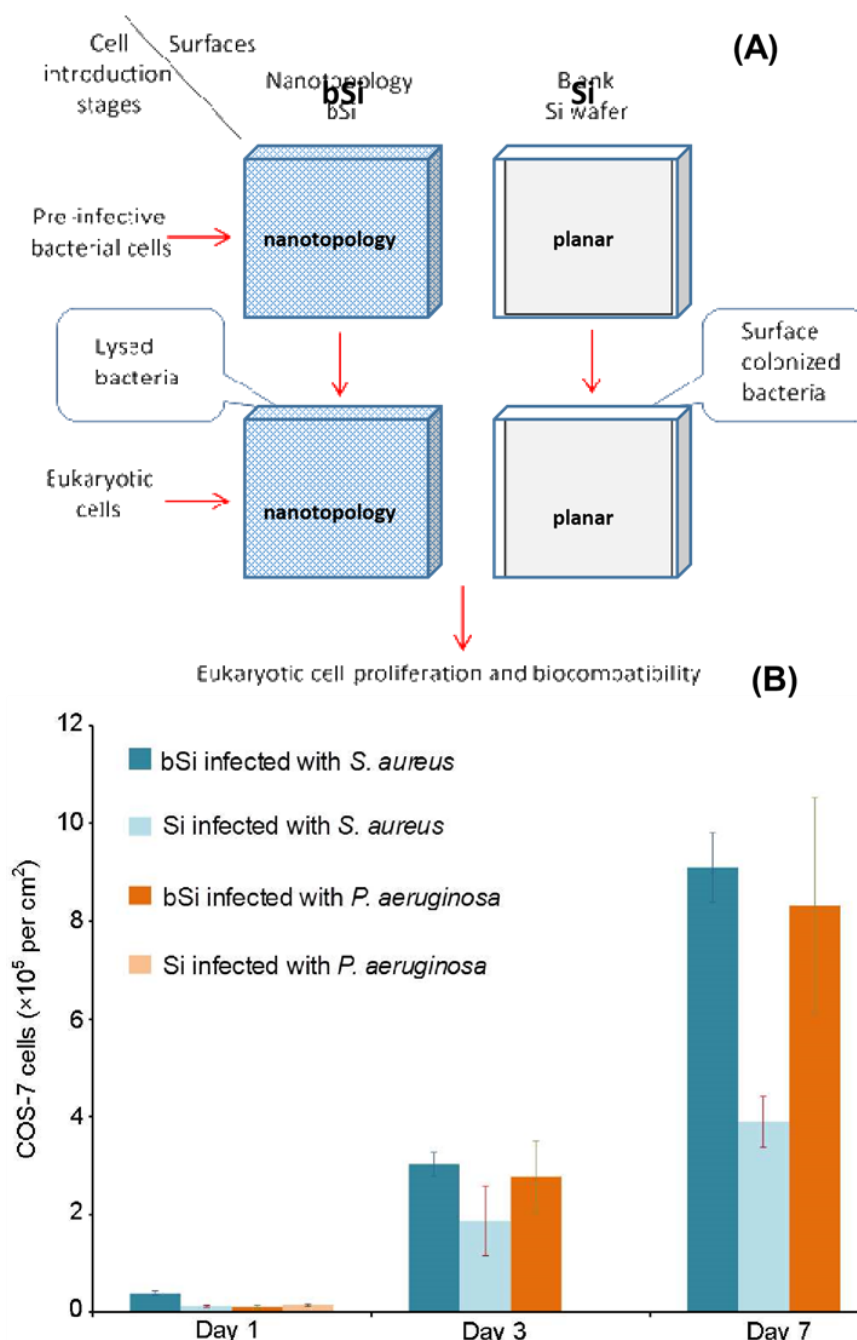


Figure S2. (A) Overall study protocol; (B) Quantification of COS-7 cells attached onto the substrate surfaces infected with pathogenic bacteria after 1, 3 and 7 days of contact. Cell quantification was based on the confocal data images, indicating the quantity of viable COS-7 cells retained on the surface at each time point.

S2.3 Inflammatory responses on bSi surfaces

The histomorphometrical measurements of material-adherent macrophages revealed that significantly more macrophages (** $p < 0.01$) were found at the material surfaces of the

non-structured silicon implants (20.61 ± 1.08 macrophages mm^2) as compared to the group of the bSi implants (8.21 ± 1.87 macrophages mm^2) (Fig. S3).

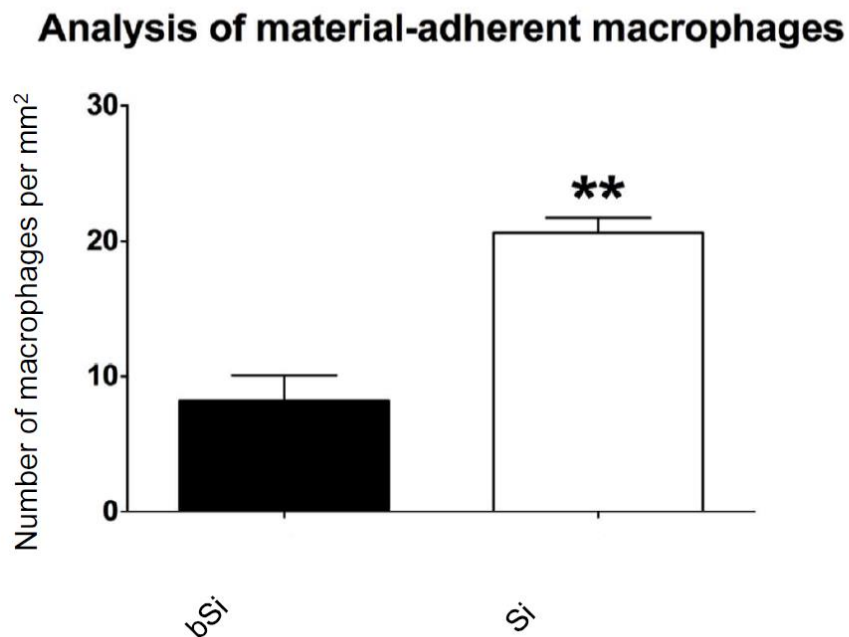


Figure S3. The number of macrophages associated with the implanted silicon surfaces. Bar chart shows the results of the analysis for the histomorphometrical measurements of material-adherent macrophages per mm^2 . Control Si showed a significantly increased number of adhered macrophages as compared to bSi (** $p < 0.01$).

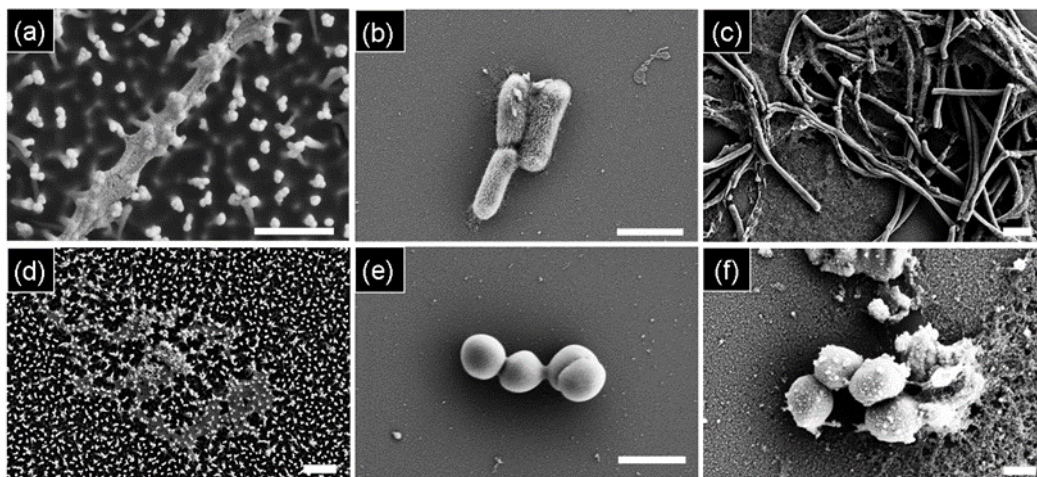


Figure S4. Typical morphology of *P. aeruginosa* (a, b & c) and *S. aureus* (d, e & f) cells after the 6 hours pre-infection process with bSi (a, d) and non-structured Si surfaces (b, e); compared to the morphology of bacterial cells after 24 hours exposing the pre-infected surfaces to COS-7 cultured in DMEM (supplemented with 1% penicillin-streptomycin). No bacterial cells could be found on bSi after one day introducing COS-7 cells, bacterial debris could not be identified under SEM. Scale bars are 2 μm .

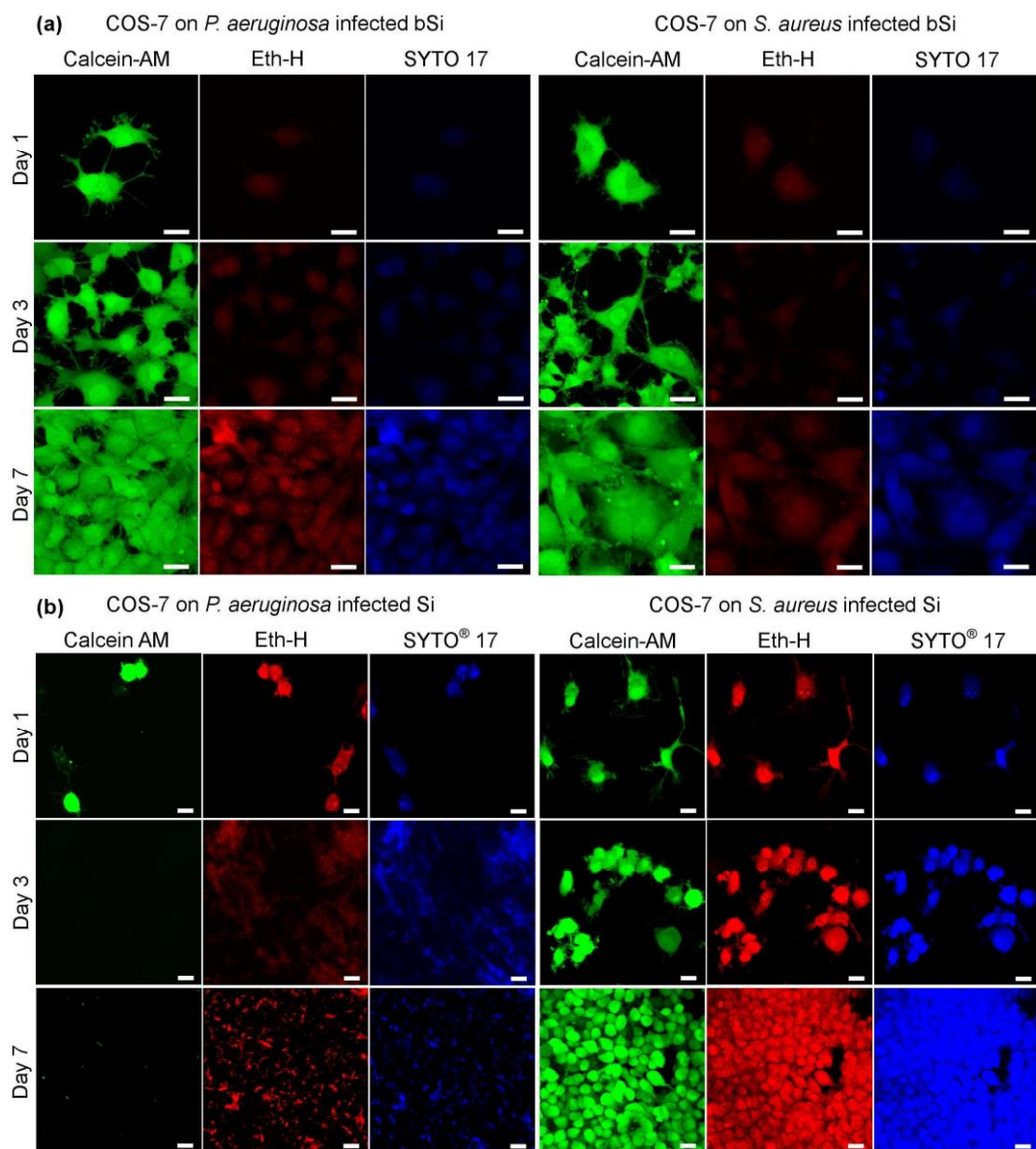


Figure S5. Typical confocal images of COS-7 cells cultured on bSi (a) and Si (b) surfaces that were pre-infected with live *P. aeruginosa* and *S. aureus* bacteria. Scale bars are 20 μm . Live COS-7 cells were stained with calcein AM (green), dead COS-7 cells were stained with ethidium homodimer-1 (red), bacterial cells were stained with SYTO® 17, presented as separated fluorescent images.

References

1. Barbeck, M.; Lorenz, J.; Kubesch, A.; Booms, P.; Boehm, N.; Choukroun, J.; Sader, R.; Kirkpatrick, C. J.; Ghanaati, S. Porcine Dermis-Derived Collagen Membranes Induce Implantation Bed Vascularization Via Multinucleated Giant Cells: A Physiological Reaction? *J. Oral Implantol.* **2015**, 41 (6), e238-e251.
2. Barbeck, M.; Lorenz, J.; Grosse Holthaus, M.; Raetscho, N.; Kubesch, A.; Booms, P.; Sader, R.; Kirkpatrick, C. J.; Ghanaati, S. Porcine Dermis and Pericardium-Based, Non

- CrossLinked Materials Induce Multinucleated Giant Cells After Their *In vivo* Implantation: A Physiological Reaction? *J. Oral Implantol.* **2015**, 41 (6), e267-e281.
3. Barbeck, M.; Udeabor, S.; Lorenz, J.; Schlee, M.; Grosse Holthaus, M.; Raetscho, N.; Choukroun, J.; Sader, R.; Kirkpatrick, C. J.; Ghanaati, S. High-Temperature Sintering of Xenogeneic Bone Substitutes Leads to Increased Multinucleated Giant Cell Formation: *In vivo* and Preliminary Clinical Results. *J. Oral Implantol.* **2015**, 41 (5), e212-e222.
 4. Ghanaati, S.; Barbeck, M.; Detsch, R.; Deisinger, U.; Hilbig, U.; Rausch, V.; Sader, R.; Unger, R. E.; Ziegler, G.; Kirkpatrick, C. J. The Chemical Composition of Synthetic Bone Substitutes Influences Tissue Reactions *In vivo*: Histological And Histomorphometrical Analysis of The Cellular Inflammatory Response to Hydroxyapatite, Beta-Tricalcium Phosphate and Biphasic Calcium Phosphate Ceramics. *Biomed. Mater.* (Bristol, U. K.) **2012**, 7 (1), 015005.
 5. Ghanaati, S.; Barbeck, M.; Orth, C.; Willershausen, I.; Thimm, B. W.; Hoffmann, C.; Rasic, A.; Sader, R. A.; Unger, R. E.; Peters, F.; Kirkpatrick, C. J. Influence of BetaTricalcium Phosphate Granule Size and Morphology on Tissue Reaction *In vivo*. *Acta Biomater.* **2010**, 6 (12), 4476-4487.
 6. Qiu, T.; Wu, X. L.; Shen, J. C.; Ha, P. C. T.; Chu, P. K. Surface-Enhanced Raman Characteristics of Ag Cap Aggregates on Silicon Nanowire Arrays. *Nanotechnology* **2006**, 17 (23), 5769-5772.
 7. Lee, S. J.; Morrill, A. R.; Moskovits, M. Hot Spots in Silver Nanowire Bundles for Surface-Enhanced Raman Spectroscopy. *J. Am. Chem. Soc.* **2006**, 128 (7), 2200-2201.
 8. Xiong, Z.; Zheng, M.; Liu, S.; Ma, L.; Shen, W. Silicon Nanowire Array/Cu₂O Crystalline Core-Shell Nanosystem for Solar-Driven Photocatalytic Water Splitting. *Nanotechnology* **2013**, 24 (26), 265402.
 9. Jawad, M. J.; Hashim, M. R.; Ali, N. K.; Crocoles, E. P.; Sharifabad, M. E. An Alternative Method to Grow Ge Thin Films on Si by Electrochemical Deposition for Photonic Applications. *J. Electrochem. Soc.* **2011**, 159 (2), D124-D128.

2.4. Pheochromocytoma (PC12) Cell Response on Mechanobactericidal Titanium Surfaces

Materials, **2018**, 11(4).

Wandiyanto, J. V.^a, Linklater, D.^{a,b}, Perera, P. G. T.^a, **Orłowska, A.**^{c,d}, Truong, V. K.^a, Thissen, H.^e, Ghanaati, S.^c, Baulin, V.^d, Crawford, R. J.^f, Juodkazis, S.^{a,b}, & Ivanova, E. P.^a.

^a School of Science, Swinburne University of Technology, Hawthorn, VIC 3122, Australia

^b Centre for Micro-Photonics, Swinburne University of Technology, Hawthorn, VIC 3122, Australia

^c Frankfurt Orofacial Regenerative Medicine, University Hospital Frankfurt, Theodor-Stern-Kai 7, D-60590 Frankfurt am Main, Germany

^d Departament d'Enginyeria Química, Universitat Rovira i Virgili, 26 Avenue dels Països Catalans, 43007 Tarragona, Spain

^e CSIRO Manufacturing, Clayton, VIC 3168, Australia

^f School of Science, RMIT University, Melbourne, VIC 3001, Australia

3.4.1 Abstract

Titanium is a biocompatible material that is frequently used for making implantable medical devices. Nanoengineering of the surface is the common method for increasing material biocompatibility, and while the nanostructured materials are well-known to represent attractive substrata for eukaryotic cells, very little information has been documented about the interaction between mammalian cells and bactericidal nanostructured surfaces. In this study, we investigated the effect of bactericidal titanium nanostructures on PC12 cell attachment and differentiation—a cell line which has become a widely used *in vitro* model to study neuronal differentiation. The effects of the nanostructures on the cells were then compared to effects observed when the cells were placed in contact with non-structured titanium. It was found that bactericidal nanostructured surfaces enhanced the attachment of neuron-like cells. In addition, the PC12 cells were able to differentiate on nanostructured surfaces, while the cells on non-structured surfaces were not able to do so. These promising results demonstrate the potential application of bactericidal nanostructured surfaces in biomedical applications such as cochlear and neuronal implants.

3.4.2 Introduction

Recent advances in the ability to fabricate large-scale topographical nanofeatures have provided researchers with the opportunity to combat the bacterial contamination of surfaces using a next-generation technology. This technology promises to provide long-lasting and durable mechanobactericidal activity without risking the emergence of bacterial resistance.^{1,2} Conventional antibacterial surfaces rely on the diffusive release of antibacterial agents with which the material has been impregnated.^{3,4} The leaching of antibiotics and other antimicrobial agents into the environment poses a considerable risk to non-target organisms and may be contributing to an increase in the emergence of multi-drug-resistant pathogenic bacteria. Therefore, antibacterial surfaces that employ non-diffusive techniques are highly preferred and thus have been the focus of a great deal of recent investigation.³

The ability of certain nanoscale structures to kill bacteria via physico-mechanical means has been investigated over the past few years.⁵⁻⁷ The first observed mechanobactericidal surface was of biological origin; the dense nanopillar array on the surface of the wings of the cicada *Psaltoda claripennis* were observed to selectively kill bacteria.^{5,6} Since this time, many new surface structures have been designed, largely modelled upon the surface nanoarchitecture of insect wings, plant leaves, and animal skin.^{5,8,9} Such surfaces utilize biomimetic nanoarchitecture

in order to achieve regular arrays of nanoscale pillars that are capable of delivering a lethal mechanical force to bacterial cell membranes coming into contact with the surface.

Resistance to bacterial contamination is of particular importance for the manufacture of orthopedic implants. Nanoengineering of titanium and titanium alloys has been performed in order to generate surfaces possessing nanotopographies that are not only antibacterial, but also display biocompatibility towards human cells.¹⁰⁻¹² Considerable progress in implant technologies over the last decade has demonstrated the significance of micro-structured topographies which are able to guide cell growth and tissue development. These surfaces also have the ability to control cell migration and alignment,¹⁰⁻¹² yet currently the impact of the surface nanoscale topographical features on the growth of mammalian cells is only an emerging area of research, and hence very little is known on this topic. In addition, it is important to proceed with cell-surface interaction investigations in a standardized manner which accounts for superficial modifications of the biomaterials and modification to the culture conditions, all of which may have an impact on the response of cells grown on the studied materials, ensuring greater accuracy of the measurements obtained.¹³ Mimicking the surface nanoarchitecture of the dragonfly, hydrothermally etched titanium surfaces have been shown to possess selective bactericidal activity while enhancing the attachment and proliferation of primary human fibroblasts.² Another study has shown that the titanium dioxide nanowire arrays inspired by cicada wing surfaces can also be selectively bactericidal, but are capable of guiding human osteoblast-like cell proliferation depending on the presence of a distinct nanostructure.¹⁴ These studies provide examples of the ability of nanostructured titanium surfaces to resist bacterial contamination yet provide a biocompatible scaffold for the attachment and proliferation of mammalian cells.

Pheochromocytoma (PC12) cells are a commonly studied representative of a neuronal cell line which is often used in *in vitro* studies to examine the degree of differentiation and neurotoxicity commonly associated with neurodegenerative diseases.^{15,16} Under common laboratory culture conditions, PC12 cells adhere poorly to culture flasks and prefer to grow while floating in cell aggregates.¹⁷ Therefore, to encourage cellular attachment, tissue culture surfaces are frequently functionalized with a protein. Once adhered to a substratum, PC12 neuron-like cells display growth, proliferation, differentiation, and development of neurite outgrowths.¹⁵

While the presence of micro-scale topographical features on substrata are known to enhance cell attachment,¹⁸⁻²⁰ the influence of these bactericidal nanostructured surfaces on the cell behavior has not been investigated to the same extent, and therefore this study was aimed to fill this gap in existing knowledge. The results demonstrate that mechanobactericidal nanostructures generated on the surface of commercially pure grade titanium can promote the

attachment of PC12 cells and enhance the extent of cell differentiation. The cell attachment behavior on the nanostructured surfaces was compared to that obtained on non-structured titanium surfaces coated with poly-L-lysine.

3.4.3 Experimental

Preparation of As-Received and Hydrothermally Etched Titanium Discs

Titanium rods, 1 cm in diameter, were cut into 2 mm billets using a Secotom 50 automatic grinder (Struers, Milton, QLD, Australia). Prior to hydrothermal treatment, Ti discs were polished with silicon carbide grinding paper (grit size 1200) and cleaned ultrasonically in MilliQ water, 100% ethanol, 100% acetone, and finally 50% ethanol for 6–8 min each, respectively. This cleaning process was performed to remove organic and inorganic contaminants produced during polishing steps. Afterward, cleaned, and polished Ti discs were dried at 37 °C overnight.

Hydrothermal treatment (HTE) of the as-received (AR) titanium billets was performed by immersion in 1 M KOH solution in a Teflon container as described elsewhere.² The resulting samples were cleaned with 75% ethanol and sterilized under UV radiation for 30 min prior to experiments

Culturing and Seeding of PC12 Cells

The pheochromocytoma cells (PC12) were purchased from the American Type Culture Collection (ATCC, Manassas, VA, USA) and were cultured in complete Gibco™ RPMI medium (Thermo Fisher Scientific, Waltham, MA, USA) supplemented with 10% Gibco™ horse serum (HS, Thermo Fisher Scientific, Waltham, MA, USA), 5% Gibco™ foetal bovine serum (FBS, Thermo Fisher Scientific, Waltham, MA, USA), and 1% Gibco™ penicillin/streptomycin (PS, Thermo Fisher Scientific, Waltham, MA, USA) at 37 °C and 5% CO₂ in a 95% humidified incubator. The medium was changed every two days and passaged accordingly when cell confluence reached 90%.

For each independent experiment, PC12 cells were seeded at a density of 10,000 cells per 100 μL on AR-Ti and HTE-Ti samples. After 1-, 5-, and 7-day incubation periods, the samples were prepared for imaging as described in the following sections. Cell proliferation and total protein count assays were performed after 1 day of incubation to study the attachment patterns. All experiments were approved under the Swinburne Biosafety Project 2014/SBC01.

Cellular Morphology

Scanning electron microscopy (SEM) was used to assess the cell morphology following incubation on AR and HTE Ti surfaces. Prior to SEM analysis, the cells were fixed with 2.5% glutaraldehyde for 25 min. The cells were then dehydrated by passing through a 30%, 50%, 70%, and 100% graded ethanol series for 15 min each. Before imaging, samples were gold sputtered using a NeoCoater MP-19020NCTR (JEOL, Tokyo, Japan). SEM images were taken using a field emission SEM (FESEM) SUPRA 40VP (Carl Zeiss, Jena, Germany) at an accelerating voltage of 3 kV at magnifications of 10,000 × for AR and 2000 × for HTE samples.

Immunohistochemistry

The PC12 cells were incubated with the Ti substrate for 1 day. After this time, the samples were initially fixed with 4% paraformaldehyde for 15 min, permeabilised in 0.1% Triton X for 5 min then blocked with 1% Bovine Serum Albumin (BSA) for 60 min. Image-IT[®] FX Signal Enhancer (Invitrogen, Carlsbad, CA, USA) was also used during the fixation stage to enhance the subsequent fluorescent signals. Samples were then treated with a primary anti-vinculin antibody (Sigma, St. Louis, MO, USA) overnight, followed by goat anti-mouse secondary antibody conjugated with Alexa Fluor 594 (Invitrogen). Actin filaments were visualised by staining the cells with Alexa Fluor 488 conjugated phalloidin (Invitrogen). Cell nuclei were labelled using TO-PRO3 (Invitrogen). To study the extent of cell differentiation after 5 and 7 days of incubation, the anti-nestin antibody (Sigma) was applied as the primary antibody. Samples were then imaged using a Fluoview FV10i microscope (Olympus, Tokyo, Japan) at 60 × magnification.

Cell Proliferation

Cell proliferation was determined using the CellTiter 96[®] Aqueous One Solution Cell Proliferation Assay (Promega, Madison, WI, USA). Tetrazolium was added to the PC12 cell culture at a 10% ratio of the final volume and incubated for 90 min at 37 °C and 5% CO₂. This allowed for the reduction of MTS (3-(4,5-dimethylthiazol-2-yl)-5-(3-carboxymethoxyphenyl)-2-(4-sulfophenyl)-2H-tetrazolium) to formazan, resulting in the formation of a colored precipitate (purple). The absorbance was recorded at a wavelength of 490 nm using a FLUOstar Omega microplate reader (BMG LABTECH, Thermo Fisher Scientific, Waltham, MA, USA).

Protein Concentration of PC12

Total protein concentrations were determined using the bicinchoninic acid protein (BCA) assay (Sigma-Aldrich, St. Louis, MO, USA). The PC12 cells were lysed with 150 μ L of protein lysis reagent (Sigma-Aldrich, NSW, Australia) and incubated for 15 min at 25 °C. After incubation, the cells were spun down at 1300 rpm for 5 min at 25 °C, then 25 μ L aliquots of the supernatant were placed on a 96-well plate (Sarstedt, Germany) together with 200 μ L of BCA reagent (bicinchoninic acid solution and copper (II) sulphate pentahydrate 4%). The sample was then incubated for 30 min at 37 °C and the absorbance was recorded at 562 nm using the FLUOstar Omega micro plate reader (BMG LABTECH).

Cell Viability

Cellular viability of PC12 was achieved by labelling them with the LIVE/DEAD Viability/Cytotoxicity Kit (Invitrogen), which is composed of calcein AM and ethidium homodimer-1 for live cell and dead cell staining, respectively. Viable cells were quantified based on the confocal imaging data, expressed as the percentage of non-viable cells over the total population.

X-ray Photoelectron Spectroscopy (XPS)

An X-ray photoelectron spectroscopic (XPS) analysis was performed using a Thermo Scientific K-alpha X-ray photoelectron spectrometer (Thermo Fisher Scientific, Waltham, MA, USA), equipped with a monochromatic X-ray source (Al K α , $h\nu = 1486.6$ eV) operating at 150 W. The spectrometer energy scale was calibrated using the Au 4f $_{7/2}$ photoelectron peak at a binding energy (BE) of 83.98 eV. During analysis, the samples were flooded with low-energy electrons to counteract any surface charging that may occur. The hydrocarbon component of the C 1s peak (BE = 284.8 eV) was used as a reference for charge correction. Photoelectrons emitted at an angle of 90° to the surface from an area of 700 \times 300 μ m 2 were analysed with 160 eV for survey spectra and then with 20 eV for region spectra. Survey spectra were recorded at intervals of 1.0 eV/step, while the region spectra were taken at intervals of 0.1 eV/step. The Shirley algorithm was used to measure the background core level spectra, and chemically distinct species in the high-resolution regions of the spectra were resolved using synthetic Gaussian–Lorentzian components after the background was removed using the Thermo Scientific Advantage Data System software (Thermo Fischer Scientific, Waltham, MA, USA). High-resolution scans were performed across each of the C 1s, O 1s, Ti 2p, K 2p peaks.

X-ray Diffractometry (XRD)

XRD (Bruker D8 Advance) was performed under ambient conditions to determine the degree of crystallinity of the Ti samples. The samples were scanned over a 2θ range of $30\text{--}85^\circ$ at a scanning rate of 1 degree per minute using Cu- $K\alpha$ radiation ($\lambda = 0.15406$ nm).

Scanning Electron Microscopy

High-resolution electron micrographs of Ti discs were recorded using a field emission SEM (FESEM; ZEISS SUPRA 40 VP, Oberkochen, BW, Germany) at 3 kV and $75,000\times$ magnification. To assess the cell morphology of bacteria, titanium discs with adherent bacteria were sputter-coated with gold using a Dynavac CS300 prior to imaging. Characterisation of the surface nanostructure (e.g., edge density, aspect ratio, and tip diameter) was performed using Image J. The colour threshold for binary SEM images was adjusted and the particles were then analysed. The particle analysis allowed an area distribution to be obtained, allowing the determination of the average edge density of the tips per square micron.

Atomic Force Microscopy (AFM)

AFM was used to study the topographical features of the surface at the nanoscale level using an Innova scanning probe microscope (Veeco, Bruker, Billerica, MA, USA) followed by a roughness analysis. The measurements were performed in tapping mode in air to minimise any damage to the tip from the interaction between tip and sample surface. The silicon cantilever used in the tapping mode (Cont20A, Veeco Probes) had a spring constant of 0.9 N m^{-1} and resonance frequency ranging between 18 kHz and 24 KHz. All samples were scanned over a $1 \times 1\ \mu\text{m}^2$ area to perform a roughness analysis of the surface. To study the surface topography, various surface roughness parameters—average roughness (S_a), root-mean-square roughness (S_q), maximum peak height (S_{max}), skewness (S_{sk}), and kurtosis (S_{ku})—were calculated using Gwyddion data processing software, and are presented in Table 1.²¹ The results obtained were expressed in terms of their mean values and the corresponding standard deviations following the commonly used protocol.^{22,23}

Table 1. Surface chemical, topological, and physico-chemical characteristics of as-received and nanostructured titanium surfaces obtained by X-ray photoelectron spectroscopy (XPS), atomic force microscopy (AFM), and water contact angle measurements. AR: as-received; HTE: hydrothermal treatment.

Samples	Chemical composition (%)				Wettability		AFM ($1 \times 1 \mu\text{m}^2$)		
	C	O	Ti	K	Water Contact Angle ($^\circ$)	S_a (nm)	S_q (nm)	S_{sk}	S_{ku}
HTE	13.5 ± 0.6	56.7 ± 0.5	22.7 ± 0.2	7.3 ± 0.1	23.1 ± 4.3	26.5 ± 3.8	33.9 ± 5.6	-0.2 ± 0.1	0.2 ± 0.1
AR	25 ± 0.3	48 ± 0.5	27 ± 0.3	27 ± 0.3	58.9 ± 4.8	6.2 ± 2.5	8.8 ± 3.9	0.1 ± 0.9	2.5 ± 1.1

Wettability

Surface wettability measurements were conducted using the sessile drop method to measure the static contact angles of MilliQ water on titanium discs. An FTA1000 (First Ten Ångströms Inc., Portsmouth, VA, USA) instrument was used to measure each water contact angle. An average of at least five measurements was determined for each Ti disc. Each measurement was recorded in 50 images in 2 s using a Prosilica GT camera (Allied Vision, Exton, PA, USA) and the contact angle was then determined using the FTA Windows Mode 4 software.

Statistical Analysis

Statistical data processing was conducted using the Statistical Package for the Social Sciences, SPSS 21.0 (SPSS, Chicago, IL, USA). Results are presented as the mean \pm standard deviation.

3.4.4 Results and discussion

Surface Characterisation

The nanostructured Ti surfaces were fabricated using the established technique.² Alkaline hydrothermal reactions are commonly used to form nanostructures on titanium because of the reliable nature of the process in fabricating a wide array of titanium dioxide structures, including nanotubes, nanowires, and nanobelts.²⁴ Hydrothermally etched titanium surfaces were characterised using standard microscopy techniques. SEM micrographs highlight the differences between the AR-Ti and HTE-Ti surfaces on the nanoscale (Figure 1A). HTE-Ti surfaces possessed a network of dense nanoscale features. The change in the surface characteristics resulting from the hydrothermal treatment was quantitatively analysed using AFM. A small ($1 \times 1 \mu\text{m}^2$) scan area was required to visualise the nanoscale changes to the unmodified Ti as a result of the hydrothermal etching. The comparative surface roughness parameters, including average

roughness (S_a), root mean square roughness (S_k), skew (S_{sk}), and kurtosis (S_{ku}), are presented in Table 1. These conventional surface roughness parameters indicate that a four-fold increase in surface roughness resulted from the hydrothermal etching process (AR-Ti $S_a = 6.2 \pm 2.5$ and HTE-Ti $S_a = 26.5 \pm 3.8$ nm). This finding is confirmed by the 3D reconstruction of the AFM scans and the associated line profiles (Figure 1B, C). The height of the nanoscale structures can be seen to vary considerably.

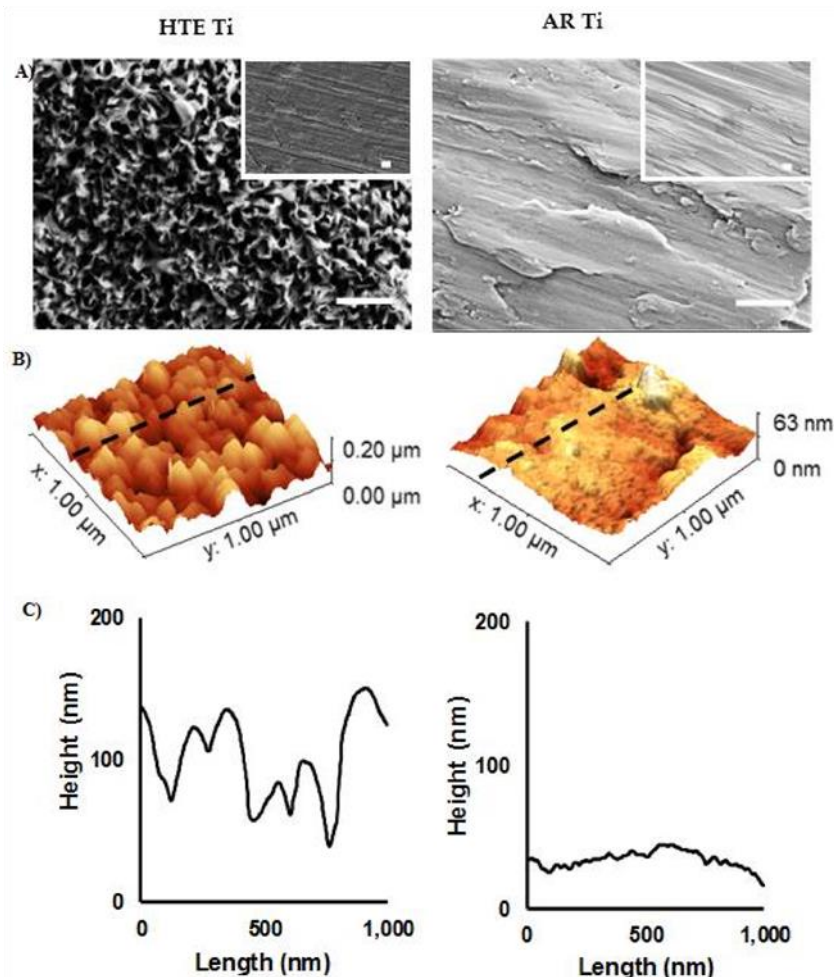


Figure 1. Surface topographic characterization of as-received and nanostructured titanium. (A) SEM images of the surfaces of AR (right) and HTE Ti (left) (scale bar = 400 nm). Insets are images taken at 5000× (scale bar = 2 μm). (B) Typical 3D AFM images and (C) corresponding surface profiles of AR and HTE Ti surfaces over 1 × 1 μm² scanning areas, showing a significant change in surface nanoarchitecture resulting from the hydrothermal treatment.

The surface chemical analysis of the AR and HTE Ti surfaces confirmed the formation of titanium dioxide (TiO₂) nanofeatures. XPS was used to define the chemical composition of both surfaces. High-resolution scans of the Ti 2p region revealed that the surface nanotopography (post-processing) was predominantly TiO₂, while the X-ray diffractograms provide confirmation of a surface with enhanced crystallinity, evidenced by an increase in the anatase (A) phase (Figure 2). No significant differences were observed in the surface chemistry of the AR and HTE-Ti samples. The hydrothermal etching of the Ti substrata resulted in an increase in the surface

wettability, decreasing the water contact angle from 58.9° to 23.1°. This increased degree of surface wettability is most likely a result of the formation of nanostructures on the Ti surface.²⁵

The physical and chemical characteristics of a surface are particularly important in ensuring the successful biointegration of an implant material, as these two factors directly influence the initial interactions between human tissue and foreign material being implanted into the body.²⁶ Surface chemistry determines the adsorption of protein from bodily fluids. Of the hydrothermally-modified Ti surfaces used in the present study, cells were primarily exposed to titanium dioxide, and the crystalline structure—as identified by XRD—was mostly anatase (Figure 2). Surface chemical characteristics between the non-structured control and hydrothermally-treated surfaces did not vary significantly enough to comment on the influence of surface chemistry on the proliferation and differentiation of PC12 neuron-like cells.

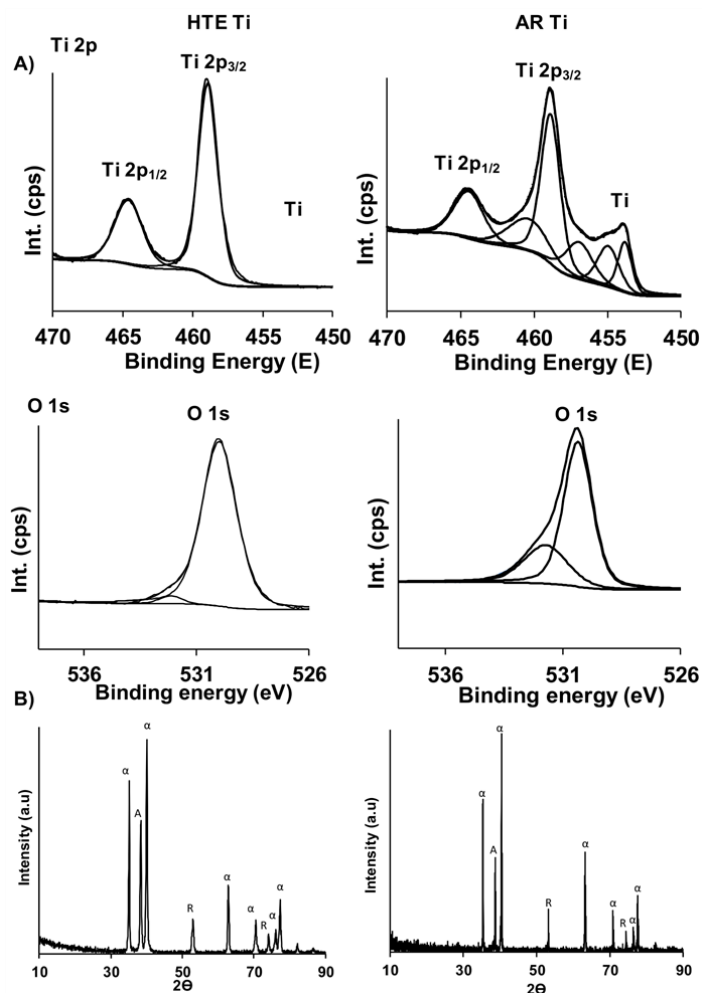


Figure 2. Surface chemistry and crystallinity characteristics of titanium surfaces. (A) XPS spectra of Ti 2p, and O 1s for the as-received (right) and HTE (left) titanium substrata. (B) X-ray diffractograms demonstrating the crystalline phases present on as-received (right) and HTE (left) substrata.

The Proliferation of PC12 Cells on Titanium Surfaces

The impact of nanostructures on the attachment and proliferation of mammalian cells on surfaces has been well-documented;¹⁸⁻²⁰ however, very little understanding has been obtained regarding the nature of the interaction taking place between neuron-like cells and the modified titanium surfaces possessing bactericidal nanostructures. As previously stated, PC12 cells adhere poorly to the smooth surfaces of culture flasks, preferentially growing as cellular aggregates in suspension.¹⁷ To encourage cellular attachment onto the surface of tissue culture flasks, they are often functionalized with protein, such as collagen. Only once attached to a substrate are the PC12 cells able to proliferate over the surface in a differentiated form.²⁷

To determine the mechanisms by which the PC12 cells underwent proliferation and differentiation on the HTE-Ti surfaces, the PC12 cells were seeded onto both the nanostructured and non-structured substrata and visualized after 1, 5, and 7 days of incubation. The nanostructured Ti surfaces were not coated with protein in order to effectively determine their suitability as substrata for initial anchorage. After day 1, analysis of the SEM and corresponding confocal laser scanning microscopy (CLSM) images showed that the PC12 cells were successfully attached onto the surface (Figure 3). At day 5, the PC12 cells exhibited a change in morphology, with the beginnings of neurite outgrowths being evident, which is an indication of successful differentiation. At day 7, the PC12 cells exhibited a large neurite growth, extending over the nanostructures. In contrast, the PC12 cells seeded onto the non-structured AR surfaces attached and proliferated over the surface, but failed to differentiate and produce neurite outgrowths, even in the presence of nerve growth factors (NGFs), retaining their rounded morphology. The expression of nestin—the type VI intermediate filament protein that is produced in nerve cells^{28,29}—can be seen in the CLSM images (stained red) at day 5 and 7 only for the differentiated cells on the HTE-Ti surfaces. It is evident that the nanostructures present on the HTE-Ti substrates provided focal adhesion points for the neuron-like cells to attach and provide further directional cues for growth and differentiation. The results presented here provide strong evidence as to the biocompatibility of the nanostructured Ti surfaces, with the surface nanostructures clearly affording the surface characteristics that are beneficial for the growth and proliferation of nerve cells. Such surfaces are suitable for use in implant applications without the need for additional surface coatings to encourage the attachment and differentiation of neurons.

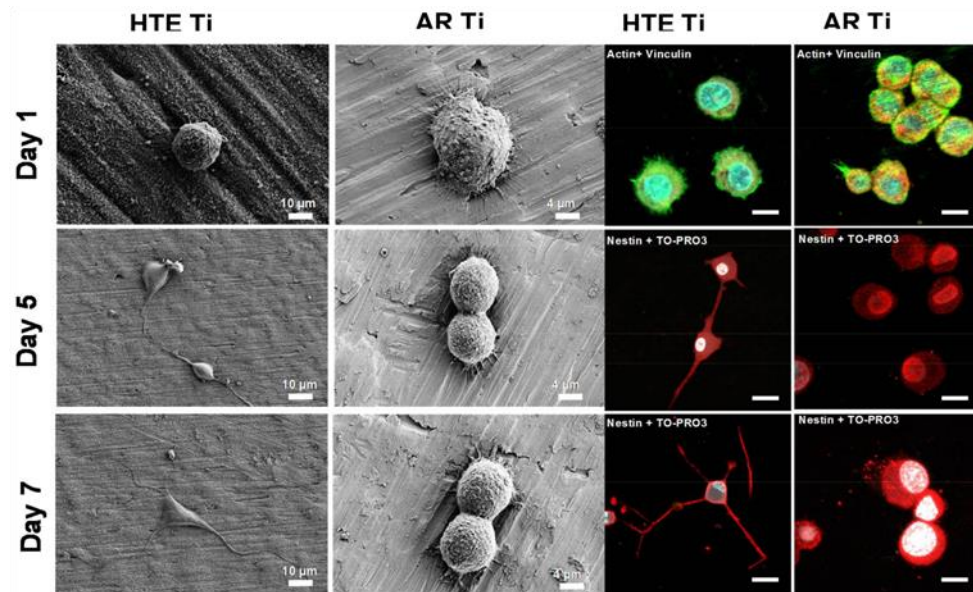


Figure 3. PC 12 cell morphology on HTE and AR Ti surfaces. The PC 12 cells were only able to differentiate on the surfaces of the nanostructured substrata in the presence of nerve growth factors (NGFs). No differentiation was observed on the non-structured AR surfaces. Expression of nestin was observed on the differentiated PC12 cells grown on the HTE-Ti substrates over a 7-day period. Immunohistochemical staining (nestin, red) of the PC12 cells showed that the cells could be differentiated on the surface of the nanostructured substrates. The cells exhibited an enhanced neurite elongation and expression of nestin, as seen on days 5 and 7. The PC12 cells grown on the AR surfaces were not observed to differentiate (scale bar = 3 μm). Actin (green) and vinculin (red) were labelled on day 1 to enable the determination of cell attachment patterns.

The viability of PC12 cells attached onto nanostructured substrata was estimated by applying a range of qualitative and quantitative bioassays. Live/dead staining yields two-color discrimination of the population of live and dead cells. Green-fluorescent calcein-AM indicates the presence of intracellular esterase activity, whereas red-fluorescent ethidium homodimer-1 indicates loss of membrane integrity. Fluorescent micrographs in Figure 4A show the proportion of live (green) and dead (red) cells on the HTE and AR substrata. The HTE-Ti surfaces supported the attachment and growth of neuron-like cells, following one day of incubation. In similarity with the smooth control, the numbers of dead cells were negligible (7.4% and 2.0%, respectively). MTS cell proliferation and viability assays (Figure 4B) give a quantitative measure of metabolically-active cells, and showed that the cells attached to all substrata remained viable for the maximum 1-week incubation period. Absorbance readings of the reduced MTS compound highlighted that the surface modification process provided a substratum that actually encouraged cellular proliferation, with increased levels of formazan being present in the culture wells containing the PC12 cells on HTE-Ti; however, no significant difference was detected in the total protein concentration for cells coming into contact with the nanostructured and non-structured substrata. Finally, in Figure 4C, neurite growth also serves to demonstrate the health of attaching nerve cells, with measurements of neurite outgrowths at 7 days showing that ~30% of the cells exhibited growths of 40–60 μm in length, whereas those on non-structured surfaces

did not produce growth extensions at all and failed to differentiate, which is typical for these cells on surfaces not coated with protein.

Previously, it was demonstrated that osteoblast-like cells responded to HTE-modified Ti surfaces through an enhanced cellular attachment and proliferation compared to non-structured titanium substrata.²⁵ On similar surfaces, primary human fibroblasts were shown to successfully attach and proliferate, with the surface providing sufficient anchorage points and cues for enhanced growth and elongation of filopodia.² Furthermore, the behavior of mesenchymal stem cells (MSCs) on Ti surfaces fabricated by the same method as used in this study was also observed.³⁰ Significantly, compared with non-structured Ti substrata, MSCs cultured on HTE-Ti substrata displayed significantly higher proliferation and differentiation levels of alkaline phosphatase and osteocalcin after 7- and 14-day cultures, respectively. Often, the biocompatibility of titanium implants is studied using oral-derived cell lines due to the heavy use of titanium to treat dental caries.³¹⁻³³ Upon its placement in the jaw, a dental implant must encounter osteoblasts from the bone, epithelial cells and underlying fibroblasts. Therefore, in a recent systematic study of human gingival fibroblasts, epithelial cells, and osteoblasts grown on alkali-hydrothermally etched Ti, it was shown that the osteogenic activity of osteoblasts was enhanced, and the adhesion activity of human epithelial cells and fibroblasts was promoted as compared to smooth surfaces.³¹ These results, and results obtained in the current study, suggest that the nanostructured titanium substrata have great potential for inducing growth and differentiation in multiple cell lines, including osteoblasts and neurons, and that the approach presented here may be exploited to fabricate titanium-based implants.

Enhanced osseointegration has frequently been observed in cases where modified Ti substratum have been implanted into an animal model, and under conditions where the Ti implants are exposed to normal bodily fluids and proteins.³⁴⁻³⁶ A study investigating the implantation and response of a modified Ti surface possessing titanium dioxide nanorods in rabbit femurs achieved better osseointegration and higher rates of bone tissue apposition of the nanostructured Ti, compared to classically treated (acid etched, grit blasted) micro-rough Ti surfaces.³⁴ Other studies have demonstrated the significantly increased primary and secondary stability of nano-modified titania implants and increased new bone formation [37,38]. More interestingly, although it has been confirmed *in vitro*, *in vivo* models have also established the influence of the shape of the nanostructures in enhancing osseointegration.^{39,40} Over a range of specific nanomorphologies investigated *in vivo* in rats, nanoleaves—being a network of vertically aligned, non-periodic “leaf-like” structures—promoted increased osteoblast cell proliferation, alkaline phosphatase activity, and collagen synthesis with reduced inflammatory responses over other shapes investigated. An inflammatory cytokine analysis of both chronic and acute

cytokines revealed no significant increase due to the presence of nanoscale features as compared to smooth controls.⁴⁰ The similar Ti nanomorphologies presented in the literature—which have been studied *in vivo*—implies that the Ti surface modifications achieved in this study will also promote both antibacterial activity and osseointegration as an implant, although here we have tested neuronal response to the surface, which is the first study of its kind according to our knowledge.

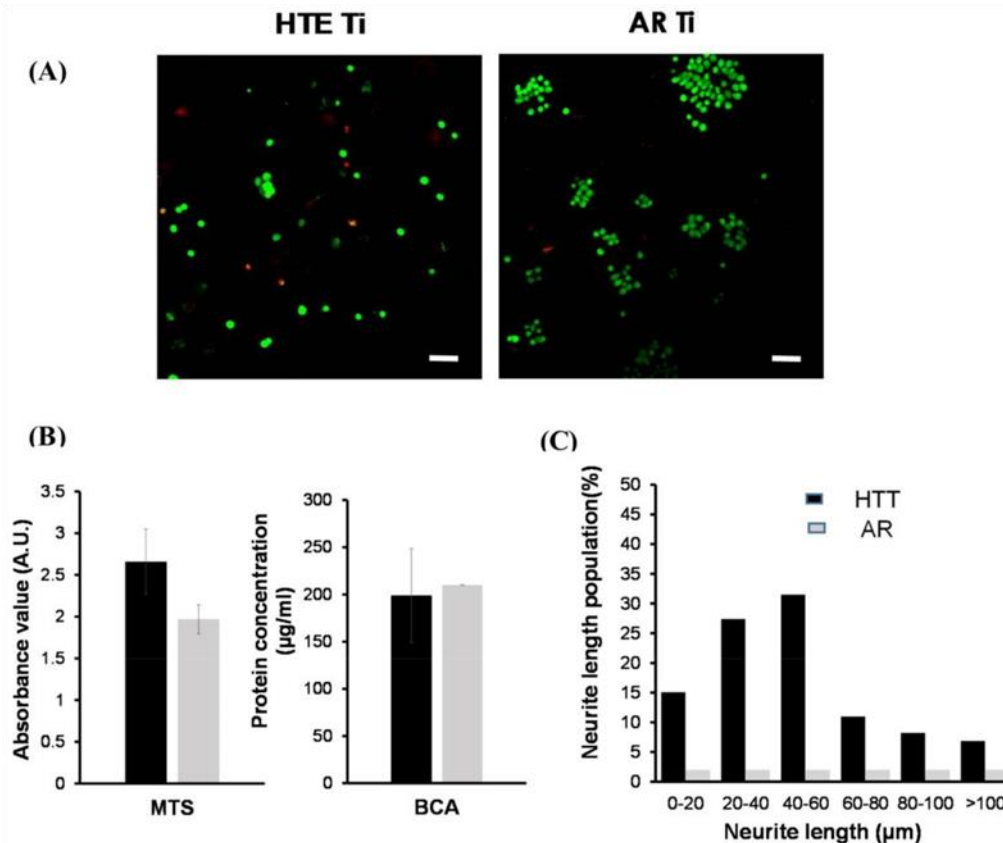


Figure 4. PC12 cell viability and differentiation on HTE and AR Ti surfaces. (A) Confocal laser scanning micrographs showing viable (green) and nonviable (red) bacterial cells on the HTE-Ti and AR-Ti surfaces. The majority of PC12 cells still survived on both surfaces after one day of incubation, and the mechanobactericidal surface of HTE-Ti did not have any killing effect towards PC12 cells (scale bar 50 µm). (B) Day 1, PC12 cell attachment and proliferation on HTE-Ti and AR surfaces. MTS (3-(4,5-dimethylthiazol-2-yl)-5-(3-carboxymethoxyphenyl)-2-(4-sulfophenyl)-2H-tetrazolium) results suggest that the HTE-Ti facilitated cell attachment. No differences were detected in the total protein content (BCA, bicinchoninic acid protein assay) of the two samples tested. (C) PC12 cell differentiation on HTE-Ti. PC12 cells present on HTE-Ti surface exhibited enhanced neurite growth for 7 days. The cells grown on the AR surfaces were not able to undergo differentiation.

The biocompatibility of materials is a prerequisite for the manufacture of orthopedic implants and for use in medical devices. Although Ti surfaces are chemically inert, surface suitability and functionality can be greatly altered through changes to surface chemistry or topography. Current approaches to the surface modification of implants do not make the distinction between mammalian and bacterial cells and may easily discourage or encourage the attachment and growth of both. Micro-nanoscale modification of surfaces can also have a

differential impact on the formation of focal adhesion points for mammalian cells, even though the surface is “antibiofouling” in nature. With this in mind, the design and fabrication of a bactericidal medical implant material that can support the proliferation and differentiation of neuron cells is particularly significant. Moreover, because the surfaces in this study capitalise on the mechanical interactions between cells and surfaces and because they can be easily fabricated using a simple, scalable process, the translation of this research on hydrothermally treated titanium surfaces into a commercial product should readily be achieved.

3.4.5 Conclusions

Commercial-grade Ti was successfully modified to create surfaces with an array of bactericidal nanofeatures. The effect of the nanostructures on PC12 cells was studied using cell viability assays and cellular morphology to assess cell–substrata interactions. It was shown that the neuron-like cells preferred to attach to the HTE-Ti substrata compared to the non-structured surfaces, even without a pre-coating of poly-L-lysine. Once attached onto the nanostructured titanium surfaces, PC12 cells demonstrated enhanced proliferation and differentiation. This study therefore confirmed the potential of nanostructured titanium surfaces to induce PC12 cells differentiation into neurons, without the need of surface pre-treatments.

3.4.6 Acknowledgments

The authors acknowledge partial funding from Marie Curie Actions under EU FP7 Initial Training Network SNAL 608184. Authors gratefully acknowledge the RMIT Microscopy and Microanalysis Facility (RMMF) for providing access to their analytical instruments.

3.4.7 References

1. Truong, V.K.; Webb, H.K.; Fadeeva, E.; Chichkov, B.N.; Wu, A.H.F.; Lamb, R.; Wang, J.Y.; Crawford, R.J.; Ivanova, E.P. Air-directed attachment of coccoid bacteria to the surface of superhydrophobic lotus-like titanium. *Biofouling* **2012**, *28*, 539–550.
2. Bhadra, C.M.; Khanh Truong, V.; Pham, V.T.H.; Al Kobaisi, M.; Seniutinas, G.; Wang, J.Y.; Juodkazis, S.; Crawford, R.J.; Ivanova, E.P. Antibacterial titanium nano-patterned arrays inspired by dragonfly wings. *Sci. Rep.* **2015**, *5*, 16817.
3. Bridier, A.; Briandet, R.; Thomas, V.; Dubois-Brissonnet, F. Resistance of bacterial biofilms to disinfectants: A review. *Biofouling* **2011**, *27*, 1017–1032.

4. Stigter, M.; Bezemer, J.; De Groot, K.; Layrolle, P. Incorporation of different antibiotics into carbonated hydroxyapatite coatings on titanium implants, release and antibiotic efficacy. *J. Control. Release* **2004**, *99*, 127-137.
5. Ivanova, E.P.; Hasan, J.; Webb, H.K.; Truong, V.K.; Watson, G.S.; Watson, J.A.; Baulin, V.A.; Pogodin, S.; Wang, J.Y.; Tobin, M.J.; et al. Natural bactericidal surfaces: Mechanical rupture of *Pseudomonas aeruginosa* cells by cicada wings. *Small* **2012**, *8*, 2489–2494.
6. Mainwaring, D.E.; Nguyen, S.H.; Webb, H.; Jakubov, T.; Tobin, M.; Lamb, R.N.; Wu, A.H.F.; Marchant, R.; Crawford, R.J.; Ivanova, E.P. The nature of inherent bactericidal activity: Insights from the nanotopology of three species of dragonfly. *Nanoscale* **2016**, *8*, 6527–6534.
7. Ivanova, E.P.; Hasan, J.; Webb, H.K.; Gervinskas, G.; Juodkazis, S.; Truong, V.K.; Wu, A.H.F.; Lamb, R.N.; Baulin, V.A.; Watson, G.S.; et al. Bactericidal activity of black silicon. *Nat. Commun.* **2013**, *4*, 2838.
8. Green, D.W.; Lee, K.K.H.; Watson, J.A.; Kim, H.Y.; Yoon, K.S.; Kim, E.J.; Lee, J.M.; Watson, G.S.; Jung, H.S. High quality bioreplication of intricate nanostructures from a fragile gecko skin surface with bactericidal properties. *Sci. Rep.* **2017**, *7*, 41023.
9. Takeda, I.; Kawanabe, M.; Kaneko, A. An investigation of cell adhesion and growth on micro/nano-scale structured surface—Self-assembled micro particles as a scaffold. *Precis. Eng.* **2016**, *43*, 294–298.
10. Wang, M.; Wu, Y.; Lu, S.; Chen, T.; Zhao, Y.; Chen, H.; Tang, Z. Fabrication and characterization of selective laser melting printed Ti–6Al–4V alloys subjected to heat treatment for customized implants design. *Prog. Nat. Sci. Mater. Int.* **2016**, *26*, 671–677.
11. Staehlke, S.; Kunz, F.; Loeffler, R.; Matschegewski, C.; Fleischer, M.; Kern, D.P.; Nebe, J.B. Regulation of T-type calcium channels in osteoblasts on micro-structured surface topography. *Adv. Mater. Res.* **2013**, *647*, 476–481.
12. Marrelli, M.; Pujia, A.; Palmieri, F.; Gatto, R.; Falisi, G.; Gargari, M.; Caruso, S.; Apicella, D.; Rastelli, C.; Nardi, G.M.; et al. Innovative approach for the *in vitro* research on biomedical scaffolds designed and customized with CAD-CAM technology. *Int. J. Immunopathol. Pharmacol.* **2016**, *29*, 778–783.
13. Marrelli, M.; Pujia, A.; Palmieri, F.; Gatto, R.; Falisi, G.; Gargari, M.; Caruso, S.; Apicella, D.; Rastelli, C.; Nardi, G.M.; et al. Innovative approach for the *in vitro* research on biomedical scaffolds designed and customized with cad-cam technology. *Int. J. Immunopathol. Pharmacol.* **2016**, *29*, 778–783.

15. Diu, T.; Faruqi, N.; Sjöström, T.; Lamarre, B.; Jenkinson, H.F.; Su, B.; Ryadnov, M.G. Cicada-inspired cell-instructive nanopatterned arrays. *Sci. Rep.* **2014**, *4*, 7122.
16. Jesky, R.; Chen, H. The neuritogenic and neuroprotective potential of senegenin against a b-induced neurotoxicity in PC 12 cells. *BMC Complement. Altern. Med.* **2016**, *16*, 26.
17. Westerink, R.H.; Ewing, A.G. The PC 12 cell as model for neurosecretion. *Acta Physiol.* **2008**, *192*, 273–285.
18. Attiah, D.G.; Kopher, R.A.; Desai, T.A. Characterization of PC 12 cell proliferation and differentiation-stimulated by ECM adhesion proteins and neurotrophic factors. *J. Mater. Sci. Mater. Med.* **2003**, *14*, 1005–1009.
19. Brammer, K.S.; Choi, C.; Frandsen, C.J.; Oh, S.; Johnston, G.; Jin, S. Comparative cell behavior on carbon-coated TiO₂ nanotube surfaces for osteoblasts vs. osteo-progenitor cells. *Acta Biomater.* **2011**, *7*, 2697–2703.
20. Gittens, R.A.; McLachlan, T.; Olivares-Navarrete, R.; Cai, Y.; Berner, S.; Tannenbaum, R.; Schwartz, Z.; Sandhage, K.H.; Boyan, B.D. The effects of combined micron-/submicron-scale surface roughness and nanoscale features on cell proliferation and differentiation. *Biomaterials* **2011**, *32*, 3395–3403.
21. Prodanov, L.; te Riet, J.; Lamers, E.; Domanski, M.; Luttge, R.; van Loon, J.J.W.A.; Jansen, J.A.; Walboomers, X.F. The interaction between nanoscale surface features and mechanical loading and its effect on osteoblast-like cells behavior. *Biomaterials* **2010**, *31*, 7758–7765.
22. Neċas, D.; Klapetek, P. Gwyddion: An open-source software for SPM data analysis. *Cent. Eur. J. Phys.* **2012**, *10*, 181–188.
23. Webb, H.K.; Truong, V.K.; Hasan, J.; Crawford, R.J.; Ivanova, E.P. Physico-mechanical characterisation of cells using atomic force microscopy—Current research and methodologies. *J. Microbiol. Methods* **2011**, *86*, 131–139.
24. Webb, H.K.; Truong, V.K.; Hasan, J.; Fluke, C.; Crawford, R.J.; Ivanova, E.P. Roughness parameters for standard description of surface nanoarchitecture. *Scanning* **2012**, *34*, 257–263.
25. Bavykin, D.V.; Friedrich, J.M.; Walsh, F.C. Protonated titanates and TiO₂ nanostructured materials: Synthesis, properties, and applications. *Adv. Mater.* **2006**, *18*, 2807–2824.
26. Puleo, D. Understanding and controlling the bone–implant interface. *Biomaterials* **1999**, *20*, 2311–2321.
27. Shi, X.; Nakagawa, M.; Kawachi, G.; Xu, L.; Ishikawa, K. Surface modification of titanium by hydrothermal treatment in Mg-containing solution and early osteoblast responses. *J. Mater. Sci. Mater. Med.* **2012**, *23*, 1281–1290.

28. Orłowska, A.; Perera, P.T.; Al Kobaisi, M.; Dias, A.; Nguyen, H.K.D.; Ghanaati, S.; Baulin, V.; Crawford, R.J.; Ivanova, E.P. The effect of coatings and nerve growth factor on attachment and differentiation of pheochromocytoma cells. *Materials* **2018**, *11*, 60.
29. Yang, K.; Jung, K.; Ko, E.; Kim, J.; Park, K.I.; Kim, J.; Cho, S.-W. Nanotopographical manipulation of focal adhesion formation for enhanced differentiation of human neural stem cells. *ACS Appl. Mater. Interfaces* **2013**, *5*, 10529–10540.
30. Cho, Y.I.; Choi, J.S.; Jeong, S.Y.; Yoo, H.S. Nerve growth factor (NGF)-conjugated electrospun nanostructures with topographical cues for neuronal differentiation of mesenchymal stem cells. *Acta Biomater.* **2010**, *6*, 4725–4733. Cai, K.; Lai, M.; Yang, W.; Hu, R.; Xin, R.; Liu, Q.; Sung, K.L.P. Surface engineering of titanium with potassium hydroxide and its effects on the growth behavior of mesenchymal stem cells. *Acta Biomater.* **2010**, *6*, 2314–2321.
31. Miao, X.; Wang, D.; Xu, L.; Wang, J.; Zeng, D.; Lin, S.; Huang, C.; Liu, X.; Jiang, X. The response of human osteoblasts, epithelial cells, fibroblasts, macrophages and oral bacteria to nanostructured titanium surfaces: a systematic study. *Int. J. Nanomed.* **2017**, *12*, 1415–1430.
32. Guida, L.; Oliva, A.; Basile, M.A.; Giordano, M.; Nastri, L.; Annunziata, M. Human gingival fibroblast functions are stimulated by oxidized nano-structured titanium surfaces. *J. Dent.* **2013**, *41*, 900–907.
33. Im, B.J.; Lee, S.W.; Oh, N.; Lee, M.H.; Kang, J.H.; Leesungbok, R.; Lee, S.C.; Ahn, S.J.; Park, J.S. Texture direction of combined microgrooves and submicroscale topographies of titanium substrata influence adhesion, proliferation, and differentiation in human primary cells. *Arch. Oral Biol.* **2012**, *57*, 898–905.
34. Salou, L.; Hoornaert, A.; Louarn, G.; Layrolle, P. Enhanced osseointegration of titanium implants with nanostructured surfaces: An experimental study in rabbits. *Acta Biomater.* **2015**, *11*, 494–502.
35. Ravanetti, F.; Chiesa, R.; Ossiprandi, M.C.; Gazza, F.; Farina, V.; Martini, F.M.; Di Lecce, R.; Gnudi, G.; Della Valle, C.; Gavini, J.; et al. Osteogenic response and osteoprotective effects *in vivo* of a nanostructured titanium surface with antibacterial properties. *J. Mater. Sci. Mater. Med.* **2016**, *27*, 52.
36. Omar, O.; Karazisis, D.; Ballo, A.; Petronis, S.; Agheli, H.; Emanuelsson, L.; Thomsen, P. The role of well-defined nanotopography of titanium implants on osseointegration: Cellular and molecular events *in vivo*. *Int. J. Nanomed.* **2016**, *11*, 1367–1382.

37. Bjursten, L.M.; Rasmusson, L.; Oh, S.; Smith, G.C.; Brammer, K.S.; Jin, S. Titanium dioxide nanotubes enhance bone bonding *in vivo*. *J. Biomed. Mater. Res. Part A* **2010**, *92*, 1218–1224.
38. Sul, S.T. Electrochemical growth behavior, surface properties, and enhanced *in vivo* bone response of TiO₂ nanotubes on microstructured surfaces of blasted, screw-shaped titanium implants. *Int. J. Nanomed.* **2010**, *5*, 87–100.
39. Ballo, A.; Agheli, H.; Thomsen, P.; Petronis, S. Nanostructured model implants for *in vivo* studies: Influence of well-defined nanotopography on de novo bone formation on titanium implants. *Int. J. Nanomed.* **2011**, *6*, 3415–3428.
40. Divya Rani, V.V.; Vinoth-Kumar, L.; Anitha, V.C.; Manzoor, K.; Deepthy, M.; Shantikumar, V.N. Osteointegration of titanium implant is sensitive to specific nanostructure morphology. *Acta Biomater.* **2012**, *8*, 1976–1989.

2.5. Synthetic biomaterials conclusions

Much of the effort in nanotechnology has focused on using nanotopography to augment material surfaces with nanometre-scale features to mimic the features of the extracellular matrix (ECM) proteins to which cells naturally adhere. However, existing approaches have achieved only partial successes in cell adhesion as well as infection prevention.

Therefore, in subchapter 3.1 study of human plasma albumin (Alb) and fibronectin (Fn) adsorption onto black silicon surface (BSi), which is synthetic bactericidal material, has been conducted to determine the effect of nanoscale topography on protein adsorption. The adsorption of albumin and fibronectin onto two types of substrata was investigated using a combination of various analytical methods, such as: Raman spectroscopy, Scanning Electron Microscopy (SEM), X-ray Photoelectron Spectroscopy (XPS) and Atomic Force Microscopy (AFM). Three different concentration of albumin (0.4, 4 and 40 $\mu\text{g}/\text{ml}$) and fibronectin (0.3, 3 and 30 $\mu\text{g}/\text{ml}$) were applied on the surface, for both maximum concentrations referred to the average physiologically present in blood. At lower concentrations (below 40 $\mu\text{g}/\text{ml}$), albumin tended to collect at the bottom of the nanopillars. However, at higher bulk concentrations, the albumin deposition shifted to the top of the nanopillars. In contrast, fibronectin preferentially adsorbed on the top of the nanopillars, no matter the concentration. Overall, both proteins (Alb and Fn) adsorbed to a greater extent on the smooth surface than on the nanotopography black silicon surface, however the adsorption profiles between the proteins differ due to their varied concentration. The resulting data provides a better understanding of the interaction between proteins and surfaces.

A more detailed study, aiming to characterize an effect of different protein coatings and NGF on cellular attachment and differentiation of PC12 cells, is described in chapter 3.2. Several techniques were used to analyze, cellular morphology was examined using brightfield phase contrast microscopy. Additionally, cell metabolism and proliferation were examine using a MTS assay. Finally, the neurite outgrowth and axonal generation of PC12 cells was appraised using wide field fluorescence microscopy. The results suggest that a combination of poly-L-lysine (PLL) / laminin (Lam) or PLL / fibronectin (Fn) is a more effective coating for enhancing cell adhesion, proliferation, and differentiation of PC12 cells than either protein alone. The interesting observation from this study is that NGF (100ng/l) significantly enhanced cell differentiation on all surfaces, but to a greater extent on the surfaces coated with PLL / Fn or PLL / Lam. This is likely because NGF promotes the differentiation of PC12 cells through integrin-mediated mechanisms, and the PLL / Fn and PLL / Lam coatings provide more ligands for integrin-mediated adhesion than the other surfaces.

In chapter 3.3, the focus was to investigate the use of black silicon substratum (BSi) to improve both biocompatibilities as for example cell adhesion and antimicrobial activity to bridge the gap between material science and biomedical application. Several *in vitro* models were employed in order to assess mechanobactericidal and cellular compatibility of BSi. Firstly, surfaces were infected with example of Gram negative; *Pseudomonas aeruginosa* and Gram positive; *Staphylococcus aureus*, the morphological changes of bacteria cells were visualized using SEM technique. Secondly, COS-7 cells were seeded on already preinfected surfaces and incubated over different period (1, 3 and 7 day). The cell viability and membrane integrity was checked with Live/Dead assay while observation was performed using confocal microscopy. Tissue reaction was assessed by using mice subcutaneous implantation model with qualitative and quantitative histological analysis of implantation bed afterwards. The results indicate that the specific nanotopology of BSi, which has been pre-infected by both pathogenic bacteria, provides an effective antibacterial mechanism by enabling the increase in COS-7 cell number over time. The *in vivo* findings indicated that a more pronounce foreign body response was provoked by the planar, nonstructured silicone surface. There was a greater number of macrophages associated with the material (~ 21 per mm²) in comparison to the samples with implanted BSi (~8 per mm²). Lastly, thinner fibrous capsule was seen in BSi samples in contrast to flat surfaces.

While black silicon seems like an attractive choice for this purpose, because it can be easily produced with a variety of diameters, real real-life applications of this material remain limited. Therefore, chapter 3.4. presents hydrothermally etched titanium, the material that offers a more versatile platform with plethora of medical use cases, such as orthopedic and dental implants. The purpose of this study was to explore how bactericidal titanium nanostructures might affect PC12 cell attachment and differentiation into neuronal-like looking cells. The PC12 viability, proliferation rate and morphology, grown on nanostructured substrata was verified using a variety of qualitative and quantitative bioassays. The results of this study show that hydrothermally etched titanium surfaces can significantly improve both cell adhesion and cell differentiation. While changes in morphology could be observed by neurite outgrowth with length of 40-60 μm in 30% of cell population on HTE-Ti surface, PC-12 cells remained round shaped on AR-Ti. Live/Dead assay show low cell death rate on both THE-Ti and AR-Ti substratum (up to 7% of cell population). Additionally, BCA test presented no difference in protein concentration on both surfaces. Finally, a trend in higher metabolic activity was detected by increase in PMS reduction by viable cells into formazan on titanium nanostructured surface in comparison to flat one.

Overall, the results of these studies have shown that the surface modification (protein coating and nanoscale features) can be used to control cell attachment, proliferation and cell differentiation which is a key parameter in the development of implantable biomaterials. Furthermore, *in vivo* studies of BSi indicate that there is milder host tissue reaction to surfaces with nanofeature in contrast to flat ones. Nevertheless, their application as implantable materials still require further studies to assess their biocompatibility. Additional cell models should be incorporated in a study design especially focusing on macrophage lines and primary cells as well as longer time points observations should be applied. Moreover, more research needs to be conducted to validate the *in vivo* effects of nanostructured surfaces. However, the results of this study provide a new perspective on how different technique of surface modification can be employed to improve the biocompatibility of materials.

3. Study of biocompatibility of nature-derived biomaterials

3.1. The case of autologous materials

Autologous also called autogenous biomaterials are materials derived from the same individual. These materials are often used in medical procedures, as they are less likely to cause an adverse reaction in the patient. Among these, platelet concentrates are commonly used in transfusion medicine, they were originally employed for the treatment and prevention of haemorrhage due to severe thrombopenia (which could be caused by medullar aplasia, acute leukaemia, or significant blood loss during long-lasting surgery). The standard platelet concentrate for transfusion is known as platelet rich plasma (PRP), and typically contains 0.5×10^{11} platelets per unit.¹ Platelets are known to contain more than 300 biologically active molecules (cytokines, growth factors and chemokines) released upon platelet-alpha activation. Platelet-derived molecules play an important role in regulating cell-cell and cell-extracellular matrix interactions and facilitate modification of their microenvironment and influence how they interact with their surroundings.² In terms of tissue regeneration, the most important molecules released are VEGF vascular endothelial growth factor (VEGF), transforming growth factor β -1 (TGF β -1), platelet-derived growth factor (PDGF), fibroblast growth factor (FGF), epidermal growth factor (EGF), matrix metalloproteinases 2 and 9 (MMP2 and -9), and interleukin 8.^{2,3} These proteins have an ability to promote cell proliferation, matrix remodelling and revascularization and therefore have been used to enhance the wound healing, bone remodelling, hair regrowth (androgenic alopecia), nerve regeneration and skin rejuvenation.^{3,4,5,6}

All platelet rich plasma (PRP) techniques share some commonalities: blood is drawn with anticoagulant prior to or during surgery and is immediately processed for centrifugation. The time span for all procedure does not extend to more than 1 hour. Centrifugation process intends to separate blood into three different layers: red blood cells (RBCs), buffy coat (leukocytes and platelets) and plasma with platelets, often called supernatant (which may exhibit a more solid form, in case fibrin polymerization, caused by adding thrombin or calcium chloride). Depending on the protocol, sometimes centrifugation is performed twice to reduce the presence of RBCs.^{1,2,5,6}

Choukroun's platelet rich fibrin (PRF) is the newest advancement in these systems. Blood is drawn without anticoagulant and immediately centrifuged. This creates a leukocyte- and platelet-rich fibrin clot (L-PRF), without the need for biochemical modification. Furthermore, in last five years, additional protocols were developed, for instance an injectable PRF (iPRF), which

is a PRF-based matrix in liquid, obtained by reducing the relative centrifugation force (RCF) and time. iPRF is often directly injected into the patient's tissue or is used as an additive to several xenogenic biomaterials to enhance their biocompatibility.¹

In order to investigate the influence of RCF on cellular content and growth factor profile release within injectable PRF (iPRF) and solid PRF, different *in vitro* comparative studies were performed in this thesis. Additionally, *in vivo* tissue response was assessed by implanting two differently obtained platelet rich fibrins using the subcutaneous implantation model in SCID (severe combined immunodeficient) mice.

References

1. Dohan Ehrenfest, D. M., Rasmusson, L., & Albrektsson, T. (2009). Classification of platelet concentrates: from pure platelet-rich plasma (P-PRP) to leucocyte- and platelet-rich fibrin (L-PRF). *In Trends in Biotechnology* (Vol. 27, Issue 3, pp. 158–167). <https://doi.org/10.1016/j.tibtech.2008.11.009>
2. Xu, J., Gou, L., Zhang, P., Li, H., & Qiu, S. (2020). Platelet-rich plasma and regenerative dentistry. *In Australian Dental Journal* (Vol. 65, Issue 2, pp. 131–142). Blackwell Publishing. <https://doi.org/10.1111/adj.12754>
3. Wu, P. I. K., Diaz, R., & Borg-Stein, J. (2016). Platelet-Rich Plasma. *In Physical Medicine and Rehabilitation Clinics of North America* (Vol. 27, Issue 4, pp. 825–853). W.B. Saunders. <https://doi.org/10.1016/j.pmr.2016.06.002>
4. Bernardi, S., Macchiarelli, G., & Bianchi, S. (2020). Autologous materials in regenerative dentistry: Harvested bone, platelet concentrates and dentin derivatives. *In Molecules* (Vol. 25, Issue 22). MDPI AG. <https://doi.org/10.3390/molecules25225330>
5. Miron, R. J., Zucchelli, G., Pikos, M. A., Salama, M., Lee, S., Guillemette, V., Fujioka-Kobayashi, M., Bishara, M., Zhang, Y., Wang, H. L., Chandad, F., Nacopoulos, C., Simonpieri, A., Aalam, A. A., Felice, P., Sammartino, G., Ghanaati, S., Hernandez, M. A., & Choukroun, J. (2017). Use of platelet-rich fibrin in regenerative dentistry: a systematic review. *In Clinical Oral Investigations* (Vol. 21, Issue 6, pp. 1913–1927). Springer Verlag. <https://doi.org/10.1007/s00784-017-2133-z>
6. Mikael, P. E., Golebiowska, A. A., Kumbar, S. G., & Nukavarapu, S. P. (2020). Evaluation of autologously derived biomaterials and stem cells for bone tissue engineering. *Tissue Engineering - Part A*, 26(19–20), 1052–1063. <https://doi.org/10.1089/ten.tea.2020.0011>

3.1.1. Reduction of relative centrifugal forces increases growth factor release within solid platelet-rich-fibrin (PRF)-based matrices: a proof of concept of LSCC (low speed centrifugation concept)

European Journal of Trauma and Emergency Surgery, **2019**, 45(3), 467–479.

El Bagdadi, K.^a, Kubesch, A.^a, Yu, X.^b, Al-Maawi, S.^a, **Orłowska, A.**^a, Dias, A.^a, Booms, P.^a, Dohle, E.^a, Sader, R.^a, Kirkpatrick, C. J.^a, Choukroun, J.^{a,c}, & Ghanaati, S.^a.

^a FORM (Frankfurt Orofacial Regenerative Medicine) Lab, Department for Oral, Cranio-Maxillofacial and Facial Plastic Surgery, University Hospital Frankfurt Goethe University, Theodor-Stern-Kai 7, 60590 Frankfurt am Main, Germany

^b Department of Orthopedics, West China Hospital/West China School of Medicine, Sichuan University, Chengdu, Sichuan, People's Republic of China

^c Private Practice, Pain Therapy Center, Nice, France

Abstract

Purpose: The present study evaluated the platelet distribution pattern and growth factor release (VEGF, TGF- β 1 and EGF) within three PRF (platelet-rich-fibrin) matrices (PRF, A-PRF and A-PRF+) that were prepared using different relative centrifugation forces (RCF) and centrifugation times.

Materials and methods: Immunohistochemistry was conducted to assess the platelet distribution pattern within three PRF matrices. The growth factor release was measured over 10 days using ELISA.

Results: The VEGF protein content showed the highest release on day 7; A-PRF+ showed a significantly higher rate than A-PRF and PRF. The accumulated release on day 10 was significantly higher in A-PRF+ compared with A-PRF and PRF. TGF- β 1 release in A-PRF and A-PRF+ showed significantly higher values on days 7 and 10 compared with PRF. EGF release revealed a maximum at 24 h in all groups. Toward the end of the study, A-PRF+ demonstrated significantly higher EGF release than PRF. The accumulated growth factor releases of TGF- β 1 and EGF on day 10 were significantly higher in A-PRF+ and A-PRF than in PRF. Moreover, platelets were located homogeneously throughout the matrix in the A-PRF and A-PRF+ groups, whereas platelets in PRF were primarily observed within the lower portion.

Discussion: The present results show an increase growth factor release by decreased RCF. However, further studies must be conducted to examine the extent to which enhancing the amount and the rate of released growth factors influence wound healing and biomaterial-based tissue regeneration.

Conclusion: These outcomes accentuate the fact that with a reduction of RCF according to the previously LSCC (described low speed centrifugation concept), growth factor release can be increased in leukocytes and platelets within the solid PRF matrices.

Introduction

Various blood concentrates are used to support tissue regeneration and wound healing in different fields. One of these systems is platelet-rich plasma (PRP), a technique that has been developed for clinical practice and tissue regeneration therapies^{1, 2} PRP is prepared by multiple centrifugation steps using patient blood to which anticoagulants have been added to achieve a platelet-rich concentrate that can be used for different indications.³ However, seeking to minimize contamination risk, eliminate additional anticoagulants and use the autologous and

natural regeneration capacity, a new system, platelet-rich fibrin (PRF), was introduced as the first blood concentrate system without additional anticoagulants.⁴

PRF is derived from patient venous blood by means of single-step centrifugation without the further addition of any type of anticoagulants. This system was developed to fulfill clinical needs by being time-saving and easy to use.⁴ PRF-based matrices include various inflammatory cells, such as platelets and leukocytes, in combination with various plasma proteins embedded in a fibrin network.⁵ The components of PRF-based matrices are known to play an important role during the process of wound healing. Platelets are the first cells to occur in the region of an injury. In addition to their role within hemostasis, platelets have inflammatory potential, including the recruitment of further inflammatory cells, such as neutrophils and macrophages, and promote angiogenesis and tissue repair.^{6, 7} In this context, platelets are able to express a series of biologically active signaling molecules and growth factors, such as platelet-derived growth factor (PDGF), vascular endothelial growth factor (VEGF) and transforming growth factor beta (TGF- β). These growth factors are essential for tissue vascularization and new tissue formation.^{8, 9} Moreover, platelets contain granules with cytokines, chemokines and other inflammatory mediators that are released after platelet aggregation to enhance hemostasis and activate and recruit cells to the site of inflammation.^{10, 11} Leukocytes also contribute to angiogenesis and lymphangiogenesis by participating in cell–cell cross talk and expressing various signaling molecules.^{12, 13} The extracellular matrix in the wound bed supports the formation of blood vessels, and fibrin provides a scaffold for the inflammatory cells.¹⁴

The structure and constituents of PRF-based matrices were previously explored by our group. An *ex vivo* histomorphometrical study showed a dense structure and specific localization of the included inflammatory cells in the lower part of PRF.⁵ In addition, a modification of the preparation setting based on the previously LSCC (described low-speed centrifugation concept) is a first step in the reduction of the applied relative centrifugation force (RCF). This step was accompanied by a mild increase of centrifugation time, resulting in a so-called advanced PRF (A-PRF).^{5, 15} Analysis of the structure and composition of A-PRF revealed a more porous structure compared to PRF.⁵ In addition, histomorphometrical analysis revealed significantly more neutrophilic granulocytes in the group of A-PRF compared with PRF.⁵

While developing PRF-based matrices, the focus was on clot formation, consistency and functional integrity the fibrin clot and the distribution of the included inflammatory cells to generate PRF-based matrices with high functionality and adequate handling. In this study, the applied RCF and centrifugation times are key elements. Further research on PRF-based matrices regarding their structure and composition indicates that adjusting the centrifugation time, *i.e.*, reducing the spinning time and applying the same RCF as in the case of A-PRF, allows the

introduction of a new PRF-based matrix, Advanced-PRF+ (A-PRF+). A previous systematic study demonstrated the influence of the RCF reduction on the leukocyte and platelet numbers as well as their role in growth factor release in fluid PRF-based matrices following the LSCC, which indicates that reducing the RCF enhances the cell number and growth factor release within PRF-based matrices.¹⁵ Based on the LSCC, we examined modifications of the RCF and centrifugation times in solid PRF-based matrices and their influence on the growth factor release within the previously introduced PRF protocols with a solid structure; PRF, A-PRF and A-PRF+. Therefore, the goal of the present study was to determine growth factor release in solid PRF-based matrices, PRF, A-PRF and A-PRF+, at six different time points over a period of 10 days. Additionally, immunohistochemical analysis was conducted to assess the platelet distribution pattern within the various PRF-based matrices.

Experimental

PRF preparation

For each protocol, peripheral blood was drawn from four healthy volunteers between 25 and 60 years of age (two females, two males) without a history of anticoagulant usage. Informed consent was obtained from each donor who participated in this study. As previously described,⁵ the venous blood was collected in 10-ml sterile glass tubes (A-PRF tubes Process for PRF™, Nice, France; Mectron, Cologne, Germany) without external anticoagulants and placed immediately in a centrifuge (Duo centrifuge, Process for PRF™, Nice, France; Mectron, Cologne, Germany). The centrifuge has a fixed angle rotor with a radius of 110 mm and no brake. After centrifugation time, the centrifugation process ends automatically, and the centrifuge stops in 2-5s. All preparation steps were performed at room temperature according to the established protocols as follows: PRF: 10 ml; 2400 rpm; 12 min; 208 g, A-PRF: 10 ml; 1300 rpm; 14 min; 208 g, A-PRF+: 10 ml; 1300 rpm; 8 min; 208 g. After centrifugation, all clots were carefully removed from the tubes and separated from the red blood cell fraction with sterile tweezers and scissors.

PRF cultivation

The total clots of PRF, A-PRF and A-PRF+ were placed in separate wells of a 6-well plate (Greiner, Bio-One International) and covered with 5 ml Roswell Park Memorial Institute medium (RPMI 1640, Gibco Thermo Fischer Scientific) without Fetal Bovine Serum and supplemented with L-glutamine and 1% penicillin/streptomycin. The clots were incubated in a humidified incubator for up to 10 days at 37 °C with 5% CO₂. The supernatants from each well were taken

after 6, 24, 48, 72 h, 7 and 10 days and stored as aliquots at -80°C . At each time point, all of the clots of PRF-based matrices were placed into new wells and covered with 5 ml fresh medium.

Growth factor measurement

The supernatants that were collected from the various PRF-based matrices at different cultivation time points were used for the quantification of different growth factors by enzyme-linked immunosorbent assay (ELISA). All collected supernatants were simultaneously centrifuged (1500 rpm; 5 min.) using a centrifuge (Thermo fisher scientific, Heraeus® Labofuge® 400 R) to exclude possible residue that could affect the photometrical measurement. Before TGF- β 1 and EGF ELISA preparation, the supernatants were diluted 1:4 with the same cell culture RPMI medium used for PRF-matrices cultivation. The protein concentrations of human VEGF, TGF- β 1 and EGF were determined by the Dou Set ELISA kit (Human VEGF DY293B, R&D Systems, detection range: 2000–31.3 pg/ ml), Human Dou Set ELISA kit (Human TGF- β 1 DY240, R&D Systems, detection range: 2000–31.3 pg/ml) and the Duo Set DuoSet ELISA kit (human EGF DY236, R&D Systems, detection range: 3.91–250 pg/mL) according to the manufacturer's instructions. Measurements were conducted using a microplate reader (Infinite® M200, Tecan, Grödig, Austria) set to 450 nm and subtracted at 570 nm from the 450 nm measurements.

Immunohistological analysis

As previously described,^{5, 16} the PRF clots were collected after 10 days and fixed in Roti®-Histofix 4%, acid free (pH 7), and 4% phosphate-buffered formaldehyde solution (Carl-Roth) for 24 h. The PRF-based matrices were dehydrated in a series of alcohol and xylene through a Tissue Processor (TP1020, Leica Biosystems Nussloch GmbH, Germany) and embedded in paraffin blocks. Afterwards, 3 μm thick sections from each sample were cut by a rotatory microtome (Leica RM2255, Wetzlar, Germany). For immunohistochemistry, the sections were deparaffinized, rehydrated and finally sonicated in citrate buffer (pH 6) at 96°C for 20 min. The sections were stained with monoclonal mouse anti-human CD61 marker (1:50, Platelet Glycoprotein IIIa/APC, Clone Y2/5, Dako) by means of an autostainer (Lab vision Autostainer 360, Thermo Fisher Scientific). Histological examination was conducted using a light microscope (Nikon Eclipse 80i, Tokyo, Japan). Three of the authors KE, SA and SG, were independently blinded for the morphological analysis. The microphotographs were prepared with a connected DS-Fi1/Digital camera (Nikon, Tokyo, Japan) and a Digital sight unit DS-L2 (Nikon, Tokyo, Japan).

Statistical evaluation

Data were expressed as the mean \pm standard deviation. Statistical analysis was conducted using Prism Version 6 (GraphPad Software Inc., La Jolla, USA). The significance of differences among means of data was analyzed using two-way analysis of variance (ANOVA) with the Tukey multiple comparisons test ($\alpha = 0.05$) of all pairs. The significant differences were regarded as significant if the p values were less than 0.05 ($*p < 0.05$) and highly significant if the p values were less than 0.005 ($**p < 0.005$), 0.0005 ($***p < 0.0005$) or 0.0001 ($****p < 0.0001$).

Results and discussion

General observation of fibrin clotting within the three investigated groups

Macroscopic observation demonstrated the formation of three slightly different clots. PRF formed a clot with a fibrin/red blood count (RBC) ratio of 1/1.66, and the clot length was measured as 3.5 cm. A-PRF showed a clot formation with a fibrin/red blood count (RBC) ratio of 1/2. Here the clot length was 3.5 cm. A-PRF+ had a fibrin/ red blood count (RBC) ratio of 1/3 and a length of 2.5 cm (Fig. 1). Moreover, while separating the fibrin clot from the RBC, it was observed that in the case of PRF and A-PRF, the adhesion between the two sections, the fibrin clot and RBC, was stronger compared with A-PRF+. Accordingly, the A-PRF+ fibrin clot was much easier to separate.

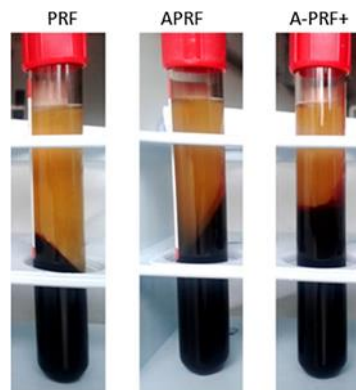


Figure 1. The PRF-based matrices immediately following centrifugation

Growth factor release kinetics from the clots

The present study focused on the determination of the released growth factor kinetics of the three PRF-based matrices, PRF, A-PRF and A-PRF+. The growth factors VEGF, EGF and TGF- β 1 were quantified for the released concentrations at each time point (6, 24, 48, 72 h, 7, and 10 days). Additionally, the accumulated growth factor quantities were calculated.

VEGF release

The general trend of the three evaluated groups at each time point was similar. The release of VEGF increased in the very early phase from 6 to 24 h in all groups. At 48 h, the growth factor release was comparable to the values at 24 h in all groups. From 48 to 72 h, a slight decrease in the release of VEGF was evidenced in all groups. From 72 h to day 7, a highly significant increase in all groups was observed ($p < 0.0005$) in an intra-individual comparison (data not shown). During the 4 days of cultivation between 72 h and day 7, the highest released concentration of VEGF over the study time was measured. Here, A-PRF+ showed the highest concentration when compared with PRF and A-PRF (PRF = 158.5 ± 36.6 pg/ml; A-PRF = 153.6 ± 40.1 pg/ml; A-PRF+ = 242.35 ± 67.9 pg/ml), which was statistically highly significant when compared to PRF and A-PRF ($p < 0.0005$). By contrast, A-PRF showed no statistically significant difference compared to PRF. From day 7 to day 10, all groups showed a decrease in the release of VEGF. This decrease was intra-individually statistically highly significant compared with day 7 (data not shown). Furthermore, after 10 days, A-PRF+ showed the highest VEGF release (PRF = 83.7 ± 28.81 pg/ml; A-PRF = 64.84 ± 15.7 pg/ml; A-PRF+ = 95.5 ± 44.7 pg/ml). At this time point, no significant difference could be identified among the groups (Fig. 2A1).

Concerning the accumulated VEGF concentration, a general trend was also evidenced by a continuous increase in the released VEGF over the study time. In the early phase (6–72 h), the release of VEGF increased in all groups, whereas the groups' concentrations were quite similar. Moreover, in the late study period (72 h–10 days), a similar tendency was observed in all groups. However, A-PRF+ released the highest concentration on day 10 when compared with PRF and A-PRF (Table 1). This difference was highly significant when comparing A-PRF+ to A-PRF ($***p < 0.0005$) and significant comparing A-PRF+ to PRF ($**p < 0.005$) at this time point (Fig. 2 A2).

TGF- β 1 release

Various TGF- β 1 release patterns were measured in PRF, A-PRF and A-PRF+. Within the PRF group, a slight increase was observed in the early study time (6–72 h) followed by a dramatic decrease in the late study time (72 h–10 days). At 72 h, PRF already showed the highest concentration over the study period. At this time point, PRF was significantly higher only when compared to A-PRF ($p < 0.0001$), whereas no significant difference was observed compared to A-PRF+ (Fig. 2B1).

The A-PRF group showed a high release value at the first time point (6 h) (PRF = 4.6 ± 1.0 ng/ml; A-PRF = 7.0 ± 1.4 ng/ml; A-PRF+ = 5.8 ± 1.4 ng/ml), the difference between A-PRF and PRF being statistically significant ($p < 0.05$). However, no statistically significant difference was

detected regarding A-PRF+. This observation was followed by irregular behavior until 72 h and a significant increase at day 7, when the highest TGF- β 1 release of A-PRF was observed. At this time point, A-PRF was significantly higher than PRF ($p < 0.0001$), whereas no significant difference was revealed for the A-PRF+ group.

A-PRF+ showed a mild decrease of the released TGF β 1 at the early study time (6–48 h). However, from 72 h to day 7, an increase in the released TGF- β 1 was observed when the highest concentration of TGF- β 1 release was reached in the case of A-PRF+. At day 7, a statistically highly significant difference was observed when compared with PRF ($p < 0.0001$), whereas no significant difference was observable compared to A-PRF (PRF = 1.9 ± 1.6 ng/ml; A-PRF = 8.5 ± 0.6 ng/ml; A-PRF+ = 8.6 ± 0.4 ng/ml). From day 7 to day 10, the release of TGF- β 1 decreased in all groups. However, A-PRF showed significantly higher values when compared with PRF ($p < 0.0001$). Similarly, A-PRF+ revealed more growth factor release, which was highly significant when compared with PRF ($p < 0.0001$). No statistically significant difference was observed when comparing A-PRF and A-PRF+ at this time point (Fig. 2B1).

The accumulated concentration of TGF- β 1 showed an increase in all groups at the early study time (6–72 h). However, at the late study time (72 h–10 days), the growth factor release differed among the various groups. PRF showed a more or less constant concentration of TGF- β 1 after 72h, whereas in the case of A-PRF and A-PRF+, an increased TGF- β 1 concentration was observed. These differences on day 10 were statistically significant when comparing A-PRF to PRF ($p < 0.0001$) and A-PRF+ to PRF ($p < 0.0001$); however, no statistically significant difference was detected when comparing A-PRF to A-PRF+ (Table 1) (Fig. 2B2).

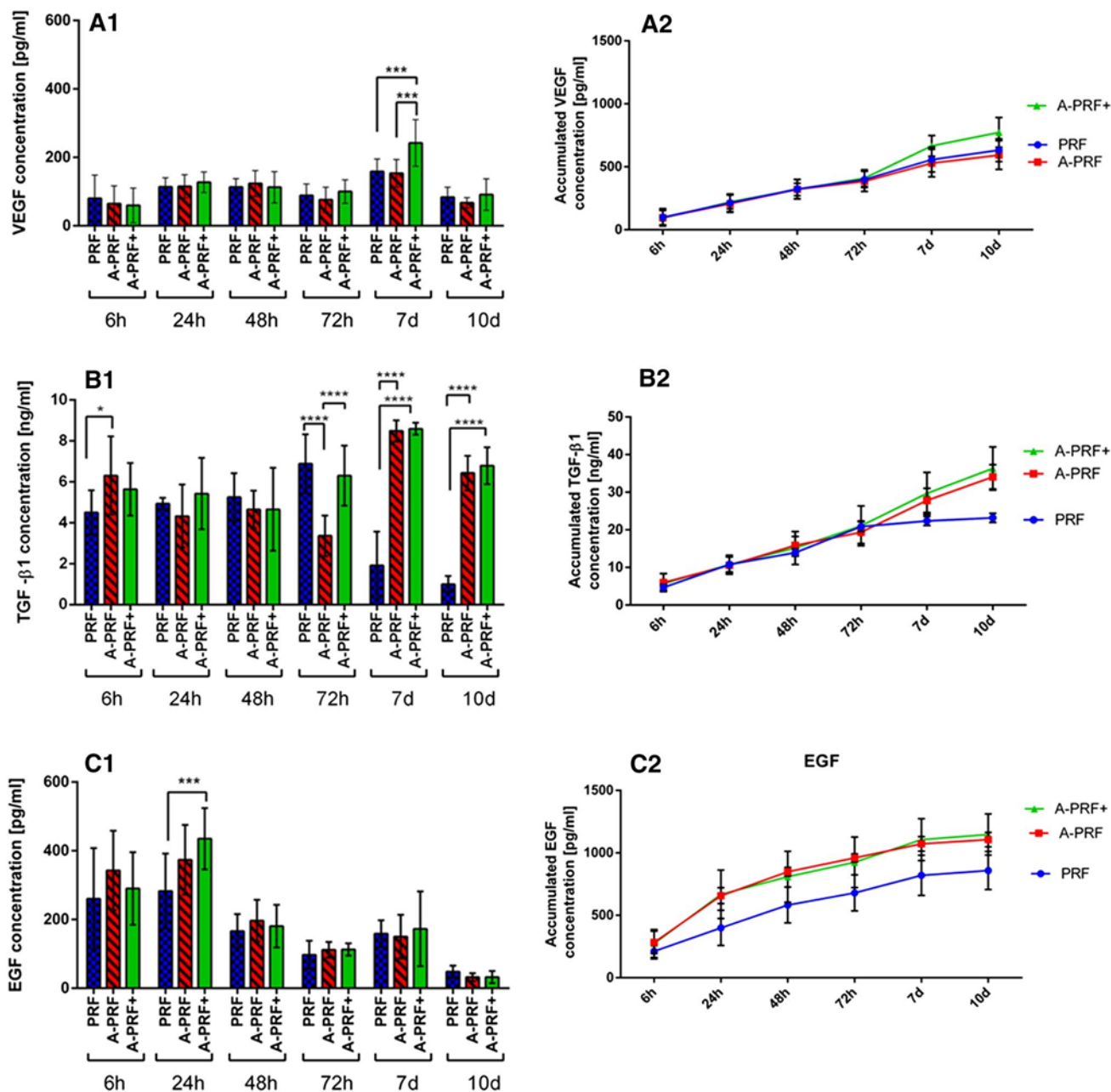


Figure 2. Statistical analysis of the growth factor releases by time (** $p < 0.0005$), (**** $p < 0.0001$). Total accumulated growth factor points as the mean \pm standard deviation for PRF, A-PRF and concentration over 10 days. A2 VEGF, B2 TGF-β1, C2 EGF A-PRF+. A1 VEGF, B1 TGF-β1 release, C1 EGF release, ($*p < 0.05$),

EGF release

A general trend was observed in all three PRF-based matrices. The rate of the released EGF increased quite early in the study time (6–24 h) to reach the highest value in all groups at 24 h. At this time point, A-PRF+ showed the highest value of the released EGF when compared with PRF and A-PRF (PRF = 282.69 ± 109.09 pg/ml; A-PRF = 373.75 ± 101.25 pg/ml; A-PRF+ = 435.17 ± 89.29 pg/ml), the difference being statistically highly significant when comparing A-PRF+ to PRF (** $p < 0.0005$); no statistical significance was observed when comparing A-PRF to

A-PRF+. Subsequently, a course change was observed when a strong reduction of the released EGF occurred in all examined groups until 72 h. After that, on day 7, a slight increase was observed in all groups. Here also, A-PRF+ was the highest (PRF = 148.28 ± 48.27 pg/ml; A-PRF = 138.70 ± 61.07 pg/ml; A-PRF+ = 173.50 ± 98.72 pg/ml) although no statistically significant difference was detectable. At the last evaluated time point on day 10, all groups showed a significant decrease in the released EGF compared with day 7 (data not shown). However, at this time point, no statistically significant differences were observed among the groups (Fig. 2C1).

The accumulated concentration of the released EGF also exhibited a general trend. All groups showed a similar curve progression in the form of increased EGF release over the study time. A-PRF and A-PRF+ also displayed similar values. Early in the study time, a remarkable increase in released EGF was evidenced in all groups. After 72 h, only a minor increase of the released EGF was observed toward the end of the study on day 10. At these time points (72 h–10 days), A-PRF and A-PRF+ showed statistically significantly higher release values when compared with PRF (A-PRF+ compared with PRF $p < 0.005$; A-PRF compared with PRF $p < 0.05$), whereas no statistically significant differences were revealed when comparing A-PRF to A-PRF+ (Table 1) (Fig. 2C2).

Table 1. Accumulated growth factor concentration of PRF, A-PRF and A-PRF+ at day 10 as the mean \pm standard deviation. Statistical analysis of A-PRF and A-PRF+ compared with PRF (* $p < 0.05$), (** $p < 0.005$), (***) $p < 0.0005$), (**** $p < 0.0001$)

Growth factor	PRF	A-PRF	A-PRF+
VEGF (pg/ml)	632.26 ± 90.58	593.15 ± 114.08	$773.88 \pm 117.66^{**}$
TGF β 1 (ng/ml)	23.18 ± 1.22	$34.081 \pm 3.21^{****}$	$36.29 \pm 5.73^{****}$
EGF (pg/ml)	858.62 ± 152.90	$1106 \pm 57.74^*$	$1147.07 \pm 164.47^{**}$

Platelet distribution in the PRF-based matrices

Immunohistochemical staining with CD-61 antibodies against platelets was conducted to determine the platelet distribution in cross sections of the three PRF-based matrices. The platelet distribution was evaluated with regard to the location in the clot. The platelets formed accumulations within all three clots. PRF, which was prepared with a high RCF, showed a different distribution pattern according to the localization. The upper and middle portions of the clot showed only a few platelets, whereas the majority of platelets were distributed in the lower portion of PRF (Fig. 3). By contrast, A-PRF, which was prepared with a reduced RCF, presented a different distribution pattern. Platelets were dispersed all over the clot (Fig. 4). A-PRF+ with a reduced RCF and a reduced centrifugation time also displayed an even platelet distribution pattern in the various locations within the clot (Fig. 5).

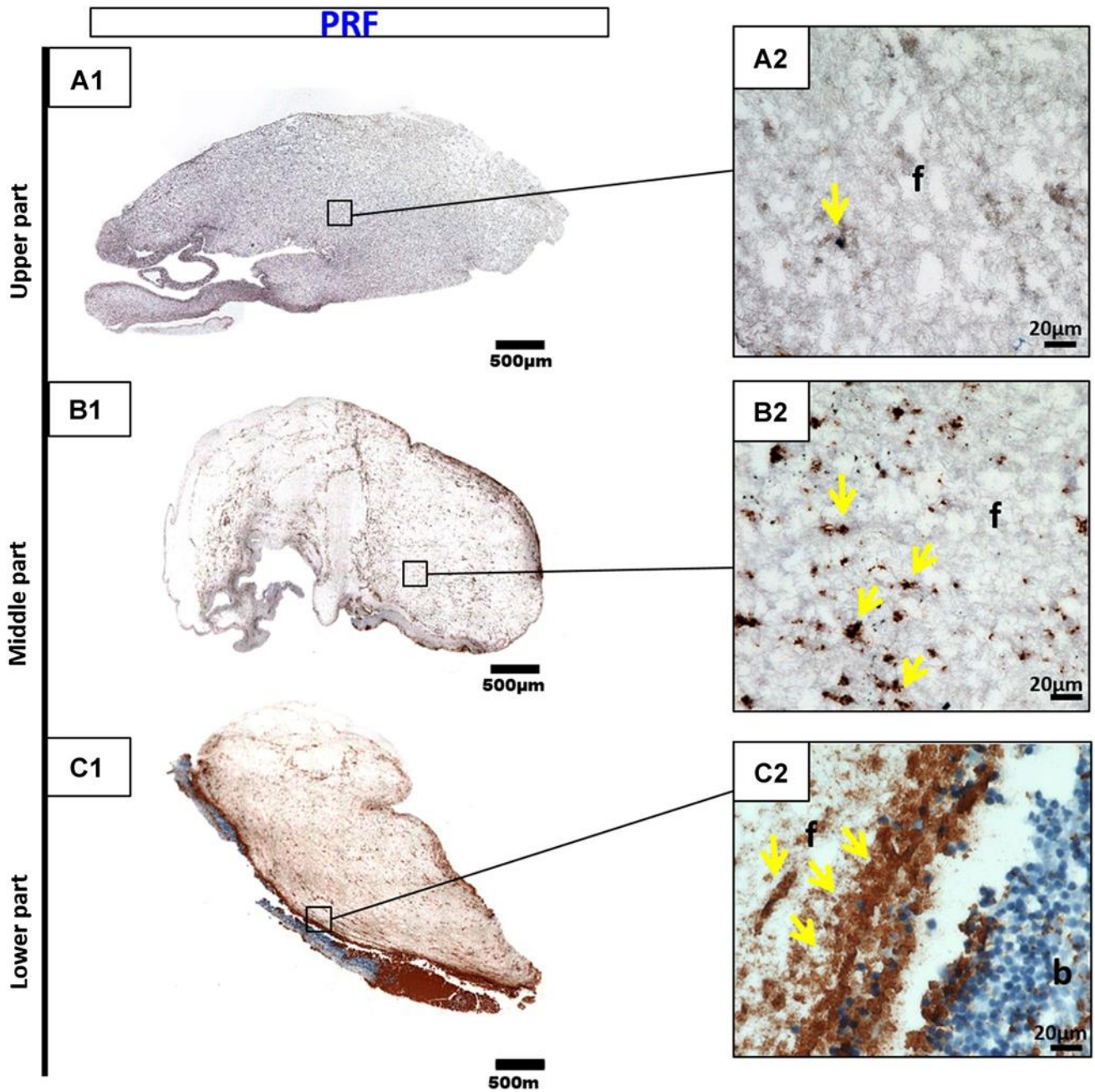


Figure 3. CD-61 immunohistochemical analysis of PRF according to the different regions. (A1, A2) upper portion; (B1, B2) middle portion; (C1, C2) lower portion (A1, B1, C1 total scan sections; scale bar 500 µm). A2, B2, C2 show the distribution pattern of platelets (yellow arrows) in higher magnification (f fibrin; b buffy coat; scale bar 20 µm)

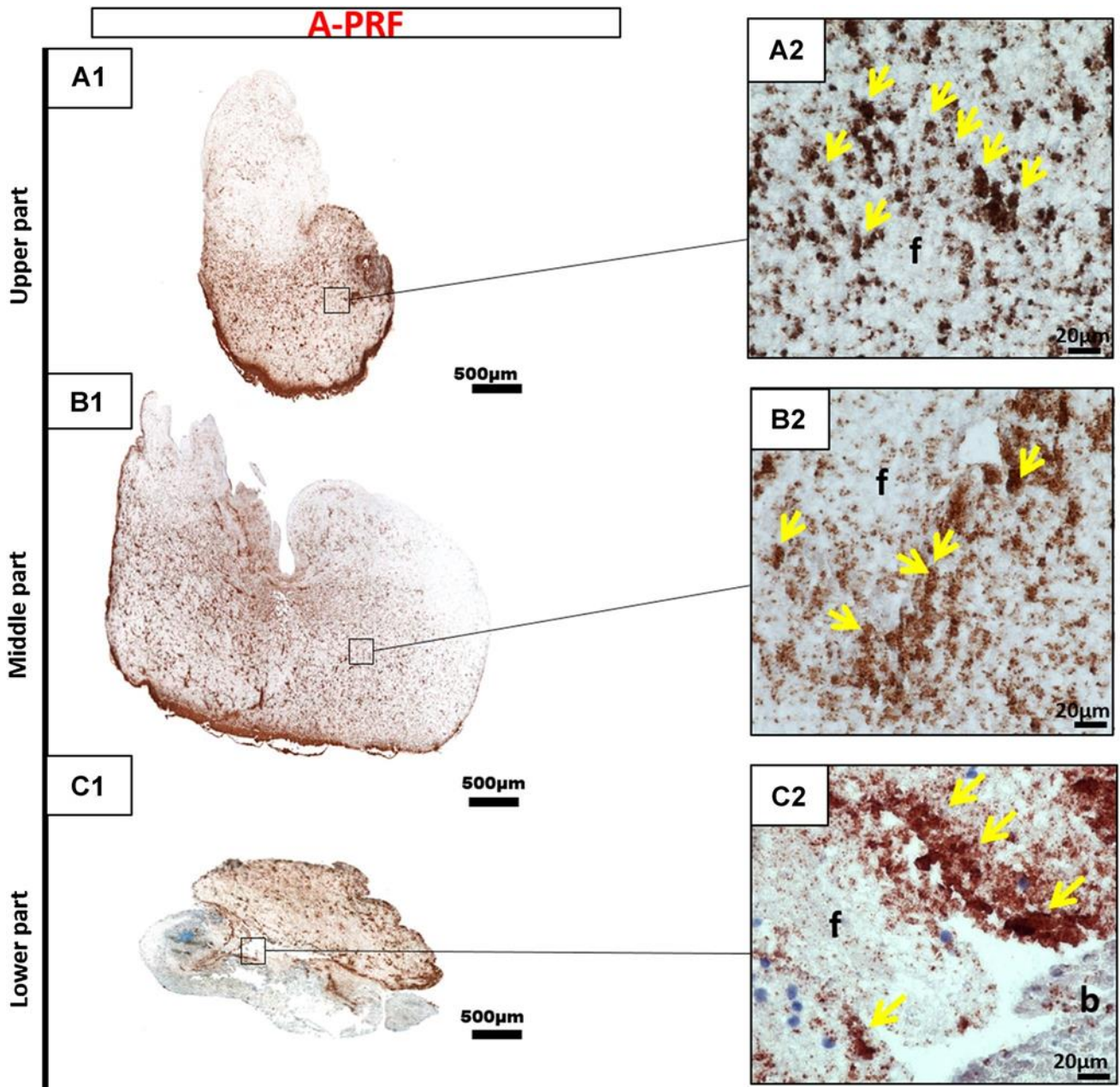


Figure 4. CD-61 immunohistochemical analysis of A-PRF according to the different regions. (A1, A2) upper portion; (B1, B2) middle portion; (C1, C2) lower portion (A1, B1, C1 total scan sections; scale bar 500 µm). A2, B2, C2 Show the distribution pattern of platelets (yellow arrows) in higher magnification (f fibrin; b buffy coat; scale bar 20 µm)

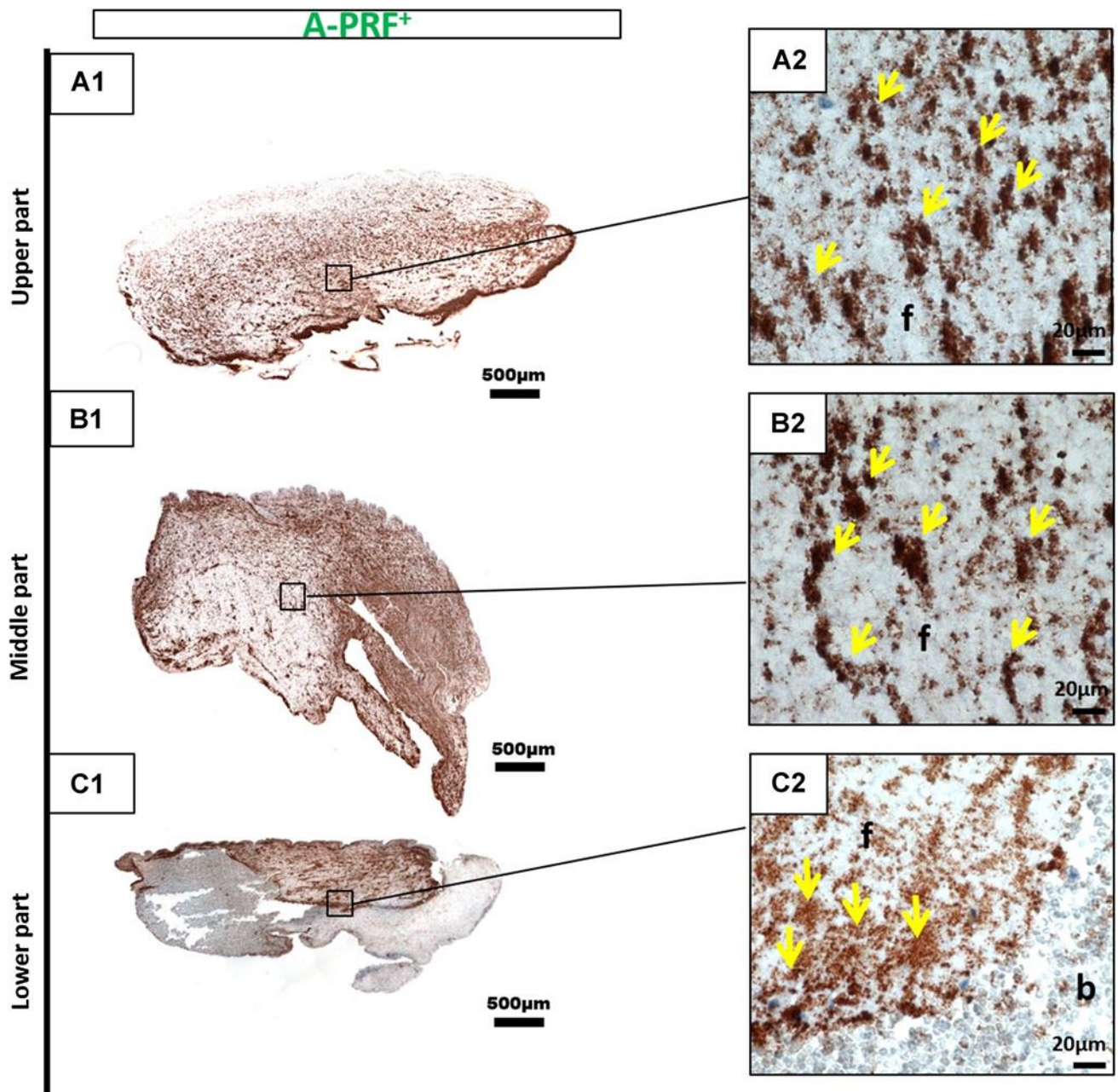


Figure 5. CD-61 immunohistochemical analysis of A-PRF according to the different regions. (A1, A2) upper portion; (B1, B2) middle portion; (C1, C2) lower portion (A1, B1, C1 total scan sections; scale bar 500 µm). A2, B2, C2 Show the distribution pattern of platelets (yellow arrows) in higher magnification (f fibrin; b buffy coat; scale bar 20 µm)

Discussion

This study presents the potential of PRF-based matrices (PRF, A-PRF and A-PRF+) for growth factor release as a modest contribution to ongoing discussions regarding the preparation of PRF-based matrices as biological scaffolds and a natural growth factor release system, which is derived from autologous blood. The results revealed continuous growth factor release of VEGF, TGF- β 1 and EGF over the study time. However, statistically significant differences among the various preparation protocols, PRF, A-PRF and A-PRF+, were demonstrated.

One of the most potent angiogenesis-stimulating growth factors is VEGF. A-PRF+ released significantly more VEGF than PRF and A-PRF on day 7. Moreover, the accumulated release of VEGF on day 10 was significantly higher in A-PRF+ than in PRF and A-PRF. However, no statistical significance was detected when evaluating A-PRF and PRF. These outcomes are quite likely related to the specific fibrin structure and cellular distribution pattern of A-PRF+. VEGF plays a crucial role in wound healing and tissue regeneration to promote vascularization and new vessel formation.¹⁷ Additionally, previous studies have demonstrated that the sustained release of VEGF promotes epithelialization and enhances collagen tissue deposition in a skin wound healing model in mice.¹⁸ Thus, the sustained and enhanced VEGF release of A-PRF+ could lead to more benefits in regeneration and vascularization and thus provide a nutrient supply to support wound healing and improve the biomaterial-guided regeneration pattern.

The release of TGF- β 1 in A-PRF and A-PRF+ indicated the maximal release values on days 7 and 10, which were significantly higher when comparing A-PRF to PRF and A-PRF+ to PRF. However, no statistically significant difference between the TGF- β 1 release of A-PRF and A-PRF+ was detected in this case. TGF- β 1 is essential for wound healing.¹⁹ Chronic wounds were observed to have a decreased expression of TGF- β receptors.²⁰ Thus, PRF matrices with an enhanced release of TGF β 1, as was the case PRF+ groups than in the PRF group. By contrast, A-PRF and A-PRF+ revealed no statistically significant difference for A-PRF and A-PRF+, could have a major influence on wound healing as a catalyzer of wound repair stages. In addition, this growth factor is known to stimulate fibroblast migration, enhance collagen synthesis and promote angiogenesis.^{21, 22} All of the latter characteristics are essential in the biomaterial-based regeneration process. Hence, PRF-based matrices as an additional autologous dose of inflammatory cells and growth factor could be promising in the field of guided bone and tissue regeneration (GTR and GBR), in which biomaterials should provide a scaffold and support the regeneration process in the defect area. The release of EGF was generally higher in the A-PRF and A-PRF+ groups when compared with PRF. Statistically highly significant differences were detected when comparing A-PRF+ with PRF after 24 h, whereas no significant difference was observed between A-PRF+ and A-PRF. The accumulated EGF release showed significantly higher rates in the case of A-PRF and A-PRF+ compared with PRF at most time points, particularly on day 10. EGF has previously been described as promoting cell growth,²¹ enhancing keratinocyte migration,²³ inhibiting apoptosis under hypoxic conditions,²⁴ and supporting reepithelization and skin healing.^{25, 26} Additionally, EGF supports the healing process of chronic wounds,²⁷ nonhealing chronic wounds and ulcers, which are, for example, observed in diabetic patients known to lack the necessary growth factors to maintain the healing process.^{28, 29} Thus, such patient groups may benefit from the application of PRF matrices as an autologous drug delivery system. Moreover, immunohistochemical

evaluation indicated an equal distribution pattern of platelets in all clot regions in the case of A-PRF and A-PRF+, whereas in PRF, the majority of the platelets were located in the lower portion of the clot. These findings may be related to the LSCC (low speed centrifugation concept), indicating that reducing the applied RCF increases the number inflammatory cells and platelets as well as the growth factor release within the PRF-based matrices.¹⁵ Because the centrifugation process depends on cell weight and density, a higher RCF may be the reason for the sedimentation of the majority of the platelets to the lower portion of the clot according to their density and size, as observed in PRF. Decreasing the RCF allows the platelets to become separated from the red blood cell phase and become equally distributed within the fibrin network. The effectiveness of PRF clots with low platelet counts and uneven platelet distribution may have less influence on clinical outcomes than clots with evenly distributed and enhanced platelet numbers because the applied clot could have uneven biological activity and thus a reduced growth factor release, as indicated in the present study. However, comparative clinical studies are necessary to evaluate the advanced PRF matrices presented here to demonstrate the extent to which the improved structure, even cellular distribution and enhanced growth factor release may affect clinical outcomes.

These observations highlight the influence of RCF reduction, *i.e.*, from PRF (708 g) to A-PRF and A-PRF+ (208 g) on platelet distribution, thereby correlating with the previously demonstrated automated cell counting that indicated significantly more platelets in PRF matrices prepared with low RCF than with high RCF application.¹⁵ A previous *ex vivo* immunohistochemical study demonstrated the distribution pattern in PRF and A-PRF, which included, in addition to platelets, a wide range of inflammatory cells that physiologically exist within the peripheral blood, such as leukocytes, including neutrophils and monocytes as well as lymphocytes.⁵ However, further immunohistochemical studies are required to determine the distribution pattern of the included leukocytes and their subgroups, particularly in A-PRF+. These cells, particularly platelets and neutrophilic granulocytes, contribute to neoangiogenesis and VEGF release.^{30, 31} In addition, platelets are the primary secretory cells of EGF and TGF- β 1,³² thus, their presence within the PRF-based matrices is a possible explanation for the observed growth factor release. These cells are essential for wound healing and tissue regeneration.^{33, 34} In the present study, release kinetics displayed an increased growth factor release over the study time and a maximum at day 7 in the case of VEGF and TGF- β 1 as well as an increased growth factor release at 24 h in the case of EGF. Based on the growth factor and release kinetics demonstrated here, one may assume that the growth factor release pattern within the various PRF-based matrices is an active release from living cells within the different PRF clots, which

most likely experienced apoptosis during the study period if 10 days reflects the reduction in growth factor release at day 10 compared with day 7 in all groups and growth factors.

Additionally, leukocytes and platelet interaction via cellular cross talk have been described in bone regeneration.⁹ In this context, the high regeneration potential of advanced PRF-based matrices could be beneficial in various clinical applications, such as enhancing the regeneration pattern of biomaterials in terms of GTR and GBR. Moreover, autologous biologizing biomaterials using PRF based matrices may improve the regeneration pattern in large-sized, soft and bony defects to catalyze wound healing and regeneration. Ongoing clinical observations in oral- and maxillofacial surgery have demonstrated that various bony defects within the jaw or head can be regenerated by different clot numbers according to the defect size. Thus, molar sockets are treated with 2–3 clots, whereas larger bony head defects are treated with up to 6 clots. Based on these observations, PRF-based matrices could be a beneficial tool to improve the regeneration of soft and bony defects after orthopedic or trauma surgery. The present study demonstrates that the application of the LSCC (low speed centrifugation concept), by decreasing the RCF from PRF toward A-PRF and A-PRF+, results in a significantly higher release of VEGF, TGF- β 1 and EGF. Notably, the accumulated release over 10 days of TGF- β 1 and EGF supports the relation between the reduction of RCF and the growth factor release. Hence, A-PRF+ and A-PRF, which were prepared with the same RCF, displayed comparable results that were significantly higher than PRF, which was prepared with more than three times higher RCF. These observations emphasize the fact that the application of the LSCC is valuable in modifying and optimizing solid PRF based matrices. However, the manipulation of the centrifugation time appeared to influence only certain growth factors, as shown in the case of A-PRF+. The accumulated VEGF release on day 10 showed a significantly higher rate in the group of A-PRF+ compared with A-PRF and PRF. It may be that the application of a low RCF but a longer centrifugation time, as demonstrated in the case of A-PRF, affected the VEGF release capacity, whereas the application of a low RCF and slightly decreased centrifugation time, as in A-PRF+, resulted in a significantly higher VEGF release. Another plausible explanation may be that the specific fibrin clot composition of A-PRF+ allows a highly increased VEGF release and thus a higher accumulated VEGF release on day 10. These data accentuate the fact that the various growth factor concentrations may be a consequence of the various total cell concentrations within the PRF-based matrices.

The various release profiles of the evaluated PRF based matrices may also be a consequence of the different growth factor binding affinities to fibrin. It has been demonstrated that growth factors, such as VEGF, have a high affinity to bind to fibrinogen and fibrin so that those factors are released in a sustained manner.³⁵ This information is reflected in the present

results by showing significantly enhanced VEGF release on day 7 in the case of A-PRF+. By contrast, EGF is released in a high concentration level at the very early time point of 24 h. One explanation for this observation may be the low binding affinity of EGF to fibrin and fibrinogen.³⁶ Another factor may be the structure of the PRF-based matrices. A-PRF and A-PRF+ exhibit a more porous structure than the densely structured PRF.⁵ The physical properties of the clot and the specific fibrin structure related to the manufacturing protocol⁵ may also influence the binding affinity and the sustained release of the various growth factors. It is possible that a more porous structure, as shown in A-PRF and A-PRF+, is one reason for an enhanced growth factor release.⁵ Thus, it remains questionable whether the growth factor release is related to the specific physical properties of the fibrin network or to the included inflammatory cells and platelets, or perhaps a combination of both. Therefore, further study is required to understand this specific complex system.

The release kinetics of growth factors in the PRF-based matrices have previously been reported in several studies.^{37, 38} Direct comparisons of these studies are limited because of the various preparation protocols in terms of RCF, centrifugation time, blood volume and the techniques used to generate the PRF-based matrices. However, one *in vitro* study analyzed the growth factor release in PRF based matrices compared with PRP.³⁹ Correlations were demonstrated in the case of the accumulated TGF- β 1 and EGF, for which both studies presented a significantly higher growth factor release in PRF matrices prepared with a low RCF application compared with PRF matrices with high RCF exposure. This accentuates the fact that reduction of the RCF enhances the release of these growth factors. Notably, the later study also showed that PRP released higher growth factor concentrations (EGF, VEGF and TGF- β 1) at the very early time points, whereas PRF-based matrices showed a continuous and higher growth factor concentration over a period of 10 days.³⁹ Moreover, this group demonstrated further evaluation of the growth factors in PRF, A-PRF and A-PRF+.⁴⁰ The results of the accumulated growth factor release on day 10 are consistent with the present findings with regard to A-PRF+ concerning TGF β 1 and EGF. Both studies presented a significantly higher release of these growth factors within A-PRF+ when compared with PRF. By contrast to Kobayashi *et al.* (2016), the present study reveals no significant differences between A-PRF and A-PRF+ with regard to TGF β 1 and EGF. Additionally, the present outcomes indicate significantly higher accumulated VEGF release on day 10 in the group of A-PRF+ compared with A-PRF and PRF, whereas Kobayashi *et al.* (2016) showed no statistically significant differences between the examined groups on day 10. At this point, it must be stressed that the two studies were of different designs. Kobayashi *et al.* (2016) evaluated different time points from the time points investigated in the present study. In addition, Kobayashi *et al.* (2016) used a shaking incubator before performing the ELISA

evaluation, whereas our group incubated the PRF-based matrices without further manipulation, which can also be a reason for the discrepancies revealed in the results. It is evident that detection of the specific growth factors is dependent on the specific methods employed. Thus, further studies in this field are necessary to develop and evaluate PRF-based matrices generated according to LSCC.

The present experimental design regarding the preparation and cultivation of PRF-based matrices may offer advantages because the PRF clots were not compressed or manipulated but nevertheless yielded the large amount of growth factors in the PRF clot. Furthermore, the clots were incubated in a cell culture environment to provide adequate gas exchange and optimal conditions for cells. The primary limitation of this study is the *in vitro* system issue. A comparison with clinical results is difficult because of the discrepancy of comparing the physiological environment *in vivo*. Thus, the cellular crosstalk and enzymatic degradation of the fibrin network would be different *in vivo*. Further *in vivo* studies are required to determine the influence of the growth factors on the regeneration pattern of PRF-based matrices, particularly those matrices that are prepared according to the LSCC. This is necessary to identify out whether the observed inflammatory cell and growth factor enhancement will contribute to an improved regeneration potential *in vivo*. Moreover, the optimal release of growth factors required in wound healing and regeneration processes remains unclear, as is whether enhancing the amount released will indeed lead to improved performance. Thus, controlled clinical studies are essential to evaluate the regeneration potential of A-PRF and A-PRF+ and to establish the extent to which homogeneously distributed platelets and an enhanced growth factor release in addition to the porous structure will contribute to improved wound healing.

Less is known regarding the interaction of the PRF-based matrices with biomaterials with a view to improving biomaterial-based regeneration. In addition, little attention has been focused on the composition of PRF-based matrices obtained from patients undergoing pharmacologic treatments and whether the growth factor release will be influenced by medication. In addition, the regeneration potential of the PRF-based matrices may also be related to the age of the donor. Therefore, it may be that as the age of donors increases, less growth factor is released and vice versa. If this scenario is true, PRF-based matrices with enhanced growth factor release may be beneficial in these specific cases. In this respect, the determination of mononuclear cell growth in PRF and penetration into the PRF-based matrices as a simulation of the regeneration process *in vitro* would be of interest in understanding the role of PRF-based matrices in biomaterials and tissue engineering. Hence, further studies of the PRF-based matrices as a complex system that influences cell growth and differentiation and provides a growth factor reservoir remain necessary.

Additionally, the current PRF-based matrices were prepared according to specific protocols with a defined amount of blood. However, it would be interesting to determine how increasing or decreasing the blood volume influences the composition of the prepared PRF-based matrices, their regenerative potential and their growth factor release. These questions are current investigation topics of our research group as we seek to enhance wound healing and tissue regeneration to decrease patient morbidity. Hence, the outcomes of this study could provide new clinical approaches in tissue and bone regeneration in terms of a combination of biomaterials with PRF-based matrices. Nevertheless, further studies, particularly clinical studies, are required to develop optimized, standardized and tailored preparation protocols for various clinical applications and to demonstrate their advantages now and in the future.

Conclusion

The present study demonstrates the influence of RCF reduction on the growth factor release and platelet distribution in solid PRF-based matrices. A-PRF+, prepared with a reduced RCF, displayed significantly higher VEGF concentration over the study period of 10 days than A-PRF and PRF, which exhibited no statistically significant difference. EGF and TGF- β 1 were comparable in A-PRF and A-PRF+, which were significantly higher than PRF. Additionally, the platelet distribution pattern appeared to be equivalent in all regions concerning A-PRF and A-PRF+, whereas PRF showed the largest accumulation of platelets in the lower portion of the clot. Long-term, sustained and slow release of growth factors from all of the PRF groups may support cell migration and cell proliferation as well as offer advantages in the wound healing process. However, the significantly enhanced release in A-PRF and A-PRF+ may render these matrices superior to PRF in specific clinical indications. These promising findings offer an excellent handling efficiency and new approaches to the clinical application of wound healing as well as soft and bone tissue regeneration. Nevertheless, further clinical studies must demonstrate the extent to which the application of LSCC to generate A-PRF and A-PRF+ will benefit clinical outcomes.

References

1. Albanese A, Licata ME, Polizzi B, Campisi G. Platelet-rich plasma (PRP) in dental and oral surgery: from the wound healing to bone regeneration. *Immun Ageing*. **2013**; 10:23. doi:10.1186/1742-4933-10-23.

2. Intini G. The use of platelet-rich plasma in bone reconstruction therapy. *Biomaterials*. **2009**; 30:4956–4966. doi:10.1016/j.biomaterials.2009.05.055.
3. Textor J. Platelet-rich plasma (PRP) as a therapeutic agent: platelet biology, growth factors and a review of the literature, in: platelet-rich plasma. *Regen Med Sport Med Orthop Recover Musculoskelet Inj*. **2013**; 61–94. doi:10.1007/978-3-642-40117-6_2.
4. Choukroun J, Adda F, Schoeffler C, Vervelle A. An opportunity in paro-implantology: PRF (in French). *Implantodontie*. **2001**; 42:55–62.
5. Ghanaati S, Booms P, Orłowska A, Kubesch A, Lorenz J, Rutkowski J, Landes C, Sader R, Kirkpatrick C, Choukroun J. Advanced platelet-rich fibrin: a new concept for cell-based tissue engineering by means of inflammatory cells. *J Oral Implantol*. **2014**; 40:679–89. doi:10.1563/aaid-joi-D-14-00138.
6. Nurden AT. Platelets, inflammation and tissue regeneration. *Thromb Haemost*. **2011**; S13–33. doi:10.1160/THS10-11-0720.
7. Rivera FJ, Kazanis I, Ghevaert C, Aigner L. Beyond clotting: a role of platelets in cns repair? *Front Cell Neurosci*. **2015**; 9:511. doi:10.3389/fncel.2015.00511.
8. Schär MO, Diaz-Romero J, Kohl S, a Zumstein M, Nestic D. Platelet-rich concentrates differentially release growth factors and induce cell migration *in vitro*. *Clin Orthop Relat Res*. **2015**; 473:1635–43. doi:10.1007/s11999-015-4192-2.
9. Nami N, Feci L, Napoliello L, Giordano A, Lorenzini S, Galeazzi M, Rubegni P, Fimiani M. Crosstalk between platelets and PBMC: new evidence in wound healing. *Platelets*. **2016**; 27:143–8. doi:10.3109/09537104.2015.1048216.
10. Everts PM, Knappe JT, Weibrich G, Schönberger JPAM, Hoffmann J, Overdevest EP, Box HAM, van Zundert A. Platelet rich plasma and platelet gel: a review. *J Extra Corpor Technol*. **2006**; 38:174–87.
11. Jenne CN, Urrutia R, Kubes P. Platelets: bridging hemostasis, inflammation, and immunity. *Int J Lab Hematol*. **2013**; 35:254– 61. doi:10.1111/ijlh.12084.
12. Soloviev DA, Hazen SL, Szpak D, Bledzka KM, Ballantyne CM, Plow EF, Pluskota E. Dual role of the leukocyte integrin M2 in angiogenesis. *J Immunol*. **2014**; 193:4712–21. doi:10.4049/jimmunol.1400202.
13. Ekström K, Omar O, Granéli C, Wang X, Vazirisani F, Thomsen P. Monocyte exosomes stimulate the osteogenic gene expression of mesenchymal stem cells. *PLoS One*. **2013**; 8:e75227. doi:10.1371/journal.pone.0075227.
14. Rybarczyk BJ, Lawrence SO, Simpson-Haidaris PJ. Matrixfibrinogen enhances wound closure by increasing both cell proliferation and migration. *Blood*. **2003**; 102:4035–43. doi:10.1182/blood-2003-03-0822.

15. Choukroun J, Ghanaati S. Reduction of relative centrifugation force within injectable PRF-(Platelet-Rich-Fibrin) concentrates advances patients' own inflammatory cells, platelets and growth factors: First introduction of the low speed centrifugation concept (LSCC). *Eur J Trauma Emerg Surg.* **2017**; doi:10.1007/ s00068-017-0767-9
16. M. Barbeck, A. Motta, C. Migliaresi, R. Sader, C.J. Kirkpatrick, S. Ghanaati. Heterogeneity of biomaterial-induced multinucleated giant cells: possible importance for the regeneration process? *J Biomed Mater Res Part A* **2016**; 104:413–8. doi:10.1002/jbm.a.35579.
17. Ozaki H, Hayashi H, Viores SA, Moromizato Y, Campochiaro PA, Oshima K. Intravitreal sustained release of VEGF causes retinal neovascularization in rabbits and breakdown of the blood-retinal barrier in rabbits and primates. *Exp Eye Res.* **1997**; 64:505–17.
18. Brem H, Kodra A, Golinko MS, Entero H, Stojadinovic O, Wang VM, Sheahan CM, Weinberg AD, S.L.C. Woo, Ehrlich HP, Tomic-Canic M. Mechanism of sustained release of vascular endothelial growth factor in accelerating experimental diabetic healing. *J Investig Dermatol.* **2009**; 129:2275–87. doi:10.1038/ jid.2009.26.
19. Lichtman MK, Otero-Vinas M, Falanga V. Transforming growth factor beta (TGF- β) isoforms in wound healing and fibrosis. *Wound Repair Regen.* **2016**; 24:215–22. doi:10.1111/wrr.12398.
20. Kim B-C, Kim HT, Park SH, Cha J-S, Yufit T, Kim S-J, Falanga V. Fibroblasts from chronic wounds show altered TGF- β -signaling and decreased TGF- β Type II Receptor expression. *J Cell Physiol* **2003**; 195:331–6. doi:10.1002/jcp.10301.
21. Alexander PB, Yuan L, Yang P, Sun T, Chen R, Xiang H, Chen J, Wu H, Radloff DR, Wang X-F. EGF promotes mammalian cell growth by suppressing cellular senescence. *Cell Res.* **2015**; 25:135–8. doi:10.1038/cr.2014.141.
22. W. Fan, M. Yang, C. Zhang, R. Xue, W. Zhang, H. Qin. Effects of Choukroun's platelet-rich fibrin on human gingival fibroblasts proliferation, migration and type I collagen secretion. *Zhonghua Kou Qiang Yi Xue Za Zhi.* **2013**; 48:72–6.
23. M.A. Seeger, A.S. Paller. The roles of growth factors in keratinocyte migration. *Adv Wound Care.* **2015**; 4:213–24. doi:10.1089/ wound.2014.0540.
24. Arda-Pirincci P, Bolkent S. The role of epidermal growth factor in prevention of oxidative injury and apoptosis induced by intestinal ischemia/reperfusion in rats. *Acta Histochem.* **2014**; 116:167–75. doi:10.1016/j.acthis.2013.07.005.
25. S. Forsberg, O. Rollman. Re-epithelialization from human skin explant cultures is promoted by ligand-activated HER3 receptor. doi:10.1016/j.jdermsci.2010.03.017.

26. Hong JP, Kim YW, Lee SK, Kim SH, Min KH. The effect of continuous release of recombinant human epidermal growth factor (rh-EGF) in chitosan film on full thickness excisional porcine wounds. *Ann Plast Surg.* **2008**; 61:457–62. doi:10.1097/SAP.0b013e31815bfeac.
27. Johnson NR, Wang Y. Coacervate delivery of HB-EGF accelerates healing of type 2 diabetic wounds. *Wound Repair Regen.* **2015**; 23:591–600. doi:10.1111/wrr.12319.
28. L. Heuch, J. Streak Gomersall. Effectiveness of offloading methods in preventing primary diabetic foot ulcers in adults with diabetes: a systematic review. *JBIS Database Syst Rev Implement Reports.* **2016**; 14:236–65. doi:10.11124/JBISRIR-2016-003013.
29. B.D. Pence, J.A. Woods, Exercise, obesity, and cutaneous wound healing: evidence from rodent and human studies. *Adv Wound Care.* **2014**; 3:71–9. doi:10.1089/wound.2012.0377.
30. Tan KW, Chong SZ, F.H.S. Wong, Evrard M, S.M.-L. Tan, Keeble J, Kemeny DM, Ng LG, Abastado J-P, Angeli V. Neutrophils contribute to inflammatory lymphangiogenesis by increasing VEGF-A bioavailability and secreting VEGF-D. *Blood.* **2013**; 122:3666–77. doi:10.1182/blood-2012-11-466532.
31. Walsh TG, Metharom P, Berndt MC. The functional role of platelets in the regulation of angiogenesis. *Platelets.* **2015**; 26:199–211. doi:10.3109/09537104.2014.909022.
32. Barrientos S, Stojadinovic O, Golinko MS, Brem H, TomicCanic M, Perspective article. Growth factors and cytokines in wound healing. *Wound Repair Regen.* **2008**; 16:585–601. doi:10.1111/j.1524-475X.2008.00410.x.
33. Kolaczkowska E, Kubes P. Neutrophil recruitment and function in health and inflammation. *Nat Rev Immunol.* **2013**; 13:159–75. doi:10.1038/nri3399.
34. Gurtner G, Werner S, Barrandon Y, Longaker M. Wound repair and regeneration. *Nature.* **2008**; 453:314–21. doi:10.1038/nature07039.
35. Sahni A, Francis CW. Vascular endothelial growth factor binds to fibrinogen and fibrin and stimulates endothelial cell proliferation. *Blood.* **2000**; 96:3772–8.
36. Martino MM, Briquez PS, Ranga A, Lutolf MP, Hubbell JA. Heparin-binding domain of fibrin(ogen) binds growth factors and promotes tissue repair when incorporated within a synthetic matrix. *Proc Natl Acad Sci USA.* **2013**; 110:4563–8. doi:10.1073/pnas.1221602110.
37. M. a. Zumstein, A. Rumian, V. Lesbats, M. Schaer, P. Boileau. Increased vascularization during early healing after biologic augmentation in repair of chronic rotator cuff tears using autologous leukocyte- and platelet-rich fibrin (L-PRF): a prospective randomized controlled pilot trial. *J Shoulder Elb Surg.* **2014**; 23:3–12. doi:10.1016/j.jse.2013.08.017.

38. Visser LC, Arnoczky SP, Caballero O, Egerbacher M. Platelet-rich fibrin constructs elute higher concentrations of transforming growth factor- β 1 and increase tendon cell proliferation over time when compared to blood clots: a comparative *in vitro* analysis. *Vet Surg.* **2010**; 39:811–7. doi:10.1111/j.1532-950X.2010.00739.x.
39. E. Kobayashi, L. Flückiger, M. Fujioka-Kobayashi, K. Sawada, A. Sculean, B. Schaller, R.J. Miron. Comparative release of growth factors from PRP, PRF, and advanced-PRF. *Clin Oral Investig.* **2016**; 20(9):2353–60. doi:10.1007/s00784-016-1719-1.
40. M. Fujioka-Kobayashi, R.J. Miron, M. Hernandez, U. Kandalam, Y. Zhang, J. Choukroun, Optimized platelet rich fibrin with the low speed concept: growth factor release, biocompatibility and cellular response. *J Periodontol.* **2017**; 88(1):112–21. doi:10.1902/jop.2016.160443

3.1.2. Reduction of the relative centrifugal force influences cell number and growth factor release within injectable PRF-based matrices

Journal of Materials Science: Materials in Medicine, **2017**, 28(12).

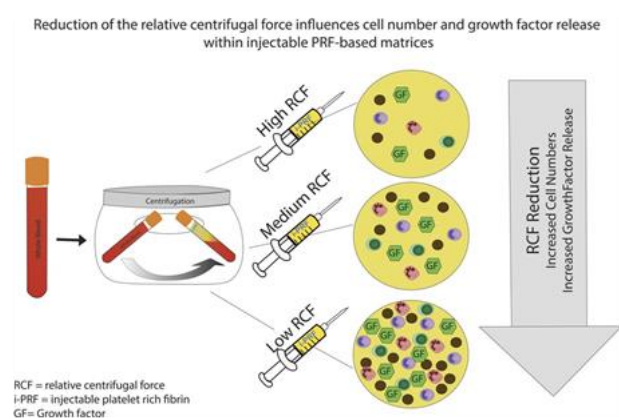
Wend, S.^a, Kubesch, A.^a, **Orłowska, A.**^a, Al-Maawi, S.^a, Zender, N.^a, Dias, A.^a, Miron, R. J.^b, Sader, R.^a, Booms, P.^a, Kirkpatrick, C. J.^a, Choukroun, J.^{a,c}, & Ghanaati, S.^a

^a Frankfurt Orofacial Regenerative Medicine (FORM) -Lab, Department for Oral, Cranio-Maxillofacial and Facial Plastic Surgery, University Hospital Frankfurt Goethe University, Frankfurt am Main, Germany

^b Department of Periodontology, College of Dental Medicine, Nova Southeastern University, Fort Lauderdale, Florida, USA

^c Private practice, Pain Therapy Center, Nice, France

Graphical abstract



Abstract

Platelet rich fibrin (PRF) is a blood concentrate system obtained by centrifugation of peripheral blood. First PRF matrices exhibited solid fibrin scaffold, more recently liquid PRF-based matrix was developed by reducing the relative centrifugation force and time. The aim of this study was to systematically evaluate the influence of RCF (relative centrifugal force) on cell types and growth factor release within injectable PRF- in the range of 60–966 g using consistent centrifugation time. Numbers of cells was analyzed using automated cell counting (platelets, leukocytes, neutrophils, lymphocytes and monocytes) and histomorphometrically (CD 61, CD-45, CD-15+, CD-68+, CD3+ and CD-20). ELISA was utilized to quantify the concentration of growth factors and cytokines including PDGFBB, TGF- β 1, EGF, VEGF and MMP-9. Leukocytes, neutrophils, monocytes and lymphocytes had significantly higher total cell numbers using lower RCF. Whereas, platelets in the low and medium RCF ranges both demonstrated significantly higher values when compared to the high RCF group. Histomorphometrical analysis showed a significantly high number of CD61+, CD-45+ and CD-15+ cells in the low RCF group whereas CD-68+, CD-3+ and CD-20+ demonstrated no statistically significant differences between all groups. Total growth factor release of PDGF-BB, TGF- β 1 and EGF had similar values using low and medium RCF, which were both significantly higher than those in the high RCF group. VEGF and MMP-9 were significantly higher in the low RCF group compared to high RCF. These findings support the LSCC (low speed centrifugation concept), which confirms that improved PRF-based matrices may be generated through RCF reduction. The enhanced regenerative potential of PRF-based matrices makes them a potential source to serve as a natural drug delivery system. However, further pre-clinical and clinical studies are required to evaluate the regeneration capacity of this system

Introduction

Platelet rich fibrin (PRF) is a blood concentrate system obtained from the peripheral blood of patients. first protocol of PRF matrices are generated using a one-step centrifugation process without necessitating the use of anticoagulants, known inhibitors of wound healing.^{1,2} Since the introduction of PRF in 2001 as a first platelet concentrate without added anticoagulants,¹ the successful applications of PRF in dentistry and medicine has seen a steady and widespread increase in popularity with many clinical indications demonstrating improvements in regenerative outcomes.³ The composition of the PRF matrix contains various inflammatory cells and growth factors embedded in a specifically structured fibrin network.² Platelets act as the

primary hemostasis cells shown to release a series of platelet-derived growth factors to recruit inflammatory cells to the impaired region and support tissue regeneration following the physiological phases of wound healing.⁴ Additionally, the interaction of platelets with leukocytes, which are also included within PRF-based matrices, further contribute to wound healing,⁵ and the fibrin network provides a scaffold for inflammatory cells as well as binding sites for growth factors.^{6,7}

While PRF has seen tremendous momentum as a regenerative modality in dentistry and medicine, the manufacturing process of the first described PRF scaffolds required a high relative centrifugal force (RCF). This resulted in a fibrin clot with a dense structure, including platelets and leukocytes that were mostly distributed unevenly throughout the scaffold accumulated at the proximal portion of the PRF clot adjacent to the isolated red cell fraction.² In order to improve the structure of PRF and enhance their regenerative potential, our group recently demonstrated that by reducing the RCF and modifying the centrifugation time in solid PRF-based matrices, a more porous fibrin structure could be manufactured with more leukocytes and growth factor release when compared to originally designed PRF scaffolds fabricated using high RCF.^{2,8,9}

In addition to solid fibrin clots,² a clinical need exists to develop an injectable PRF-based matrix for various clinical procedures including direct injections as well as to combine with various biomaterials to improve their angiogenic potential. Previous findings from research conducted by our group with solid PRF-based matrices revealed that the RCF and the centrifugation time were crucial factors for modifying the structure and composition of PRF-based matrices.^{2,8} Moreover, solid physiological clot formation is supported by the glass surface of the collecting tubes used to generate solid PRF matrices. Therefore, the manufacturing of an injectable blood concentrate without the need for anticoagulants was achieved by developing specific plastic tubes favoring the liquid phase after centrifugation. Recently, our group conducted a study to assess the influence of the applied RCF on leukocyte and platelet numbers within three different PRF-based matrices (i-PRF) with decreasing RCF content. The findings from that study showed that reducing RCF led to a significant enrichment in the i-PRF PRF scaffolds with greater leukocytes, platelets, and growth factor release after 8 min centrifugation time [10]. Based on these results, the low speed centrifugation concept (LSCC) was introduced as a potential tool to modify PRF scaffolds by fine tuning the centrifugation settings.¹⁰

Currently, the clinically-utilized liquid injectable PRF formulation (i-PRF) has been described using a 3 min centrifugation period in order to produce a liquid platelet concentrate containing primarily liquid fibrinogen and thrombin prior to fibrin formation. The aim of the present study was to further analyze the influence of RCF reduction on i-PRF matrices using

various centrifugation speeds. Systematic analysis included a wide RCF range (966–60 g-force) and a stepwise decrease of the RCF by halving the revolutions per minute (rpm) from 2800 rpm to 1400 rpm to 700 rpm. Thereby, we questioned whether the so-called LSCC effect would systematically alter these newer centrifugation times, *i.e.*, 3 min. In the present study, the centrifugation time of 3 min was maintained in the three test groups to focus solely on the influence of the RCF. Thus, the goal of this study was a comparative analysis of three different injectable PRF based matrices generated by systematic decreases in RCF by 4 times and 16 times while maintaining the centrifugation time. The focus was placed on the regenerative properties of the matrices, including the total number and distribution pattern of platelets and leukocytes, including their subfamilies along with the release of several growth factors and cytokines within the i-PRF matrices.

Experimental

Injectable platelet-rich fibrin (i-PRF) preparation

Blood was drawn from three healthy volunteers in an age range between 20–60 years without anticoagulant ingestion. The donors provided informed consent for their participation in this study. Injectable PRF matrices were prepared, as previously described [10]. Briefly, 10 ml of peripheral blood was collected in sterile plain plastic tubes (i-PRF, Process for PRF, Nice, France) and immediately centrifuged (Duo Centrifuge, PROCESS for PRF, Nice, France). Systematic decreases in RCF were performed in steps as follows:

- High RCF: 10 ml; 2800 rotations per minute (rpm); for 3 min; 966 g.
- Medium RCF: 10 ml; 1400 rotations per minute (rpm); for 3 min; 241 g.
- Low RCF: 10 ml; 700 rotations per minute (rpm); 3 min; 60 g.

After centrifugation, injectable PRF was collected using an ordinary syringe (5 ml Terumo® Syringe, Leuven, Belgium) with a needle (20 G x ½", Terumo®, Leuven, Belgium) through means of aspirating the upper yellowish layer without manipulating the red blood cell fraction

PRF-matrices cultivation

The prepared injectable PRF matrices (500 µl per well) were filled in 24-well cell culture plates (CELLSTAR®, Greiner bio-one) and incubated at 37 degrees for one hour until total clotting. Afterwards, 500 µl Dulbecco's Modified Eagle Medium (Biochrom GmbH, Berlin, Germany) was added per well and further incubated at 37 degrees for one hour. Subsequently, the supernatants were collected and frozen at –80 °C for growth factor and cytokine analysis.

Enzyme-linked immunosorbent assay (ELISA)

The protein concentrations of vascular epithelial growth factor (VEGF), transforming growth factor (TGF- β 1), platelet-derived growth factor (PDGF BB), matrix metalloproteinase 9 (MMP9) and epidermal growth factor (EGF) were quantified using ELISA-kits (Quantikine[®] ELISA, R&D Systems, Minneapolis, USA) according to the manufacturer's instructions, as follows (Table 1). The optical density was determined using a microplate reader (Infinite[®] M200, Tecan, Grödig, Austria) set at 450 nanometers. Next, the final concentrations of each sample were calculated using the graphing and statistics software GraphPad Prism 6 (GraphPad Software, Inc., La Jolla, USA). The experiments were performed in triplicate for each blood donor and preparation protocol.

Table 1. The used ELISA and detection ranges for the different growth factors

Growth factor/cytokine	Catalogue number	Detection range
VEGF	DVE00	15.6–1000 pg/mL
TGF- β 1	DB100B	31.2–2000 pg/mL
PDGF BB	DBB00	31.2–2000 pg/mL
EGF	DEG00	3.9–250 pg/mL
MMP 9	DMP900	0.3–20 ng/mL

Automated cell-counting

Automated cell-counting was performed as described before.¹⁰ For each specific experimental condition, the injectable matrices of the three groups were treated with EDTA (BD, New Jersey) for anticoagulation. This intervention was unavoidable for automated cell counting measurements. Subsequently, ADVIA[®] LabCell[®] Automation Solution (Siemens, France) analysis was performed at a medical laboratory (Labazur laboratory, Nice, France). The focus of the analyses was detecting the number of leukocytes, neutrophil granulocytes, monocytes, lymphocytes and platelets per microliter in each group.

Tissue processing and histological preparation

The clotted i-PRF matrices were fixed in 4% formaldehyde solution for 24 h and processed in various solutions as previously described.^{2, 11, 12} Briefly, a dehydration through an alcohol series with various concentrations was performed. Then, the samples were treated with xylene and embedded in paraffin. Three samples per donor and group were cut using a rotary microtome (Leica RM 2255, Wetzlar, Germany) to obtain 6 slices of 2–3 μ m thickness.

Subsequently, the sections were deparaffinized using xylene and rehydrated by passing through a series of alcohol with decreasing concentrations. One section per donor and group was stained in H.E. for an overview analysis of the structure and cells. Six sections were used for specific immunohistochemistry.

Platelets (CD61), leukocytes (CD 45), T-lymphocytes (CD3), B-lymphocytes (CD20), neutrophil granulocytes (CD15) and monocytes (CD68). Standardized immunohistochemical staining was performed according to standardized methods as previously described [2, 13, 14]. In brief, the deparaffinized and rehydrated sections were placed on slides and treated with citrate buffer (pH 6) at 96 °C for 20 min. Then, the slides were washed and cooled under running tap water. Before transferring the slides to the autostainer (Lab Vision™ Autostainer 360, ThermoScientific), the samples were washed with TBS. Next, the autostainer was loaded with a suitable solution and antibody for each specific cell type (Table 2) according the manufacturer's instruction. Additionally, and UltraVision™ Quanto Detections System HRP AEC was used. After autostaining, the slides were counterstained with hemalum for 30 s and washed with water. Finally covered with Aquatex® (Merck Millipore, Darmstadt, Germany).

Table 2. The immunohistochemical markers used in this study and their specifications

Antibody	Targeted cell	Epitope demasking	Concentration
CD 61 (Dako)	Platelets	Citrate-buffer, pH 6.0	1:50
CD 45 (Dako)	Leukocytes	Citrate-buffer, pH 6.0	1:100
CD 3 (Thermo Fisher)	T-lymphocytes	Citrate-buffer, pH 6.0	RTU
CD 20 (Thermo Fisher)	B-lymphocytes	Citrate-buffer, pH 6.0	RTU
CD 15 (Thermo Fisher)	Neutrophil Granulocytes	Tris-EDTA, pH 8.0	RTU
CD 68 (Dako)	Monocytes	Citrate-buffer, pH 6.0	1:200

Histological evaluation

Three of the authors were blinded and evaluated the slides independently. Histological analysis was performed using a light microscope (Nikon Eclipse Ni, Tokyo, Japan). Representative histological images were captured with a Nikon DS-Fi1 digital camera and a Nikon Digital sight unit DS-U3 (Nikon, Tokyo, Japan).

Histomorphometrical evaluation

As described before,² within each group, two immunohistochemically stained slides for each donor, and cell type were digitalized in a total scan using a Nikon Eclipse 80i microscope in combination with an automatic scanning table (Prior Scientific, Rockland, Maine), which was connected to a Nikon DS-Fi/1 digital camera and a computer with the Nikon NIS – Elements AR software, version 4.0. (Nikon, Tokyo, Japan). The total sample area calculated using the

measurement function of NIS Elements and positive-stained cells were counted manually by a NIS-Elements software counting tool to determine the cell number of each stained cell type per square millimeter.

Statistical evaluation

Statistical analysis was performed using the graphing and statistics software GraphPad Prism 6 (GraphPad Software, Inc., La Jolla, USA). The measured data are expressed as the mean \pm standard deviation (SD). Statistical significance was determined using one-way and two-way analysis of variance (ANOVA) with a Tukey multiple comparisons test ($\alpha=0.05$). The values were reported as significant at $p < 0.05$ (*) and highly significant at $p < 0.01$ (**) and $p < 0.001$ (***)

Results and discussion

Automated cell count

The number of leukocytes and leukocyte subfamilies showed a consistent trend in the examined groups across the cells investigated. In general, a decrease in RCF resulted in an increase in cell numbers. Significantly higher numbers of leukocytes were found in the low RCF group when compared to the high ($p < 0.001$) and medium ($p < 0.001$) RCF groups. No statistically significant differences were observed between the medium and high RCF ranges. Lymphocytes showed a similar trend with significantly higher numbers in the low RCF group when compared to medium RCF ($p < 0.01$) and high RCF groups ($p < 0.01$). Once again, no statistically significant difference was observed between the medium RCF and high RCF groups. The analysis of the total number of neutrophil granulocytes showed significantly higher numbers in the low RCF group when compared to the medium ($p < 0.01$) and high ($p < 0.01$) RCF groups, while there was no statistically significant difference between medium RCF and high RCF (Fig. 1a). Similarly, a significantly higher number of monocytes was found in the low RCF group when compared to the medium RCF and high RCF groups ($p < 0.01$) (Fig. 1b). There were also significantly more platelets in both the low RCF and medium RCF groups compared to the high RCF group ($p < 0.001$). No statistically significant differences were detected between the low RCF and medium RCF groups (Fig. 1c).

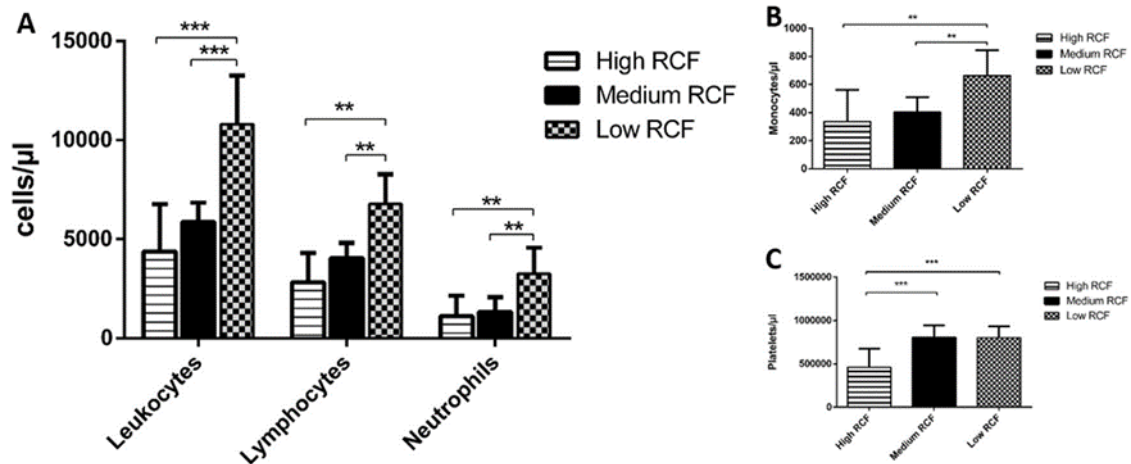


Figure 1. Comparative diagrams of automated cell counting results. (A) Leukocytes, lymphocytes and neutrophils. (B) Monocytes. (C) Platelets. Statistical analysis showed significant differences at $p < 0.05$ (*) and highly significant differences at $p < 0.01$ (**) and $p < 0.001$ (***)

Qualitative histological observation

General analysis of the evaluated groups showed that the total number of cells (platelets and leukocytes) was reduced with increased RCF (Fig. 2). The analysis of high RCF group showed a PRF-based matrix consisting mainly of a fibrin network in which single platelets and leukocytes were observable and distributed through the evaluated samples (Fig. 3A1, B1). In the case of medium RCF, more platelets and leukocytes were found throughout the fibrin scaffold when compared to the high RCF group (Fig. 3A3, B2). Whereas the low RCF group demonstrated a fibrin matrix most evenly and densely populated with platelets and leukocytes compared to the other two tested groups (Fig. 3A3, B3). The findings from these qualitative observations support the findings from the automated cell counting experiments demonstrating that lower RCF resulted in more cells throughout the PRF-based matrices.

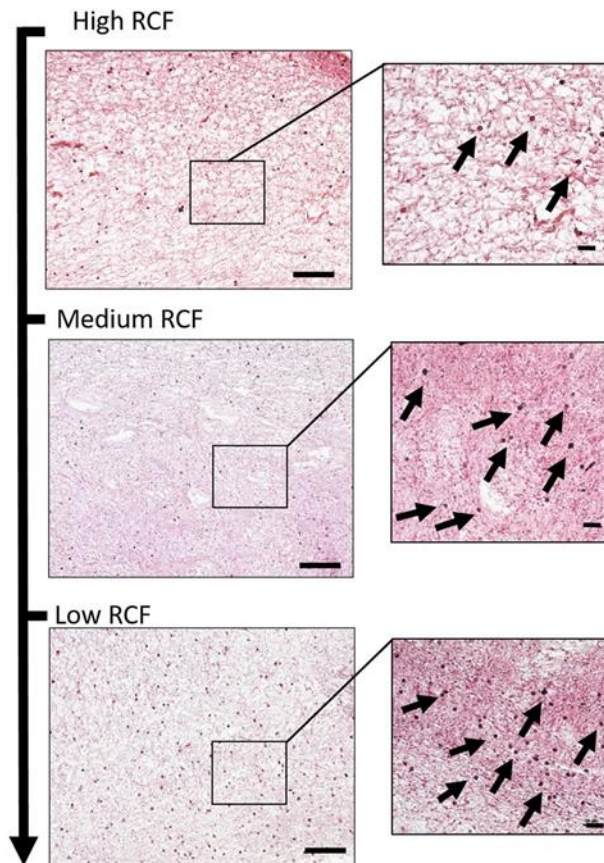


Figure 2. Representative histological images of the clotted injectable PRF in different RCF ranges (H&E staining; left column; scale bar = 100 μm ; Right column; scale bar = 20 μm ; arrows = cells)

Quantitative histomorphometrical analysis

The number of CD-61 positive cells (platelets) was significantly higher in the groups of low and medium RCF ($p < 0.001$ and $p < 0.05$, respectively). Whereas no statistical significant difference was detected between the medium and low RCF groups (Fig. 3C). The histomorphometrical analysis of CD-45 positive cells (leukocytes) showed that a significantly higher number of platelets was found in the low RCF group compared to the medium and high RCF groups ($p < 0.05$). However, no statistical significant difference was found between the medium and high RCF groups (Fig. 3D). The leukocyte subgroup CD-15 positive cells (neutrophil granulocytes) revealed different cell numbers within the three examined injectable PRF matrices. The low RCF group included the highest number of CD-15 cells whereas the medium and high RCF groups showed significantly lower values ($p < 0.001$). No significant difference was observed between the medium and high RCF groups. The analysis of CD-20 positive cells (B cells) showed comparable values within the three i-PRF matrices. The distribution of CD 68-positive cells (monocytes) within the evaluated matrices showed comparable outcomes between in the low and medium RCF groups, while the high RCF group demonstrated the lowest rate of CD-68-positive cells. Nevertheless, no statistically significant differences were detected between the

three groups. Additionally, CD-3 positive cells (T-lymphocytes) were found lowest in the low RCF group whereas medium RCF had the most CD-3 positive cells. Nevertheless, no statistically significant differences were observed (Fig. 4).

Growth factor and cytokine release

Growth factor release was then quantified by ELISA using the three injectable PRF-matrices at different RCF. The general trend in response to changes in the RCF showed that there was a tendency towards increased growth factor release with lower RCF. PDGF-BB release showed significantly higher values in the low and medium RCF groups when compared to the high RCF group ($p < 0.05$). No statistically significant difference was detected between the low and medium RCF groups. Furthermore, VEGF showed the highest value in the low RCF group, followed by medium RCF and high RCF ($p < 0.01$), with no statistical significance between the low and medium RCF and comparing the medium to the high groups. EGF showed the highest release in the low RCF group, significantly higher when compared to the high RCF group ($p < 0.05$). The medium RCF group also showed a significantly higher rate when compared to the high RCF group ($p < 0.05$). Thus, no statistically significant difference was detected between the high RCF and medium RCF groups (Fig. 5A). Similarly, the release of TGF- β 1 showed a similar trend whereby the low RCF and medium RCF demonstrated significantly more growth factor release when compared to the high RCF group ($p < 0.001$) and medium RCF was compared to high RCF ($p < 0.001$). In summary, the findings demonstrated that by reducing the RCF, a higher growth factor release of multiple blood-derived growth factors could be observed (Fig. 5B).

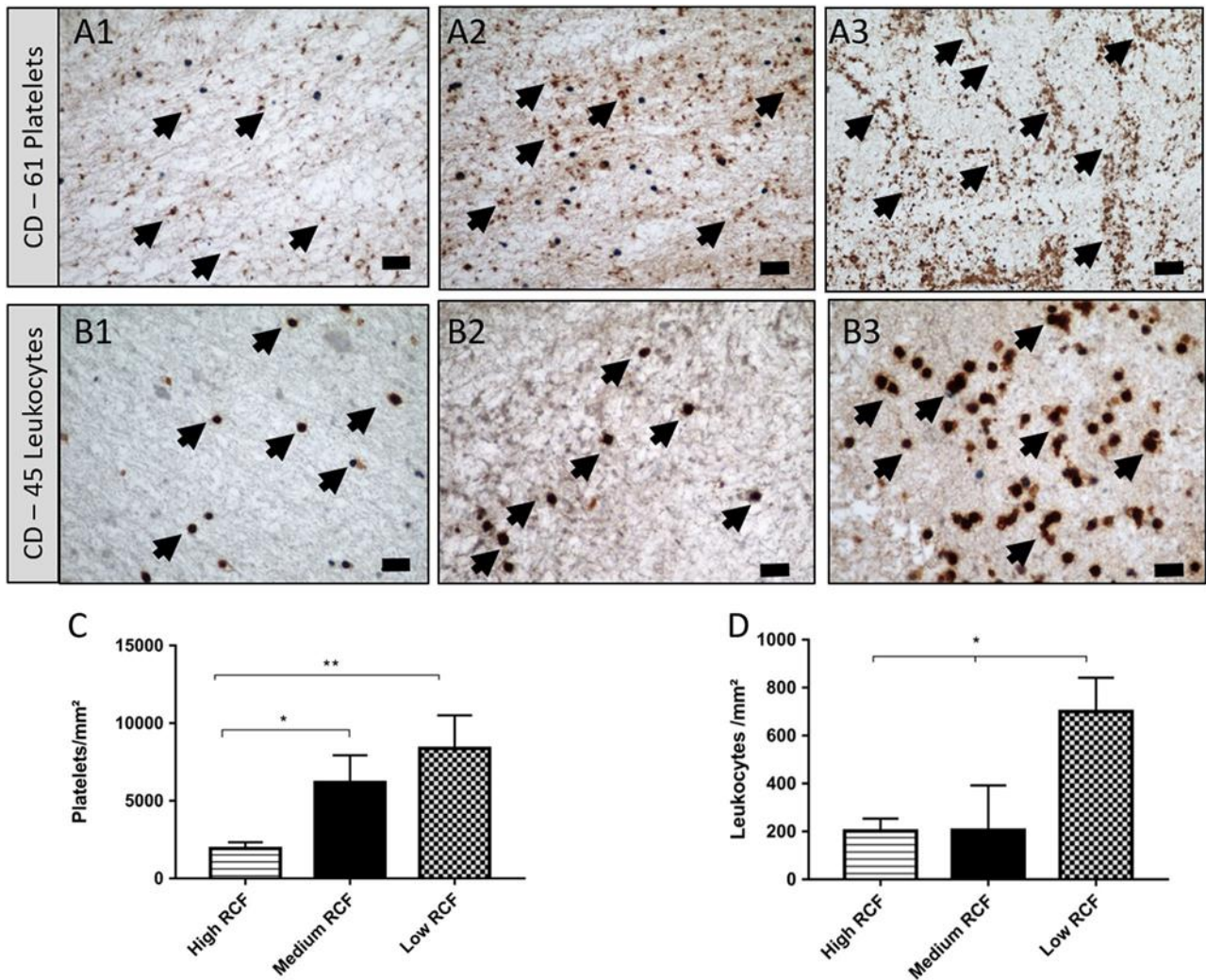


Figure 3. Histological micrographs of the platelets and leukocytes number in clotted injectable PRF. (A1-A3) CD 61 staining, black arrows = CD 61 positive platelets, scale bars = 20 μm. (A1) High RCF range, (A2) medium RCF range (A3) low RCF range. (B1-B3) CD 45 staining, black arrows = CD 45 positive leukocytes, scale bars = 20 μm. (B1) High RCF range, (B2) medium RCF range (B3) low RCF range. (C) Statistical analysis of the CD 61positive evaluated cells. (D) Statistical analysis of the CD 45- positive evaluated cells. Statistical analysis showed significant differences at $p < 0.05$ (*) and highly significant differences at $p < 0.01$ (**) and $p < 0.001$ (***)

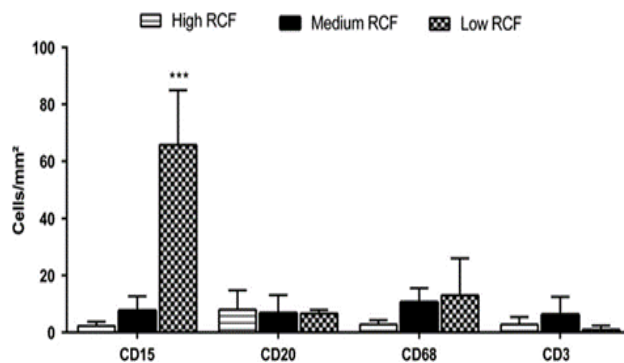


Figure 4. Statistical analysis of the measured inflammatory cells; CD 15 = neutrophils, CD-20 = B-Lymphocytes, CD-68 = monocytes; CD-3 = T-lymphocytes. There was a statistically significant difference in the amounts of CD-15 positive cells (***) $p < 0.001$

Cytokine release

The analysis of MMP 9 showed there was a significantly higher amount within the low RCF group compared to the medium RCF ($p < 0.001$) and high RCF groups ($p < 0.001$). Whereas the medium and high RCF groups had similar values without statistically significant differences. (Fig. 5B).

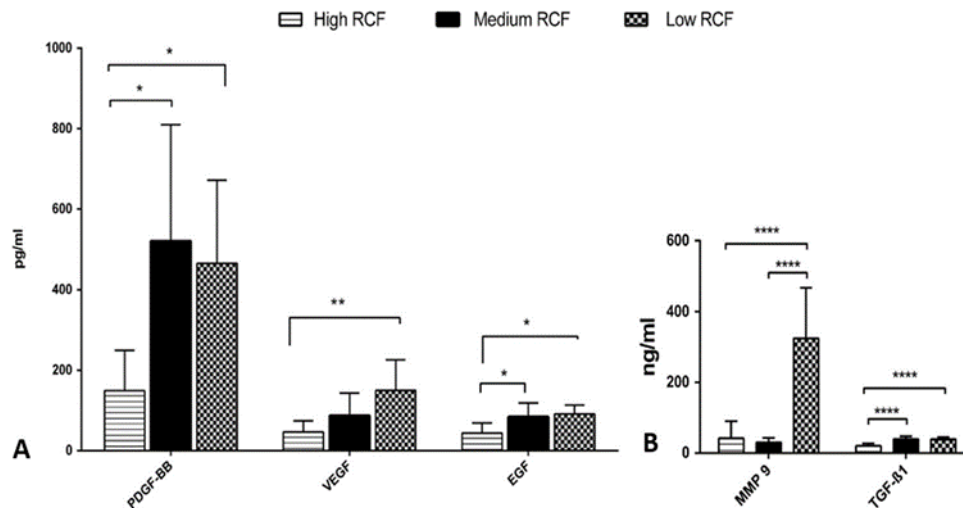


Figure 5. Comparative diagrams for the evaluated growth factor release using ELISA. a PDGFBB, VEGF, EGF. b TGF-β1 and MMP-9. Statistical analysis showed significant differences at $p < 0.05$ (*) and highly significant differences at $p < 0.01$ (**) and $p < 0.001$ (***)

Discussion

The relative centrifugation force and centrifugation time are key elements that could be modified to enhance the structure and composition of PRF-based matrices.^{2, 8, 10} Moreover, the introduction of the LSCC (low speed centrifugation concept) showed convincingly that the influence of RCF reduction on injectable and solid PRF-based matrices was responsible for an increase in cell numbers and growth factor release.^{8, 10} The present study demonstrated a systematic analysis of the RCF as a consequence of different rpm (revolutions per minute) settings during the preparation of injectable PRF-based matrices. As such, three injectable PRF-based matrices were manufactured following a stepwise decrease in halving the rpm and due to the centrifuge radius of 110 mm, a 4 time RCF decrease (medium RCF) and a 16 time decrease (low RCF) was investigated. We then focused on the number of various inflammatory cells and the release of different growth factors and cytokines within the evaluated PRF-based matrices.

The results from the automated cell counting experiments demonstrated that there was a general trend whereby lower RCF resulted in higher cell numbers. Leukocytes and their subfamilies, *i.e.*, neutrophils and monocytes as well as lymphocytes, were found in significantly higher numbers in the low RCF samples compared to medium and high RCF samples, although no statistically significant differences were observed between the medium and high RCF. Thus,

the first RCF reduction produced no significant differences in the mentioned cell types, whereas the second RCF reduction (low RCF) resulted in significantly higher cell numbers within the injectable PRF matrices. This frequently observed phenomenon showed that modification of the RCF had a major impact on the inflammatory cell numbers within the i-PRF matrices. Other than leukocytes and their subfamilies, the influence of RCF on platelets led to significant differences in the first RCF reduction between the high and medium RCF ranges, whereas no statistically significant difference was observed between the medium and low RCF range. These observations indicate that the cellular response to altering the RCF might be sensitive to cell-specific properties, such as weight, size and density. It may be that up to a specific decrease in RCF, the impact on specific inflammatory cells subsides. These findings correlate well with the results of our recent study, which indicated that PRF-based matrices following 8 min of centrifugation prepared with a reduced RCF included a significantly higher number of inflammatory cells compared to a PRF-matrix with a higher RCF application.¹⁰ The results from that study showed sustained significant differences between the high and medium range as well as between the medium and low range regarding leukocytes and platelets. Thus, altering the centrifugation time (from 8 to 3 min) might also have an impact on the included cells within the PRF-based matrices.¹⁰ Therefore, the present results demonstrated that following the LSCC, it was possible to influence the number of specific cells selectively, which might be a promising approach for generating specific PRF-based matrices according to clinical specifications and thus influence cell-cell communication by increasing Leukocytes and platelets that are major players in specific processes associated with wound healing and subsequently improving the regeneration process.¹⁵

General morphological and qualitative histological observations showed that there were obvious differences in the platelets and inflammatory cells. The stepwise decrease in RCF from the high to low RCF range were accompanied by an increased amount of platelets and inflammatory cells. These observations were further confirmed quantitatively using histomorphometry. The results showed a significantly higher rate of platelets and leukocytes in the low RCF groups compared to the high RCF group. In the case of leukocytes, the first step RCF reduction was not associated with significant differences whereas the platelets maintained their number between the high and medium RCF ranges. Additionally, CD-15 positive cells in the case of the low RCF group when compared to the medium and high groups. These results further approve our findings using automated cell count. However, no statistically significant difference was detected between the medium and high RCF groups. In addition, other cells, such as CD-20, CD-3 and CD-68 positive cells showed an increasing trend as RCF decreased but no statistically significant differences were observed between the evaluated groups. In contrast to the

histological analysis, there was a major discrepancy in the leukocytes subgroups and lymphocytes results derived from automated cell counting. These observations may be related to the high total number of leukocytes and platelets that is significantly influenced by the RCF reduction. In this case these changes are visible even in a 3–5 μm cross-section of the samples. In addition, due to the comparably small number of each leukocytes subgroup and lymphocytes physiologically existing in healthy blood, these cell groups are affected by the limitations of performing histomorphometric analysis that cannot represent the precise distribution pattern of the whole sample. In contrast, automated cell counting is a more accurate technique that analyzes a defined sample volume and includes all cell numbers representing more precise data, as shown in the results of flow cytometry.

The inflammatory cells evaluated in this study play an essential role in wound healing, which is a common factor in every surgical field.¹⁶ Platelets are involved in primary wound closure and have the capacity to release various signaling molecules, including several growth factors to recruit inflammatory cells to the region of injury.^{4, 17} Moreover, leukocytes and their subfamilies, such as neutrophils, monocytes and macrophages, are involved in the regeneration process within different tissue types.^{18, 19} Their appearance in the impaired site support angiogenesis and lymphangiogenesis.²⁰ The cross talk between platelets and leukocytes was previously shown to promote bone regeneration.²¹ Furthermore, neutrophils are the main players in the early wound healing phase. They function as phagocytes and release neutrophilic extracellular traps to prevent pathogenic activity and wound infection.^{22, 23} The regenerative potential of monocytes in releasing different cytokines and proteins, such as bone morphogenetic protein 2 (BMP-2), has been previously described in the literature.^{21, 24, 25} In addition, a recent *in vivo* study by our group demonstrated that the combination of monocytes isolated from human peripheral blood with bone substitute material resulted in significantly higher vascularization of the implantation bed compared to a pure bone substitute material.¹⁴ Finally, in addition to their immunological role, lymphocytes influence the osteogenic differentiation of mesenchymal stromal cells²⁶ and release cytokines, such as IL-17, which have a stimulating potential on osteoblasts during new bone formation.²⁷ Due to the liquid consistency of the injectable PRF, combinations with biomaterials, such as bone substitute granules or collagenous membranes, are possible and might lead to the enrichment of biomaterials with autologous crucial inflammatory cells. Such combinations might be beneficial to enhance the capacity and bioactivity of the applied biomaterials. However, one limitation of the present *in vitro* study is that it cannot provide any conclusions about functionality of these cells. Thus, further *in vivo* and clinical studies are needed to demonstrate the extent to which

including i-PRF within the wound as well as in combination with biomaterials may influence tissue regeneration.^{28–33}

The analysis of the growth factors EGF and TGF- β 1 revealed the highest growth factor release in the low RCF group that was significantly higher compared to high RCF. However, medium RCF also showed significantly higher growth factor release compared to high RCF. No statistically significant difference was detected between medium and low RCF and similar results were observed for PDGF β . These observations made it clear that the decrease in RCF resulted in a higher growth factor release. Therefore, significant differences were only observed when modifying the RCF within a high spectrum field, *i.e.*, from high RCF to medium RCF or high RCF to low RCF. Comparisons between the medium and low RCF range revealed no statistically significant differences. These findings correlated with the prior platelet trend as the RCF amount changed. Therefore, the growth factor release might be related to the number of releasing cells, *e.g.*, platelets. The present results underline the results of our previous *in vitro* study, which demonstrated that PRF-based matrices prepared according to the LSCC, *i.e.*, reduced RCF release, led to significantly higher values in EGF, TGF- β 1 and VEGF over 10 days compared to PRF prepared with a higher RCF.⁸

Additionally, VEGF only showed significantly higher values in low RCF compared to high RCF, whereas no statistically significant difference was found between the medium and high range or the medium and low RCF range. In our previous study using an 8 min centrifugation time with various RCFs, more VEGF release was observed at lower RCF ranges when compared to the high RCF range.

In this context, the centrifugation time in combination with a specific RCF range might play a role in growth factor release. The present outcomes made it obvious that for VEGF, modifying the RCF within the high range (*i.e.*, from high to medium) did not influence the VEGF release significantly. In this context, there might be specific RCF ranges in which specific parameters can be influenced selectively to tailor the preparation protocols to the patients' needs and suitable clinical applications. However, further studies are needed to determine this possible postulation. Finally, the cytokine expression of MMP-9 was significantly higher in the low RCF group compared to the other evaluated samples. Thus, no significant differences were found between the high and medium RCF samples.

Growth factors are important signaling molecules in the process of wound healing and tissue regeneration.¹⁵ The enhanced growth factor release within the i-PRF matrices prepared with the LSCC might have the potential to accelerate wound healing and contribute to an improved regeneration pattern in chronic wounds that lack certain growth factors.²⁸ PDGF is first released from the alpha granules of platelets during the early phases of wound healing and

has a high potential to recruit various cells, such as fibroblasts, mesenchymal stem cells and osteoblasts, which emphasizes its vital role in tissue and bone regeneration.²⁹ During the phases of wound healing, fibroblast migration and collagen synthesis are promoted by TGF- β 1, which also has an impact on tissue vascularization.^{30, 31} In addition, EGF is involved in supporting cell growth,³² keratinocyte migration³³ and re-epithelialization of wounds.³⁴ Whereas VEGF is the master regulator for angiogenesis and new vessel formation, which makes it an essential factor for promoting tissue regeneration.^{35, 36} For the vascularization process, the required activation and immobilization of VEGF is promoted by matrix metalloproteases, such as MMP-9, which also allow for recruitment of marrow progenitors.^{37, 38} In this context, i-PRF-based matrices, especially those prepared according to the LSCC could serve as a reservoir of growth factors and supply the application region with key molecules to support and improve the regeneration process.

The present results showed selective reactions of various growth factors in response to modifying RCF. These findings are probably related to the specific characteristics of particular growth factors and their molecular structure, density and size. Interestingly, platelets exhibited the lowest density compared to other blood-derived inflammatory cells, whereas other cells with a higher density, such as neutrophilic granulocytes, monocytes and lymphocytes, appeared to be significantly influenced additionally in the medium to low RCF spectrum. Due to the composition of the PRF-based matrices and the different included components, it has to be respected that PRF-matrices are a complex system. Therefore, modifying the composition of PRF-based matrices with the LSCC could provide a tool to influence the cell-cell communication by selectively altering a specific growth factor or cell type.

All in all, this systematic approach of RCF decrease demonstrated that using the LSCC, which was demonstrated in different *ex vivo*, *in vitro* and *in vivo* studies, enhanced the regenerative potential by significantly increasing the number of inflammatory cells and growth factor release over time.^{2, 8, 10} Thus, PRF-based matrices with enhanced regenerative potential could serve as a drug delivery system and be a useful therapeutic approach in different applications combined with biomaterials in guided bone and tissue regeneration as well as dressing wounds with impaired wound healing. Further *in vivo* and clinical studies are needed to show the functionality and regenerative potential of this system as well as to explore its impact on wound healing and patient morbidity.

Conclusion

The present study showed that decreasing the RCF resulted in a significantly higher number of inflammatory cells, platelets and significantly higher growth factor/cytokine release. However, specific cell types and growth factors were differentially influenced within the different RCF ranges. These findings show that it is possible to modify the components within PRF matrices by selectively modifying the RCF. The liquid consistency of the novel injectable PRF and its improved composition would allow for it to be combined with various biomaterials to increase their biological activity and potentially enhance the properties of membranes and bone grafts during guided bone and tissue regeneration (GTR/GBR) procedures. Additionally, the results demonstrated that the LSCC (low speed centrifugation concept) led to improved characteristics of PRF-based matrices by reducing the applied RCF. Thus, further preclinical and clinical studies are necessary to investigate whether the application of PRF-matrices generated according to the LSCC will further benefit wound healing.

Acknowledgements

The authors would like to thank Mrs. Verena Hoffmann for her excellent technical assistance. This work was partially funded by Marie Curie Actions under EU FP7 Initial Training Network SNAL 608184

References

1. Choukroun J, Adda F, Schoeffler C, Vervelle A. Une opportunité en paro-implantologie: le PRF. *Implantodontie* **2001**; 42:55–62
2. Ghanaati S, Booms P, Orłowska A, Kubesch A, Lorenz J, Rutkowski J, Landes C, Sader R, Kirkpatrick C, Choukroun J. Advanced Platelet-Rich Fibrin: A New Concept for Cell-Based Tissue Engineering by Means of Inflammatory Cells. *J Oral Implantol* **2014**; 40:679–89. <https://doi.org/10.1563/aaid-joi-D-14-00138>
3. Miron RJ, Fujioka-Kobayashi M, Bishara M, Zhang Y, Hernandez M, Choukroun J. Platelet-Rich Fibrin and Soft Tissue Wound Healing: A Systematic Review. *Tissue Eng Part B Rev* **2017**; 23:83–99. <https://doi.org/10.1089/ten.TEB.2016.0233>
4. Jenne CN, Urrutia R, Kubes P. Platelets: bridging hemostasis, inflammation, and immunity. *Int J Lab Hematol* **2013**; 35:254–61. <https://doi.org/10.1111/ijlh.12084>

5. Schmidt-Bleek K, Kwee BJ, Mooney DJ, Duda GN. Boon and Bane of Inflammation in Bone Tissue Regeneration and Its Link with Angiogenesis. *Tissue Eng Part B Rev* **2015**; 21:354–64. <https://doi.org/10.1089/ten.TEB.2014.0677>
6. Clark Ra. Fibrin and wound healing. *Ann N Y Acad Sci* **2001**; 936:355–67. <https://doi.org/10.1111/j.1749-6632.2001.tb03522.x>
7. Sahni A, Francis CW. Vascular endothelial growth factor binds to fibrinogen and fibrin and stimulates endothelial cell proliferation. *Blood* **2000**; 96:3772–78.
8. El Bagdadi K, Kubesch A, Yu X, Al-Maawi S, Orłowska A, Días A, Booms P, Dohle E, Sader R, Kirkpatrick CJ, Choukroun J, Ghanaati S. Reduction of relative centrifugal forces increases growth factor release within solid platelet-rich-fibrin (PRF)-based matrices: a proof of concept of LSCC (low speed centrifugation concept), *Eur. J Trauma Emerg Surg.* **2017**. 1007/s00068-017-0785-7
9. Miron RJ, Fujioka-Kobayashi M, Hernandez M, Kandalam U, Zhang Y, Ghanaati S, Choukroun J. Injectable platelet rich fibrin (i-PRF): opportunities in regenerative dentistry? *Clin Oral Investig* **2017**. <https://doi.org/10.1007/s00784-017-2063-9>
10. Choukroun J, Ghanaati S. Reduction of relative centrifugation force within injectable platelet-rich-fibrin (PRF) concentrates advances patients' own inflammatory cells, platelets and growth factors: the first introduction to the low speed centrifugation concept. *Eur J Trauma Emerg Surg* **2017**. <https://doi.org/10.1007/s00068-017-0767-9>
11. Ghanaati S, Orth C, Unger RE, Barbeck M, Webber MJ, Motta A, Migliaresi C. C. James Kirkpatrick, Fine-tuning scaffolds for tissue regeneration: effects of formic acid processing on tissue reaction to silk fibroin. *J Tissue Eng Regen Med* **2010**;4 :464–72. <https://doi.org/10.1002/term.257>
12. Barbeck M, Lorenz J, Kubesch A, Böhm N, Booms P, Choukroun J, Sader R, Kirkpatrick CJ, Ghanaati S. Porcine Dermis-Derived Collagen Membranes Induce Implantation Bed Vascularization Via Multinucleated Giant Cells: A Physiological Reaction? *J Oral Implantol* **2015**; 41:e238–e51.
13. Barbeck M, Motta A, Migliaresi C, Sader R, Kirkpatrick CJ, Ghanaati S. Heterogeneity of biomaterial-induced multinucleated giant cells: Possible importance for the regeneration process? *J Biomed Mater Res—Part A*. **2016**; 104:413–18.
14. Barbeck M, Unger RE, Booms P, Dohle E, Sader RA, Kirkpatrick CJ, Ghanaati S, Monocyte preseeding leads to an increased implant bed vascularization of biphasic calcium phosphate bone substitutes via vessel maturation, *J Biomed Mater Res—Part A* **2016**; 1–8. <https://doi.org/10.1002/jbm.a.35834>

15. Gurtner G, Werner S, Barrandon Y, Longaker M. Wound repair and regeneration. *Nature* **2008**; 453:314–21.
16. Nami N, Feci L, Napoliello L, Giordano A, Lorenzini S, Galeazzi M, Rubegni P, Fimiani M. Crosstalk between platelets and PBMC: New evidence in wound healing. *Platelets* **2016**; 27:143–8.
17. Nurden AT Platelets, inflammation and tissue regeneration, *Thromb Haemost*; **2011** S13-33.
18. McNally AK, Anderson JM. Phenotypic expression in human monocyte-derived interleukin-4-induced foreign body giant cells and macrophages *in vitro*: Dependence on material surface properties. *J Biomed Mater Res A* **2015**; 103(4):1380–90.
19. Vannella KM, Wynn TA. Mechanisms of Organ Injury and Repair by Macrophages. *Annu Rev Physiol* **2017**; 79:593–617.
20. Soloviev DA, Hazen SL, Szpak D, Bledzka KM, Ballantyne CM, Plow EF, Pluskota E. Dual Role of the Leukocyte Integrin M2 in Angiogenesis. *J Immunol* **2014**; 193:4712–21.
21. Ekström K, Omar O, Granéli C, Wang X, Vazirisani F, Thomsen P. Monocyte exosomes stimulate the osteogenic gene expression of mesenchymal stem cells. *PLoS ONE* **2013**
22. Brinkmann V, Reichard U, Goosmann C, Fauler B, Uhlemann Y, Weiss DS, Weinrauch Y, Zychlinsky A. Neutrophil extracellular traps kill bacteria. *Science* **2004**; 303:1532–5.
23. Mócsai A. Diverse novel functions of neutrophils in immunity, inflammation, and beyond. *J Exp Med* **2013**; 210:1283–99.
24. Pirraco RP, Reis RL, Marques AP. Effect of monocytes/macrophages on the early osteogenic differentiation of hBMSCs. *J Tissue Eng Regen Med* **2013**; 7:392–400.
25. Omar OM, Granéli C, Ekström K, Karlsson C, Johansson A, Lausmaa J, Wexell CL, Thomsen P. The stimulation of an osteogenic response by classical monocyte activation. *Biomaterials* **2011**; 32:8190–204.
26. Grassi F, Cattini L, Gambari L, Manferdini C, Piacentini A, Gabusi E, Facchini A, Lisignoli G. T cell subsets differently regulate osteogenic differentiation of human mesenchymal stromal cells *in vitro*. *J Tissue Eng Regen Med* **2016**; 10:305–14.
27. Croes M, Cumhur Öner F, van Neerven D, Sabir E, Kruyt MC, Blokhuis TJ, Dhert WJ, Alblas J. Proinflammatory T cells and IL-17 stimulate osteoblast differentiation. *Bone* **2016**; 84:262–70.
28. Kim B-C, Kim HT, Park SH, Cha J-S, Yufit T, Kim S-J, Falanga V. Fibroblasts from chronic wounds show altered TGF- β -signaling and decreased TGF- β Type II Receptor expression. *J Cell Physiol* **2003**; 195:331–336.

29. Digiovanni CW, Petricek JM. The Evolution of rhPDGF-BB in Musculoskeletal Repair and its Role in Foot and Ankle Fusion Surgery. *Foot Ankle Clin NA*. **2010**; 15:621–640.
30. Lichtman MK, Otero-Vinas M, Falanga V. Transforming growth factor beta (TGF- β) isoforms in wound healing and fibrosis. *Wound Repair Regen* **2016**; 24:215–22.
31. Roberts AB, Sporn MB, Assoian RK, Smith JM, Roche NS, Wakefield LM, Heine UI, Liotta LA, Falanga V, Kehrl JH. Transforming growth factor type beta: rapid induction of fibrosis and angiogenesis *in vivo* and stimulation of collagen formation *in vitro*. *Proc Natl Acad Sci U S A* **1986**; 83:4167–71.
32. Alexander PB, Yuan L, Yang P, Sun T, Chen R, Xiang H, Chen J, Wu H, Radloff DR, Wang X-F. EGF promotes mammalian cell growth by suppressing cellular senescence. *Cell Res* **2015**; 25:135–38.
33. Seeger MA, Paller AS. The Roles of Growth Factors in Keratinocyte Migration. *Adv Wound Care* **2015**; 4:213–24.
34. Forsberg S, Rollman O. Re-epithelialization from human skin explant cultures is promoted by ligand-activated HER3 receptor. *J Dermatol Sci* **2010**; 59:7–15.
35. Moens S, Goveia J, Stapor PC, Cantelmo AR, Carmeliet P. The multifaceted activity of VEGF in angiogenesis – Implications for therapy responses. *Cytokine Growth Factor Rev* **2014**; 25:473–82
36. Koch S, Claesson-Welsh L. Signal Transduction by Vascular Endothelial Growth Factor Receptors, *Cold Spring Harb. Perspect Med* **2012**; 2:a006502–a006502.
37. Carmeliet P, Jain RK. Molecular mechanisms and clinical applications of angiogenesis. *Nature* **2011**; 473(7347):298–307.
38. Heissig B, Nishida C, Tashiro Y, Sato Y, Ishihara M, Ohki M, Gritli I, Rosenkvist J, Hattori K. Role of neutrophil-derived matrix metalloproteinase-9 in tissue regeneration. *Histol Histopathol* **2010**; 25:765–70.

3.1.3. A low-speed centrifugation concept leads to cell accumulation and vascularization of solid plateletrich fibrin: an experimental study *in vivo*

Platelets, **2019**, 30(3), 329–340.

Kubesch, A.^a, Barbeck, M.^a, Al-Maawi, S.^a, **Orłowska, A.^a**, Booms, P. F.^a, Sader, R. A.^a, Miron, R. J.^b, Kirkpatrick, C. J.^a, Choukroun, J.^{a,c}, & Ghanaati, S.^a

^a Frankfurt Orofacial Regenerative Medicine (FORM) -Lab, Department for Oral, Cranio-Maxillofacial and Facial Plastic Surgery, University Hospital Frankfurt Goethe University, Frankfurt am Main, Germany

^b Department of Periodontology, College of Dental Medicine, Nova Southeastern University, Fort Lauderdale, Florida, USA

^c Private practice, Pain Therapy Center, Nice, France

Abstract

Platelet-rich fibrin (PRF) is generated from the patients' own venous blood by a single centrifugation step without the additional use of anticoagulants. Based on the previously described LSCC (low-speed centrifugation concept), our group showed that modification of the centrifugation setting, that is, reducing the relative centrifugal force (RCF) and mildly increasing the centrifugation time, resulted in modified solid and liquid PRF-matrices with increased number of platelets, leukocytes, and growth factors' concentrations. The aim of this study was to determine whether RCF reduction might also result in different tissue reactions toward the two PRF-based matrices, especially vascularization and cell distribution *in vivo*. Two centrifugation protocols (PRF-high [719 g] and PRF-medium [222 g]) were compared in a subcutaneous implantation model of SCID mice at 5 and 10 days. Histological and histomorphometrical analyses were performed to quantify lymphocyte, neutrophil, human macrophage, and monocyte populations. CD31 was used to detect newly formed vessels, while all human cells were detected by using human vimentin as a pan-cellular marker. The results demonstrated that PRF-high elicited a dense and stable fibrin structure and prevented cellular penetration of the host tissue. By contrast, PRF-medium was more porous, had a significantly higher *in vivo* vascularization rate, and included significantly more human cells, especially at day 10, compared to PRF-high. These findings highlight the possibility of modifying the structure and composition of PRF matrices and thus selectively altering their regenerative potential *in vivo*. Clinical studies now must evaluate the different PRF matrices for bone and soft-tissue regeneration to validate possible benefits using personalized preparation protocols.

Introduction

In the field of regenerative medicine, minimally invasive and feasible concepts with a high regenerative potential are needed. Vascularization is imperative for successful wound healing and regeneration of the defective tissue area and influences biomaterial integration in the surrounding tissue by providing an effective connection to the blood vessel network of the host peri-implant tissue.¹

Techniques to increase *in vivo* vascularization include either changes of the physicochemical material properties of the biomaterial itself^{2,3} or pre-seeding technologies involving osteoblasts, mesenchymal cells,⁴ or endothelial cells.^{5,6} Nonetheless, elaborate approaches that require cell isolation, cultivation, and the availability of an aseptic environment to prepare the scaffolds in proximity to the operating theatre are complex and thus limit their

translational application in a clinical setting. Thus, a clinically relevant technique for increasing biomaterial vascularization is necessary to overcome these limitations. An *in vivo* study was able to demonstrate that the addition of whole blood enhances biomaterial vascularization when compared to biomaterial implantation alone in an animal subcutaneous model.⁷ Thus, in searching for a clinically applicable concept, efforts in biomaterial research have recently focused on autologous blood-derived scaffolds as a viable approach.⁸⁻¹⁰

To eliminate elaborated production procedures and still obtain a pre-seeded tissue-like construct from autologous blood, platelet rich fibrin (PRF) was introduced.⁸ A fibrin-based matrix derived from peripheral blood can be obtained through a single centrifugation process, thus dispensing with the addition of anticoagulants or other additives, which minimize the risk of transcontamination.^{8,11} The preparation procedure of this system was designed to be suitable for clinical settings and is thus easy to implement through the accessible venous blood. The centrifugation procedure, together with the specific surface condition of the glass-based tubes, activates the physiological coagulation process and results in a three-dimensional fibrin clot.

Recently, our group investigated the influence of the relative centrifugation force on the resulting PRF clot characteristics.

Thus, tuning the preparation parameter of PRF, *i.e.*, reducing the applied RCF with a simultaneous slight increase in centrifugation time resulted in two PRF clots with different properties. Accordingly, an immunohistochemical analysis showed that PRF clots prepared using medium RCF of 222 g exhibit an evenly distributed and significantly higher number of neutrophil granulocytes as a leukocyte subfamily, compared to PRF prepared with high RCF of 719 g. Moreover, a qualitative histological analysis revealed a looser fibrin structure in the case of the medium RCF clot compared to the dense structure in the case of the high RCF clot.¹¹ The three-dimensional fibrin matrix provides a scaffold for the various included physiological inflammatory cells and mimics the extracellular matrix in some respects. This matrix presents an autologous complex system, which includes a variety of inflammatory cells, growth factors, and plasma proteins. The role of these elements is essential for wound healing and tissue regeneration.¹² Platelets are known to release different growth factors, including platelet-derived growth factor (PDGF), vascular endothelial growth factor (VEGF), which is involved in tissue vascularization, and transforming growth factor-beta (TGF- β), which has a regulatory effect on cells involved in new tissue formation.^{13,14} In addition, leukocytes are an integral part of the wound healing process through cellular crosstalk and thus contribute to angiogenesis and lymphangiogenesis,¹⁵ while the fibrin network serves as a source of growth factors.^{16,17} The release of specific growth factors such as VEGF, EGF, and TGF β -1 was evaluated in an *in vitro* study that analyzed the influence of altering the RCF in solid PRF-based matrices on the growth factor release. The

results showed a significantly higher growth factor release over a period of 10 days in the case of medium RCF-PRF when compared to high RCF-PRF and platelet-rich plasma, a different plasma concentrate system.¹⁸

Nevertheless, the cellular reaction of the different PRF-based matrices within the host tissue and especially their vascularization rates is unknown. Based on the previous *ex vivo* and *in vitro* observations, we questioned the extent to which the previous protocol modification of RCF influences the *in vivo* regeneration capacity of the PRF variations. To the best of our knowledge, this comparative study is the first to evaluate two different PRF-based matrices centrifuged with high RCF versus medium RCF, *in vivo*. The goal of the present study was to determine whether altering the preparation parameter affects the cellular reaction, implantation bed vascularization, and thus the regenerative potential of the PRF-based matrices.

Experimental

Manufacture of PRF

The PRF matrices were obtained in accordance with previously published protocols.¹¹ The present *in vivo* study is a continuation of a previously published *ex vivo* study with four donors,¹¹ according to which the PRF of each donor showed a characteristic protocol-related cell distribution and matrix deposition. Thus, based on the maxim of reducing animal experiments (3Rs: reduction, replacement, refinement) in the present study, the blood of one donor was used to generate multiple PRF-matrices for the two experimental groups (*i.e.*, high RCF vs. medium RCF) investigated. The donor of the blood for this study had no history of anticoagulation medication usage. This subject was one of the four donors in the previously published study that analyzed the differences between the same PRF groups in an *ex vivo* setting. Peripherally drawn blood from the donor was obtained using the tubes described below (Process for PRF™) and centrifuged with a (PC-O2, PROCESS for PRF, Nice, France). Informed consent was given by the subject.

This centrifuge has a fixed angle rotor with a radius of 88 mm. The following centrifugation protocols and RCF were used following the previously described methods:¹¹

- PRF-high: Sterile glass tube (10 ml), 2700 rpm, 719 g for 12 min
- PRF-medium: Sterile glass tube (10 ml), 1500 rpm, 222 g for 14 min

The relation between the rpm and RCF was calculated according to the following formula:

$$RCF = 1,12 \times Radius \times (rpm/1000)^2$$

Implantation and explanation procedure

The *in vivo* experiments of this study were conducted at the Institute of Pathology, University Medical Center of the Johannes Gutenberg University, Mainz, Germany, following a previously published method.⁴ The Committee on the Use of Live Animals in Teaching and Research in Rhineland Palatinate, Germany, approved the experimental setup for this study (reference: 23 177-07/10 10-1-029).

Briefly, a total of 20 six-week-old female SCID mice (Charles River Laboratories, Germany) were held under standard conditions with artificial light/dark cycles of 12 h and were supplied with water *ad libitum* and standard mouse pellets (Laboratory Rodent Chow, Altromin, Germany) at the Laboratory Animal Unit of the Institute of Pathology, University Medical Center at Johannes Gutenberg University in Mainz, Germany.

Prior to the implantation procedure, the experimental animals were divided into three groups. The SCID mice in the first group received the PRF-high clots at two time points, *i.e.*, 5 and 10 days of implantation ($n = 4$ animals per time point), while the animals in the second group underwent implantation of the PRF-medium for the same two time points and with $n = 4$ animals per time point. A third group of four animals (*i.e.*, $n = 2$ animals per time point) was deployed as the control group (implantation procedure without material insertion) to control surgery quality. In the first group, PRF-high clots were prepared, compressed in the PRF box, and placed in a sterile dental strip crown (Frasaco GmbH, Tettngang, Germany). The pores in the dental strip crowns were added by using a sterile 3-mm punch-biopsy tool. In the second group, PRF-medium was compressed in the PRF box and placed in the sterile dental strip crowns described above. The dental strip crowns were used to avoid the pressure of the overlying animal tissue on the fibrin-based scaffolds and thus avoid pressure induced premature degradation and dissolution. The basic setup of a pressure-free implantation is described in Figure 1. In the control group, two animals per time point underwent a sham operation and served as quality assurance for the performed surgeries.

Four PRF-based matrices for each group (PRF-high and PRF medium) per time point were implanted under sterile conditions in preformed subcutaneous pockets of the subscapular region of SCID mice using an established implantation model.⁴ Additionally, two PRF-based matrices from each group were placed in formalin fixative after undergoing all manufacturing procedures described for the implanted ones. This was done to delineate the condition of the PRF scaffolds of each group before implantation. All animals survived the operation and showed no signs of infection or wound healing disorders. Furthermore, no abnormal sleeping or eating pattern was observed in any of the experimental groups. After the respective time periods, the

animals were sacrificed with an overdose of ketamine and xylazine. Thereafter, the PRF-based matrices of both experimental groups were explanted in conjunction with the surrounding tissue and were fixed with 4% formaldehyde for 24 h for a histological (*i.e.*, histochemical and immunohistochemical) workup following the previously published methods.¹¹ After fixation, the explants were cut in three identical segments from left to right and were placed in embedding cassettes.

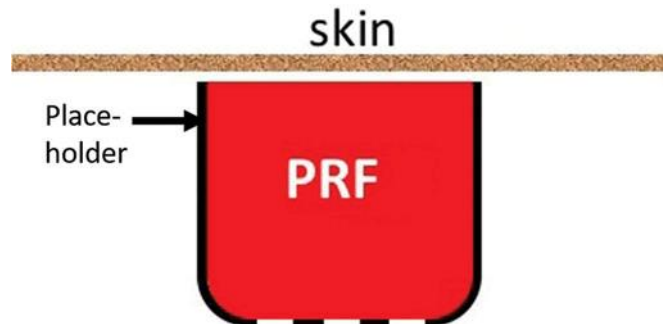


Figure 1. Pressure-free implantation. This figure demonstrates the subcutaneous implantation of the PRF-based matrices based on a pressure-free concept. Black dashed line = pores in dental strip crowns.

(Immuno-)histological preparation and staining methods

To prepare the samples for microscopic evaluation, tissue processing was conducted in a series of increasing alcohols and xylene. After subsequent paraffin embedding, from the central segment, 15 consecutive tissue sections with a thickness of 2–4 μm were produced with a rotation microtome (SLEE CUT 5062, Mainz, Germany) and mounted on precoated slides (SuperFrost® Plus, ThermoFisher Scientific, Dreieich, Germany). Prior to staining, the sections were subjected to dewaxing and rehydration by immersing the slides consecutively in xylene and ethanol in decreasing concentrations. Subsequently, histochemical and immunohistochemical staining was conducted as follows.

The first three slides were histochemically stained by hematoxylin and eosin (H&E), Giemsa, and Azan as these histochemical staining methods allow differentiation between the clot and the peri-implant tissue according to previously published methodologies.^{2,3} Twelve further slides were utilized to detect immunohistochemically molecules specific for the different blood cells and for murine macrophages as listed in Table I. An autostainer (Lab Vision™ Autostainer 360-2D, ThermoFisher Scientific, Dreieich, Germany) was used for these procedures.

In brief, to prepare the slides for immunohistochemistry, pretreatment was performed with a citrate buffer pH 6.0 solution at 96°C for 15–20 min with Proteinase K or EDTA pH 9.0 (depending on the antibody, see Table I). Afterwards, the slides were rinsed with tris buffered

saline and placed in the autostainer along with the obligatory solutions and antibodies in accordance with the manufacturer's specifications. For these staining reactions, the EnVision detection system (DAKO Deutschland GmbH, Hamburg, Germany) was used. Subsequently, the slides were removed from the autostainer, immersed in hemalum for 30 s and washed under running tap water. Afterwards, the slides were sufficiently dried and covered with cover slips using a water based mounting medium (Aquatex, Merck, Germany). For these staining reactions, the EnVision detection system (DAKO Deutschland GmbH, Hamburg, Germany) was used. Subsequently, the slides were removed from the autostainer, immersed in hemalum for 30 s and washed under running tap water. Afterwards, the slides were sufficiently dried and covered with cover slips using a water based mounting medium (Aquatex, Merck, Germany).

Table I. Antibodies used in this study. RTU: Ready-to-use.

Antibody	Targeted cell	Clone	Type (mono or poly)	Epitope demasking	Concentration
Anti-F4/80	Murine macrophages	BM8	Monoclonal rat anti-mouse	Proteinase K	1:100
Anti-CD3	T-lymphocytes	SP?	Polyclonal rabbit antihuman	Citrate buffer pH 6.0	RTU
Anti-CD15	Neutrophils	Ab-3	Monoclonal mouse antihuman	Citrate buffer pH 6.0	RTU
Anti- CD20	B-lymphocytes	Ab-1 L26	Monoclonal mouse antihuman	Citrate buffer pH 6.0	RTU
Anti-CD34	Mesenchymal precursor cells	QBend/10	Monoclonal mouse antihuman	EDTA pH 9.0	RTU
Anti-CD68	Monocytes	KP1	Monoclonal mouse antihuman	Citrate buffer pH 6.0	1:200
Anti-CD31	Endothelial cells	SZ31	Monoclonal rat anti-mouse	Citrate buffer pH 6.0	1:10
Anti-Vimentin	Human intermediate filament	V9	Monoclonal mouse antihuman	Citrate buffer pH 6.0	1:100

Histological analysis

For the histological examination, a light microscope (PrimoStar HD, Carl Zeiss Microscopy GmbH, Jena, Germany) was used, and the photomicrographs were taken with an integrated digital camera.

The focus of the analysis was on the scaffold–tissue interactions and was conducted independently by three investigators (i.e., AK, MB, and SG). The tissue reactions induced by the scaffolds were examined with respect to the fibrin matrix network structure, tissue ingrowth into the fibrin-based scaffolds, detection of the stained human inflammatory cells within the PRF-based matrices, and, finally, the extent of implantation bed vascularization.

Histomorphometrical measurements

Both slides which were histochemically stained via Giemsa and Azan and all of the immunohistochemically stained slides were digitized using a special microscopy system that included an Eclipse 90i microscope (Nikon, Tokyo, Japan), an automatic scanning table (Prior, USA), and a DS-Fi/1 digital camera (Nikon, Tokyo, Japan). Additionally, a computer system running the NIS – Elements AR software (version 4.1, Nikon, Tokyo, Japan) was used. This system was used for preparation of the so-called total scans, which are large-scale images obtained by

stitching together 40–100 single images containing the scaffolds and the peri-implant tissue at 100× magnification. These total scans were histomorphometrically measured as follows. The Azan-stained slides were used for the analysis of the fibrin structure. In this context, the scans were used for the measurements of the fibrin pores using the area tool of the NIS-Elements software. The Giemsa-stained slides permitted analysis of the cell penetration into the scaffolds by measuring their distance from the scaffold-tissue interface using the length tool of the NIS-Elements research software. To determine the vascularization rate for each animal, a slide stained with CD31 was used to measure both the vessel density and the percentage of vascularization after determining the total area of the respective scaffolds. Hence, the number of vessels and their respective areas were measured using the abovementioned software and were divided, based on the total implantation area to calculate both these vascularization parameters.

Furthermore, the distribution of the different cell types, *i.e.*, T-lymphocytes, B-lymphocytes, neutrophils, and human monocytes/macrophages, CD34+ mesenchymal precursor cells, vimentin-positive cells, and murine macrophages, was determined by using the NIS-Elements software and relating their respective numbers to the total implant area to calculate the number of positive cells per square millimeter.

Statistical methods

The statistical analysis was conducted by using the collected data of the two experimental groups (*i.e.*, with $n = 4$ samples in each group/time point).

The data were statistically analyzed using a one-way analysis of variance (ANOVA) and a Fisher's least significant differences multiple comparisons *post-hoc* test with GraphPad Prism (version 6.1, GraphPad Software, La Jolla, USA). Therefore, intraindividual (•) and interindividual (*) significant differences were reported as significant (•;/*) at P value < 0.05 and as highly significant (••/**) at P value < 0.01 and (•••/***) at P value < 0.001 . Finally, the quantitative data were presented graphically as the mean + standard deviation.

Results and discussion

All animals survived the surgery. No macroscopic or microscopic abnormal reaction, infection, or any complications were observed in the control group as well as both test groups. The control group underwent sham operation (without biomaterial) to control the surgery quality. Therefore, this group was not included in the statistical analysis of this study. The results focus on the PRF based scaffold-related cellular reaction and vascularization.

Qualitative and quantitative analysis of architecture of PRF based scaffolds prior to implantation

The histological analysis showed that the fibrin network of the PRF-medium scaffolds had a more porous structure compared to that of the PRF-high scaffolds (Figure 2A and B). The histomorphometrical analysis of the porosity of the fibrin networks confirmed that the pores of the PRF-medium scaffolds had a significantly higher mean diameter ($4.59 \pm 1.45 \mu\text{m}$) compared to that of the PRF scaffolds ($1.16 \pm 0.32 \mu\text{m}$) ($***P < 0.001$) (Figure 2C).

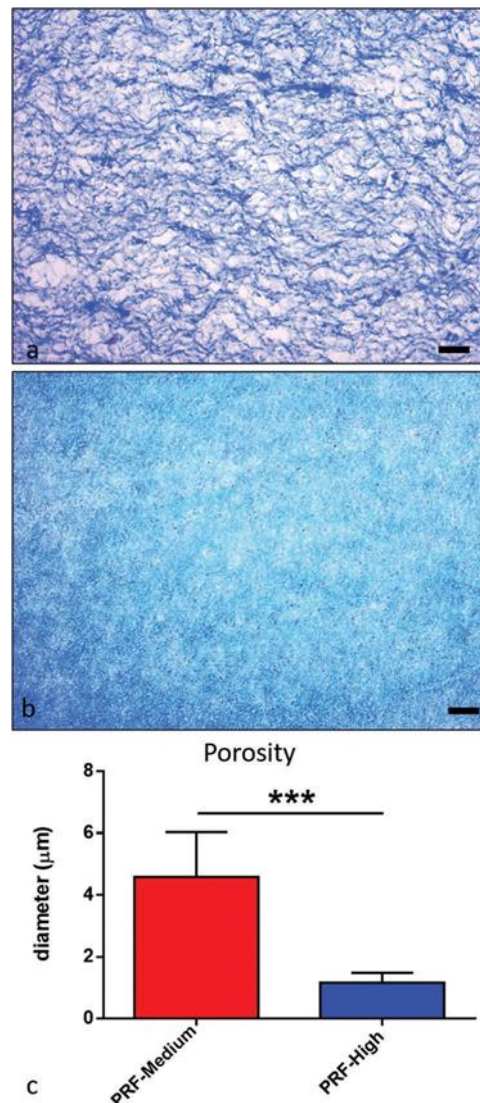


Figure 2. Fibrin architecture. Panels (A) and (B) show representative histological images of the structures of the fibrin networks of the PRF medium and PRF-high scaffolds, respectively. Histochemical Azan-staining; scale bar = $20 \mu\text{m}$. Panel (C) shows the results of the histomorphometrical measurements of the pore diameters of both scaffold types. The fibrin network of the PRF-medium and scaffolds exhibits a more porous structure compared to that of the PRF-high scaffolds ($***P < 0.001$).

Qualitative analysis of the tissue reaction to PRF-based scaffolds

The histological analysis demonstrated that both scaffold types were detectable within the subcutaneous connective tissue on day 5 after implantation (Figure 3A and B). At the tissue–biomaterial interface of both scaffolds, only mononuclear cells, which were identified mainly as macrophages, were detected. Additionally, single granulocytes and fibroblasts were found. On day 10 after implantation, only mononuclear cells that were mainly of the macrophage line were observed in the interfaces of the scaffolds (Figure 3C and D). In case of the PRF-medium scaffolds, the cells invaded the outer scaffold regions together with some vessels, while low numbers of cells penetrated the scaffolds in the case of the PRF-high implants at this time point (Figure 3C and D).

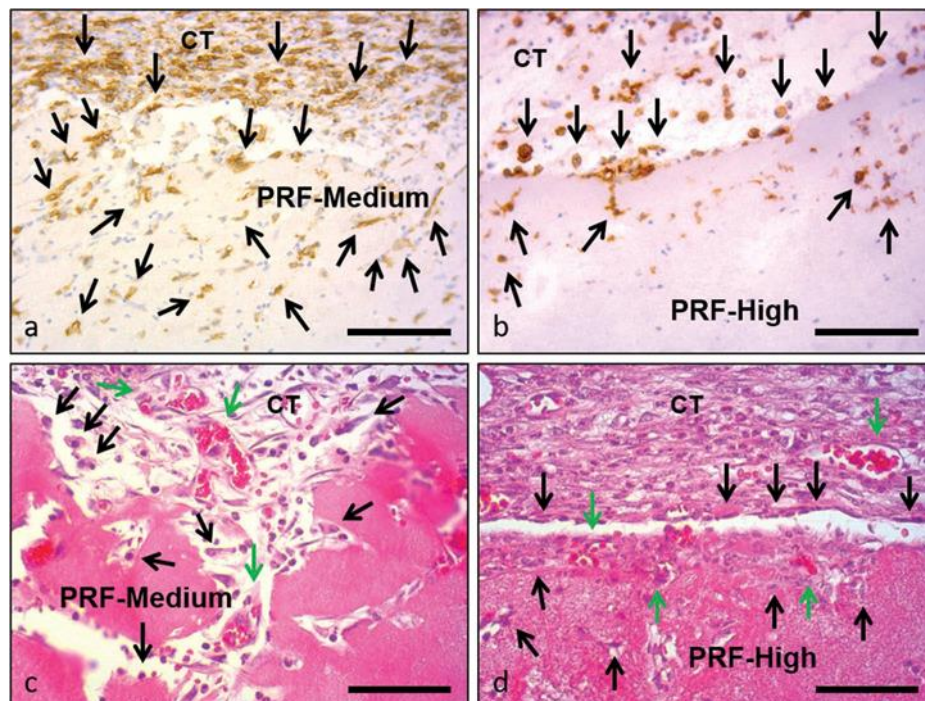


Figure 3. Tissue reaction. (A) and (B) show the cellular tissue response to both groups, which was driven by mononuclear cells, such as murine macrophages (F4/80-staining; scale bars = 100 μ m), on day 5. (C) and (D) also show that there were only mononuclear cells on day 10 (H&E-staining; scale bars = 100 μ m). Black arrows = mononuclear cells/(murine) macrophages, green arrows = vessels.

Qualitative and quantitative cell penetration analysis

The histological analysis of cell penetration showed that a higher number of cells penetrated the peripheral regions of the PRF-medium scaffolds at both time points compared to the group of the PRF-high scaffolds (Figure 4A–D). At both time points, the invaded cells also reached higher penetration depths in the case of the PRF-medium scaffolds compared to the PRF-high group (Figure 4A–D). Histomorphometrical analysis of the cellular penetration additionally showed that a significantly higher number of cells ($*P < 0.05$) had invaded the PRF-

medium scaffolds ($203.3 \pm 44.84 \mu\text{m}$) on day 5 after implantation in comparison to the PRF-high scaffolds ($79.33 \pm 17.39 \mu\text{m}$) (Figure 4E). On day 10 after implantation, a significantly higher number of cells (** $P < 0.01$) also penetrated the PRF-medium scaffolds ($540.50 \pm 85.44 \mu\text{m}$) in comparison to the PRF-high scaffolds ($163.30 \pm 31.90 \mu\text{m}$) (Figure 4E). A significant increase (••• $P < 0.001$) in the number of invaded cells was only found in the PRF-medium group, while the number in the PRF-high group was at a comparable level on days 5 and 10 after implantation (Figure 4E). Moreover, significantly higher penetration depths (** $P < 0.01$) were found in the PRF-medium group ($31.85 \pm 5.65\%$) compared to the PRF-high group ($9.38 \pm 3.88\%$) on day 5 after implantation (Figure 4F). On day 10 after implantation, significantly higher cellular penetration depths (** $P < 0.01$) were still observable in the group of PRF medium scaffolds ($39.97 \pm 9.57\%$) compared to the values in the PRF-high group ($14.48 \pm 2.38\%$) (Figure 4F).

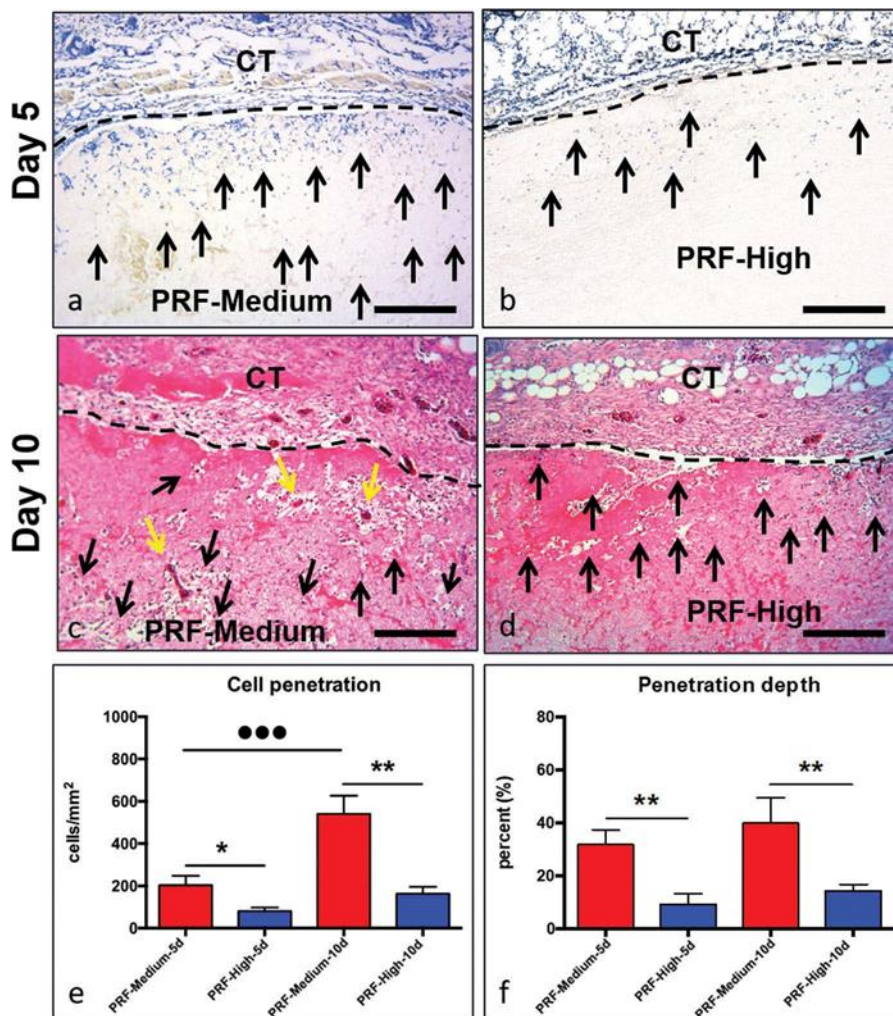


Figure 4. Cell penetration. (A–D) show representative histological images of the cell penetration into both scaffolds of the PRF High and PRF Medium on days 5 (A and B) and 10 (C and D) after implantation (black arrows = invaded cells, yellow arrows = vessels, black dashed line = interface between the scaffolds and the surrounding peri-implant tissue, CT = connective tissue). In the case of the PRF Medium, a visibly higher number of cells was found to have invaded the fibrin scaffolds at greater depths at both time points compared to the PRF-High group (A, B): Giemsa staining; scale bars = 100 μm). (C, D): H&E-staining; scale bars = 100 μm). (E) and (F) show the results of the

histomorphometrical analyses of the number of invaded cells per mm² (E) and their penetration depth (F) (* $P < 0.05$, ** $P < 0.01$, *** $P < 0.001$)

Qualitative and quantitative analysis of implantation bed vascularization

The histological analysis of the implantation bed vascularization indicated that the scaffolds in the PRF-medium group had a higher vascularization rate, starting with day 5 up to day 10 compared to that in the PRF-high group (Figure 5A–D). The histomorphometrical analysis revealed that both a significantly higher number of vessels per square millimeter and a significantly higher percentage of vascularization (* $P < 0.05$) were measured in the case of the PRF medium scaffolds (2.24 ± 0.79 vessels/mm² and $0.19 \pm 0.03\%$) in comparison to the values in the PRF high (0.96 ± 0.13 vessels/mm² and $0.04 \pm 0.03\%$) on day 5 after implantation (Figure 5E and F). In addition, on day 10 after implantation, both vascularization parameters in the PRF medium group (4.46 ± 1.25 vessels/mm² and $0.32 \pm 0.12\%$) showed significantly higher values (** $P < 0.01$) compared to those in the PRF-high group (0.96 ± 0.15 vessels/mm² and $0.06 \pm 0.04\%$) (Figure 5E and F). Only in the group of PRF-medium was a significant increase ($P < 0.05$) in the vessel density found between day 5 and day 10 after implantation (Figure 5E).

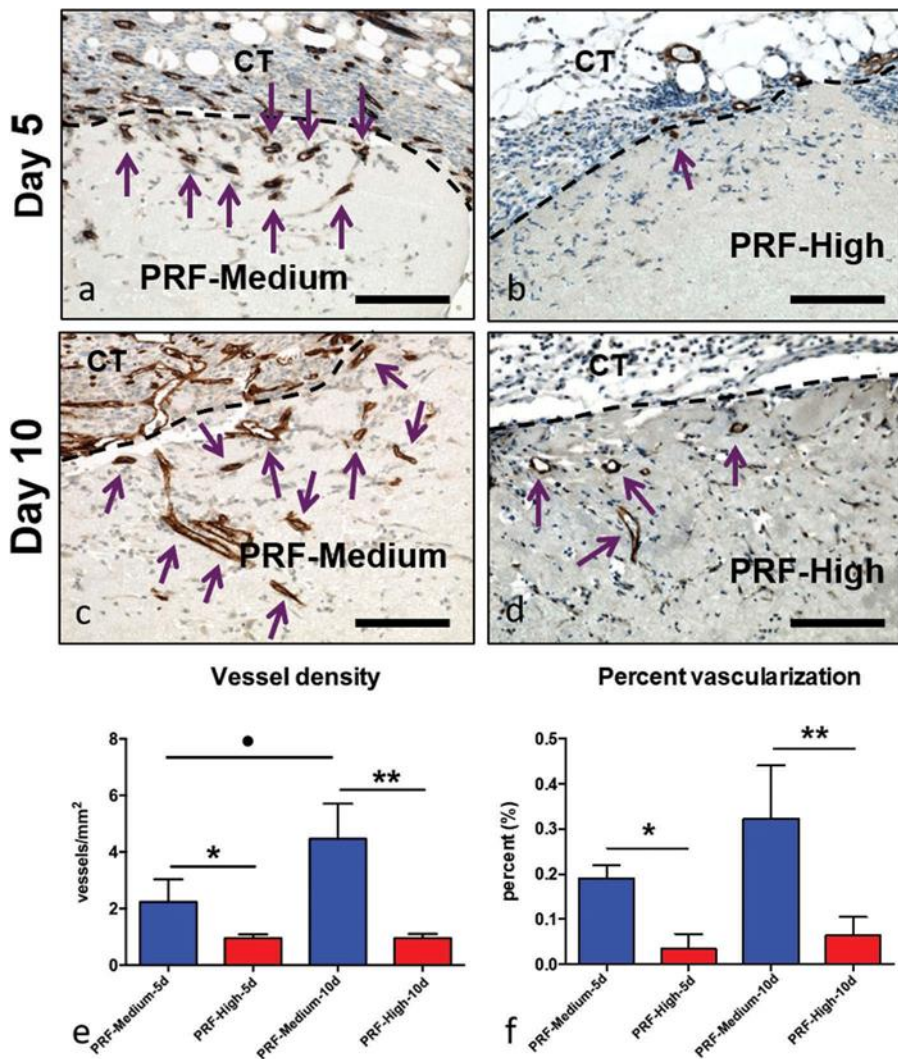


Figure 5. Implantation bed vascularization. Panels a–d show representative immunohistochemical images of the vascularization patterns of the PRF medium and the PRF high scaffolds on day 5 (A,B) and day 10 (C,D) after implantation. At both time points, the PRF medium scaffolds show higher ingrowth of blood vessels (purple arrows) extending from the surrounding connective tissue (CT) (black dashed line = interface between the scaffolds and the surrounding tissue) (CD31-immunostainings; scale bars = 100 μm). (E) and (F) show the results of the histomorphometrical analyses of the blood vessel density (E) and the percentage of implantation bed vascularization (F) (* $P < 0.05$, ** $P < 0.01$, • $P < 0.05$).

Qualitative and quantitative analysis of implantation bed vascularization

The histological analysis of the implantation bed vascularization indicated that the scaffolds in the PRF-medium group had a higher vascularization rate, starting with day 5 up to day 10

compared to that in the PRF-high group (Figure 5A–D). The histomorphometrical analysis revealed that both a significantly higher number of vessels per square millimeter and a significantly higher percentage of vascularization (* $P < 0.05$) were measured in the case of the PRF-medium scaffolds (2.24 ± 0.79 vessels/mm² and $0.19 \pm 0.03\%$) in comparison to the values in the PRF high (0.96 ± 0.13 vessels/mm² and $0.04 \pm 0.03\%$) on day 5 after implantation (Figure

5E and F). In addition, on day 10 after implantation, both vascularization parameters in the PRF medium group (4.46 ± 1.25 vessels/mm² and $0.32 \pm 0.12\%$) showed significantly higher values (** $P < 0.01$) compared to those in the PRF high group (0.96 ± 0.15 vessels/mm² and $0.06 \pm 0.04\%$) (Figure 5E and F). Only in the group of PRF medium was a significant increase ($\bullet P < 0.05$) in the vessel density found between day 5 and day 10 after implantation (Figure 5E).

Qualitative and quantitative analysis of the total number of human cells within the PRF scaffolds

The histological analysis of the human cells based on vimentin immunodetection within both PRF scaffolds showed that comparable numbers were present in the implantation bed of both groups on day 5 after implantation (Figure 6A and B). Interestingly, the cells were mostly found within the peripheral region of the scaffolds near the scaffold–tissue interfaces and appeared to be involved in the tissue reactions to both scaffold types, comparable to their murine equivalents (Figure 6A and B). On day 10 after implantation, markedly higher numbers of human cells were detected in the implant beds of the PRF-medium group compared to those of the PRF-high scaffolds (Figure 6C and D). In both groups, the human cells still appeared to be integrated in the tissue reactions to the scaffolds near the border to the peri-implant tissue (Figure 6A–D). A histomorphometrical analysis indicated that on day 5 after implantation, comparable numbers of human cells were found within the implantation beds of the PRF medium scaffolds (80.49 ± 51.43 vimentin-positive cells/mm²) and those of the PRF high scaffolds (57.33 ± 27.67 vimentin-positive cells/mm²) (Figure 6E). On day 10 after implantation, a significantly higher number ($*P < 0.05$) of human cells was found in the group of PRF medium scaffolds (17.98 ± 6.87 vimentin-positive cells/mm²) compared to the values in the PRF high group (4.53 ± 1.46 vimentin-positive cells/mm²) (Figure 6E). Only in the PRF high group was a significant decrease ($\bullet P < 0.05$) of the number of human cells found (Figure 6E).

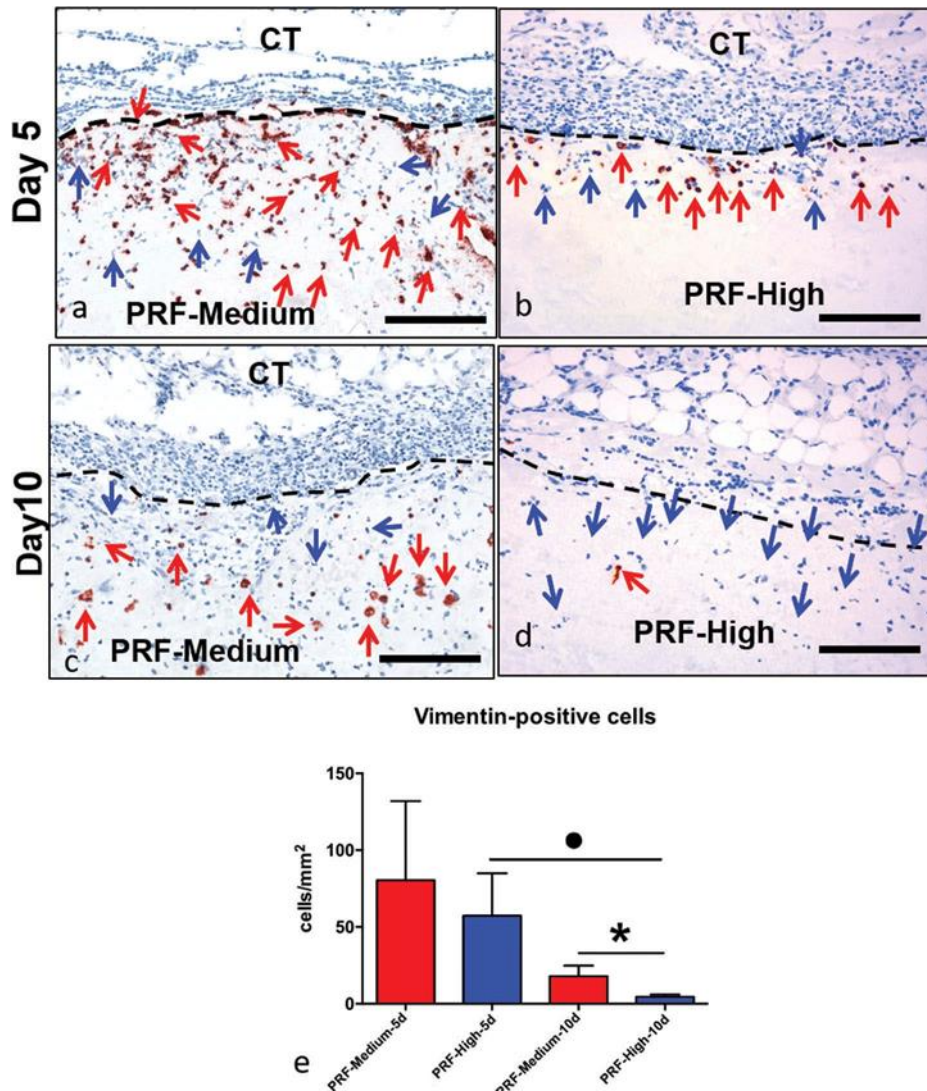


Figure 6. Total number of human cells. (A-D) show representative histological images of the incorporated human cells (brown dye, red arrows) identified by vimentin immunodetection within the PRF high and PRF medium scaffolds on day 5 (A, B) and day 10 (C, D) after implantation (black dashed line = interface between the scaffolds and the surrounding tissue). The human cells were mainly found within the peripheral regions of the implant beds of both scaffold types in the proximity of the invading murine cells (blue arrows) (Giemsa staining). On day 5 after implantation, comparable numbers of human cells were found in both groups, while a higher number of human cells was detectable in the PRF medium group (vimentin-immunostaining; scale bars = 100 μ m) on day 10. (E) shows the results of the histomorphometrical measurement of human cells incorporated in both scaffold types (* $P < 0.05$, • $P < 0.05$).

Qualitative and quantitative analysis of CD68-positive cells within the PRF scaffolds on day 5 after implantation

The immunodetection of the CD68 antigen showed that comparable numbers of human macrophages were observable within the peripheral implant regions of both scaffold types, especially on day 5 after implantation (Figure 7A and B). The histomorphometrical analysis also confirmed that higher numbers of human macrophages were found in the group of PRF medium

scaffolds (19.29 ± 6.40 CD68+ cells/mm²) and in the group of PRF high scaffolds (10.56 ± 9.86 CD68+ cells/mm²) (Figure 7C). However, this difference was not statistically significant.

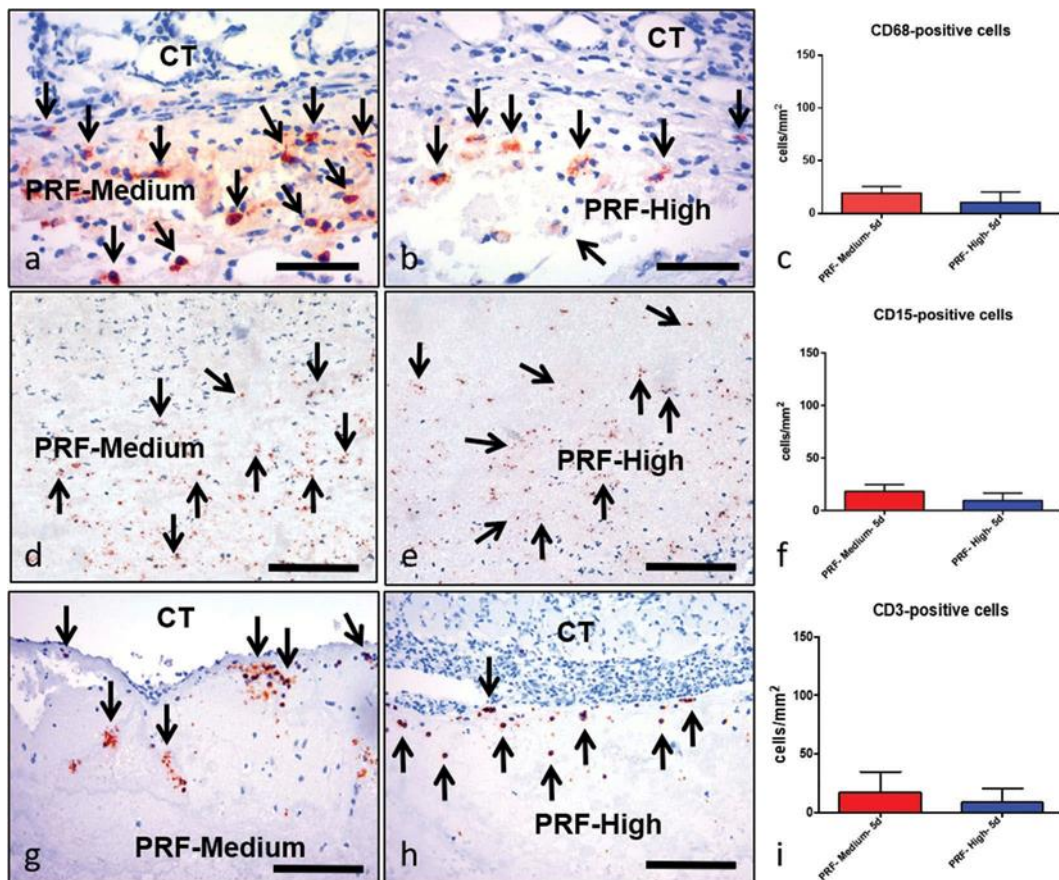


Figure 7. Human macrophages (CD68+), neutrophils (CD15+), and T-lymphocytes (CD3+). (A-B) show immunohistochemical staining (*i.e.*, CD68-immunostainings; scale bars = 100 μ m) for PRF high and PRF medium, (C) shows the histomorphometrical analysis of CD-68-positive cells within the PRF high and PRF medium scaffolds. (D-E) show immunohistochemical staining (*i.e.*, CD15immunostainings, 200 \times magnification, scale bars = 100 μ m). Panel f shows the histomorphometrical analysis of CD-15-positive cells within the PRF high and PRF medium scaffolds. (G, H) show the immunohistochemical staining (*i.e.* CD3-immunostainings; scale bars = 100 μ m). (I) shows the histomorphometrical analysis of CD3-positive cells within the PRF high and PRF medium scaffolds. Black arrows = brow dye; incorporated human cells, CT = connective tissue.

Qualitative and quantitative analysis of CD15-positive cells within the PRF scaffolds on day 5 after implantation

The immunodetection of the CD15 antigen also revealed comparable numbers of neutrophils in the implantation beds of both scaffold types (Figure 7D and E). This observation was confirmed by the histomorphometrical measurement, comparable numbers of CD15+ cells being detected in the group of the PRF medium scaffolds (18.15 ± 6.49 CD15-positive cells/mm²) and in the group of PRF-high scaffolds (9.49 ± 6.12 CD15-positive cells/mm²) (Figure 7F).

Qualitative and quantitative analysis of CD3-positive cells within the PRF scaffolds on day 5 after implantation

Immunodetection of the CD3 antigen revealed comparable numbers of human T-lymphocytes in the implant beds of both scaffold types (Figure 7G and H). The histomorphometrical measurements confirmed that larger numbers of T-lymphocytes were present in the implant bed of the PRF-medium scaffolds (16.71 ± 17.98 CD3+ cells/mm²) and in that of the PRF-high scaffolds (8.42 ± 11.93 CD3-positive cells/mm²) (Figure 7I). However, no statistically significant difference was detected.

Qualitative and quantitative analysis of CD68+, CD15+, and CD3+ cells

On day 10, only a few CD68+, CD15+, and CD3+ cells were detected within the implantation area (data not shown). Accordingly, a histomorphometrical analysis for CD3-, CD15-, and CD68-positive cells was only conducted at the earlier time point (5 days).

Qualitative and quantitative analysis of CD20+ and CD34+

At both time points, *i.e.*, day 5 and day 10, there was only a sporadic presence of CD20+ cells, and no CD34+ cells were detected within the implantation bed of the two PRF groups (data not shown). Thus, no histomorphometrical analysis was conducted for these two cell markers.

Discussion

In a clinical setting, rapid integration of biomaterials is crucial for their contribution to the biomaterial-based reconstructed tissue area and thus for the clinical condition and extent of patient morbidity. In this context, vascularization is a critical factor in the field of tissue engineering. The tools and systems therefore should be easily applicable in a clinical setting. To achieve this, the biomaterial matrix should be enhanced by the autologous regenerative properties, *i.e.*, the inflammatory cells and components of the extracellular matrix.

To accelerate wound healing using a biomaterial-based tissue engineering approach, PRF was developed by centrifugation of the patient's peripheral blood without the addition of any anticoagulants or supplements.^{8,11} In previous studies, our group was able to demonstrate differences in the structure and cell composition by modifying the applied relative centrifugal force (RCF) and centrifugation time according to the so-called LSCC (low-speed centrifugation concept).^{11,19} By decreasing the RCF and correspondingly increasing the centrifugation time, we were able to generate "advanced PRF" with more inter-fibrinous spaces. Interestingly, the

reduction of RCF resulted in more neutrophils within the matrices.¹¹ These findings on PRF-based matrices have so far been conducted *ex vivo*.¹¹ Furthermore, an *in vitro* study of our group compared the growth factor release of three different PRF-based matrices, including two of the same specific preparation parameters as the here examined PRF matrices. The data gathered indicated that reducing the RCF leads to significantly higher growth factor release (TGF- β 1 and EGF) at different time points over a 10day period.²⁰ However, the release of VEGF was similar in both PRF protocols.²⁰ Despite these findings, to date, there are still no available data on the influence of PRF-based matrices on tissue integration after their implantation *in vivo*. Therefore, we set out to determine whether the observed structural changes between the two protocols, *i.e.*, PRF high and PRF medium, would have an impact on the regenerative potential in terms of tissue reaction and especially vascularization *in vivo*.

Prior to discussing the *in vivo* data, two core issues need to be addressed: donor selection and the process of implantation. For this study, we selected one healthy donor to reduce the animal numbers according to the maxim of the 3Rs (reduce, replace, and refine).²¹ In our previously published *ex vivo* research,¹¹ we investigated and evaluated PRF matrices according to the same protocols as applied here, generated from four healthy donors, males and females aged 20–60 years. While there are certain differences in terms of blood composition and, accordingly, in the composition of the fibrin clot, the histological observations confirmed that in all investigated subjects, PRF-based matrices generated with the PRF-medium protocol appeared to be less compact, possessed higher fibrin porosity, and contained more inflammatory cells when compared to matrices generated with the PRF-high protocol.¹¹ This finding justifies the use of only one blood donor while keeping the number of animals in each group small but still large enough ($n = 4$ per time point and group) for a subsequent statistical analysis.

The subcutaneous implantation model in SCID mice was previously shown to serve as a suitable system to investigate tissue engineering concepts including human cells and their contribution to vascularization as a preclinical *in vivo* evaluation approach.^{4,5,22} Previously, our group has shown that the implantation of biomaterials pre-cultured with mesenchymal cells, osteoblasts, or monocytes leads to an enhanced vascularization compared to the implantation of pure biomaterial.^{4,22,23} In this study, we investigated a concentrate of human cells embedded within a three-dimensional fibrin scaffold according to different preparation parameters, *i.e.*, PRF high and PRF medium.

Concerning the issue of implantation, it is known that fibrin is part of the endogenous wound healing response and plays a central role in primary hemostasis. Usually, the fibrin clot degrades quickly.²⁴ Furthermore, within the subcutaneous region of an animal, there is pressure

on the implanted material during animal movement, which, in the case of PRF, leads to premature and fast degradation. The latter finding was observed in previously performed *in vivo* pilot studies with PRF-based matrices by our group, in which we were not able to properly detect the matrices after *in vivo* implantation (data not shown). To overcome these problems, Frasaco dental strip crowns were used in this study as placeholders for both groups PRF-high and PRF medium. The Frasaco dental strip crowns are made of plastic and did not elicit any abnormal tissue reactions, such as inflammation or encapsulation (data not shown). The incorporation of the PRF-based matrices into the Frasaco dental strip crowns permitted adequate evaluation of the peri-implant tissue reaction without having the pressure of the overlying soft tissue.

The RCF modification in the tow preparation protocols resulted in two differently structured scaffolds, which have shown a specific inflammatory response, cellular penetration, and vascularization pattern. Both the histological and histomorphometrical data demonstrated highly significant differences between the two evaluated PRF groups with respect to their structure characteristics. The PRF-based matrices within the PRF-medium group appeared to have a looser fibrin structure with larger inter-fibrinous spaces, whereas PRF-high showed less porous structure with densely packed fibrin. Correspondingly, the data on cell penetration and vascularization underline the fact that a looser fibrin structure with higher porosity leads to a significant increase in cell penetration into the PRF-based matrix and thus facilitates host vascularization of the scaffold as shown in PRF medium. This is supported by the findings of the significantly increased cell penetration on day 5 and day 10 in the PRF medium group, when compared to the PRF high group. By contrast, PRF high showed a dense and stable fibrin structure which was more resistant to cellular penetration. Thus, it is possible that the porous structure in the case of PRF medium facilitated cellular penetration, allowing endothelial cells to migrate easily into the scaffold and promote angiogenesis. However, in the case of PRF high, the dense structure rather serves as a “barrier membrane” or a place holder. These data demonstrate that even single parameter changes within the centrifugation settings, *i.e.*, reduction of RCF according to LSCC, can influence the physico-chemical properties of the extracellular matrix, *i.e.*, fibrin structure and porosity within the PRF matrices, thus allowing selective modification of *in vivo* vascularization.

In the previously published study, the focus was on detecting blood-derived inflammatory cells within the PRF-based matrices and examination of their distribution in accordance with the differing production settings.¹¹ In the present study, we set out to identify a selection of the investigated blood cells in our samples using immunohistochemistry,¹¹ narrowing down the selection to those cells that were most relevant and dominant during the early phase of inflammation. The focus was thus placed on detecting CD3-, CD15-, and CD68-positive cells

within the implantation area. As mentioned earlier, the sporadically found CD20+ and CD34+ precursor cells were not subjected to analysis. To differentiate between human and murine cells in the implantation area and ultimately within the PRF-based matrices, the samples were stained with an antibody against vimentin. Vimentin can be detected in the cytoplasm of all mesenchymal cells, and immunohistochemical staining for human vimentin is therefore used to detect human cells within the murine implantation field.⁴ The evaluation of the vimentin-stained slides revealed that human cells could be detected in both matrices at both time points. In the PRF medium matrices, the number of vimentin-positive cells was higher than in the PRF high matrices. This difference in cell numbers was only significant on day 10 of the study. There appeared to be a decrease in vimentin-positive cells from day 5 to day 10, but this decrease was only significant in the PRF high group. These findings highlight the fact that PRF-based matrices prepared with respect to the LSCC, i.e., the reduced RCF exhibit a higher number of leukocytes and platelets. Moreover, the microenvironment within the PRF medium may be one factor for improved survival of the included cells compared to PRF high, where a significant decrease in cell numbers was observed from days 5 to 10.

On day 10, only a few human cells were detected within the implantation area, and so, the histomorphometrical analysis for CD3-, CD15-, and CD68-positive cells was only conducted at the earlier time point (5 days). Here, no significant difference between the PRF high and PRF medium could be observed. These observations may be due to the limitation of the histological analysis methods. In this study, we analyzed a cross-section of the scaffolds in the central segments of the explanted tissue and not the complete fibrin scaffold. The *in vivo* cross-section was within the core of the implantation bed and not along the longitudinal axis, as was the case in the previously published *ex vivo* study.¹¹ On the other hand, as the selected cells play a role in the process of early inflammation,²⁵ they may not be detectable 5 days after implantation or even at later time points, i.e., 10 days.

Generally, PRF matrices exhibit a marked proangiogenic potential by releasing different growth factors such as VEGF,^{18,20} which is the main stimulus for angiogenesis.²⁶ The fact that the previous *in vitro* investigation of these two specific preparation protocols demonstrated no significant difference in the VEGF release²⁰ indicates that other factors involved in the angiogenesis might have contributed to significantly higher vascularization in the PRF medium RCF group *in vivo*. It appears that the inflammatory cells within the fibrin scaffold act in concert with the host cells to attract the host cells to migrate into the scaffold and thus enable an enhanced inflammatory cell-initiated vascularization, which highlights the correlation between inflammation and vascularization. In addition, the amount of RCF might have an effect on the cellular viability to release signaling molecules and interact with the host cells as a natural

bioactive system to guide angiogenesis. The here observed results for the solid PRF matrices are supported by our previous *in vitro* studies using a liquid PRF matrices, i.e., injectable PRF. *Ex vivo* and *in vitro* studies analyzed the influence of the applied RCF on the number of platelets, leukocytes, and the released growth factors. A systematical reduction of the used RCF and constant centrifugation time was performed in three steps from high RCF to medium RCF and low RCF.^{19,27} The results showed that injectable PRF matrices prepared using medium or low RCF contain significantly higher number of platelets and leukocytes compared to those prepared using high RCF. Additionally, the concentrations of released growth factors after 1 or 24 h (VEGF, PDGF-BB, EGF, and TGF- β 1) were significantly higher in the case of injectable PRF matrices prepared using medium or low RCF compared to those prepared using high RCF (19,27). These *in vitro* data correspond with the here presented angiogenesis effect *in vivo* which was enhanced by the reduction of the applied RCF.

Since its introduction, PRF demonstrates its suitability for clinical application by the clinical successes seen in different fields of application, such as periodontal defect regeneration or the vitality preservation of teeth in dentistry,^{28,29} bone regeneration and reconstruction in facial and oral surgery pain management,³⁰ and wound healing.³¹ However, to date, it is unknown whether altering the composition and structure of the PRF and the amount of included cells will have any benefit in the clinical outcomes. Therefore, the present results are of great interest for future clinical applications.

The present findings highlight the fact that it is possible to modify the structure and composition of PRF-based matrices selectively to obtain an optimized construct toward personalized PRF for the various indications.

Considering PRF as a cell-based tissue engineering concept to serve as a wound healing catalyzer, it appears that using a preparation protocol that is adapted to the LSCC such as PRF medium could have some benefits regarding vascularization. Moreover, the inclusion of a highly concentrated number of autologous inflammatory cells could enhance its potential to integrate within the application area and accelerate the regeneration process. In this context, PRF matrices within the medium RCF may be a clinically applicable approach for cell-based tissue engineering.

In other clinical scenarios such as wound sealing, a denser fibrin structure similar to PRF high RCF might be more beneficial to serve as a barrier, without allowing cellular penetration. According to the principles of guided bone and tissue regeneration,³² a complex tissue defect including two types of tissue, i.e., soft and hard tissue, exhibits a competition in tissue regeneration in which soft tissue proliferates and regenerates faster than the hard tissue. Hence, a barrier membrane is suggested to separate the soft and hard tissue to allow the delayed hard

tissue to regenerate the defect and prevent soft tissue ingrowth.³³ In this case, a stable dense structure that is resistant to cellular penetration may be suitable to isolate different tissue types, whereas a cell-loaded and more porous structure could be used as a filling within the hard tissue defect in order to accelerate the regeneration process by means of inflammatory cell-mediated integration and vascularization. However, to validate these hypotheses, systematic and controlled clinical studies are needed.

Presently, in tissue engineering and biomaterial research, biomaterials are loaded with different cells such as endothelial cells, mesenchymal cells, and monocytes in mono- or co-culture.^{4,6,22} Previously, we were able to show that inclusion of monocytes isolated from peripheral blood significantly increases the vascularization pattern of biomaterials, compared to biomaterial implantation alone.²² However, cell isolation and the cultivation of different cell types are sensitive, elaborate procedures. By contrast, using PRF matrices that include a high number of inflammatory cells is clinically applicable without the burden of isolation, co-cultivation, and other associated drawbacks, including the intensive regulatory process. Nevertheless, since PRF is a complex system of various cells and plasma proteins, further research is required to gain a better understanding of how the cells included in PRF matrices that are prepared within the medium RCF range might influence the surrounding microenvironment to support tissue regeneration. Additionally, further studies regarding the LSCC must investigate how far the reduction of RCF will enable further modification of the structure of PRF-based matrices and show the possible benefits that may be derived for clinical applications to generate individual PRF-based matrices for specific clinical indications.

Currently, clinically applicable cell-based tissue regeneration focuses on bone marrow concentrates, such as the BMAC[®] system.³⁴ Nevertheless, this system requires the addition of heparin and further anticoagulants as well as specific manufacturing conditions and surgical skills.³⁵ Additionally, harvesting bone marrow is a more complicated surgical procedure and can lead to higher patient morbidity. The marrow cells in this system are isolated by centrifugation.³⁶ Here, it is unclear whether the derived stem cells could lose their phenotype and specific characteristics after their supplementation with anticoagulants and centrifugation and whether these cells will still be able to differentiate to the required cell types. In contrast, PRF matrices, especially those prepared within the medium RCF, can be considered a natural drug delivery system, in which the inflammatory cells, together with the porous fibrin structure and the released growth factors, contribute to a stimulation of host vascularization, thus leading to its rapid incorporation. PRF can accordingly be considered a clinically applicable tool to enhance the regenerative potential of biomaterials after their combination with this easy-to-access peripheral blood-derived matrix without the use of additional anticoagulants.¹⁹ Moreover, it

remains to be elucidated which structure is optimal for wound healing and tissue regeneration in specific fields to achieve standardized and tailored PRF-based matrices for specific clinical indications. All these concerns are present research subjects in our group, with the aim of achieving a better understanding of the PRF-based regeneration system. It is hoped that this will provide better clinical outcomes and reduce patient morbidity.

Conclusions

The present study demonstrated that altering the relative centrifugation force has a significant influence on the *in vivo* cellular reaction to the generated PRF matrices. PRF high showed a dense and stable fibrin structure with significantly lower pore size compared to PRF medium. Thus, significantly higher *in vivo* vascularization and higher total numbers of human cells, especially on day 10 after scaffold implantation, were found in PRF medium compared to PRF high. The findings highlight the angiogenic potential of PRF-based matrices and indicate that reducing the RCF using the LSCC selectively alters the fibrin structure and included cell number. By considering the cells within the PRF-based matrices as sources of growth factors and thus as a complex natural drug-delivery system, modification of the preparation protocol might be a tool to increase the regenerative potential within the specific regions of interest. In conclusion, solid and liquid PRF-based matrices and especially those generated with respect to LSCC can be beneficial for both clinical as well as basic science researchers to better understand cell–cell communication in wound healing processes and tissue regeneration.

Acknowledgments

The authors would like to thank the excellent technical support of Mrs. Verena Hoffmann.

References

1. Ghanaati S, Fuchs S, Webber MJ, Orth C, Barbeck M, Gomes ME, Reis RL, James Kirkpatrick C. Rapid vascularization of starch-poly (caprolactone) *in vivo* by outgrowth endothelial cells in co-culture with primary osteoblasts. *J Tissue Eng Regen Med* **2011** Jun;5(6): e136–143.
2. Ghanaati S, Orth C, Unger RE, Barbeck M, Webber MJ, Motta A, Migliaresi C, James Kirkpatrick C. Fine-tuning scaffolds for tissue regeneration: effects of formic acid processing on tissue reaction to silk fibroin. *J Tissue Eng Regen Med* **2010**; 4: 464–472.

3. Ghanaati S, Schlee M, Webber MJ, Willershausen I, Barbeck M, Balic E, Görlach C, Stupp SI, Sader RA, Kirkpatrick CJ, Ghanaati S. Evaluation of the tissue reaction to a new bilayered collagen matrix *in vivo* and its translation to the clinic, *Biomed. Mater* **2011**; 6: 15010–15012.
4. Ghanaati S, Unger RE, Webber MJ, Barbeck M, Orth C, Kirkpatrick JA, Booms P, Motta A, Migliaresi C, Sader RA, Kirkpatrick CJ. Scaffold vascularization *in vivo* driven by primary human osteoblasts in concert with host inflammatory cells. *Biomaterials* **2011**; 32: 8150–8160.
5. Fuchs S, Ghanaati S, Orth C, Barbeck M, Kolbe M, Hofmann A, Eblenkamp M, Gomes M, Reis RL, Kirkpatrick CJ. Contribution of outgrowth endothelial cells from human peripheral blood on *in vivo* vascularization of bone tissue engineered constructs based on starch polycaprolactone scaffolds. *Biomaterials* **2009**; 30: 526–534.
6. Unger RE, Ghanaati S, Orth C, Sartoris A, Barbeck M, Halstenberg S, Motta A, Migliaresi C, Kirkpatrick CJ. The rapid anastomosis between prevascularized networks on silk fibroin scaffolds generated *in vitro* with cocultures of human microvascular endothelial and osteoblast cells and the host vasculature. *Biomaterials* **2010**; 31: 6959–6967.
7. Barbeck M, Najman S, Stojanovic S, Mitic Z, Zivkovic JM, Choukroun J, Kovacevic P, Sader R, Kirkpatrick CJ, Ghanaati S. Addition of blood to a phylogenetic bone substitute leads to increase *in vivo* vascularization, *Biomed. Mater* **2015**; 10: 55007.
8. Choukroun J, Adda F, Schoeffler C, Vervelle A. Une opportunité en parodontologie: le PRF. *Implantodontie* **2001**; 42: 55–62.
9. Eppley BL, Pietrzak WS, Blanton M. Platelet-rich plasma: a review of biology and applications in plastic surgery. *Plast Reconstr Surg* 2006; 118: 147e–159e.
10. Bhanot S, Alex JC. Current applications of platelet gels in facial plastic surgery. *Facial Plast Surg* **2002**; 18: 27–33.
11. Ghanaati S, Booms P, Orłowska A, Kubesch A, Lorenz J, Rutkowski J, Landes C, Sader R, Kirkpatrick C, Choukroun J. Advanced platelet-rich fibrin: A new concept for cell-based tissue engineering by means of inflammatory cells. *J Oral Implantol* 2014; 40: 679–689.
12. Litvinov RI, Weisel JW. What is the biological and clinical relevance of fibrin?. *Semin Thromb Hemost* **2016**; 42: 333–343.
13. Ekström K, Omar O, Granéli C, Wang X, Vazirisani F, Thomsen P. Monocyte exosomes stimulate the osteogenic gene expression of mesenchymal stem cells. *PLoS One* **2013**; 8: e75227.
14. Perut F, Filardo G, Mariani E, Cenacchi A, Pratelli L, Devescovi V, Kon E, Marcacci M, Facchini A, Baldini N, Granchi D. Preparation method and growth factor content of

- platelet concentrate influence the osteogenic differentiation of bone marrow stromal cells. *Cytotherapy* **2013**; 15: 830–839.
15. Nami N, Feci L, Napoliello L, Giordano A, Lorenzini S, Galeazzi M, Rubegni P, Fimiani M. Crosstalk between platelets and PBMC: new evidence in wound healing. *Platelets* **2016**; 27: 143–148.
 16. Soloviev DA, Hazen SL, Szpak D, Bledzka KM, Ballantyne CM, Plow EF, Pluskota E. Dual role of the leukocyte integrin M 2 in angiogenesis. *J Immunol* **2014**; 193: 4712–4721.
 17. Schmidt-Bleek K, Kwee BJ, Mooney DJ, Duda GN. Boon and bane of inflammation in bone tissue regeneration and its link with angiogenesis. *Tissue Eng Part B Rev* **2015**; 21: 354–364.
 18. Kobayashi E, Flückiger L, Fujioka-Kobayashi M, Sawada K, Sculean A, Schaller B, Miron RJ. Comparative release of growth factors from PRP, PRF, and advanced-PRF, *Clin. Oral Investig* **2016** Dec;20(9):2353–2360.
 19. Choukroun J, Ghanaati S. Reduction of relative centrifugation force within injectable platelet-rich-fibrin (PRF) concentrates advances patients' own inflammatory cells, platelets and growth factors: the first introduction to the low speed centrifugation concept. *Eur J Trauma Emerg Surg* **2018** Feb;44(1):87–95.
 20. El Bagdadi K, Kubesch A, Yu X, Al-Maawi S, Orłowska A, Dias A, Booms P, Dohle E, Sader R, Kirkpatrick CJ, Choukroun J, Ghanaati S. Reduction of relative centrifugal forces increases growth factor release within solid platelet-rich-fibrin (PRF)-based matrices: a proof of concept of LSCC (low speed centrifugation concept). *Eur J Trauma Emerg Surg* **2017** Mar 21. doi:10.1007/s00068-017-0785-7
 21. Vitale A, Manciocco A, Alleva E. The 3R principle and the use of non-human primates in the study of neurodegenerative diseases: the case of Parkinson's disease. *Neurosci Biobehav Rev* **2009**; 33: 33–47.
 22. Barbeck M, Unger RE, Booms P, Dohle E, Sader RA, Kirkpatrick CJ, Ghanaati S. Monocyte preseeding leads to an increased implant bed vascularization of biphasic calcium phosphate bone substitutes via vessel maturation. *J Biomed Mater Res Part* **2016** Dec;104 (12):2928–2935.
 23. Fuchs S, Jiang X, Schmidt H, Dohle E, Ghanaati S, Orth C, Hofmann A, Motta A, Migliaresi C, Kirkpatrick CJ. Dynamic processes involved in the pre-vascularization of silk fibroin constructs for bone regeneration using outgrowth endothelial cells. *Biomaterials* **2009**; 30: 1329–1338.

24. Wolbank S, Pichler V, Ferguson JC, Meinel A, Van Griensven M, Goppelt A, Redl H. Non-invasive *in vivo* tracking of fibrin degradation by fluorescence imaging. *J Tissue Eng Regen Med* **2015**; 9: 973–976.
25. Kolaczowska E, Kuberski P. Neutrophil recruitment and function in health and inflammation. *Nat Rev Immunol* **2013**; 13: 159–175.
26. Sahni A, Francis CW. Vascular endothelial growth factor binds to fibrinogen and fibrin and stimulates endothelial cell proliferation. *Blood* **2000**; 96: 3772–3778.
27. Wend S, Kubersch A, Orłowska A, Al-Maawi S, Zender N, Dias A, Miron RJ, Sader R, Booms P, Kirkpatrick CJ, Choukroun J, Ghanaati S. Reduction of the relative centrifugal force influences cell number and growth factor release within injectable PRF-based matrices. *J Mater Sci Mater Med* **2017**; 28: 188.
28. Chang Y-C, Zhao J-H. Effects of platelet-rich fibrin on human periodontal ligament fibroblasts and application for periodontal infrabony defects. *Aust Dent J* **2011**; 56: 365–371.
29. Hiremath H, Saikalyan S, Kulkarni SS, Hiremath V. Second-generation platelet concentrate (PRF) as a pulpotomy medicament in a permanent molar with pulpitis: a case report. *Int Endod J* **2012**; 45: 105–112.
30. Ozgul O, Senses F, Er N, Tekin U, Tuz HH, Alkan A, Kocyigit ID, Atil F. Efficacy of platelet rich fibrin in the reduction of the pain and swelling after impacted third molar surgery: randomized multicenter split-mouth clinical trial. *Head Face Med* **2015**; 11: 37.
31. Chignon-Sicard B, Georgiou CA, Fontas E, David S, Dumas P, Ihrari T, Lebreton E. Efficacy of leukocyte- and platelet-rich fibrin in wound healing: a randomized controlled clinical trial. *Plast Reconstr Surg* **2012**; 130: 819e–829e.
32. Gottlow J. Guided tissue regeneration using bioresorbable and nonresorbable devices: initial healing and long-term results. *J Periodontol* **1993**; 64: 1157–1165.
33. Bottino MC, Thomas V, Schmidt G, Vohra YK, Chu T-MG, Kowolik MJ, Janowski GM. Recent advances in the development of GTR/GBR membranes for periodontal regeneration—a materials perspective. *Dent Mater* **2012**; 28: 703–721.
34. Duttonhoefer F, Hieber SF, Stricker A, Schmelzeisen R, Gutwald R, Sauerbier S. Follow-up of implant survival comparing ficoll and bone marrow aspirate concentrate methods for hard tissue regeneration with mesenchymal stem cells in humans. *Biores Open Access* **2014**; 3: 75–76.
35. Sauerbier S, Stricker A, Kuschnierz J, Bühler F, Oshima T, Xavier SP, Schmelzeisen R, Gutwald R. *In vivo* comparison of hard tissue regeneration with human mesenchymal

stem cells processed with either the FICOLL method or the BMAC method. *Tissue Eng Part C Methods* **2010**; 16: 215–223.

36. Sauerbier S, Giessenhagen B, Gutwerk W, Rauch P, Xavier SP, Oshima T, Nagursky H, Gutwald R, Schmelzeisen R. Bone marrow aspirate concentrate used with bovine bone mineral to reconstruct vertical and horizontal mandibular defects: report of two techniques. *Int J Oral Maxillofac Implants* n.d.; 28: e310–4.

3.1.4. Autogenous biomaterials conclusions

This chapter studies platelet rich fibrine (PRF) and its sensitivity to relative centrifugal force (RCF). PRF is a fibrin-based biomaterial that has been shown to promote cell adhesion, proliferation, and differentiation. However, the effect of RCF during PRF preparation has not been studied in depth. The aim of this research was to investigate the effect of RCF during matrix preparation on the structure and function of PRF using *in vitro* and *in vivo* models.

In chapter 3.1.1 The purpose of this study was to observe the variation in platelet distribution and growth factor release (VEGF, TGF- β 1, EGF) within three different solid PRF matrices (PRF, A-PRF, A-PRF+). These matrices were prepared using different relative centrifugal force (RCF) and centrifugation times, such as A-PRF+ (208g; 8 min), A-PRF (208g; 14min) and PRF (708g; 12 min). The results show that increased RCF during preparation significantly enhances the fibrin content of PRF, while decreasing RCF significantly influences cell count, specifically platelets. Different growth factor release was checked after 6h, 24h, 48h, 72h, 7 days and 10 days incubation time in cultural medium. The protein VEGF was found to be most prevalent on day 7; A-PRF+ presented a significantly higher rate than both A-PRF and PRF. A-PRF+ showed significantly higher accumulated release levels of growth factor release (TGF- β 1 and EGF) on day 10 in comparison with PRF and A-PRF. The release of TGF- β 1 was significantly higher in the A-PRF and A-PRF+ groups on days 7 and 10 compared with the PRF group. The release of EGF was highest at 24 hours in all groups, but the A-PRF+ group showed significantly higher EGF release than the PRF group. TGF- β 1 and EGF growth factor release was significantly higher on day 10 in A-PRF+ and A-PRF groups as compared to PRF group. These results underscore that by reducing centrifugal force (RCF) according to the previously described low speed centrifugation concept (LSCC), leukocytes and platelets can release growth factors to a greater extent within solid PRF matrices.

The main focus of chapter 3.1.2. is evaluation of RCF impact on liquid PRF form and its cell content together with growth factor release. The parameters used for each protocol were as follows: high RCF (966g for 3min), medium RCF (241g for 3 min) and low RCF (60g for 3min). Overall, automated cell count (platelets and leukocytes: neutrophils, monocytes and lymphocytes) revealed that the cell number increase with a decrease of RCF. The trend of gradual increase from around 5000 leukocytes per μ l in high RCF protocol up to 11000 leukocytes per μ l could be seen. The similar ongoing raise trend in number of lymphocytes could be as well observed by ~ 2.5 folds in low RCF when compared to high RCF. The number of neutrophils and monocytes was found the highest in low RCF by reaching ~ 4000 neutrophils per μ l and ~ 700 monocytes per μ l. Platelets in low and medium RCF were ~ two fold higher in high

RCF. Additionally, leukocyte histochemical detection showed the highest number in low RCF in comparison to medium RCF and high RCF. ELISA method was employed in order to quantify concentration of growth factors, such as PDGF-BB, TGF- β 1, VEGF and MMP-9. Similar values for PDGF-BB, TGF- β 1 and EGF release were observed by using low and medium RCF protocols and both of them presented to be significantly higher in comparison to high RCF example. Moreover, it has been presented that VEGF levels were 3 folds higher in low RCF than in high RCF and MMP-9 levels were 16 folds higher in low RCF than in high RCF. These findings affirm the LSCC (low speed centrifugation concept), which demonstrates that cell and growth factor enriched PRF-based matrices can be made through RCF reduction.

The aim of the study enclosed in chapter 3.1.3. was to compare the tissue reactions to two different kinds of PRF-based matrices, in terms of vascularization and cell distribution, *in vivo*. In a subcutaneous implantation model of SCID mice, PRF-high (719 g) and PRF-medium (222 g) centrifugation protocols were studied at 5 and 10 days. Histology and histomorphometry were used to quantify various cell populations: lymphocytes, neutrophils, human macrophages and monocytes. To detect newly formed vessels, CD31 was used. All human cells were detected by using vimentin as a pan-cellular marker. The findings showed that PRF-high produced dense and steady fibrin structure that prevented cells from entering host tissue. In contrast, PRF-medium was more porous with a mean diameter \sim 4 times. A faster *in vivo* vascularization rate could be also observed in PRF-medium with an approximation of 2 newly formed capillaries per mm^2 on the day 5 up to almost 5 capillaries per mm^2 detected on day 10. In contrast high PRF presented only 1 per mm^2 newly formed capillary on day 5 and the same value on day 10. In general, the highest number of vimentin labelled cells within PRF matrix was found on 5th day post implantation in both samples mediumPRF and highPRF. Moreover, cell degradation was noticed in both protocols on day 10 as the number of them decreased (not native mice cells). Overall, slight increase in CD68+, CD15+ and CD3+ positive cells was noted in animal where PRF-medium was utilized. These findings demonstrate the potential to modify the structure and composition of PRF matrices, and in doing so, selectively alter their regenerative capabilities *in vivo*.

In general, these studies indicate that modification of RCF can be used to acquire, as well as tailor matrices with special characteristic (more porous, higher content of growth factor, more leukocytes *etc.*) that can be used for specific applications, like guided bone formation or guided tissue regeneration. Nevertheless, it is important to mention that this research is still in its early stage, as well as it is limited mostly to *in vitro* and *in vivo* studies. More research needs to be conducted to validate the *in vivo* effects of the different PRF preparations. The mechanism behind these differences is still not well understood and requires further investigation. However,

the results of this study provide a new perspective on how RCF can be employed to improve the biocompatibility of fibrin-based biomaterials.

3.2. The case of xenogenic materials

Currently, there is a wide array of different biomaterials that can be used to support hard and soft tissue regeneration following the principles of guided bone regeneration (GBR) and guided tissue regeneration (GTR).^{1,2} In this context, collagen membranes are used as a support for delayed tissue regeneration in bone defects, as well as to stop early soft tissue growth into the damaged area. Furthermore, a barrier membrane used in dental procedures should ideally possess the following qualities: being able to integrate with host tissue, cell-occlusive, permeable for nutrients and easy to handle.^{2,3}

Different collagen membranes of animal origin have been engineered for GTR or GBR procedures. Due to the fact that collagen is a major protein found in the connective tissues of all mammals, these membranes offer a high level of homology.⁴ From the 28 collagen types that have been identified in vertebrates, collagen type I is the most widespread and best-characterized member of the family. In humans, collagens make up for ~30% of the body's total protein amount. They can be found in all tissues and organs, such as skin, bone, and tendon, etc. Collagen proteins play a vital role in various biological processes, such as blood vessel and extracellular matrix formation, cell adhesion and migration, as well as tissue morphogenesis and repair. They exist as either elongated fibres or network-forming collagens and give stability and elasticity to the tissue by their remarkable tensile strength. Different cells synthesize collagen molecules, such as endothelial or smooth muscle cells, but predominantly by fibroblasts.^{5,6}

Collagen-derived membranes are natural biomaterials that are very effective due to their quick adaptation to mechanical forces. They also play an important role in haemostatic reactions.⁶ Platelets have cell surface-exposed collagen-specific receptors that, when bound to a ligand, induce degranulation and blood clotting.⁷ Therefore, collagen helps stabilize wounds and has been widely used as a haemostatic agent and biological dressing in medicine and pharmacology.⁸ Furthermore, collagen acts as a chemoattractant for different cell types involved in the wound healing process, including gingival and periodontal ligament fibroblasts.⁶ Collagen is degraded quickly and without inflammation when exposed to the oral cavity, which makes collagen membranes a viable option for use in challenging flap procedures. As collagen membranes are not synthesized *de novo*, they need to undergo processing using different chemical and physical methods.^{1,9} This purification process includes deactivation of potential pathogens and donor-cells, which may also affect the native structure. As such, the resultant structure and surface characteristics of natural biomaterials depend on the donor tissues and the processing techniques used. Furthermore, other methods are used to enhance the stability of collagen-based biomaterials including different types of cross-linking. However, this process

(especially chemical crosslinking) may result in inducing more pronounced foreign body reaction.⁹⁻¹¹

In order to investigate the tissue reaction and influence of MNGCs formation, several collagen membranes were studied using *in vivo* subcutaneous implantation model in rat. Additionally, the PRF based model for cellular penetration and PRF absorption coefficient was employed, providing an environment to observe interactions between the material and cells in a more controlled manner as well as allowing study of permeability and liquid absorption capacity of a collagen membrane. This PRF based evaluation system complements *in vivo* studies and might potentially reduce number of animals used in biomaterial experiments in the future.

References

1. Bottino, M. C., Thomas, V., Schmidt, G., Vohra, Y. K., Chu, T. M. G., Kowolik, M. J., & Janowski, G. M. (2012). Recent advances in the development of GTR/GBR membranes for periodontal regeneration - A materials perspective. *In Dental Materials* (Vol. 28, Issue 7, pp. 703–721). <https://doi.org/10.1016/j.dental.2012.04.022>
2. Pellegrini, G., Pagni, G., & Rasperini, G. (2013). Surgical approaches based on biological objectives: GTR versus GBR techniques. *International Journal of Dentistry*, 2013. <https://doi.org/10.1155/2013/521547>
3. Hardwick, R., Scantlebury, T., Sanchez, R., Whitley, N. & Ambruster, J. (1994) Membrane design criteria for guided bone regeneration of the alveolar ridge. In: Buser, D., Dahlin, C. & Schenk, R.K., eds. *Guided bone regeneration in implant dentistry*
4. Stavropoulos, F., Dahlin, C., Ruskin, J. D., & Johansson, C. (2004). A comparative study of barrier membranes as graft protectors in the treatment of localized bone defects: An experimental study in a canine model. *In Clinical Oral Implants Research* (Vol. 15, Issue 4, pp. 435–442). <https://doi.org/10.1111/j.1600-0501.2004.01029.x>
5. Copes, F., Pien, N., van Vlierberghe, S., Boccafoschi, F., & Mantovani, D. (2019). Collagen-based tissue engineering strategies for vascular medicine. *In Frontiers in Bioengineering and Biotechnology* (Vol. 7, Issue JUL). Frontiers Media S.A. <https://doi.org/10.3389/fbioe.2019.00166>
6. Lynn, A. K., Yannas, I. v., & Bonfield, W. (2004). Antigenicity and immunogenicity of collagen. *In Journal of Biomedical Materials Research - Part B Applied Biomaterials* (Vol. 71, Issue 2, pp. 343–354). <https://doi.org/10.1002/jbm.b.30096>

7. Nuyttens, B. P., Thijs, T., Deckmyn H., Broos K. (2011) Platelet adhesion to collagen. *Thrombosis Research*, (127, supp-S2). [https://doi:10.1016/s0049-3848\(10\)70151-1](https://doi:10.1016/s0049-3848(10)70151-1)
8. Fleck, C. A., & Simman, R. (2010). Modern collagen wound dressings: Function and purpose. *In Journal of the American College of Certified Wound Specialists* (Vol. 2, Issue 3, pp. 50–54). <https://doi.org/10.1016/j.jcws.2010.12.003>
9. Rodella, L. F., Favero, G., & Labanca, M. (2011). Biomaterials in Maxillofacial Surgery: Membranes and Grafts. *In International journal of Biomedical science* (Vol. 7, Issue 2). www.ijbs.org
10. Solomon, S. M., Sufaru, I. G., Teslaru, S., Ghiciuc, C. M., & Stafie, C. S. (2022). Finding the Perfect Membrane: Current Knowledge on Barrier Membranes in Regenerative Procedures: A Descriptive Review. *In Applied Sciences* (Switzerland) (Vol. 12, Issue 3). MDPI. <https://doi.org/10.3390/app12031042>
11. Sasaki, J.-I., Abe, G. L., Li, A., Thongthai, P., Tsuboi, R., Kohno, T., & Imazato, S. (2021). Barrier membranes for tissue regeneration in dentistry. *Biomaterial Investigations in Dentistry*, 8(1), 54–63. <https://doi.org/10.1080/26415275.2021.1925556>

3.2.1. Biologization of Collagen-Based Biomaterials Using Liquid-Platelet-Rich Fibrin: New Insights into Clinically Applicable Tissue Engineering

Materials, 2019, 12(23).

Al-Maawi, S.^a, Herrera-Vizcaíno, C.^a, **Orłowska, A.**^a, Willershausen, I.^{a,b}, Sader, R.^a, Miron, R. J. ^c,
Choukroun, J.^{a,d}, & Ghanaati, S.^a.

^a Department for Oral, Cranio-Maxillofacial, and Facial Plastic Surgery, Frankfurt Orofacial Regenerative Medicine (FORM) Lab, University Hospital Frankfurt Goethe University, 60590 Frankfurt am Main, Germany

^b Department of Orthodontics and Orofacial Orthopedics, University of Erlangen, 91052 Erlangen, Germany

^c Department of Periodontology, University of Bern, 3004 Bern, Switzerland;

^d Private practice, Pain Therapy Center, 06100 Nice, France

Abstract

Platelet-rich fibrin (PRF) is a blood concentrate derived from venous blood that is processed without anticoagulants by a one-step centrifugation process. This three-dimensional scaffold contains inflammatory cells and plasma proteins entrapped in a fibrin matrix. Liquid-PRF was developed based on the previously described low-speed centrifuge concept (LSCC), which allowed the introduction of a liquid-PRF formulation of fibrinogen and thrombin prior to its conversion to fibrin. Liquid-PRF was introduced to meet the clinical demand for combination with biomaterials in a clinically applicable and easy-to-use way. The aim of the present study was to evaluate, *ex vivo*, the interaction of the liquid-PRF constituents with five different collagen biomaterials by histological analyses. The results first demonstrated that large variability existed between the biomaterials investigated. Liquid-PRF was able to completely invade Mucograft® (MG; Geistlich Biomaterials, Wolhusen, Switzerland) and to partly invade Bio-Gide® (BG; Geistlich Biomaterials, Wolhusen, Switzerland) and Mucoderm® (MD; Botiss Biomaterials, Berlin, Germany), and Collprotect® (CP; Botiss Biomaterials, Berlin,

Germany) showed only a superficial interaction. The BEGO® collagen membrane (BCM; BEGO Implant Systems) appeared to be completely free of liquid-PRF. These results were confirmed by the different cellular penetration and liquid-PRF absorption coefficient (PAC) values of the evaluated membranes. The present study demonstrates a system for loading biomaterials with a complex autologous cell system (liquid-PRF) in a relatively short period of time and in a clinically relevant manner. The combination of biomaterials with liquid-PRF may be clinically utilized to enhance the bioactivity of collagen-based biomaterials and may act as a biomaterial-based growth factor delivery system.

Introduction

The function of biomaterials in regenerative medicine is to support soft and hard tissue regeneration through material-induced tissue reactions. When looking for the “ideal” biomaterial, several requirements must be considered, including tissue compatibility, physiochemical stability, the rates of vascularization and degradation, and the biomaterial-specific immune response.¹ Recently, various collagen-based biomaterials were introduced for use in guided bone and tissue regeneration (GBR/GTR). These materials are mostly resorbable, naturally derived collagenous biomaterials mainly with xenogeneic origins. Previous *in vivo* experiments evaluated the cellular reaction towards collagen-based biomaterials after subcutaneous implantation.² Different types of tissue reactions were observed, including the

induction of mononuclear cells (MNCs), such as monocytes, lymphocytes, macrophages, and fibroblasts, or signs of a foreign body reaction, which is characterized by the formation of additional multinucleated giant cells (MNGCs).^{2,3}

In vivo evaluation of a porcine-derived bilayer collagen membrane showed stepwise integration, inducing only MNCs, over a 60-day period.⁴ Analysis of the vascularization rate revealed a mild vascularization pattern without material penetration, which emphasizes the ability of collagen-based biomaterials to integrate within the implantation region without undergoing transmembranous vascularization.^{4,5} Additional investigations evaluating porcine-derived collagenous membranes of different thicknesses and physicochemical compositions revealed the presence of MNGCs. In these cases, the occurrence of MNGCs was associated with an enhanced vascularization rate and disintegration of the membranes accompanied by premature ingrowth of the peri-implantation region into the central region of the biomaterials.^{6,7} These observations showed that although all biomaterials were derived from the same origin, different cellular reactions were induced based on their processing techniques and physicochemical properties.

The role of collagen-based biomaterials in GBR has been explored *in vivo*, showing the crucial influence of new bone formation when comparing bony defects covered with a collagen membrane to those without collagen membranes.⁸ However, the biomaterial characteristics may influence the underlying bone area. Several investigations have confirmed the function of different collagen-based biomaterials as bioactive components involved in bone regeneration in combination with different bone substitutes.⁹ These findings are relevant for clinical applications of pure biomaterials.^{10,11} Moreover, previously published, *in vivo* cell-based, tissue engineering studies that considered the use of biological concepts, such as the combination of biomaterials with primary human cells or pre-seeding with monocytes, have demonstrated their effects on the vascularization patterns in the biomaterials at hand, and the consequently enhanced regenerative capacities.¹² However, cell-based tissue engineering is a sensitive technique that requires special conditions, which are mostly not available in clinical settings. A clinically applicable system was, therefore, highly needed to reap the benefits of these observations.

This blood concentrate is derived from the patient's peripheral blood after a one-step centrifugation without anticoagulants to generate a platelet and leucocyte-rich matrix. The presence of platelets, leucocytes, and fibrin was previously shown to be essential for wound healing.^{13,14} In addition to the potential of leucocytes to influence angiogenesis and lymphomagenesis, this fibrin network, containing leucocytes and platelets, is a source of cytokines and growth factors, which are the main players in the process of wound healing.¹⁵ The use of specific plastic tubes favors nonclotting platelet-rich fibrin (PRF) and results in the

development of a liquid-PRF-based matrix (liquid-PRF) produced without the need for anticoagulants. Previously, a systematic study investigated the influence of the applied relative centrifugal force (RCF) on the composition and bioactivity of PRF matrices.¹⁶ In that study, it was shown that liquid-PRF generated with the lowest RCF contained the highest concentration of platelets and leukocytes and released significantly higher concentrations of different growth factors compared to two other liquid-PRF matrices prepared at higher RCF.¹⁶ Therefore, the low-speed centrifugation concept (LSCC) was described to standardize the centrifugation of blood concentrates.

The combination of autologous biological products; *i.e.*, PRF-based matrices with xenogeneic biomaterials, has been of great clinical interest. The application of PRF matrices with different centrifugation protocols in combination with collagen-based biomaterials was previously described in several clinical studies, especially in periodontology.¹⁷ However, the results are not consistent. Some studies showed a positive effect of the addition of PRF to collagen-based biomaterials, while others did not show any effect.¹⁸ It may be that the biomaterial-specific physicochemical characteristics, such as surface structure, absorption capacity, porosity, and thickness, may influence the interaction between the collagen-based biomaterial and PRF. However, to date, no published studies have evaluated the feasibility of combining collagen-based biomaterials and PRF in detail. Therefore, the aim of the present study was to evaluate the interaction of liquid-PRF with five different collagenous biomaterials by histological analyses to identify the most promising combination for clinical use. To the best of our knowledge, this was the first study to analyze the combination of different commercially available collagen-based biomaterials and liquid-PRF *ex vivo*. Particular attention was focused on the absorption capacities and penetration patterns of the leucocytes and platelets within the collagen-based biomaterials after liquid-PRF application, and on the interaction between collagen and fibrin.

Experimental

Collagen Membranes

Mucograft® (MG; Geistlich Biomaterials, Wolhusen, Switzerland) is a bilayered collagen matrix derived from porcine peritoneum and skin. The collagen is derived from a certified porcine source and is processed to purify it from genetically active constituents. The matrix consists of type I and type III collagen and is processed using standardized methods and sterilized by gamma irradiation without chemical treatment or additional cross-linking. The bilayered

structure of the matrix consists of a thin, smooth, compact layer with low porosity and a three-dimensional spongy layer with higher porosity. These layers are connected using a biophysical interweaving process. The pore system of the matrix is manufactured via defined parameters and lyophilization to include both small and large pores (5–200 μm). This variously-sized pores serve as a matrix for tissue and cell adherence and stabilize the blood clot after application.

Bio-Gide[®] (BG; Geistlich Biomaterials, Wolhusen, Switzerland) is a porcine-derived collagen membrane containing type I and III collagen without cross-linking. This bilayered membrane is manufactured using a standardized process to eliminate immunologically active constituents, microorganisms, and other residues. Collagen is obtained from a veterinary-certified porcine source and is sterilized by gamma irradiation. The pure bilayered collagen membrane consists of a smooth, thin, compact layer with low porosity and a three-dimensional, more porous spongy layer. This structure should support bone formation and inhibit connective tissue ingrowth in bony defects.

Mucoderm[®] (MD; Botiss Biomaterials, Berlin, Germany) is a porcine dermis-based collagen matrix. The membrane is purified by a multistep cleaning method, lyophilized, and sterilized by gamma irradiation to produce a three-dimensional non-cross-linked membrane of collagen and elastin.

Collprotect[®] (CP; Botiss Biomaterials, Berlin, Germany) is a bilayered cross-linked collagen membrane containing type I and type III collagen and elastin. The membrane is obtained from porcine dermis. Purification methods, such as multistep cleaning, lyophilization, and gamma irradiation, were performed to generate a stable three-dimensional bilayered collagen membrane.

BEGO[®] collagen membrane (BCM; BEGO Implant Systems) is a non-cross-linked, stratified membrane obtained from porcine pericardium. Donor animals are selected in a veterinary-controlled porcine source. The extracted collagen is treated by a controlled purification process, lyophilized, and sterilized with ethylene oxide gas.

Scanning Electron Microscopy

The ultrastructure of the collagen-based biomaterials was examined under a DSM 962 SEM (scanning electron microscope, Zeiss, Oberkochen, Germany) operated with a LaB6 cathode, which can be used to obtain medium resolution photographs. After sputter coating the samples with 20–30 nm gold in a cold sputter unit, images were taken at 10 keV acceleration energy and an object distance of approximately 12.0 cm. The SEM images were analyzed with the Kontron KS 300 image analysis program (Carl Zeiss Vision, Eching, Germany).

Liquid-PRF Preparation

The application of PRF in this study was approved by the responsible Ethics Commission of the state of Hessen, Germany (265/17). Liquid-PRF was obtained from venous blood without additional anticoagulants as previously described.¹⁶ Three healthy volunteers, aged 18–50 years with no anticoagulant usage, donated peripheral blood for this study after informed consent was obtained. Four sterile, 10 mL plastic tubes (Process for PRF, France, radius 110 mm) full of blood were obtained from each participant. The filled tubes were immediately placed in the centrifuge, with two tubes placed directly opposite each other for balance during centrifugation. The liquid centrifugation protocol (10 mL, 600 rpm, 44 × g for 8 min) according to LSCC was performed in a programmed centrifuge (Duo centrifuge; PROCESS for PRF, Nice, France). The tubes that were used did not contain any type of anticoagulants in order to avoid interference with platelet activity. After centrifugation, the tubes showed a multiphasic liquid that contained an upper phase of a yellow–orange-colored liquid (liquid-PRF) and a lower red phase of the remaining blood constituents. The tubes were carefully opened to avoid mixing the phases, and 1–2 mL of the upper liquid (liquid-PRF) was collected using a 10 mL syringe with a needle (B Braun inject®) and transferred to a flask.

Liquid-PRF Application

Four samples (10 × 10 mm) were prepared from each collagenous biomaterial using scissors. The material sample was placed on a 4 × 6 cell culture plate, and the prepared 500 µL liquid-PRF was applied to the collagen-based biomaterial samples, covering the entire sample. The membranes were kept in liquid-PRF until clotting (15 min at room temperature). Then, the samples were fixed in 4% formaldehyde for 24 h.

Histological Preparation

The fixed samples were processed according to previously described techniques.⁵ Briefly, after processing, six 3–4 µm sections were cut from each sample using a rotary microtome (Leica RM2255; Wetzlar, Germany). Next, the samples were stained with different histochemical stains. The first slice was stained with hematoxylin and eosin (H&E) according to standard protocols, and the other five slices were stained with Azan–Mallory, Masson–Goldner, and Giemsa.

Histological Analysis

Morphological and qualitative histological analyses of the prepared slices were performed using a Nikon ECLIPSE 80i microscope (Tokyo, Japan). We focused on the interaction with liquid-PRF, particularly the locations and distributions of leucocytes and platelets, and the liquid-PRF invasion of the biomaterials. Additionally, histological photographs were captured using a Nikon DS-Fi1/Digital camera with a digital sight control unit.

Histomorphometrical and Statistical Analysis

Four Giemsa-stained slides of each biomaterial were used for the histomorphometric analysis of cellular penetration. Total scans were created using a light microscope (Nikon, Tokyo, Japan) with a scanning table (Prior, Rockland, MA, USA) connected to a DS-Fi/1 digital camera (Nikon) and a PC running NIS Elements AR software (version 4.1; Nikon). A total scan is a merge of 50–100 single images of the region of interest. Subsequently, the thickness of the biomaterials was measured (in μm) using the measurement tools in NIS Elements. The penetration distance into the biomaterials was measured in μm . Cellular penetration into the central region (thickness/2) of the biomaterial was set to 100%.

Fluid Absorption Capacity

The capacity of each biomaterial to absorb liquid-PRF was measured using a gravimetric method and named the PRF absorption coefficient (PAC). This method was based on the difference in sample weight before versus after the application of a specific liquid. In this experiment, two different liquids were tested: distilled water and liquid-PRF. Three segments of 0.8 mm diameter (d) from each biomaterial were extracted using biopsy punches (SmithKline Beecham, NW, UK) weighed in a dry state (W_0) and then placed in 24-well cell culture plates. Five hundred microliters of liquid-PRF were deposited on top of the biomaterials; incubation for 15 min at room temperature was then performed—until clotting. The weight of the biomaterials after incubation was registered (W_1), and the absorption coefficient was calculated using the following formula: $\text{PAC} = (W_1 - W_0)/W_0$. The same procedure was repeated with distilled water as a control measurement (WAC).

Statistical Analysis

The results are expressed as the means and standard deviations. GraphPad Prism 7 (GraphPad Software, Inc., La Jolla, USA) was used to generate charts and perform statistical

analyses using one-way analysis of variance with Tukey's multiple comparisons test ($\alpha = 0.05$). Values were considered significant if $p < 0.05$ (*) and highly significant at $p < 0.01$ (**), $p < 0.001$ (***), and $p < 0.0001$ (****).

Results and discussion

The results revealed the structural details of the biomaterials before combination with PRF to evaluate differences in the physical structures *ex vivo*. This may be relevant to understanding the interaction between the material and liquid-PRF, as described in the following sections

Ultrastructure of the Collagen-Based Biomaterials without PRF

Mucograft® (MG): The structure of MG was observed in the cross section as a bilayered collagen matrix. The layers could be differentiated because of their variation in porosity. The compact layer (CL) was thinner and exhibited lower porosity than the spongy layer (SL; Figure 1A). The surface of the CL was smooth and even (Figure 1A1). In contrast, the surface of the spongy layer was more heterogeneous. Collagen fibers of different diameters were observed in a defined arrangement, which made the surface of the SL rough (Figure 1A2).

Bio-Gide® (BG): In the cross section, the ultrastructure of BG showed two different layers; i.e., the CL and SL. The arrangement of the collagen fibers allowed the identification and differentiation of the layers. Most of the collagen fibers in the CL were arranged vertically, which imparted low porosity, whereas the collagen fibers within the SL were arranged in parallel horizontally direction, which contributed to its more porous appearance (Figure 1B). The surface of the CL consisted of collagen fibers that were close to each other, imparting a smooth, even surface with small intercollagenous spaces and low porosity (Figure 1B1). The SL showed a dynamic distribution of collagen fibers, which provided a more porous structure and a rather surface (Figure 1B2).

Mucoderm® (MD): In the cross section, MD showed uniformly arranged collagen fibers that appeared to be tightly interwoven (Figure 1C). The surface structure exhibited a high roughness (Figure 1C1, C2). The porous system was compact and consistent.

Collprotect® (CP): In cross section, the membrane appeared homogenous, with irregularly arranged collagen fibers. Different-sized pores were unequally distributed throughout the cross section (Figure 1D). The surfaces of both sides appeared to be different. The rough side exhibited a very uneven surface with upward-directed fibers (Figure 1D1). In contrast, the smooth side

was comparably smooth, with fine collagen fibers that formed a slightly wavy surface (Figure 1D2).

BEGO® collagen membrane (BCM): A cross section of the BCM showed parallelly-arranged collagen fibers with uniform porosity (Figure 1E). The surfaces of the membrane differed according to their morphology. The smooth surface was evenly wavy without obvious pores (Figure 1E1), whereas the rough surface was compact but more porous, with collagen fibers arranged in different directions (Figure 1E2).

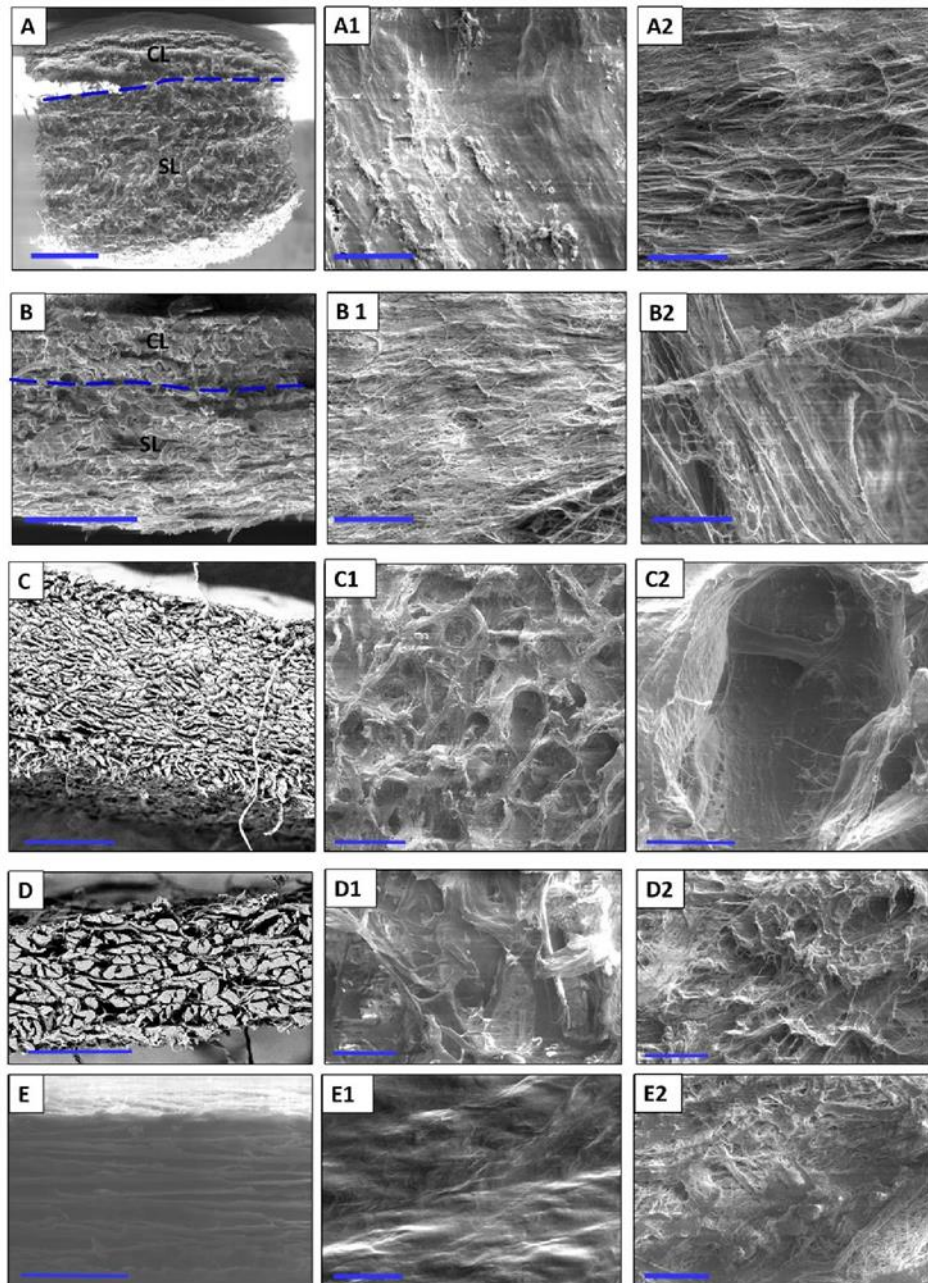


Figure. 1 Representative scanning electron microscopy images showing the ultrastructure of the evaluated biomaterials. (A) MG in a cross section ($\times 25$, 10 Kv, scale bar = 1 mm); (A1) the smooth surface of MG ($\times 500$, 5 kV, scale bar = 50 μm); (A2) the rough surface of MG ($\times 500$, 5 kV, scale bar = 50 μm). (B) Cross section of BG ($\times 200$, 10 kV, scale bar = 200 μm); (B1) the smooth surface of BG ($\times 500$, 5 kV, scale bar = 50 μm); (B2) the rough surface of BG ($\times 500$, 5 kV, scale bar = 50 μm). (C)

Cross section of MD ($\times 50$, 15 kV, scale bar = 500 μm); (C1) the surface of MD ($\times 100$, 5 kV, scale bar = 200 μm); (C2) the surface of MD at a higher magnification ($\times 500$, 5 kV, scale bar = 50 μm). (D) Cross section of CP ($\times 200$, 15 kV, scale bar = 200 μm); (D1) the rough side of CP ($\times 500$, 5 kV, scale bar = 50 μm); (D2) the smooth side of CP ($\times 500$, 5 kV, scale bar = 50 μm); (E) cross section of BCM ($\times 500$, 15 kV, scale bar = 50 μm); (E1) smooth surface of BCM ($\times 500$, 5 kV, scale bar = 50 μm); (E2) the rough surface of BCM ($\times 500$, 5 kV, scale bar = 50 μm).

Histological Evaluation of Material–PRF Interaction

Qualitative histological analysis of each tissue was performed, focusing on the interaction between the liquid-PRF and each collagen-based biomaterial. A particular emphasis was placed on the distribution of leucocytes and platelets within the biomaterials, and the fibrin saturation.

Mucograft[®] (MG): Liquid-PRF was detectable between the collagen fibers of the matrix, and liquid-PRF had invaded the entire collagen matrix; i.e., the SL and CL (Figure 2A, A1). Additionally, the pores appeared to be mostly full of liquid-PRF, and the leucocytes and platelets had reached the central region of the collagen matrix and were evenly distributed. These cells were clearly observable in the superficial layer and within the core of the membrane. A PRF-clot was observable on the surface of the matrix (Figure 3A, A1).

Bio-Gide[®] (BG): After liquid-PRF application, the bilayered collagen membrane showed a variable distribution pattern. Leucocytes and platelets were located between the collagen fibers on the superficial parts of the CL (Figure 2B, B1). In contrast, the SL appeared to be largely free of cells. In addition, there were no leucocytes or platelets in the central region of the collagen membrane. While a stable, continuous liquid-PRF clot was located adjacent to the surface of the membrane on the SL (Figure 3B, B1), only a sporadic liquid-PRF was observed on the surface of the CL.

Mucoderm[®] (MD): Both sides of the biomaterial interacted with the liquid-PRF matrix. However, the interaction was only observed on the very superficial layers of the membrane (Figure 2C, C1). There was almost no liquid-PRF invasion within the superficial layers, although some single leucocytes and platelets were observed (Figure 3C, C1). These cells did not enter the material body or reach the center. Accordingly, most of the collagenous material contained no fibrin or leucocytes. In addition, some PRF clot formation was observed on the collagen membrane surface.

Collprotect[®] (CP): Both sides of the membrane had leucocytes and platelets between the collagen fibers of the superficial layer (Figure 2D, D1). However, the central region of the membrane was free of leucocytes and platelets (Figure 3D, D1). Liquid-PRF did not invade the membrane; therefore, no fibrin was observed in any part of the membrane; however, a PRF clot did form on the surface of the membrane.

BEGO® collagen membrane (BCM): The liquid-PRF did not enter the collagen membrane. No leucocytes or platelets were found in any region of the membrane (Figure 2E, E1), and no fibrin was observed within the membrane. Additionally, the membrane appeared to be embedded within a PRF clot, without allowing the liquid-PRF to enter the membrane central region (Figure 3E, E1).

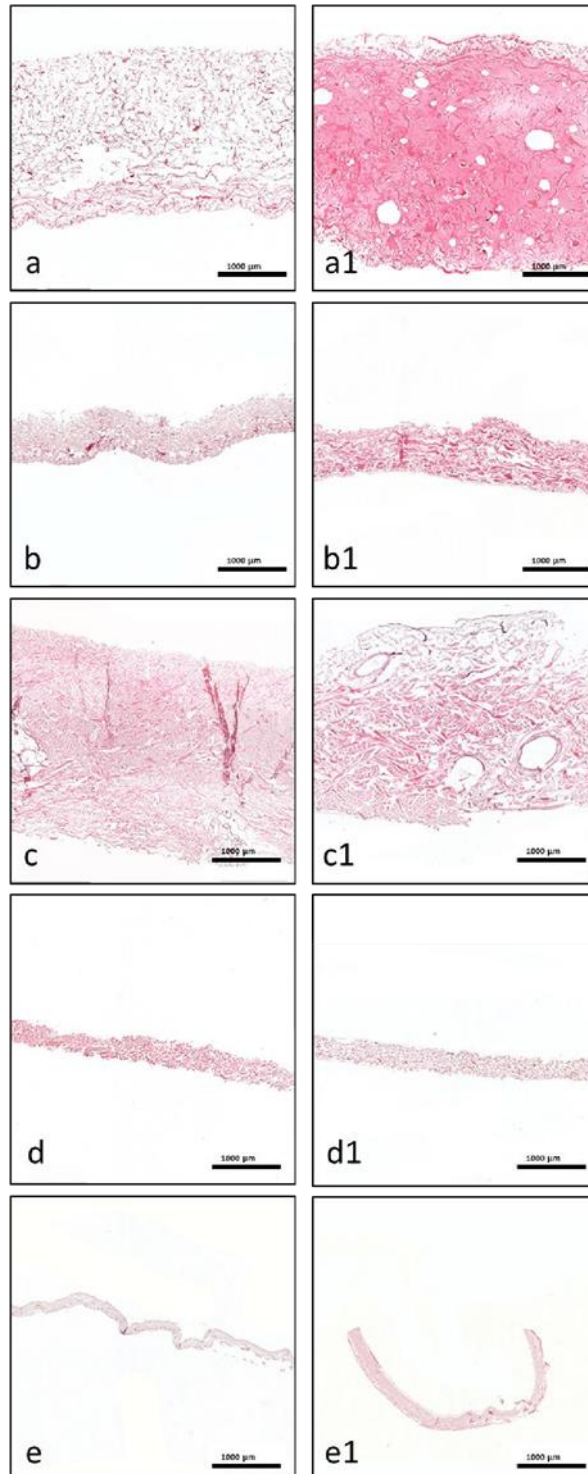


Figure 2. Representative histological micrographs. (a–e) Cross sections of blank membranes without liquid-PRF as a control (H&E staining, scale bar = 1000 µm). (a1–e1) Cross sections of

membranes after liquid-PRF incubation (H&E staining, scale bar = 1000 μm). (a, a1) MG, (b, b1) BG, (c, c1) MD, (d, d1) CP, and (e, e1) BCM.

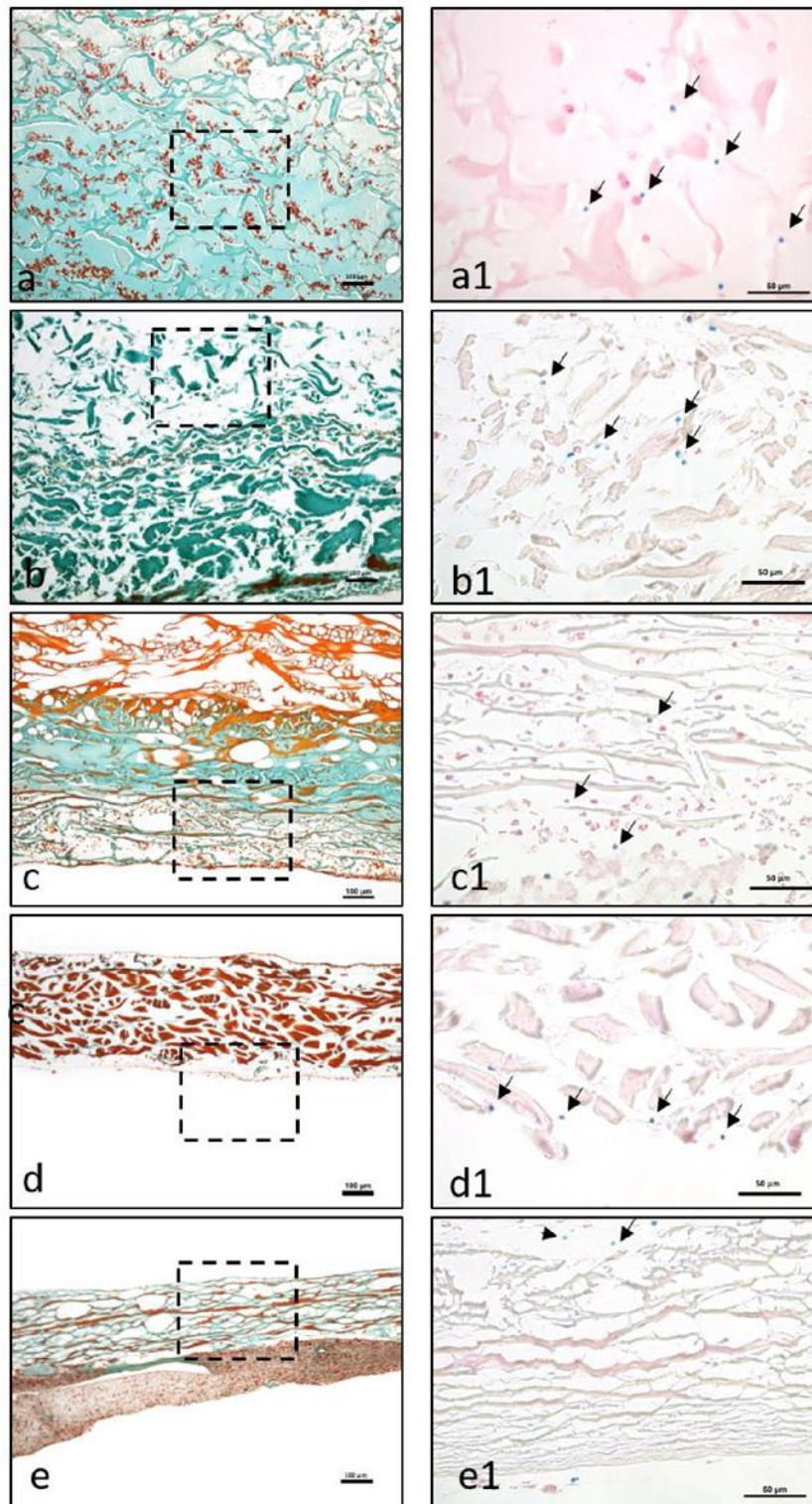


Figure 3. The interaction between liquid-PRF and the evaluated membranes. (a–e) The formation of PRF-clots on the membrane (a) or on the membrane surface (b–e). (a–e) Masson Goldner staining. Dashed lines refer to the area, which is presented at a higher magnification in (a1–e1). (a1–e1) A higher magnification of the membrane-cell interaction in the different membrane types. Arrows point to the cell localization in the different membranes. Giemsa staining (a, a1) MG, (b, b1) BG, (c, c1) MD, (d, d1) CP, and (e, e1) BCM.

Histomorphometrical Results of the PRF Penetration Pattern within the Different Collagen-Based Biomaterials

Cellular penetration of the platelets and leukocytes into the different biomaterials was evaluated histomorphometrically. The analysis revealed that MG showed the highest percentage of cellular penetration, and compared to all other evaluated materials, the difference was highly significant ($p < 0.0001$ ****). The cellular penetration of BG was significantly higher than that of MD ($p < 0.0001$ ****), CP ($p < 0.001$ ***), and BMC ($p < 0.0001$ ****). CP showed significantly higher cellular penetration than BMC ($p < 0.05$ *). However, there were no statistically significant differences between MD and CP or MD and BCM (Figure 4).

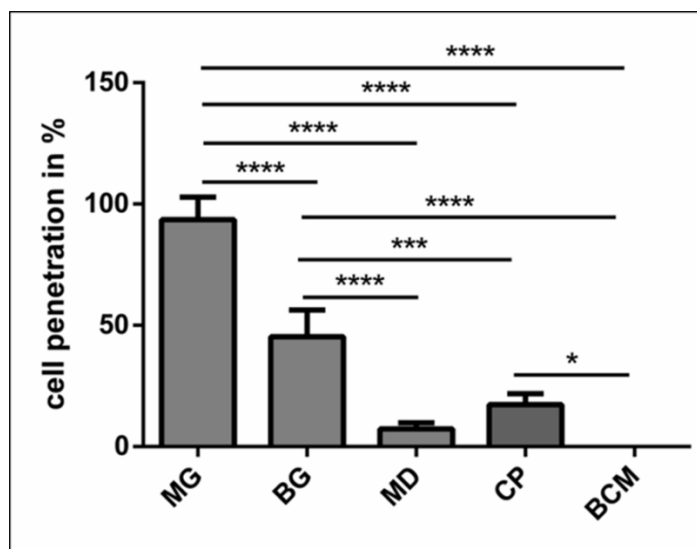


Figure 4. Statistical analysis of the cell penetration in percent with regard to the biomaterial thickness. Statistically significance at $p < 0.05$ (*) and high significance at $p < 0.01$ (**), $p < 0.001$ (***) and $p < 0.0001$ (****).

Water and Liquid-PRF Absorption Coefficient (WAC/PAC) in the Different Collagen-Based Biomaterials

Similar absorption patterns were observed for both WAC and PAC. In the case of the WAC, MG absorbed a significantly higher amount of water compared to BG (**** $p < 0.0001$), MD (**** $p < 0.0001$), CP (**** $p < 0.0001$), and BCM (**** $p < 0.0001$). No statistically significant differences were found between the other groups.

For the PAC, the results demonstrated that MG can absorb a high content of liquid-PRF components and increase its original weight up to 10 times (10.12 ± 1.29). BG increased its weight four times (4.37 ± 1.50) after being immersed in liquid-PRF. MD showed the lowest PAC with an increase of two times its original weight (2.83 ± 0.53). CP exhibited a middle range of PAC values with an increase of five times its weight (5.05 ± 2.21) after immersion in liquid-PRF. In the case of BCM, the measurements showed an increase of six times its original weight (6.12

± 0.97). Thereby, MG absorbed significantly more liquid-PRF compared to BG (**** $p < 0.0001$), MD (**** $p < 0.0001$), CP (** $p < 0.01$), and BCM (** $p < 0.01$). No statistically significant differences were found between the other groups (Figure 5).

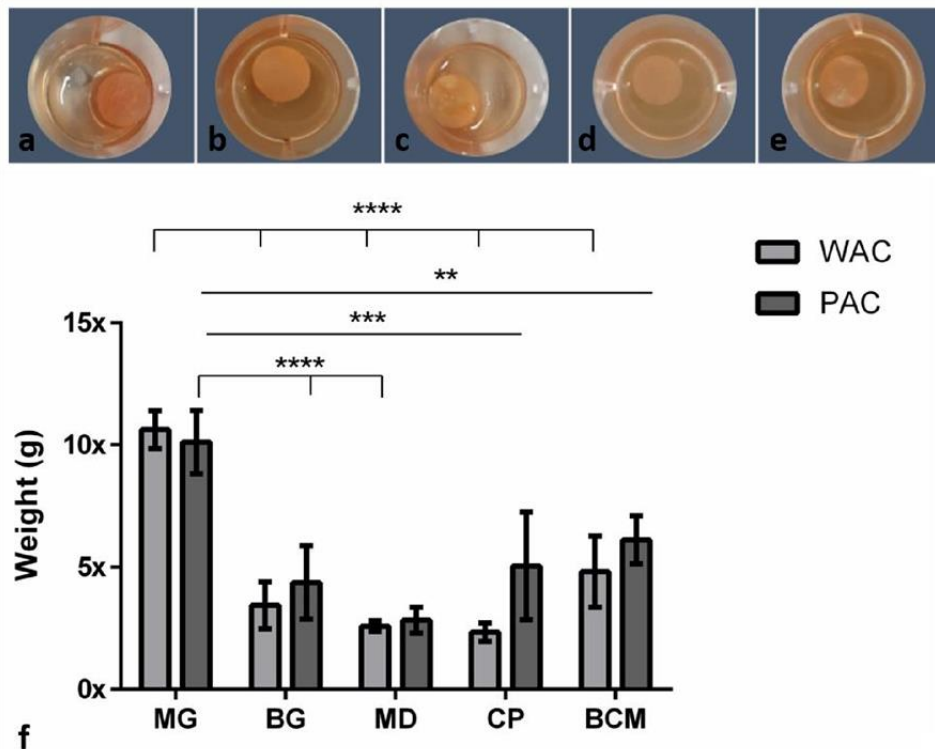


Figure 5. (a–e) The different membranes incubated in liquid-PRF: (a) MG, (b) BG, (c) MD, (d) CP, and (e) BCM. (f) Water absorption coefficient (WAC) and liquid-PRF absorption coefficient (PAC). Differences were considered statistically significant at $p < 0.05$ (*) and as highly significant at $p < 0.01$ (**), $p < 0.001$ (***) and $p < 0.0001$ (****).

Classification of Collagen Liquid-PRF Interaction

The histological observations allowed the classification of collagen-based biomaterials based on their interactions with liquid-PRF. Thereby, three different interaction types were observed. MG allowed total penetration of liquid-PRF into its central region and represented reaction type I (class I). MD, CP, and BG showed only some penetration of PRF into the collagen-based biomaterials. However, the central region was free of liquid-PRF. These materials represented interaction type II (class II). Finally, BCM was completely occlusive over the penetration of liquid-PRF, and therefore represented a further, type III interaction (class III) (Figure 6).

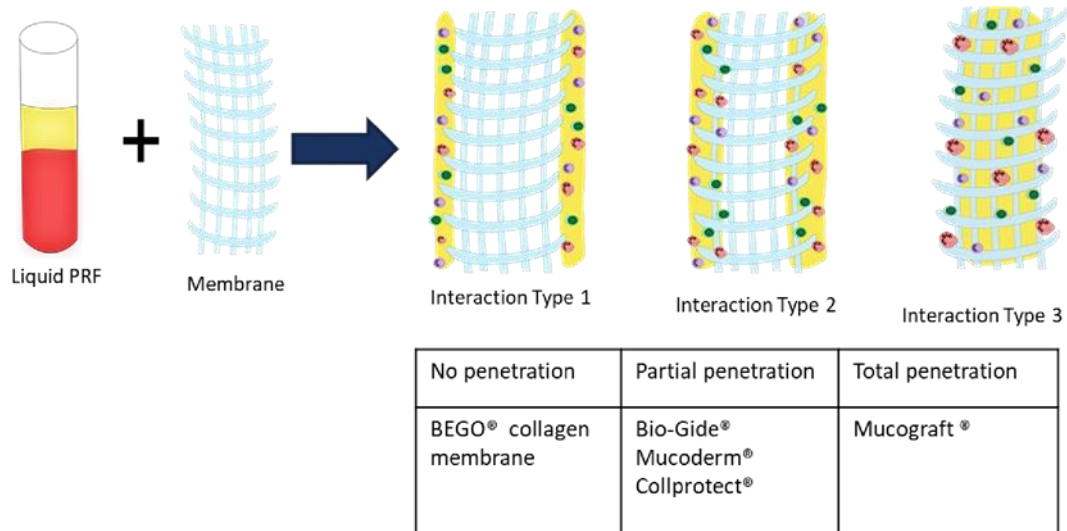


Figure 6. Classification of collagen-based biomaterials based on their interactions with liquid-PRF.

Discussion

The development of biomaterials for use in cell-based tissue engineering has focused on the *in vitro* preculturing of biomaterials. This technique showed enhanced vascularization after the addition of isolated cells, such as endothelial cells, mesenchymal cells, or primary human osteoblasts, in mono or cocultures.¹⁴ The procedure of cell isolation and preculturing of biomaterials is dependent on various factors, including harvesting human tissue, cell isolation, and cultivation under aseptic conditions in laboratories. Precultivation of biomaterials can take up to two weeks.¹⁹ In addition, cell cultures are sensitive to viral and bacterial infection and environmental changes.²⁰ These factors are practical limitations and drawbacks for routine clinical use. With the introduction of PRF,^{13,21} scientific developments have met the requirements for clinical application; thus, cell-based tissue engineering and regeneration have become clinically applicable. In contrast to isolated cells, PRF is a complex system that includes human platelets, leukocytes, and plasma proteins within a fibrin matrix.²² Those components are key elements in wound healing and tissue regeneration. Leukocytes promote regeneration by releasing signaling molecules involved in angiogenesis, cellular cross-talk,^{15,23} and cell-cell communication during bone formation.²⁴ Platelets are essential for wound healing and tissue regeneration, as they express numerous platelet-derived growth factors (PDGFs), such as vascular endothelial growth factor (VEGF), which promotes vascularization, and transforming growth factor-beta (TGF- β), which influences the function of cells involved in new tissue formation, such as fibroblasts.^{23,25,26} Thus, the interplay between these cells leads to better performance in regeneration.²⁷ The so-called low-speed centrifugation concept (LSCC) leads to significant enrichment of liquid-PRF-based matrices with leukocytes and platelets.¹⁶ Furthermore, liquid-PRF has a suitable consistency and is easy to handle. The reasoning behind

combining collagen membranes with liquid-PRF is to make use of the liquid-PRF constituents, such as leukocytes, platelets, and fibrin, to support guided bone and tissue regeneration (GTR/GBR).

This study presented a histological analysis of the combination of autologous liquid-PRF matrix and xenogeneic collagen-based biomaterials. However, to date, it is unknown which type of collagen-based biomaterial is most suitable for combination with liquid-PRF. Therefore, this *ex vivo* study was the first to analyze the interaction pattern between PRF and different collagen-based biomaterials with the aim of understanding the capacity and suitability of biomaterials to incorporate PRF. The results are potentially useful for translation into specific clinical indications with improved regeneration potential. The results of the present study showed differences in the structural composition of the collagen membranes observed by scanning electron microscopy and variations in the interactions between the collagen-based biomaterials and liquid-PRF, supporting previous findings that the cellular-biomaterial interaction is partially determined by the structural characteristics of the biomaterial [28,29].

MG is a collagen matrix composed of a smooth and rough surface. When mixed with liquid-PRF, the collagen matrix appeared completely loaded with liquid-PRF, including leukocytes, platelets and fibrin matrix, which were evenly distributed throughout the collagen matrix. Additionally, MG showed the higher PAC of all the membranes included in this study, ratifying the histological findings. The present *ex vivo* results also underlined the ability of MG to serve as an “enriched” scaffold with liquid-PRF, including cells and fibrin matrix. According to the literature, one of the most common clinical indications of MG in dentistry is the coverage of periodontal recession defects by GTR. In a previous clinical study by our group, MG was used to cover skin defects to induce soft tissue regeneration in patients undergoing skin cancer removal [30]. The histological results revealed an integrated membrane, inducing a mononuclear cellular reaction and a desirable clinical appearance [30]. The interaction between the collagen-based matrix and liquid-PRF, *i.e.*, complete enrichment of the collagen matrix with liquid-PRF, may lead to a better tissue regeneration process in clinical applications as an effect of the regeneration potential of liquid-PRF. However, further clinical studies are required.

BG is a collagen bilayered membrane with one compact and one spongy layer. In this scenario, in the cell–biomaterial interaction, liquid-PRF showed a different distribution within BG. The CL allowed cells (leukocytes and platelets) and the fibrin matrix to partially enter the membrane, whereas the SL was free of liquid-PRF. Therefore, the central region of the material showed no liquid-PRF cellular penetration. Interestingly, the SL, which was free of liquid-PRF, had a well-adhered liquid-PRF clot on the surface. The results confirm the primary clinical use for BG, which is GBR. As stated by the manufacturer, the SL should face the bony defect, and the

CL should be adapted to the soft tissue. Clinically, by applying the “enriched” membrane to a bone defect, BG would preserve its clinical indication, and the liquid-PRF clot on the surface would face the bone defect to support its regeneration.

In comparison, MD and CP allowed less liquid-PRF intake, as observed histologically and by the PAC measurements. These collagen-based biomaterials had leukocytes and platelets only in the most superficial layer. Those cellular–biomaterial interactions could be explained by the biomaterials’ compact structures with fibers of larger size, which were presumably impeding the expansion of biomaterials and reducing their PAC properties.

MD contained liquid-PRF fibrin between the most superficial collagen fibers, and both biomaterials showed a stable liquid-PRF clot on their surface. These materials have been used clinically in GBR/GTR. In this scenario, the result once again confirmed the membranes’ clinical indication for GBR/GTR due to the observed liquid-PRF formation of a PRF clot on their surface. Remarkably, in a previous *in vivo* study by our group using a subcutaneous model in Wistar rats, a pathological cellular reaction lead by MNGCs was observed on the surface of these liquid-PRF collagen-based biomaterials. The implications of an enriched collagen biomaterial, i.e., covered with a liquid-PRF clot, as to whether the inflammatory cellular reaction would be modulated, is a topic of research that requires further investigation.

The final biomaterial tested, BCM, appeared to be surrounded by a large liquid-PRF clot, and histologically no leukocytes, platelets, or fibrin were observed invading the membrane. Nevertheless, the PAC measurements of BMC showed an absorbing coefficient of five. These results suggest that BMC and the aforementioned collagen membranes may have also absorbed other components of liquid-PRF, which were not the focus of this histological evaluation. According to the manufacturer, BCM is to be used for GBR/GTR, which is in accordance with the formation of a liquid-PRF clot on the surface of the membrane. In this context, the adherent liquid-PRF clot would interact with the surrounding tissue. The rationale behind this cellular–biomaterial interaction liquid-PRF could be related to the physicochemical characteristics of the biomaterial due to the methods used to sterilize the membranes. BCM is the only biomaterial investigated in this study that is sterilized with ethylene oxide gas;⁷ the other evaluated membranes are sterilized with gamma irradiation,^{4–6} which might influence the physicochemical composition of the biomaterial and its interaction with liquid-PRF.

Remarkably, MD, CP, and BCM showed commonalities *ex vivo*. These collagenous materials prevented the liquid-PRF components from entering the membrane central region, leading to the formation of a PRF clot on the surfaces. Additionally, the ultrastructural analyses of the various collagen-based biomaterials showed different characteristics.

It seems that the physiochemical composition and surface properties of these biomaterials are critical elements for cellular interaction. These characteristics are probably related to the techniques used to process the biomaterials during manufacturing and the harvesting compartment. The various interaction patterns observed in this study are of great clinical relevance. Based on the results presented here, including three different interaction types (class I–III), this approach may be useful as a tool to further classify and evaluate the capacity of different collagen-based biomaterials to assess their regenerative capacities. However, this study did not provide any results about the bioactivity of the different membranes, after combination with PRF. Therefore, further studies are needed to further verify this system.

Interestingly, although all of the biomaterials evaluated here are of porcine origin, variable interactions with liquid-PRF were observed. Evidently, these differences depended on the biomaterial properties, since the protocol to obtain liquid-PRF was consistent. Accordingly, the physiochemical compositions of the particular biomaterials might influence their interactions with inflammatory cells. Therefore, liquid-PRF might be a useful tool for *ex vivo* examination of the initial response towards novel biomaterials to predict the *in vivo* cellular response.

Previous *in vitro* studies have shown that PRF-based matrices can be considered delivery systems because of their ability to release different growth factors.¹⁶ When combining xenogeneic biomaterials with autologous liquid-PRF, the question raised is to what extent the addition of liquid-PRF, as a dose of physiological inflammatory cells, can influence the biomaterial-related cellular reaction. It might be that the total cellular penetration of the biomaterial, including the fibrin matrix within the collagen matrix, could act as a biomaterial-based delivery system, leading to enhanced vascularization and tissue regeneration, as the regenerative potential of collagen-based biomaterials and fibrin-based liquid-PRF are used simultaneously.

Furthermore, the present study utilized a protocol of 600 RPM for 8 min to produce liquid-PRF, which was previously introduced by the low-speed centrifugation concept.¹⁶ Additionally, a systematic study investigated the influence of reducing the RCF as a proof of LSCC by using a 3 min centrifugation time and showed similar results.³¹ More recently, it was further shown that the 8 min protocol utilized in our study represents a superior and more effective means to concentrate platelets compared to many commercially available protocols.³² Previous studies have described the role of collagen-based biomaterials as a bioactive compartment in GTR by demonstrating the effect of placing a collagen membrane on newly formed bone.^{8,9} Accordingly, the combination of liquid-PRF with collagen-based biomaterials introduced in this study aimed

to optimize the bioactivity of biomaterials to achieve better regeneration using a clinically applicable system. The present study proved that it is possible to load xenogeneic collagen-based biomaterials with a complex mixture of autologous cells (liquid-PRF) using a clinically applicable method in less than 15 min. Additionally,

we showed a histological analysis of each distribution pattern of liquid-PRF after its application on various biomaterials. However, the present observations do not provide any information as to what extent this biologically complex system, *i.e.*, liquid-PRF with various collagen-based biomaterials, will influence the functionality of the included cells and growth factors. Additionally, the influence of PRF on the mechanical properties of the biomaterials and the activation of the cells in PRF after contact with the biomaterial surface must be further evaluated. Thus, ongoing systematic investigations, including *ex vivo*, *in vivo*, and *in vitro* studies, are needed to evaluate the functionality and potential of this system. Moreover, controlled clinical studies will provide knowledge about the sufficiency of this combination system for the regeneration process and its effects on patient morbidity.

Conclusion

The present study analyzed the combination of an autologous liquid-PRF matrix as a drug delivery system, with five different xenogeneic collagen-based biomaterials histologically. Emphasis was placed on the distribution of leucocytes and platelets within the collagen membrane, and the interaction between the collagen membrane and liquid-PRF. Although all of the evaluated membranes were of porcine origin, three different types of interactions were observed, including total cellular penetration, partial cellular penetration, and no cellular penetration. The present study showed that it is possible to load biomaterials with a complex cell system (liquid-PRF) using a clinically applicable method within 15 min. PRF could serve as a drug delivery system to support GTR/GBR and enhance biomaterial bioactivity. Additionally, this *ex vivo* system could be used to assess the initial reactions of novel biomaterials, and thus reduce the number of animals used for *in vivo* studies. However, further investigations are required to evaluate the regeneration potential of this combination system and its clinical impact on patient morbidity

Acknowledgments

The authors would like to thank Verena Hoffmann for her excellent technical assistance.

References

1. Bunyaratavej, P.; Wang, H.L. Collagen membranes: A review. *J. Periodontol.* **2001**, *72*, 215–229.
2. Al-maawi, S.; Orłowska, A.; Sader, R.; Kirkpatrick, C.J.; Ghanaati, S. *In vivo* cellular reactions to different biomaterials—Physiological and pathological aspects and their consequences. *Semin. Immunol.* **2017**.
3. Miron, R.J.; Zohdi, H.; Fujioka-Kobayashi, M.; Bosshardt, D.D. Giant cells around bone biomaterials: Osteoclasts or multi-nucleated giant cells? *Acta Biomater.* **2016**, *46*, 15–28.
4. Ghanaati, S. Non-cross-linked porcine-based collagen I-III membranes do not require high vascularization rates for their integration within the implantation bed: A paradigm shift. *Acta Biomater.* **2012**, *8*, 3061–3072.
5. Ghanaati, S.; Schlee, M.; Webber, M.J.; Willershausen, I.; Barbeck, M.; Balic, E.; Görlach, C.; Stupp, S.I.; Sader, R.A.; Kirkpatrick, C.J.; et al. Evaluation of the tissue reaction to a new bilayered collagen matrix *in vivo* and its translation to the clinic. *Biomed. Mater.* **2011**, *6*, 15010–15012. [CrossRef]
6. Barbeck, M.; Lorenz, J.; Kubesch, A.; Böhm, N.; Booms, P.; Choukroun, J.; Sader, R.; Kirkpatrick, C.J.; Ghanaati, S. Porcine Dermis-Derived Collagen Membranes Induce Implantation Bed Vascularization Via Multinucleated Giant Cells: A Physiological Reaction? *J. Oral Implantol.* **2015**, *41*, e238–e251.
7. Barbeck, M.; Lorenz, J.; Holthaus, M.G.; Raetscho, N.; Kubesch, A.; Booms, P.; Sader, R.; Kirkpatrick, C.J.; Ghanaati, S. Porcine Dermis and Pericardium-Based, Non-Cross-Linked Materials Induce Multinucleated Giant Cells After Their *In vivo* Implantation: A Physiological Reaction? *J. Oral Implantol.* **2015**, *4*, e267–e281. [CrossRef]
8. Turri, A.; Elgali, I.; Vazirisani, F.; Johansson, A.; Emanuelsson, L.; Dahlin, C.; Thomsen, P.; Omar, O. Guided bone regeneration is promoted by the molecular events in the membrane compartment. *Biomaterials* **2016**, *84*, 167–183.
9. Elgali, I.; Turri, A.; Xia, W.; Norlindh, B.; Johansson, A.; Dahlin, C.; Thomsen, P.; Omar, O. Guided bone regeneration using resorbable membrane and different bone substitutes: Early histological and molecular events. *Acta Biomater.* **2016**, *29*, 409–423.
10. Schmitt, C.M.; Moest, T.; Lutz, R.; Wehrhan, F.; Neukam, F.W.; Schlegel, K.A. Long-term outcomes after vestibuloplasty with a porcine collagen matrix (Mucograft®) versus the free gingival graft: A comparative prospective clinical trial. *Clin. Oral Implants Res.* **2016**, *27*, e125–e133.

11. Fouad, W.; Osman, A.; Atef, M.; Hakam, M. Guided maxillary sinus floor elevation using deproteinized bovine bone versus graftless Schneiderian membrane elevation with simultaneous implant placement: Randomized clinical trial. *Clin. Implant Dent. Relat. Res.* **2018**
12. Ghanaati, S.; Orth, C.; Unger, R.E.; Barbeck, M.; Webber, M.J.; Motta, A.; Migliaresi, C.; Kirkpatrick, C.J. Fine-tuning scaffolds for tissue regeneration: Effects of formic acid processing on tissue reaction to silk fibroin. *J. Tissue Eng. Regen. Med.* **2010**, *4*, 464–472.
13. Choukroun, J.; Adda, F.; Schoeffler, C. Uneopportunit  en paro-implantologie: Le PRF. *Implantodontie* **2001**, *42*, 55–62.
14. Litvinov, R.I.; Weisel, J.W. What Is the Biological and Clinical Relevance of Fibrin? *Semin. Thromb. Hemost.* **2016**, *42*, 333–343.
15. Soloviev, D.A.; Hazen, S.L.; Szpak, D.; Bledzka, K.M.; Ballantyne, C.M.; Plow, E.F.; Pluskota, E. Dual Role of the Leukocyte Integrin M 2 in Angiogenesis. *J. Immunol.* **2014**, *193*, 4712–4721.
16. Choukroun, J.; Ghanaati, S. Reduction of relative centrifugation force within injectable platelet-rich-fibrin (PRF) concentrates advances patients' own inflammatory cells, platelets and growth factors: The first introduction to the low speed centrifugation concept. *Eur. J. Trauma Emerg. Surg.* **2018**, *44*, 87–95.
17. Aroca, S.; Keglevich, T.; Barbieri, B.; Gera, I.; Etienne, D. Clinical Evaluation of a Modified Coronally Advanced Flap Alone or in Combination with a Platelet-Rich Fibrin Membrane for the Treatment of Adjacent Multiple Gingival Recessions: A 6-Month Study. *J. Periodontol.* **2009**, *80*, 244–252.
18. Ghanaati, S.; Herrera-Vizcaino, C.; Al-Maawi, S.; Lorenz, J.; Miron, R.J.; Nelson, K.; Schwarz, F.; Choukroun, J.; Sader, R. Fifteen years of platelet rich fibrin (PRF) in dentistry and oromaxillofacial surgery: How high is the level of scientific evidence? *J. Oral Implantol.* **2018**.
19. Ghanaati, S.; Unger, R.E.; Webber, M.J.; Barbeck, M.; Orth, C.; Kirkpatrick, J.A.; Booms, P.; Motta, A.; Migliaresi, C.; Sader, R.A.; et al. Scaffold vascularization *in vivo* driven by primary human osteoblasts in concert with host inflammatory cells. *Biomaterials* **2011**, *32*, 8150–8160.
20. Jones, J.A.; Dadsetan, M.; Collier, T.O.; Ebert, M.; Stokes, K.S.; Ward, R.S.; Hiltner, P.A.; Anderson, J.M. Macrophage behavior on surface-modified polyurethanes. *J. Biomater. Sci. Polym. Ed.* **2004**, *15*, 567–584.
21. Choukroun, J.; Diss, A.; Simonpieri, A.; Girard, M.-O.; Schoeffler, C.; Dohan, S.L.; Dohan, A.J.J.; Mouhyi, J.; Dohan, D.M. Platelet-rich fibrin (PRF): A second-generation platelet

- concentrate. Part V: Histologic evaluations of PRF effects on bone allograft maturation in sinus lift. *Oral Surg. Oral Med. Oral Pathol. Oral Radiol. Endod.* **2006**, 101, 299–303.
22. Ghanaati, S.; Booms, P.; Orłowska, A.; Kubesch, A.; Lorenz, J.; Rutkowski, J.; Landes, C.; Sader, R.; Kirkpatrick, C.; Choukroun, J. Advanced Platelet-Rich Fibrin: A New Concept for Cell-Based Tissue Engineering by Means of Inflammatory Cells. *J. Oral Implantol.* **2014**, 40, 679–689.
23. Ekström, K.; Omar, O.; Granéli, C.; Wang, X.; Vazirisani, F.; Thomsen, P. Monocyte exosomes stimulate the osteogenic gene expression of mesenchymal stem cells. *PLoS ONE* **2013**, 8, e75227.
24. Perut, F.; Filardo, G.; Mariani, E.; Cenacchi, A.; Pratelli, L.; Devescovi, V.; Kon, E.; Marcacci, M.; Facchini, A.; Baldini, N.; et al. Preparation method and growth factor content of platelet concentrate influence the osteogenic differentiation of bone marrow stromal cells. *Cytotherapy* **2013**, 15, 830–839.
25. Aminabadi, N.A. Plasma rich in growth factors as a potential therapeutic candidate for treatment of recurrent aphthous stomatitis. *Med. Hypotheses* **2008**, 70, 529–531.
26. Herath, T.D.K.; Larbi, A.; Teoh, S.H.; Kirkpatrick, C.J.; Goh, B.T. Neutrophil-mediated enhancement of angiogenesis and osteogenesis in a novel triple cell co-culture model with endothelial cells and osteoblasts. *J. Tissue Eng. Regen. Med.* **2018**, 12, e1221–e1236.
27. Schmidt-Bleek, K.; Kwee, B.J.; Mooney, D.J.; Duda, G.N. Boon and Bane of Inflammation in Bone Tissue Regeneration and Its Link with Angiogenesis. *Tissue Eng. Part B Rev.* **2015**, 21, 354–364.
28. Chia-Lai, P.; Orłowska, A.; Al-Maawi, S.; Dias, A.; Zhang, Y.; Wang, X.; Zender, N.; Sader, R.; Kirkpatrick, C.J.; Ghanaati, S. Sugar-based collagen membrane cross-linking increases barrier capacity of membranes. *Clin. Oral Investig.* **2017**.
29. Al-Maawi, S.; Vorakulpipat, C.; Orłowska, A.; Zrnc, T.A.; Sader, R.A.; Kirkpatrick, C.J.; Ghanaati, S. *In vivo* Implantation of a Bovine-Derived Collagen Membrane Leads to Changes in the Physiological Cellular Pattern of Wound Healing by the Induction of Multinucleated Giant Cells: An Adverse Reaction? *Front. Bioeng. Biotechnol.* **2018**, 6.
30. Lorenz, J.; Blume, M.; Barbeck, M.; Teiler, A.; Kirkpatrick, C.J.; Sader, R.A.; Ghanaati, S. Expansion of the peri-implant attached gingiva with a three-dimensional collagen matrix in head and neck cancer patients-results from a prospective clinical and histological study. *Clin. Oral Investig.* **2016**.
31. Wend, S.; Kubesch, A.; Orłowska, A.; Al-Maawi, S.; Zender, N.; Dias, A.; Miron, R.J.; Sader, R.; Booms, P.; Kirkpatrick, C.J.; et al. Reduction of the relative centrifugal force influences

cell number and growth factor release within injectable PRF-based matrices. *J. Mater. Sci. Mater. Med.* **2017**, 28.

32. Miron, R.J.; Chai, J.; Zheng, S.; Feng, M.; Sculean, A.; Zhang, Y. A Novel Method for Evaluating and Quantifying Cell Types in Platelet Rich Fibrin and an Introduction to Horizontal Centrifugation. *J. Biomed. Mater. Res.* **2019**.

3.2.2. Sugar-based collagen membrane cross-linking increases barrier capacity of membranes

Clinical Oral Investigations, **2018**, 22(4), 1851–1863.

Chia-Lai, P.^a, **Orłowska, A.**^a, Al-Maawi^a, S., Dias, A.^a, Zhang, Y.^a, Wang, X.^{a,b}, Zender, N.^a, Sader, R.^a, Kirkpatrick, C. J.^a, & Ghanaati, S^a.

^a Department for Oral, Cranio-Maxillofacial and Facial Plastic Surgery, FORM (Frankfurt Orofacial Regenerative Medicine) Lab, University Hospital Frankfurt Goethe University, Theodor-Stern-Kai 7, 60590 Frankfurt am Main, Germany

^b Department of Oral and Maxillofacial Plastic and Trauma surgery, Capital Medical University School of Stomatology, Beijing, China

Abstract

Objectives: This study examines the permeability and barrier capacity of a sugar cross-linked resorbable collagen membrane *ex vivo* and *in vivo*.

Materials and methods: In an *ex vivo* study, injectable platelet-rich fibrin (i-PRF), a peripheral blood-derived human leukocyte and-platelet-rich plasma was used to analyze membrane permeability. *in vivo* subcutaneous implantation in Wistar rats (n = 4 per time point and group) was used to investigate the barrier capacity of the membrane. The induced *in vivo* cellular reaction was evaluated at 3, 15, and 30 days and compared to sham OP (control) without biomaterial using histological, immunohistochemical, and histomorphometric methods.

Results: *Ex vivo*, the membrane was impenetrable to leukocytes, platelets, and fibrin from peripheral human blood concentrate (PRF). *In vivo*, the membrane maintained its structure and remained impervious to cells, connective tissue, and vessels over 30 days. CD-68-positive cell (macrophage) numbers significantly decreased from 3 to 15 days, while from day 15 onwards, the number of multinucleated giant cells (MNGCs) increased significantly. Correspondingly, a rise in implantation bed vascularization from 15 to 30 days was observed. However, no signs of degradation or material breakdown were observed at any time point. Conclusion *Ex vivo* and *in vivo* results showed material impermeability to cellular infiltration of human and murine cells, which highlights the membrane capacity to serve as a barrier over 30 days. However, whether the induced MNGCs will lead to material degradation or encapsulation over the long term requires further investigation.

Clinical relevance: The data presented are of great clinical interest, as they contribute to the ongoing discussion concerning to what extent an implanted material should be integrated versus serving only as a barrier membrane.

Introduction

Guided bone regeneration (GBR) is a widely used procedure in different surgical fields, especially in oral and maxillofacial surgery.¹ The principle aim is to substitute and support impaired regions due to diseases or traumatic events and to enhance the amount of bone available, such as prior to implant therapy in oral surgery. Since the rate of bone formation is slower than the rate of fibrogenesis, the role of the membrane is first and foremost to prevent the ingrowth of epithelium and connective tissue into the augmentation region.²⁻⁴ Further requirements are to act as a place holder, to maintain space for delayed osteogenesis, and to stabilize the wound in order to achieve primary wound closure.⁵

Currently, two types of membranes are commercially available: resorbable and non-resorbable membranes. In the 1990s, non-resorbable membranes, such as expanded polytetrafluoroethylene (e-PTFE), titanium mesh, and titanium-reinforced PTFE, were used in the GBR technique. Although these barriers proved very effective in preventing the invasion of soft tissue physically,^{6, 7} their technique sensitivity and increased patient morbidity (due to obligatory membrane retrieval) were major limitations. To avoid these drawbacks, biomaterials development has been focused on generating resorbable membranes. Among these, collagen, as a ubiquitous molecule, has shown suitable and beneficial properties. Consequently, collagen-based biomaterials have demonstrated favorable GBR results⁸ while bypassing the shortcomings of non-resorbable membranes. However, collagen membranes are predisposed to degradation within their implantation beds,⁹ which undermines their ability to function as true barriers.

During wound healing, different inflammatory cells are involved in the regeneration process of the affected tissue as a cellular response to the injury. In the early wound healing stage and during hemostasis, platelet accumulation occurs to build a platelet plug, which then becomes a fibrin matrix.¹⁰ This phase is then followed by the recruitment of different physiologic mononuclear cells, such as leukocytes and their subtypes, which allows phagocytosis of contaminated and necrotic tissue, first by neutrophils and then by macrophages.^{10, 11} Additionally, platelets and leukocytes release numerous growth factors to mediate vascularization¹² and allow the shift to the process of new tissue formation by recruiting keratinocytes and fibroblasts.¹⁰ However, the implantation of biomaterials within the defect area adds an additional factor in the processes of wound healing and tissue regeneration. After biomaterial implantation, an interaction with the biomaterial occurs that results in a biomaterial-specific cellular reaction.

Previously, our group conducted a series of *in vivo* studies to analyze the cellular reactions towards various collagen membranes of different origins and attributes using a subcutaneous implantation model in small animals. The collected data have shown that, generally, there are two different types of cellular reactions that most likely depend on the physicochemical properties and the processing techniques of the biomaterials. Membranes that induced a physiological reaction by means of mononuclear cells underwent an integration process and maintained their structure over a period of 60 days.^{7, 13} This process was revealed in non-cross-linked bilayered collagen membranes of porcine origin composed of collagen types I and III,⁷ as well as in a collagen-based matrix that included collagen types I and III harvested from porcine peritoneum and skin.¹³ Furthermore, the main reaction towards these two collagen-based materials was dominated by mononuclear cells, which ultimately led to its integration within the host tissue without material breakdown.¹³ In addition, the cellular reaction in translational

clinical cases, including histological evaluation of human samples, corresponded to the *in vivo* observed outcomes.¹³

Other biomaterials demonstrated a different type of cellular reaction that included non-physiological cells, such as multinucleated giant cells (MNGCs), which are a sign of a foreign body reaction.¹⁴ In a comparative *in vivo* study, two collagen-based biomaterials with different thicknesses were analyzed in a subcutaneous implantation model. Both the thick collagen matrix and the thin bilayered collagen membrane induced the formation of MNGCs, a manifestation of a foreign body reaction,^{14, 15} which not only led to increased vascularization in the implantation regions but also to membrane breakdown in terms loss of the native structure.¹⁴ Similarly, another *in vivo* study investigated the cellular responses towards two non-cross-linked collagen-based biomaterials, both of porcine origin but differing in their harvesting compartments and thicknesses, and found that they underwent disintegration by the induction of MNGCs, which led to a breakdown after 30 days in both biomaterials.¹⁵

Therefore, the induced cellular reaction decisively influences the degradation and regeneration process of collagen-based biomaterials and their role as a barrier membrane.

To further increase the resistance of collagen-based biomaterials to degradation, various chemical and physical crosslinking methods, such as ultraviolet light, glutaraldehyde, and enzymatic ribose cross-linking, have been used to boost the biomechanical properties of the collagen fibers.¹⁶ Various studies have shown that supplementary cross-linking confers stability on collagen membranes after implantation.^{17–19} However, cross-linking was also associated with foreign body reaction and fibrosis, which might be due to chemical manipulation of the collagen structure.²⁰ Recently, GLYMATRIX™ technology (Datum Dental Ltd., 1 Bat Sheva Street, Lod 7120101 Israel), a novel technique which uses ribose—a naturally occurring sugar molecule—to crosslink collagen, has been developed.²¹ The manufacturing process involves the extraction of collagen into monomeric fibrils, which are then reconstructed and cross-linked to form an improved collagen-based biomaterial. In this study, the capacity of such a sugar cross-linked collagen membrane, OSSIX® PLUS (OS, REGEDENT, Zurich, CH) to serve as a barrier was evaluated *in vivo* using a subcutaneous implantation model in Wistar rats. Special interest was directed at the induced cellular reaction in terms of cell types, membrane permeability, vascularization, and degradation patterns. Additionally, a blood concentrate system of injectable platelet-rich fibrin (iPRF), which contains numerous human peripheral blood cells, was used for evaluation of membrane permeability *ex vivo*.

Experimental

OSSIX® PLUS membrane

OSSIX® PLUS membrane (OS) is a sugar cross-linked resorbable collagen membrane derived from porcine tendons.²² The native tissue undergoes a series of purification processes to isolate monomeric collagen and to remove all potential immunogenic tissue remnants. Subsequently, the monomeric collagen is reconstituted into collagen fibrils and then glycosylated with ribose, a naturally occurring sugar, using GLYMATRIX™ technology.²¹ Sterilization was achieved with ethylene oxide. The collagen membrane is CE-marked. According to the manufacturer, OS maintains barrier functionality for 4–6 months. Furthermore, since it is purported to be resistant to the oral environment, membrane exposure during implantation will not impede wound healing or guided bone regeneration (GBR).²² The biomaterial is specified to be impermeable to cells, but permits the passage of fluid and plasma proteins.

Experimental design of the *ex vivo* study part

Injectable platelet-rich fibrin (iPRF) is a blood concentrate system obtained by the centrifugation of human peripheral blood.²³ This system exists in a solid²³ and a liquid form.²⁴ PRF is a fully autologous concentrate system that does not require the addition of any external chemicals or anticoagulants. After blood collection, the tubes are immediately centrifuged using a specific, established centrifugation protocol.²⁵ In the case of the liquid, injectable PRF (i-PRF), the resultant blood concentrate contains a high number of platelets, leukocytes, and plasma proteins suspended in a soluble fibrinogen matrix.²⁴ Because iPRF is not treated with anticoagulants, the physiological coagulation process is not inhibited. Therefore, iPRF forms a clot of cell-loaded fibrin after 10–15 min.

i-PRF preparation and application

In the *ex vivo* section of this study, three healthy volunteers between 18 and 60 years of age, and who were not under any anticoagulant therapy, donated peripheral blood for research purposes. All three volunteers gave written informed consent beforehand. From each participant, venous blood was collected in four 10-ml sterile plastic tubes (Process for PRF, Nice, France). The tubes were immediately centrifuged in a pre-programmed centrifuge (Duo centrifuge, Process for PRF, Nice, France) according to the iPRF centrifugation protocol (10 ml, 700 rpm, 60 ×g, for 3 min).²⁵ After this centrifugation process, a multiphasic liquid consisting of a yellowish-orange upper phase and a reddish lower phase was obtained. The former is iPRF,

whereas the latter includes the remaining blood constituents. Using a blunt needle, 1–2 ml of the iPRF liquid was collected into a 5-ml syringe (Injekt®, B. Braun Medical Inc., Bethlehem, PA, USA) for further use. In the process, care was taken to prevent the two phases from mingling or an accidental uptake of the lower phase.

Four 10 × 10-mm samples of OS were first placed inside a 4 × 6 cell culture plate and then covered by 500 µl iPRF. After 15 min at room temperature, the iPRF liquid formed fibrin clots on the OS samples. These OS membrane-fibrin clot samples were then fixed in 4% paraformaldehyde for 24 h to allow for subsequent histological analysis. This experiment was performed in triplicate at independent time points.

Experimental design of the *in vivo* study part

This study was approved by the Committee on the Use of Live Animals in Teaching and Research of the State of Hessen, Germany. A total of 24 Wistar rats were obtained from Charles River Laboratories (Sulzfeld, Germany) and housed in the Laboratory Animal Unit, Institute of Pathology, Goethe University Frankfurt, Germany. The animals were allowed an acclimation period of 1 week, which enabled them to become accustomed to the new laboratory environment before the experiments began. Throughout the entire study period, the animals were fed regularly with mouse pellets (Laboratory Rodent Chow, Altromin, Lage, Germany) and given water *ad libitum*. Artificial light–dark cycles of 12 h each simulated day and night rhythms.

Based on the study design, the 24 rats were first assigned randomly into two groups. The animals in the first group ($n = 4$ animals/time point) were implanted with OS, whereas the second group ($n = 4$ animals/time point) served as a sham-operated control in order to evaluate the inflammatory pattern during wound healing without biomaterial implantation. The evaluated time points were 3, 15, and 30 days after implantation. The implantation of OS was performed under sterile conditions in accordance with previously established subcutaneous implantation methods as previously described.¹³ All animals survived the operational procedure and through the respective evaluation time points without any complications.

Tissue preparation for histology and histochemistry

After explanation at the designated time points, tissue samples as well as *ex vivo* samples were processed by the methods described in previously published studies.^{26–28} First, the samples were fixed in 4% neutral buffered formaldehyde for 24 h. These samples were then placed into embedding cassettes (Histosette, VWR, Deutschland) and dehydrated in baths of progressively concentrated ethanol (70–100%) before alcohol clearance with xylene. Finally, the tissue

segments were impregnated with molten paraffin wax and embedded into paraffin blocks. After sufficient cooling, the paraffin blocks were cut with a rotatory microtome (Rotationsmikrotom RM2255, Leica, Germany) to produce serial sections of 3- μm thickness. To evaluate the tissue sections under a microscope, they were stained as follows: the first section was stained with Mayer's hematoxylin and eosin (H&E), while the second section was stained with Azan. The third section was stained with Masson's trichrome stain, and the fourth section underwent tartrate-resistant acid phosphatase (TRAP) staining. The latter stain was specifically used to identify TRAP activity in target cells. The fifth and sixth and seventh sections were stained immunohistochemically with anti-mouse CD-31, CD-68, and vWF respectively, as previously described.^{13, 15} In brief, immunohistochemistry was conducted with a Lab Vision™ Autostainer 360-2D (ThermoFisher Scientific, Germany). After deparaffinization, the slides were pretreated with citrate buffer and proteinase K, followed by H₂O₂ (UltraVision™ Quanto Detection System, ThermoFisher Scientific, Germany) and avidin and biotin blocking solutions (Avidin/Biotin Blocking Kit, Vector Laboratories, US). The first antibody used was anti-CD-68 (MCA341GA; 1:400; 30 min), anti-CD-31 (orb10314; 1:200; 2 h), or anti-vWF (ab6994; 1:500; 2 h), whereas the second antibody was goat anti-rabbit IgG-B (sc-2040, 1:200, Santa Cruz Biotechnology, USA). Subsequently, the avidinbiotin-peroxidase complex (ABC) (30 min) and the Histostain-Plus IHC Kit including AEC (20 min) were applied (ThermoFisher Scientific, Germany). Counterstaining was performed using Mayer's hematoxylin. CD-31 and vWF highlight murine blood vessels, while CD-68 detects macrophages in the tissue sections. The negative control for the immunohistochemical staining used was the absence of incubation for primary antibody, while the positive control was applied according to the manufacturer's instruction (anti-CD-31, rat lung; Anti-vWF, human tongue; and anti-CD-68, rat lymph node).

Qualitative histological analysis

Systematic histological assessment was performed by means of a Nikon ECLIPSE 80i microscope (Nikon, Tokyo, Japan) equipped with a motorized stage (ProScan III, Prior, Rockland, MA, USA) and NIS Elements software (Nikon, Tokyo, Japan) as described in preceding publications.¹⁴ Qualitative and quantitative histological analysis focused on the cellular reaction and inflammatory pattern towards the implanted biomaterial, vascularization of the implantation bed, signs of fibrosis, encapsulation, and membrane degradation.

Quantitative histological analysis

Membrane thickness

Adopting the same histomorphometry methods as mentioned in earlier studies,²⁷ the peri-implant tissue of each animal was first digitized prior to histomorphometric analysis. Initially, a total scan including 100–130 individual micrographs was taken automatically by the Nikon ECLIPSE 80i microscope. This was made possible by the motorized stage, which moved automatically within coordinates specified in the NIS Elements software. These single images were then compounded to generate a single large total scan at $\times 100$ magnification. The thickness of the OS membrane of each animal at each of the three time points (3, 15, and 30 days) was then measured at up to 15 distinct points along its length. The mean of these measurements was calculated as the absolute membrane thickness in micrometers. The values obtained from the later time points were also compared to that of day 3, assigned to a value of 100%.

Number of multinucleated giant cells and CD-68-positive mononuclear cells

To analyze the material-associated MNGCs histomorphometrically, TRAP- and CD-68-stained slides were first converted to total scan digital images as previously mentioned. The “annotations and measurements” function of the NIS Elements software was used to manually count the numbers of MNGCs and their subpopulations (TRAP-positive and -negative giant cells), as well as CD-68-positive cells, separately. The respective cell numbers were then computed in relation to the implantation area (MNGCs/ mm^2 ; CD-68/ mm^2), and statistical comparison of the different time points was performed to determine the tissue response elicited by OS over the course of the study.

Statistical analysis

The results from the abovementioned histomorphometric analysis were presented as the means \pm standard deviation and were evaluated for significant differences at the different time points using a one-way analysis of variance (ANOVA) using GraphPad Prism 6.0 software (GraphPad Software Inc., La Jolla, CA, USA). Differences were considered statistically significant if the *P* values were $* < 0.05$ and highly significant if the *P* values were, $** < 0.01$, and $*** < 0.001$ and $**** < 0.0001$. The compiled data were plotted with GraphPad Prism 6.0 software to represent the results graphically.

Results

Ex vivo histological analysis

The OS membrane was easily identified and exhibited a highly dense structure without detectable pores. The interaction with the iPRF revealed that no leukocytes or platelets from the iPRF penetrated into the biomaterial. Instead, OS prevented the inflammatory cells from entering the membrane body. Moreover, the extracellular fibrin was not included within the biomaterial, which resulted in the formation of a cell-rich fibrin clot on both surfaces of the membrane (Fig. 1A, B).

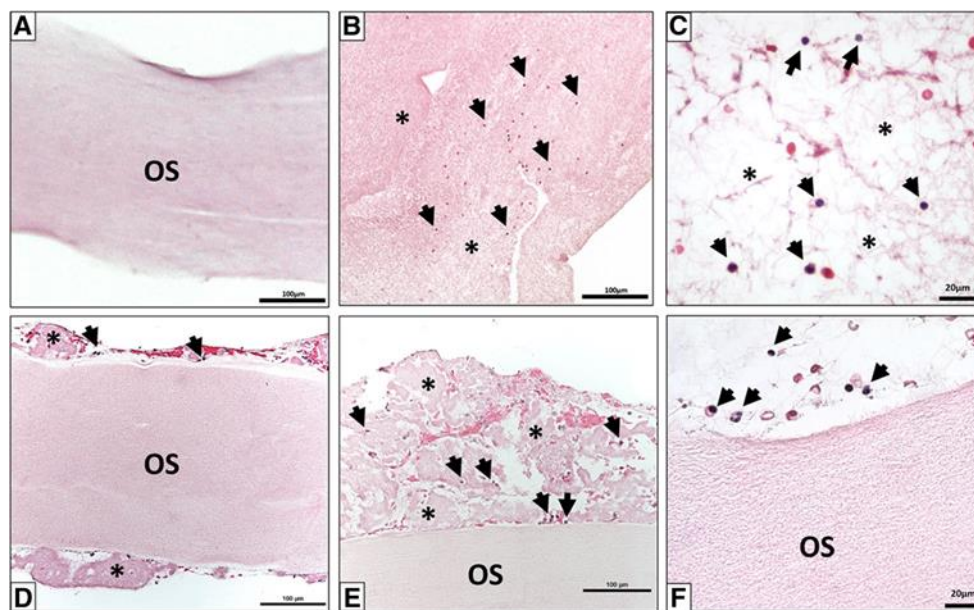


Figure 1. (A) The native structure of OS membrane *ex vivo* as a control in H&E staining. (B) iPRF alone in H&E staining; asterisk = fibrin clot, black arrows = human leukocytes. (C) iPRF alone; black arrows = human leukocytes, asterisk= fibrin clot in H&E staining. (D) A cross section of the OS membrane treated with i-PRF in H&E staining. (E) The interface between i-PRF and OS in H&E staining; asterisk = fibrin clot, black arrows = human leukocytes. (F) Black arrows = human leukocytes in H&E staining

In vivo histological and histomorphometric analysis

All tested animals survived their respective operations, and healing was uneventful. During the entire experiment, no animals were observed to have necrosis or signs of atypical inflammation.

Tissue reaction to the OS membrane

The OS membrane was clearly visible within the murine subcutaneous implantation bed 3 days after implantation (Fig. 2A). It showed a homogeneous structure of densely packed collagen. Both surfaces of this compact membrane were lined with a layer of mononuclear cells

(Fig. 2A, B), of which a large amount were CD-68-positive, i.e., macrophages. No penetration by peri-implant cells or extracellular matrix was noted at this time point (Fig. 4A, A1). Thus, the membrane per se was free of cells. Single vessels were found within the periimplantation area, but the membrane itself exhibited no vascularization (Fig. 3A).

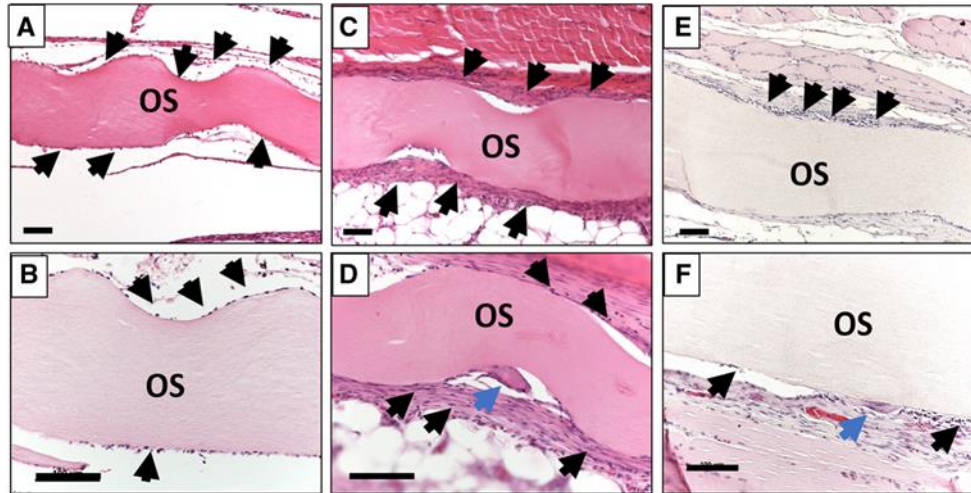


Figure 2. (A) The membrane (OS) within the implantation bed on day 3. Mononuclear cells were detected on both membrane surfaces (black arrows). (B) Mononuclear cells on the membrane (OS) surface (black arrows) on day 3. (C) The membrane (OS) within the implantation region on day 15. There is an increased number of mononuclear cells on both membrane surfaces (black arrows). (D) Mononuclear cells (black arrows), as well as multinucleated giant cells (blue arrow) on the membrane surface (OS) on day 15. (E) The membrane within the implantation bed (OS) on day 30. (F) Mononuclear (black arrows) and multinucleated giant cells adhering to the membrane (OS) surface on day 30.

On day 15 post-implantation, the membrane did not show any signs of degradation (Fig. 2C, D). In comparison to day 3, more mononuclear cells were observed in the implantation bed (Fig. 5B), several of which were CD-68 positive (Fig. 4B, B1). Additionally, a small number of MNGCs located predominantly at the biomaterial-tissue interface was seen (Fig. 2D). A majority of these MNGCs was TRAP-negative (Fig. 5C). At this time point, the membrane maintained its structure, preventing cellular infiltration into the membrane central region. Moreover, connective tissue formation was observed only within the peri-implantation region, and no connective tissue ingrowth was detected within the membrane. Although micro-vessel formation was noted in proximity to the membrane, the membrane body itself remained avascular (Fig. 5A, Fig. 3B). Additionally, no signs of membrane breakdown were observed at this time point.

At day 30 after implantation, no evidence of degradation of the membrane was perceived (Fig. 2E). The membrane displayed a stable dense structure and inhibited cellular infiltration of all kinds. Instead, an organized, cell-rich connective tissue was seen on both membrane surfaces (Fig. 5E). In comparison to day 15, the number of mononuclear cells adjacent to the membrane increased significantly (Fig. 2E, F). These included CD-68-positive cells (Fig. 4C, C1). In addition,

more biomaterial-adherent MNGCs were identified within the implantation region (Fig. 2F), which remained on the membrane surface and did not enter the biomaterial body. The majority of the MNGCs showed no TRAP expression. Nevertheless, no signs of membrane breakdown were found (Fig. 5F). Although the membrane continued to be impermeable to cells and connective tissue, there were no indications that it was segregated from the surrounding tissue by encapsulation or fibrosis.

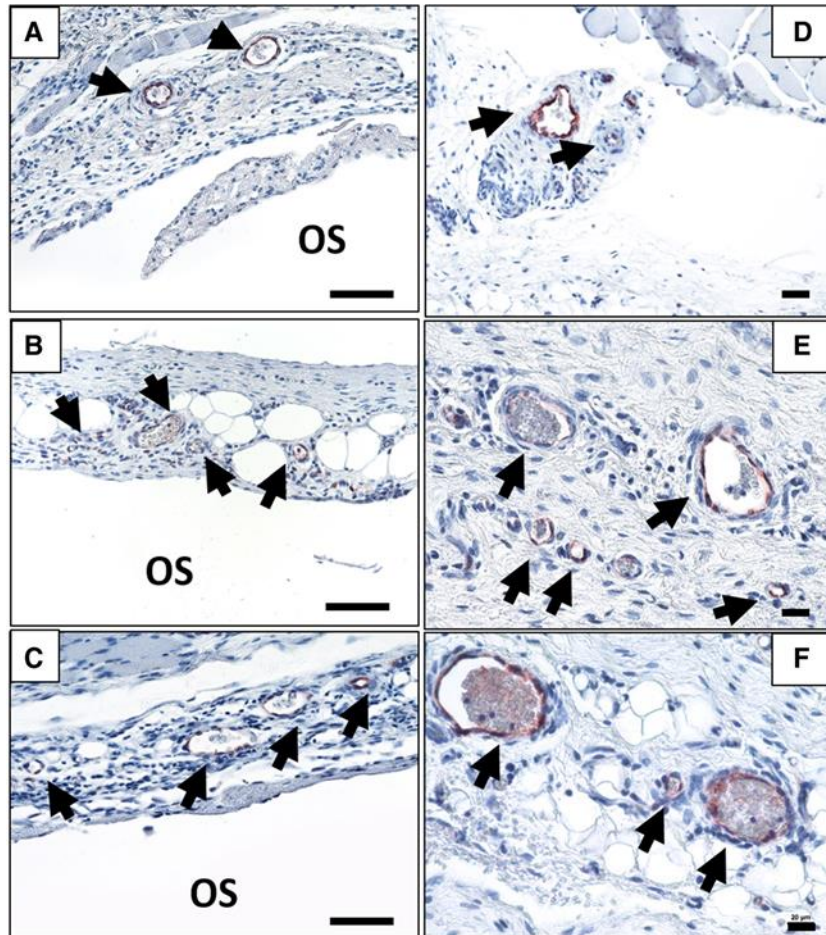


Figure 3. The vascularization pattern over the investigation time points using immunohistochemical stains: (A-C) = anti-CD-31; scale bar = 100 μm, (D-F) = anti-vWF; scale bar = 20 μm. Black arrows indicate vessels and OS indicates the membrane

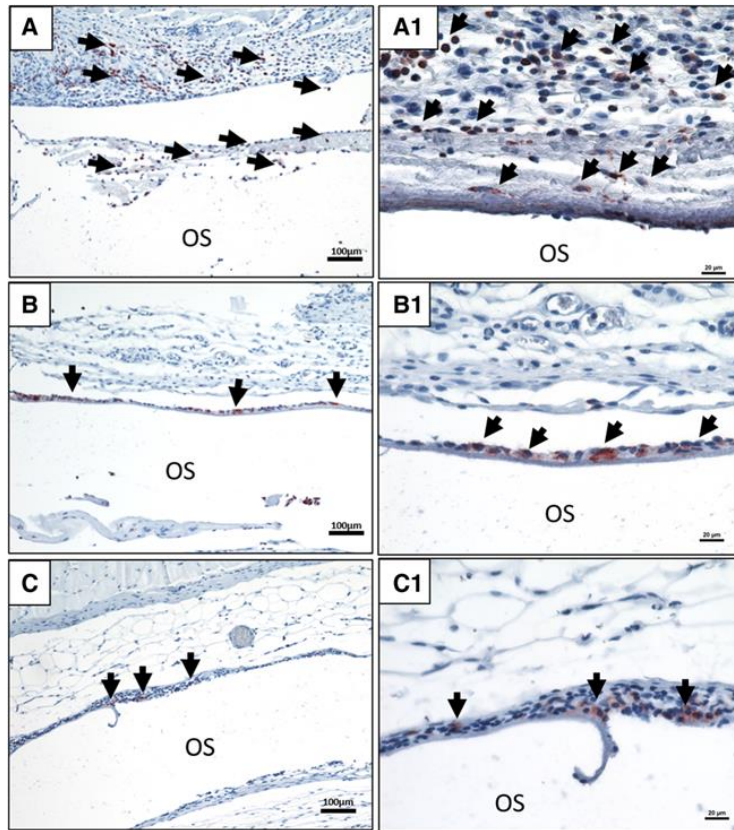


Figure 4. The CD-68-positive cells on the biomaterial surface at day 3 (A; A1); day 15 (B; B1) and day 30 (C; C1). Black arrows = CD-68-positive mononuclear cells, i.e., macrophages. OS indicates the biomaterial. In B and C, the biomaterial was detached and washed during the staining process.

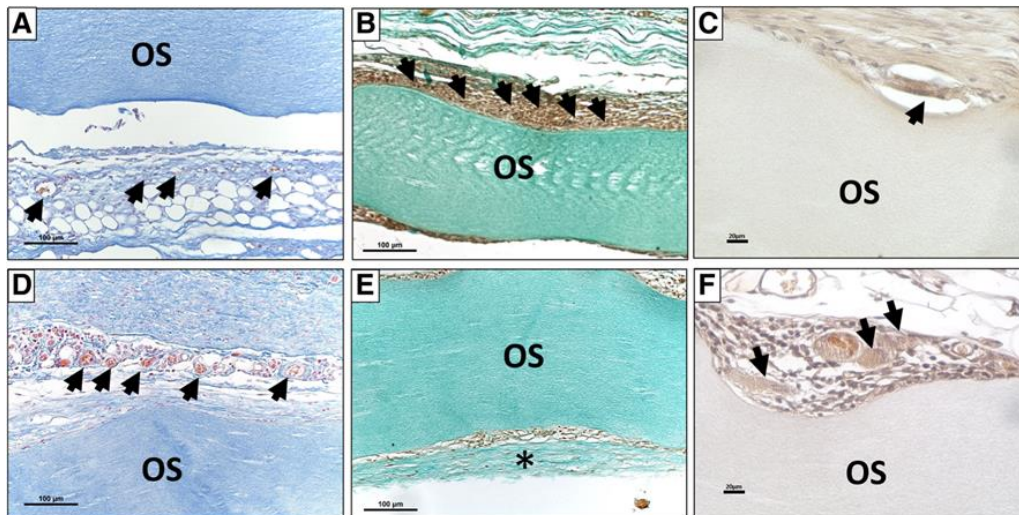


Figure 5. Detailed representative micrographs on days 15 and 30. (A) Vessels (black arrows) were detected near the membrane (OS) at day 15, (Azan staining; scale bar = 100 μ m). (B) Accumulation of mononuclear cells (black arrows) on the membrane (OS) surface at day 15, (Masson Goldner staining; scale bar = 20 μ m). (C) TRAP-negative multinucleated giant cells (black arrows) adherent on the membrane (OS) surface at day 30 (TRAP staining; scale bar = 20 μ m). (D) Increased numbers of vessels (black arrows) were detected in proximity to the membrane (OS) at day 30, (Azan staining; scale bar = 100 μ m). (E) Formation of organized connective tissue including mononuclear cells (asterisk) on the membrane (OS) surface at day 30, (Masson Goldner; scale bar = 20 μ m). (F) TRAP-negative multinucleated giant cell (black arrows) adherent on the membrane (OS) surface at day 30 (TRAP staining; scale bar = 20 μ m)

Histomorphometric analysis of OS membrane thickness

The histomorphometric analysis of the OS membrane revealed that there was no decrease in membrane thickness between day 3 and day 30 after implantation. In contrast, the measured membrane thickness showed a slight increase over the study period, which was not statistically significant (day 3 = 274.68 ± 27.75 ; day 15 = 287.59 ± 27.83 ; day 30 = 302.60 ± 15.19), (Fig. 6A). Due to the possibility of artifacts arising from the histological and implantation procedures, the membrane thickness was calculated as a percentage to obtain a more accurate evaluation. The thickness of day 3 was set at 100%, and all mean values of successive time points were calculated in relation to day 3. The percentage of thickness revealed a slight increase of the membrane thickness towards day 30. However, no statistically significant differences were detected over the duration of the study (day 15 = $104.70\% \pm 15.93\%$; day 30 = $110.11\% \pm 15.77\%$; Fig. 6B).

Histomorphometric analysis of CD-68-positive macrophages

At day 3 post-implantation, the macrophage density in the peri-implant area was significantly higher than that of day 15 ($P < 0.1$) and day 30 ($P < 0.1$). There was no statistically significant increase in the density of the macrophages in the implantation bed between day 15 and day 30. A similar trend was observed within the control group, which showed that the number of macrophages decreased significantly from day 3 to 15, (day 3 vs. day 15 ($P < 0.5$); day 3 vs. day 30 ($P < 0.1$)). In contrast, there was no statistically significant difference between days 15 and 30 (data not shown). However, the number of macrophages within the OS group was significantly higher than that of the control group at all time points (day 3 ($P < 0.001$); day 15 ($P < 0.1$); day 30 ($P < 0.001$), Fig. 7B).

Histomorphometric analysis of multinucleated giant cells

At day 3 after implantation, no MNGCs could be detected within the area of implantation. Their presence was first observed at day 15 after implantation. The number of MNGCs at day 15 was highly significant compared to day 3 ($P < 0.001$). Moreover, the majority of the MNGCs was TRAP-negative, and the difference between day 3 and day 15 was statistically significant ($P < 0.01$). The membrane-adherent TRAP-positive MNGCs at day 15 showed no statistical significance when compared between day 3 and day 15. However, at day 30, the total number of MNGCs increased significantly.

Histomorphometric analysis of the implantation bed vascularization

Histomorphometric evaluation of the implantation bed showed that no ingrowth of vessels into the membrane was detected at any time points during the study. The percentage of vascularization in the peri-implantation bed increased steadily over the course of the study. At day 3 after implantation, the percentage of vascularization was comparable to that of the control group. At day 15 post-implantation, there was no statistically significant increase in the vascularization percentage compared to day 3. In addition, no statistically significant difference was detected between the test group and the control group. However, at day 30, the percentage of vascularization was significantly higher in comparison to day 3 ($P < 0.0001$) and day 15 ($P < 0.001$), respectively. At this time point, the vascularization percentage in the test group was significantly higher than that in the control group ($P < 0.05$). Similarly, the percentage of vascularization increased gradually in the sham-operated groups as well (Fig. 6C).

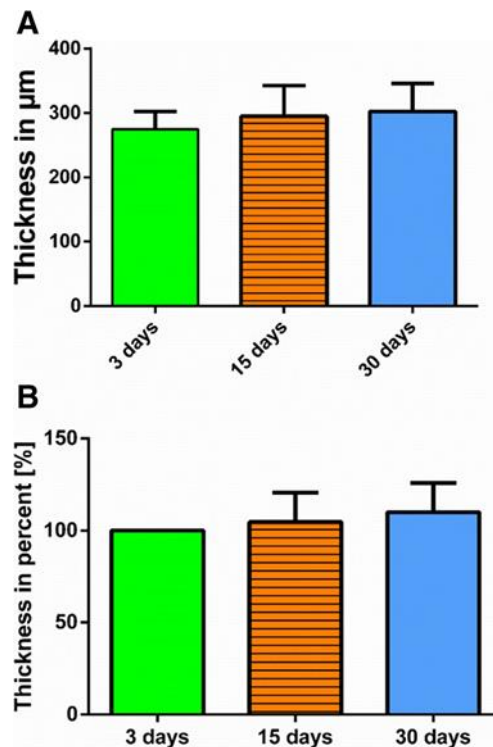


Figure 6. (A) Illustration of the histomorphometric analysis of the membrane thickness in micrometers. (B) Illustration of the histomorphometric analysis of the membrane thickness as a percentage relative to day 3

The number of vessels detected per square millimeter at day 3 was significantly higher than that of the control group ($P < 0.01$). Comparing the values at day 15 to day 3, no statistically significant difference between the test groups was found. However, at day 15, the value in the test group was significantly higher than that of the control group ($P < 0.01$). Moreover, at day 30 post-implantation, there was a marked increase in the number of vessels per square millimeter. This value was highly statistically significant compared to both day 3 and day 15 ($P < 0.0001$). At

this time point, the difference in vessel number per square millimeter was also highly significant compared to the control group ($P < 0.0001$) (Fig. 7D).

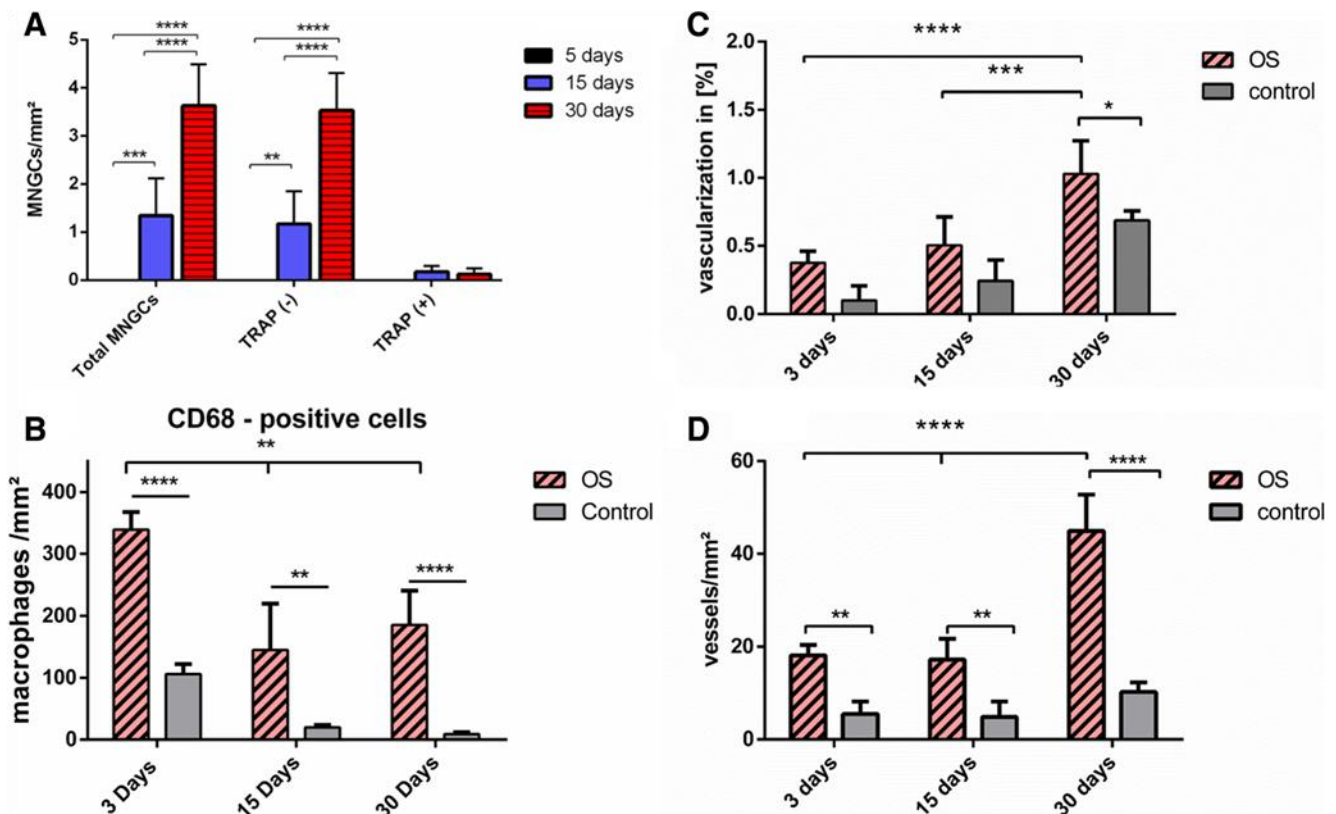


Figure 7. (A) Comparative graphical presentation of the histomorphometric statistical analysis over the study period. Values are illustrated as means and SD. a The number of total multinucleated giant cells (MNGCs) and TRAP-positive and TRAP-negative MGCSs per square millimeter. (B) The total number of macrophages (CD-68-positive cells) millimeter. b The total number of macrophages (CD-68-positive cells) per square millimeter. (C) The vascularization rate over the study time in the OS test group and the control group. The vessel area was calculated as a percentage of the total examined area. (D) The number of vessels per square millimeter in the OS test group and the control group. * = $P < 0.05$, ** = $P < 0.1$, *** = $P < 0.01$, and **** = $P < 0.001$

Discussions

The present study evaluated a collagen membrane reinforced using a ribose cross-linking technique. The aim of the study was to analyze cellular permeability of this biomaterial *ex vivo* and its barrier capacity *in vivo*. Special interest was directed to the cellular reaction towards this biomaterial in terms of the induced cell types and vascularization and degradation pattern compared to the control sham operation group, which imitated the physiological wound healing process.

In the *ex vivo* part, the focus was placed on evaluating the cellular permeability of the biomaterial. Looking at the clinical scenario, after biomaterial application, the membrane first comes in contact with the blood. Therefore, injectable platelet rich fibrin (iPRF), which is a blood concentrate system derived from centrifuged human peripheral blood, was chosen for this examination. I-PRF can be considered a cell suspension containing cells that are involved in

wound healing, such as platelets and leukocytes.²⁹ In this context, the pattern of interaction with iPRF might provide several hints concerning the initial cellular interactions with the biomaterial. The results of the *ex vivo* part showed that OS was occlusive to the cells and fibrin of the iPRF and prevented cellular penetration into the membrane body. These results underline the impenetrability of OS to soluble plasma and proteins, such as the fluid fibrin.

The *in vivo* study focused on the barrier capacity of OS over 30 days and the induced cells in comparison to the cells involved in wound healing of the control group. *In vivo* histological analysis revealed no cellular penetration of the membrane at any time point. In short, both *ex vivo* human cells and *in vivo* murine inflammatory cells were not detected within the membrane. This comparison between the *ex vivo* and *in vivo* studies is noteworthy, as it was demonstrated in this study that it is possible to determine the barrier capacity and to obtain clues regarding the cellular response of biomaterials by using a human-derived cell-rich blood concentrate, iPRF, to reach results similar to those obtained by *in vivo* animal experiments. However, further applications of this method are necessary to evaluate the potential of iPRF to serve as an alternative to *in vivo* animal experimentation to assess immediate and early tissue reactions towards biomaterials.

Histological analysis of the cellular reaction showed that the membrane induced an initial mononuclear cell-based reaction at day 3. At this time point, a large number of CD-68 positive cells, macrophages, were detected within the implantation bed. Thus, at the mid-term evaluation time point, day 15, a course change in the inflammatory pattern was observed. During this time, the number of CD-68-positive cells significantly decreased, coincident with the appearance of multinucleated giant cells (MNGCs). The trend of the CD-68 accumulation was similar to the control group wound healing. However, OS induced significantly higher numbers of CD68 cells at all time points. In addition, no MNGCs were found in the control group at any time point. This significant reduction in the number of CD-68 cells towards days 15 and 30 in the OS group might be related to the physiological presence of macrophages in an increased number during the initial phase of the wound healing and their physiological persistence period within the wounded site, as was the case in the control group.¹⁰ However, the high number of CD-68-positive cells within the OS group in comparison to the control group showed a higher rate of inflammation due to the biomaterial, which might have led to the persistence of a specific type of macrophages that is not only involved in wound healing but also in so-called “frustrated phagocytosis”,^{30, 31} a process of foreign body giant cell formation in which macrophages fuse to form MNGCs after their efforts to phagocytize the implanted biomaterial proved futile. From day 15 to day 30, the number of CD-68-positive cells showed no significant difference, but the number of MNGCs significantly increased. It might be deduced that newly recruited

macrophages progressively fused to form MNGCs as the collagen biomaterial continued to persist in the implantation region. In this context, the observed cellular response also might be partly due to the surface topography of OS, as the surface properties of biomaterials influence the type of proteins that adhere to the biomaterial surfaces.¹³ This impacts the adhesion and subsequent polarization of macrophages downstream, the amount and types of cytokines they secrete, and, eventually the fusion of these macrophages into MNGCs.^{32, 33}

The material-adherent MNGCs were mostly TRAP-negative. Only single TRAP-positive MNGCs were located within the implantation region, and their numbers displayed no statistically significant increase over the study period. The presence of MNGCs within the implantation bed indicated a foreign body reaction towards the evaluated membrane,³¹ although the role of biomaterial-related MNGCs is still mostly unexplored.

The aforementioned significant increase in the total number of MNGCs between day 3, day 15, and day 30 also contributed to a significant rise in implantation bed vascularization between the analyzed time points. The MNGCs might have contributed to the increase in implantation bed vascularization, since it is known that MNGCs secrete vascular endothelial growth factor, a main protagonist of neoangiogenesis.^{12, 34} These findings verify the present results, which highlight the correlation between the enhanced vascularization and the increase in the number of MNGCs within the implantation bed of collagen-based biomaterials. Taken together, the significant increase in the number of MNGCs and the significant rise in implantation bed vascularization over the course of the study are indicative of a foreign body reaction.

Interestingly, recent studies have shown that the presence of MNGCs within the implantation bed of the non-crosslinked collagen membrane led to its disintegration by premature connective tissue ingrowth and eventual membrane breakdown. In these studies, the correlation between the increased number of MNGCs and the enhanced implantation bed vascularization bears resemblance to our current findings.^{13, 35} Although MNGCs boast enhanced oxidative and phagocytic capabilities compared to macrophages alone,^{36, 37} the significant increase in the vascularization and number of MNGCs in the present study did not alter the integrity of OS over 30 days. In contrast, the membrane remained fully intact, without exhibiting any signs of cellular penetration, degradation, or membrane breakdown over the observation period of 30 days. Moreover, as OS is derived from porcine tendons, it is different from the other membranes investigated earlier by our study group, which are either processed from the porcine dermis and/or pericardium.¹³⁻¹⁵ In this context, the quality and the harvesting compartment of the used collagen might play a crucial role in its degradation pattern and therefore its barrier function.

Other studies conducted by our group have shown that several biomaterials induce a full physiological reaction without the formation of MNGCs, such as a non-cross-linked gamma-sterilized collagen membrane that maintained its structure over a period of 60 days. It underwent a slow and controlled integration by inducing a mere mononuclear reaction that was similar to the wound healing physiological reaction that was observed in the control group of the present study. Moreover, these mononuclear cells were accompanied by a mild vascularization. This membrane elicited a physiological mononuclear reaction and mild vascularization pattern. The integration of the membrane was achieved by allowing the host cells to slowly migrate into the membrane scaffold while preserving the function, structure, and the functional barrier of the membrane.¹³

Despite the formation of MNGCs, in an *in vivo* study in a dog model, OS was used to cover critical size defects within the jaw after tooth extraction. After 25 weeks, OS showed signs of ossification and led to enhanced bone regeneration compared to sham OP.³⁸ The manufacturing technique of OS also makes it highly interesting, as the collagen fibrils are reconstituted *de novo* from extracted monomeric collagen, whereas conventional membranes are assembled from residual *in situ* collagen after the removal of all immunogenic components from the donor tissue. Another distinct characteristic of OS is the incorporation of ribose to cross-link the collagen fibrils by a patented glycation process, GLYMATRIX™.²¹ In a way, OS simulates glycation by glucose, a well-documented occurrence in aging tissue and diabetes, which grants collagen fibers resistance to degradation by collagenase.^{39, 40}

In comparison, other cross-linking methods, such as chemical cross-linking with glutaraldehyde, evoked a more aggressive inflammatory reaction.⁴¹ In addition, clinical human studies have shown that even when exposed to the oral environment, OS sustained GBR and GTR functions compared.^{18, 42} Additionally, a case series in which OS was applied for GBR in implant-related bony defects showed that 25–29 weeks after primary healing, new bone formation was observed in close proximity to the OS showing partial signs of ossification.⁴³

The actual results in OS resemble the cellular reaction observed with e-PTFE, a non-resorbable membrane that displayed a similar inflammatory pattern and cellular reaction to the currently evaluated membrane OS. In brief, e-PTFE elicited an initial mononuclear cell-based reaction, which was followed by the formation of MNGCs. e-PTFE, which served as a *bona fide* physical barrier, prevented cellular infiltration for an investigation period of 60 days. Accordingly, the e-PTFE membrane was encapsulated within a vessel- and MNGC-rich connective tissue after 60 days.⁷ No encapsulation could be detected at the latest time point of this study. Nevertheless, the limited evaluation period of 30 days is likely insufficient to evaluate whether the membrane will ultimately undergo encapsulation. Therefore, further long-term

studies are needed to assess to what extent the presence of MNGCs within the implantation bed of this specific cross-linked biomaterial might influence the regeneration process, which is thought to be guided by OS. Additionally, one limitation of the *in vivo* part of this study is analyzing only sugar-based without PRF. Thereby, this study cannot make any statement about the *in vivo* cellular reaction to OS-iPRF combination. The implantation of iPRF in small animals would require the use of severe combined immunodeficiency (SCID) mice to avoid any immune reaction to the implanted human cells. Ongoing research is towards understanding the *in vivo* cellular reaction to PRF and its combination with different biomaterials. This application might be a tool to modulate the cellular reaction towards biomaterials by means of pre-loading with iPRF in advance.

Conclusions

The present study evaluated, the permeability and barrier capacity of a ribose cross-linked collagen membrane *ex vivo* as well as *in vivo*, with specific respect to the induced cell types. *Ex vivo*, the membrane was impermeable to human cells derived from peripheral blood. *In vivo*, the membrane showed a stable structure and allowed no cellular penetration over 30 days. The *in vivo* cellular reaction was initiated by mononuclear cells, which progressed to the formation of multinucleated giant cells (MNGCs) from day 15 onwards. Over the course of the experiment, a significant increase in the number of MNGCs was associated with a significant rise in implantation bed vascularization. This is indicative of a foreign body reaction. However, no breakdown was observed at any time point. The data gathered prove that ribose cross linking enhanced the barrier functionality of the collagen membranes. On these grounds, further long-term studies are necessary to investigate the degradation pattern of this specific cross-linked biomaterial.

Acknowledgements

The authors would like to thank Mrs. Verena Hoffmann for her excellent technical assistance. This work was partially funded by Marie Curie Actions under EU FP7 Initial Training Network SNAL 608184.

References

1. Bottino MC, Thomas V, Schmidt G, Vohra YK, Chu T-MG, Kowolik MJ, Janowski GM (2012) Recent advances in the development of GTR/GBR membranes for periodontal

- regeneration—a materials perspective. *Dent Mater* 28(7):703–721. <https://doi.org/10.1016/j.dental.2012.04.022>
2. Cen L, Liu W, Cui L, Zhang W, Cao Y (2008) Collagen tissue engineering: development of novel biomaterials and applications. *Pediatr Res* 63(5):492–496. <https://doi.org/10.1203/PDR.0b013e31816c5bc3>
 3. Dahlin C, Linde A, Gottlow J, Nyman S (1988) Healing of bone defects by guided tissue regeneration. *Plast Reconstr Surg* 81(5): 672–676. <https://doi.org/10.1097/00006534-198805000-00004>
 4. Patino MG, Neiders ME, Andreana S, Noble B, Cohen RE (2002) Collagen as an implantable material in medicine and dentistry. *Research* 220
 5. Wang H-L, Boyapati L (2006) BPASS^ principles for predictable bone regeneration. *Implant Dent* 15:8–17. <https://doi.org/10.1097/01.id.0000204762.39826.0f>
 6. Buser D, Dula K, Hirt HP, Schenk RK (1996) Lateral ridge augmentation using autografts and barrier membranes: a clinical study with 40 partially edentulous patients. *J Oral Maxillofac Surg* 54: 420–432 3
 7. Ghanaati S (2012) Non-cross-linked porcine-based collagen I-III membranes do not require high vascularization rates for their integration within the implantation bed: a paradigm shift. *Acta Biomater* 8(8):3061–3072. <https://doi.org/10.1016/j.actbio.2012.04.041>
 8. Sheikh Z, Qureshi J, Alshahrani AM, Nassar H, Ikeda Y, Glogauer M, Ganss B (2016) Collagen based barrier membranes for periodontal guided bone regeneration applications. *Odontology*. <https://doi.org/10.1007/s10266-016-0267-0>
 9. Bunyaratavej P, Wang HL (2001) Collagen membranes: a review. *J Periodontol* 72(2):215–229. <https://doi.org/10.1902/jop.2001.72.2.215>
 10. Gurtner G, Werner S, Barrandon Y, Longaker M (2008) Wound repair and regeneration. *Nature* 453(7193):314–321. <https://doi.org/10.1038/nature07039>
 11. Shevach EM, Rosenthal AS (1973) Function of macrophages in antigen recognition by guinea pig T lymphocytes. II. Role of the macrophage in the regulation of genetic control of the immune response. *J Exp Med* 138:1213–1229 <http://www.ncbi.nlm.nih.gov/pubmed/4126770>. Accessed 20 March 2017
 12. Moens S, Goveia J, Stapor PC, Cantelmo AR, Carmeliet P (2014) The multifaceted activity of VEGF in angiogenesis—implications for therapy responses. *Cytokine Growth Factor Rev* 25(4):473–482. <https://doi.org/10.1016/j.cytogfr.2014.07.009>
 13. Ghanaati S, Schlee M, Webber MJ, Willershausen I, Barbeck M, Balic E, Görlach C, Stupp SI, Sader RA, Kirkpatrick CJ, Ghanaati S (2011) Evaluation of the tissue reaction to a new

- bilayered collagen matrix *in vivo* and its translation to the clinic. *Biomed Mater* 6(1): 15010–15012. <https://doi.org/10.1088/1748-6041/6/1/015010>
14. Barbeck M, Lorenz J, Kubesch A, Böhm N, Booms P, Choukroun J, Sader R, Kirkpatrick CJ, Ghanaati S (2015) Porcine dermis-derived collagen membranes induce implantation bed vascularization via multinucleated giant cells: a physiological reaction? *J Oral Implantol* 41(6):e238–e251. <https://doi.org/10.1563/aaid-joi-D-1400274>
 15. Barbeck M, Lorenz J, Holthaus MG, Raetscho N, Kubesch A, Booms P, Sader R, Kirkpatrick CJ, Ghanaati S (2015) Porcine dermis and pericardium-based, non-cross-linked materials induce multinucleated giant cells after their *in vivo* implantation: a physiological reaction? *J. Oral Implantol.* 41(6):e267–e281. <https://doi.org/10.1563/aaid-joi-D-14-00155>
 16. Brunel G, Piantoni P, Elharar F, Benqué E, Marin P, Zahedi S (1996) Regeneration of rat calvarial defects using a bioabsorbable membrane technique: influence of collagen cross-linking. *J Periodontol* 67(12):1342–1348. <https://doi.org/10.1902/jop.1996.67.12.1342>
 17. Friedmann A, Strietzel FP, Marezki B, Pitaru S, Bernimoulin J-P (2002) Histological assessment of augmented jaw bone utilizing a new collagen barrier membrane compared to a standard barrier membrane to protect a granular bone substitute material. *Clin Oral Implants Res* 13(6):587–594. <https://doi.org/10.1034/j.1600-0501.2002.130603.x>
 18. Moses O, Pitaru S, Artzi Z, Nemcovsky CE (2005) Healing of dehiscence-type defects in implants placed together with different barrier membranes: a comparative clinical study. *Clin Oral Implants Res* 16(2):210–219. <https://doi.org/10.1111/j.1600-0501.2004.01100.x>
 19. Friedmann A, Gissel K, Soudan M, Kleber B-M, Pitaru S, Dietrich T (2011) Randomized controlled trial on lateral augmentation using two collagen membranes: morphometric results on mineralized tissue compound. *J Clin Periodontol* 38(7):677–685. <https://doi.org/10.1111/j.1600-051X.2011.01738.x>
 20. Rothamel D, Schwarz F, Sager M, Herten M, Sculean A, Becker J (2005) Biodegradation of differently cross-linked collagen membranes: an experimental study in the rat. *Clin Oral Implants Res* 16(3):369–378. <https://doi.org/10.1111/j.1600-0501.2005.01108.x>
 21. OSSIX® PLUS—GLYMATRIX™ Technology in Brief, (n.d.)
OSSIX® PLUS Instructions for Use IFU-MKT-OSP-016 ver OSSIX® PLUS The Resorbable Collagen Membrane Instructions for Use for OSSIX® PLUS, (2016)

22. Ghanaati S, Booms P, Orłowska A, Kubesch A, Lorenz J, Rutkowski J, Landes C, Sader R, Kirkpatrick C, Choukroun J (2014) Advanced platelet-rich fibrin: a new concept for cell-based tissue engineering by means of inflammatory cells. *J Oral Implantol* 40(6):679–689. <https://doi.org/10.1563/aaid-joi-D-14-00138>
23. Choukroun J, Ghanaati S (2017) Reduction of relative centrifugation force within injectable platelet-rich-fibrin (PRF) concentrates advances patients' own inflammatory cells, platelets and growth factors: the first introduction to the low speed centrifugation concept. *Eur J Trauma Emerg Surg*. <https://doi.org/10.1007/s00068017-0767-9>
24. Miron RJ, Fujioka-Kobayashi M, Hernandez M, Kandalam U, Zhang Y, Ghanaati S, Choukroun J (2017) Injectable platelet rich fibrin (i-PRF): opportunities in regenerative dentistry? *Clin Oral Investig*. <https://doi.org/10.1007/s00784-017-2063-9>
25. Ghanaati S, Kirkpatrick C, Kubesch A, Lorenz J, Sader R, Udeabor S, Barbeck M, Choukroun J (2014) Induction of multinucleated giant cells in response to small sized bovine bone substitute (BioOss TM) results in an enhanced early implantation bed vascularization. *Ann Maxillofac Surg* 4:150. <https://doi.org/10.4103/2231-0746.147106>
26. Ghanaati S, Orth C, Unger RE, Barbeck M, Webber MJ, Motta A, Migliaresi C, James Kirkpatrick C (2010) Fine-tuning scaffolds for tissue regeneration: effects of formic acid processing on tissue reaction to silk fibroin. *J Tissue Eng Regen Med* 4:464–472. <https://doi.org/10.1002/term.257>
27. Serrano C, García-Fernández L, Fernández-Blázquez JP, Barbeck M, Ghanaati S, Unger R, Kirkpatrick J, Arzt E, Funk L, Turón P, del Campo A (2015) Nanostructured medical sutures with antibacterial properties. *Biomaterials* 52:291–300. <https://doi.org/10.1016/j.biomaterials.2015.02.039>
28. Choukroun J, Ghanaati S (2016) Reduction of relative centrifugation force within injectable PRF—(platelet-rich-fibrin) concentrates advances patients' own inflammatory cells, platelets and growth factors: first introduction of the low speed centrifugation concept (LSCC), *Eur J Trauma Emerg Surg*. accepted
29. MacLauchlan S, Skokos EA, Meznarich N, Zhu DH, Raouf S, Shipley JM, Senior RM, Bornstein P, Kyriakides TR (2009) Macrophage fusion, giant cell formation, and the foreign body response require matrix metalloproteinase 9. *J Leukoc Biol* 85(4): 617–626. <https://doi.org/10.1189/jlb.1008588>
30. Anderson JM, Rodriguez A, Chang DT (2008) Foreign body reaction to biomaterials. *Semin Immunol* 20(2):86–100. <https://doi.org/10.1016/j.smim.2007.11.004>

31. McNally AK, Anderson JM (2011) Macrophage fusion and multinucleated giant cells of inflammation. *Adv Exp Med Biol* 713:97–111. https://doi.org/10.1007/978-94-007-0763-4_7
32. McNally AK, Anderson JM (2003) Foreign body-type multinucleated giant cell formation is potently induced by alpha-tocopherol and prevented by the diacylglycerol kinase inhibitor R59022. *Am J Pathol* 163(3):1147–1156. <http://www.ncbi.nlm.nih.gov/pubmed/12937156>. Accessed 27 Jan 2017. [https://doi.org/10.1016/S00029440\(10\)63474-8](https://doi.org/10.1016/S00029440(10)63474-8)
33. Ghanaati S, Barbeck M, Orth C, Willershausen I, Thimm BW, Hoffmann C, Rasic A, Sader RA, Unger RE, Peters F, Kirkpatrick CJ (2010) Influence of β -tricalcium phosphate granule size and morphology on tissue reaction *in vivo*. *Acta Biomater* 6(12): 4476–4487. <https://doi.org/10.1016/j.actbio.2010.07.006>
34. Lorenz J, Kubesch A, Korzinskas T, Barbeck M, Landes C, Sader RA, Kirkpatrick CJ, Ghanaati S (2015) TRAP-positive multinucleated giant cells are foreign body giant cells rather than osteoclasts: results from a split-mouth study in humans. *J Oral Implantol* 41(6):e257–e266. <https://doi.org/10.1563/AAID-JOI-D-14-00273>
35. McNally AK, Anderson JM (2005) Multinucleated giant cell formation exhibits features of phagocytosis with participation of the endoplasmic reticulum. *Exp Mol Pathol* 79(2):126–135. <https://doi.org/10.1016/j.yexmp.2005.06.008>
36. Enelow RI, Sullivan GW, Carper HT, Mandell GL (1992) Cytokine-induced human multinucleated giant cells have enhanced candidacidal activity and oxidative capacity compared with macrophages. *J Infect Dis* 166(3):664–668. <https://doi.org/10.1093/infdis/166.3.664>
37. Zubery Y, Goldlust A, Alves A, Nir E (2007) Ossification of a novel cross-linked porcine collagen barrier in guided bone regeneration in dogs. *J Periodontol* 78(1):112–121. <https://doi.org/10.1902/jop.2007.060055>
38. Gautieri A, Redaelli A, Buehler MJ, Vesentini S (2014) Age- and diabetes-related nonenzymatic crosslinks in collagen fibrils: candidate amino acids involved in advanced glycation end-products. *Matrix Biol* 34:89–95. <https://doi.org/10.1016/j.matbio.2013.09.004>
39. Bourne JW, Lippell JM, Torzilli PA (2014) Glycation cross-linking induced mechanical-enzymatic cleavage of microscale tendon fibers. *Matrix Biol* 34:179–184. <https://doi.org/10.1016/j.matbio.2013.11.005>
40. Rothamel D, Schwarz F, Sculean A, Herten M, Scherbaum W, Becker J (2004) Biocompatibility of various collagen membranes in cultures of human PDL fibroblasts

- and human osteoblast-like cells. *Clin Oral Implants Res* 15(4):443–449.
<https://doi.org/10.1111/j.1600-0501.2004.01039.x>
41. Klinger A, Asad R, Shapira L, Zubery Y (2010) *In vivo* degradation of collagen barrier membranes exposed to the oral cavity. *Clin Oral Implants Res* 21(8):873–876.
<https://doi.org/10.1111/j.1600-0501.2010.01921.x>
42. Zubery Y, Nir E, Goldlust A (2008) Ossification of a collagen membrane cross-linked by sugar: a human case series. *J Periodontol* 79(6):1101–1107.
<https://doi.org/10.1902/jop.2008.070421>

3.2.3. *In vivo* Implantation of a Bovine-Derived Collagen Membrane Leads to Changes in the Physiological Cellular Pattern of Wound Healing by the Induction of Multinucleated Giant Cells: An Adverse Reaction?

Frontiers in Bioengineering and Biotechnology, **2018**, 6(8).

Al-Maawi, S.^a, Vorakulpipat, C.^a, **Orłowska, A.**^a, Zrnc, T. A.^b, Sader, R. A.^a, Kirkpatrick, C. J.^a, & Ghanaati, S.^a.

^a Department for Oral, Cranio-Maxillofacial and Facial Plastic Surgery, Frankfurt Orofacial Regenerative Medicine Lab, University Hospital Frankfurt Goethe University, Frankfurt am Main, Germany

^b Department of Oral and Maxillofacial Surgery, Medical University of Graz, Graz, Austria

Abstract

The present study evaluated the tissue response toward a resorbable collagen membrane derived from bovine achilles tendon (test group) in comparison to physiological wound healing (control group). After subcutaneous implantation in Wistar rats over 30 days, histochemical and immunohistochemical methods elucidated the cellular inflammatory response, vascularization pattern, membrane protein and cell absorbance capacity. After 30 days, the test-group induced two different inflammatory patterns. On the membrane surface, multinucleated giant cells (MNGCs) were formed after the accumulation of CD-68-positive cells (macrophages), whereas only mononuclear cells (MNCs) were found within the membrane central region. Peri-implant vascularization was significantly enhanced after the formation of MNGCs. No vessels were found within the central region of the membrane. Physiological wound healing revealed no MNGCs at any time point. These dynamic changes in the cellular reaction and vascularization within the test-group are related typical indications of a foreign body reaction. Due to the membrane-specific porosity, mononuclear cells migrated into the central region, and the membrane maintained its integrity over 30 days by showing no breakdown or disintegration. The *ex vivo* investigation analyzed the interaction between the membrane and a blood concentrate system, liquid platelet-rich fibrin (liquid PRF), derived from human peripheral blood and consisting of platelets, leukocytes and fibrin. PRF penetrated the membrane after just 15 min. The data question the role of biomaterial-induced MNGCs as a pathological reaction and whether this is acceptable to trigger vascularization or should be considered as an adverse reaction. Therefore, further pre-clinical and clinical studies are needed to identify the types of MNGCs that are induced by clinically approved biomaterials.

Introduction

The biomaterial physicochemical properties play a major role in induced cellular reactions (Ghanaati et al., 2012). Synthetic biomaterials are precisely synthesized under controlled conditions to produce a specific biomaterial porosity, thickness and surface topography (Moore et al., 2001). In contrast, natural biomaterials e.g., allogeneic and xenogeneic biomaterials are mostly derived from a particular region of the donor body without *de novo* synthesis (Ghanaati et al., 2011). Thereby, these materials undergo strict processing using different chemical and physical methods to reach an adequate state of purification and deactivation of potential pathogens and donor-cells, which may also affect the native structure (Ghanaati et al., 2014). In this sense, the resultant structure and surface characteristics of natural biomaterials depend on

the donor tissues and the processing techniques used for their purification (Al-Maawi et al., 2017).

The type of the triggered cellular reaction in response to a biomaterial is imperative for the success of tissue engineering strategies (Dollinger et al., 2018). After biomaterial application, interaction with the surrounding host tissues and cells leads to the induction of a specific cellular inflammatory reaction that may characterize the biomaterial regeneration capacity (Ghanaati, 2012). In a complex process, the cellular reaction toward the implanted biomaterial occurs in concert with wound healing. Initially, the biomaterial surface capacity to absorb specific proteins such as fibrin is a trend-setting property for the subsequent cellular reactions and was described to be involved in the foreign body reaction (Anderson et al., 2008). The formation of a provisional matrix on the interface between the implanted biomaterial and the host tissue is the initial nexus for the host cells to interact with the biomaterial (Anderson et al., 2008). Different *in vitro* and *in vivo* models are utilized to understand the patterns of inflammatory responses to biomaterials and assess their biocompatibility and potential adverse reactions.

In the last decade, our group has presented a systematic series of *in vivo* investigations to analyze the cellular reactions toward different biomaterials using a subcutaneous implantation model (Al-Maawi et al., 2017). Basically, two types of cellular reactions were observed. A physiological reaction that includes the induction of solely mononuclear cells was observed in the case of a non-cross-linked bilayer collagen membrane leading to its integration within the host tissue (Ghanaati, 2012; Al-Maawi et al., 2017). In this *in vivo* study, the porcine-derived biomaterial maintained its structure over 60 days and showed the capacity to serve as a functional barrier without undergoing a premature breakdown or degradation. Moreover, transmembraneous vascularization was not necessary for the integration of this collagen membrane (Ghanaati, 2012). A similar reaction was detected within the implantation bed of a non-cross-linked collagen matrix made from porcine skin and peritoneum (Ghanaati et al., 2011). This biomaterial evoked only mononuclear cells over 60 days and maintained its native structure, which led to its integration within the implantation region. In addition, these findings were successfully translated to the clinic, showing the same mononuclear cell-based reaction (Ghanaati et al., 2011).

The second type of tissue response included the formation of multinucleated giant cells (MNGCs) as a pathological cellular reaction toward the biomaterials (Al-Maawi et al., 2017). The presence of MNGCs within the subcutaneous implantation bed of two non-cross-linked, collagen-based biomaterials of different thicknesses led to their disintegration in terms of premature loss of their native structure as well as an influx of the host connective tissue into the membrane after 30 days, leading to biomaterial disintegration. Thus, the cellular reaction

toward biomaterials depends on their physicochemical properties (Barbeck et al., 2015; Al-Maawi et al., 2017). The role of biomaterial induced MNGCs within the regeneration process is not yet fully understood. Different aspects are discussed in the literature to whether these cells may have any contribution to the regeneration process by expressing possible anti-inflammatory mediators (Miron and Bosshardt, 2018). On the other hand, a literature review has shown that biomaterial induced MNGCs actually express similar proinflammatory pattern as pathological MNGCs known from inflammatory diseases such as tuberculosis (Al-Maawi et al., 2017).

In addition to the manufacturing techniques, further methods are used to enhance the stability of collagen-based biomaterials including different types of cross-linking. However, cross linking techniques, especially chemical cross linking was shown to induce a high foreign body reaction (Rothamel et al., 2005). To avoid this, clinical techniques were introduced to provide the membrane higher biomechanical stability without cross linking. In this sense, the collagen double layer technique was introduced for enhanced membrane stability during guided bone regeneration (Abou Fadel et al., 2018). However, degradable biomaterials cannot be considered as a physically occlusive barrier as it is the case for nonresorbable biomaterials (Ghanaati, 2012). Recent studies have shown that resorbable biomaterials serve rather as a functional barrier for a defined time period and get then integrated into the implantation region (Ghanaati et al., 2011; Ghanaati, 2012).

Further developments have focused on harvesting collagen from different animal groups and compartments. Thereby, a novel collagen biomaterial with a specific structural architecture was derived from bovine achilles tendon. The aim of the present study was to analyze the *in vivo* cellular response toward this biomaterial. A subcutaneous implantation model in Wistar rats was used to analyze the cellular reaction in comparison to physiological wound healing without a biomaterial over 30 days. Special focus was placed on the inflammatory pattern, vascularization and regenerative capacity. A liquid platelet-rich fibrin (liquid PRF), which is a blood concentrate system derived from centrifuged human peripheral blood components including fibrin, leukocytes and platelets, was used to examine the protein absorption capacity and interaction with human cells as a novel *ex vivo* assessment system.

Experimental

SYMBIOS® Collagen Membrane SR

SYMBIOS R Collagen Membrane SR (SB, Dentsply Implants, Germany) is a slowly resorbing membrane matrix engineered from highly purified type I collagen fibers derived from bovine

achilles tendon. According to the manufacturer, the harvested collagen underwent a purification and processing procedure including the use of sodium hydroxide for the inactivation of pathogens such as those associated with bovine spongiform encephalopathy (BSE). The processing and purification methods met the European and international standards for animal tissue sourcing.

***Ex vivo* Study**

The *ex vivo* part of the study focused on the histological analysis of the initial biomaterial-cell interaction to assess the membrane capacity to absorb human proteins and interact with mononuclear cells from the peripheral blood.

Liquid Platelet-Rich Fibrin (Liquid PRF) Preparation PRF is a blood concentrate system derived from centrifuged human peripheral blood. This concentrate contains a high number of platelets and leukocytes in addition to fibrinogen and plasma proteins. Liquid PRF was chosen to mimic the initial interaction between the biomaterial and the host tissue after biomaterial application.

Three healthy volunteers between 20 and 60 years old donated blood for this study. All volunteers gave written informed consent beforehand. The liquid PRF preparation was performed as previously published (Chia-Lai et al., 2017; Wend et al., 2017). Peripheral blood was collected using 10ml plastic tubes (orange tubes, PROCESS for PRF, France) and clinically approved butterflies. Two 10-ml tubes per donor were collected and immediately placed in a preprogrammed centrifuge (DUOTM, PROCESS for PRF, France). Centrifugation was performed for 8 min at 600 rpm, 44 g. The resultant upper layer (liquid PRF) was collected using a syringe with a needle (BD Microlance™ 3, Germany). Nine biomaterial samples (3 per donor) 10 × 10 mm² in size were placed in a 24-well plate. One milliliter of liquid PRF was added to each biomaterial sample and incubated for 15 min. Thereafter, the samples were fixed in 4% buffered formalin for 24 h for further histological analysis.

***In vivo* Experimental Design: Animal Surgery**

The present *in vivo* protocol was approved by the committee on the Use of Live Animals in Teaching and Research (State, Darmstadt, Hessen Germany). A total number of 32 female 8-week-old Wistar rats were purchased from Charles River Laboratories (Germany) and housed for a week before use at the Animal Welfare Office and Central Facility (Goethe University, Frankfurt, Germany). The animals were randomly distributed into 2 groups (n = 16 animals per group). The surgical procedure followed standardized methods as previously described

(Ghanaati, 2012). In brief, after intraperitoneal anesthesia (10 ml of ketamine (50 mg /ml) with 1.6 ml of 2% xylazine), the first group (n = 4 per time point) of animals was placed under anesthesia, and a sterile collagen membrane (SYMBIOS R Collagen Membrane SR, DentsplyImplants, Germany) was implanted under strict sterile conditions into a subcutaneous pocket within the rostral subscapular region. The second group was sham operated (n = 4 per time point) to analyze the cellular reaction under physiological wound healing. The animals were sacrificed by means of an overdose (ketamine and xylazine 4 times the anesthetic dose). After the evaluation time points at 3, 10, 15, and 30 days post-operation, the biomaterial including the periimplantation region in the first group as well as the sham operated region in the second group were explanted and fixed in 4% buffered formalin for 24 h for further histological preparation.

Tissue Preparation for Histology and Immunohistochemistry

The histological processing and staining procedures were performed as previously described (Ghanaati, 2012; Barbeck et al., 2016). Briefly, the explants were cut into three identical segments, which included the margins and the center of the implantation area. Subsequently, the *ex vivo* and *in vivo* samples were processed using a series of graded alcohol and xylene followed by paraffin embedding. For the histological and immunohistochemical staining, four consecutive 3–4- μm slices from the central segment were cut using a rotation microtome (Rotationsmicrotom RM2255, Leica, Germany). After deparaffinization and rehydration, histochemical staining of the *in vivo* and *ex vivo* samples included Mayer's hematoxylin and eosin (H and E), Azan stain and Masson-Goldner stain. To identify tartrate-resistant acid phosphatase (TRAP) activity of the cells, specific staining was performed for TRAP as previously described (Ghanaati et al., 2013). A Sample from previous (Ghanaati et al., 2010a) study showing TRAP-positive cells in Wistar rats served as a positive control for TRAP-staining (data not shown). Two more slices of the *in vivo* samples were used for further immunohistochemical staining to determine blood vessel density and identify macrophages. Immunohistochemical staining was performed using a Lab Vision™ Autostainer 360-2D instrument (ThermoFisher Scientific, Germany) as previously described (Barbeck et al., 2016). Next, endogenous peroxidase activity was blocked using 4% H_2O_2 in methanol, and endogenous avidin- and biotin-binding proteins were blocked by avidin and biotin blocking solutions (Avidin/Biotin Blocking Kit, Vector Laboratories, USA). The first antibody anti CD-68 (MCA341GA; 1:400; 30 min) for macrophages and Anti-Actin, α -Smooth Muscle (SMA) A5228; 1:1,000; 2 h) for vascular endothelial cells. *Ex vivo* samples were stained using anti CD-61 (Dako; 1:50; 1 h) to

stain platelets. Thereafter, the secondary antibody goat anti-rabbit IgG-B (sc-2040; 1:200, Santa Cruz Biotechnology, USA) was applied. Subsequently, the avidin-biotin-peroxidase complex (ABC, ThermoFisher Scientific, Germany) for CD-68 and the Histostain-Plus IHC Kit including AEC (ThermoFisher Scientific, Germany) for SMA were applied for 30 min and 20 min, respectively. As negative controls, immunological staining in the absence of the primary antibody was performed on 2 control sections. For visualization by light microscopy, the sections used for immunohistochemistry were counterstained with Mayer's hematoxylin.

Qualitative Histological Analysis

Qualitative histopathological evaluation was performed using a Nikon ECLIPSE 80i light microscope (Nikon, Japan). The analysis focused on characterizing of the cellular reactions, inflammatory responses and vascularization. A further aim of the histological analysis was to examine the interaction of the biomaterial with liquid PRF *ex vivo*. Photomicrographs were captured using a camera DS-Fi1 (Nikon, Japan).

Quantitative Histomorphometric Analysis

Quantitative histomorphometric analysis of the stained slides was performed with a light microscope (ECLIPSE 80i; Nikon, Japan) including a motorized scanning stage (ProScan III, Prior, USA) connected to a PC running NIS Elements software (Nikon, Japan). As previously described (Ghanaati, 2012; Barbeck et al., 2015a), images of the total implantation beds (total scans), large images of the sample including the collagen membrane and the peri-implant tissue, were reconstructed automatically by merging 100-130 individual micrographs. To evaluate the mean membrane thickness at each time point, the total scans of the H and E-stained slides were used. Fifteen distinct points along the length of the biomaterial per animal were measured manually using the "annotations and measurements" function of the NIS Elements software (Nikon, Tokyo, Japan). The mean of these measurements per slide was calculated as the absolute membrane thickness in μm . The values obtained from later time points were calculated as a percent, while the membrane thickness at day 3 was defined as 100% to avoid artifacts due to histological preparation. The number of MNGCs as well as CD-68-positive macrophages was counted manually using the "count" tool in NIS Elements on the total scans of the TRAP staining and CD-68 staining, respectively, in each animal. The total number of each cell type was calculated with respect to the total implant area on the slides (cell number/ mm^2) at each time point. The SMA-stained slides were used for evaluation the vascularization pattern. The number and the area (in mm^2) of vessels within the implantation beds were determined by manually

marking the vessels within the digitized scans. Thus, the total number of vessels was calculated in relation to the total area (in vessels/mm²) and as a percentage of the vessel area (as a fraction of the total implant area in %).

Statistical Analysis

The results from the calculated histomorphometrical analysis were evaluated for significant differences at different time points using one-way and two-way analyses of variance (ANOVA). Statistical significance was defined via p-values (*/ $p < 0.05$; **/ $p < 0.01$; ***/ $p < 0.001$ and ****/ $p < 0.0001$) using GraphPad Prism 7 Software (La Jolla, USA). The results are presented as the mean \pm standard deviation, and GraphPad Prism 7 was used to produce charts and complete the statistical analysis.

Results and discussion

***Ex vivo* Histological Analysis**

The interaction between the liquid PRF and the collagen membrane SB was analyzed histologically. The membrane showed a specific structure with differently oriented collagen fibers (Figure 1A). The membrane absorbed PRF, showing a fibrin clot within its porous structure (Figures 1B, C). In addition, leukocytes and platelets were detected within the central region of the membrane (Figures 1D, E).

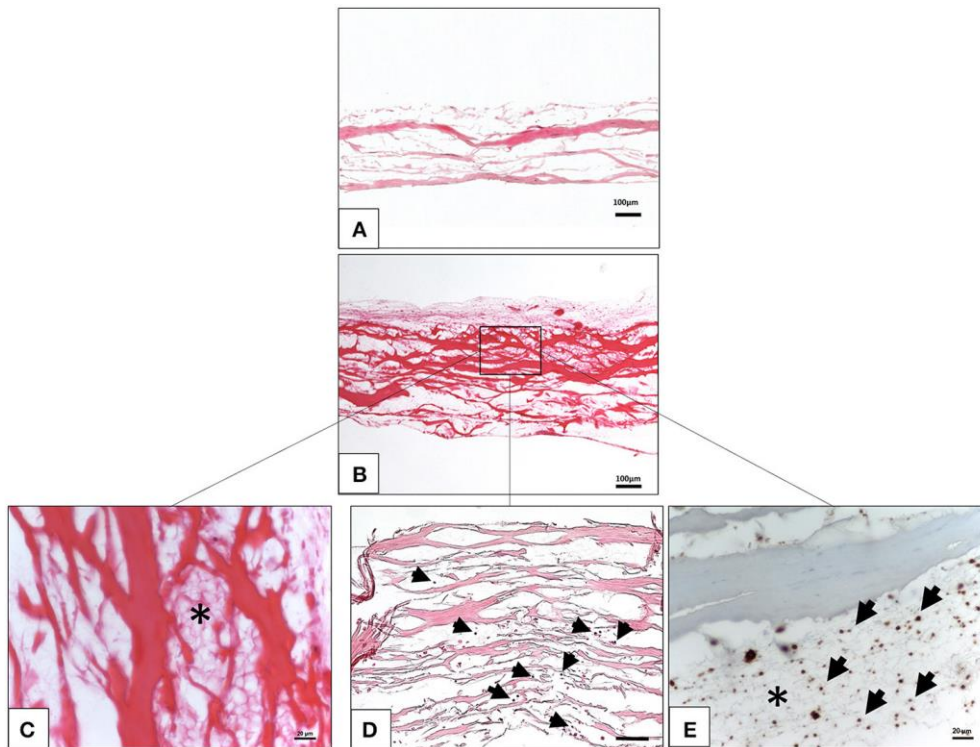


Figure 1. *Ex vivo* interaction between liquid platelet-rich fibrin and the collagen membrane SB. (A) A control of the SB illustrating the membrane-specific porous structure (H and E staining; scale bar = 100µm). (B) Total penetration of leukocytes and platelets from liquid PRF into the SB central region (H and E staining; scale bar = 100µm). (C) High magnification micrograph showing the fibrin network (*) within the SB collagen fibers (H and E staining; scale bar = 20µm). (D) High magnification micrograph showing the leukocytes (black arrows) within the SB collagen fibers (H and E staining; scale bar = 100µm). (E) High magnification micrograph showing the platelets (black arrows) and fibrin network (*) within the SB collagen fibers (anti CD-61 staining; scale bar = 20µm).

***In vivo* Histological and Histomorphometrical Analyses**

All animals survived the implantation period. The wound healing was appropriate in the test group as well as in the sham operated animals. No signs of infection or atypical feeding or sleeping behaviors were observed during the evaluation period.

Qualitative Analysis of the Cellular Reaction Over Time

For the test group, the biomaterial was detected within the implantation region at all-time points. Three days after implantation, the membrane maintained its native structure and integrity and induced mononuclear cells, which were found on the membrane surface (Figures 2A–D). The biomaterial central region was mostly free of cells (Figure 2A).

After 10 days, the biomaterial showed a stable structure. More mononuclear cells were accumulated on both sides of the membrane. Moreover, mononuclear cells started invading the membrane and were found within the pores of the membrane (Figure 2B). CD-68-positive macrophages were accumulated on the biomaterial surface (Figure 4A). At this time point, single

MNGCs were sporadically found within the biomaterial implantation bed and on the biomaterial surface. Most of the MNGCs showed no TRAP activity (data not shown). Additionally, micro vessels were detected in proximity to the biomaterial. However, no vessels were detected within the membrane central region.

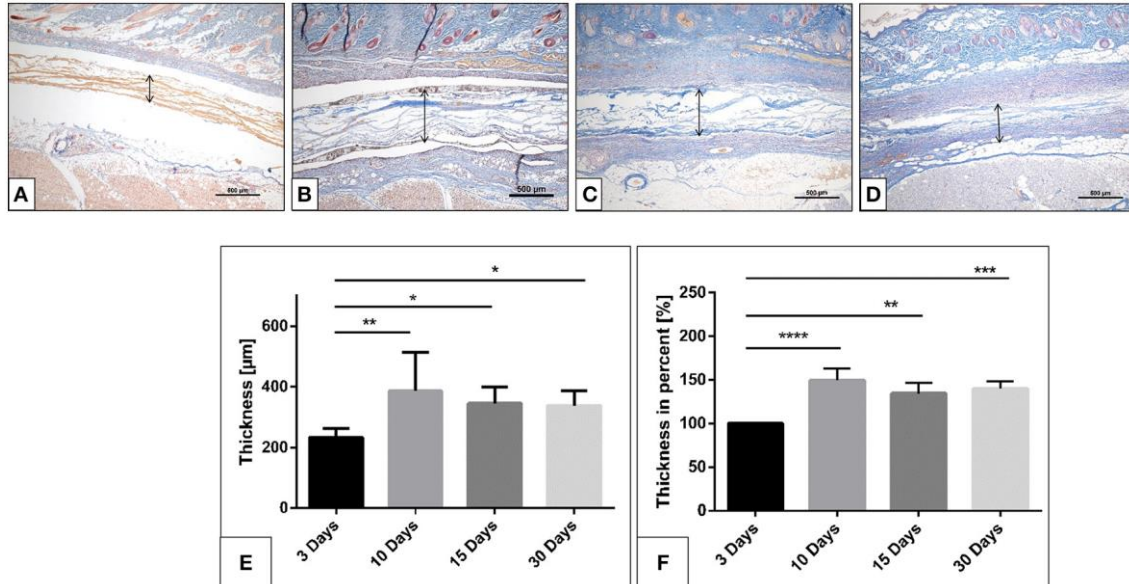


Figure. 2 The collagen membrane SB within the implantation bed over the investigates time points. (A) after 3 days; (B) after 10 days; (C) after 15 days; (D) after 30 days. (Azan staining; x40 magnification; scale bars = 500μm). (E, F) Histomorphometrical image of the membrane thickness and percentage thickness over 30 days (* $p < 0.05$; ** $p < 0.01$; *** $p < 0.001$; and **** $p < 0.0001$).

Fifteen days following implantation, the membrane maintained its integrity and showed stable structure. No signs of breakdown were observed. The membrane was embedded in a cell- and vessel-rich connective tissue. At this time point, more mononuclear cells invaded the membrane and reached its central region. The membrane interfibrillar area contained connective tissue (Figures 3A, B). The number of MNGCs increased remarkably, while fewer CD-68-positive macrophages were found in proximity to the biomaterial (Figure 4B). However, in general, the MNGCs showed no TRAP expression. The implantation bed showed higher vascularization at 15 days than at the previous time point. However, the MNGCs persisted but were not increased in number and were located on the membrane surface. Thus, no infiltration of no vessels were found within the membrane central region (Figures 2D, 3A and B). At 30 days after implantation, the membrane was detectable within the implantation bed, showing a stable volume and sustained integrity. No signs of breakdown or disintegration were revealed. The membrane was embedded in a cell and vessel-rich host connective tissue and allowed the infiltration of mononuclear cells and connective tissue into its central region without losing its native structure (Figure 3D). Similar to the observations at day 10, some CD-68-positive macrophages were observed close to the biomaterial surface (Figure 4C). However, MNGCs within the central region was observed. At this time point, most of the MNGCs showed no TRAP

activity (Figure 3D). The implantation area showed new, well-vascularized connective tissue, while the biomaterial retained its native structure and included the newly formed connective tissue (Figures 2E, 3C and D).

In the control group, the physiological wound healing was uneventful during the observation period. The cellular reaction included only mononuclear cells. No MNGCs were observed at any time point. At day 3, a high number of macrophages (CD-68-positive) was observed within the evaluation area. The number of macrophages decreased progressively toward day 30. A mild vascularization pattern was detected in the healing area with an increasing tendency from day 3 to day 30.

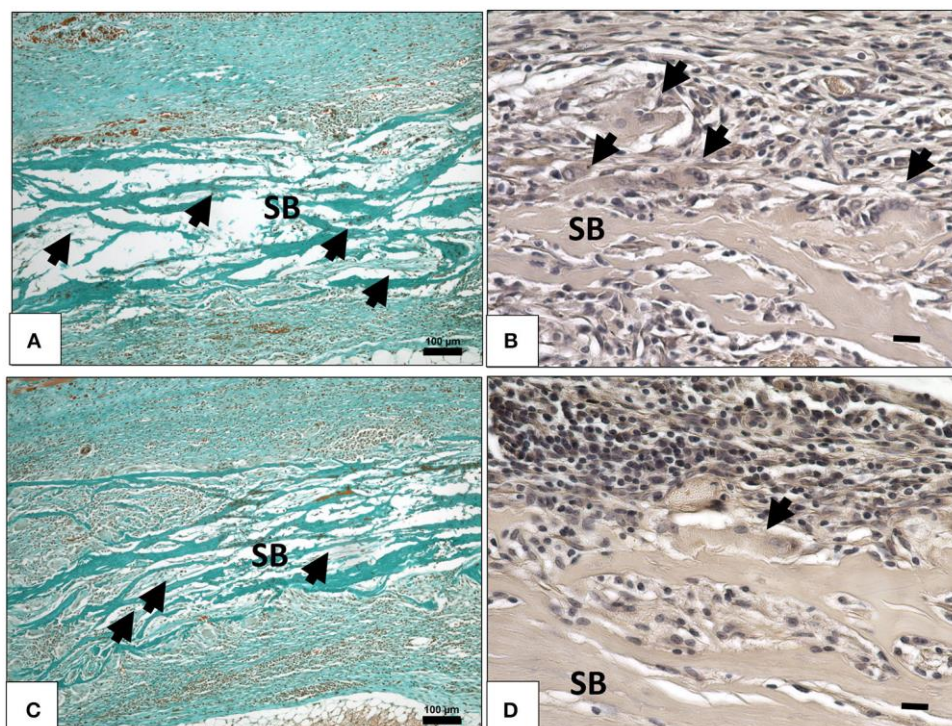


Figure 3. (A) Cellular and connective tissue infiltration (black arrows) of the collagen membrane (SB) on day 15, (Masson Goldner staining; scale bar= 100µm). (B) TRAP- negative MNGCs (black arrows) on the membrane surface (SB) on day 15, (TRAP staining; scale bar = 20µm). (C) Cellular and connective tissue infiltration (black arrows) of the collagen membrane (SB) on day 30, (Masson Goldner staining; scale bar = 100µm). (D) TRAP-negative MNGCs (black arrows) on the membrane surface (SB) on day 30, (TRAP staining; scale bar = 20µm).

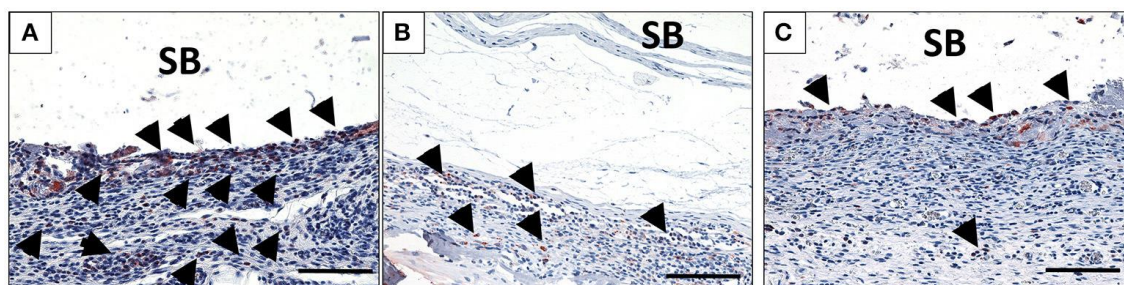


Figure 4. The behavior of macrophage (black arrows) accumulation on days 10 (A), 15 (B), and 30 (C) on the surface of the biomaterial (CD-68) immunohistochemical staining; scale bar =100µm).

Quantitative Histomorphometrical Analysis

Evaluation of the Membrane Thickness Over Time

The membrane maintained its stable structure over the observation time period. The histomorphometrical analysis showed that on day 3 the membrane exhibited a mean thickness of $233.5 \pm 29.4 \mu\text{m}$. The mean thickness increased toward day 10 ($366.4 \pm 104.8 \mu\text{m}$). The membrane thickness at day 15 ($345.3 \pm 54.2 \mu\text{m}$) was comparable to that at day 10. Thus, no statistically significant difference was detected between day 15 and day

10. Finally, a similar value was measured on day 30 ($325.7 \pm 51.3 \mu\text{m}$). The statistical analysis showed a significant difference in the membrane thickness on day 3 and those measured on days 10 ($**p < 0.01$), 15 ($*p < 0.05$) and 30 ($*p < 0.05$). However, no statistically significant differences were found among the thicknesses measured on days 10, 15, and 30 (Figure 2C).

The analysis of the percent thickness in relation to day 3 showed a similar pattern. Thereby, the mean percent thickness increased after 10 days ($149.2 \pm 13.5\%$). The membrane maintained the percent thickness on days 15 ($134.5 \pm 12.1\%$) and 30 ($139.9 \pm 8.2\%$). Statistically significant differences were detected between the measured percent thickness on day 3 and those measured on days 10 ($****p < 0.0001$), 15 ($**p < 0.01$), and 30 ($***p < 0.001$). Whereas no statistically significant differences were found comparing the thickness measured on days 10, 15, and 30 (Figure 2F).

Evaluation of the Number of CD-68-Positive Cells (Macrophages) Over Time

The number of CD-68-positive macrophages was calculated histomorphometrically per square millimeter. Three days after implantation, some CD-68-positive cells were found within the implantation bed in the test group ($33.7 \pm 12.5 \text{ cells/mm}^2$), whereas a significantly higher number was found within the implantation bed in the control group ($105.9 \pm 16.3 \text{ cells/mm}^2$; $***p < 0.0001$). The number of these cells increased by day 10 ($185.9 \pm 8.5 \text{ cells/mm}^2$) in the test group. On the contrary, there was a rapid decrease in the number of CD-68-positive cells in the control group ($19.6 \pm 3.7 \text{ cells/mm}^2$). At this time point, the highest number of macrophages was measured in the test group throughout the study period and was significantly higher than in the control group ($***p < 0.0001$). By day 15, the number of macrophages was decreased in the test group ($118.9 \pm 8.5 \text{ cells/mm}^2$) and in the control group ($12.5 \pm 4.2 \text{ cells/mm}^2$). At this time point, the difference was still highly significant ($p < 0.0001$). Similar numbers of macrophages observed on day 15 were observed on day 30 in the respective test (109.8 ± 14.4

cells/mm²) and control groups (8.9 ± 2.9 cells/mm²). At this timepoint, significantly higher number of CD-68 positive cells was detected within the test group compared to the control group (••••*p* < 0.0001). Within-group analyses in the test group showed that the increase in the number of macrophages from day 3 to 10 was highly significant (*****p* < 0.0001). Moreover, the decrease from day 10 to 15 showed a statistically significant difference (****p* < 0.001). Additionally, the difference in macrophage number between day 10 and 30 was statistically highly significant (*****p* < 0.0001). Despite the decrease from day 10 onward, the numbers of macrophages on days 15 and 30 were higher. The difference was statistically highly significant when comparing the numbers between day 3 and day 15 (*****p* < 0.0001) and between day 3 and day 30 (*****p* < 0.0001). However, no statistically significant difference was observed in the macrophage numbers between days 15 and 30 (Figure 5A).

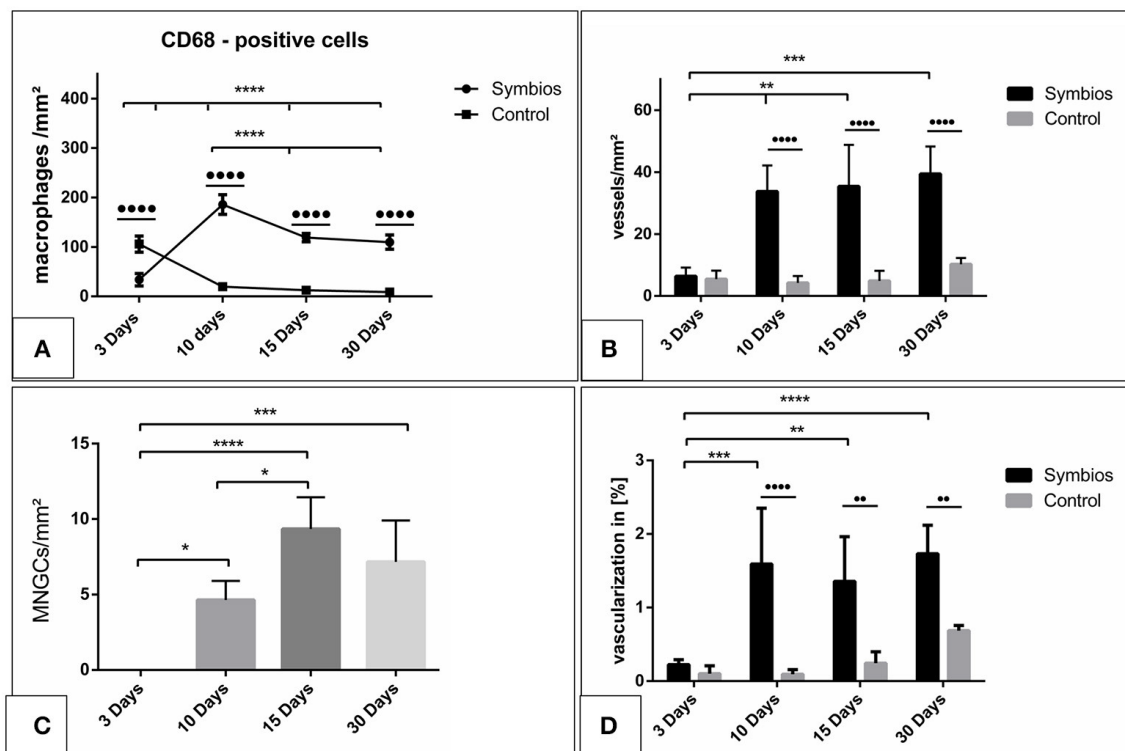


Figure 5. Histomorphometrical analysis. (A) The numbers of CD-68-positive cells (macrophages) per square millimeter over the time. (B) The vascularization pattern over the time in vessels per square millimeter in comparison to the control group. (C) The numbers of multinucleated giant cells (MNGCs) per square millimeter over the time. (D) The percent vascularization of the implantation bed over the time in comparison to the control group. (*/*p* < 0.05; **/*p* < 0.01; ***/*p* < 0.001; and ****/*p* < 0.0001).

Evaluation of the Number of Multinucleated Giant Cells Over Time

No MNGCs were observed in the control group at any time point; therefore, it was not considered for the statistical analysis.

The number of the MNGCs was determined histomorphometrically per square millimeter. Three days after implantation, no MNGCs were found within the implantation bed of the

biomaterial. After 10 days, a moderate number of MNGCs were present within the biomaterial implantation bed (4.6 ± 1.3 MNGCs/mm²). The number of the MNGCs increased significantly toward day 15 (9.3 ± 2.1 MNGCs/mm²). However, after 30 days, a slight decrease in the MNGC number was detected (7.2 ± 2.7 MNGCs/mm²) compared to the number of MNGCs at day 15.

Statistical analysis showed a significant difference in the MNGC number between days 3 and 10 ($*p < 0.05$). The number of MNGCs was significantly higher on day 15 than on day 3 ($****p < 0.0001$) and on day 10 ($*p < 0.05$). The slight decrease from day 15 to 30 showed no statistically significant difference. Moreover, no statistically significant difference was observed in the MNGC numbers between days 30 and 10. However, the number of MNGCs was significantly higher on day 30 than on day 3 ($***p < 0.001$). Generally, the MNGCs showed no TRAP expression. Therefore, no histomorphometrical analysis of the TRAP expression was performed (Figure 5C).

Evaluation of the Vascularization Pattern Over Time

The vascularization pattern was evaluated histomorphometrically in the biomaterial implantation bed as well as the sham operation group.

The vessel density on day 3 within the SB implantation bed (6.4 ± 2.8 vessels/mm²) and the control group (5.3 ± 2.7 vessels/mm²) showed comparable results. Thus, no statistically significant difference was revealed at this time point. Ten days after implantation, the SB implantation bed (33.7 ± 8.4 vessels/mm²) showed a higher vascularization rate than that on day 3. The difference was statistically significant ($**p < 0.01$). The vessel density within the control group increased only slightly on day 10 (5.9 ± 2.2 vessels/mm²). Therefore, the vessel density within the SB group showed a significantly higher rate than that in the control group ($****p < 0.0001$). After 15 days, the vessel density within the SB implantation bed was increased slightly (35.4 ± 13.4 vessels/mm²). No statistically significant difference was detected compared to day 10. However, the vessel density was significantly higher than that on day 3 ($**p < 0.01$). In addition, a minor increase in the vessel number was observed in the control group (6.3 ± 3.8 vessels/mm²). The SB group showed a significantly higher vessel number than the control group at this time point ($****p < 0.0001$). On day 30, an increase in the vessel density within the SB group was observed (39.4 ± 8.8 vessels/mm²). However, no statistically significant difference was revealed between days 10 and 15. The number of vessels was significantly higher than the vessel density on day 3 ($***p < 0.001$). The vascularization of the control group showed an increase in the vessel density (10.2 ± 2.1 vessels/mm²). However, the SB group showed a significantly higher vessel density compared to the control group at this time point ($****p <$

0.0001; Figure 5B). The vascularization was quantified with respect to the implantation area in both the SB group and the control group. The percent vascularization increased over 30 days in both groups. On day 3, both groups showed comparable values (SB: $0.2 \pm 0.07\%$; control: $0.15 \pm 0.08\%$), and there was no statistically significant difference. The percent vascularization increased in the SB group significantly by day 10 ($1.6 \pm 0.06\%$). At this time point, the percent vascularization within the SB implantation bed was significantly higher than that in the control group ($0.12 \pm 0.06\%$; $****p < 0.001$). Subsequently, on day 15, the percent vascularization rate within the SB group ($1.3 \pm 0.6\%$) showed a slight decrease compared to the previous time point. However, the vascularization was significantly higher than that on day 3 ($**p < 0.01$), whereas no statistically significant difference was detected compared to the vascularization on day 10. The difference between the vascularization in the SB group and in the control group ($0.2 \pm 0.1\%$) showed a significantly higher vascularization in the SB group at this time point ($**p < 0.001$). Finally, after 30 days, the percent vascularization increased in the SB group ($1.7 \pm 0.3\%$). This value was significantly higher than the percent vascularization on day 3 ($****p < 0.0001$). In contrast, no statistically significant differences were evident compared to the percent vascularization on days 15 or 10. The percent vascularization within the control group ($0.7 \pm 0.07\%$) increased compared to the previous time point. Nevertheless, the percent vascularization was significantly higher in the SB group than in the control group at this time point ($**p < 0.01$; Figure 5D).

Additionally, similar kinetics were detected in the vascularization and induction of MNGCs. The vascularization pattern increased corresponding to the increasing number of the induced MNGCs over time (Figures 6A–C).

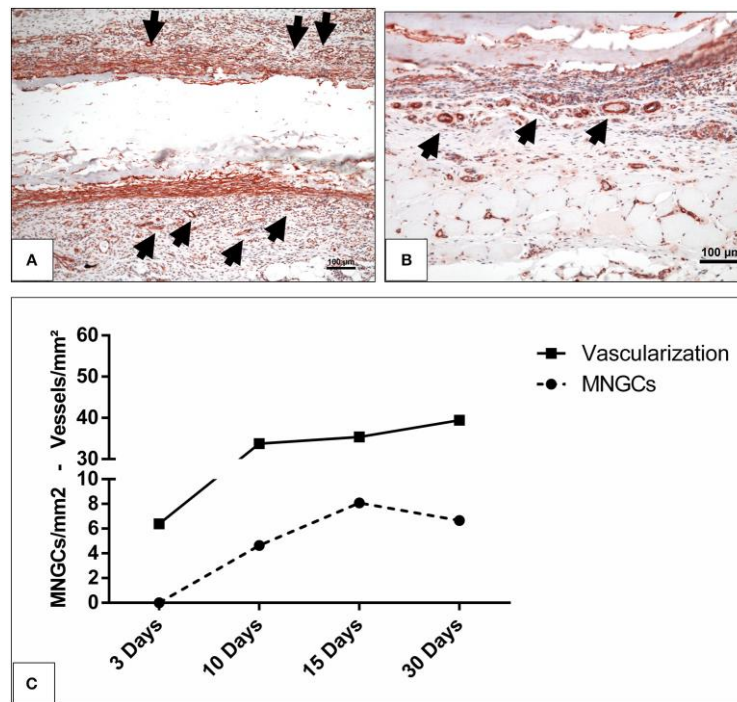


Figure 6. The vascularization pattern (A) on day 10 and (B) on day 15 highlighted with immunohistochemical staining of SMA. Black arrowheads, vessels; scale bar, 100µm. (C) The correlation between the induced MNGCs and the vascularization in the test group.

Discussion

Numerous collagen-based membranes are available as naturally derived xenogeneic membranes that should meet the defined requirements to serve as a scaffold and maintain integrity for a suitable time period. However, the naturally derived xenogeneic collagen-based biomaterials must undergo different purification and processing procedures that influence their native structure. In this context, the cellular reaction toward different membranes is primarily related to the membrane-specific physicochemical properties (Dadsetan et al., 2004; Ghanaati et al., 2012).

The *in vivo* tissue response toward a novel collagen-based biomaterial SB that is derived from bovine achilles tendon showed that SB initially induced a mononuclear cell-based reaction on day 3. At this time point, single mononuclear cells had already infiltrated the membrane. Immunohistochemical staining showed that some of the mononuclear cells were CD-68-positive, representing the presence of macrophages on the SB surface. The mid-term cellular reaction on day 10 was characterized by a high number of macrophages (CD-68-positive) on the membrane surface, reflecting a significant increase in their number compared the number of macrophages observed on day 3. Additionally, some MNGCs were found on the biomaterial surface at this time point. The induction of MNGCs was accompanied by significantly increased vascularization. However, the localization of the mononuclear cells was rather triggered within the central region, whereas MNGCs were only located on the membrane surface (Figure 3).

MNGCs the potential to express vascular endothelial growth factor, which may explain the enhanced vascularization within the implantation bed after their formation (Moens et al., 2014). This phenomenon was previously observed within the implantation bed of different biomaterials including synthetic and xenogeneic bone substitute materials and collagen based membranes (Ghanaati et al., 2010a; Barbeck et al., 2015). By day 15, a course change was detected in the number of the macrophages and MNGCs (Figure 4). The macrophage number decreased significantly in comparison to that observed on day 10. Simultaneously, the number of the MNGCs increased significantly compared to that observed on day 10. Macrophages are precursors cells of MNGCs (Anderson et al., 2008; Chen et al., 2010). Their interaction with the biomaterial surface and the inflammatory microenvironment around the implanted biomaterial is essential for the fusion and formation of MNGCs, which possess an enhanced oxidative capacity (Enelow et al., 1992; McNally and Anderson, 2002; Chang et al., 2009). This process was previously described as “frustrated phagocytosis”. Thus, after the frustrated attempts of macrophages to degrade the biomaterial, they fuse to form MNGCs (Xia and Triffitt, 2006; MacLauchlan et al., 2009). Accordingly, the dynamic changes observed here in the numbers of macrophages and MNGCs might be due to their fusion and the process of MNGC formation. At the last observation time point, neither the macrophages nor the MNGCs showed a significant change in the number of cells. These findings were similar to the rate of vascularization, which showed a stable level from day 10 onwards. All the parameters presented here, including the formation of MNGCs and enhanced vascularization, are circumstantial evidence of a foreign body reaction (Mcnally and Anderson, 2015). In this sense, it is questionable whether an exuberant vascularization is required for the regeneration process. It was previously shown that a mild vascularization that is derived by mononuclear, similar to the physiological vascularization pattern is sufficient for membrane integration *in vivo* (Ghanaati, 2012).

The present results showed that the occurrence of MNGCs is induced by the implanted biomaterial, thus no MNGCs were observed within the control group, which simulated physiological wound healing. Previous assumptions questioned whether the formation of MNGCs is a physiological reaction related to biomaterial resorption or might be associated with collagen-based biomaterials harvested from a specific compartment (Barbeck et al., 2015b). However, MNGCs were observed within the implantation bed of different biomaterials including collagen-based biomaterial (Barbeck et al., 2015b) and silk-based polymers (Ghanaati et al., 2010c), as well as different synthetic and xenogeneic bone substitute materials (Ghanaati et al., 2010b). The biomaterial-induced MNGCs show common characteristics with pathological MNGCs (Langerhans’ giant cells) that exist in sarcoidosis and tuberculosis (Al-Maawi et al., 2017). These are not only morphological characteristics in terms of the number of nuclei but also in the

expressed surface proteins such as CD-68, Integrin β 1/2 and HLA-DR (Al-Maawi et al., 2017). In this sense, the question arises as to whether the presence of MNGCs within the implantation bed of clinically applicable biomaterials is an acceptable reaction or rather an adverse reaction after chronic inflammation.

It is noteworthy that collagen-based biomaterials, such as non-cross-linked bilayer collagen matrix from porcine skin and peritoneum, induced solely mononuclear cells and maintained their native structure over a period of 60 days. This collagen matrix allowed slow penetration into the biomaterial superficial layer but served as a functional barrier within its central region and was integrated within the host tissue (Ghanaati et al., 2011).

Additionally, in the present study MNGCs were only localized on the surface of the biomaterial and did not enter the biomaterial body, while the mononuclear cells migrated into the membrane body and were integrated after 30 days. Therefore, the vascularization was enhanced at the peri-implantation region, but no vessels were observed within the membrane central region in terms of transmembraneous vascularization. The occurrence of inflammatory responses with two different outcomes, i.e., mononuclear cells vs. MNGCs, is noteworthy. This specific inflammatory pattern may be beneficial to recruit vessels to the implantation region without manipulating the membrane structure. This may be related to the specific architecture of the biomaterial that includes pores within the membrane body, which allowed the mononuclear cells to migrate into the center region and integrate within the biomaterial so that the macrophages were not over-accumulated at the surface, resulting in a high number of MNGCs. In addition, despite the presence of MNGCs, the SB maintained its integrity over 30 days and allowed only mononuclear cells to enter its central region while resisting the MNGCs (Figure 3). Thereby, no signs of breakdown or disintegration in terms of loss of the initial structure, were detected during the evaluation period. Additionally, within the observation period of this study, the biomaterial did not show typical signs of encapsulation as it was previously found in non-resorbable biomaterials (Ghanaati, 2012) Furthermore, it is interesting to further elucidate whether the presence of MNGCs will lead to a classical foreign body reaction and encapsulation of the biomaterial or whether these cells could be involved within the resorption process of the biomaterial.

In contrast, other non-cross-linked, collagen-based biomaterials that induced MNGCs underwent disintegration after a clear backdown leading to their disintegration (Barbeck et al., 2015b). In that case, the loss of integrity allowed premature ingrowth of the peri-implantation connective tissue into the membrane body including MNGC- and vessel-rich granulation tissue (Barbeck et al., 2015b). This phenomenon was not observed in this study during the evaluation

period. Within the limitations of this study, it is presumable that the membrane may experience disintegration after 60 days or more.

Another naturally derived biomaterial of silk fibroin underwent disintegration after the induction of MNGCs. The silk fibroin showed transmembraneous vascularization and a loss of integrity after 60 days (Ghanaati, 2012). However, most of the induced MNGCs in silk fibroin expressed TRAP, which might be a sign for their pro-inflammatory activity (Ghanaati, 2012). On the other hand, the present results showed mostly no TRAP-positive MNGCs, which might represent a different MNGC type that did not contribute to the disintegration of the biomaterial. Another parameter may be the harvesting compartment of the SB, i.e., bovine achilles tendon. This may include a different collagen quality that does not evoke a severe pro-inflammatory reaction.

Furthermore, different processing and purification methods have an impact on changing the surface characteristics of the native collagen, which leads to different tissue responses (Jones et al., 2004). This may influence the cellular activation and thus the macrophage polarization and expression pattern, which possibly influence their fusion to MNGCs (Jones et al., 2004; Kajahn et al., 2012). However, further studies are needed to determine the interaction between differently activated macrophages and the formation of MNGCs for a better understanding of the mononuclear cells and multinucleated giant cell activation and polarization.

The *ex vivo* results of the interaction between SB and the liquid PRF showed that the membrane was infiltrated by liquid PRF including leukocytes and platelets. Therefore, the membrane absorbed the liquid PRF and allowed cellular invasion during the early time period (Figure 1). However, *in vivo* results after 3 days showed some cellular infiltration into the superficial layer of the membrane, whereas the central region was still free of murine cells of the peri-implantation region. This occurs because of the difference between the qualities of subcutaneous tissue and the liquid PRF. Thereby, *in vivo* cellular infiltration require longer time period until cells migrate from the extracellular matrix of the peri-implantation region into the membrane compartment. Nevertheless, cellular infiltration was then reached after an initial time period of 10–15 days *in vivo*.

Accordingly, the *in vivo* thickness measurements showed that the SB thickness increased significantly from day 3 to day 10 and then maintained the thickness level over 30 days. This occurred because the SB allowed cells and connective tissue to enter the membrane body. The specific structure and interfibrillar compartments allowed the membrane to include the host cells and connective tissue and thus increase in thickness without undergoing a breakdown or disintegration (Figure 3). Recently, the application of this method for the evaluation of a sugar

cross-linked porcine derived collagen membrane showed that the membrane was occlusive to the fibrin and cells of PRF (ChiaLai et al., 2017). These results were in correlation to the *in vivo* evaluation using subcutaneous implantation. This frequent agreement in the *ex vivo* and *in vivo* results make liquid PRF a potential tool to investigate the membrane absorbance capacity and provide information about the *in vivo* cellular reaction while avoiding animal experiments. Recent studies used blood serum and plasma proteins to investigate the biomaterial surface absorption capacity (Nguyen et al., 2016). In the present study, a more complex system was used i.e., liquid PRF, which includes not only plasma proteins but also cells (Platelets and leukocytes). Thereby, the focus of the present study was placed on the cellular infiltration of the collagen-based membrane by the cells and the formation of the fibrin network within the membrane pores. Additionally, to further elucidate the mechanisms of protein absorbance and the interaction between collagen and PRF, further methods are required such as atomic force microscopy. These aspects are further topics of our research group and are presently under investigation to elucidate the capacity of different collagen-based biomaterials to incorporate PRF with special focus on different plasma proteins respecting the competitive protein exchange and the Vroman effect (Hirsh et al., 2013).

In addition, the specific porous structure and the ability to include the host connective tissue might be a reason for the maintained integrity after inducing a foreign body reaction by MNGCs. It might be that including the host cells within the membrane is favorable for the regeneration process to serve as a scaffold to promote guided tissue regeneration. In an animal study using a tooth dehiscence model for periodontological regeneration, a collagen biomaterial of bovine achilles origin showed comparable results to a non-cross-linked, porcine derived collagen membrane, which led to successful tissue regeneration (Behfarnia et al., 2012). Furthermore, a clinical study showed that bovine-derived collagen membranes are suitable for successful root coverage (Schlee et al., 2012).

In summary, the present findings raise the need for further research to characterize the types of biomaterial-related MNGCs and whether they should be accepted as a biomaterial related cellular reaction or considered as an adverse reaction following chronic inflammation. These findings are clinically highly interesting to evaluate the clinical suitability of different biomaterials and define suitable indications with respect to the biomaterial physicochemical properties.

Conclusion

The present study evaluated the cellular reaction toward a novel collagen membrane derived from bovine achilles tendon. The tissue response showed an initial reaction of mononuclear cells followed by the formation of MNGCs from day 10 onwards, whereas no MNGCs were detected within the control group that mimicked physiological wound healing. The presence of these cells was accompanied by a reduction in the CD-68-positive cell number (macrophages), indicating their fusion to form MNGCs, which were only localized on the membrane surface. Along with the enhanced MNGC number, the vascularization of the periimplantation area increased significantly. No transmembraneous vascularization was found within the membrane body, and only mononuclear cells were able to migrate. These characteristics refer to a foreign body reaction toward the biomaterial surface. Thereby, the role of the MNGCs induced by this biomaterial requires further investigation.

Ex vivo and *in vivo* experiments showed that the biomaterial allows protein absorbance and mononuclear cells to migrate into its central region. These findings were observed along with the *in vivo* increase in thickness reflecting the membrane capacity to incorporate the host cells and connective tissue and form a scaffold without undergoing any signs of breakdown or disintegration. These findings raise the question of whether the formation of MNGCs should be accepted as a biomaterial-related reaction or considered as an adverse reaction.

Acknowledgments

The authors would like to thank the excellent technical support of Mrs. Verena Hoffmann and Mrs. Yunxin Zhang

References

- Abou Fadel, R., Samarani, R., and Chakar, C. (2018). Guided bone regeneration in calvarial critical size bony defect using a double-layer resorbable collagen membrane covering a xenograft: a histological and histomorphometric study in rats. *Oral Maxillofac. Surg.* 22, 203–213. doi: 10.1007/s10006-0180694-x
- Al-Maawi, S., Orłowska, A., Sader, R., James Kirkpatrick, C., and Ghanaati, S. (2017). *In vivo* cellular reactions to different biomaterials—Physiological and pathological aspects and their consequences. *Semin. Immunol.* 29, 49–61. doi: 10.1016/j.smim.2017.06.001

- Anderson, J. M., Rodriguez, A., and Chang, D. T. (2008). Foreign body reaction to biomaterials. *Semin. Immunol.* 20, 86–100. doi: 10.1016/j.smim.2007.11.004
- Barbeck, M., Lorenz, J., Holthaus, M. G., Raetscho, N., Kubesch, A., Booms, P., et al. (2015a). Porcine dermis and pericardium-based, non-crosslinked materials induce multinucleated giant cells after their *in vivo* implantation: a physiological reaction? *J. Oral Implantol.* 41, e267–e281. doi: 10.1563/aaid-joi-D-14-00155
- Barbeck, M., Lorenz, J., Kubesch, A., Böhm, N., Booms, P., Choukroun, J., et al. (2015b). Porcine dermis-derived collagen membranes induce implantation bed vascularization via multinucleated giant cells: a physiological reaction? *J. Oral Implantol.* 41, e238–e251. doi: 10.1563/aaid-joi-D-14-00274
- Barbeck, M., Motta, A., Migliaresi, C., Sader, R., Kirkpatrick, C. J., and Ghanaati, S. (2016). Heterogeneity of biomaterial-induced multinucleated giant cells: possible importance for the regeneration process? *J. Biomed. Mater. Res. Part A* 104, 413–418. doi: 10.1002/jbm.a.35579
- Barbeck, M., Udeabor, S., Lorenz, J., Schlee, M., Holthaus, M. G., Raetscho, N., et al. (2015c). High-temperature sintering of xenogeneic bone substitutes leads to increased multinucleated giant cell formation: *in vivo* and preliminary clinical results. *J. Oral Implantol.* 41, e212–e222. doi: 10.1563/aaid-joi-D-1400168
- Behfarnia, P., Khorasani, M. M., Birang, R., and Abbas, F. M. (2012). Histological and histomorphometric analysis of animal experimental dehiscence defect treated with three bio absorbable GTR collagen membrane. *Dent. Res. J. (Isfahan)*. 9, 574–581. doi: 10.4103/1735-3327.104876
- Chang, D. T., Colton, E., Matsuda, T., and Anderson, J. M. (2009). Lymphocyte adhesion and interactions with biomaterial adherent macrophages and foreign body giant cells. *J. Biomed. Mater. Res. A* 91, 1210–1220. doi: 10.1002/jbm.a.32218
- Chen, S., Jones, J. A., Xu, Y., Low, H.-Y., Anderson, J. M., and Leong, K. W. (2010). Characterization of topographical effects on macrophage behavior in a foreign body response model. *Biomaterials* 31, 3479–3491. doi: 10.1016/j.biomaterials.2010.01.074
- Chia-Lai, P.-J., Orłowska, A., Al-Maawi, S., Dias, A., Zhang, Y., Wang, X., et al. (2017). Sugar-based collagen membrane cross-linking increases barrier capacity of membranes. *Clin. Oral. Investig.* 22, 1851–1863. doi: 10.1007/s00784-017-2281-1
- Dadsetan, M., Jones, J. A., Hiltner, A., and Anderson, J. M. (2004). Surface chemistry mediates adhesive structure, cytoskeletal organization, and fusion of macrophages. *J. Biomed. Mater. Res. A* 71, 439–448. doi: 10.1002/jbm.a.30165
- Dollinger, C., Ciftci, S., Knopf-Marques, H., Guner, R., Ghaemmaghami, A. M., Debry, C., et al. (2018). Incorporation of resident macrophages in engineered tissues: multiple cell type response

to microenvironment controlled macrophage-laden gelatine hydrogels. *J. Tiss. Eng. Regen. Med.* 12, 330–340. doi: 10.1002/term.2458

Enelow, R. I., Sullivan, G. W., Carper, H. T., and Mandell, G. L. (1992). Cytokine-induced human multinucleated giant cells have enhanced candidacidal activity and oxidative capacity compared with macrophages. *J. Infect. Dis.* 166, 664–668. doi: 10.1093/infdis/166.3.664

Ghanaati, S. (2012). Non-cross-linked porcine-based collagen I-III membranes do not require high vascularization rates for their integration within the implantation bed: a paradigm shift. *Acta Biomater.* 8, 3061–3072. doi: 10.1016/j.actbio.2012.04.041

Ghanaati, S., Barbeck, M., Booms, P., Lorenz, J., Kirkpatrick, C. J., and Sader, R. A. (2014). Potential lack of “standardized” processing techniques for production of allogeneic and xenogeneic bone blocks for application in humans. *Acta Biomater.* 10, 3557–3562. doi: 10.1016/j.actbio.2014.04.017

Ghanaati, S., Barbeck, M., Detsch, R., Deisinger, U., Hilbig, U., Rausch, V., et al. (2012). The chemical composition of synthetic bone substitutes influences tissue reactions *in vivo*: histological and histomorphometrical analysis of the cellular inflammatory response to hydroxyapatite, betatricalcium phosphate and biphasic calcium phosphate ceramics. *Biomed. Mater.* 7:015005. doi: 10.1088/1748-6041/7/1/015005

Ghanaati, S., Barbeck, M., Orth, C., Willershausen, I., Thimm, B. W., Hoffmann, C., et al. (2010a). Influence of β -tricalcium phosphate granule size and morphology on tissue reaction *in vivo*. *Acta Biomater.* 6, 4476–4487. doi: 10.1016/j.actbio.2010.07.006

Ghanaati, S., Orth, C., Barbeck, M., Willershausen, I., Thimm, B. W., Booms, P., et al. (2010b). Histological and histomorphometrical analysis of a silica matrix embedded nanocrystalline hydroxyapatite bone substitute using the subcutaneous implantation model in wistar rats. *Biomed. Mater.* 5:035005. doi: 10.1088/1748-6041/5/3/035005

Ghanaati, S., Orth, C., Unger, R. E., Barbeck, M., Webber, M. J., Motta, A., et al. (2010c). Fine-tuning scaffolds for tissue regeneration: effects of formic acid processing on tissue reaction to silk fibroin. *J. Tissue Eng. Regen. Med.* 4, 464–472. doi: 10.1002/term.257

Ghanaati, S., Schlee, M., Webber, M. J., Willershausen, I., Barbeck, M., Balic, E., et al. (2011). Evaluation of the tissue reaction to a new bilayered collagen matrix *in vivo* and its translation to the clinic. *Biomed. Mater.* 6:015010. doi: 10.1088/1748-6041/6/1/015010

Ghanaati, S., Udeabor, S. E., Barbeck, M., Willershausen, I., Kuenzel, O., Sader, R. A., et al. (2013). Implantation of silicon dioxide-based nanocrystalline hydroxyapatite and pure phase betatricalciumphosphate bone substitute granules in caprine muscle tissue does not induce new bone formation. *Head Face Med.* 9:1. doi: 10.1186/1746-160X-9-1

- Hirsh, S. L., McKenzie, D. R., Nosworthy, N. J., Denman, J. A., Sezerman, O. U., and Bilek, M. M. (2013). The Vroman effect: competitive protein exchange with dynamic multilayer protein aggregates. *Colloids Surfaces B Biointerfaces* 103, 395–404. doi: 10.1016/j.colsurfb.2012.10.039
- Jones, J. A., Dadsetan, M., Collier, T. O., Ebert, M., Stokes, K. S., Ward, R. S., et al. (2004). Macrophage behavior on surface-modified polyurethanes. *J. Biomater. Sci. Polym. Ed.* 15, 567–84. doi: 10.1163/156856204323046843
- Kajahn, J., Franz, S., Rueckert, E., Forstreuter, I., Hintze, V., Moeller, S., et al. (2012). Artificial extracellular matrices composed of collagen I and high sulfated hyaluronan modulate monocyte to macrophage differentiation under conditions of sterile inflammation. *Biomatter* 2, 226–236. doi: 10.4161/biom.22855
- MacLauchlan, S., Skokos, E. A., Meznarich, N., Zhu, D. H., Raoof, S., Shipley, J. M., et al. (2009). Macrophage fusion, giant cell formation, and the foreign body response require matrix metalloproteinase 9. *J. Leukoc. Biol.* 85, 617–626. doi: 10.1189/jlb.1008588
- McNally, A. K., and Anderson, J. M. (2002). $\beta 1$ and $\beta 2$ integrins mediate adhesion during macrophage fusion and multinucleated foreign body giant cell formation. *Am. J. Pathol.* 160, 621–630. doi: 10.1016/S0002-9440(10)64882-1
- McNally, A. K., and Anderson, J. M. (2015). Phenotypic expression in human monocyte-derived interleukin-4-induced foreign body giant cells and macrophages *in vitro*: dependence on material surface properties. *J. Biomed. Mater. Res. A.* 103, 1380–1390. doi: 10.1002/jbm.a.35280
- Miron, R. J., and Bosshardt, D. D. (2018). Multinucleated giant cells: good guys or bad guys? *Tiss. Eng. B Rev.* 24, 53–65. doi: 10.1089/ten.teb.2017.0242
- Moens, S., Goveia, J., Stapor, P. C., Cantelmo, A. R., and Carmeliet, P. (2014). The multifaceted activity of VEGF in angiogenesis – Implications for therapy responses. *Cytokine Growth Factor Rev.* 25, 473–482. doi: 10.1016/j.cytogfr.2014.07.009
- Moore, W. R., Graves, S. E., and Bain, G. I. (2001). Synthetic bone graft substitutes. *ANZ J. Surg.* 71, 354–361. doi: 10.1046/j.1440-1622.2001.2128.x
- Nguyen, D. H. K., Pham, V. T. H., Al Kobaisi, M., Bhadra, C., Orłowska, A., Ghanaati, S., et al. (2016). Adsorption of human plasma albumin and fibronectin onto nanostructured black silicon surfaces. *Langmuir* 32, 10744–10751. doi: 10.1021/acs.langmuir.6b02601
- Rothamel, D., Schwarz, F., Sager, M., Herten, M., Sculean, A., and Becker, J. (2005). Biodegradation of differently cross-linked collagen membranes: an experimental study in the rat. *Clin. Oral Implants Res.* 16, 369–378. doi: 10.1111/j.1600-0501.2005.01108.x

Schlee, M., Ghanaati, S., Willershausen, I., Stimmlmayr, M., Sculean, A., and Sader, R. A. (2012). Bovine pericardium based non-cross linked collagen matrix for successful root coverage, a clinical study in human. *Head Face Med.* 8:6. doi: 10.1186/1746-160X-8-6

Wend, S., Kubesch, A., Orłowska, A., Al-Maawi, S., Zender, N., Dias, A., et al. (2017). Reduction of the relative centrifugal force influences cell number and growth factor release within injectable PRF-based matrices. *J. Mater. Sci. Mater. Med.* 28:188. doi: 10.1007/s10856-0175992-6

Xia, Z., and Triffitt, J. T. (2006). A review on macrophage responses to biomaterials. *Biomed. Mater.* 1, R1–R9. doi: 10.1088/1748-6041/1/1/R01

3.2.4. Multinucleated giant cells within the *in vivo* implantation bed of a collagen-based biomaterial determine its degradation pattern

Clinical Oral Investigations, **2021**, 25(3), 859–873.

Tanneberger, A. M.^a, Al-Maawi, S.^a, Herrera-Vizcaíno, C.^a, **Orłowska, A.**^a, Kubesch, A.^a, Sader, R.^a, Kirkpatrick, C. J.^a, & Ghanaati, S.^a

^a Department for Oral, Cranio-Maxillofacial and Facial Plastic Surgery, FORM (Frankfurt Orofacial Regenerative Medicine) Lab, University Hospital Frankfurt Goethe University, Theodor-Stern-Kai 7, 60590 Frankfurt am Main, Germany

Abstract

Objectives: The aim of the present study was to characterize the cellular reaction to a xenogeneic resorbable collagen membrane of porcine origin using a subcutaneous implantation model in Wistar rats over 30 days.

Materials and methods: *Ex vivo*, liquid platelet-rich fibrin (PRF), a leukocyte and platelet-rich cell suspension, was used to evaluate the blood cell membrane interaction. The material was implanted subcutaneously in rats. Sham-operated rats without biomaterial displayed physiological wound healing (control group). Histological, immunohistological, and histomorphometric analyses were focused on the inflammatory pattern, vascularization rate, and degradation pattern.

Results: The membrane induced a large number of mononuclear cells over the observation period, including lymphocytes, macrophages, and fibroblasts. After 15 days, multinucleated giant cells (MNGCs) were observed on the biomaterial surface. Their number increased significantly, and they proceeded to the center of the biomaterial on day 30. These cells highly expressed CD-68, calcitonin receptor, and MMP-9, but not TRAP or integrin- β 3. Thus, the membrane lost its integrity and underwent disintegration as a consequence of the induction of MNGCs. The significant increase in MNGC number correlated with a high rate of vascularization, which was significantly higher than the control group. Physiological wound healing in the control group did not induce any MNGCs at any time point. *Ex vivo* blood cells from liquid-PRF did not penetrate the membrane. *Conclusion* The present study suggests a potential role for MNGCs in biomaterial degradation and questions whether it is beneficial to accept them in clinically approved biomaterials or focus on biomaterials that induce only mononuclear cells. Thus, further studies are necessary to identify the function of biomaterial-induced MNGCs.

Clinical relevance: Understanding the cellular reaction to biomaterials is essential to assess their suitability for specific clinical indications and outline the potential benefit of specific group of biomaterials in the respective clinical indications.

Introduction

The principle of guided tissue regeneration (GTR) and guided bone regeneration (GBR) is based on the separation of different cells and tissues that compete during the healing process.^{1,2} Different collagen-based biomaterials have been utilized in oral and maxillofacial surgery to promote healthy soft tissue regeneration (GTR) or bone regeneration (GBR) while inhibiting the

ingrowth of undesirable fibrotic tissue into the bony defect.^{1, 3-5} In addition to biocompatibility and suitability in clinical handling, membranes are required to fulfill a so-called barrier function and to act as a place holder.^{1, 6, 7}

Xenogeneic collagen-based membranes were used successfully in GTR/GBR methods.⁸⁻¹⁰ Collagen is an ubiquitous protein in human and animal tissue that undergoes enzymatic degradation via matrix metalloproteases (MMP) released by neutrophils, monocytes/macrophages, eosinophils, and fibroblasts recruited during wound healing.^{11, 12} In addition to the angiogenic potential of collagen type I, it plays an important role in tissue regeneration.^{7, 13, 14}

Currently a wide range of different collagen-based biomaterials is available for clinical applications.¹⁵ However, the regenerative mechanisms of the membranes are still not fully explored.¹⁶ Additionally, different manufacturing and processing techniques influence the biomaterials' specific surface and physicochemical properties such as porosity, polarity, and hydrophilicity. Accordingly, the biomaterial attracts a different type of cellular reaction.^{17, 18} Previous studies have shown different collagen-based materials of the same origin, *i.e.*, porcine induce different cellular reactions according to their properties after their implantation *in vivo*.^{19, 20} In this context, the formation of biomaterial-induced multinucleated giant cells (MNGCs) has been frequently observed.²¹⁻²⁴ Different studies discussed the morphological and possible functional similarities of these cells to physiologically existing osteoclasts and disease-related MNGCs.^{21, 25, 26} Further studies showed that their formation leads rather to a premature biomaterial disintegration and enhanced vascularization *in vivo*.^{19, 23} However, the reason for their formation and the role of these cells in the biomaterial-based regeneration process are still unexplored.

This study aimed to analyze the cellular reaction of a resorbable membrane consisting of collagen and elastin. Their combination in an interwoven structure is thought to provide the membrane a high *in vivo* stability. This novel collagen-based membrane, Creos™ Xenoprotect (CXP, Nobel Biocare, Gothenburg, Sweden; Remaix, Matricel GmbH, Herzogenrath, Germany), is derived from porcine collagen and elastin, which are manufactured to a highly purified non-cross-linked collagen membrane. Special attention was paid to the cellular response and degradation pattern of the specifically reinforced collagen membrane CXP.

Additionally, this study evaluated the biomaterial-induced MNGCs and their differentiation. Moreover, liquid platelet rich fibrin (PRF), a blood concentrate system obtained from the peripheral blood, was used to examine the initial interaction between collagen and fibrin, including the physiological existence of blood cells derived from peripheral blood to analyze the initial permeability of the biomaterial *ex vivo*.

Experimental

Creos™ Xenoprotect (CXP)

According to the manufacturer, CXP is a xenogeneic, biodegradable, non-chemically cross-linked collagen membrane of porcine origin, which is indicated in clinical cases requiring GBR and GTR. This collagen membrane is marked as Conformité Européene (CE). The hydrophilic membrane is composed of collagen and elastin fiber networks, which supply it with high mechanical strength and avoid invasion of the surrounding tissue.

***Ex vivo* analysis of the biomaterial-blood interaction**

PRF is a blood concentrate system that is produced by the centrifugation of human peripheral blood. PRF is composed of platelets, leukocytes, and plasma proteins. In this study, PRF was used as a cell suspension to evaluate the membrane-cell interaction and occlusion. The *ex vivo* analysis was performed as previously described.^{22, 23} Three healthy volunteers participated in this study, and informed consent was obtained before blood withdrawal according to a local ethical approval (265/17). Using a 24-gauge butterfly needle, 10 ml of blood was withdrawn from the antecubital vein direct into 10-ml liquid-PRF tubes covered with plastic in the interior (Process for PRF, Nice, France). The tube was quickly transported to a tabletop centrifuge (Duo centrifuge, Process for PRF, Nice, France (11 cm rotor, fixed angel)) and processed at low speed to allow the concentration of blood cells in high numbers using a relatively low centrifugation force (44×g and 8 min) [27]. The blood was fractioned into a superior liquid segment containing liquid-PRF and a lower segment of erythrocytes. The superior segment was collected using a 1-ml pipette tip and transported in 5-ml plastic tubes for homogenization. Concomitantly, the Creos™ Xenoprotect (CXP) membranes were cut into 1-cm² segments and placed in 24-well cell culture plates. Before coagulation of liquidPRF, 1 ml was deposited on top of the membranes until they were covered and kept at room temperature for 15 min until clot formation. The samples were fixed with formaldehyde (Roti-Histofix 4% acid free pH 7, Carl-Roth, Germany) over 24 h for histological evaluation.

***In vivo* analysis of the cellular reaction**

The design, analysis, and reporting of the experiments were conducted following the ARRIVE guidelines for animal research.²⁸ The experiments were approved by the government regulating agency of Darmstadt and the ethical committee from the University of Goethe of Frankfurt am Main (FK/ 1023). Animal husbandry, care, and surgeries were carried out in the

animal care facility ((ZFE) Frankfurt am Main, Germany) of the Department of Medicine of Johann Wolfgang Goethe University Frankfurt. Twenty-four female Wistar rats (*Rattus norvegicus*) were purchased from Charles River (Sulzfeld, Germany) with an average age of 7–8 weeks and weighing between 190 and 220 g. The experiments were performed in summer 2016. The animals were housed in groups for 1 week prior to surgery for acclimatization in a controlled environment (temp, 20 °C; light/dark cycles of 12 h; and humidity of 40% to 70%) and fed regular rodent pellets and water *ad libitum*. The animals were provided from Charles River in groups of 4 in one cage and were prepared by an independent person from the animal facility. In sequence, animals in each cage (n = 4) were alternately used either for implantation (test group) or for the control group. The surgical intervention was performed following a standardized and established model as previously described.^{29, 30} Anesthesia was induced through intraperitoneal injection of a mixture of ketamine/xylazine (100 mg/kg/5 mg/kg). The animals were placed in the prone position, and the depth of anesthesia was verified by the absence of the toe reflex. A subcutaneous pocket was prepared by generating a 2-cm incision in the rostral skin and dissection of the subcutaneous tissue into the interscapular area. The biomaterial was cut in segments of 1 cm² and placed above the muscle fascia. The tissue was sutured using a 4–0 polypropylene suture (Prolene Ethicon). Tramadol (1–3 mg/kg/d) was administered orally for pain management through the drinking water for 1 day. Four animals were included in the experimental group, and four served as controls (sham surgery) to evaluate the physiological wound healing per time point. In the control group of animals, anesthesia and surgery were performed as described for the experimental group, but without the implantation of a biomaterial. Tissue explantation involving the biomaterial and the surrounding implantation bed was performed on day 3, 15, and 30 and fixed with formaldehyde (Roti-Histofix 4% acid free pH 7, Carl-Roth, Germany) over 24 h for histological evaluation.

Tissue processing and histological preparation

Histological preparation was performed as previously described.^{31, 32} The fixed tissue mentioned above was segmented and distributed in embedding cassettes (Histosette, VWR, Deutschland) before processing in increasing concentrations of alcohol and xylol, followed by the infiltration of paraffin wax under a vacuum using an automatic tissue processor (Leica TP1020). After processing, the samples were embedded in paraffin blocks, and slides from all blocks with a thickness of 3 µm were obtained from consecutive sections using a rotation microtome (Leica RM2255) and stained with hematoxylin and eosin for screening. The block containing the most representative sagittal section of the biomaterial was selected, and nine

consecutive slides were obtained and stained as described previously; the first four slides were stained with Mayer's hematoxylin and eosin (H&E) (1), Azan (2), Masson-Goldner (3), and TRAP (4). The remaining five slides were immunohistochemically stained using an autostainer (Lab Vision™ Autostainer 360, Thermo Scientific, Germany). Antigen retrieval was performed using the heat-induced epitope retrieval (HIER) method. The slides were immersed in citrate buffer, pH 6.0, and heated using a water bath (VWR®, Germany) at 95 °C for 20 min. Subsequently, after protein blocking (Avidin/Biotin Blocking Kit, Vector Laboratories, USA), antigens were immunodetected with mouse anti-rat CD-68 monoclonal antibody (Bio-Rad; MCA341GA; concentration 1:400; 30 min) as a pan marker for the monocyte lineage (5). Goat anti-rabbit IgG-B (Santa Cruz Biotechnology, USA. sc-2040; 1:200; 60 min) was used as the secondary antibody with further amplification of the antigen using the avidin-biotin complex method (ABC, Thermo Fisher Scientific, Germany). Finally, the slides were stained with α -smooth muscle actin (α -SMA) (Sigma-Aldrich, Germany; A5228; concentration 1:20.000; 120 min) for vascular endothelial cells (6), MMP-9 (ab58803, 1: 250) (7), calcitonin receptor (ab11042, 1:200) (8), integrin- β 3 (ab225742, 1:2000), and (9) followed by anti-mouse secondary antibody (HRP Ultravision Quanto Detection System, Thermo Fisher Scientific). Chromogenic visualization was obtained by applying AEC (3-amino-9-ethylcarbazole) peroxidase (Thermo Fisher Scientific, Germany) for CD-68 and α -SMA or DAB (diaminobenzidine (DAB) Quanto chromogen and substrate) for calcitonin receptor, integrin- β 3 and MMP-9 and counterstaining with Mayer's hematoxylin. From the set of samples, two supplementary, randomly selected slides were added as a negative control without application of the primary antibody. For immunohistochemical staining, rat bone was used as positive control. As negative controls, the primary antibodies were replaced by antibody substrate and used to stain rat bone as described.

Qualitative histological evaluation

The stained slides were systematically evaluated by the authors (AT, SA, and SG) using a light microscope (Nikon Eclipse 80i, Tokyo, Japan). The cellular reaction in the implantation bed, characteristics of the biomaterial, and vascularization were compared within the experimental group (inter-comparison) at all time points and with the control group (inter-comparison). Representative histological images were captured with a Nikon DS-Fi1 digital camera and a Nikon Digital sight unit DS-U3 (Nikon, Tokyo, Japan), which were controlled using Nikon's NIS-Elements imaging software (Nikon, Tokyo, Japan). Six samples per animal were stained from which two samples per animal from the center region were used for histomorphometry.

Quantitative histological analysis

Histomorphometry was performed following established parameters as previously described.^{29, 33} All stained slides were scanned with the Nikon ECLIPSE 80i histological microscope at high magnification using the large image settings in the NIS-Elements software (Nikon, Tokyo, Japan). Using an automatically motorized stage, a total of 100–200 images were obtained at $\times 200$ for each sample and used to construct the “total scan,” allowing complete visualization of the sample and histomorphometric analyses.

Measurement of vascularization

After obtaining the “total scan” of α -SMA positively stained structures on day 3, 15, and 30, the vascular structures in the implantation bed and within the biomaterial were manually counted using the annotation and measurement function in the NIS-Elements software (Nikon, Tokyo, Japan). To obtain different perspectives regarding the angiogenesis process during implantation of the biomaterial, the quantified vascular structures were first expressed as the density and then calculated by dividing the total vascular structures by the total area of the sample (vessel/mm²). Second, the lumen area of the vascular structures was quantified and expressed as a percentage (%).

Quantification of multinucleated giant cells (MNGCs) and CD-68-positive mononuclear cells

As described previously, the slides were scanned using the large image capture tool (“total scan”) in the Nis element software (Nikon, Tokyo, Japan). The positively stained MNGCs and their subtypes, TRAP positive or TRAP negative, as well as CD-68-positive monocytes were quantified using the manual “annotations and measurements” tool in the NIS-Elements software. For each individual slide, the total number of counted cells was divided by the total area of the implantation bed as a relative measurement to evaluate the cellular reaction of the Creos™ Xenoprotect (CXP) membrane. The results are expressed as MNGCs/mm² (TRAP-/TRAP+) and CD-68-positive monocytes/mm², and they were statistically evaluated for all time points (on day 3, 15, 30).

Statistics

Sample size calculation ($n = 4$) was assessed according to previous studies.^{22, 26, 34} Primary outcomes were the characterization of the cellular reaction in terms of the induction of multinucleated giant cells (MNGCs) and vascularization. Secondary outcomes were signaling

molecule expression (TRAP and CD-68, calcitonin receptor, MMP-9 and integrin- β 3). All the output data were introduced into GraphPad Prism 7.0 software (GraphPad Software Inc., La Jolla, CA, USA) and statistically evaluated by one-way and two-way analysis of variance (ANOVA). The results were all expressed as the mean and standard deviation (SD) and depicted as column bars. Differences were considered statistically significant if the p values were $* < 0.05$ and highly significant if the p values were $** < 0.01$, $*** < 0.001$, and $**** < 0.0001$

Results and discussion

***Ex vivo* analysis of the cellular interaction with Creos Xenoprotect (CXP)**

Liquid-PRF, as a blood concentrate system containing a large number of platelets and leukocytes, was used to evaluate the cellular interaction and membrane permeability *ex vivo* over 15 min as previously described.²⁶ Fifteen minutes after application, the liquid-PRF formed a fibrin clot. Histological analysis showed that the membrane was not penetrated by the leukocytes and platelets from liquid-PRF (Fig. 1A-C). A fibrin clot including leukocytes and platelets was formed on both surfaces of the membrane (Fig. 1B). However, membrane cross sections showed no cellular penetration into the membrane body in any of the evaluated CXP samples (Fig. 1C).

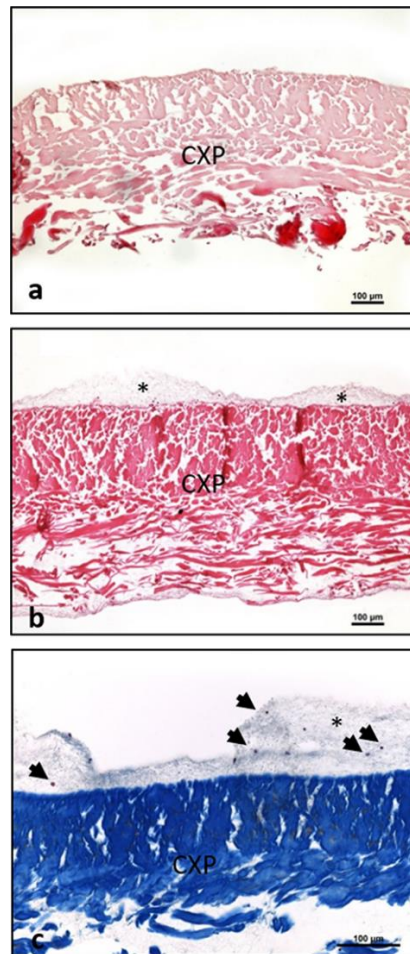


Figure. 1 *Ex vivo* interaction between membrane Creos™ Xenoprotect (CXP), blood-derived cells, and fibrin from liquid-PRF. (A) A control cross section of the native membrane *ex vivo*, H and E staining; (B) CXP after liquid-PRF application. A fibrin clot is formed on the membrane surface (*); H and E staining; (C) High magnification of fibrin clot formation on the membrane surface (*) including blood cells (arrows). The membrane was not invaded by cells.

Qualitative analysis of the *in vivo* cellular reaction

In the following section, the observed cellular reaction is described for both Creos™ Xenoprotect (CXP) and control group.

Control group

The sham-operated control group was used to mimic wound healing without biomaterial implantation as previously described.^{22,23} All animals survived the operation and the observation time period without any complications or atypical feeding or sleeping behaviors. No wound dehiscence, infection, or wound healing disorders were observed at any time point. Across the healing time points, *i.e.*, day 3, 15, 30, only mononuclear cells (*e.g.*, monocytes, macrophages, fibroblasts, lymphocytes) were observed within the wound healing region. No multinucleated giant cells (MNGCs) were detected at any time point.

Qualitative analysis of the *in vivo* cellular reaction to Creos™ Xenoprotect (CXP)

All animals survived the operation and the observation time period without any complications or atypical feeding or sleeping behaviors. No wound dehiscence, infection, or wound healing disorders were observed at any time point. The membrane was detectable within the implantation area after 3 days (Fig. 2A). A large number of mononuclear cells accumulated on the surface, including lymphocytes, monocytes, and macrophages. Some of the mononuclear cells expressed CD-68. Some cells started invading the CXP toward its center region. However, the central area was generally free of cells. New vessel formation was observed in the peri-implant region (Fig. 2B).

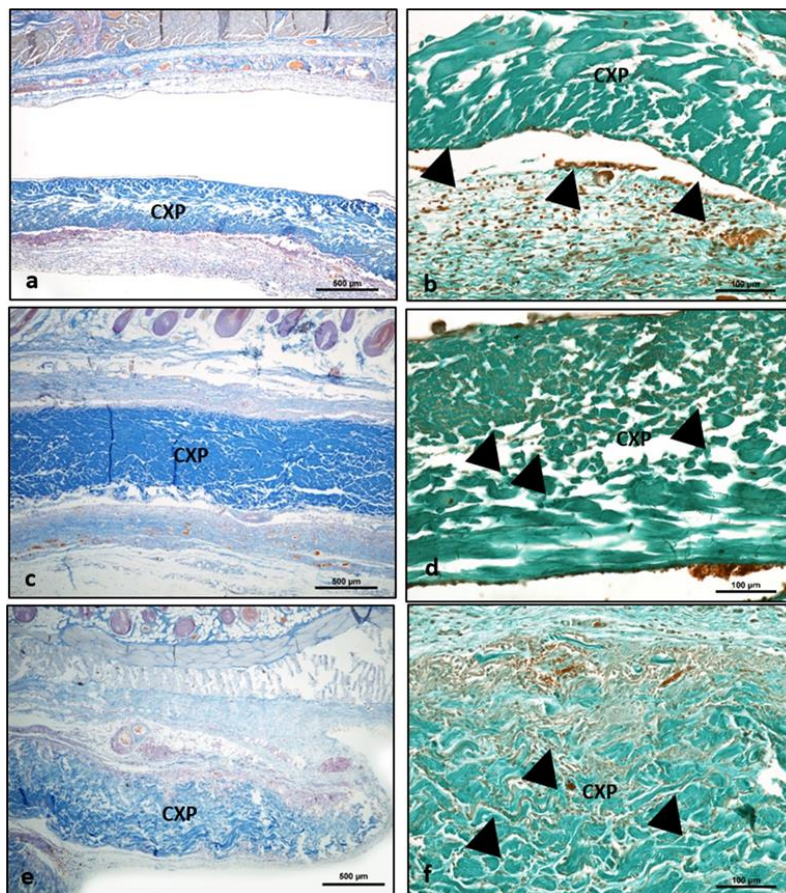


Figure 2. The cellular reaction to Creos™ Xenoprotect (CXP). a and b Day 3. c and d Day 15. e and f day 30. Left column - Azan staining; Right column - Masson-Goldner staining; Arrows, peri-implantation tissue/ cells

After 15 days, the number of mononuclear cells increased, illustrating a wall of inflammatory cells on the CXP surface (Fig. 2C). Thus, more cells invaded CXP toward its central region. At this time point, no capsule formation was observed. The membrane displayed a stable structure and maintained its integrity without allowing connective tissue ingrowth from the peri-implantation area (Fig. 2C). Single MNGCs could be detected on the biomaterial surface. Most of the induced MNGCs were TRAP negative. Additional vessels were detected in proximity to the

membrane in comparison with the initial time point on day 3. However, no vessel formation was observed within the biomaterial body (Fig. 2D).

On day 30 following implantation, the membrane was invaded by mononuclear cells that reached the central region. Immunohistochemical staining showed that some mononuclear cells within the implantation bed of CXP expressed CD-68. Compared with day 15, a greater number of MNGCs formed on the surface of CXP (Fig. 2E). These cells started to invade the membrane, followed by connective tissue ingrowth that progressed toward the central region of the membrane. The membrane showed a high rate of degradation and influx of connective tissue as markers of disintegration (Fig. 2F). Most of the induced MNGCs showed no TRAP and integrin- β 3 activity. In addition, vessel formation was observed within the superficial region of the membrane. However, a high expression of CD-68, calcitonin receptor, and MMP-9 was observed (Fig. 3A–E).

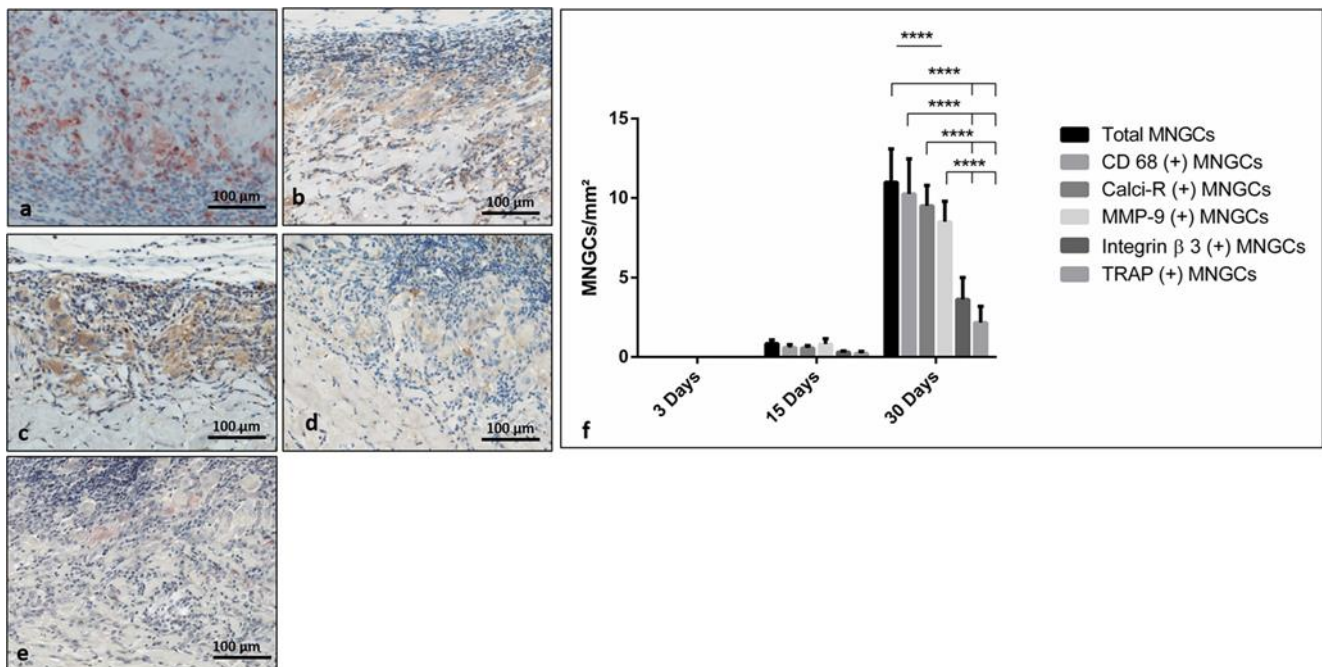


Figure 3. Immunohistochemical staining of the different expression markers in multinucleated giant cells (MNGCs). Positive cells are stained in red/ brown. a Anti-CD-68. b Anti-calcitonin receptor. c Anti-MMP-9. d Anti-integrin- β 3. e TRAP staining. f Statistical analysis of the histomorphometrically measured MNGC number per square millimeter. * $p < 0.05$; ** $p < 0.01$; *** $p < 0.001$; **** $p < 0.0001$

Quantitative histomorphometric analysis

The comparative statistical analysis of the quantified data of material-induced multinucleated giant cells (MNGCs), number of cells expressing CD-68, and the vascularization rate is presented in the following section.

Material-induced multinucleated giant cells (MNGCs)

In the control group, no MNGCs were observed at any time point. In the Creos™ Xenoprotect (CXP) test group, the membrane induced MNGCs starting on day 15 (Fig. 4A). Toward day 30 (Fig. 4B), the number of induced MNGCs per square millimeter increased significantly compared with the previous time points on day 15 ($p < 0.0001$) and 3 days ($p < 0.0001$) (Fig. 4C). On day 15, some MNGCs expressed TRAP. However, their number was not statistically significant compared with the TRAP-negative MNGCs. After 30 days, TRAP activity was detected in the analyzed material-induced MNGCs, but their number was significantly reduced ($p < 0.0001$) compared with the TRAP-negative MNGCs representative of most of the material-induced MNGCs at this time point (Fig. 4C). Differences were detected especially on day 30. The number of MNGCs expressing CD-68 was the highest, followed by calcitonin receptor and MMP-9. However, the number of MNGCs expressing MMP-9 was significantly lower compared with the total number ($**** p < 0.0001$). Additionally, the number of MNGCs expressing TRAP and integrin- $\beta 3$ was the lowest. Both were significantly lower compared with the total MNGCs number ($**** p < 0.0001$), CD-68-positive MNGCs ($**** p < 0.0001$), calcitonin receptor ($**** p < 0.0001$), and MMP-9 ($**** p < 0.0001$) (Fig. 3F).

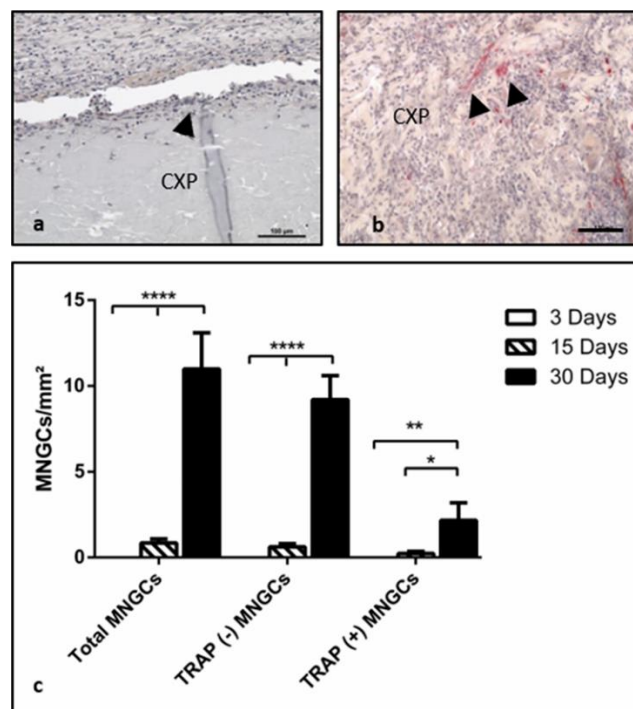


Figure 4. Biomaterial-induced multinucleated giant cells (MNGCs). A TRAP-negative MNGCs (arrowhead) on Creos™ Xenoprotect (CXP) surface on day 15. b TRAP-positive cells (arrowheads) invaded CXP on day 30. TRAP staining; $\times 200$ magnification. c Statistical analysis of the histomorphometrically measured MNGC number per square millimeter. * $p < 0.05$; ** $p < 0.01$; *** $p < 0.001$; **** $p < 0.0001$

Vascularization pattern over time

The vessel density was evaluated histomorphometrically in the CXP group and control group over the evaluation time period of 30 days.

Intraindividual analysis revealed a progressive increase in vascularization in the CXP group in which the vessel density increased notably from day 3 to day 15. However, the difference was not statistically significant. Toward day 30, a significant increase in vessel density was observed compared with day 3 ($p < 0.0001$) and day 15 ($p < 0.01$) (Fig. 5A-E). In the control group, the vessel density increased from day 3 to day 30 without a statistically significant difference.

On day 3, the interindividual analysis showed that the vessel density in the CXP group was significantly higher than that of the control group at the same time point ($p < 0.05$). Similarly, a significantly higher vessel density was detected in the CXP group on day 15 compared with the control group ($p < 0.0001$) on the same day. Finally, on day 30, the vessel density was higher in the CXP group than the control group, demonstrating a highly significant difference at that same time point ($p < 0.0001$) (Fig. 5A-E).

A similar pattern was observed when evaluating the percent vascularization. The percent vascularization increased progressively in both groups. The intraindividual group. However, the CXP group showed a significantly higher percentage of vascularization on day 30 compared with day 3 ($p < 0.01$) (Fig. 5B-E).

The interindividual analysis revealed significantly higher vascularization in the CXP group compared with the control group on both day 15 ($p < 0.01$) and day 30 ($p < 0.01$). However, no statistically significant difference was detected on day 3 (Fig. 5B-E).

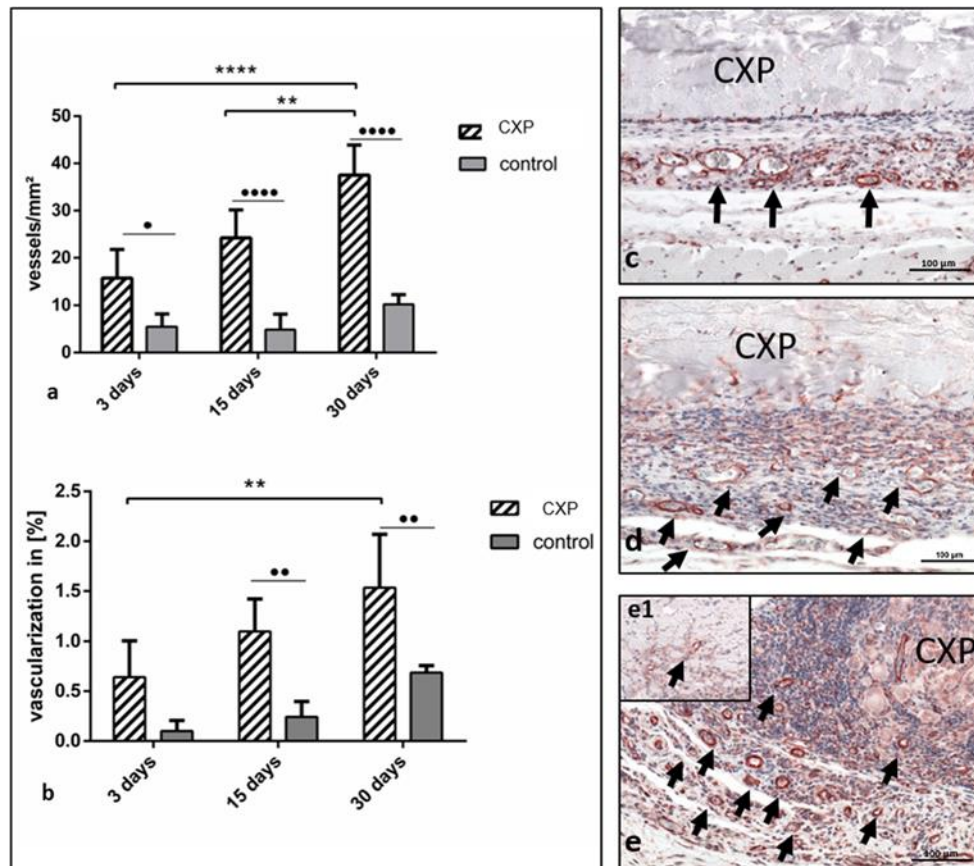


Figure 5. Vessel formation within Creos™ Xenoprotect (CXP). Statistical analysis of the histomorphometrically measured vessel number per square millimeter. * $p < 0.05$; ** $p < 0.01$; *** $p < 0.001$; **** $p < 0.0001$. (A) Vessel density, (B) vascularization rate as a percent, (C–E) immunohistochemical staining of α -SMA marked vessels (arrows) (C) day 3, (D) day 15, and (E) and (E1) day 30.

CD-68 expression in mononuclear cells

Histomorphometric measurements of CD-68 expressing cells were calculated per square millimeter in the CXP (Fig. 6A–C) and control group (Fig. 6D–F).

On day 3, the number of CD-68-positive cells was significantly higher in the control group ($p < 0.001$) compared with the test group. Toward day 15, the number of CD-68-positive mononuclear cells was decreased in the control group. However, in the CXP test group, the number of CD-68-positive cells increased significantly. Consequently, a significantly higher cell number per square millimeter was detected in the CXP compared with the control group ($p < 0.001$). Thirty days after implantation, the number of CD-68-positive cells was further reduced compared with day 15 in the control group. By contrast, the CXP group showed a slight increase in CD-68-positive cells compared with day 15. The difference between the tested groups at this time point was statistically highly significant, demonstrating an increase in the CXP compared with the control group ($p < 0.0001$) (Fig. 6G).

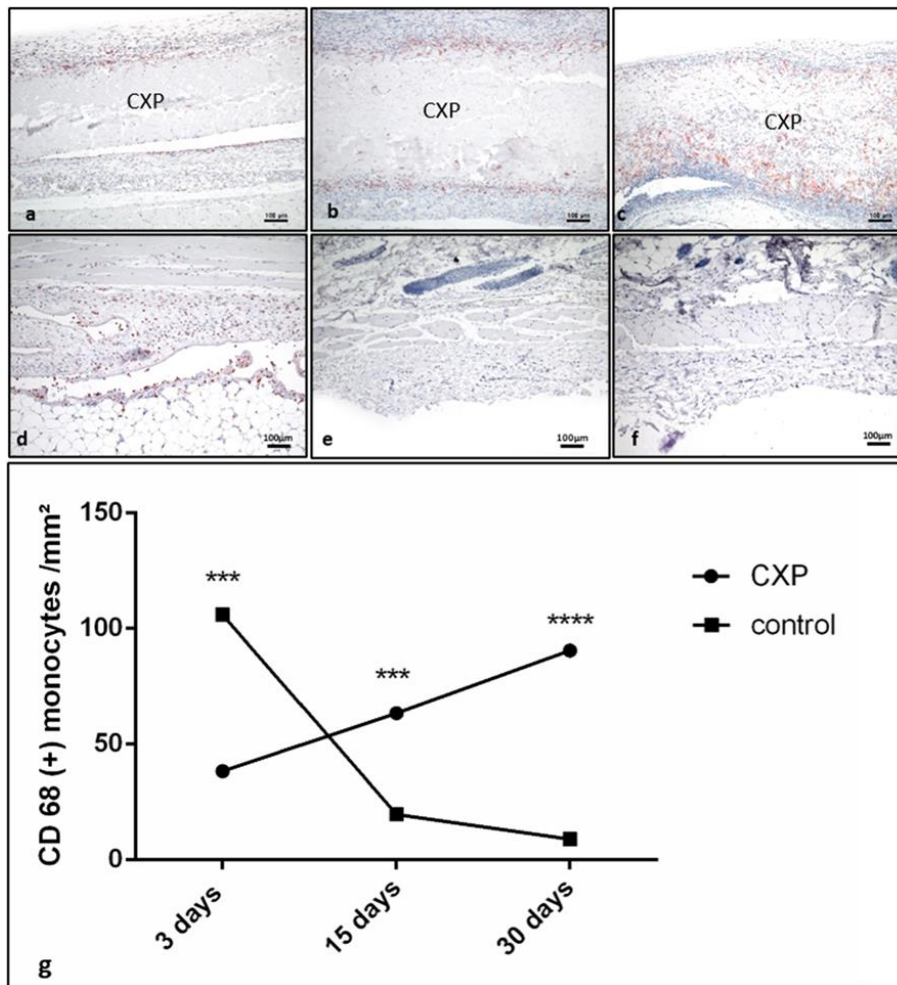


Figure 6. Immunohistochemical staining of CD-68-positive cells (A) day 3, (B) day15, and (C) day 30 in the Creos™ Xenoprotect (CXP) group and (D) day 3, (E) day 15, and (F) day 30 in the control group. (G) Statistical analysis of the histomorphometrically measured CD-68-positive mononuclear cell number per square millimeter. * $p < 0.05$; ** $p < 0.01$; *** $p < 0.001$; **** $p < 0.0001$

Discussion

In the last few years, the European market has experienced an influx of different collagen-based membranes and matrices that were introduced for applications in GTR and GBR.²⁶ Collagen-based biomaterials are derived from different origins, including allogeneic and xenogeneic materials. In addition, different harvesting species and compartments were used to manufacture well-engineered, biocompatible, and clinically practical membranes and matrices. The most common harvesting compartments are porcine pericardium, dermis, and skin [19]; bovine Achilles tendon;²³ and porcine tendon.²² Collagen is a favorable material for application as a resorbable scaffold or membrane in tissue engineering³⁵ because it is a highly conserved protein that exists in most mammals and is therefore well tolerated as a naturally derived biomaterial.¹¹ Additionally, physiological native collagen exhibits good features to support cell migration, proliferation, and angiogenesis.³⁶ Although collagen-based biomaterials consist of the same construction unit, *i.e.*, collagen, which is mostly preserved in its natural structure, different

processing and purification methods are applied to eliminate pathogens and avoid the risk of xenotransplantation of immunologically active material.³⁷ Moreover, some manufacturers implement further techniques to reinforce the biomaterial stability by means of chemical or physical cross-linking methods.²² These changes in the physical and chemical properties of materials have a prominent influence on the induced cellular reaction *in vivo* after biomaterial implantation into the host tissue.²⁶ Therefore, the present study aimed to analyze the cellular reaction to a novel non-chemically cross-linked collagen membrane to understand its pattern of regeneration and degradation. A wound healing model was used as a control to mimic physiological wound healing without the biomaterial. The authors believe that the most accurate control in this case is the physiological wound healing without biomaterial as demonstrated in previous studies.²³ It is not reasonable to compare different commercially available collagen-based biomaterials, as the manufacturing and processing methods significantly influence the cellular reaction as previously published.^{19, 38} Therefore, to the best of our knowledge, no reliable parameters are presently known to characterize an appropriate control in terms of a collagen-based biomaterial. In this context, in this study, the physiological wound healing was considered as a control to assess biomaterial-related changes in relation to the physiological regeneration pattern. However, summarizing the reactions from different data can provide evidence to other researches. In this context, one of the limitations of the present study is the analysis of only one membrane in comparison with physiological healing. Additionally, the present data can be compared with previously published studies that used the same standardized model and evaluation methods but analyzed different collagen-based biomaterials. This study presents two preclinical models to characterize the cell-matrix interaction *ex vivo* and *in vivo*. *Ex vivo*, a leukocyte and platelet-rich cell suspension (liquid-PRF) was used to mimic the first interaction between the Creos™ Xenoprotect (CXP) membrane and the host cells, i.e., blood cells, as previously described.^{22, 23} The *ex vivo* results showed that the blood-derived leukocytes and platelets accumulated on the membrane surface and could not penetrate the biomaterial. Moreover, a fibrin clot was formed on the biomaterial surface, including the blood derived cells. Similar results were observed in previous studies that used liquid-PRF to investigate other collagen-based membranes of bovine and porcine origin. Regardless of the rate of porosity, the membranes were occlusive to blood cells in liquid-PRF.^{22, 23} PRF was used as a cell suspension to evaluate the initial biomaterial interaction with blood cells and the biomaterial capacity of absorbing blood components. In this case, only one biomaterial was tested to compare the *in vivo* and the *ex vivo* results in order to understand the absorption capacity of this specific biomaterial.

The *ex vivo* results were in accordance with the *in vivo* observations 3 days after implantation. In this case, the membrane induced only physiological mononuclear cells (*e.g.*, monocytes, macrophages, lymphocytes), which were also observed in the control group and did not allow the cells to enter the biomaterial body. However, toward day 30 following implantation, the membrane induced a large number of multinucleated giant cells (MNGCs), which were first only located on the biomaterial surface (day 15) but then proceeded to infiltrate the biomaterial body (day 30) along with the mononuclear cells and peri-implantation connective tissue. Remarkably, the control group did not show any induction of MNGCs at any time point. This observation supports the suggestion that MNGCs are rather biomaterial-related cells that are not involved in physiological wound healing and regenerative processes.²⁶ Biomaterial-induced MNGCs are frequently observed in the implantation bed of different biomaterials.^{26, 39} In addition, common surface molecules and secretors are found between the biomaterial-induced MNGCs and other pathological MNGC types that are found, for example, in sarcoidosis.²⁶

Previous *in vitro* and *in vivo* studies have shown that MNGCs are formed by the fusion of macrophages after their frustrated attempt to degrade the biomaterial in a process called “frustrated phagocytosis” as an indication of a foreign body reaction.^{22, 23, 40} However, MNGC induction and formation depend primarily on the biomaterial surface characteristics and, thereby, the adhesive molecules expressed by the cells.⁴¹ Interestingly, the present study demonstrated a dynamic decrease in the number of macrophages (CD-68-positive mononuclear cells) in the control group as a physiological life cycle of macrophages.⁴² In contrast, the CXP group showed a significant increase over of persisting macrophages in the implantation bed. This phenomenon is associated with a chronic inflammation as one sign of a foreign body reaction.⁴³ Consequently, persisted macrophages fused to form biomaterial-induced MNGCs as observed in the present similar membrane.²³ Thus, both studies observed the formation of MNGCs in response to collagen membrane CXP. The MNGCs observed herein were further characterized as TRAP-positive and TRAP-negative MNGCs. TRAP positive MNGCs were detected on day 30, results starting with day 15 until day 30. The present findings are in agreement with a previous *in vivo* study investigating a together with obvious biomaterial disintegration, which indicated a loss of integrity, fragmentation, and a loss of the initial structure. Thus, peri-implantation connective tissue was able to find its way into the central region of the membrane between membrane fragments. These observations are supported by a recent *in vitro* study, which have shown that both types of TRAP expression are associated with collagen degradation.⁴⁴ These findings showed that the biomaterial-induced TRAP positive MNGCs in this case were associated with a high inflammatory reaction. TRAP is a degrading enzyme that exists

in 2 isoforms, type 5a and type 5b, that have been suggested to have different functions.^{44–46} It was first described in osteoclasts;^{47, 48} however, recent studies have shown that TRAP may be considered as a pro-inflammatory signaling molecule.^{49, 50} Similar findings were observed when analyzing the expression of MNGCs in inflammatory diseases such as sarcoidosis. TRAP type 5a was highly expressed in MNGCs and macrophages of sarcoidosis tissue. This study also suggested that TRAP type 5a is derived from systemic inflammatory of macrophages and thereby may be a biomarker of inflammation.

Another interesting finding of the present study was the correlation between the number of MNGCs and the rate of vascularization. With an increased number of MNGCs, a high vascularization rate was measured on day 15 and 30, which was significantly higher than in the control group, *i.e.*, not comparable to the physiological vascularization that occurs during wound healing (supraphysiological). The large number of vessels was potentially induced by the pro-inflammatory microenvironment resulting from the persistence of CD-68positive cells and induction of MNGCs. In a previous *in vivo* study, biomaterial-induced MNGCs were shown to produce vascular endothelial growth factor (VEGF) *in vivo*.³¹ Additionally, the number and kinetics of the biomaterial induced MNGCs have been shown to directly influence its degradation pattern. A recent study analyzed a bovine-derived collagen-based membrane gained from Achilles tendon in the same implantation model. The bovine-derived membrane also induced MNGCs but in a different pattern. In this case, there was no statistically significant increase of the MNGCs number from day 15 to 30. Thereby, the membrane did not undergo a total disintegration, as it was observed by the present membrane.²³ These results show that even though most of the clinically used membranes are collagen based, different *in vivo* reactions are observed according to the biomaterial-specific physicochemical properties, manufacturing technique, surface morphology and structure. In this context, our group performed a standardized series of studies to classify different polymeric biomaterials according to the *in vivo* induced cellular reaction. The results showed that there are three different cellular reaction patterns based on the biomaterial properties.⁵¹ Class I includes biomaterials that do not induce MNGCs at any time point; class II includes biomaterials that induce MNGCs with a constant number over 30 days; and class III includes biomaterials that induce MNGCs with continuous increasing number over 30 days.⁵¹ Based on this classification, the here analyzed membrane fits in class III.

Previously, biomaterial-induced MNGCs were considered as osteoclasts, because of their morphological similarities. However, biomaterial-induced MNGCs and osteoclasts express some signaling molecules in common such as CD-68.²¹ A previous histological study that evaluated the expression pattern of biomaterial-induced MNGCs in human biopsies showed that biomaterial-

induced MNGCs show a high expression of inflammatory signaling molecules such as Cox-2 or CCR-7 and rather low expression of other markers such as CD-163 or CD-206.⁵² Additionally, osteoclasts are known to express markers like RANKL, calcitonin receptor, integrin- β 3, and TRAP. However, little is known about the expression of these markers in the biomaterial-induced MNGCs. A recent *in vitro* study showed that calcitonin receptors show rather a low expression in biomaterial-induced MNGCs.²¹ By contrast, the present study showed a high expression of calcitonin receptor in the biomaterial-induced MNGCs. Different studies showed that the high expression of calcitonin receptor inhibits the activity of osteoclasts.⁵³ It may be presumed that a similar effect of this molecule will play a role in the biomaterial degradation. However, further research is needed to understand this mechanism. Additionally, biomaterial-induced MNGCs highly expressed MMP-9, a matrix metalloprotease. MMP-9 was found to be expressed in both osteoclasts,⁵⁴ foreign body MNGCs, and disease-related MNGCs such as tuberculosis.^{55, 56} In addition, the upregulation of MMP-9 in an inflammatory process has been shown to play an important role in the fusion of macrophages to form MNGCs.⁵⁵ This molecule has been additionally shown to be involved in collagen degradation in different localization.^{57, 58} In this context, the high expression of MMP-9 in the biomaterial-induced MNGCs is a potential marker for their role in the biomaterial degradation.

A further study characterized the type of MNGCs according to the expressed type of integrin. Integrins β 1 and β 2 have been described in the process of foreign body MNGC fusion, while integrin- β 3 is rather expressed in osteoclasts.⁵⁹ The present finding confirms these data, as the biomaterial induced MNGCs in this study showed a rather low expression of integrin- β 3. Similar findings were observed in the case of TRAP expression. Based on these data, the present study showed that biomaterial-induced MNGCs may have similarities with osteoclasts, especially in the inflammatory markers (CD-68, MMP-9), but not in marker that are related to bone adhesion and resorption (integrin- β 3, TRAP).

To date, little is known about the role of biomaterial induced MNGCs in the process of regeneration.²⁵ One function may be to support biomaterial degradation in resorbable biomaterials. However, other collagen-based membranes, such as non-cross-linked collagen I and III porcine-derived membrane and matrix, were evaluated *in vivo* using similar subcutaneous implantation models as demonstrated in the present study. These collagen-based materials did not induce any MNGCs at any time point over an observation time of 60 days.^{20, 34} They induced only mononuclear cells, which are physiologically involved in the process of regeneration, such as macrophages, lymphocytes, and fibroblasts; preserved their native structure over the study period; and were well integrated into the host tissue after 60 days. Additionally, their slow degradation without a loss of function was primarily associated with macrophages. These

observations show that biomaterials do not induce foreign body MNGCs per se and that it is possible to produce biomaterials that induce only mononuclear cells as a physiological reaction. At this point, the question arises whether MNGCs have any contribution to the process of regeneration and whether clinicians should accept this reaction in clinical applications. The disintegration of the membrane evaluated herein after 30 days showed that the membrane might be alternately used for indications for which rapid biomaterial degradation and induction of a high rate of vascularization are required rather than for indications in which long-term stability is necessary.

The present study also demonstrated that the wound healing microenvironment after biomaterial implantation is more complex than physiological wound healing. The present study analyzed only one membrane in comparison with the physiological wound healing. Because of the high number of different parameters that may influence the cellular reaction, it would be interesting to manufacture the same collagen membrane and modify only one parameter such as cross-linking to be able to separately evaluate this parameter in a more standardized and systematic study. Collagen-based membranes were previously considered to serve as an inactive barrier to separate two types of tissue in terms of GTR or GBR. However, recent *in vivo* studies have shown that the applied collagen membrane significantly influences the underlying augmentation area.¹⁶ A previous *in vivo* study investigated the same collagen membrane that was evaluated in this study (CXP) using a bone defect model, further comparing it with a porcine-derived collagen membrane.⁶⁰ The results revealed different rates of newly formed bone according to the implanted collagen membrane, although both membranes were of porcine origin.⁶⁰ These outcomes demonstrate that despite of the identical origin, different collagen membranes contribute differently to the GBR process based on their interaction with the surrounding tissue and the induced cellular reaction. Thus, understanding the cellular reaction to biomaterials is essential to assess their suitability for specific clinical indications. However, further controlled clinical studies are needed to outline the potential benefit to the specific group of biomaterials in the respective clinical indications.

Taken together, the present study showed that biomaterial implantation leads to changes in the physiological cellular kinetics of wound healing in a biomaterial-specific cellular reaction. *Ex vivo* and *in vivo* interactions with the host tissue showed that the CXP biomaterial investigated herein was initially occlusive to host tissue cells, but the induction and accumulation of MNGCs led to its disintegration after 30 days. The present findings mandate further characterization of the biomaterial-induced MNGCs to outline their potential functions in the process of regeneration.

Conclusion

This study characterized the cellular reaction to a novel collagen-based membrane of porcine origin *ex vivo* and *in vivo* in comparison with physiological wound healing.

The tissue response revealed an initial accumulation of mononuclear cells, such as monocytes, macrophages, lymphocytes, and fibroblasts, at the early time point in both *ex vivo* and *in vivo* examinations. From day 15 onward, the membrane induced MNGCs that were first localized on the membranes surface and then proceeded toward the central membrane region, followed by connective tissue influx from the periimplantation region. During physiological wound healing, no MNGCs were observed at any time point. After material implantation, a dynamic change was observed in the number of CD-68-positive cells (macrophages), which correlated with the induction of MNGCs. MNGCs highly expressed CD-68, calcitonin receptor, and MMP-9 but not integrin- β 3 and TRAP. These findings support that biomaterial-induced MNGCs are rather a sign of a foreign body reaction. The induced MNGCs led to membrane disintegration after 30 days and a loss of integrity. Thus, the present study calls for further preclinical and controlled clinical research to characterize the biomaterial-induced MNGCs and to elucidate their potential function in the degradation process.

Acknowledgments

The authors would like to thank Mrs. Verena Hoffmann for the excellent technical support

References

1. Gottlow J (1993) Guided tissue regeneration using bioresorbable and non-resorbable devices: initial healing and long term results. *J Periodontol* 64:1157–1165
2. Bottino MC, Thomas V, Schmidt G, Vohra YK, Chu T-MG, Kowolik MJ, Janowski GM (2012) Recent advances in the development of GTR/GBR membranes for periodontal regeneration—a materials perspective. *Dent Mater* 28:703–721. <https://doi.org/10.1016/j.dental.2012.04.022>
3. Karring T (1986) The role of bone regeneration in post-surgical periodontal wound healing. *Orthod Fr* 57 Pt 2:435–442
4. Dahlin C, Sennerby L, Lekholm U, Linde A, Nyman S (1989) Generation of new bone around titanium implants using a membrane technique: an experimental study in rabbits. *Int J Oral Maxillofac Implants* 4:19–25

5. Hämmerle CH, Karring T (1998) Guided bone regeneration at oral implant sites. *Periodontol.* 2000(17):151–175 <http://www.ncbi.nlm.nih.gov/pubmed/10337322>. Accessed January 17, 2017
6. Eickholz P, Kim T-S, Holle R, Hausmann E (2001) Long-term results of guided tissue regeneration therapy with non-resorbable and bioabsorbable barriers. I. Class II Furcations. *J Periodontol* 72: 35–42. <https://doi.org/10.1902/jop.2001.72.1.35>
7. Schenk RK, Buser D, Hardwick WR, Dahlin C (n.d.) Healing pattern of bone regeneration in membrane-protected defects: a histologic study in the canine mandible. *Int J Oral Maxillofac Implants* 9:13–29
8. Lundgren D, Sennerby L, Falk H, Friberg B, Nyman S (1994) The use of a new bioresorbable barrier for guided bone regeneration in connection with implant installation. Case reports. *Clin Oral Implants Res* 5:177–184
9. Zellin G, Gritli-Linde A, Linde A (1995) Healing of mandibular defects with different biodegradable and non-biodegradable membranes: an experimental study in rats. *Biomaterials.* 16:601–609
10. Sheikh Z, Qureshi J, Alshahrani AM, Nassar H, Ikeda Y, Glogauer M, Ganss B (2016) Collagen based barrier membranes for periodontal guided bone regeneration applications. *Odontology.* <https://doi.org/10.1007/s10266-016-0267-0>
11. Bunyaratavej P, Wang HL (2001) Collagen membranes: a review. *J Periodontol* 72:215–229. <https://doi.org/10.1902/jop.2001.72.2.215>
12. Armstrong DG, Jude EB (2002) The role of matrix metalloproteinases in wound healing. *J Am Podiatr Med Assoc* 92:12–18
13. Fuchs S, Ghanaati S, Orth C, Barbeck M, Kolbe M, Hofmann A, Eblenkamp M, Gomes M, Reis RL, Kirkpatrick CJ (2009) Contribution of outgrowth endothelial cells from human peripheral blood on *in vivo* vascularization of bone tissue engineered constructs based on starch polycaprolactone scaffolds. *Biomaterials.* 30:526–534. <https://doi.org/10.1016/j.biomaterials.2008.09.058>
14. Fuchs S, Jiang X, Schmidt H, Dohle E, Ghanaati S, Orth C, Hofmann A, Motta A, Migliaresi C, Kirkpatrick CJ (2009) Dynamic processes involved in the pre-vascularization of silk fibroin constructs for bone regeneration using outgrowth endothelial cells. *Biomaterials.* 30:1329–1338. <https://doi.org/10.1016/j.biomaterials.2008.11.028>
15. Turri A, Elgali I, Vazirisani F, Johansson A, Emanuelsson L, Dahlin C, Thomsen P, Omar O (2016) Guided bone regeneration is promoted by the molecular events in the membrane compartment. *Biomaterials.* 84:167–183. <https://doi.org/10.1016/j.biomaterials.2016.01.034>

16. Elgali I, Turri A, Xia W, Norlindh B, Johansson A, Dahlin C, Thomsen P, Omar O (2016) Guided bone regeneration using resorbable membrane and different bone substitutes: early histological and molecular events. *Acta Biomater* 29:409–423. <https://doi.org/10.1016/j.actbio.2015.10.005>
17. Ghanaati S, Orth C, Unger RE, Barbeck M, Webber MJ, Motta A, Migliaresi C, James Kirkpatrick C (2010) Fine-tuning scaffolds for tissue regeneration: effects of formic acid processing on tissue reaction to silk fibroin. *J Tissue Eng Regen Med* 4:464–472. <https://doi.org/10.1002/term.257>
18. Brodbeck WG, Shive MS, Colton E, Nakayama Y, Matsuda T, Anderson JM (2001) Influence of biomaterial surface chemistry on the apoptosis of adherent cells. *J Biomed Mater Res* 55:661–668 <http://www.ncbi.nlm.nih.gov/pubmed/11288096>. Accessed March 21, 2017
19. Barbeck M, Lorenz J, Holthaus MG, Raetscho N, Kubesch A, Booms P, Sader R, Kirkpatrick CJ, Ghanaati S (2015) Porcine dermis and pericardium-based, non-cross-linked materials induce multinucleated giant cells after their *in vivo* implantation: a physiological reaction? *J. Oral Implantol.* 41:e267–e281. <https://doi.org/10.1563/aaid-joi-D-14-00155>
20. Ghanaati S (2012) Non-cross-linked porcine-based collagen I-III membranes do not require high vascularization rates for their integration within the implantation bed: a paradigm shift. *Acta Biomater* 8:3061–3072. <https://doi.org/10.1016/j.actbio.2012.04.041>
21. Miron RJ, Zohdi H, Fujioka-Kobayashi M, Bosshardt DD (2016) Giant cells around bone biomaterials: osteoclasts or multi-nucleated giant cells? *Acta Biomater* 46:15–28. <https://doi.org/10.1016/j.actbio.2016.09.029>
22. Chia-Lai P, Orłowska A, Al-Maawi S, Dias A, Zhang Y, Wang X, Zender N, Sader R, Kirkpatrick CJ, Ghanaati S (2017) Sugar-based collagen membrane cross-linking increases barrier capacity of membranes. *Clin Oral Investig.* <https://doi.org/10.1007/s00784017-2281-1>
23. Al-Maawi S, Vorakulpipat C, Orłowska A, Zrnc TA, Sader RA, Kirkpatrick CJ, Ghanaati S (2018) *In vivo* implantation of a bovinederived collagen membrane leads to changes in the physiological cellular pattern of wound healing by the induction of multinucleated giant cells: an adverse reaction? *Front Bioeng Biotechnol* 6. <https://doi.org/10.3389/fbioe.2018.00104>
24. Ghanaati S, Barbeck M, Detsch R, Deisinger U, Hilbig U. et al (2012) The chemical composition of synthetic bone substitutes influences tissue reactions *in vivo* :

- histological and histomorphometrical analysis of the cellular inflammatory response to hydroxyapatite, beta-tricalcium phosphate and biphasic calcium phosphatase. *Biomed Mater* 7(1):015005. <https://doi.org/10.1088/1748-6041/7/1/015005>
25. Miron RJ, Bosshardt DD (2018) Multinucleated giant cells: good guys or bad guys? *Tissue Eng Part B Rev* 24:53–65. <https://doi.org/10.1089/ten.TEB.2017.0242>
 26. Al-Maawi S, Orłowska A, Sader R, James Kirkpatrick C, Ghanaati S (2017) *In vivo* cellular reactions to different biomaterials— physiological and pathological aspects and their consequences. *Semin Immunol* 29:49–61. <https://doi.org/10.1016/j.smim.2017.06.001>
 27. Choukroun J, Ghanaati S (2018) Reduction of relative centrifugation force within injectable platelet-rich-fibrin (PRF) concentrates advances patients' own inflammatory cells, platelets and growth factors: the first introduction to the low speed centrifugation concept. *Eur J Trauma Emerg Surg* 44:87–95. <https://doi.org/10.1007/s00068-017-0767-9>
 28. Kilkenny C, Browne WJ, Cuthill IC, Emerson M, Altman DG (2010) Improving bioscience research reporting: the ARRIVE guidelines for reporting animal research. *PLoS Biol* 8:e1000412. <https://doi.org/10.1371/journal.pbio.1000412>
 29. Ghanaati S, Udeabor SE, Barbeck M, Willershausen I, Kuenzel O, Sader RA, Kirkpatrick CJ (2013) Implantation of silicon dioxidebased nanocrystalline hydroxyapatite and pure phase betatricalciumphosphate bone substitute granules in caprine muscle tissue does not induce new bone formation. *Head Face Med* 9:1. <https://doi.org/10.1186/1746-160X-9-1>
 30. Ghanaati SM, Thimm BW, Unger RE, Orth C, Kohler T, Barbeck M, Müller R, Kirkpatrick CJ (2010) Collagen-embedded hydroxylapatite-beta-tricalcium phosphate-silicon dioxide bone substitute granules assist rapid vascularization and promote cell growth. *Biomed Mater* 5:25004. <https://doi.org/10.1088/17486041/5/2/025004>
 31. Ghanaati S, Barbeck M, Orth C, Willershausen I, Thimm BW, Hoffmann C, Rasic A, Sader RA, Unger RE, Peters F (2010) Influence of β -tricalcium phosphate granule size and morphology on tissue reaction *in vivo*. *Acta Biomater* 6:4476–4487. <https://doi.org/10.1016/j.actbio.2010.07.006>
 32. Ghanaati S, Barbeck M, Lorenz J, Stuebinger S, Seitz O, Landes C, Kovács AF, Kirkpatrick CJ, Sader RA (2013) Synthetic bone substitute material comparable with xenogeneic material for bone tissue regeneration in oral cancer patients: first and preliminary histological, histomorphometrical and clinical results. *Ann Maxillofac Surg* 3:126–138. <https://doi.org/10.4103/2231-0746.119221>

33. Ghanaati S, Fuchs S, Webber MJ, Orth C, Barbeck M, Gomes ME, Reis RL, James Kirkpatrick C (2011) Rapid vascularization of starch-poly(caprolactone) *in vivo* by outgrowth endothelial cells in co-culture with primary osteoblasts. *J Tissue Eng Regen Med* 5. <https://doi.org/10.1002/term.373>
34. Ghanaati S, Schlee M, Webber MJ, Willershausen I, Barbeck M, Balic E, Görlach C, Stupp SI, Sader RA, Kirkpatrick CJ (2011) Evaluation of the tissue reaction to a new bilayered collagen matrix *in vivo* and its translation to the clinic. *Biomed Mater* 6:015010. <https://doi.org/10.1088/1748-6041/6/1/015010>
35. Lorenz J, Blume M, Barbeck M, Teiler A, Kirkpatrick CJ, Sader RA, Ghanaati S (2016) Expansion of the peri-implant attached gingiva with a three-dimensional collagen matrix in head and neck cancer patients-results from a prospective clinical and histological study. *Clin Oral Investig*. <https://doi.org/10.1007/s00784-0161868-2>
36. Regazzoni C, Winterhalter KH, Rohrer L (2001) Type I collagen induces expression of bone morphogenetic protein receptor type II. *Biochem Biophys Res Commun* 283:316–322. <https://doi.org/10.1006/bbrc.2001.4813>
37. Ghanaati S, Barbeck M, Booms P, Lorenz J, Kirkpatrick CJ, Sader RA (2014) Potential lack of “standardized” processing techniques for production of allogeneic and xenogeneic bone blocks for application in humans. *Acta Biomater* 10:3557–3562. <https://doi.org/10.1016/j.actbio.2014.04.017>
38. Barbeck M, Lorenz J, Kubesch A, Böhm N, Booms P, Choukroun J, Sader R, Kirkpatrick CJ, Ghanaati S (2015) Porcine dermis-derived collagen membranes induce implantation bed vascularization via multinucleated giant cells: a physiological reaction? *J Oral Implantol* 41:e238–e251. <https://doi.org/10.1563/aid-joi-D-1400274>
39. McNally AK, Anderson JM (2005) Multinucleated giant cell formation exhibits features of phagocytosis with participation of the endoplasmic reticulum. *Exp Mol Pathol* 79:126–135. <https://doi.org/10.1016/j.yexmp.2005.06.008>
40. Enelow RI, Sullivan GW, Carper HT, Mandell GL (1992) Cytokine-induced human multinucleated giant cells have enhanced candidacidal activity and oxidative capacity compared with macrophages. *J Infect Dis* 166:664–668
41. Dadsetan M, Jones JA, Hiltner A, Anderson JM (2004) Surface chemistry mediates adhesive structure, cytoskeletal organization, and fusion of macrophages. *J Biomed Mater Res* 71A:439–448. <https://doi.org/10.1002/jbm.a.30165>
42. Klopffleisch R (2016) Macrophage reaction against biomaterials in the mouse model - phenotypes, functions and markers. *Acta Biomater* 43:3–13. <https://doi.org/10.1016/j.actbio.2016.07.003>

43. Klopffleisch R, Jung F (2017) The pathology of the foreign body reaction against biomaterials. *J Biomed Mater Res A* 105:927–940. <https://doi.org/10.1002/jbm.a.35958>
44. Mira-Pascual L, Patlaka C, Desai S, Paulie S, Näreoja T, Lång P, Andersson G (2020) A novel sandwich ELISA for tartrate-resistant acid phosphatase 5a and 5b protein reveals that both isoforms are secreted by differentiating osteoclasts and correlate to the type I collagen degradation marker CTX-I *in vivo* and *in vitro*. *Calcif Tissue Int* 106:194–207. <https://doi.org/10.1007/s00223-01900618-w>
45. How J, Brown JR, Saylor S, Rimm DL (2014) Macrophage expression of tartrate-resistant acid phosphatase as a prognostic indicator in colon cancer. *Histochem Cell Biol* 142:195–204. <https://doi.org/10.1007/s00418-014-1181-6>
46. Ahmed GJ, Tatsukawa E, Morishita K, Shibata Y, Suehiro F, Kamitakahara M, Yokoi T, Koji T, Umeda M, Nishimura M, Ikeda T (2016) Regulation and biological significance of formation of osteoclasts and foreign body giant cells in an extraskeletal implantation model. *Acta Histochem Cytochem* 49:97–107. <https://doi.org/10.1267/ahc.16007>
47. Lorenz J, Kubesch A, Korzinskas T, Barbeck M, Landes C, Sader RA, Kirkpatrick CJ, Ghanaati S (2015) TRAP-positive multinucleated giant cells are foreign body giant cells rather than osteoclasts: results from a split-mouth study in humans. *J Oral Implantol* 41:e257–e266. <https://doi.org/10.1563/AAID-JOI-D-14-00273>
48. Halling Linder C, Ek-Rylander B, Krumpel M, Norgård M, Narisawa S, Millán JL, Andersson G, Magnusson P (2017) Bone alkaline phosphatase and tartrate-resistant acid phosphatase: potential co-regulators of bone mineralization. *Calcif Tissue Int* 101:92–101. <https://doi.org/10.1007/s00223-017-0259-2>
49. Janckila AJ, Slone SP, Lear SC, Martin A, Yam LT (2007) Tartrateresistant acid phosphatase as an immunohistochemical marker for inflammatory macrophages. *Am J Clin Pathol* 127:556–566. <https://doi.org/10.1309/DGEA9BE2VE5VCFYH>
50. Luukkonen J, Pascual LM, Patlaka C, Lång P, Turunen S, Halleen J, Nousiainen T, Valkealahti M, Tuukkanen J, Andersson G, Lehenkari P (2017) Increased amount of phosphorylated proinflammatory osteopontin in rheumatoid arthritis synovia is associated to decreased tartrate-resistant acid phosphatase 5B/5A ratio. *PLoS One* 12:e0182904. <https://doi.org/10.1371/journal.pone.0182904>
51. Al-Maawi S, Rutkowski J, Sader R, Kirkpatrick CJ, Ghanaati S (2020) The biomaterial-induced cellular reaction allows a novel classification system regardless of the biomaterials origin. *J Oral Implantol*. <https://doi.org/10.1563/aaid-joi-D-19-00201>
52. Zhang Y, Al-Maawi S, Wang X, Sader R, Kirkpatrick CJ, Ghanaati S (2018) Biomaterial-induced multinucleated giant cells express proinflammatory signaling molecules: a

- histological study in humans. *J Biomed Mater Res A*:jbm.a.36594. <https://doi.org/10.1002/jbm.a.36594>
53. Del Fattore A, Teti A, Rucci N (2008) Osteoclast receptors and signaling. *Arch Biochem Biophys* 473:147–160. <https://doi.org/10.1016/j.abb.2008.01.011>
54. Helming L, Gordon S (2008) The molecular basis of macrophage fusion. *Immunobiology*. 212:785–793. <https://doi.org/10.1016/j.imbio.2007.09.012>
55. MacLauchlan S, Skokos EA, Meznarich N, Zhu DH, Raof S, Shipley JM, Senior RM, Bornstein P, Kyriakides TR (2009) Macrophage fusion, giant cell formation, and the foreign body response require matrix metalloproteinase 9. *J Leukoc Biol* 85:617– 626. <https://doi.org/10.1189/jlb.1008588>
56. Zhu XW, Price NM, Gilman RH, Recarvarren S, Friedland JS (2007) Multinucleate Giant cells release functionally unopposed matrix metalloproteinase-9 *in vitro* and *in vivo*. *J Infect Dis* 196: 1076–1079. <https://doi.org/10.1086/521030>
57. Du M, Wang Y, Liu Z, Wang L, Cao Z, Zhang C, Hao Y, He H (2019) Effects of IL-1 β on MMP-9 expression in cementoblastderived cell line and MMP-mediated degradation of type I collagen. *Inflammation*. 42:413–425.
58. Macarie RD, Vadana M, Ciortan L, Tucureanu MM, Ciobanu A, Vinereanu D, Manduteanu I, Simionescu M, Butoi E (2018) The expression of MMP-1 and MMP-9 is up-regulated by smooth muscle cells after their cross-talk with macrophages in high glucose conditions. *J Cell Mol Med* 22:4366–4376. <https://doi.org/10.1111/jcmm.13728>
59. Barbeck M, Booms P, Unger R, Hoffmann V, Sader R, Kirkpatrick CJ, Ghanaati S (2017) Multinucleated giant cells in the implant bed of bone substitutes are foreign body giant cells - new insights into the material-mediated healing process. *J Biomed Mater Res A* 105: 1105–1111. <https://doi.org/10.1002/jbm.a.36006>
60. Omar O, Dahlin A, Gasser A, Dahlin C (2018) Tissue dynamics and regenerative outcome in two resorbable non-cross-linked collagen membranes for guided bone regeneration: a preclinical molecular and histological study *in vivo*. *Clin Oral Implants Res* 29:7– 19. <https://doi.org/10.1111/clr.13032>

3.2.5. Xenogenic biomaterial conclusions

This chapter focus on the biocompatibility of xenogeneic materials, in particular, of collagen membranes. These materials were evaluated using traditional *in vivo* models (such as subcutaneous implantation model in rats) as well as an *ex vivo* interaction with liquid PRF matrix.

A comparative study of five different collagen membranes is described in chapter 3.2.1. using cellular penetration % and liquid – PRF absorption coefficient (PAC) as indicatives. Liquid-PRF (fibrin and cells) was found to be able to completely invade Mucograft® (MG) membrane by reaching its center, while Bio-Gide® (BG) only approximately 50%. Mucoderm® (MD) and Collprotect® (CP) only demonstrated superficial interaction with liquid-PRF. Lastly, BEGO® (BCM) collagen membrane appeared to be free of liquid-PRF entirely. The results of the PAC analysis presented that MG was able to absorb a high content of liquid-PRF components, increasing its original weight by 10 folds (10.12 ± 1.29). In case of BG membrane, the increase in weight was four folds (4.37 ± 1.50) after being immersed in liquid-PRF. The measurements showed that MD had the lowest PAC with an increase of two folds its original weight (2.83 ± 0.53). CP demonstrated a middle range of PAC values, increasing five folds in weight (5.05 ± 2.21) after immersion in liquid-PRF whereas, the BCM test presented an increase of six folds its original weight (6.12 ± 0.97).

The pairing of biomaterials with liquid-PRF can be used clinically to improve the bioactivity of collagen-based biomaterials as well as it may act as a growth factor delivery system that is based on biomaterials. Additionally, it can complement *in vitro* and *in vivo* studies and reduce number of animals needed in the process.

In chapter 3.2.2, *ex vivo* study utilizing PRF study as means of membrane cellular penetration was used together with *in vivo* subcutaneous implantation model. *Ex vivo* results exhibit that there was no cellular penetration after 15 min of PRF application. In terms of subcutaneous implantation model, the membrane retained its structure and neither cells nor blood vessels could be found within its center after 30-day period. Macrophages were reduced in numbers from 3 days to 15 days, from approximately 320 to 150 per mm^2 . Moreover, from day 15 onwards, there was a significant increase in the number of multinucleated giant cells (MNGCs) reaching almost 4 cells per mm^2 . In parallel, increase in neovascularization around the implant site was observed by more than 45 newly formed capillaries. The data presented in this study suggest that OSSIX PLUS® can be used as barrier membrane as it does not disintegrate, however this should be investigated and validated further over a longer period of time.

Chapter 3.2.3 focuses on analysis of bovine Achilles tendon derived membrane, commercially named SYMBIOS®. The investigation methods used were the same as in chapter

3.2.2. The research focused on the interaction between a blood concentrate system (PRF) and SYMBIOS® membrane and revealed presence of leukocytes, platelets, and fibrin with membrane's center 15 min after the deposition. *In vivo* data indicates the peak in the number of macrophages was observed at day 10 after implantation procedure, achieving up to 200 cells per mm². MNGCs were not detected at any time point, while mononuclear cells could be observed in the middle of the membrane. The membrane retained its integrity over 30 day period. At day 10, as well as 30, approximately 40 of newly formed capillaries per mm² (areas indicated by CD31 immunohistochemical staining) were counted. This data do not contribute to the theory of MNGCs presence necessity in new vessel formation process.

Investigation of tissue reaction to Creos Xenoprotect® membrane was conducted and describe in detail in chapter 3.2.4. The same *ex vivo* and *in vivo* models were employed as previously mentioned in above chapters. Fifteen-minute application of PRF concentrate assessment did not show any cellular membrane penetration. Histological data obtained from subcutaneous implantation model did not show any presence of macrophages or MNG cells on day 3. A slight increase in the number of these cells could be seen on day 15 (1 cell per mm²), reaching approximately 12 CD68+ and MNG cells per mm² on day 30. First newly formed blood vessel could be observed on day 3 (15 per mm²). The number of blood vessel was gradually growing over time, up to 40 per mm². The result of the study indicates that MNGCs could play a pivotal role in degradation process of a material.

Overall, the results of these studies show that all tested collagen membranes are biocompatible and support cell adhesion and proliferation. In addition, Ossix Plus® and Creos Xenoprotect® membranes promote foreign body reaction, described by multinucleated giant cell formation and collagen deposition around the materials. Interestingly, together with the gradual increase of a MNGCs within implantation bed over time, an increase in the number of blood vessels was noticed. This leads to the conclusion that moderate presence of MNGCs does not affect biocompatibility of a material in harmful manner, but on the contrary might have a positive effect on neovascularization of the implant environment. Moreover, OSSIX PLUS® and Creos Xenoprotect® membranes were found to be non-permeable to the liquid PRF matrix (fibrin leukocytes and platelets), which suggests that they could be used as a barrier to prevent the ingrowth of undesired cells.

It is important to mention that this research is still in its early stage, as well as it is limited mostly to *in vivo* observation up to 30 days post implantation. On these grounds, further long-term experiments (60 days) and controlled clinical studies are necessary to be evoked. Additionally, as it has been a debate for long time of defining the role of MNGCs in neovascularisation process further studies are necessary to be conducted to identify the

function of biomaterial induced MNGCs. Furthermore, as results obtained from the PRF-based model closely align with *in vivo* findings regarding membrane permeability and function and thus it proves that the model could be potentially used to complement or even replace *in vivo* studies in some cases. Though, it is necessary to emphasize that this research is still preliminary as well as materials which have been applied are only reduce to collagen membrane therefore, other materials should be used to verify that findings.

4. Study of biocompatibility of PP-13

4.1. The pyrrolopyrimidine colchicine-binding site agent PP-13 reduces the metastatic dissemination of invasive cancer cells *in vitro* and *in vivo*

Biochemical Pharmacology, **2019**, 160, 1–13.

Gilson, P.^{a,b}, Couvet, M.^a, Vanwonderghem, L.^a, Henry, M.^a, Voltaire, J.^a, Baulin, V.^c, Werner, M.^c, **Orłowska, A.**^c, Josserand, V.^a, Mahuteau-Betzer, F.^d, Lafanechère, L.^e, Coll, J. L.^a, Busser, B.^{a,b}, & Hurbin, A.^a

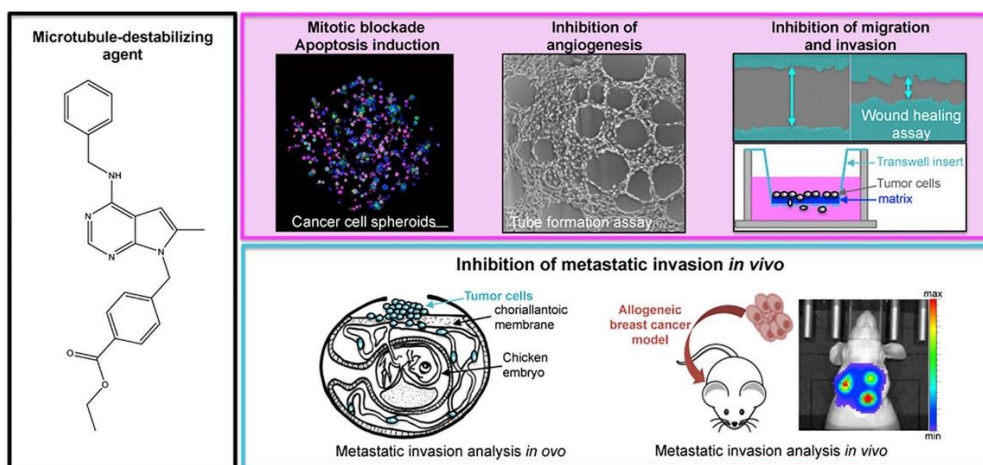
^a Cancer Target and Experimental Therapeutics, Institute for Advanced Biosciences, INSERM U1209, CNRS UMR5309, Grenoble Alpes University, Grenoble, France

^b Biochemistry Department, Grenoble University Hospital, Grenoble, France

^c Departament d'Enginyeria Química, Universitat Rovira i Virgili, Tarragona, Spain

^d Institut Curie, PSL Research University, CNRS, INSERM UMR9187/U1196, Orsay, France

^e Regulation and Pharmacology of the Cytoskeleton, Institute for Advanced Biosciences, INSERM U1209, CNRS UMR5309, Grenoble Alpes University, Grenoble, France.



Abstract

Standard chemotherapies that interfere with microtubule dynamics are a chemotherapeutic option used for the patients with advanced malignancies that invariably relapse after targeted therapies. However, major efforts are needed to reduce their toxicity, optimize their efficacy, and reduce cancer chemoresistance to these agents. We previously identified a pyrrolo[2,3d]pyrimidine-based microtubule-depolymerizing agent (PP-13) that binds to the colchicine site of β -tubulin and exhibits anticancer properties in solid human cancer cells, including chemoresistant subtypes. Here, we investigated the therapeutic potential of PP-13 *in vitro* and *in vivo*. PP-13 induced a mitotic blockade and apoptosis in several cancer cells cultured in two-dimensions or three-dimensions spheroids, in conjunction with reduced cell proliferation. Capillary-like tube formation assays using HUVECs showed that PP-13 displayed antiangiogenic properties. It also inhibited cancer cell motility and invasion, in *in vitro* wound-healing and transwell migration assays. Low concentration PP-13 (130 nmol.L⁻¹) treatment significantly reduced the metastatic invasiveness of human cancer cells engrafts on chicken chorioallantoic membrane. In nude mice, 0.5 or 1 mg.kg⁻¹ PP-13 intraperitoneally administered three-times a week reduced the sizes of paclitaxel-refractory orthotopic breast tumors, delayed the progression of metastasis, and decreased the global metastatic load compared to 0.5 mg.kg⁻¹ paclitaxel or vehicle alone. PP-13 did not show any apparent early adverse effect *in vivo*. These data suggest that PP-13 is a promising alternative to standard chemotherapy in antimitotic drug-refractory tumors, especially through its impact on metastasis.

Introduction

Despite recent innovations in targeted anticancer strategies over the last decade, non-selective chemotherapies are still widely used for the clinical management of various patients with advanced malignancies.¹ Microtubules represent one of the most common targets for chemotherapies, as they are crucial for the maintenance of cell shape, intracellular transport cell motility, and chromosome migration during cell division.² Taxanes and vinca-alkaloids are the two main classes of microtubule-targeting agents and are classically known to induce microtubule stabilization and depolymerization, respectively.³ Therapeutic doses of all compounds from these two families lead to the alteration of the dynamic state of the microtubules, which ultimately induces multipolar divisions and causes cell death.^{4, 5} Beyond their cytotoxic activity, most microtubule-binding agents display antimetastatic, antiangiogenic or vascular-disrupting properties, supporting their use as therapeutic agents for cancer

treatment.⁶⁻⁸ However, the troublesome side effects of microtubule inhibitors, particularly myelosuppression and peripheral neurotoxicity, and the emergence of chemoresistance, predominantly from the overexpression of efflux transporters, drastically limits their therapeutic outcomes,³ hence underscoring the need for alternative agents.

We recently identified a novel pyrrolopyrimidine-based microtubule-depolymerizing agent (PP-13) that was effective *in vitro* on a wide range of human cancer cells.⁹ PP-13 has no kinase activity, directly binds to the colchicine binding site of β -tubulin, interferes with microtubule organization and induces spindle multipolarity, transient mitotic cell cycle arrest and apoptosis.⁹ Interestingly, in marked contrast to conventional microtubule-damaging drugs, PP-13 escapes resistance mechanisms linked to the presence of efflux pumps, which underlies its potential anticancer activity for multidrug-resistant cancer cells.⁹ Based on the efficacy of PP-13 against human cancer cell proliferation and multi drug resistant cancer cells, the aim of the present study was to investigate the therapeutic potential of PP-13 against highly invasive and aggressive cancer cell lines *in vitro* and *in vivo*. The effects of PP-13 were analyzed in HeLa cervical cancer cells, A549 NSCLC cells and 4T1 murine mammary cancer cells that were cultured in two-dimensions monolayers or in three dimensions-spheroids. The impact of PP-13 on cell migration, metastasis and angiogenesis was evaluated. Since no colchicine binding-site agent is currently used in clinic for cancer treatment, we assessed the clinical potential of PP-13 activity in comparison with paclitaxel, a standard anti-mitotic chemotherapy that is routinely used for the treatment of a wide range of solid cancers, and is considered a reference treatment for *in vitro* and *in vivo* studies of new microtubule-targeting agents.

Experimental

Materials

Paclitaxel was obtained from Sigma-Aldrich (Saint-Quentin-Fallavier, France). PP-13 was obtained from Institut Curie (CNRS Chemical library, 2004 version), as described in.⁹ All drugs were dissolved in sterile anhydrous dimethyl sulfoxide (DMSO, Carl Roth, Karlsruhe, Germany) at a 10 mmol.L⁻¹ stock solution. Phospho-histone H3 (H3P), and active caspase-3 antibodies were purchased from Cell Signaling Technology (Ozyme, Saint-Quentin-LesYvelines, France), and conjugated Alexa Fluor 633 goat anti-rabbit antibodies were from Thermo Fisher Scientific (Saint-Aubin, France).

Cell lines and culture

The human HeLa and A549 cell lines and the murine 4T1 cells were obtained from the American Type Culture Collection (ATCC, Manassas, VA, USA). HeLa cells expressing mEGFP- α -tubulin and mRFP-H2B (HeLa-EGFP/RFP) were a generous gift from Dr. D. Gerlich [10]. The 4T1 cells were stably transfected with a plasmid expressing the fusion histone H2B-RFP (provided by Dr. C. Albigès-Rizo, Institute for Advanced Biosciences, Grenoble, France) (4T1-RFP) or with the pGL4.50[luc2/CMV/Hygro] vector encoding the firefly luciferase reporter gene luc2 (Promega, Charbonnière, France) (4T1-rvLuc2) using JetPEI (Polyplus Transfection, Illkirch, France) according to the manufacturer's protocol. Transfected cells were selected with G418 antibiotic (Invivogen Europe, Toulouse, France, ant-gn-5) and amplified. All cells were routinely tested for the presence of mycoplasma (MYCOALERT® Mycoplasma Detection Kit, Lonza, Amboise, France) and used within three months after thawing. A549, HeLa, and HeLa-EGFP/RFP cell lines were authenticated by DNA STR profiling (ATCC Cell line Authentication Service, Manassas, VA, USA). Human umbilical vein endothelial cells (HUVECs, passage two to five; Lonza) were cultured in complete medium of the EGM-2 BulletKit (Lonza, Amboise, France).

Two-dimensions (2D) cell culture

Cells were maintained in culture at 37°C in the appropriate medium with 10% FBS in a 5% CO₂ humidified atmosphere, and the cell morphology was routinely checked.

Three-dimensions (3D) cell culture

Spheroids were generated by plating A549 (4000 cells/well), HeLa-EGFP/RFP (1000 cells/well), or 4T1-RFP (2000 cells/well) cells into 96-well round bottom ultra-low attachment (ULA) spheroid microplates (Corning, Tewksbury, MA, USA). The spheroid culture was performed in medium with 10% FBS in a humidified atmosphere with 5% CO₂. Spheroid formation and growth were assessed by microscopic examination using an inverted microscope and by imaging the spheroids at each time point.

***In vitro* cytotoxicity assays**

Cell proliferation assays were conducted in 96-well culture plates. 2D-cultured cells and spheroids were cultured for 24 h and 72 h, respectively, prior to treatment with PP-13 or paclitaxel in medium containing 10% FBS for 72 h. The cell viability was quantified using CELLTITER 96® AQueous One Solution cell proliferation assay (Promega, Charbonnière, France)

in 2D cell models or by using the CELLTITER-GLO® 3D Cell Viability Assay (Promega, Charbonnière, France) in spheroids. The drug concentrations required to inhibit cell growth by 50% (IC50) were interpolated from the dose-response curves.

Immunofluorescence analyses of spheroids

After PP-13 treatment, the spheroids were washed, fixed overnight at 4°C in 4% paraformaldehyde, and then washed, frozen and cut into 7- μ m sections before mounting onto SuperFrost UltraPlus slides (Thermo Fisher Scientific, Saint-Aubin, France). Cryosections were rehydrated in PBS-glycine, permeabilized for 1 h in PBS with 2% Triton X-100, washed in PBS-glycine, blocked in 10% goat serum and incubated overnight at 4°C with primary antibodies. The sections were then washed in 0.2% Tween-20/PBS and incubated for 1 h with conjugated secondary antibodies. Hoechst was used to counterstain the cell nuclei. Fluorescence microscopy was carried out using a confocal microscope (LSM 710; Carl Zeiss, Jena, Germany). An objective Plan Aplanachromat 20 \times /0.8 NA in air and an objective Plan Aplanachromat 63 \times /1.4 NA in oil were used. The H3P and active caspase-3 expression levels in spheroids were counted based on color thresholding image adjustment using ImageJ software (NIH, Bethesda, MD, USA) and the images were blinded. The percentage of H3P was physically wounded the cell monolayers, and increasing concentrations of PP-13 or DMSO were added into the medium. Images of the cells invading the scratch wound were monitored for 12 h using the IncuCyte S3 Live-Cell analysis system (Essen Bioscience, Hertfordshire, UK). The relative wound density was analyzed using the IncuCyte S3 software. Transwell migration and invasion assays A549, 4T1-rvLuc2 and HeLa cells were plated (75000 cells) on top of a transwell chamber with Matrigel (Corning, Tewksbury, MA, USA) under starvation conditions, and complete medium was added into the well. After 24 h of incubation with PP-13 or DMSO, cells that reached the bottom of the transwell were stained with methylene blue and observed by microscopy (AxioImager M2, Carl Zeiss, Jena, Germany). Ten images were obtained per condition and were blinded for quantification. Cell invasion was quantified using a fully connected, three-layer back-propagation neuronal network, as previously described.¹² Briefly, the input layer of the network was prepared to receive 12 9 12 pixel images, with three-color channels totaling up to 12 9 12 9 3 input neurons. A total of twenty-four neurons in the hidden layer were utilized. The output layer consists of two neurons corresponding to the two classes E (empty space between structures) and S (structure) with respect to which each pixel and its neighborhood were classified. A training set of ~10-20 images of each kind were created for training. An extended training set of ~ five hundred pictures per species was generated by rotating each picture by

twenty-four equidistant angles, as well as rescaling to 90, 100, and 110% of the original size. Training was performed by (on average) two thousand forward passes per extended training set picture, with full error back propagations. Feedforward and error-backward propagations employ well-known sigmoidal characteristics based on the logistic function. The target signals for the two output neurons were [1, 0] corresponding to E, and [0, 1] corresponding to S, respectively.

***In vitro* capillary-like tube formation assay**

A 15-well Ibidi angiogenesis microslide (Ibidi, Clinisciences, Nanterren France) was coated with 10 μL of Matrigel matrix (Corning) and incubated for 30 minutes at 37°C for gel polymerization. Twenty thousand HUVECs were seeded on top of the polymerized gel matrix in complete medium with increasing concentrations of PP-13 or 0.1% DMSO. The microslide was then placed in a 37°C heated stage in a 5% CO₂ humidified atmosphere. Images were acquired after 6 h of incubation by a phase-contrast microscope with an Achromat 5 \times /0.12 NA objective, blinded and analyzed using the automated WimTube image analysis tool (Wimasis GmbH, Munich, Germany).

***In vivo* studies using chick embryo tumor model**

A chick embryo tumor growth and metastasis assay (InOvotion, Grenoble, France) was performed as previously described.⁹ According to French legislation, no ethical approval is needed for scientific experimentations using oviparous embryos (decree number 2013–118, February 1, 2013; art. R-214–88). Briefly, fertilized white leghorn eggs (SFPA, Hendrix Genetics group, Saint Briec, France) were incubated at 38°C with 60% relative humidity for nine days. The chorioallantoic membrane (CAM) was then dropped, and a 1-cm² window cut into the eggshell above the CAM (at day nine). A total of three million A549 cells were added directly onto the CAM of each egg. The eggs were randomly allocated into three groups. Group size was determined based on the expertise of InOvotion showing that $n \geq 15$ was the minimum number of eggs to show significant effects. At day ten, when tumors began to be detectable, the eggs were treated every other day for ten days by adding 100 μL of either 50 $\mu\text{mol.L}^{-1}$ paclitaxel ($n = 17$), 0.13 $\mu\text{mol.L}^{-1}$ PP-13 ($n = 18$), or 0.5% DMSO in PBS (vehicle, $n = 18$) dropwise onto the tumor. The concentration of paclitaxel was chosen as a positive control to induce significant tumor growth inhibition without toxicity for embryos.

The concentration of PP-13 has been arbitrarily chosen according to *in vitro* experiments (IC₅₀) and following the expertise of InOvotion. The upper portion of the CAM was then

removed, and the tumors were carefully cut away and weighed. In parallel, a 1 cm² portion of the lower CAM was collected, genomic DNA was extracted, and qPCR analysis was performed by using primers specific for genomic human Alu/repetitive sequences⁹ to evaluate the number of A549 cells. Finally, scoring the number of dead embryos and looking for morphological or functional abnormalities in the surviving embryos was carried out to evaluate the toxicity of the treatment.

***In vivo* studies using mice tumor model**

All animal studies were performed in accordance with the European Economic Community guidelines and the “Principles of Laboratory Animal Care” (NIH publication N 86-23 revised 1985) and were approved by the institutional guidelines and the European Community (EU Directive 2010/63/EU) for the use of experimental animals (authorization for the experiment: APAFIS#8854-2017031314338357 v1).

Six-week-old female NMRI nude mice (Janvier Labs, Le Genest-Saint Isle, France) were anesthetized using 4% isoflurane/air for anesthesia induction and 1.5% thereafter, and luciferase-modified mouse 4T1 cancer cells (4T1-rvLuc2 cells, 20000 cells per 50 µL) were injected into the mammary fat pad. The mice were immediately randomly divided into four groups of eight mice, receiving vehicle (0.9% NaCl, 1% DMSO, 30% PEG, 1% Tween-80, referred to as control), 0.5 mg.kg⁻¹ paclitaxel, 0.5 mg.kg⁻¹ PP-13, or 1 mg.kg⁻¹ PP-13. Group size was determined based on our expertise showing that $n \geq 8$ per group was the minimum number of mice to show significant effects on metastases. Based on the results obtained on chick embryo tumor model showing the effect of PP-13 at very low dose, two low concentrations of PP-13 were chosen (0.5 and 1 mg.kg⁻¹). Similar low concentration (0.5 mg.kg⁻¹) was chosen for paclitaxel to compare this standard chemotherapy with PP-13, and based on preliminary experiments showing sub-therapeutic effect of 0.5 mg/kg-1 paclitaxel on tumor and metastases growth (data not shown). Intraperitoneal administration of 200 µL of treatment was performed three times per week for five weeks. The mice were examined daily for behavior and morbidity and were weighed three times per week. The primary tumor growth was monitored three times per week using a caliper, and the tumor volume was calculated as follows:¹³ tumor volume = length x width² x 0.4. The thoracic metastasis growth was followed once per week by *in vivo* bioluminescence imaging (IVIS KINETIC, Perkin Elmer, Waltham, MA, USA) 5 min after the intraperitoneal injection of 150 mg.kg⁻¹ of luciferin (Promega, E1605), as previously described.¹⁴ Twenty-two days after 4T1-rvLuc2 cell implantation, 0.1 mg.kg⁻¹ buprenorphine was injected subcutaneously for analgesia and the primary breast tumors were excised under general

anesthesia. The mice were carefully observed during the day following the surgery. After five weeks, the mice were sacrificed and blood samples were collected by cardiac puncture using a heparinized syringe. The lungs, axillary and brachial lymph nodes, kidney and liver were harvested for further imaging and/or analyses.

***Ex vivo* studies of mice tissue samples**

Blood samples were evaluated for hematological parameters with a medical automated hematology analyzer (Micros-60, Horiba ABX, Montpellier, France), and biochemical analyses were performed by the Charles Rivers Laboratory (Massachusetts, USA). Bone marrow was obtained after having carefully sectioned mice femurs at each joint and flushing the bone cavity with PBS. Cells from the plasma and bone marrow samples were washed in PBS, cytopspin (Cytospin 4, Fisher Scientific, Illkirch, France) and stained with MayGrunwald-Giemsa solution (MGG) with the automated XE-5000 Instrument (Sysmex, Roissy, France). Global cell abundance evaluation and megakaryocyte and leukocyte counting were then performed for both samples by an experienced hematologist. Tumor tissues were frozen in OCT-embedding medium (VWR international, Fontenay-sous-Bois, France) and cut into 7 μm thick sections using a cryomicrotome for immunohistochemical analyses. Immunohistochemical examinations were performed after fixation with 4% paraformaldehyde and staining with anti-CD31 antibody (Pharmingen, BD Biosciences, Le Pont de Claix, France), using an AxioImager M2 microscope (Carl Zeiss, Jena, Germany). Segmentation of tissues was performed using a fully connected, three-layer back-propagation neuronal network, as previously described.¹²

Statistical analyses

All analyses were performed using the GraphPad Prism software (GraphPad Software Inc., San Diego, California, USA). Statistical comparisons between two groups or more were conducted with Mann-Whitney test, Kruskal-Wallis test, or Friedman test with Dunn's multiple comparisons *post hoc* test. Statistical comparisons between mice groups among time were determined by two-way ANOVA with Bonferroni's *post hoc* test. Statistical significance was defined for p values ≤ 0.05 .

Results and discussion

PP-13 treatment decreases cancer cell proliferation *in vitro*

To investigate the therapeutic effect of PP-13, we chose three cell lines displaying high levels of proliferation, migration and invasiveness: the human HeLa cervical cell line and its derivative subclone expressing mEGFP-tubulin and mRFP-H2B (HeLa-EGFP/RFP), the human A549 lung cancer cell line, and the mouse 4T1 mammary cancer cells expressing mRFP-H2B (4T1-RFP) or luciferase (4T1-rvLuc2). We first analyzed the toxicity of PP-13 in these cell lines cultured in monolayers or in 3D-spheroids. PP-13 had a significant effect on the proliferation of these cell lines, strongly reducing their viability (Fig. 1A). The IC50 values of PP-13 (50% growth inhibition) were relatively similar for the three cell lines cultured in monolayers (Table 1).⁹ These IC50 values did not vary significantly when the cells were grown in spheroids, except for A549 (Table 1 and Fig. 1A and 1B). Indeed, the A549 spheroids appeared to strongly resist PP-13 treatment compared to A549 cells in the monolayer cell culture. Similar effects were observed in these cell lines with the reference antimitotic chemotherapy paclitaxel (Table 1 and Fig. 1). We have shown that paclitaxel has a reducing effect on 4T1 cell viability in 2D culture compared to A549 (~five-fold lower) and HeLa (~ten-fold lower) cells, thus reflecting the resistance of 4T1 cells to paclitaxel. In addition, although 4T1-RFP spheroids were surprisingly more sensitive to low doses of paclitaxel than monolayer 4T1-RFP cells, high concentrations of paclitaxel failed to inhibit more than 50% of the cell proliferation of both A549 and 4T1 spheroids. Thus, PP-13 affected the proliferation of invasive cells *in vitro*, including those that are resistant to paclitaxel.

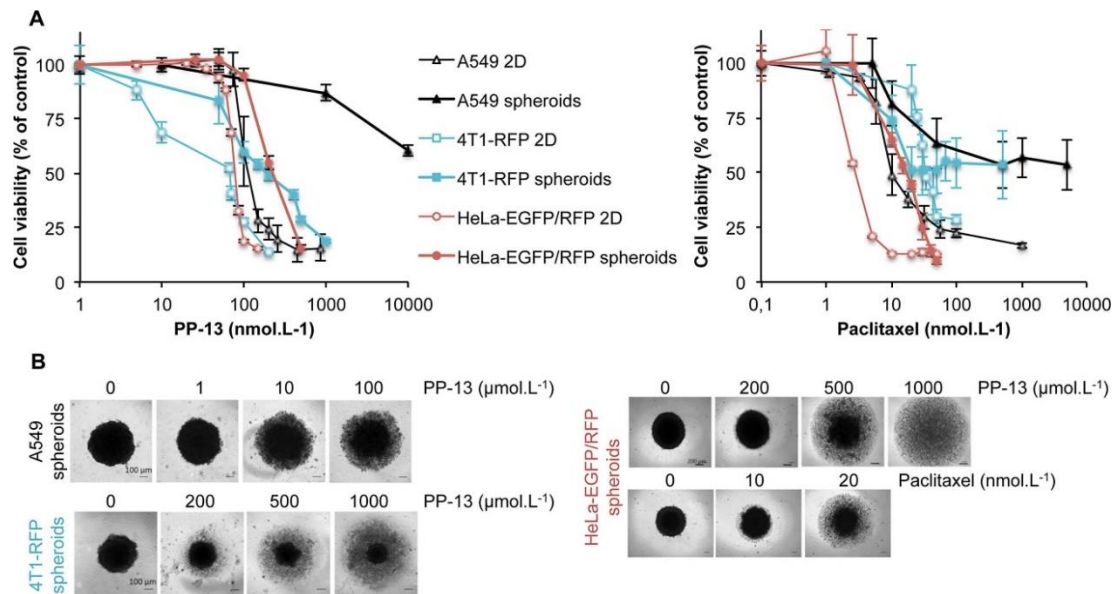


Figure 1. Viability of cancer cells treated with PP-13 or paclitaxel. (A) A549, 4T1 mRFP-H2B (4T1-RFP), and HeLa mEGFP- α -tubulin mRFP-H2B (HeLaEGFP/RFP) were cultured in two-dimensions (2D) or in spheroids, and treated for 72 h with increasing concentrations of PP-13 (left) or paclitaxel (right), and the cell viability was assessed. Data represent the mean \pm SD from three independent experiments, each performed in triplicate. (B) Representative images of treated spheroids are shown; Scale bars: 100 μ m.

PP-13 treatment induces mitotic blockade in cancer cell spheroids

We previously demonstrated that PP-13 induced a transient mitotic blockade by interfering with mitotic spindle organization and microtubule dynamics in monolayer cell cultures.⁹ Here, we analyzed the effect of PP-13 on mitosis in spheroids. The cell viability of HeLaEGFP/RFP spheroids was not impacted by a short 24 h treatment of 200 nmol.L⁻¹ PP-13 (data not shown). Alpha-tubulin and phosphorylated histone H3 (H3P), a marker of late G2/M cell cycle phase, were analyzed by confocal microscopy on HeLa-EGFP/RFP spheroid sections (Fig. 2A). We observed that PP-13 led to mitotic defects, including multiple misoriented and shortened mitotic spindles (green arrows) associated with chromosomes miscongression (blue arrows). In addition, we showed a significant increase in the level of H3P after 24 h of PP-13 treatment, reflecting the strong accumulation of cells in mitosis in the HeLa-EGFP/RFP spheroids (Fig. 2C). As expected, paclitaxel also enhanced the level of H3P in HeLaEGFP/RFP spheroids but to a lower extent than PP-13 and with an effect mainly on the cells at the periphery of the spheroids (Fig. 2B and 2C). Accumulation of H3P in response to PP-13 treatment was also increased in A549 spheroids compared to untreated control (Fig. 2C), and was confirmed by western blot of the three spheroid types (Fig. 2D). Finally, after 72 h of PP13 treatment, the HeLa-EGFP/RFP spheroids showed a significant increase in cleaved caspase-3 (Fig. 2E and 2F). Therefore, in spheroid cultures, PP-13 induced mitotic spindle disorganization, mitotic blockade, inhibition of cell growth and apoptosis.

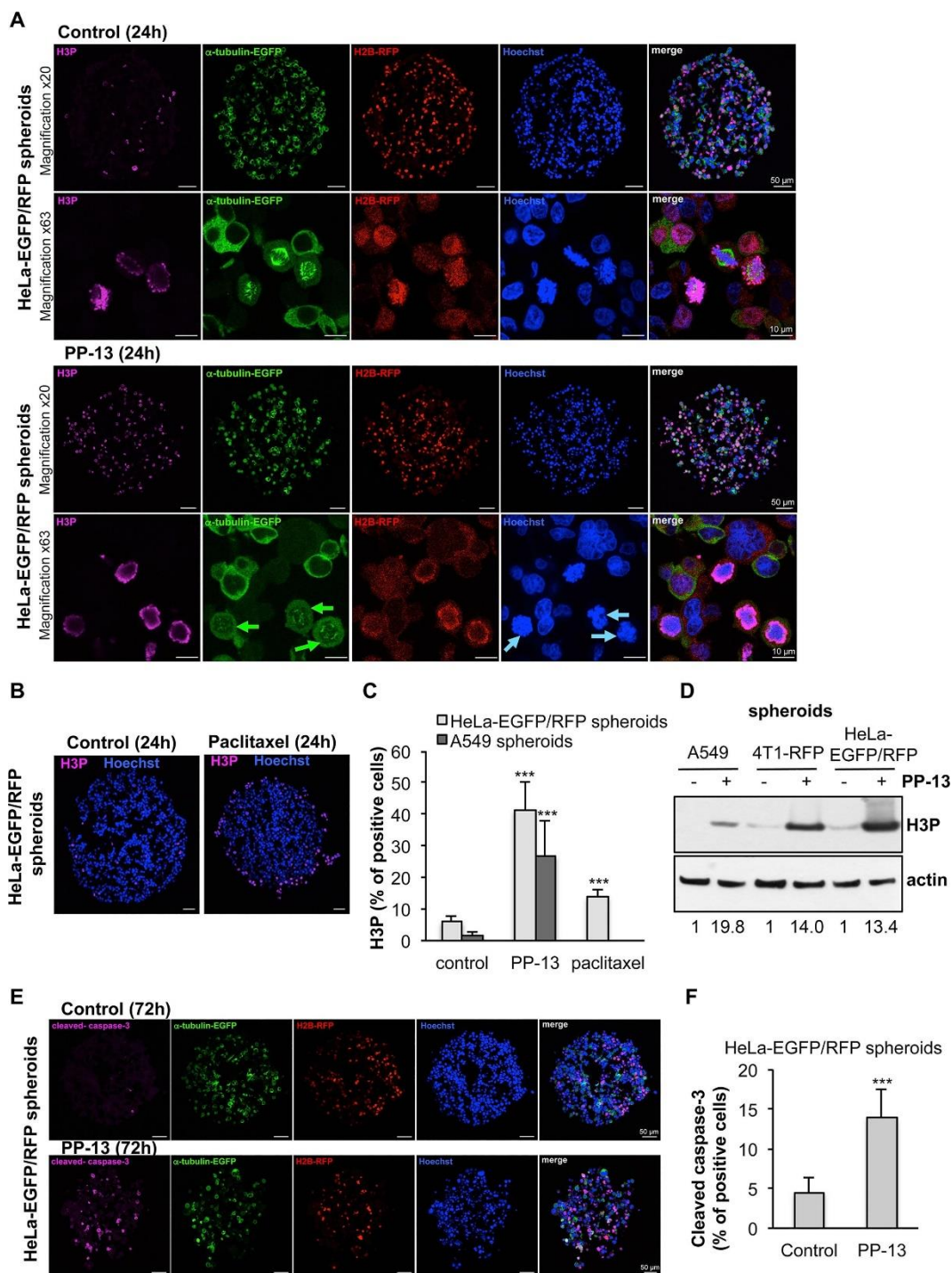


Figure 2. Effects of PP-13 on cancer cell spheroids. HeLa mEGFP-tubulin mRFP-H2B (HeLa-EGFP/RFP) spheroids were treated with vehicle (control), 200 nmol.L⁻¹ PP-13, or 15 nmol.L⁻¹ paclitaxel for 24 h (A-D) or for 72 h (E-F). A549 spheroids were treated for 24 h with vehicle (control) or 10 μmol.L⁻¹ PP-13 (C-D). 4T1 mRFP-H2B (4T1-RFP) spheroids were treated for 24 h with vehicle (control) or 200 nmol.L⁻¹ PP-13 (D). (A) Representative confocal microscopy images of microtubules (α-tubulin-EGFP) and phosphorylated histone H3 (H3P, a marker of late G2/M cell cycle phase) immunodetection in spheroid sections treated with vehicle (control) or PP-13. In purple: H3P, in green: α-tubulin, in red: H2B-RFP, in blue: Hoechst-stained nuclei. The green and blue arrows indicate multipolar mitotic spindles and miscongressed chromosomes, respectively. Scale bars: 50 μm and 10 μm. (B) Representative confocal microscopy images of H3P analyzed by immunofluorescence on spheroids sections treated with vehicle (control), or paclitaxel. In pink: H3P, in blue: Hoechst-stained nuclei. Scale bars: 50 μm. (C) The percentage of H3P was calculated as the number of H3P-positive cells in control (n = 7, HeLa-EGFP/RFP; n=11, A549), PP-13 (n = 13,

HeLa-EGFP/RFP; n=11, A549), or paclitaxel (n = 9, HeLa-EGFP/RFP) spheroids, with two or three sections per spheroid. Data are expressed as the mean \pm SD. *** $p < 0.0001$ between control and treated conditions; Mann-Whitney U-test. (D) Western blot analysis of H3P in A549, 4T1-RFP, or HeLa-EGFP/RFP pooled spheroids (n = 10 spheroids in each condition). Actin was used as a loading control. Values indicate relative H3P/actin ratio. (E) Representative confocal microscopy images of cleaved caspase-3 immunodetection in spheroid sections. In purple: cleaved caspase-3, in green: α -tubulin, in red: H2B-RFP, in blue: Hoechst-stained nuclei. Scale bars: 50 μ m. (F) Quantification of cleaved caspase-3 in spheroids (control, n = 9 spheroids; PP-13, n = 7 spheroids; with two or three sections per spheroids). Data are expressed as the mean \pm SD. *** $p < 0.0001$ between control and treated conditions; MannWhitney U-test.

PP-13 inhibits angiogenesis *in vitro*

Because most of the microtubule-targeting agents also exhibit antiangiogenic properties^{3, 6, 15, 16} we investigated the effects of PP-13 on capillary-like structure formation *in vitro* using HUVECs plated on a Matrigel basement membrane. In control conditions, endothelial cells aligned and formed organized networks of capillary-like structures after 6 h (Fig. 3A). PP-13 treatment reduced the total number of branching points, the number of loops, the length of the tubes, and the total cell-covered area compared to the control (Fig. 3B). Altogether, PP13 altered the ability of HUVECs to form tube-like structures. The concentrations of PP-13 that were used had limited impact on HUVEC proliferation (Fig. 3C). Hence, this suggested that PP-13 displayed antiangiogenic properties *in vitro*.

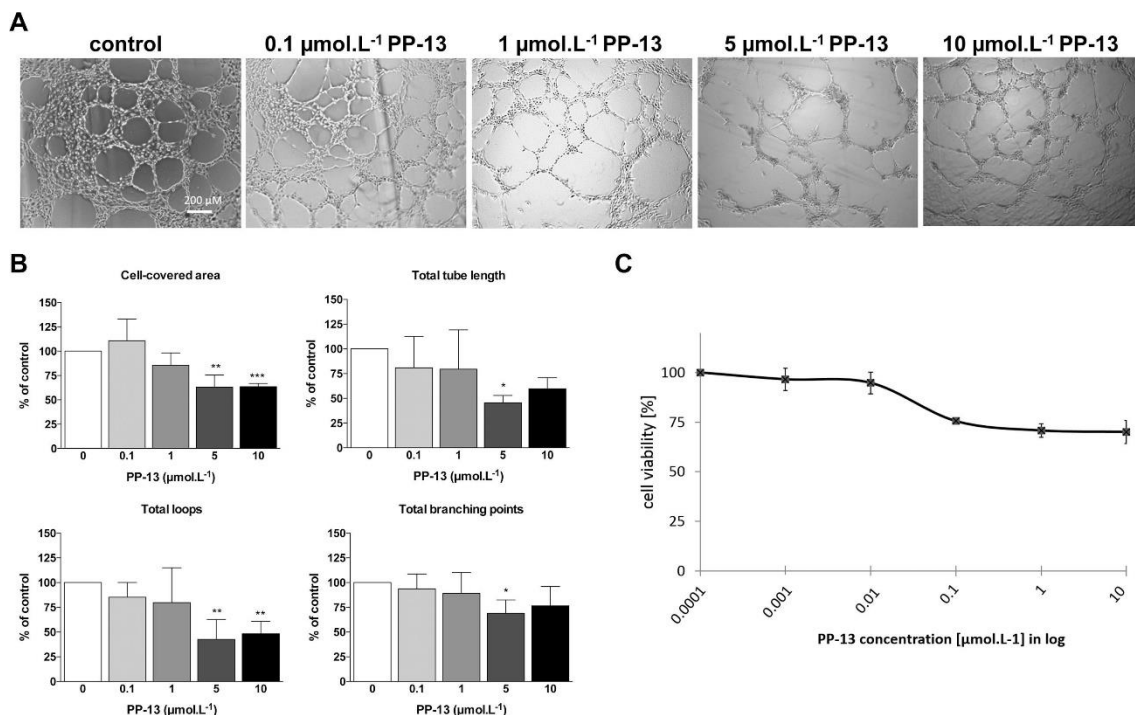


Figure 3. *In vitro* effects of PP-13 on angiogenesis. HUVECs were treated with vehicle (control) or increasing concentrations of PP-13, as indicated, for 6 h. (A) Capillary-like tube formation assay: representative images of the HUVEC capillary-like tube formation in each condition. Scale bar: 200 μ m. (B) Quantification of the tube length, the cell-covered area, the number of loops and the number of branching points. Data are expressed as the mean \pm SD and as the percentages of vehicle condition to control the seeding variations between the experiments (n = 5). * $p < 0.05$; ** $p < 0.01$; *** $p < 0.001$ between control and treated conditions; Kruskal-Wallis test with Dunn's multiple

comparisons post hoc test. (C) HUVEC cell viability was assessed. Data represent the mean \pm SD (n \geq 3).

PP-13 inhibits the migration of cancer cells *in vitro*

Given the essential role of microtubules in cell motility, we investigated whether the PP-tubulin inhibitor impacted HeLa, A549, and 4T1-rvLuc2 cell migration and invasiveness *in vitro*. The impact of PP-13 on the motility of cells was examined using an *in vitro* wound healing assay. We observed that PP-13 significantly reduced the motility of the three cell lines in a dose-dependent manner, and as paclitaxel (Fig. 4A and 4B). The effect of PP-13 on invasive migration was assessed with Matrigel in transwell chambers. PP-13 exerted a strong inhibitory effect on the invasion of the three cell lines (Fig. 4C and 4D). Paclitaxel also inhibited the invasion of these cells. These results indicated that PP-13 is able to slow down cell motility and invasion *in vitro*.

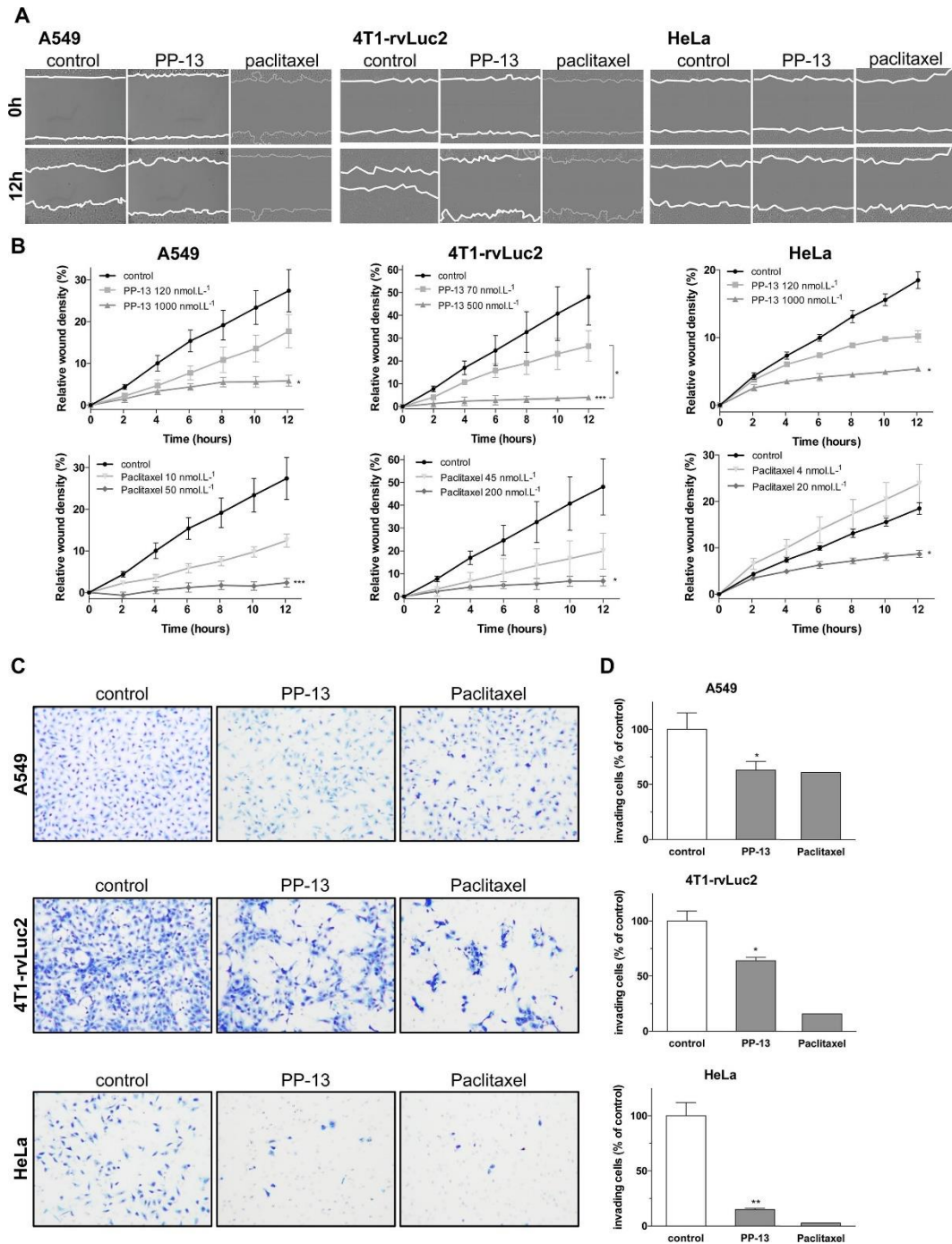


Figure 4. *In vitro* effects of PP-13 on cancer cell migration and invasion. (A-B) Wound-healing assay in A549, HeLa, and 4T1-rvLuc2 cells treated with vehicle (control) or increasing concentrations of PP-13 or paclitaxel for 12 h. (A) Representative images from wound-healing assay experiment at 0 h and 12 h. Cells were treated with vehicle (control), 1 $\mu\text{mol.L}^{-1}$ (A549 and HeLa) or 0.5 $\mu\text{mol.L}^{-1}$ (4T1-rvLuc2) PP-13, 20 nmol.L⁻¹ (HeLa) or 50 nmol.L⁻¹ (A549) or 200 nmol.L⁻¹ (4T1-rvLuc2) paclitaxel. The white lane delineates the edges of the wound. (B) Relative wound density over time in cells treated as indicated. The relative wound density at 0 h is arbitrarily set to 0%. Data are expressed as the mean \pm SD. Experiments were performed at least five times in triplicate. * $p < 0.05$; ** $p < 0.01$; *** $p < 0.001$ compared to control or treated conditions as indicated; Friedman test with Dunn's multiple comparisons post hoc test. (C, D) Matrigel invasion assay of A549, 4T1rvLuc2 and HeLa cells treated with vehicle (control), 200 nmol.L⁻¹ (4T1-rvLuc2) or 500 nmol.L⁻¹ (A549, HeLa) PP-13, or 20 nmol.L⁻¹ (HeLa), 40 nmol.L⁻¹ (A549), or 150 nmol.L⁻¹ (4T1-rvLuc2) paclitaxel for 24 h. (C) Representative images from methylen-blue stained cells treated with vehicle (control), PP-13, or paclitaxel. The red squares show the quantified cells. (D)

Quantification of invasion of cells treated with vehicle (control), PP-13, or paclitaxel. Cells were counted in ten fields per condition and in three independent experiments. Data are expressed as the mean \pm SD and as the percentages of vehicle condition to control variations between the experiments. * $p < 0.05$; ** $p < 0.01$ between control and treated conditions; Mann-Whitney U-test.

PP-13 inhibits the migration of cancer cells *in vivo*

We previously showed that PP-13 reduces tumor growth and metastatic invasion *in vivo* by using H358 NSCLC cells engrafted onto chicken chorioallantoic membranes (CAMs).⁹ Here, we used A549 NSCLC cells engrafted onto the CAMs to evaluate the efficacy of PP-13 on the migration of invasive cancer cells. The tumors were treated every other day with vehicle (control), PP-13, or paclitaxel (Fig. 5A). At the end of the experiment, the tumors were recovered from the upper CAMs and weighed. We used a very low concentration of PP13 (0.13 $\mu\text{mol.L}^{-1}$) compared to the $> 10 \mu\text{mol.L}^{-1}$ PP-13 IC₅₀ in the A549 spheroid cell culture (Table 1), which did not inhibit A549 tumor growth (Fig. 5B). Analysis of the presence of A549 cells at the lower CAM by qPCR, allowing for the accurate detection of tumor cell dissemination, showed that this low dose of PP-13 significantly reduced the metastatic ability of A549 cells compared to the control (Fig. 5C). Paclitaxel was used as a positive control at a concentration known to inhibit A549 tumor growth and metastatic dissemination without inducing significant toxicity (Fig. 5B and 5C).⁹ These results suggested that PP-13 inhibited invasion *in vivo*. Furthermore, treatment with PP-13 did not significantly increase the mortality (two embryos died in the control group, and one embryo died in both paclitaxel and PP-13-treated groups) or abnormalities (no abnormality observed on surviving embryos for the different experimental groups) on chicken embryos, indicating that it was well tolerated.

Table 1. Sensitivity of cancer cell lines to PP-13 and paclitaxel.

Cell lines and condition		PP-13 IC ₅₀ [nmol.L ⁻¹]	Paclitaxel IC ₅₀ [nmol.L ⁻¹]
HeLa	2D	120 \pm 10.0	4.0 \pm 3.5
HeLa-EGFP/RFP	2D	75 \pm 7.1	2.8 \pm 0.4
	Spheroids	185 \pm 49.5	17 \pm 0.6
A549	2D	120 \pm 40	9 \pm 4.9
	Spheroids	> 10,000	> 500
4T1-RFP	2D	66.5 \pm 2.1	35 \pm 2.1
	Spheroids	200 \pm 5.8	17.5 \pm 3.5
4T1-rvLuc2	2D	69.3 \pm 9.0	45 \pm 3.0

The drug concentrations required to inhibit cell growth by 50% (IC₅₀) at 72 h in HeLa cells, HeLa mEGFP- α -tubulin and mRFP-H2B cells (HeLa-EGFP/RFP), A549 cells, 4T1 mRFP-H2B cells (4T1-RFP) and 4T1-rvLuc2 cells cultured in 2D-monolayer (2D) or spheroids. Data represent the mean \pm SD of three independent experiments, each performed in triplicate.

PP-13 impairs tumor progression and metastasis in an allogeneic breast cancer model

To further evaluate the effect of PP-13 on tumor growth and metastasis formation, we used the allogeneic model of 4T1-rvLuc2 cell engraftment in the mammary fat pads of mice. We chose this model because once engrafted orthotopically in the mammary gland, 4T1-rvLuc2 mouse cancer cells metastasize to multiple distant sites (lymph nodes, lungs, liver, bone, brain), thus mimicking human breast cancers.¹⁷ As soon as the 4T1-rvLuc2 cells were inoculated, the mice were randomly divided into four groups: one control group, one group treated with paclitaxel (0.5 mg.kg⁻¹) and two groups treated with PP-13 (0.5 and 1 mg.kg⁻¹) (Fig. 5D). The low concentrations of PP-13 were chosen based on the results obtained on chick embryo tumor model showing an inhibitory effect of PP-13 at very low dose, and were compared to the same concentration of the standard chemotherapy paclitaxel. Intraperitoneal injections of each treatment were performed three times per week. The tumor progression was not affected at early time points, but the final tumor volumes were significantly lower after three weeks for the two groups treated with PP-13 in this rapidly progressing breast cancer model (Fig. 5E). The potential antiangiogenic activity of PP-13 *in vivo* was assessed sections performed on primary tumors stained with an anti-CD31 antibody. The microvessel density was counted and showed no significant difference between the treatments at the concentrations used and at this time-point (Fig. 5F).

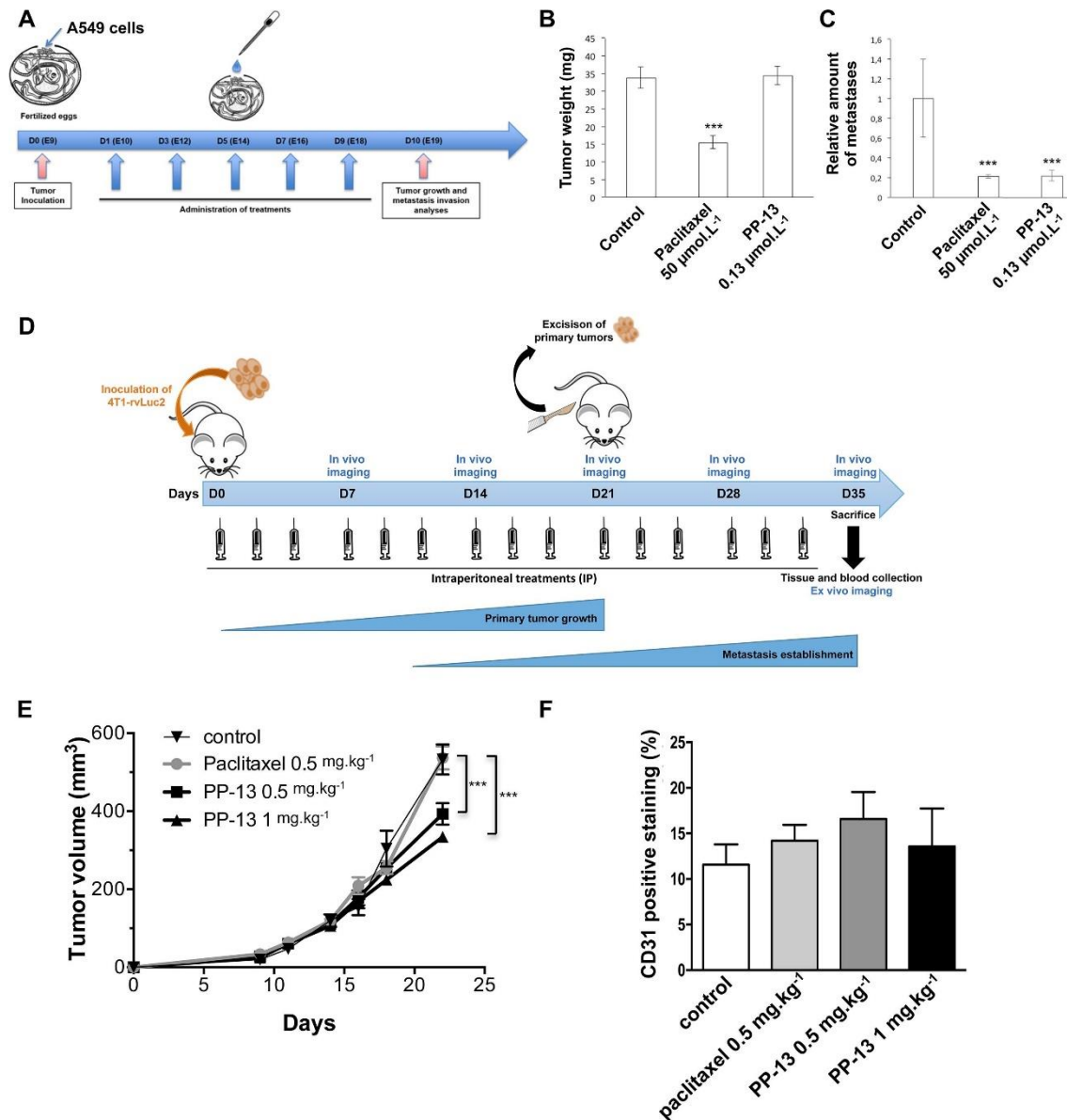


Figure 5. Effects of PP-13 *in vivo*. (A) Schematic representation of the *in ovo* assay principle. A549 cells were engrafted onto chick embryo chorioallantoic membranes (CAMs) at E9, were randomized into three groups, and treatments with 0.5% DMSO (control, $n = 18$), 50 µmol.L⁻¹ paclitaxel (positive control of tumor growth inhibition, $n = 17$), or 0.13 µmol.L⁻¹ PP-13 (low dose, $n = 18$) were administered every other day for 10 days. (B) Tumors were excised and weighted at the end of the treatments. The histogram represents the effect of treatments on A549 tumor weight (means ± SEM, $n = 16$). *** $p < 0.001$ compared to control; Kruskal-Wallis test. (C) The presence of A549 cells in the lower CAM at the end of the experiment was evaluated by qPCR in ten random embryos per group. The histogram represents the effect of treatments on A549 metastases in the lower CAM (means ± SEM, $n = 10$). The relative amount of metastases in the lower CAM in the control group is arbitrarily set to one to control interindividual variations. *** $p < 0.001$ compared to control; Kruskal-Wallis test. (D) Schematic representation of orthotopic breast tumors and metastatic growth and of the treatment plan. The mice were inoculated with 4T1-rvLuc2 cells and randomized into four groups of eight mice. Vehicle (control), 0.5 mg.kg⁻¹ paclitaxel, or 0.5 or 1 mg.kg⁻¹ PP-13 were administered intraperitoneally three times a week. Thoracic bioluminescence imaging was performed once a week for five weeks. After three weeks, the primary tumors were resected. (E) Primary tumor volume. Data represent the mean ± SEM in each group ($n = 8$). *** $p < 0.001$ compared to control group; two-way ANOVA with Bonferroni post hoc test. (F) Histogram shows the CD31 positive staining quantification on frozen 4T1-tumor sections, expressed as the mean ± SD. The CD31 levels were determined after counting positive

stained blood vessel area as described in methods, in three sections per tumor and in three tumors per group.

No significant difference between the treatments was observed in Ki67 immunostaining either (data not shown). *In vivo* bioluminescence imaging was used to follow the development of thoracic metastases before and after primary tumor resection. Paclitaxel had no effect on the bioluminescence signal compared to the control treatment and even slightly enhanced it at day 28 (Fig. 6A and 6B). In contrast, the signal of thoracic metastasis was reduced with PP-13 treatment. Of note, both PP-13 and paclitaxel treatment reduced the number of mice with thoracic metastases compared to the control treatment from 2 weeks of treatment (Table 2). These results were confirmed by measuring bioluminescence in the lungs *ex vivo* at the end of the experiment (day 35) (Fig. 6C). This showed a non-significant 66% reduction in the lung metastasis signal in mice treated with 1 mg.kg⁻¹ PP-13 compared to control mice (Fig. 6D).

Table 2. PP-13 decreased the number of mice with thoracic and lymph node metastases

Treatments	Mice with thoracic metastases (day 14)		Mice with invaded lymph nodes (day 35)	
	Number	%	Number	%
Control	6/8	75	6/8	75
Paclitaxel 0.5 mg.kg ⁻¹	3/8	37.5	5/7	71
PP-13 0.5 mg.kg ⁻¹	5/8	62.5	4/8	50
PP-13 1 mg.kg ⁻¹	4/8	50	1/8	13

Mice with 4T1-rvLuc2 tumors were treated with vehicle (control), paclitaxel 0.5 mg.kg⁻¹, or PP-13 (0.5 and 1 mg.kg⁻¹) (see Fig. 5D). Number and percentages of mice with thoracic metastases at day 14, and with invaded axillary and brachial lymph nodes at day 35 are shown in each group.

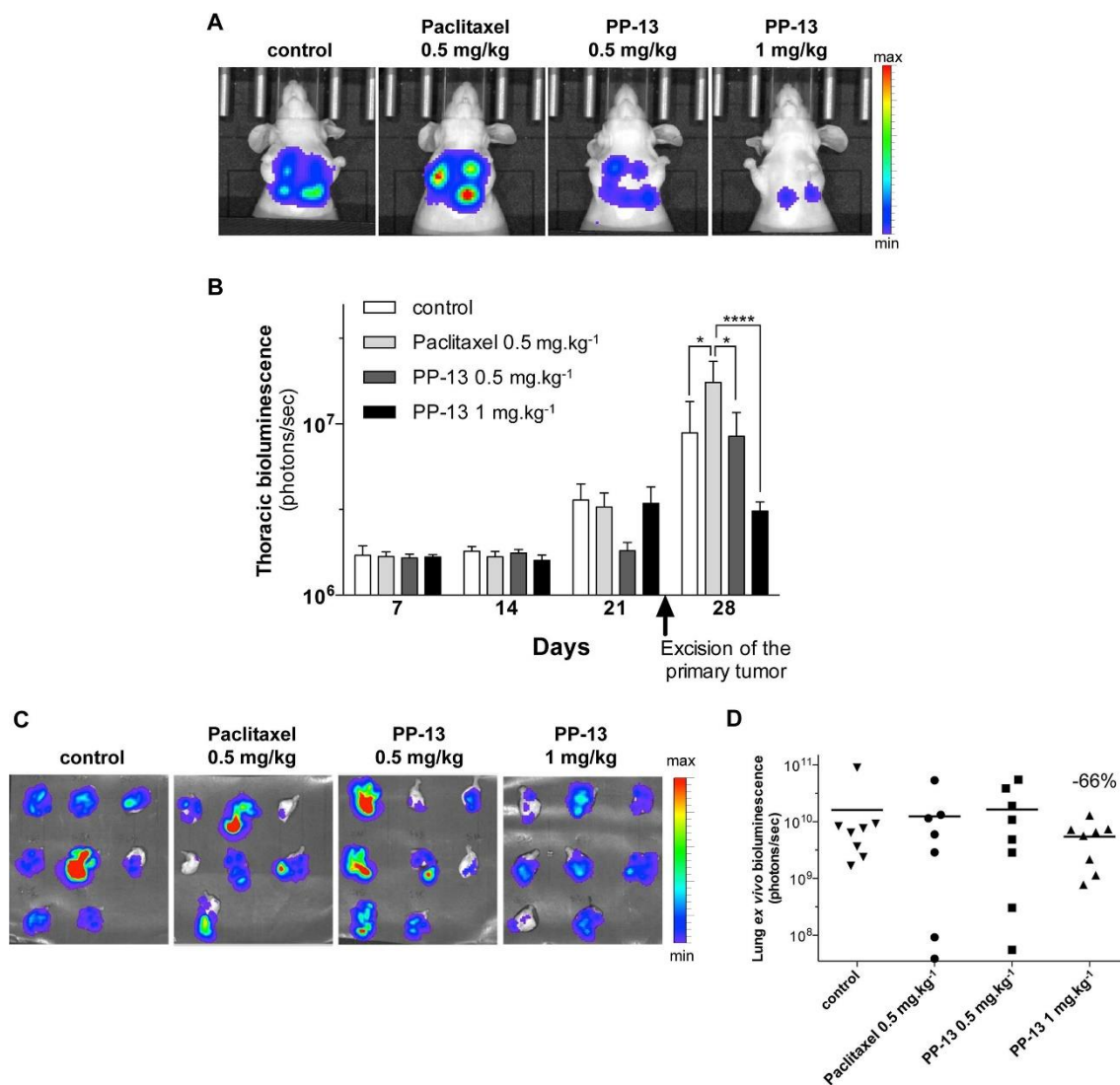


Figure 6. Effects of PP-13 on thoracic metastases in orthotopic breast tumor model. Mice with 4T1-rvLuc2 tumors were treated with vehicle (control), paclitaxel 0.5 mg.kg⁻¹, or PP-13 (0.5 and 1 mg.kg⁻¹), 3 times a week (see Fig. 5D). (A) *In vivo* bioluminescence images of the thoracic metastases (ventral view) in one representative mouse per group at day twenty eight. (B) Overtime quantification of *in vivo* bioluminescence signal in thoracic areas over the duration of the experiment (ventral and dorsal views). Data are expressed as the mean \pm SEM (n = 8). * $p < 0.05$; **** $p < 0.0001$ compared to control or to paclitaxel-treated groups; twoway ANOVA with Bonferroni post hoc test. (C) *Ex vivo* bioluminescence images of lungs at the end of the experiment (day 35). (n = 8, except in paclitaxel-treated group, n = 7). (D) *Ex vivo* bioluminescence signal in each lung at the end of the experiment (day 35). Bars: mean bioluminescence signal (n = 8, except in paclitaxel-treated group, n = 7). Number indicates the reduction (%) in mean bioluminescence signal in 1 mg.kg⁻¹ PP-13-treated group, compared to control group.

In addition, *ex vivo*, the axillary and brachial lymph nodes showed a significant decrease in signal in both of the PP-13-treated groups compared to the control and paclitaxel-treated groups (Fig. 7A and 7B). The percentage of mice with axillary and brachial lymph node metastases was reduced in a dose-dependent manner in the PP-13-treated groups compared to the control and paclitaxel treated groups (Table 2), as was the number of metastatic axillary and

brachial lymph nodes (Fig. 7A). Taken together, these results showed that PP-13 decreased tumor and metastatic dissemination in this breast cancer model.

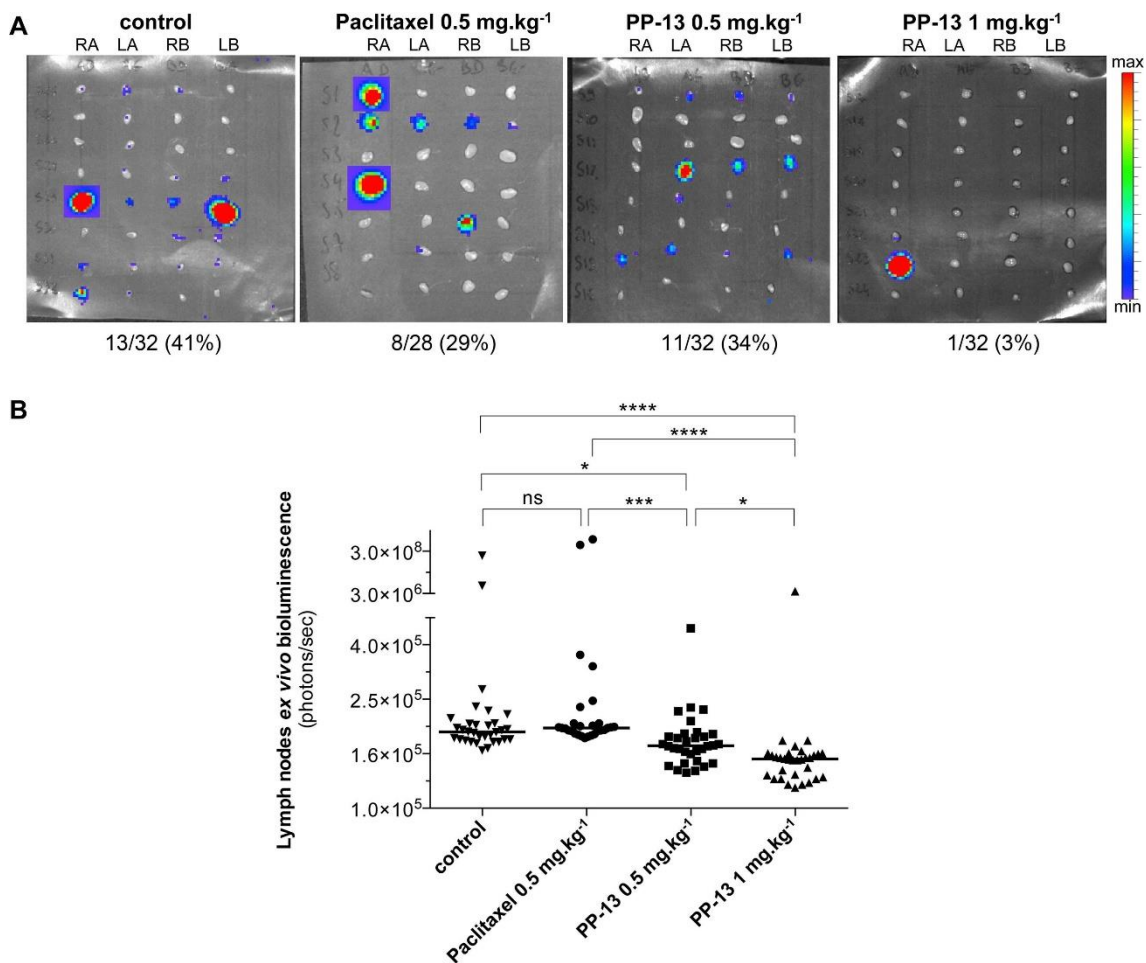


Figure 7. Effects of PP-13 on lymph node metastases. Axillary and brachial lymph nodes were collected at the end of the experiment (day thirtyfive) in 4T1-rvLuc2 mice treated as indicated. (A) *Ex vivo* bioluminescence images of lymph nodes. RA, right axillary lymph node; LA, left axillary lymph node; RB, right brachial lymph node; LB, left brachial lymph node. Each line shows the lymph nodes of one mouse ($n = 8$, except in paclitaxel-treated group, $n = 7$). Numbers indicates the invaded lymph nodes and their percentages in each group. (B) *Ex vivo* bioluminescence signal in each lymph node. Bars: median bioluminescence signal ($n = 32$ lymph nodes/group, 8 mice/group except in paclitaxel-treated group: 7 mice, 28 lymph nodes). * $p < 0.05$; *** $p < 0.001$; **** $p < 0.0001$ compared to control or treated groups; Kruskal-Wallis with Dunn's multiple comparisons post hoc test. ns, not significant.

PP-13 shows no adverse side effects *in vivo*

We assessed the toxicity of PP-13 and paclitaxel *in vivo*. There was no body-weight loss in the control and PP-13-treated mice over the course of the experiment, while mice exposed to paclitaxel displayed a significant decrease in body weight at the end of the experiment (Table 3). In addition, one of the eight mice in each of the paclitaxel and control groups died before the end of the experiment probably because of tumor progression, while all PP-13-treated mice survived suggesting that PP-13 may control tumor progression. We paid particular attention to some of the side effects described for conventional spindle poisons in patients. Serum

biochemical analysis showed significant decreases in phosphorus, creatinine, and glucose in paclitaxel-treated mice compared to the control group (Table 4). No significant changes in serum biochemical values were reported in PP-13-treated mice, except a small and isolated decrease in blood urea nitrogen that did not reflect any renal toxicity in this context. In addition, macroscopic analyses of the organs of the treated mice did not show evidence of damage (data not shown). Hematological analysis of the blood and bone marrow cells from mice treated with PP-13 did not reveal any apparent signs of myelosuppression or other hematological abnormalities compared to the control (Table 5). In contrast, paclitaxel treatment led to a significant reduction in the white blood cell (WBC) count and a slight increase in the mean corpuscular hemoglobin concentration (MCHC).

Overall, these data suggest that PP-13 displays a favorable safety profile, as it slows both tumor and metastasis progression and is well tolerated at these doses compared to the control and paclitaxel.

Table 3. Mice body-weight.

Mice body-weight.		
Treatments	Mice body-weight at day 28 (%)	Mice body-weight at day 35 (%)
Control	118.75 ± 2.56	115.75 ± 3.57
Paclitaxel 0.5 mg.kg ⁻¹	119.38 ± 1.41	111.29 ± 1.85*
PP-13 0.5 mg.kg ⁻¹	113.25 ± 0.86	108.25 ± 3.75
PP-13 1 mg.kg ⁻¹	116.13 ± 1.84	116.13 ± 1.72

Mice with 4T1-rvLuc2 tumors were treated with vehicle (control), paclitaxel 0.5 mg.kg⁻¹, or PP-13 (0.5 and 1 mg.kg⁻¹) (see Fig. 5D). Mice body-weight is expressed as mean ± SEM (n=8, except in paclitaxel-treated group at day 35, n=7), and as percentage of initial body-weight (day 0). * *p* < 0.05; two-way ANOVA with Bonferroni post-test (day 35 compared today 28).

Table 4. Biochemical analyses of mice.

Plasma biochemistry	Control (n = 6) Mean ± SD	paclitaxel 0.5 mg.kg ⁻¹ (n = 6) Mean ± SD	PP-13 1 mg.kg ⁻¹ (n = 6) Mean ± SD
Potassium (mEq/L)	6.3 ± 0.8	6.6 ± 0.9	5.8 ± 0.8
Chloride (mEq/L)	113.2 ± 1.8	110.3 ± 3.4	113.0 ± 1.7
Calcium (mg/dL)	9.7 ± 0.3	9.6 ± 0.1	9.7 ± 0.4
Phosphorus (mg/dL)	8.2 ± 1.9	5.4 ± 0.2*	6.5 ± 0.7
Glucose (g/L)	2.1 ± 0.4	1.6 ± 0.1*	2.1 ± 0.3
Aspartate amino- transferase (UI/L)	201.5 ± 48.2	188.5 ± 56.4	205.7 ± 34.7
Alanine amino- transferase (UI/L)	33.3 ± 11.3	48.5 ± 10.4	38.0 ± 12.2
Alkaline phosphatase (UI/L)	52.5 ± 12.3	50.2 ± 9.3	58.5 ± 15.2
Total bilirubin (mg/ dL)	0.2 ± 0.1	0.2 ± 0.2	0.2 ± 0.1
Total proteins (g/L)	42.0 ± 2.1	43.7 ± 1.9	43.7 ± 2.2
Albumin (g/L)	23.0 ± 1.5	23.8 ± 2.1	24.5 ± 2.3
Globulins (g/dL)	1.9 ± 0.2	2.0 ± 0.2	1.9 ± 0.1
Cholesterol (g/L)	0.7 ± 0.1	0.7 ± 0.1	0.8 ± 0.1
Triglycerides (g/L)	0.5 ± 0.1	0.6 ± 0.1	0.6 ± 0.1
Creatinine (mg/L)	9.7 ± 3.4	2.3 ± 0.5*	4.0 ± 3.9
Blood Urea Nitrogen (g/L)	0.2 ± 0.02	0.2 ± 0.04	0.1 ± 0.02*

Plasma biochemical values of mice after control, paclitaxel or PP-13 treatments were assessed. Data represent the mean ± SD of 6 mice per group. Data were analyzed using Mann-Whitney U test. * Significant as compared to control group.

Table 5. Hematological and bone marrow analyses of mice.

		Control (n = 8)	paclitaxel 0.5 mg/kg (n = 8)		PP-13 1 mg/kg (n = 8)	
		Mean ± SD	Mean ± SD	p value	Mean ± SD	p value
Hematological analyses	Red blood cells (RBC) (T/L)	8.2 ± 0.6	7.2 ± 1.0	NS	7.6 ± 0.5	NS
	Haemoglobin (g/dL)	13.7 ± 1.0	12.4 ± 1.7	NS	13.2 ± 0.7	NS
	Haematocrit (%)	40.8 ± 3.3	35.5 ± 4.6	NS	38.1 ± 2.2	NS
	Mean corpuscular hemoglobin concentration (MCHC) (g/dL)	33.6 ± 0.5	35.0 ± 0.7	p < 0.01	34.5 ± 0.5	NS
	Mean Corpuscular Hemoglobin (MCH) (pg)	16.8 ± 0.4	17.2 ± 0.3	NS	17.3 ± 0.3	NS
	Mean corpuscular volume (MCV) (μm ³)	50.0 ± 1.2	49.2 ± 1.3	NS	50.3 ± 1.3	NS
	Red cell distribution index (RDI) (%)	15.0 ± 1.0	14.9 ± 0.8	NS	14.6 ± 0.9	NS
	White blood cells (WBC) (G/L)	18.3 ± 3.5	11.8 ± 4.0	p < 0.05	17.0 ± 2.9	NS
	lymphocytes (% of WBC)	50.1 ± 8.2	39.1 ± 16.9	NS	47.5 ± 6.4	NS
	Monocytes (% of WBC)	23.9 ± 4.9	26.0 ± 6.6	NS	21.1 ± 1.2	NS
	Granular cells (% of WBC)	26.0 ± 4.0	35.0 ± 11.8	NS	31.1 ± 6.9	NS
Hematological analyses of the bone marrow	Cell abundance in the bone marrow [#]	2.4 ± 0.9	3.1 ± 0.4	NS	2.9 ± 0.7	NS
	Megakaryocytes	16.0 ± 6.5	28.7 ± 12.5	NS	18.0 ± 11.0	NS
	Granular line (%)	74.9 ± 9.0	63.4 ± 13.0	NS	65.3 ± 11.1	NS
	Erythroblastic line (%)	14.3 ± 9.6	22.1 ± 14.4	NS	28.6 ± 9.2	NS
	Lymphocytes (%)	6.1 ± 4.1	8.4 ± 3.4	NS	5.2 ± 3.6	NS
	Monocytes (%)	4.8 ± 2.7	6.1 ± 3.9	NS	2.8 ± 2.2	NS

Complete blood count and white blood cells count and evaluation of the global cell abundance and megakaryocyte and leukocyte counts in the bone marrow, from mice treated with control, paclitaxel, or PP-13. Data represent the mean ± SD of 8 mice per group. NS: not significant. # From score 1 (low abundance) to score 4 (high abundance). Data were analyzed using one-way analysis of variance.

Discussion

The new pyrrolo[2,3d]pyrimidine-based colchicine-binding site agent PP-13 showed promising anticancer properties *in vitro*.⁹ In this study, we explored the therapeutic potential of PP-13, particularly in conditions leading to invasive cancer cell phenotype, and compared the effects of PP-13 with those of paclitaxel, a widely used tubulin-targeting agent in solid tumors. We showed that PP-13 inhibited proliferation, migration and angiogenesis *in vitro*, which may potentiate its antineoplastic activity, and reduced metastatic dissemination in paclitaxel-resistant tumors *in vivo*, with no detectable adverse side effects. We confirmed the *in vitro* antitumor effects of PP-13 in spheroids. The PP-13-treated spheroids showed enhanced H3P levels associated with defects in mitotic spindle organization and chromosome congression, thus confirming in three-dimensions models that PP-13 induced an early mitotic blockade. Late caspase-3-dependent apoptotic mechanisms contributed to the decrease in spheroid growth, as was previously described in two dimensions cell cultures.⁹ Spheroids are currently considered to be a more suitable model than monolayer cell cultures because they better mimic the *in vivo* three-dimensions tumor environment and cell-cell and cell-extracellular matrix interactions.¹⁸⁻²⁰ Large spheroids ($\geq 300 \mu\text{m}$ diameter), such as those generated in our experiments, display a hypoxic core resulting from chemical gradients of oxygen and nutrients that are correlated with chemoresistance, as reported in developing tumors.²¹ We observed differences in the IC₅₀ values of PP-13 between monolayer cell culture and spheroids. In particular, A549 cells were resistant to PP-13 when cultured in spheroids, in contrast to monolayer cell culture, suggesting that the effect of PP-13 observed on two-dimensions-culture cell proliferation is reduced in spheroids. The presence of various environmental factors affecting the tumor development (e.g., cell-cell adhesion, cell-cycle distribution, local pH, extracellular matrix)²⁰ could explain the lower sensitivity of spheroid cancer cells to drugs compared to two dimensions cell cultures, as was also observed in different *in vivo* tumor models.²²⁻²⁴ The physicochemical properties of PP-13 could also be responsible for the lower sensitivity in three-dimensions cell culture. Despite opposite mechanisms of action (microtubule stabilization or depolymerization),³ both PP-13 and paclitaxel lead to the disruption of the microtubule organization and the induction of cancer cell cycle arrest and apoptosis.

Angiogenesis and cancer cell migration are attractive therapeutic targets.²⁵ The widely used capillary-like tube formation assay aids in studying the effects of new molecules on many steps of neoangiogenesis, including endothelial cell adhesion, migration, and tubule formation.²⁶ With this approach, we showed that PP-13 interfered with the tubule assembly *in vitro* by decreasing both the number of loops and branch nodes, the total length of the formed tubes

and the cell-covered area. Using *in vivo* 4T1 primary breast tumor models, we did not observe any impact of PP-13 on microvessel density, suggesting that such PP-13 concentrations were inadequate to induce antiangiogenic activities and/or that the study time was not suitable to inhibit endothelial cells *in vivo* in this rapidly progressing breast cancer orthotopic model.

PP-13 inhibited cell motility and invasion both *in vitro* and *in vivo*. *In vitro*, we found that PP-13 inhibited cancer cell migration in the three metastatic tumor cell types. In addition, PP-13 reduced metastatic invasion in H358⁹ and A549 NSCLC cells engrafted onto chicken CAMs at concentrations that did not inhibit cell proliferation in A549 spheroids. Accordingly, PP-13 did not inhibit A549 tumor growth in chicken CAMs. This confirmed the lower effect of PP-13 on cell proliferation in spheroids and *in vivo* compared to monolayer cell culture. The orthotopic mouse model of breast cancer that was used is clinically relevant to predict the influence of the organ microenvironment on tumor cell behavior and to study the cancer cell invasion and metastatic growth.²⁷ Although PP-13 did not inhibit *in vivo* tumor cell migration and metastasis seeding at the concentrations used, we observed that the growth of the metastases was delayed, and their size remained small in both lungs and lymph nodes when the cells migrated from the primary tumor. Although PP-13 had both antiproliferative and antimigration effects *in vitro*, the *in vivo* experiments indicated that the effect of the drug on the inhibition of invasion was stronger than its antiproliferative effects.

Overall, our data indicate that PP-13 could be a potent agent to decrease the growth of both primary tumors and their metastases, especially for triple-negative breast cancers (TNBC), which account for nearly 15% of breast cancers and have poor therapeutic options and prognoses.²⁸ The 4T1 allogeneic transplant mouse model mimics TNBC in humans and is associated with a high propensity to metastasize, primarily in the lymph nodes and lungs. The therapeutic arsenal for TNBC mainly consists of anthracyclines and taxane-based chemotherapies; however, the emergence of resistance and frequent tumor recurrence support the need to identify alternative drugs for the management of refractory tumors. The 4T1 model thus represents an interesting approach to screen new molecules for TNBC therapy, especially since it spontaneously metastasizes in the same regions as in TNBC and easily develops resistance to chemotherapies classically used in TNBC.^{29, 30} Compared to paclitaxel, which was used as a reference treatment to reduce metastasis while limiting the adverse effects, PP-13 moderately inhibited primary tumor growth and delayed metastatic growth.

PP-13 treatment did not show any sign of toxicity compared to the controls; there was notably an absence of myelosuppression, which is classically observed with conventional antimitotic drug treatments or colchicine binding-site agents.³ At the same dose, paclitaxel led to a significant decrease in white blood cell count, as has been previously reported,³¹ as well as

a slight reduction in plasma glycaemia, phosphorus and creatinine and an increase in MCHC. Further investigations with higher concentrations of PP-13 will be needed to establish the maximal antitumor effect of PP-13, and the therapeutic index of the molecule, and long-term survival. In addition, PP-13 has no kinase activity⁹ but may target other molecule than tubulin, that remains to determine.

In summary, PP-13 significantly reduced the cancer cell migration and neoangiogenesis processes *in vitro*. PP-13 also led to a reduction in both tumor growth and metastatic dissemination *in vivo* in a mouse orthotopic TNBC model without any significant toxicity. These findings suggest that PP-13 should be an efficient anticancer therapy and an alternative option to conventional spindle poisons such as taxanes or vinca-alkaloids.

Acknowledgements

We acknowledge the assistance of Alexei Grichine, Mylène Pezet and Jacques Mazzega (Optical Microscopy Platform - Cell Imaging, INSERM U1209). We kindly thank Dr. Lucie Sancey for critical evaluation of the data, and Lilya Mediouni for her help. This work was supported by the Institut Curie, the CNRS, the INSERM, and grants from “La Fondation de France” and “La Ligue contre le Cancer (comité de l’Isère)”. The *in vivo* evaluation was performed by the OPTIMAL facility, which is part of the France Live Imaging Program (FLI-Grenoble; French program “Investissement d’Avenir”; grant “Infrastructure d’avenir en Biologie Santé,” ANR-11-INBS-0006).

References

1. Miller, K. D. et al. Cancer treatment and survivorship statistics, 2016. *CA. Cancer J. Clin.* (2016). doi:10.3322/caac.21349
2. Jordan, M. A. & Wilson, L. Microtubules as a target for anticancer drugs. *Nat. Rev. Cancer* 4, 253–265 (2004).
3. Dumontet, C. & Jordan, M. A. Microtubule-binding agents: a dynamic field of cancer therapeutics. *Nat. Rev. Drug Discov.* 9, 790–803 (2010).
4. Fanale, D. et al. Stabilizing versus Destabilizing the Microtubules: A Double-Edge Sword for an Effective Cancer Treatment Option? *Analytical Cellular Pathology* (2015). doi:10.1155/2015/690916
5. Jordan, M. A. Mechanism of action of antitumor drugs that interact with microtubules and tubulin. *Curr. Med. Chem. Anti-Cancer Agents* 2, 1–17 (2002).
6. Schwartz, E. L. Antivascular actions of microtubule-binding drugs. *Clin. Cancer Res. Off. J. Am. Assoc. Cancer Res.* 15, 2594–2601 (2009).
7. Bates, D. & Eastman, A. Microtubule destabilizing agents: far more than just anti-mitotic anti-cancer drugs: MDA mechanisms of action. *Br. J. Clin. Pharmacol.* (2016). doi:10.1111/bcp.13126 21
8. Kanthou, C. & Tozer, G. M. Microtubule depolymerizing vascular disrupting agents: novel therapeutic agents for oncology and other pathologies. *Int. J. Exp. Pathol.* 90, 284–294 (2009).
9. Gilson, P. et al. Identification of pyrrolopyrimidine derivative PP-13 as a novel microtubule-destabilizing agent with promising anticancer properties. *Scientific Reports* DOI:10.1038/s41598-017-09491-9 (2017).
10. Pasquier, E., Honoré, S. & Braguer, D. Microtubule-targeting agents in angiogenesis: where do we stand? *Drug Resist. Updat. Rev. Comment. Antimicrob. Anticancer Chemother.* 9, 74–86 (2006).
11. Pasquier, E., André, N. & Braguer, D. Targeting microtubules to inhibit angiogenesis and disrupt tumour vasculature: implications for cancer treatment. *Curr. Cancer Drug Targets* 7, 566–581 (2007).
12. Pulaski, B. A. & Ostrand-Rosenberg, S. Mouse 4T1 breast tumor model. *Curr. Protoc. Immunol.* Chapter 20, Unit 20.2 (2001).

13. Lovitt, C. J., Shelper, T. B. & Avery, V. M. Advanced Cell Culture Techniques for Cancer Drug Discovery. *Biology* 3, 345–367 (2014).
14. Hirschhaeuser, F. et al. Multicellular tumor spheroids: an underestimated tool is catching up again. *J. Biotechnol.* 148, 3–15 (2010).
15. Mehta, G., Hsiao, A. Y., Ingram, M., Luker, G. D. & Takayama, S. Opportunities and Challenges for use of Tumor Spheroids as Models to Test Drug Delivery and Efficacy. *J. Control. Release Off. J. Control. Release Soc.* 164, 192–204 (2012).
16. Däster, S. et al. Induction of hypoxia and necrosis in multicellular tumor spheroids is associated with resistance to chemotherapy treatment. *Oncotarget* 8, 1725–1736 (2016). 22
17. Edmondson, R., Broglie, J. J., Adcock, A. F. & Yang, L. Three-Dimensional Cell Culture Systems and Their Applications in Drug Discovery and Cell-Based Biosensors. *Assay Drug Dev. Technol.* 12, 207–218 (2014).
18. Breslin, S. & O'Driscoll, L. The relevance of using 3D cell cultures, in addition to 2D monolayer cultures, when evaluating breast cancer drug sensitivity and resistance. *Oncotarget* 7, 45745–45756 (2016).
19. Nirmalanandhan, V. S., Duren, A., Hendricks, P., Vielhauer, G. & Sittampalam, G. S. Activity of anticancer agents in a three-dimensional cell culture model. *Assay Drug Dev. Technol.* 8, 581–590 (2010).
20. Hanahan, D. & Weinberg, R. A. Hallmarks of Cancer: The Next Generation. *Cell* 144, 646–674 (2011).
21. Xie, D., Ju, D., Speyer, C., Gorski, D. & Kosir, M. A. Strategic Endothelial Cell Tube Formation Assay: Comparing Extracellular Matrix and Growth Factor Reduced *Extracellular Matrix*. *J. Vis. Exp. JoVE* (2016). doi:10.3791/54074
22. Man, S., Munoz, R. & Kerbel, R. S. On the development of models in mice of advanced visceral metastatic disease for anti-cancer drug testing. *Cancer Metastasis Rev.* 26, 737–747 (2007).
23. Kaur, P. et al. A mouse model for triple-negative breast cancer tumor-initiating cells (TNBC-TICs) exhibits similar aggressive phenotype to the human disease. *BMC Cancer* 12, 120 (2012).
24. Bao, L. et al. Increased expression of P-glycoprotein is associated with doxorubicin chemoresistance in the metastatic 4T1 breast cancer model. *Am. J. Pathol.* 178, 838–852 (2011).
25. Luo, T. et al. (-)-Epigallocatechin gallate sensitizes breast cancer cells to paclitaxel in a murine model of breast carcinoma. *Breast Cancer Res. BCR* 12, R8 (2010). 23

26. Perez, E. A. Paclitaxel in Breast Cancer. *The Oncologist* 3, 373–389 (1998).
27. Steigemann, P. et al. Aurora B-mediated abscission checkpoint protects against tetraploidization. *Cell* 136, 473–484 (2009).
28. Busser, B. et al. Amphiregulin promotes BAX inhibition and resistance to gefitinib in non-small-cell lung cancers. *Mol. Ther. J. Am. Soc. Gene Ther.* 18, 528–535 (2010).
29. Zheng, Q., Milthorpe, B. K. & Jones, A. S. Direct neural network application for automated cell recognition. *Cytom. Part J. Int. Soc. Anal. Cytol.* 57, 1–9 (2004).
30. Prunier, C. et al. LIM Kinase Inhibitor Pyr1 Reduces the Growth and Metastatic Load of Breast Cancers. *Cancer Res.* 76, 3541–3552 (2016).
31. Amphiregulin promotes resistance to gefitinib in nonsmall cell lung cancer cells by regulating Ku70 acetylation. (2017)
32. Jeannot, V. et al. Targeting CD44 receptor-positive lung tumors using polysaccharidebased nanocarriers: Influence of nanoparticle size and administration route. *Nanomedicine Nanotechnol. Biol. Med.* 12, 921–932 (2016).

Supplementary Data

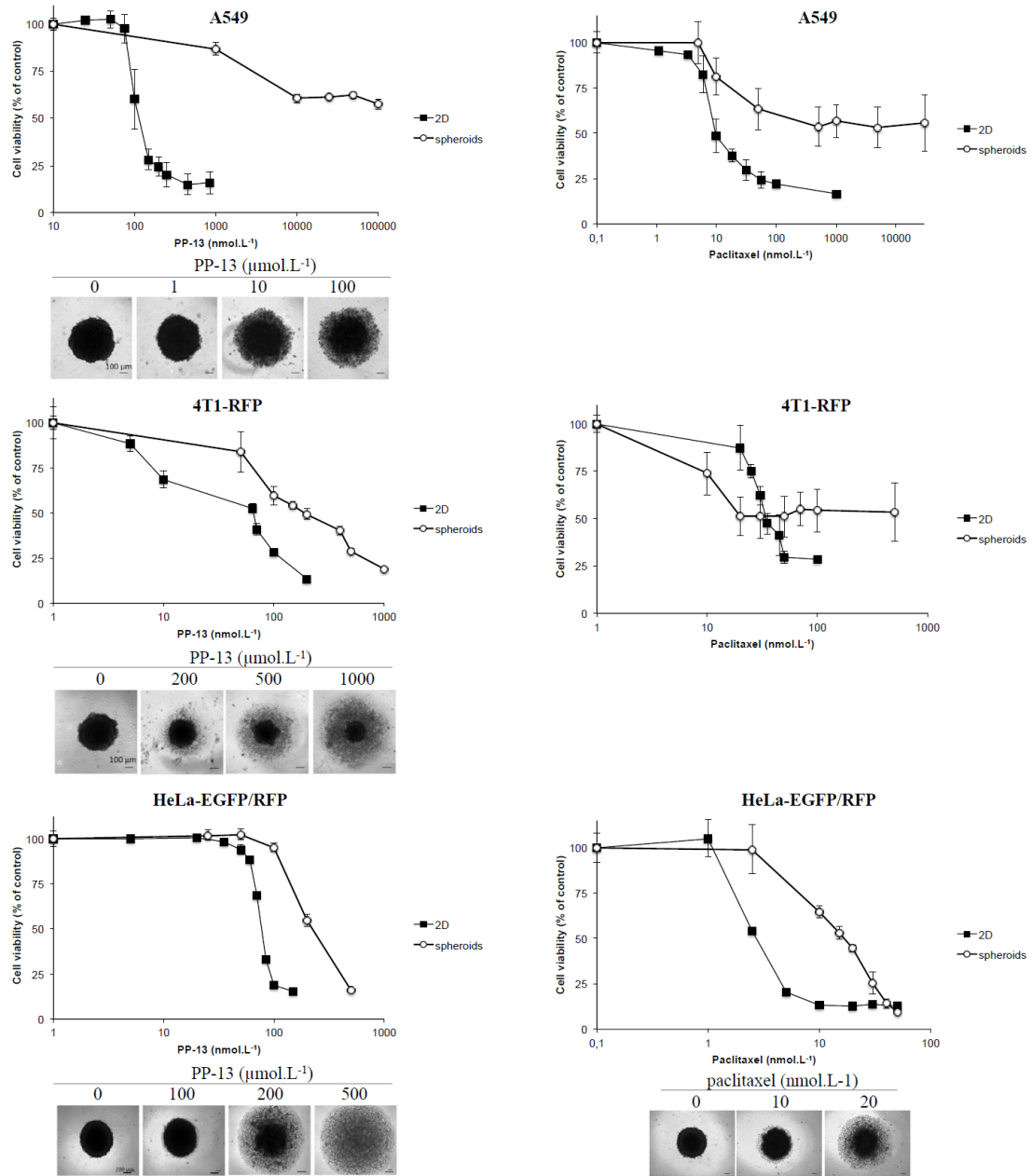


Figure S1. Viability of cancer cells treated with PP-13 or paclitaxel. A549, 4T1 mRFP-H2B (4T1-RFP), and HeLa mEGFP- α -tubulin mRFP-H2B (HeLa-EGFP/RFP) were cultured in 2D or in spheroids, and treated for 72 h with increasing concentrations of PP-13 or paclitaxel as indicated. The cell viability was assessed. Data represent the mean \pm SD from 3 independent experiments. Representative images of spheroids are shown.

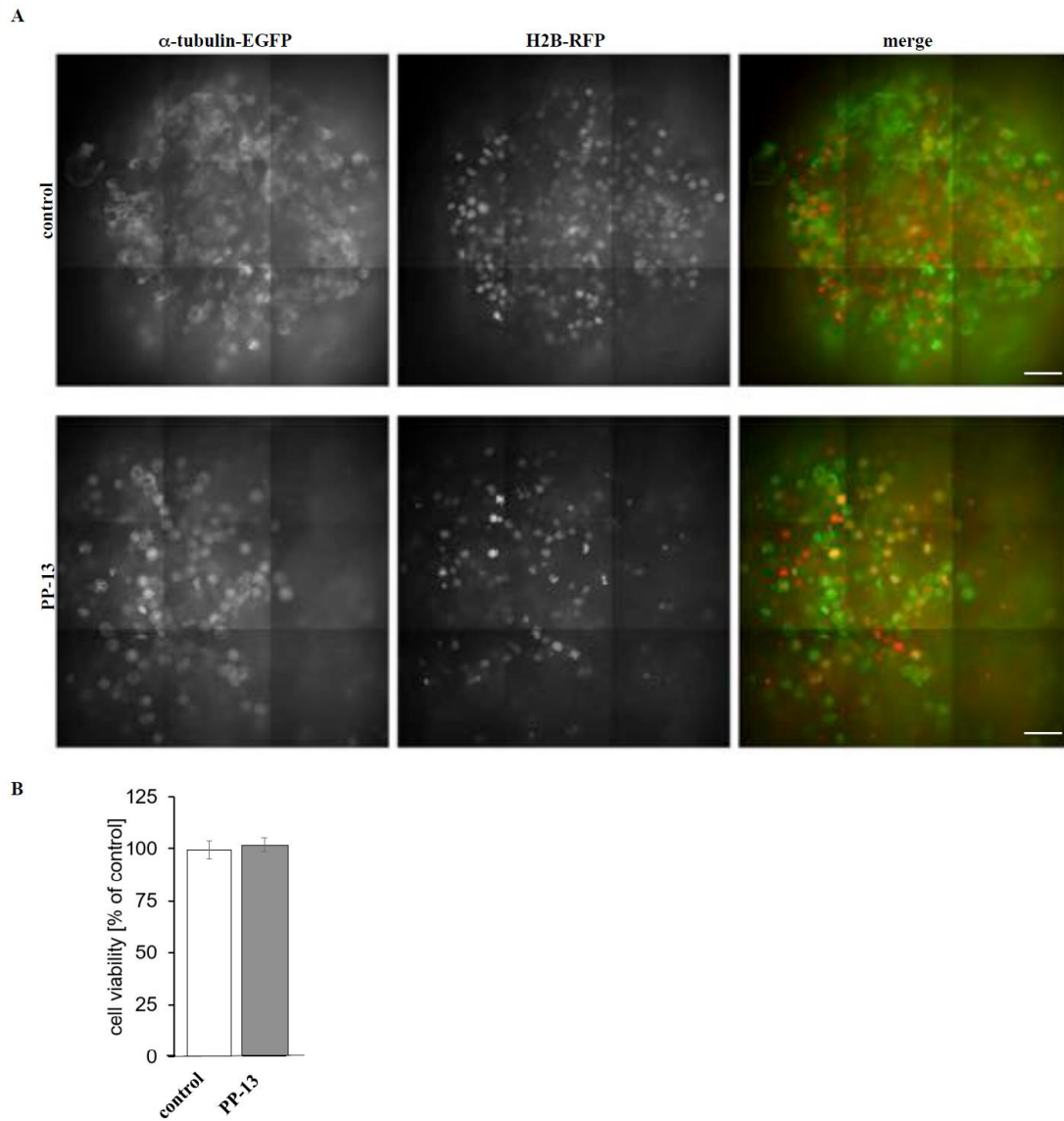


Figure S2. Effects of PP-13 on HeLa-EGFP/RFP spheroids. HeLa mEGFP- α -tubulin mRFP-H2B (HeLa-EGFP/RFP) spheroids were treated for 24 h with vehicle (control), or 200 nmol.L-1 PP-13. (A) Representative images of HeLa-EGFP/ RFP spheroids visualized by a spinning disk confocal laser video microscope (Andromeda iMic, FEI, Munich, Germany) equipped with a Plan-Apochromat 20X/1.4 oil objective and an EMCCD camera iXion3897 (Andor, Belfast, UK). In red: H2BRFP, in green: α -tubulin-EGFP. Scale bars: 50 μ m. (B) Cell viability of spheroid cells was assessed at 24 h.

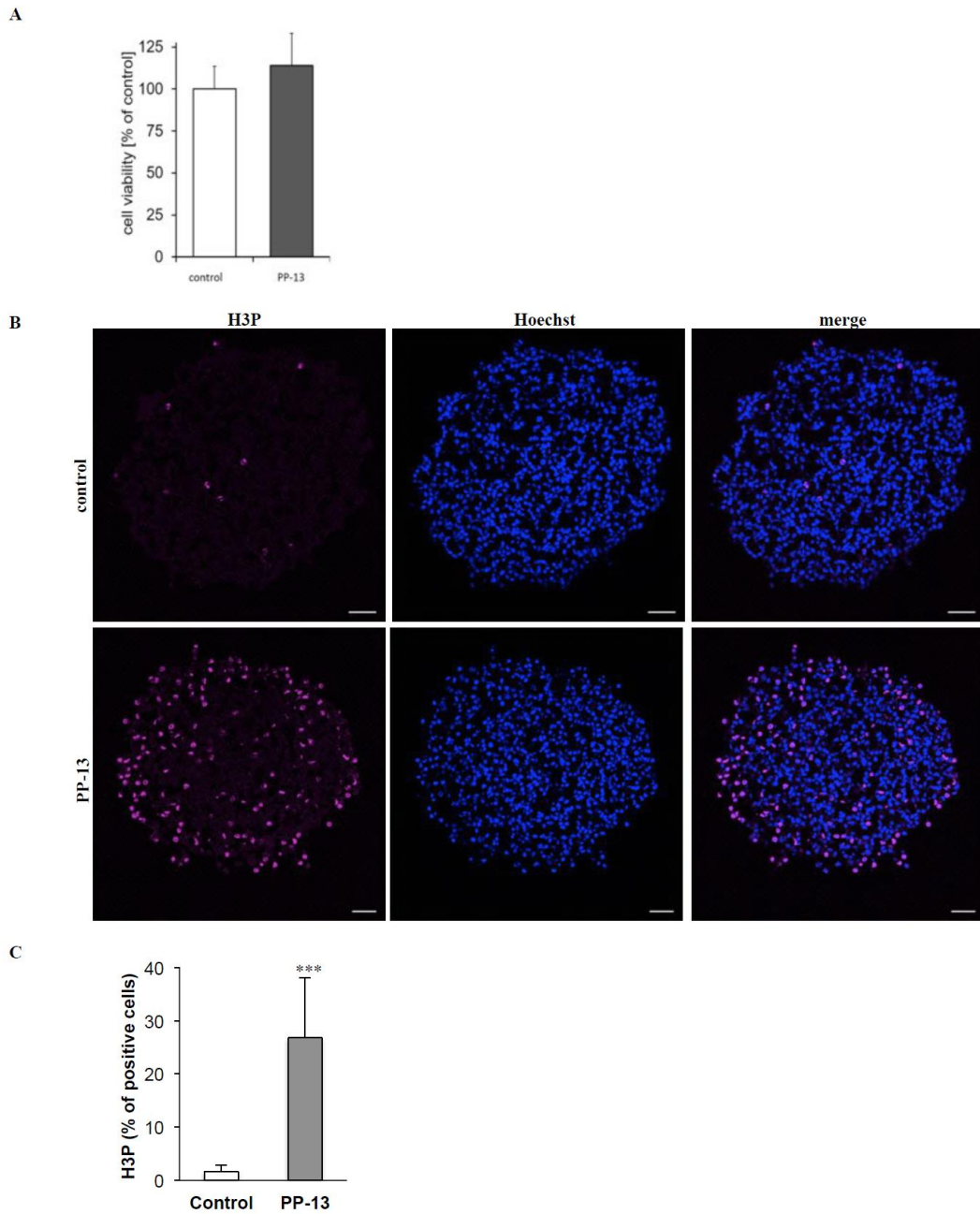


Figure S3. Effects of PP-13 on A549 spheroids. A549 spheroids were treated for 24 h with vehicle (control) or PP-13 (10 $\mu\text{mol}\cdot\text{L}^{-1}$). (A) Cell viability of A549 spheroids after 24 h control or PP-13 treatment. (B) Representative confocal microscopy images of phosphorylated histone H3 (H3P) analyzed by immunofluorescence on A549 spheroid sections. In pink: H3P, in blue: Hoechst-stained nuclei. Scale bars: 50 μm . (C) Quantification of H3P in A549 spheroids. The percentage of H3P was calculated as the number of H3P-positive cells in 11 control spheroids and 11 treated spheroids, with 2 or 3 sections per spheroid. *** $p < 0.0001$ between control and treated conditions, Mann-Whitney U-test.

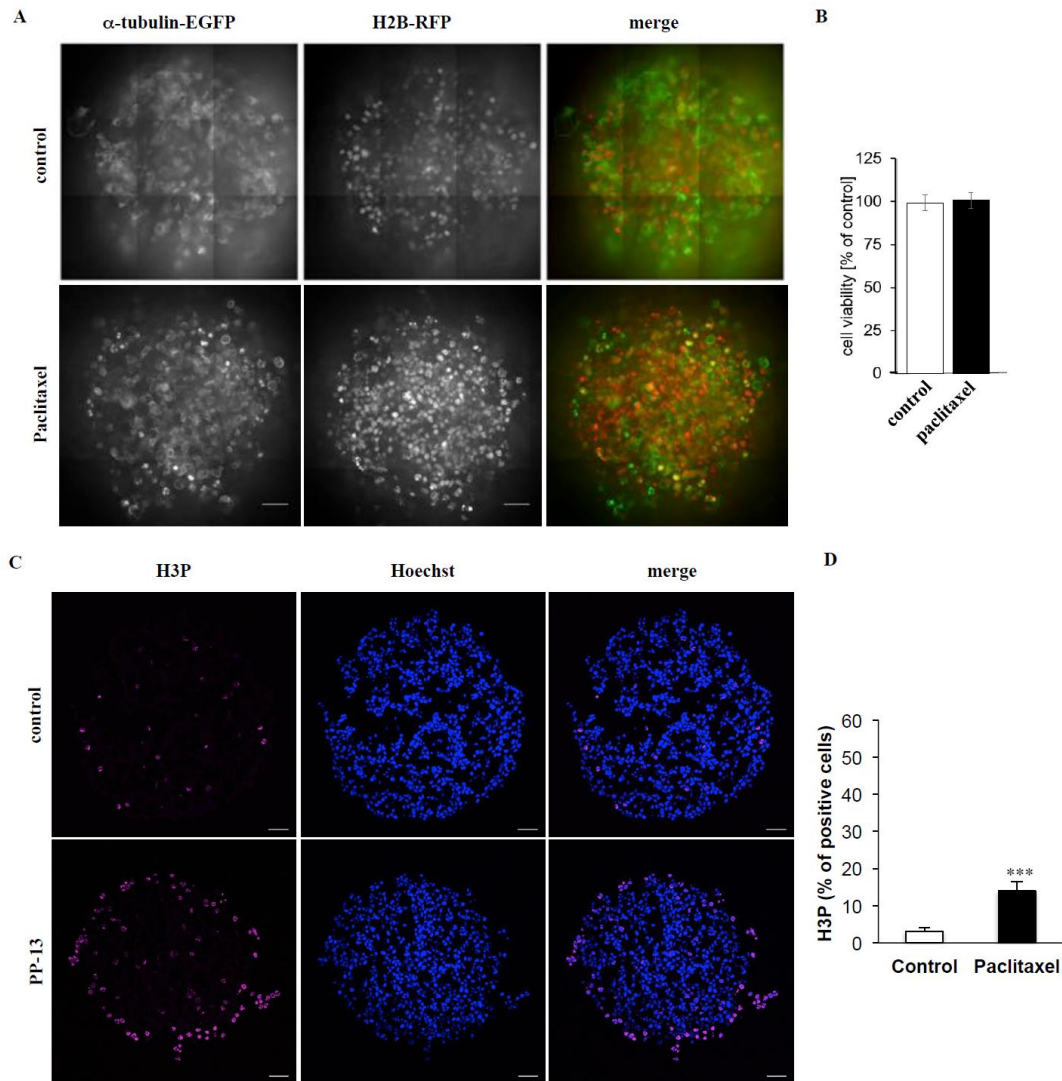


Figure S4. Effects of paclitaxel on HeLa-EGFP/RFP spheroids. HeLa-EGFP/RFP spheroids were treated for 24 h with vehicle (control), or 15 nmol.L⁻¹ paclitaxel. (A) Representative images of spheroids were visualized by a spinning disk confocal laser videomicroscope (Andromeda iMic, FEI, Munich, Germany) equipped with a Plan-Apochromat 20X/1.4 oil objective and an EMCCD camera iXion3897 (Andor, Belfast, UK). In red: H2B-RFP, in green: α -tubulin-EGFP. Scale bars: 50 μ m. (B) Cell viability of spheroid cells was assessed at 24 h. (C) Representative confocal microscopy images of H3P analyzed by immunofluorescence on HeLa-EGFP/RFP spheroids sections. In pink: H3P, in blue: Hoechst-stained nuclei. Scale bars: 50 μ m. (D) Quantification of H3P in HeLa-EGFP/RFP spheroids treated with paclitaxel. The percentage of phosphorylated histone H3 (H3P) was calculated as the number of H3P-positive cells in 10 control and 9 paclitaxel-treated spheroids, with 2 or 3 sections per spheroid. *** $p < 0.0001$ between control and treated conditions, Mann-Whitney U-test.

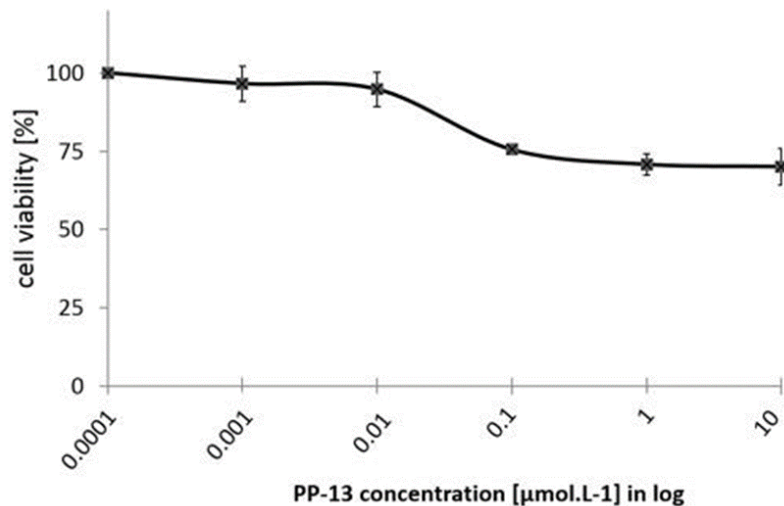


Figure S5. Effect of PP-13 on HUVECs viability. HUVECs were treated with vehicle (control) or increasing concentrations of PP-13 as indicated for 6 h, and cell viability was assessed. Data represent the mean \pm SD from ≥ 3 experiments.

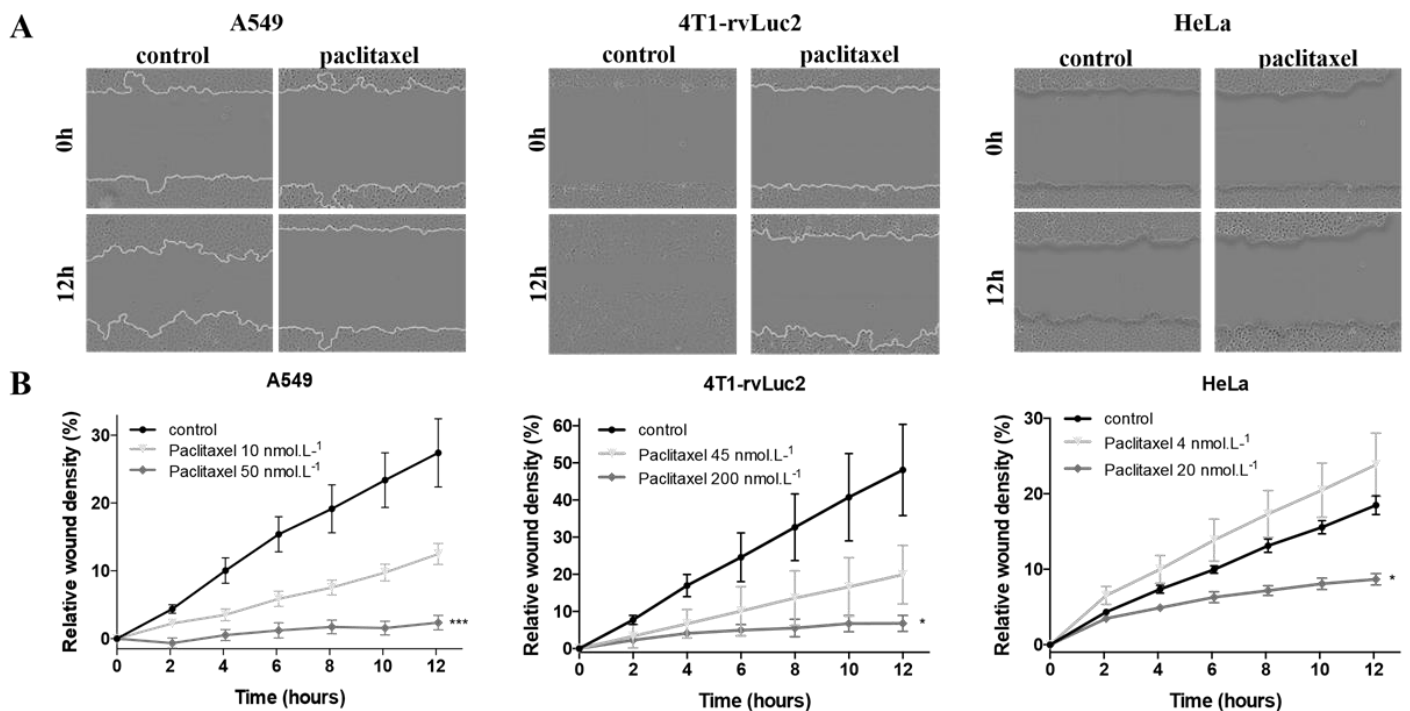


Figure S6. *In vitro* effects of paclitaxel on cancer cell migration. Wound-healing assay in A549, 4T1-rvLuc2 and HeLa cells treated with DMSO (control) or paclitaxel as indicated. (A) Representative images from wound-healing assay experiment at 0 h and 12 h. Cells were treated with DMSO (control) or 50 nmol.L⁻¹ (A549), 200 nmol.L⁻¹ (4T1-rvLuc2), and 20 nmol.L⁻¹ (HeLa) paclitaxel. The white lane delineates the edges of the wound. (B) Graphs represent the relative wound density among time in cells treated with DMSO (control) or 10 and 50 nmol.L⁻¹ (A549), 45 and 200 nmol.L⁻¹ (4T1rvLuc2), and 4 and 20 nmol.L⁻¹ (HeLa) paclitaxel. Data are expressed as mean \pm SD. * $p < 0.05$; *** $p < 0.001$, compared to control (Friedman test with Dunn's multiple comparisons test).

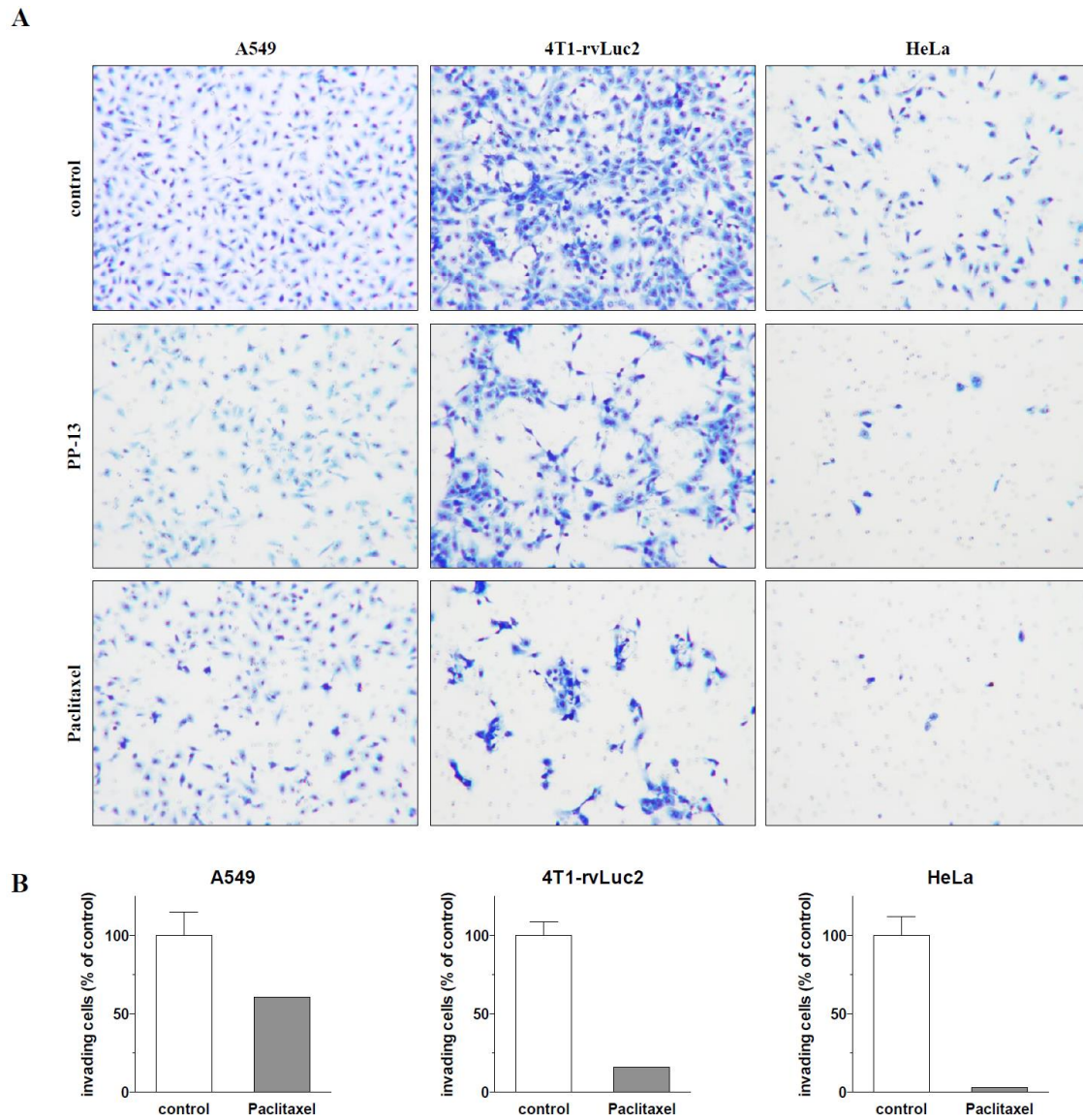


Figure S7. *In vitro* Matrigel invasion assay. (A) Representative images from methylen-blue stained cells treated with vehicle (control), 200 (4T1-rvLuc2), or 500 (A549, HeLa) nmol.L-1 PP-13, or 20 (HeLa), 40 (A549), or 150 (4T1-rvLuc2) nmol.L-1 paclitaxel. The red squares show the quantified cells. (B) Histograms represent the quantification of invasion of A549, 4T1-rvLuc2 and HeLa cells treated with vehicle (control), 20 (HeLa), 40 (A549), or 150 (4T1-rvLuc2) nmol.L-1 paclitaxel. Counting of cells was performed using a fully connected, three-layer back-propagation neuronal network, as previously described (Zheng et al. 2004, Cytom Part A).

A

Number of embryos after 10 days of treatments	Total	Alive	Dead
Control	18	16	2
Paclitaxel 50 $\mu\text{mol.L}^{-1}$	17	16	1
PP-13 0.13 $\mu\text{mol.L}^{-1}$	18	17	1

B

Toxicity checkpoints probed on embryos	Control	Paclitaxel 50 $\mu\text{mol.L}^{-1}$	PP-13 0.13 $\mu\text{mol.L}^{-1}$
Head Size, closure, eyes, ear, face and branchial arc derivatives, mobility	0	0	0
Body Size, axis deformation, ventral and dorsal closures, caudal formation, sexual area	0	0	0
Limbs Size, axis morphology, mobility	0	0	0
Skin Appendage formation, attachment, blood vessel	0	0	0
Extra-embryonic structures Vascularization, transparency, attachment, blood vessel	0	0	0

Figure S8. PP-13 did not induce toxicity in chicken embryos. A549 cells were xenografted on chick embryochorioallantoic membranes (CAMs), and treatments with 0.5% DMSO (control), 50 $\mu\text{mol.L}^{-1}$ paclitaxel (positive control of tumor growth inhibition), or 0.13 $\mu\text{mol.L}^{-1}$ PP-13 (low dose) were administered. (A) The table shows the numbers of dead and surviving embryos for the different experimental groups after 10 days of treatment. (B) The table shows the numbers of abnormality observed on surviving embryos for the different experimental groups after 10 days of treatment. 0 = no abnormality.

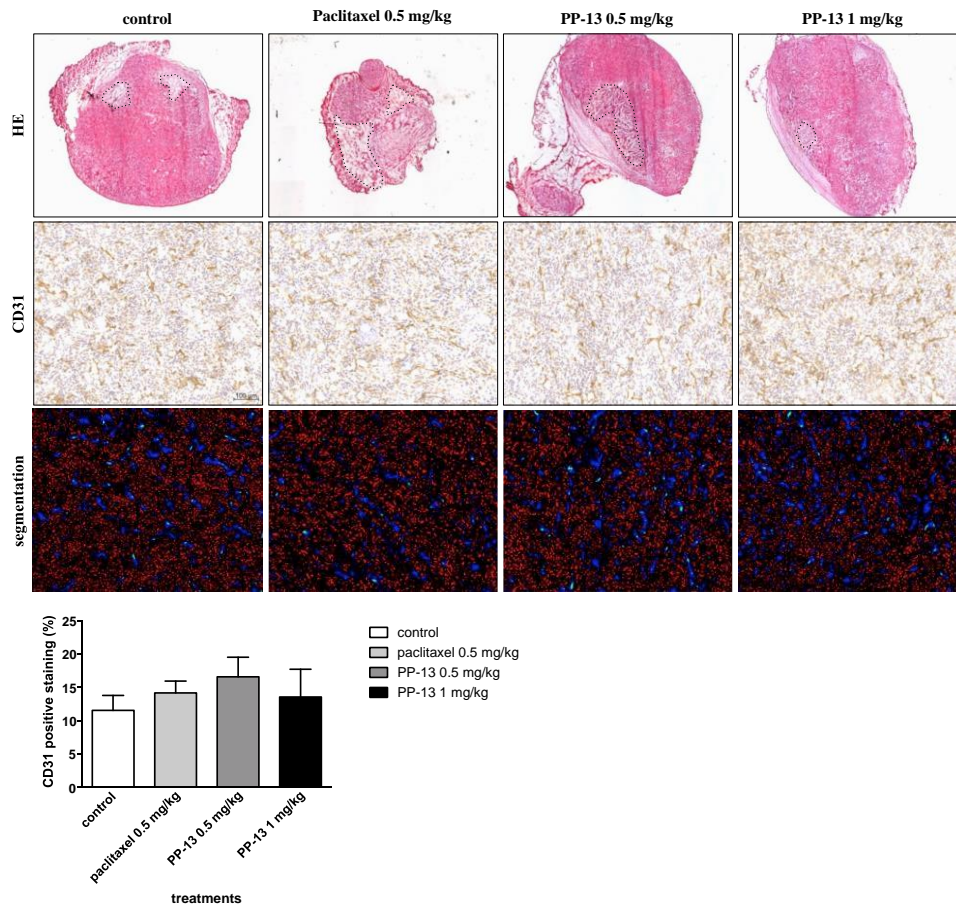


Figure S9. Immunostaining of mice tumor sections and quantification. Hematoxylin and eosin (HE) staining, and CD31 immunostaining on frozen 4T1-tumor sections from mice treated with vehicle, paclitaxel (0.5 mg/kg) or PP-13 (0.5 and 1 mg/kg). Tumor tissues were frozen in OCT-embedding medium (VWR international, Fontenay-sous-Bois, France) and cut into 7 μm thick sections using a cryomicrotome for immunohistochemical analysis. Histological observations were performed after fixation with 4% paraformaldehyde and staining with HE. One representative image of one tumor in each group is shown. Dotted lines delineate necrosis zones. Magnification $\times 2.5$. Immunohistochemical examinations were performed after fixation with 4% paraformaldehyde and staining with anti-CD31 antibody, using an Axiomager M2 microscope (Carl Zeiss, Jena, Germany). One representative magnification of one tumor in each group is shown. Bar, 100 μm . The CD31 levels were determined as shown in the segmentation pictures after counting positive stained blood vessel area (blue and green colors) in 3 sections per tumor and in 3 tumors per group. One representative magnification of one segmentation in each group is shown. Segmentation of tissues was performed using a fully connected, three-layer back-propagation neuronal network, as previously described (Zheng et al. 2004, Cytom Part A). Blue and green: CD31-stained blood vessels; red: nuclei. Histogram shows the CD31 positive staining expressed as the mean \pm SD.

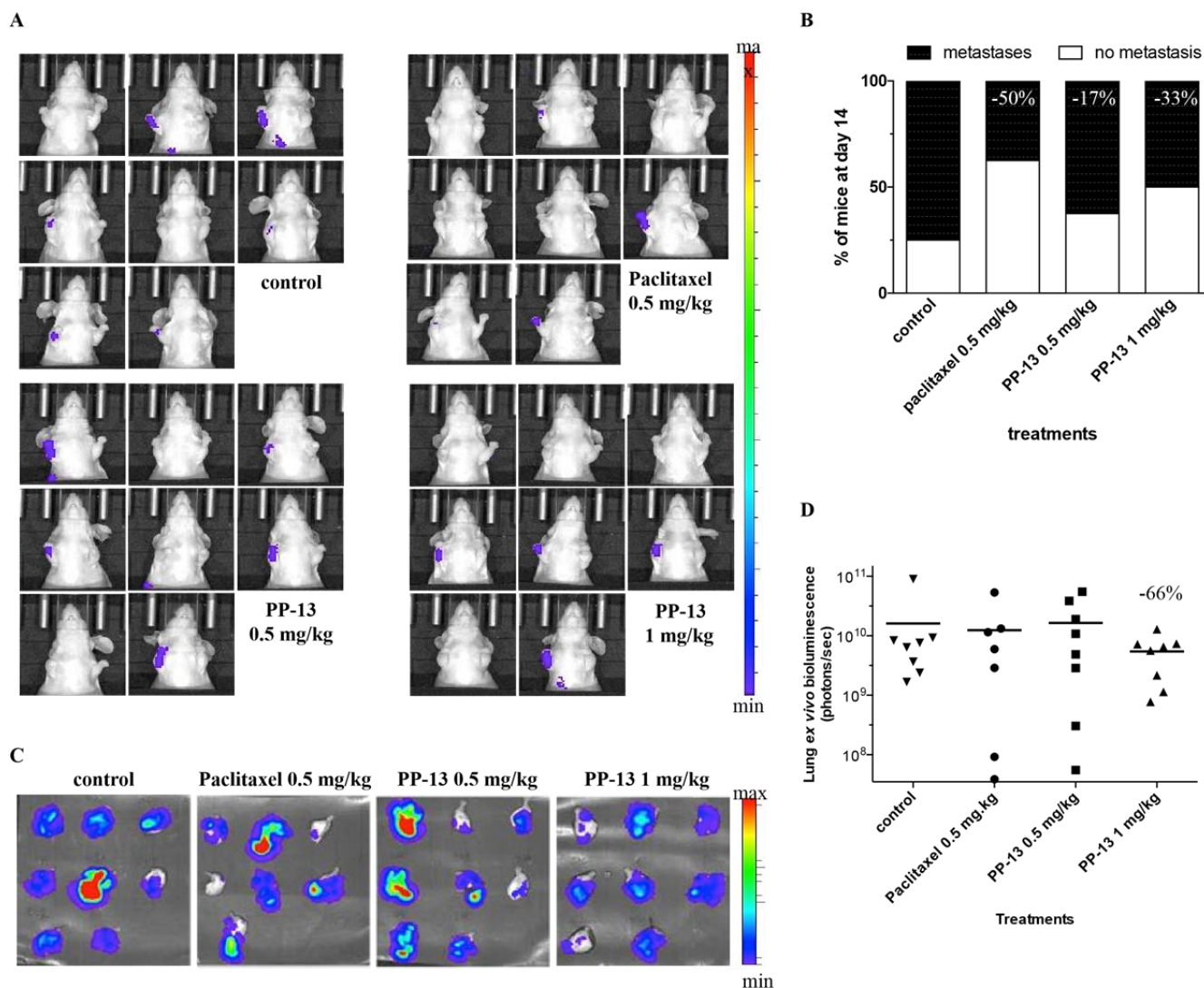


Figure S10. Effects of PP-13 on orthotopic breast tumor model *in vivo*. Mice with 4T1-rvLuc2 tumors were treated with vehicle (control), paclitaxel 0.5 mg/kg, or PP-13 (0.5 and 1 mg/kg), 3 times a week. (A) *In vivo* thoracic bioluminescence image of each mouse at day 14. (B) Percentage of mice with and without thoracic metastases at day 14 in each group (n = 8). Numbers indicate the reduction in mice with lung metastases in each treatment group, compared to control group. (C) *Ex vivo* bioluminescence images of lungs at the end of the experiment (day 35). (D) *Ex vivo* bioluminescence signal in each lung at the end of the experiment (day 35). Bars: mean bioluminescence signal (n = 8). Number indicates the reduction in mean bioluminescence signal in 1 mg/kg PP-13-treated group, compared to control group.

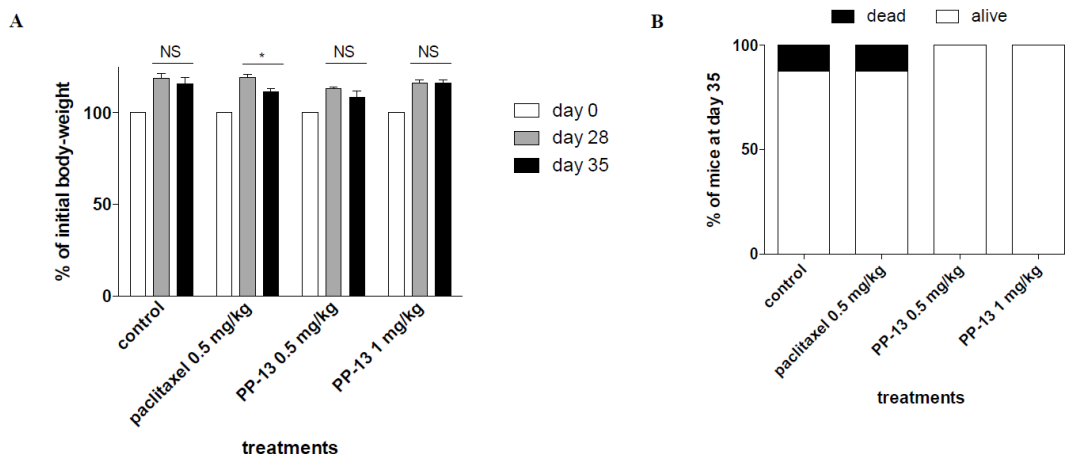


Figure S11. Effects of PP-13 on orthotopic breast tumor model *in vivo*. (A) Mice body-weight at day 0, day 28 and day 35 in each group. Data represent the mean \pm SEM and are expressed as percentage of initial weight ($n = 8$). * $p < 0.05$, two-way ANOVA with Bonferroni post-tests; NS not significant. (B) Percentage of mice dead or alive at the end of the experiment (day 35) in each group ($n = 8$).

Plasma biochemistry	Control (n=6)	paclitaxel 0.5 mg/kg (n=6)		PP-13 1 mg/kg (n=6)	
	Mean \pm SD	Mean \pm SD	<i>p</i> value	Mean \pm SD	<i>p</i> value
Potassium (mEq/L)	6.3 \pm 0.8	6.6 \pm 0.9	NS	5.8 \pm 0.8	NS
Chloride (mEq/L)	113.2 \pm 1.8	110.3 \pm 3.4	NS	113.0 \pm 1.7	NS
Calcium (mg/dL)	9.7 \pm 0.3	9.6 \pm 0.1	NS	9.7 \pm 0.4	NS
Phosphorus (mg/dL)	8.2 \pm 1.9	5.4 \pm 0.2	< 0.005	6.5 \pm 0.7	NS
Glucose (g/l)	2.1 \pm 0.4	1.6 \pm 0.1	< 0.037	2.1 \pm 0.3	NS
Aspartate amino-transferase (UI/L)	201.5 \pm 48.2	188.5 \pm 56.4	NS	205.7 \pm 34.7	NS
Alanine amino-transferase (UI/L)	33.3 \pm 11.3	48.5 \pm 10.4	NS	38.0 \pm 12.2	NS
Alkaline phosphatase (UI/L)	52.5 \pm 12.3	50.2 \pm 9.3	NS	58.5 \pm 15.2	NS
Total bilirubin (mg/dL)	0.2 \pm 0.1	0.2 \pm 0.2	NS	0.2 \pm 0.1	NS
Total proteins (g/L)	42.0 \pm 2.1	43.7 \pm 1.9	NS	43.7 \pm 2.2	NS
Albumin (g/L)	23.0 \pm 1.5	23.8 \pm 2.1	NS	24.5 \pm 2.3	NS
Globulins (g/dL)	1.9 \pm 0.2	2.0 \pm 0.2	NS	1.9 \pm 0.1	NS
Cholesterol (g/l)	0.7 \pm 0.1	0.7 \pm 0.1	NS	0.8 \pm 0.1	NS
Triglycerides (g/l)	0.5 \pm 0.1	0.6 \pm 0.1	NS	0.6 \pm 0.1	NS
Creatinine (mg/l)	9.7 \pm 3.4	2.3 \pm 0.5	< 0.004	4.0 \pm 3.9	NS
Blood Urea Nitrogen (g/l)	0.2 \pm 0.02	0.2 \pm 0.04	NS	0.1 \pm 0.02	< 0.018

Figure S12. Biochemical analyses of mice. Plasma biochemical values of mice after control, paclitaxel or PP-13 treatments were assessed. Data represent the mean \pm SD of 6 mice per group. Data were analyzed using one-way analysis of variance.

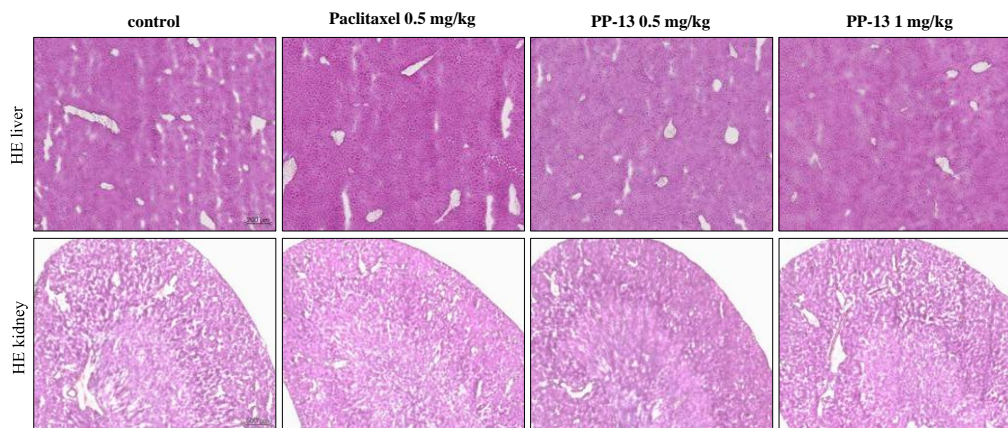


Figure S13. Hematoxylin and eosin (HE) staining on frozen liver and kidney sections from 4T1-mice treated with vehicle, paclitaxel (0.5 mg/ kg) or PP-13 (0.5 and 1 mg/kg). Organ tissues were frozen in OCT-embedding medium (VWR international, Fontenay-sous-Bois, France) and cut into 7 μm thick sections using a cryomicrotome for analysis. Histological observations were performed after fixation with 4% paraformaldehyde and staining with HE. One representative image of each group is shown. Bars, 200 μm (liver) and 500 μm (kidney).

		Control (n=8)	paclitaxel 0.5 mg/kg (n=8)	PP-13 1 mg/kg (n=8)		
		Mean ± SD	Mean ± SD	<i>p</i> value	Mean ± SD	<i>p</i> value
Hematological analyses	Red blood cells (RBC) (T/L)	8.2 ± 0.6	7.2 ± 1.0	NS	7.6 ± 0.5	NS
	Haemoglobin (g/dL)	13.7 ± 1.0	12.4 ± 1.7	NS	13.2 ± 0.7	NS
	Haematocrit (%)	40.8 ± 3.3	35.5 ± 4.6	NS	38.1 ± 2.2	NS
	Mean corpuscular hemoglobin concentration (MCHC) (g/dL)	33.6 ± 0.5	35.0 ± 0.7	<i>p</i> < 0.01	34.5 ± 0.5	NS
	Mean Corpuscular Hemoglobin (MCH) (pg)	16.8 ± 0.4	17.2 ± 0.3	NS	17.3 ± 0.3	NS
	Mean corpuscular volume (MCV) (μM ³)	50.0 ± 1.2	49.2 ± 1.3	NS	50.3 ± 1.3	NS
	Red cell distribution index (RDI) (%)	15.0 ± 1.0	14.9 ± 0.8	NS	14.6 ± 0.9	NS
	White blood cells (WBC) (G/L)	18.3 ± 3.5	11.8 ± 4.0	<i>p</i> < 0.05	17.0 ± 2.9	NS
	lymphocytes (% of WBC)	50.1 ± 8.2	39.1 ± 16.9	NS	47.5 ± 6.4	NS
	Monocytes (% of WBC)	23.9 ± 4.9	26.0 ± 6.6	NS	21.1 ± 1.2	NS
	Granular cells (% of WBC)	26.0 ± 4.0	35.0 ± 11.8	NS	31.1 ± 6.9	NS
Hematological analyses of the bone marrow	Cell abundance in the bone marrow [#]	2.4 ± 0.9	3.1 ± 0.4	NS	2.9 ± 0.7	NS
	Megakaryocytes	16.0 ± 6.5	28.7 ± 12.5	NS	18.0 ± 11.0	NS
	Granular line (%)	74.9 ± 9.0	63.4 ± 13.0	NS	65.3 ± 11.1	NS
	Erythroblastic line (%)	14.3 ± 9.6	22.1 ± 14.4	NS	28.6 ± 9.2	NS
	Lymphocytes (%)	6.1 ± 4.1	8.4 ± 3.4	NS	5.2 ± 3.6	NS
	Monocytes (%)	4.8 ± 2.7	6.1 ± 3.9	NS	2.8 ± 2.2	NS

Figure S14. Hematological and bone marrows analyses of mice. Complete blood count and white blood cells count and evaluation of the global cell abundance and megakaryocyte and leukocyte

counts in the bone marrow, from mice treated with control, paclitaxel, or PP-13. Data represent the mean \pm SD of 8 mice per group. # from score 1 (low abundance) to score 4 (high abundance). Data were analyzed using one-way analysis of variance.



UNIVERSITAT
ROVIRA I VIRGILI